DOE/NV/25946--404

Nevada Test Site–Directed Research and Development

FY 2007 Report

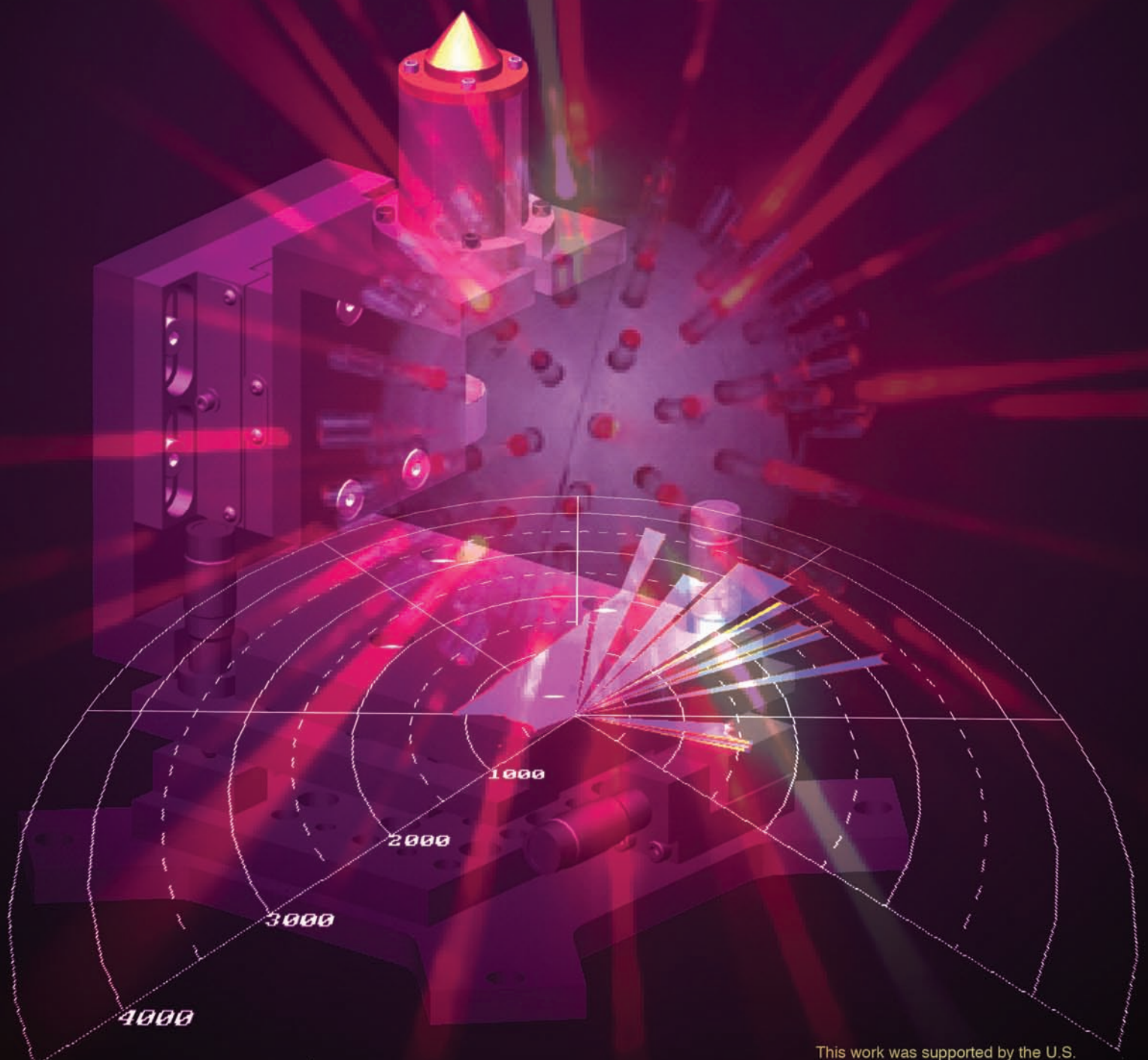

Site Directed R & D SDRD

This work was supported by the U.S. Department of Energy, National Nuclear Security Administration, Nevada Site Office, under Contract No. DE-AC52-06NA25946.

Report Date: April 2008

Disclaimer

Availability Statement

Available for sale to the public from—

U.S. Department of Commerce
National Technical Information Service
5285 Port Royal Road
Springfield, VA, 22161-0002
Telephone: 800.553.6847
Fax: 703.605.6900
E-mail: orders@ntis.gov
Online Ordering: http://www.ntis.gov/ordering.htm

Available electronically at http://www.osti.gov/bridge

Available for a processing fee to U.S. Department of Energy and its contractors, in paper, from—

U.S. Department of Energy
Office of Scientific and Technical Information
P.O. Box 62
Oak Ridge, TN 37831-0062
Telephone: 865.576.8401
Fax: 865.576.5728
E-mail: reports@adonis.osti.gov

DOE/NV/25946--404

Nevada Test Site–Directed Research and Development

FY 2007 Report

This work was supported by the U.S. Department of Energy, National Nuclear Security Administration Nevada Site Office, under Contract No. DE-AC52-06NA25946.

Report Date: April 2008

Electronics

Photonics

SDRD FY 2007

The Nevada Test Site–Directed Research and Development (SDRD) program completed a very successful year of research and development activities in FY 2007. Twenty-nine new projects were selected for funding this year, and eight projects started in FY 2006 were brought to conclusion. The total funds expended by the SDRD program were $5.67 million, for an average per-project cost of $153 thousand. An external audit conducted in September 2007 verified that appropriate accounting practices were applied to the SDRD program. Highlights for the year included: programmatic adoption of 8 SDRD–developed technologies; the filing of 9 invention disclosures for innovation evolving from SDRD projects; participation in the tri-Lab Laboratory Directed Research and Development (LDRD) and SDRD Symposium that was broadly attended by Nevada Test Site (NTS), National Nuclear Security Administration (NNSA), LDRD, U.S. Department of Homeland Security (DHS), and U.S. Department of Defense (DoD) representatives; peer reviews of all FY 2007 projects; and the successful completion of 37 R&D projects, as presented in this report.

In response to a company-wide call, authors throughout the NTS complex submitted 182 proposals for FY 2007 SDRD projects. The SDRD program has seen a dramatic increase in the yearly total of submitted proposals—from 69 in FY 2002 to 182 this year—while the number of projects funded has actually decreased from a program high of 57 in FY 2004. The overall effect of this trend has helped ensure an increasingly competitive program that benefited from a broader set of innovative ideas, making project selection both challenging and rewarding. Proposals were evaluated for technical merit, including such factors as innovation, probability of success, potential benefit, and mission applicability. Authors and reviewers benefited from the use of a shortfalls list entitled the "NTS Technology Needs Assessment" that was compiled from NTS, National Weapons Laboratory (NWL), and NNSA sources. This tool continues to be of considerable value in aligning the SDRD program with mission priorities, and was expanded in FY 2007 to include technology development needs from the DHS and other agencies with missions closely aligned to that of the NTS.

Several metrics have been selected and tracked as indicators of the overall effectiveness of the SDRD program at developing innovative solutions to NTS mission technology requirements. A compilation of these metrics appears in Figures 1 through 3. Since the introduction of the SDRD program, more than 55% of the inventions disclosed to the contractor's intellectual property office have been generated in the pursuit of SDRD projects. The graph in Figure 1 shows the number of disclosed SDRD-engendered inventions (dark green) plotted against the total number of projects funded that year.

The dark orange bars in Figure 2 represent a histogram of the number of projects from a particular fiscal year in which developed technologies were subsequently picked up by programs. They are plotted against the total number of projects funded for that year (light orange). It typically requires some period of time for SDRD success stories to be communicated to programmatic decision makers, and for funding decisions to be made to implement these technologies. It is therefore highly likely that the number of deployed technologies enabled by SDRD activities will continue to increase over time.

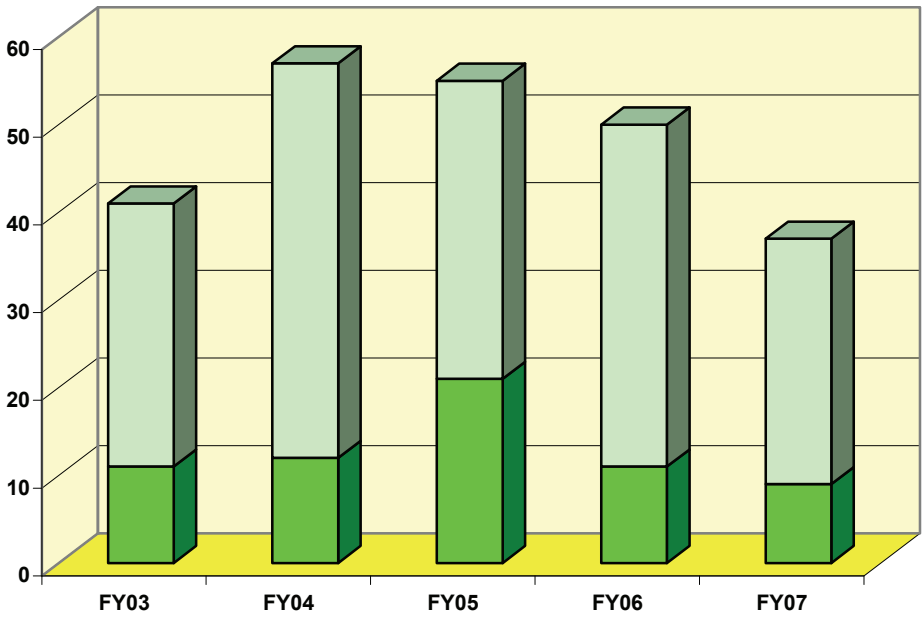

Figure 1. Inventions disclosed (dark green) plotted against the total number of SDRD projects funded in that year (pale green)

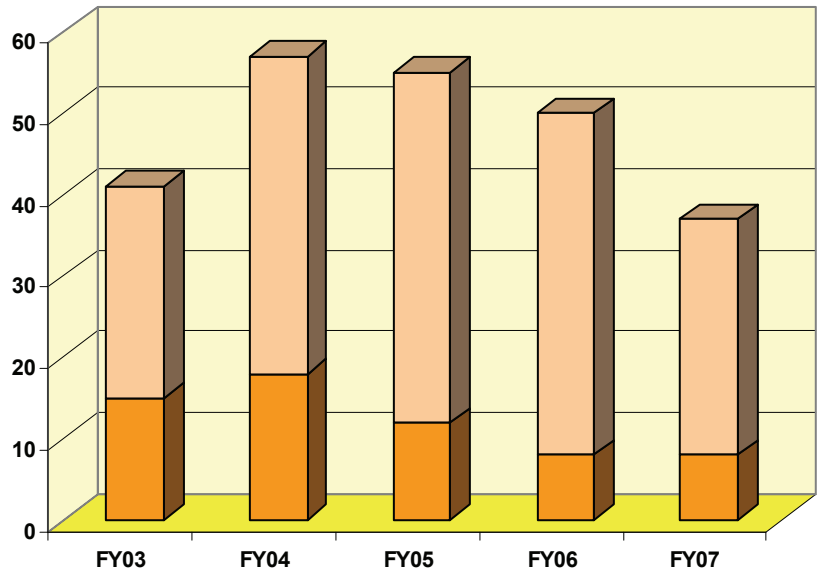

Figure 2. SDRD Projects (dark orange) contributing technologies subsequently picked up by NTS programs plotted against the total number of projects funded for that year (pale orange)

The third metric, shown in Figure 3, is an indicator of how well the SDRD program is strategically aligned with the NTS mission. Each year, the "NTS Technology Needs Assessment" is updated with the most current technology development requirements as foretold by NNSA strategic plans and management, NTS contractor managers and technical staff, and NWL management and staff. In the annual process of revising this document, which identifies anticipated technology needs currently under development as well as the "gaps" that still need addressing, the number of prior-year gaps since addressed by SDRD–funded projects are tabulated. These addressed needs are presented as the blue bars in Figure 3.

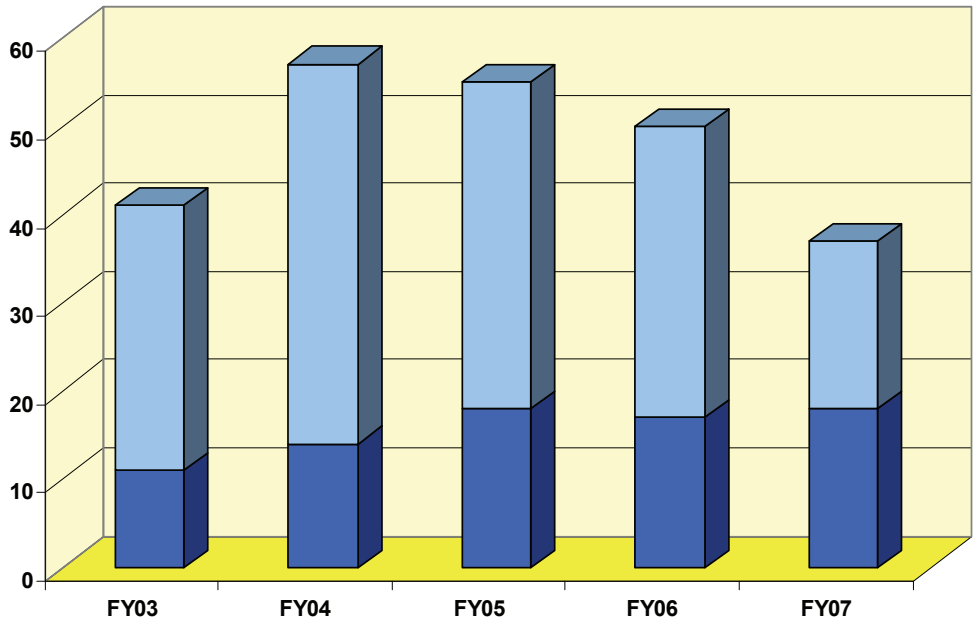

Figure 3. Number of projects (dark blue) that addressed technology development needs identified in the yearly NTS Technology Needs Assessment

This final program report covers SDRD project activities that occurred from October 2006 through September 2007. The numerous achievements it describes are a tribute to the skill and enthusiasm Principal Investigators brought to their individual projects. While many of the R&D efforts drew to successful and natural conclusions, some spawned follow-on work that may lead to further research. The desired result of all SDRD activities is to develop and/or refine technologies that are ultimately implemented by programs. Some of the following project reports clearly identify R&D efforts with those kinds of results. Others, best characterized as feasibility studies, resulted in negative findings—the entirely valid conclusion, often reached in the pursuit of "high-risk" research—that a particular

technology is currently impractical. Both types of results help move National Security Technologies toward a more vital technology base by identifying technologies that can be directly applied to our programmatic mission.

In conclusion, FY 2007 saw continued evolution of a strong, innovative R&D program that benefited from increased competitiveness and a maturation of the planning and management techniques vital to aligning SDRD with anticipated needs for future NTS mission requirements. The 37 projects selected for FY 2007 showcase a wealth of creative approaches to innovative technical research with high potential payoff. These endeavors benefited from an impressive cross section of resources and capabilities, and addressed development needs in a variety of technologies, with potential applications to a broad selection of programmatic activities.

I would like to extend a very special thank you to the editing team of Katharine Streeton, Heidi Utz, and Michele Vochosky for compiling, editing, and publishing this report; to Nancie Nickels for her support with cover, divider, and CD graphics; to Project Controls Engineer Pat Herrin for her valuable contributions to tracking progress and costs on the array of FY 2007 projects; to Richard Martinez and his team for compiling the financial data necessary to fulfill congressionally mandated reporting requirements; and to SDRD site representatives Howard Bender, Rob Buckles, Paul Guss, Chris Hagen, Steve Iversen, and Bill Nishimura, for helping implement and manage a very productive year of R&D at the NTS!

Wil Lewis, SDRD Program Manager

Los Alamos Operations (LAO)
P.O. Box 809
Los Alamos, New Mexico 87544

Livermore Operations (LO)
P.O. Box 2710
Livermore, California 94551-2710

Nevada Test Site (NTS)
P.O. Box 98521
Las Vegas, Nevada 89193-8521

North Las Vegas (NLV)
P.O. Box 98521
North Las Vegas, Nevada 89193-8521

Remote Sensing Laboratory – Andrews Air Force Base (RSL–A)
P.O. Box 380
Suitland, Maryland 20752-0108
(Andrews Air Force Base)

Remote Sensing Laboratory – Nellis Air Force Base (RSL–N)
P.O. Box 98521
Las Vegas, Nevada 89193-8521
(Nellis Air Force Base)

Special Technologies Laboratory (STL)
5520-B Ekwill Street
Santa Barbara, California 93111

this page intentionally left blank

A

AC	alternating current
ADC	analog-to-digital converter
AFB	Air Force Base
AGL	above ground level
AIR	active infrared
ALOHA	Aerial Location of Hazardous Atmospheres
AMS	Aerial Measuring System
API	application programming interface(s)

B

BAT	Burst Alert Telescope
BIB	Blocked Impurity Band
BNL	Brookhaven National Laboratory
bp	base pair
BTI	Bubble Technology Industries

C

CBE	chemical, biological, and explosive
CARS	coherent anti-Stokes Raman scattering
CCD	charge-coupled device
CdTe	cadmium telluride
$CHCl_3$	trichloromethane
CMOS	complementary metal oxide semiconductor
COTS	commercial off-the-shelf
CPO	Charged Particle Optics
CSDA	continuous slowing down approximation
CZT	$Cd_{1-x}Zn_xTe$ [ternary compound]

D

DAQ	data acquisition (system or unit)
DARHT	dual-axis radiographic hydrodynamic test (facility)
DC	direct current
D-D	deuterium-deuterium
D-T	deuterium-tritium
DEM	digital elevation model
DHS	U.S. Department of Homeland Security

DNA	deoxyribonucleic acid
DoD	U.S. Department of Defense
DOE	U.S. Department of Energy
DOS	density of states
DPF	dense plasma focus
DPSS	diode-pumped solid-state (laser)
DRI	Desert Research Institute
DRIE	deep reactive ion etch [process]
DWT	discrete wavelet transformation

E

EDS	electron dispersive x-ray analysis
e-h	electron-hole (pair)
EMI	electromagnetic interference
EML	Environmental Measurement Laboratory
ENVI	Environment for Visualization
EO	electro-optic
EPIcode	Emergency Prediction Information Code
EPMA	Embedded Piezoresistive Microcantilever Array
ETA	Experimental Test Accelerator

F

FAC2	fraction of data within a factor of 2
FB	fractional bias
FEA	field emitter array(s)
FePO4	(iron as strengite)
FE-SEM	field emission-scanning electron miscroscope
FFT	fast Fourier transform
FHT	fast Hartley transform
FIFO	First-In First-Out (scheme)
FIR	far infrared
FPGA	field programmable gate array
FRET	fluorescent resonance energy transfer
FTIR	Fourier transform infrared spectroscopy
FWHM	full-width at half-maximum
FY	fiscal year

G

GaAs	gallium arsenide
GaN	gallium nitride
GC	gross counts
GPS	global positioning system
GSFC	Goddard Space Flight Center
GSM	Global System for Mobile Communications (System)
GUI	graphical user interface

H

HDPE	high-density polyethylene
HEDP	high-energy density physics
HEU	highly enriched uranium
HF	hybrid fiber
HPAC	Hazard Prediction Assessment Capability
HPGe	high-purity germanium
HV	high voltage, high voltage

I

IC	integrated circuit
ICF	inertial-confinement fusion
IDE	integrated development environment
IDL	Interactive Data Language [software package developed by Research Systems, Inc.]
IDWT	inverse discrete wavelet transformation
IED	improvised explosive device
IFFT	inverse fast Fourier transform
I/O	in/out (bus)
IP	Internet protocol
IPA	isopropyl alcohol
IR	infrared
ITO	indium-tin-oxide

J

JFET	junction field-effect transistor

L

LANL	Los Alamos National Laboratory
LAO	Los Alamos Operations (NSTec)
LBNL	Lawrence Berkeley National Laboratory
LCA	Laser Calibration Assembly [mastering hardware]
LCD	liquid crystal display
LDRD	Laboratory Directed Research and Development
LED	light-emitting diode
LEU	low-enriched uranium
LIF	laser-induced fluorescence
LiF	lithium fluoride
LIFI	laser-induced fluorescence imaging
LIFELO	last in–first elected–last out
LINAC	linear accelerator
LLD	lower-lever discriminator
LLE	Laboratory for Laser Energetics
LLNL	Lawrence Livermore National Laboratory
LO	Livermore Operations (NSTec)
LSO	lutetium oxyorthosilicate
LSOP	laser safe operating procedure
LT-GaAs	"low-temperature"–grown gallium arsenide
LWIR	long-wave infrared

M

MCA	multichannel analyzer
MCNP	Monte Carlo N-Particle [transport code]
MCNPX	Monte Carlo N-Particle Extended version [transport code]
MCP	microchannel plate
MEH-PPV	Poly(2-methoxy-5(2-ethyl) hexoxy-phenylene-vinylene
MeOH	methyl alcohol
MFPF	Multi Frequency Phase Fluorimeter
MG	geometric mean bias
MIL	Matrox Imaging Library [software package]
MLE	maximum likelihood estimator
MOSFET	metal-oxide semiconductor field-effect transistor

N

NASA	National Aeronautics and Space Administration
NCBI	National Center for Biotechnology Information

NDA	nondisclosure agreement
Nd:YAG	neodymium:yttrium-aluminum-garnet (laser)
NEMO	neutron monitor
NFMRB	negative fast/medium ramp board
NIF	National Ignition Facility
NiO	nickel oxide
NIST	National Institute of Standards and Technology
NLV	North Las Vegas (NSTec)
NMSE	normalized mean square error
NNSA	U.S. Department of Energy, National Nuclear Security Administration
NPTEC	Nonproliferation Test and Evaluation Complex
NRS	neutron resonance spectroscopy
NSLS	National Synchrotron Light Source
NSTec	National Security Technologies, LLC
NTS	Nevada Test Site
NUGVARDI	Networked Unmanned Ground Vehicle for Autonomous Radiation Detection Indoors
NUGVARDO	Networked Unmanned Ground Vehicle for Autonomous Radiation Detection Outdoors
NVG	night vision goggle(s)
NWL	National Weapons Laboratory/Laboratories

O

1-D	one-dimensional
OPO	optical parametric oscillators
OPPP	One-Path Photogrammetry Program [software package]

P

PC	principal component (band)
PCA	principal components analysis
PCB	printed circuit board
PCF	photonic crystal fiber
PCR	polymerase chain reaction
PDV	photon Doppler velocimetry
PEM	photoelectromagnetic
PID	photoionization detectors
PL	photoluminescence
PNA	protein nucleic acid
POSS	polyhedral oligomeric silsesquioxanes

Q

QD	quantum dots

R

R	correlation coefficient
R&D	research & development
RAM	random access memory
RDAD	Real-time Data Acquisition and Dissemination
RDX	hexahydro-1,3,5-trinitro-1,3,5-triazine [explosive]
REDAR	Realtime and Environmental Acquisition Recorder
RF	radio frequency
RFI	radio frequency interference
RGB	red-green-blue [color model]
RITS	radiographic integrated test stand
RMS	root mean square
RNA	ribonucleic acid
ROI	region of interest
ROIC	readout integrated circuit
ROM	read-only memory
RSL	Remote Sensing Laboratory (NSTec)
RSL–A	Remote Sensing Laboratory – Andrews Air Force Base
RSL–N	Remote Sensing Laboratory – Nellis Air Force Base

S

SCIPUFF	Second Order Closure Integrated Puff
SDRD	(Nevada Test) Site–Directed Research and Development
SEM	scanning electron miscroscope
SFG	sum-frequency generation
SMF	single-mode fiber
SNL	Sandia National Laboratories
SNR	signal-to-noise ratio
SPR	short-pulsed reactor
SPRT	sequential probability ratio test (algorithm)
SPXRD	single-pulse x-ray diffraction
SRIM	stopping and range of ions in matter [code]
STL	Special Technologies Laboratory (NSTec)
STNG	sealed-tube neutron generator
STR-PCR	short tandem repeat polymerase chain reaction
SVI	surface-visible imaging

T

2-D	two-dimensional
3-D	three-dimensional
T&E	Test & Evaluation
TEM	transmission electron microscope
THz	terahertz
THz-TDS	terahertz time-domain spectroscopy (system)
TIFF	Tagged Image File Format
Ti:S	titanium sapphire [laser]
TNBS	trinitrobenzenesulfonic (acid)
TNT	trinitrotoluene [explosive]
TOF	time of flight [measurements]
T-T	tritium-tritium
TTL	tagging, tracking, and locating

U

UCB	University of California, Berkeley
UCD	University of California, Davis
UCSB	University of California, Santa Barbara
UGV	unmanned ground vehicle
UIC	University of Illinois at Chicago
UNLV	University of Nevada, Las Vegas
UNR	University of Nevada, Reno
UV	ultraviolet
U(VI)	uranium(VI) [complexes]
UV Vis	ultraviolet-visible (spectroscopy or spectrophotometry)

V

VC	vitreous carbon
VG	geometric variance
VISAR	velocity interferometer system for any reflector
VPF	velocity per fringe
VPN	virtual private network
VUV	vacuum ultraviolet

W

WO_3	tungsten oxide

X

XRD	x-ray diffraction

Y

YAG	yttrium-aluminum-garnet (laser)

Accelerators and Pulsed Power

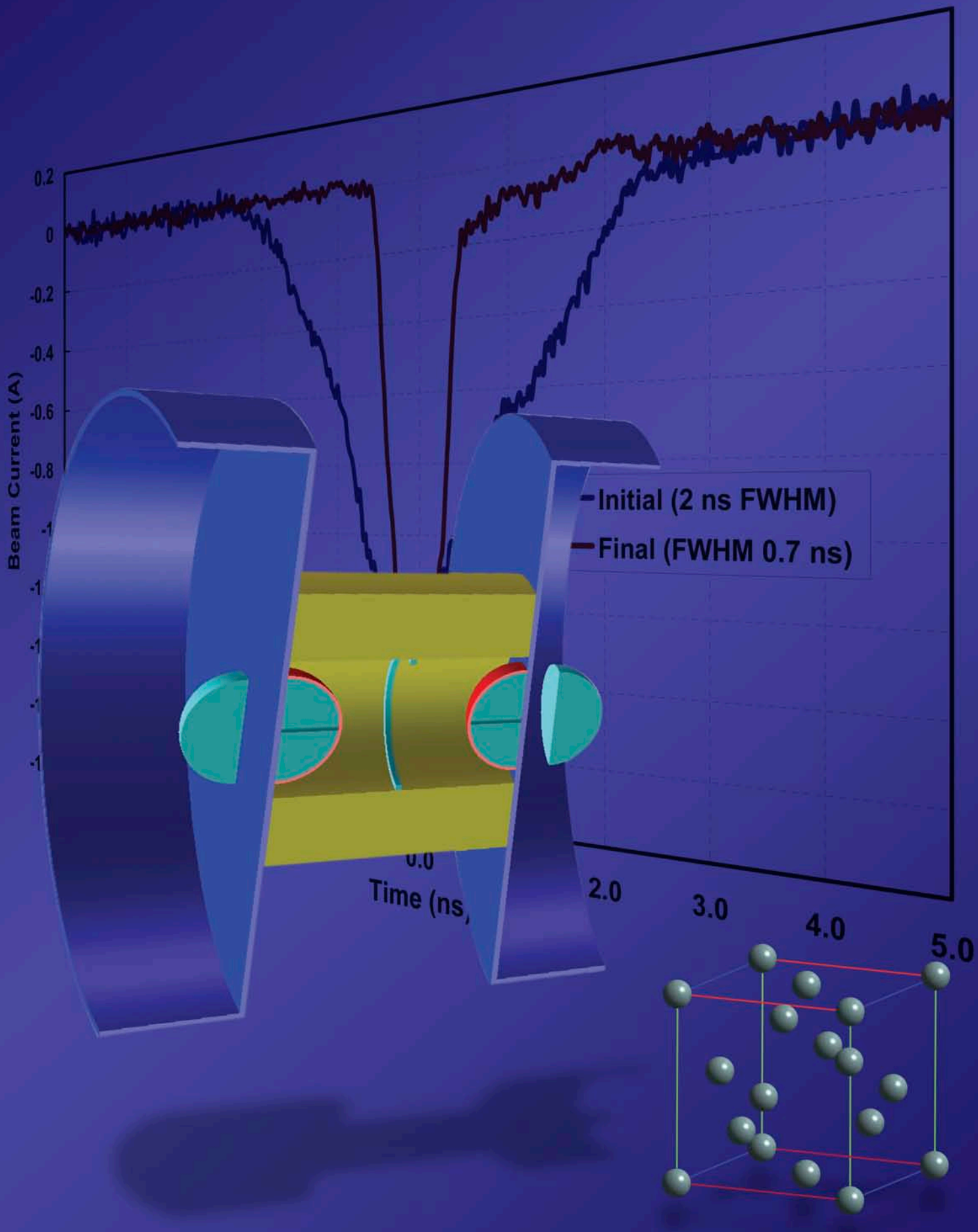

Fast-pulsed Assembly Design

E. Chris Hagen[1]
North Las Vegas

D. R. Lowe, R. J. O'Brien
University of Nevada, Las Vegas, Nevada

James L. Pigg
Los Alamos Technical Associates, Los Alamos, New Mexico

The project team studied the feasibility of designing a target-multiplier assembly that would enhance the neutron yield from a dense plasma focus (DPF) neutron generator. The materials studied for neutron multiplication were Be, ^{235}U, and ^{238}U. The team modeled a "cave" geometry that was conceived to maximize the neutron fluence in a small volume using two DPF tubes and two hemispheres of multiplying material. Criticality and safety issues were also investigated. Modeling results indicated that DPF yields can be safely increased by a factor of 300 using Be and ^{238}U.

Background

In the last six years, National Security Technologies (NSTec) has made considerable progress in the development of DPF pulsed-power machines to generate nuclear fusion, producing neutrons, gamma-rays, and other fusion products. Multiplying enclosures that simulate weapons neutron spectra have been successfully designed in previous SDRD projects (Meehan, 2006; Pigg, 2004).

Recent successes of the DPF program increased the level of neutron outputs to 2×10^{11} neutrons with a pulse width of 50 ns using the deuterium-deuterium (D-D) reaction. A larger capacitor bank that projects a pure deuterium output to 5×10^{12} has been constructed and awaits testing; the yield increase (by a factor of 80) gained by using a deuterium-tritium (D-T) gas mix implies a D-T yield of 4×10^{14}. DT fusion results in neutron energies of 14.1 MeV, rather than the 2.45 from DD fusion.

Project

The scope of this research was to design a target-multiplier assembly that would use the DPF neutrons as a driver (using them would raise the neutron yield to the 10^{16} region). Two applications were targeted for these enhanced neutron fields. The first was a neutron beam for physics experiments, imaging, and time-of-flight (TOF) measurements. The second was an irradiator for materials studies. In this work, we established that DPF yields can safely be raised by a factor of up to 300 using Be and

[1] hagenec@nv.doe.gov, 702-295-4712

^{238}U multipliers. Expanding on this concept, we then designed a "neutron cave" (i.e., a small volume in which the neutron fluence is high). The feasibility of a third application was also established: that of using the DPF multiplier as a driver for epithermal neutrons for neutron resonance spectroscopy (NRS).

Two types of anode-cathode configurations exist for the DPF. These geometries are named after their inventors—Mather and Fillipov. The Fillipov tube was chosen for this work because its geometry allows close proximity to the neutron-emitting plasma. The modeling, design, and calculations were done on the Beowulf cluster at the University of Nevada, Las Vegas (UNLV) by Lowe and O'Brien. The materials used for neutron multiplication studies were Be (n,2n), ^{238}U(n,f), and ^{235}U (n,f). Both low-enriched uranium (LEU) and highly enriched uranium (HEU) were modeled. The reflecting materials compared were polyethylene and carbon. The methodology used allowed the multiplying materials to be a constant K_{eff} (where K_{eff} is the effective neutron multiplication factor); material amounts were varied with geometry to maintain this K_{eff} value. Sensitivity analyses were performed on the very high K_{eff} models to avoid near-criticality designs.

Many physics experiments require a specific fission-to-fusion neutron ratio. This flexibility requirement was considered in all design iterations.

For the irradiator version of the configuration, the total neutrons through 1 cm^3 was the most important parameter, so this was maximized. However, the neutron delivery time and the energy distribution are also important to the experimenter, so these are also presented. The time history of the pulse was also calculated. Finally the practicality of the optimized designs was established via sensitivity calculations. A CAD model of the irradiation cell or cave is also presented.

Beam Generation

A design iteration process was executed that calculated the flux over 4-pi that could be obtained with a single Fillipov tube. There were no design limitations regarding material, size, physical supports, or any other physical parameters. A cartoon of the Fillipov tube DPF machine and the surrounding fissionable material is shown in Figure 1.

The Monte Carlo N-Particle Extended code (MCNPX) calculations shown in Table 1 assume that the z-pinch device can produce 1×10^{14} 14-MeV neutrons per pulse. This table describes the 25 iterations that were made to show how the neutron flux changed with sphere material, size, cladding location, and cladding thickness. The cladding served as a multiplying blanket, and materials with (n,2n) were suitable for this purpose. In the course of these runs, the cladding was eliminated or limited to Be.

Table 1. Log of MCNPX runs for beam multiplying structure

# Hemispheres	Hemisphere Material	Radius	K_{eff}	Cladding Material	Cladding Thickness	Cladding Location	Yield Increase into 4 pi
1	^{235}U	10.55 cm	0.95	Be	2.5 cm	under sphere, 15-cm hole	5
1	^{235}U	10.70 cm	0.95	Be	2.5 cm	under sphere, 20-cm hole	5
1	^{235}U	8.70 cm	0.95	Be	5.0 cm	around sphere	6
1	^{233}U	7.30 cm	0.95	none			6
1	^{235}U	10.0 cm	0.95	Be	2.5 cm	under sphere, 1-cm hole	6
1	^{235}U	10.1 cm	0.95	Be	2.5 cm	under sphere, 5-cm hole	6
1	^{235}U	10.0 cm	0.95	Be	2.5 cm	under sphere, 10-cm hole	6
1	^{235}U	10.0 cm	0.95	Be	2.5 cm	under sphere	6
1	^{235}U	9.3 cm	0.95	Be	2.5 cm	around sphere	7
1	^{235}U	10.7 cm	0.95	none			9
2	^{235}U	8.53 cm	0.95	Be	2.5 cm	around sphere	13
2	^{235}U	9.7 cm	0.95	none			16
1	^{233}U	7.70 cm	0.995	none			36
1	^{235}U	9.18 cm	0.995	Be	5.0 cm	around sphere	40
1	^{235}U	11.33 cm	0.995	Be	2.5 cm	under sphere, 20-cm hole	42
1	^{235}U	10.62 cm	0.995	Be	2.5 cm	under sphere, 5-cm hole	44
1	^{235}U	10.53 cm	0.996	Be	2.5 cm	under sphere, 1-cm hole	50
1	^{235}U	10.92 cm	0.995	Be	2.5 cm	under sphere, 10-cm hole	53
1	^{235}U	9.85 cm	0.995	Be	2.5 cm	around sphere	54
1	^{235}U	10.53 cm	0.996	Be	2.5 cm	under sphere	54
1	^{235}U	11.17 cm	0.995	Be	2.5 cm	under sphere, 15-cm hole	61
2	^{235}U	8.81 cm	0.995	Be	2.5 cm	around sphere	120
1	^{235}U	9.90 cm	0.998	Be	2.5 cm	around sphere	144
1	^{235}U	11.25 cm	0.995	none			150
2	^{235}U	10.25 cm	0.995	none			332

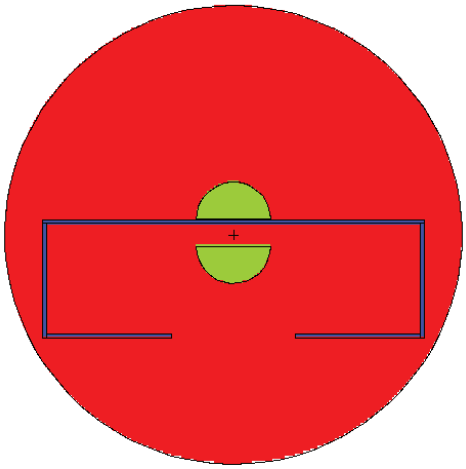

Figure 1. An example of the geometry for a given case, where red represents air, green represents ^{235}U, and blue represents aluminum.

UNLV's Nevada Radiological Center for Advanced Computational Methods team used MCNPX (version 2.6.a) as the primary particle transport code for this study. Each iteration required a two-step process; first, models were run in criticality mode to determine the K_{eff} of the system in order to change the physical parameters of the system as necessary to meet the desired K_{eff} value. Second, the general particle transport code was run using a 14-MeV point source to drive the fissionable material. UNLV's 330-node Beowulf cluster was used extensively for this project and allowed the researchers to run these iterations in a timely manner (i.e., about 10 hours per iteration as compared to 500 hours per iteration if only one computer were used).

Mesh tallies produce a visual spectrum of any type of particle and its energy range. Figure 2 shows the neutron flux, averaged over all time, for all energies, given a 14-MeV point source at the location of the cross hair. Visual representations showed how/if the neutron flux from each of the spheres interacted.

Neutron and gamma flux predictions were also made for the single ^{235}U sphere without cladding. A point source 12 cm from the vertex of the hemisphere was used to determine the neutron and gamma spectra and TOF at that location. Figure 3 shows the two spectra, and Figure 4 shows the neutron and gamma energy spectra for the same case.

To better understand how the Be multipliers played a role in output, a graph was created to show the relative output over 4-pi for various moderator configurations. On the *x* axis, the hole size in the moderator is increasing, hence the amount of moderator in the system is decreasing. We expected to see a linear relationship; however, Figure 5 shows our results.

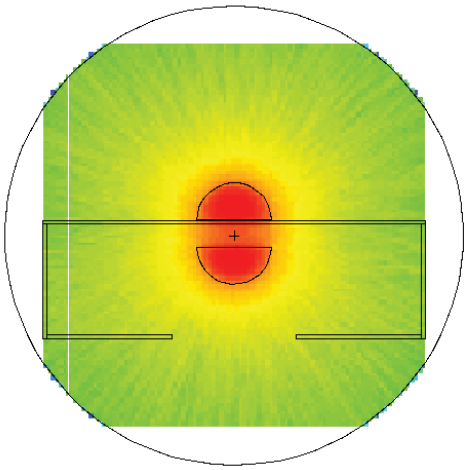

Figure 2. Neutron intensity plot with the higher intensities near red

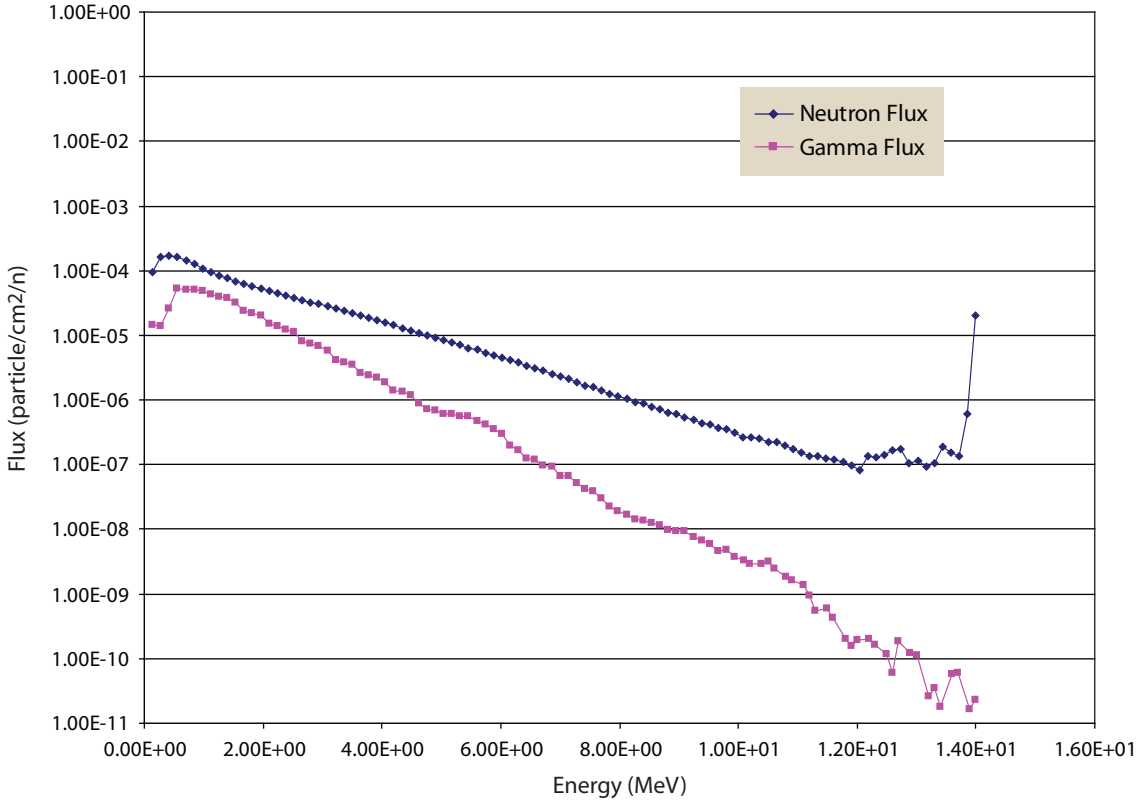

Figure 3. Neutron and gamma flux as a function of energy

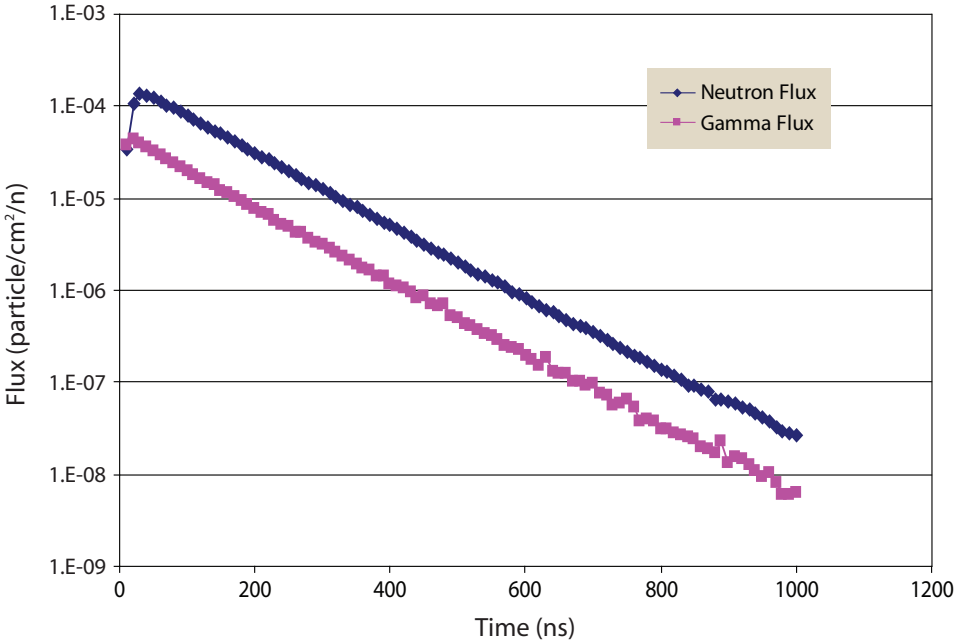

Figure 4. Time history of optimal assembly die-away

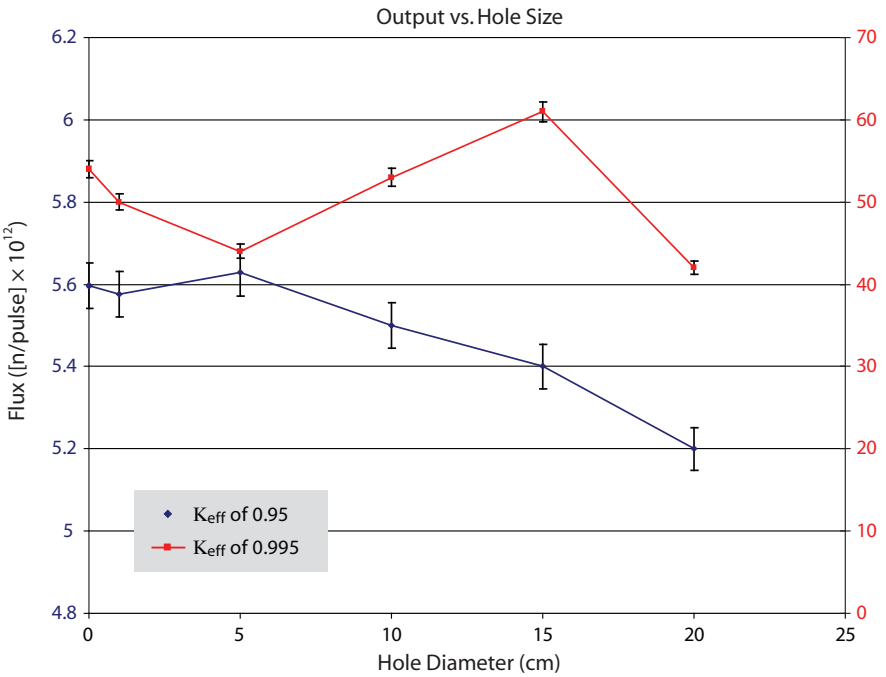

Figure 5. Effects of "leakage" holes in multiplying blanket

Further investigation revealed that hole diameter was not the driving factor in neutron output. The results of a sensitivity analysis, shown in Figure 6 with K_{eff} values for each data point, verified that the small changes in K_{eff}, of about 0.001 at K_{eff}s near 1.00, can change the neutron output by 50%. Hence, K_{eff} was the driving factor in these simulations. Detailed analyses to accurately determine the effect of the hole size were beyond the scope of this study.

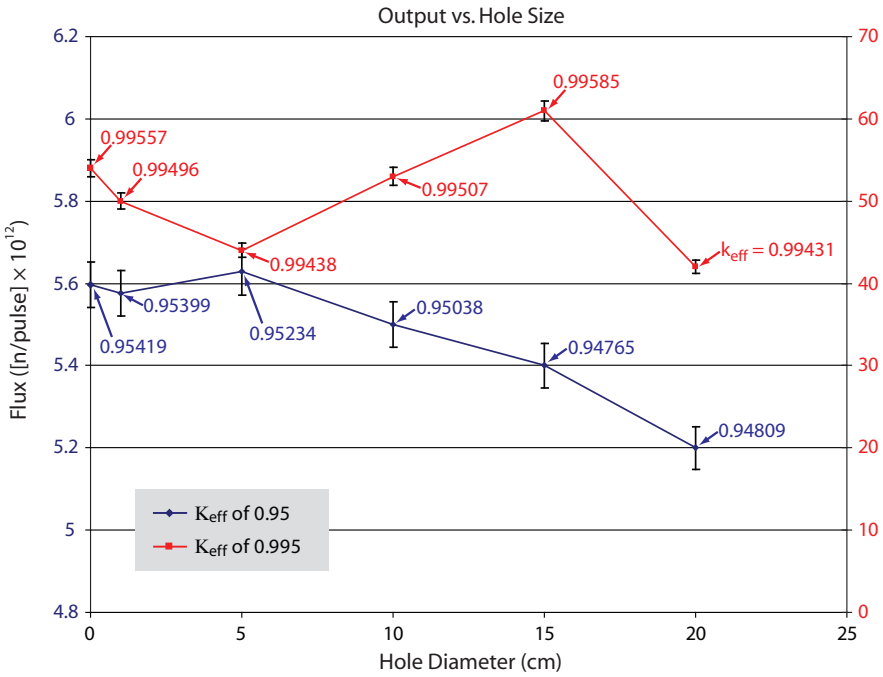

Figure 6. Sensitivity analysis of multiplying blanket hole size vs. output

Irradiator Cell

Conceptual Design

A "cave" concept was created to maximize the fission-fusion spectrum neutron flux through 1 cm^3 using two DPF Fillipov tubes and the ^{235}U hemispheres from previous simulations. This design provided high neutron fluence irradiation in a large volume. The cave design allowed multiple scattering inside the reflecting tube, combining the initial fusion neutron output of both DPFs with fission neutrons from the ^{235}U hemispheres. An initial conceptual design is illustrated in Figure 7 as modeled in MCNPX. A spherical tally volume of 1 cm^3 was used at the center of the assembly. This tally volume is where neutron fluence was reported.

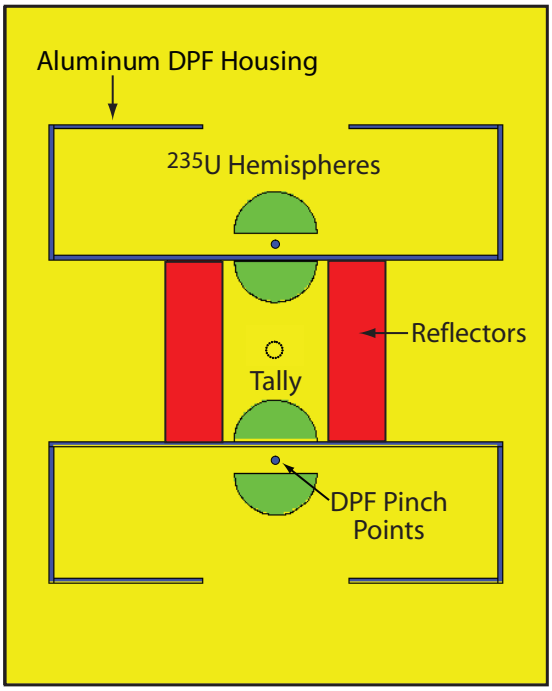

Figure 7. Initial conceptual design for irradiator cell as modeled in MCNPX

MCNPX Testing of Irradiator Cell Designs

Several MCNPX simulations of the conceptual design from Figure 7 were run to find the optimal configuration of geometry and materials to maximize neutron irradiation to the 1-cm^3 cell. These varying geometries and materials included:

- ^{235}U hemisphere sizes
- Holes in the hemispheres
- Use of LEU instead of ^{235}U
- Use of reflector materials including uranium, carbon, and polyethylene
- Be cladding on the hemispheres
- Cladding inside the reflector

This design for the irradiator cell maximized neutron flux through the center tally position by utilizing both DPF pinch points and fission neutrons created in the ^{235}U hemispheres. Neutron tracks are illustrated by intensity in Figure 8 for the irradiator cell concept.

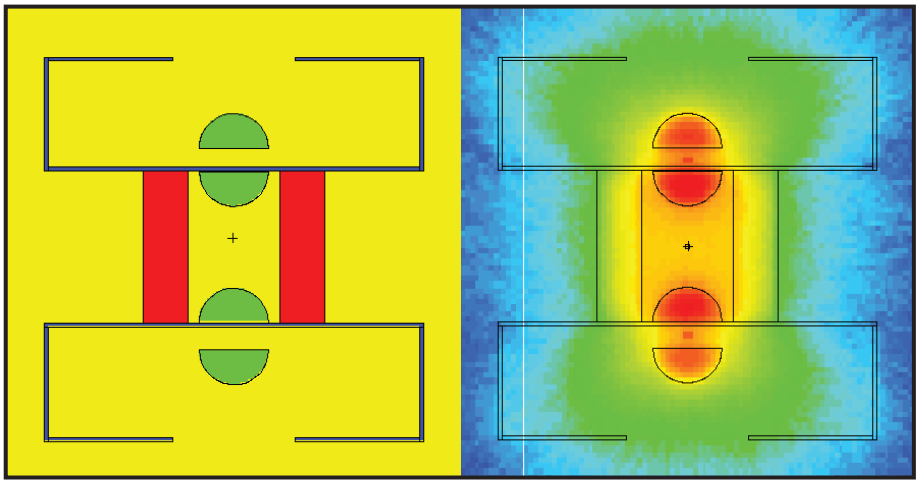

Figure 8. Neutron irradiator cell design (left) and neutron tracks by intensity (right)

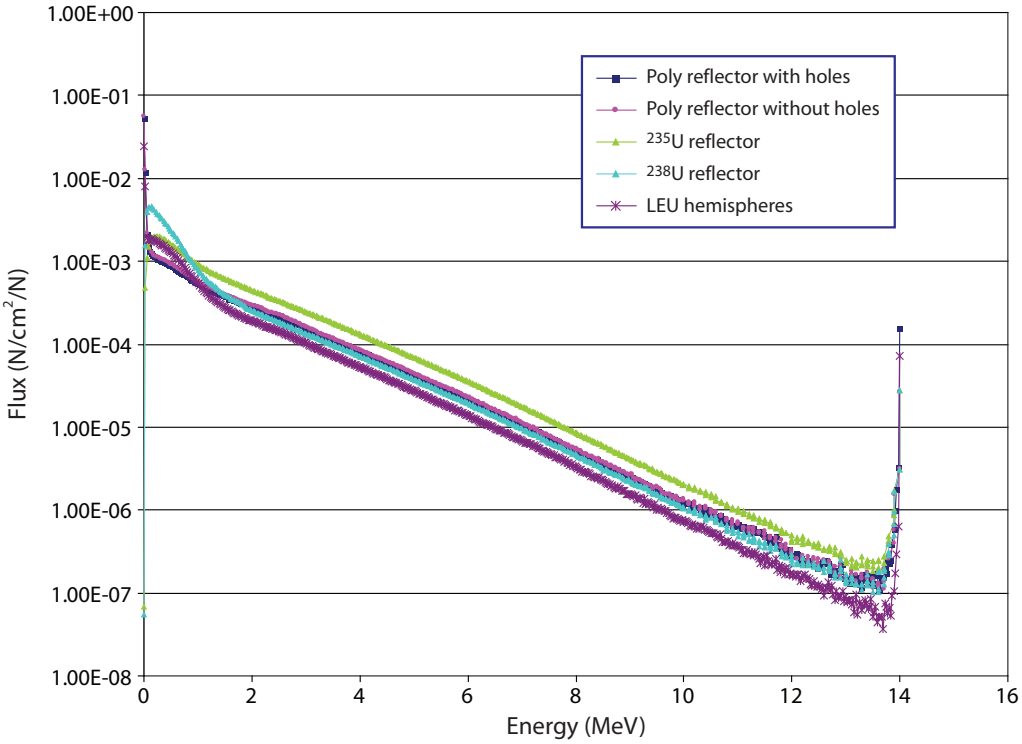

Figure 9. Fission-fusion neutron spectra in the center of the irradiator

A major advantage of this irradiator cell configuration was the magnitude of neutrons passing though the irradiated cell that were achievable without having to be directly next to the DPF pinch point. The irradiator cell utilizing this cave design can achieve neutron yields comparable to the output capability of the DPF fusion sources, while also producing a fission-fusion neutron spectrum (Figure 9). Yields at the center tally location are reported here as percentages. These percentages refer to the number of neutrons crossing the 1-cm^3 cell divided by the number of neutrons produced in both DPF sources. A percentage yield reported as 68% for a configuration would mean that 68 neutrons crossed the tally volume for every 100 emitted by *both* sources, or 50 neutrons from each source. Seventeen designs iterations are presented with their specifications and K_{eff} and flux results.

For each configuration, an initial setup of materials and geometries was determined before simulation. Once assembled in MCNPX, all configurations were first modified to achieve near-critical K_{eff} values of close to 0.99. These criticality values represent the assembly with no DPF neutron pulse. K_{eff} values of ~0.995 or higher were desired; this required fine-tuning hemisphere size and assembly configurations. With a higher K_{eff} value, more neutron multiplication occurs when the DPF is pulsed. Once the desired K_{eff} value was achieved for each assembly, the configuration was then simulated in MCNPX with DPF pulses of 14.1-MeV DT fusion neutrons.

Iteration 1: This configuration, the most basic, used the initial conceptual design of Figures 8 and 9. We used ^{238}U as a reflector material. The resulting neutron flux percentage through the center cubic centimeter was 28%.

Iteration 2: Iteration 1 was modified to include a pure ^{235}U reflector rather than ^{238}U. Reflector thickness was reduced. The resulting neutron flux was 25%.

Iteration 3: A polyethylene reflector was substituted for the previous reflector. Flux increased to 31%.

Iteration 4: A hole was added in each internal hemisphere to allow a direct path of fusion neutrons to the center tally volume. Flux remained the same (31%). Higher flux of 14.1 neutrons through the tally volume was achieved, as illustrated in Figure 9. All subsequent iterations utilized holes in the inner hemispheres.

Iteration 5: The ^{235}U spheres were replaced with LEU for comparison. Flux was reduced to 23%. This was an important benchmark due to the relative ease of security in using LEU as opposed to HEU. This configuration was not optimized, because it was tangential to our work scope. It would be a difficult case because most of the neutrons start outside the cave. It is nonetheless conservative to say that we can achieve 1% of the optimal design with HEU and the accordant relative ease of deployment.

Iteration 6: Be cladding 0.5-cm thick was added to the inner spheres of ^{235}U to make use of the (n,2n) reaction. With a ^{238}U reflector, neutron flux jumped to 75%.

Iteration 7: Additional Be cladding was added to the inner reflector walls. Neutron flux was greatly reduced to 34% because of this; the method was not investigated further.

Iteration 8: A carbon reflector replaced the ^{238}U reflector, dropping the yield to 25%. Since carbon is a pure reflector and polyethylene is a moderator, this suggested that the carbon thickness was inadequate and too many neutrons were escaping the experimental cavity.

Iteration 9: This configuration achieved the highest yield by adding a ^{235}U "donut" to the inside reflector. The addition of the small amount of ^{235}U provided additional neutron yield at the center through fissions in the donut from neutrons scattered in the poly. This configuration produced 128% flux, and is illustrated in Figure 10.

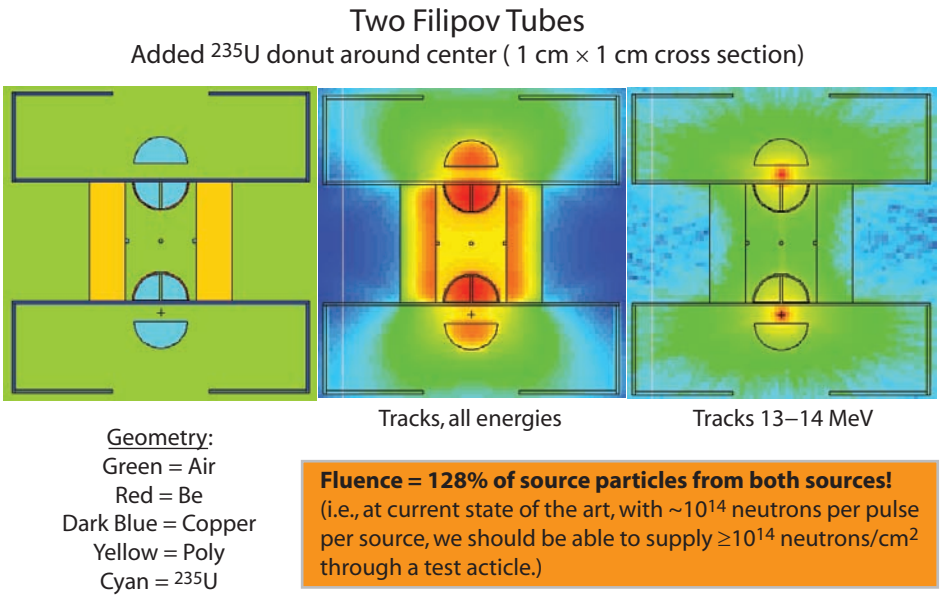

Figure 10. Iteration 9 with donut ^{235}U achieved the highest neutron yield

Iteration 10: The success of the ^{235}U donut led to the investigation of a ^{235}U liner inside the reflector. Yield was 87%, comparable to Iteration 6, but did not approach the yield of Iteration 9.

Iteration 11: Three-percent enriched uranium was used in the hemispheres to experiment with fuel-grade uranium. A ^{235}U liner was added to the poly reflector. Yield was low, as expected, at only 3.9%, and required large quantities of uranium to achieve a near-critical configuration.

Iteration 12: Iteration 10 was repeated with a natural uranium liner. Yield was reduced to 39%.

Iteration 13: For this iteration, the ^{235}U donut was removed to examine the effect on yield. The configuration of Iteration 9 was repeated without the ^{235}U donut; yield dropped dramatically to 33%. The donut design was included on all future iterations.

Iteration 14: Initial modification of the donut size was simulated in this iteration. Increasing the cross section of the donut from 1 × 1 cm to 4 × 1 cm led to a reduction in yield (59%). It is possible that a more efficient donut design could be found with further modification and optimization.

Iteration 15: Iteration 9 was repeated with a graphite reflector instead of poly. The poly moderator-reflector remained the best choice, as yield dropped to 58% when it was replaced with graphite (carbon). A later run could establish the leakage in the carbon reflector.

Iteration 16: The size of the internal cave from Iteration 9 was reduced to bring the ^{235}U donut and reflecting walls closer to the tally volume in an attempt to raise the yield. These tests were done to obtain a benchmark of this system vs. SPR II, formerly at Sandia National Laboratories. However, the yield was reduced to 52%, probably due to the fact that the amount of ^{235}U in the hemispheres had to be reduced to remain below a K_{eff} of 1.

Iteration 17: The thickness of the carbon reflector was doubled. This reduced the neutron leakage from the system. Therefore, the uranium had to be reduced to 8.76 cm to maintain the same K_{eff}, and that caused the yield to be reduced by 42%. The salient conclusion was that the important quantities were good reflectors and distributed sources. The material that had to be removed to avoid going critical could be redistributed in the system in the form of more rings around the cave. The likely result of this assembly would have a multiplication on the order of 1000. An illustration of our final optimal design concept is shown in Figure 11.

Sensitivity Analysis

Throughout these simulations, it was observed that small changes in the K_{eff}, on the order of ±0.001, would lead to large changes in the fluence. A brief sensitivity analysis was performed similar to the sensitivity analysis involving K_{eff} and hole size from the single-DPF design. The design of Iteration 13 was varied with K_{eff} values in Figure 12, and flux was tallied in the cubic centimeter. Small changes in K_{eff} led to large changes in the yield as expected. Therefore, K_{eff} values for all 17 iterations should be considered when comparing yields.

Criticality Safety of ^{235}U Donut

The inherent safety of the assembly is that the system remains subcritical when not pulsed. However, the safety of the ^{235}U was examined to ensure that this piece could be safely built, handled, and operated. The total donut mass from Iteration 9 was 1365.65 g. This mass was simulated as a sphere, a worst-case situation for criticality, for both air and water. In air, the sphere had a K_{eff} of 0.32478 ±0.00027; submerged in water, it had a K_{eff} of 0.45606 ±0.00095. These results showed that the mass would remain safe and subcritical in a spherical configuration.

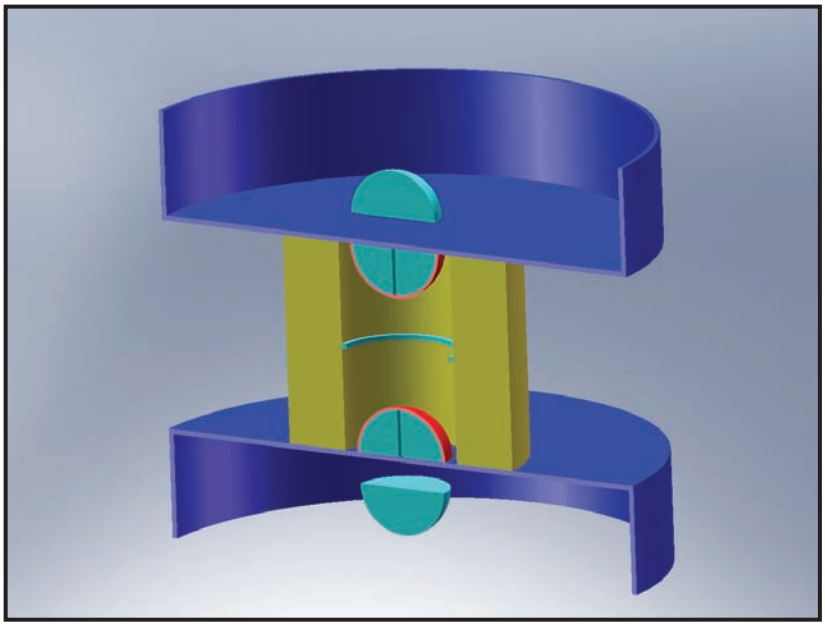

Figure 11. Final neutron cave design

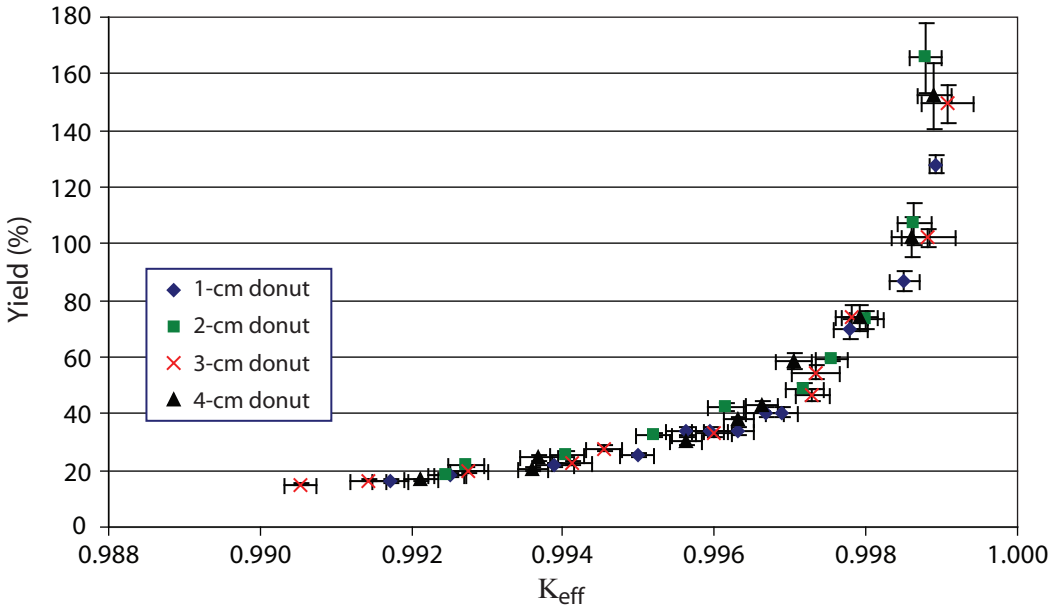

Figure 12. Changes in neutron fluence as K_{eff} varies in the same assembly

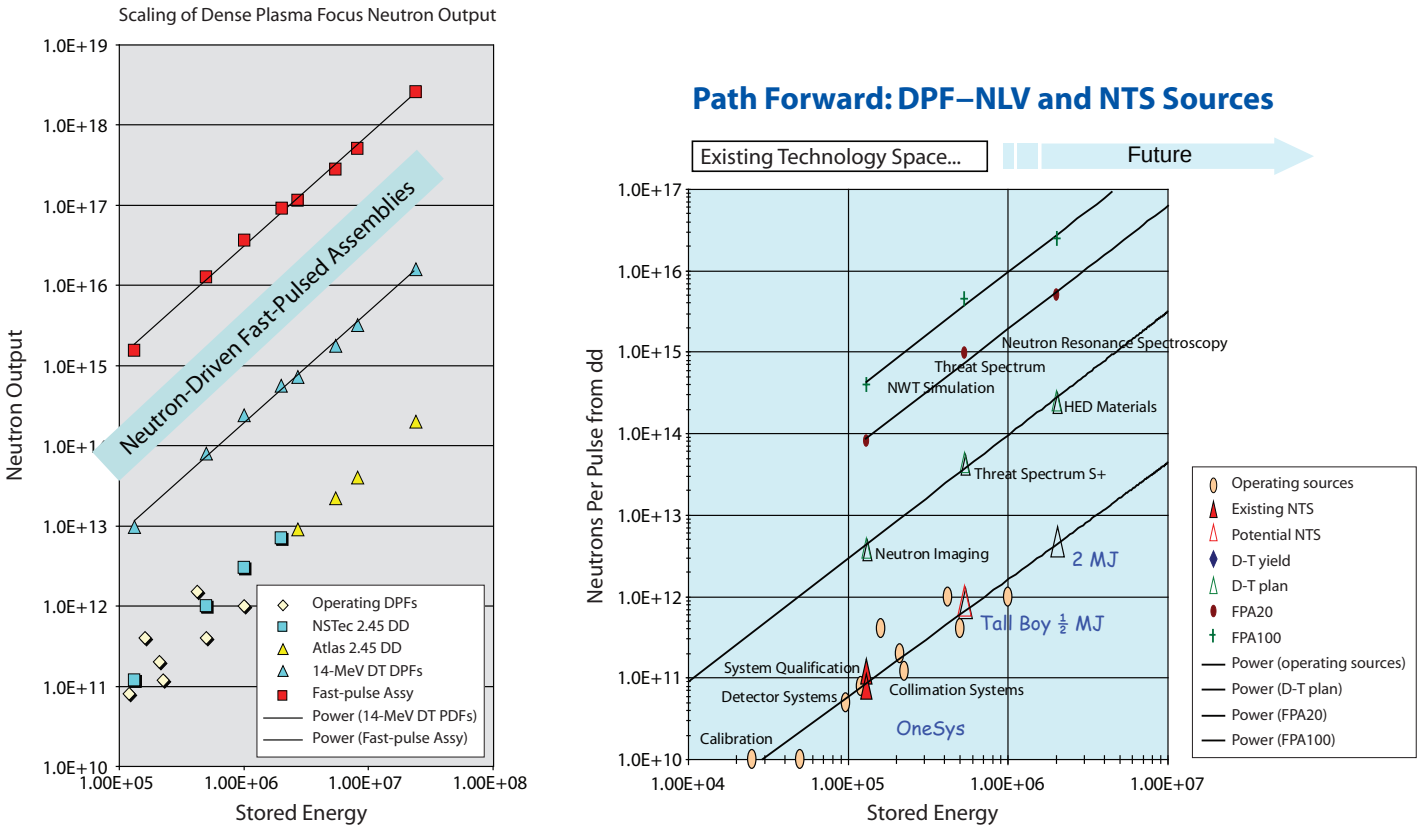

Figure 13. Projected yields of DPFs including multipliers; yields for DT-driven fast-pulsed assemblies are shown as red squares on left, red circles on right). The abscissas represent stored-bank energy. Operational NSTec DPFs are depicted on the left-hand graph as yellow diamonds and on the right-hand graph as orange ovals. The operational parameter space for several applications is shown on the right.

Conclusion

We have established that we can very safely increase the neutron yield of a DPF burst by up to 300 with the addition of ^{235}U and Be multipliers, along with carbon and polyethylene reflectors. The neutron flux is intense enough to perform several neutron physics experiments, including:

- Imaging—backlighter for high-resolution image of dense objects
- TOF measurements
- Neutron cross-section measurements
- Materials damage studies

- Weapons physics experiments and instrumentation validation
- Detector development
- Readiness applications
- Neutron-initiated nuclear reaction studies
- Neutron interrogation of black boxes that might contain special nuclear materials
- Nuclear medicine application beyond the present scope of NSTec

As the power in DPF machines increase, the multiplication available in assembly structures will remain in the 10–300 region, depending on configuration. Figure 13 shows the projected increases that could eventually be achieved at NSTec. These accelerators, with the multiplying materials, are shown as the top series in the Figure 13 graphs.

References

Meehan, B. T., "Design and Test of a Fast-pulsed Assembly for the Dense Plasma Focus," *Nevada Test Site–Directed Research, Development, and Demonstration*, FY 2005, Bechtel Nevada/National Security Technologies, LLC, Las Vegas, Nevada, 2006, 15–20.

Pigg, J. L., E. C. Hagen, "Tailored Neutron Source," *Nevada Test Site–Directed Research, Development, and Demonstration*, FY 2003, Bechtel Nevada, Las Vegas, Nevada, 2004, 43–46.

this page intentionally left blank

Exploring Phase Transitions/Shock Dynamics Using THz Spectroscopy

Craig A. Kruschwitz,[1] *Ming Wu*
Los Alamos Operations

This research sought to explore phase transitions of metals and laser-induced shock dynamics using time-resolved terahertz (THz) spectroscopy. The THz spectral fingerprint of a solid is sensitive to its lattice structures and components. Thus, THz spectroscopy will provide a powerful and sensitive method to identify phase transitions of solid metals. Combined use of laser-induced shock in solid metal and time-resolved THz spectroscopy can generate a pump-probe scheme for the possible study of shock dynamics in solid metals. Our team performed the first in a proposed series of experiments on the U12IR beam line at the National Synchrotron Light Source (NSLS) to study phase transitions and shock dynamics in solid metals. These were static experiments aimed at investigating the $\alpha \leftrightarrow \beta$ phase transition in tin (Sn). We used the high-brightness terahertz spectroscopic capabilities of U12IR to attempt to determine the phonon spectrum of Sn α and β phases.

Background

The detection of phase changes and the study of the kinetics of shock-induced phase transitions are problems of great, long-standing interest to the weapons program. In recent years, various efforts have been made toward developing a technique capable of determining phase changes over the short time scales (microseconds or less) of shock propagation. Among these techniques are surface polarimetry, high-speed pyrometric measurements, x-ray diffraction, and dynamic resistivity measurements. So far, such techniques have proven challenging to apply due to technical issues or data ambiguities.

Our team planned to investigate the possibility of using time-resolved THz spectroscopy as a phase-transition diagnostic. Successful determination of the vibrational spectrum-versus-time of the sample of interest would provide an unambiguous indicator of solid-solid phase transitions. The scientific significance of this research, then, would be twofold: demonstration of the feasibility of employing THz spectroscopy for detecting phase transitions in high-speed shock experiments; and the use of THz spectroscopy to measure the phonon spectrum of metal, which to our knowledge has never been done before.

The goal of the experiments we proposed was to explore phase transitions of metals and laser-induced shock dynamics using time-resolved THz spectroscopy. Since a solid's THz spectral fingerprints are sensitive to its lattice structures and components, THz spectroscopy provides a powerful and sensitive

[1] kruschca@nv.doe.gov, 505-663-2023

method with which to identify phase transitions of solid metals. The combined use of laser-induced shock in solid metal and time-resolved THz spectroscopy can generate a pump-and-probe scheme to study shock dynamics.

In the last few decades, experiments with hundreds of picoseconds' time resolution using either impact- or laser-driven shocks have been conducted. In this research, picosecond time-resolved nonlinear coherent anti-Stokes Raman scattering (CARS) spectroscopy monitored shock-induced chemical reaction propagation on a metal surface, or vibrational sum-frequency generation (SFG) was used to watch a planar laser–driven shock front pass over a thick layer of molecules. The proposed time-resolved THz spectroscopy would study shock dynamics inside of solid metals on the same time scale, instead of simply probing coated molecular species on the metal surfaces. Detection sensitivity of linear-absorption THz spectroscopy should be much higher than nonlinear spectroscopy, such as CARS, SFG, and Raman spectroscopy (Carr, 2003).

Our plan was to perform at least two sets of experiments in FY 2007, with additional sets proposed for future studies. The first, which were performed in the May–August 2007 beam cycle at the NSLS, were a series of static experiments aimed at measuring the phonon spectrum of the Sn α and β phases. With these experiments we hoped to use the material's THz signature to determine when a phase transition had occurred or was occurring. For future experiments, we could produce a shock in the samples of interest with a high-intensity laser, and then use THz spectroscopy to probe the shocked material for phase changes. For these experiments, we plan to investigate Sn again (this time, investigating the beta-gamma phase transformation that occurs above 9 GPa, easily accessible with a moderate-power laser) and possibly bismuth, given its rich, solid-phase structure in the 2–9 GPa pressure region.

Of principle interest in this year's static experiments was tin in its α and β phases. The transition between the low-temperature α phase (grey) and the β (white) phase begins near 13°C. Grey tin has a diamond crystal structure, while white tin has a body-centered, tetragonal crystal structure (Figure 1). The phonon density of states (DOS) for the two phases is markedly different, as has been simulated using density functional theory methods and demonstrated by neutron diffraction experiments (Pavone, 1998). Tin, therefore, is an excellent candidate for our investigation, especially given its frequent use in shock physics experiments.

Project

We procured a heating and continuous-flow cryostatic cooling stage and reflectance measurement unit from Bruker Optics. The cryostat was used to heat and cool the samples, inducing the desired phase transformations. The heating/cooling stage has a temperature range as high as 500K and as low as liquid He temperatures. Liquid helium was used in the cryostat for cooling the samples. Additionally, several tin samples were procured from the Lebow Company (Goleta, CA). These samples were 10-mm-diameter, free-standing foils mounted on stainless-steel rings. Foils had thicknesses of

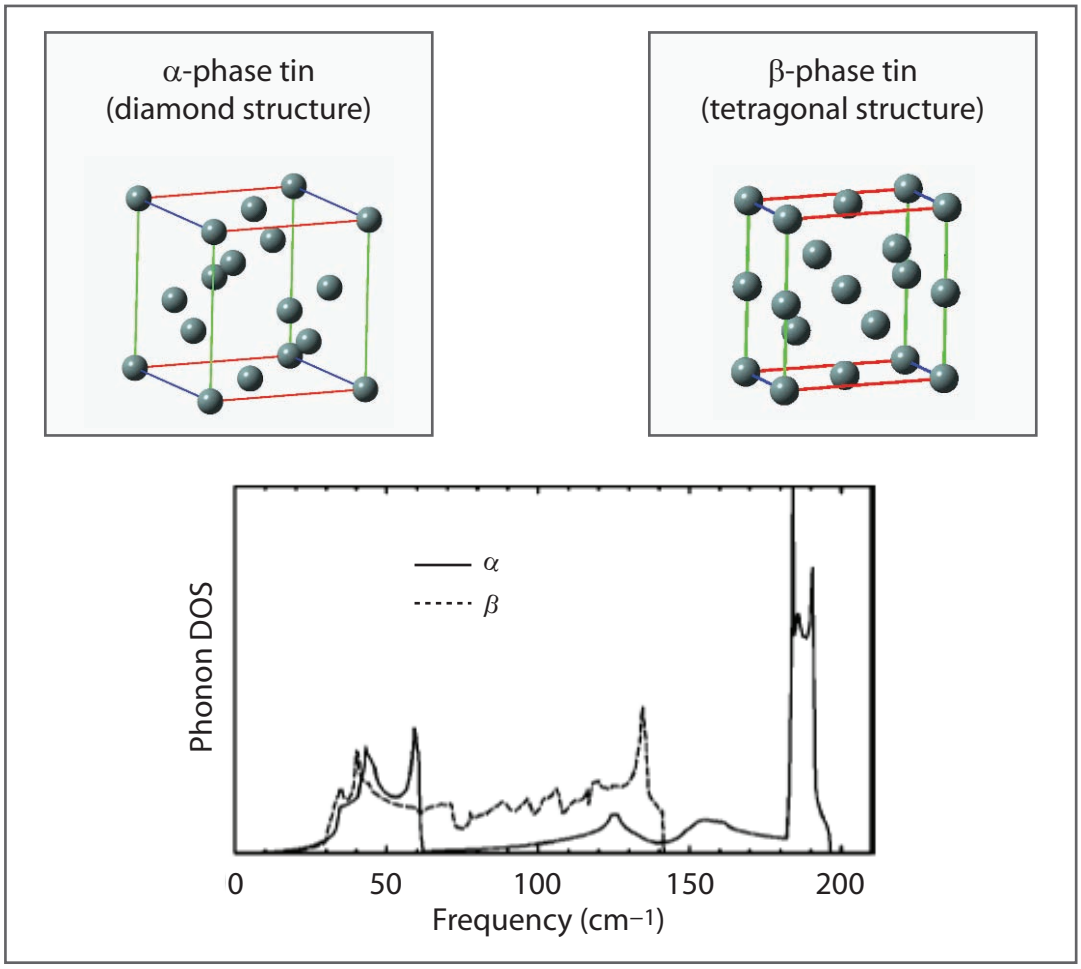

Figure 1. Unit cell of Sn α and β phase and calculated phonon density of states for each. Calculations were performed using density functional theory (Pavone, 1998).

0.25 μm, 0.5 μm, 1 μm, 2 μm, and 5 μm. The 0.25-μm foils were obtained for attempted transmission measurements, while the others were used to measure reflection. In practice, we found that the 5-μm foils were best suited for the reflection measurements because of their greater strength and more uniform surface. Samples of the 2-μm and 5-μm foils appear in Figure 2.

Experiments were conducted at the NSLS U12IR beam line from July 27 to August 5, 2007. The U12IR beam line uses the synchrotron to provide a THz source from ~8 to 4000 cm^{-1}, with a peak at ~40 cm^{-1}. A Bruker Optics IFS 125HR Fourier transform infrared (FTIR) spectrometer has been specially designed for use on the beam line. This FTIR has a maximum resolution of 0.001 cm^{-1} and was operated for these experiments with a liquid He–cooled Si bolometer with a spectral range

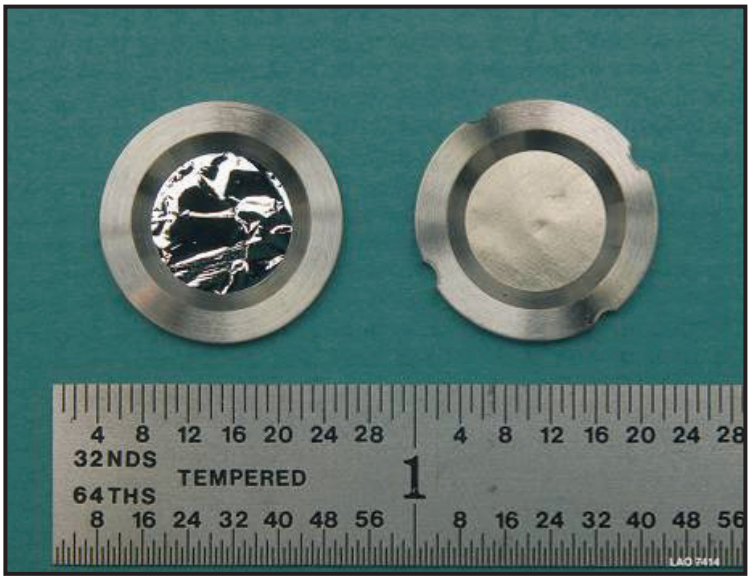

Figure 2. 2-μm and 5-μm Sn samples

of ~15–400 cm^{-1}. The IFS 125HR also has a built-in Hg arc-lamp far infrared (FIR) source, which can be used in lieu of the synchrotron. The cryostat and reflectance unit we procured from Bruker Optics were specially designed to operate out of the box on this spectrometer, which spared us long hours of setup and alignment. Figure 3 shows our experimental setup on the U12IR beam line. Figure 4 depicts the reflectance unit installed in the FTIR. For heating/cooling experiments, the sample holder was easily replaced by the cryostat.

Our first experiments were attempts at transmission measurements using the thinnest (0.25-μm) samples. These were placed directly in the beam path, and the resulting spectra were measured. Unfortunately, these experiments were unsuccessful, as the samples were apparently too thick for adequate transmission. Thus, we moved on to reflectance measurements.

Initial reflectance measurements were conducted at room temperature using the basic sample holder (Figure 4). We successfully obtained reflectance spectra from the Sn (using 5-μm samples) in this mode and so installed the cryostat and proceeded with the low-temperature measurements. Using the temperature controller, we adjusted the cryostat temperature to various values between 60K and 242K. Spectra were taken at each temperature using the synchrotron light as a source. Afterward, we took a series of spectra with the FIR source on the FTIR. When all measurements on the Sn sample were completed, a gold reference mirror was placed in the cryostat. We then took background spectra (at room temperature) over an entire synchrotron cycle. This procedure was repeated with the FIR source.

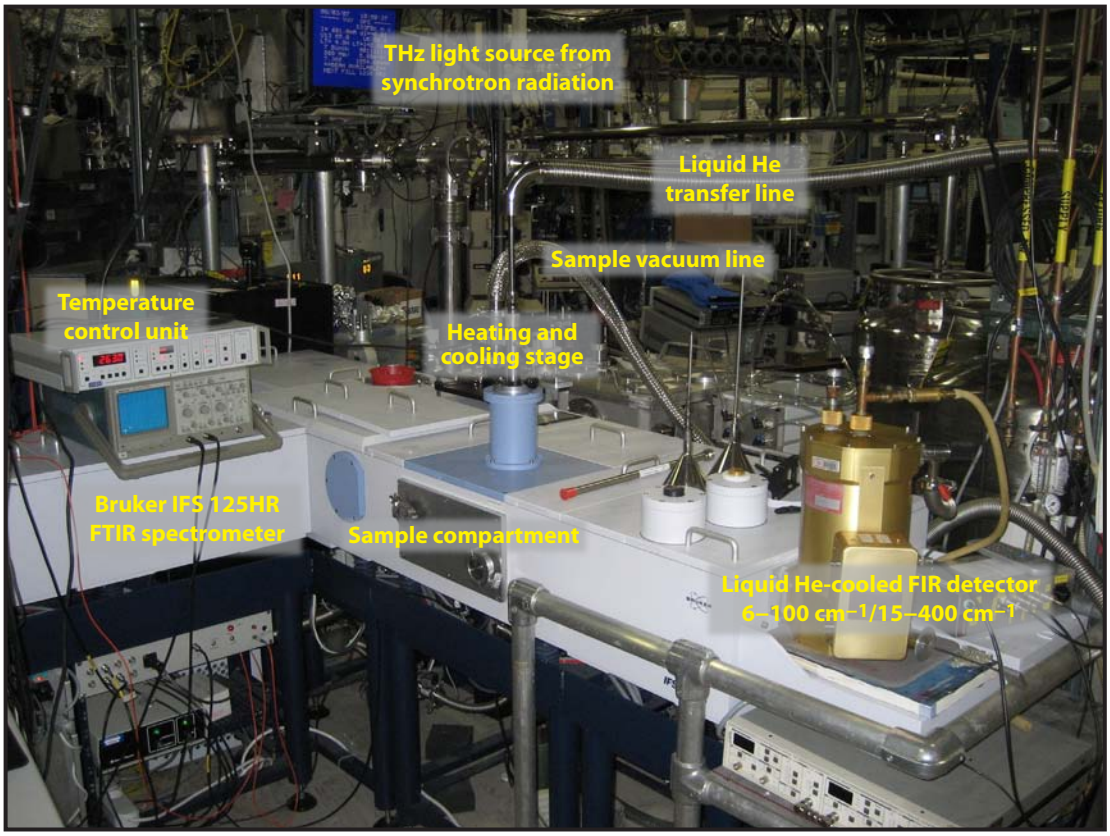

Figure 3. Experimental setup, showing the FTIR, cryostat, liquid He transfer line, temperature and He flow–controller/meter, and He-cooled Si bolometer

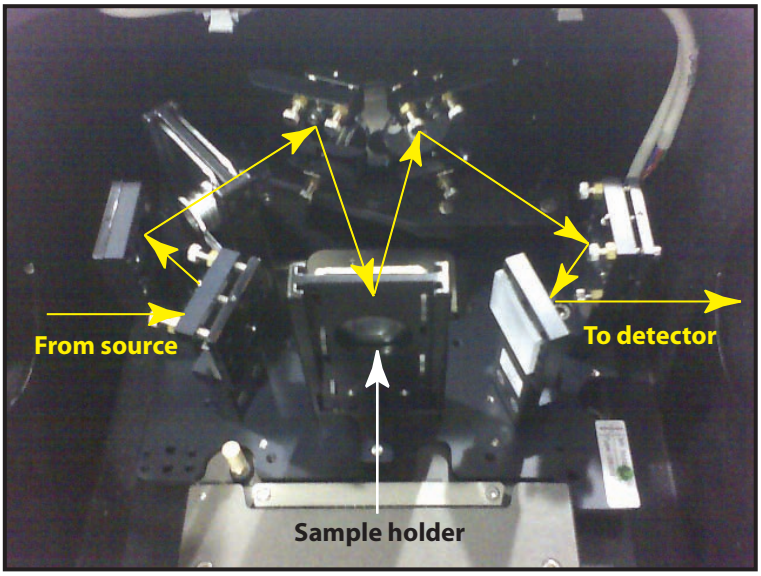

Figure 4. Reflectance unit installed in the Bruker Optics IFS 125HR FTIR

The data were processed by dividing the raw sample spectra by the background spectra. In essence, this removed the contributions of the FTIR optics, cryostat windows, and reflectance unit mirror, and gave a spectra of the Sn sample. Spectra obtained with the synchrotron source at temperatures ranging from 60K to 295K (room temperature) appear in Figure 5. You can clearly see the considerable changes in the spectra as the temperature drops below the $\alpha \leftrightarrow \beta$ phase-transition temperature (286K). A broad spectral feature exists between ~50 and 70 cm^{-1}, which grows more pronounced and shifts slightly to a lower frequency as the temperature drops.

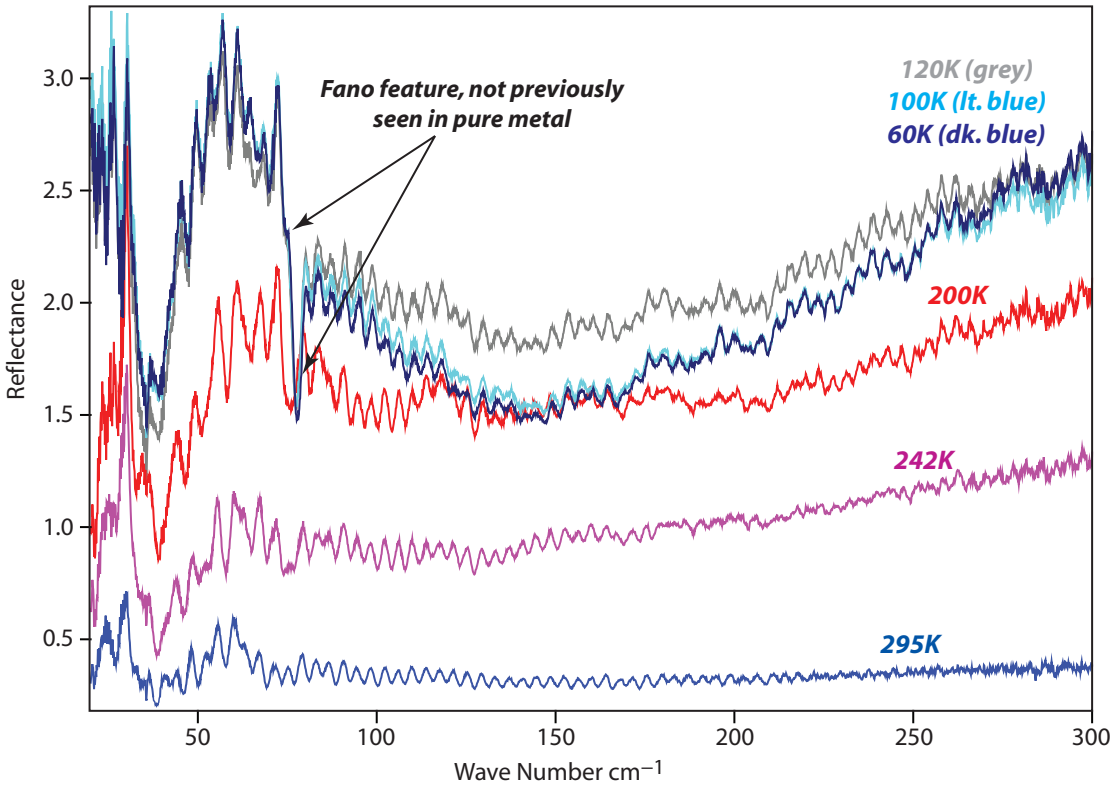

Figure 5. Sn reflectance spectra at various temperatures using synchrotron THz source

Of particular interest, however, is the appearance of a prominent spectral feature at ~80 cm^{-1}. This feature is reminiscent of a Fano resonance, often seen in reflectance spectra, usually of a thin film coated on a metal substrate. A Fano resonance occurs when a discrete quantum state couples to a continuum of states (Fano, 1961; Terakura, 1977). In the case of a thin coating on a metal substrate, a Fano resonance occurs due to coupling between a vibrational mode of the coating material and the continuum described by the electron conduction bands in the metal substrate. In our case, however, no coating exists, and the resonance appears to be occurring entirely within the metal itself, a phenomenon

never before observed. Also, the fact that the resonance only seems to occur at temperatures below the transition temperature strongly indicates that it may be associated with the phase transition. Thus, we believe this may be due to a coupling between a vibrational state of α–Sn and the conduction band. Further evidence that this is the case can be inferred from the fact that the feature is also strongly present in the reflectance spectra obtained using the FIR source (Figure 6). We would not expect to see strong spectra features due solely to phonon modes in these spectra because the incoherent light from the FIR source cannot couple to the dipole moment presented by the infrared active phonons, while the synchrotron light can. Thus, the fact that the Fano feature is so prominent in the FIR spectra indicates that it is not, in fact, due to phonon excitation. Further experiments, however, will be necessary to determine whether this is truly the case.

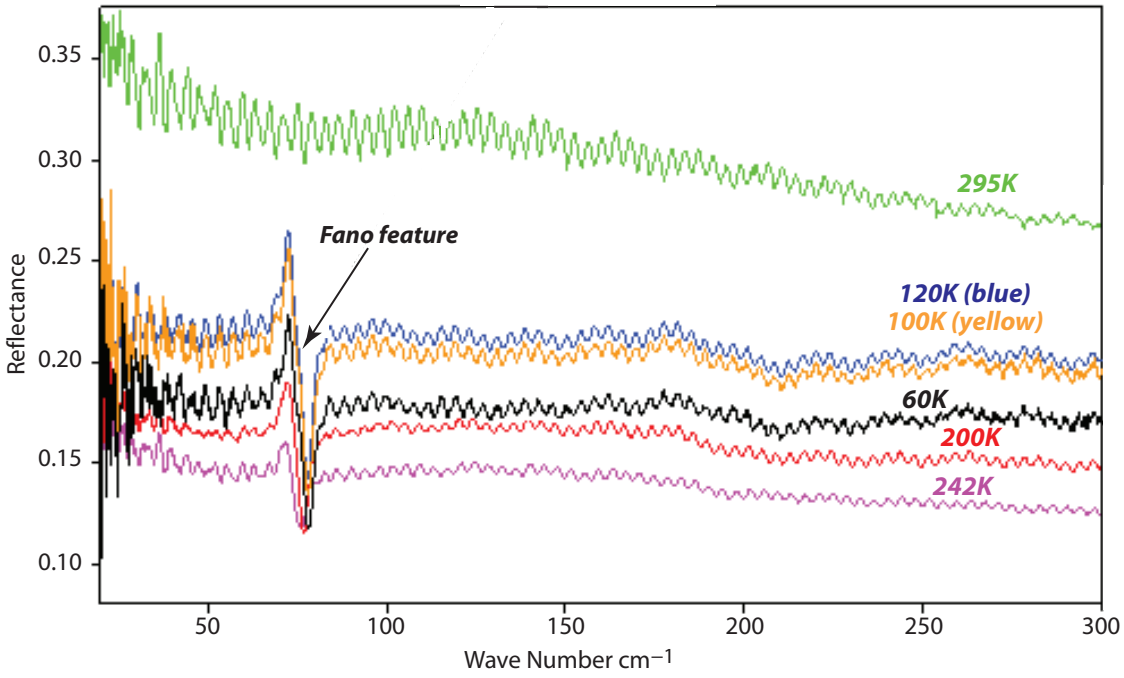

Figure 6. Sn reflectance spectra at various temperatures using the FIR source

Conclusion

The experiments conducted this year successfully used THz spectroscopy to detect the α↔β phase transition in Sn. In addition to significant changes in the reflectance spectra between ~20 and 300 cm^{-1} below the transition temperature, an unexpected strong resonance deeply reminiscent of a Fano feature was observed near 80 cm^{-1}. To our knowledge, such a feature has never before been observed in a pure metal sample and is due to a coupling between a phonon mode and the electron conduction band in α–Sn. However, further experiments are necessary to investigate this phenomenon and verify this explanation. All in all, we believe that the results of these static experiments show that THz spectroscopy shows great promise as a phase-transition detection method in metals.

Acknowledgments

The authors thank Brookhaven National Laboratory personnel, particularly G. L. Carr and Randy Smith, and U12IR beam line employees for providing useful technical suggestions, offering much-needed help, and making our visit to their facility successful and enjoyable.

References

Carr, G. L., "Dynamics of GaAs photocarriers probed with pulsed infrared radiation," *Nucl. Inst. Meth. B* **199** (2003) 323–327.

Fano, U., "Effects of configuration interaction on intensities and phase shifts," *Phys. Rev.* **124,** 6 (December 1961) 1866–1878.

Pavone, P., S. Baroni, S. de Gironcoli, "α↔β phase transition in tin: a theoretical study based on density-functional perturbation theory," *Phys. Rev. B* **57,** 17 (May 1998) 10421–10423.

Terakura, K., "A theory of Fano effects in the electronic structure of d band metals and alloys," *J. Phys. F* **7,** 9 (1977) 1773–1780.

Injector Design for a 10-picosecond Electron Accelerator

Cynthia Christensen, Ronald Sturges,[1] David Schwellenbach, Nicholas Wilcox
Los Alamos Operations

The goal of this project was to investigate the feasibility of developing a new injector design that would improve the bandwidth performance of S-band accelerators like the upgraded 1 MeV Los Alamos Operations (LAO) pulsed x-ray source. An injector capable of producing a <350-ps, 100-keV pulse was designed, modeled and characterized. It is expected that when integrated into an accelerator operating at the S-band period of 350 ps, the output pulse width will be defined by the microstructure pulse width, which for the pulsed x-ray source is approximately 10 ps.

Background

The LAO pulsed x-ray source (Figure 1) is currently being upgraded from 100 keV to 1 MeV by the addition of S-band accelerating sections. It has been calculated that the inherent microstructure of the S-band accelerator produces a pulse train of ≈10-ps-wide pulses at the S-band period of 350 ps (2856 MHz). The 100-kV pulsed x-ray source was originally designed to be the front end of an L-band accelerator having a period of 770 ps (1.3 GHz). For high bandwidth applications, such as those developed for the Test Readiness program and the National Ignition Facility, this microstructure can be exploited to give a single, fast pulse with the S-band width and variable repetition rates from single shot up to at least 100 Hz. For an S-band accelerator to deliver a single, clean pulse, the input pulse to the accelerator must have a width less than the S-band period; the input pulse must have a FWHM of <350 ps.

Project

Our ultimate goal was to investigate the feasibility of modifying an S-band accelerator to generate a 10-ps electron pulse with high peak current in the 1-MeV range. The existing electron injector and subharmonic bunching systems were characterized in order to define where improvements were feasible.

Initial Capabilities

At the start of the project, the pulsed x-ray source injector and bunching systems delivered a pulse with a FWHM of <750 ps. This was achieved with an injected pulse of 2 ns FWHM with subharmonic bunching to reduce this width to the required 750 ps. The injected pulse is formed by delivering a

[1] sturgere@nv.doe.gov, 505-663-2042

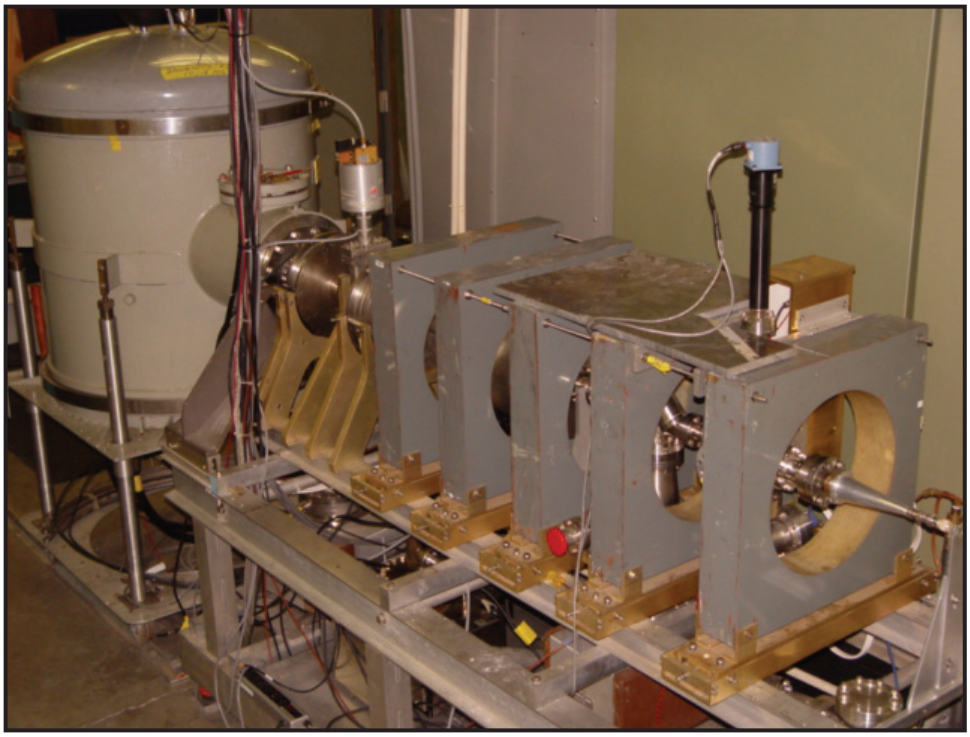

Figure 1. 100-keV pulsed x-ray source at LAO

2-ns pulse with a pulse height of 1.5 kV to the electron gun. Initial calculations indicated that a new injector design would be needed to provide an injected pulse shorter than 1.5 ns, and the subharmonic buncher would have to be improved to reduce this width to <350 ps.

Injected Pulse

The impedance of the gun and connecting hardware was not a limiting factor for pulse widths >1 ns. One approach to reducing pulse width was to redesign the gun or gun adapter to decrease the capacitance. After study, it was determined that a new gun design would require significant changes to the accelerator hardware, so this approach was rejected. These studies showed the capacitance of the gun body broadened an input pulse of 0.5 ns to a final injected pulse of ~1 ns. This injected pulse width meets the requirements without gun-body modification.

Commercially available pulsers were researched and initial design studies were performed on an in-house pulser design. The pulsers had to meet not only the 0.5-ps pulse width specification, but also required a pulse-to-pulse time jitter of <10 ps. The Grant Applied Physics Model HYPS pulser met these specifications off the shelf and had the added advantage of variable pulse height. Therefore, the option to create an in-house design was put aside.

The pulse width and jitter specifications of the Model HYPS were bench-tested and met the published values. With the Model HYPS installed, a series of beam tests were run to determine injector performance at various accelerating voltages. The results at 100 kV, the preferred operating condition for the S-band accelerator, appear in Table 1. All timing measurements were made using Tektronix TDS6154C (15 GHz) and DPO701604 (16 GHz) oscilloscopes. Representative scope traces of the injected pulse of the initial and upgraded systems appear in Figure 2.

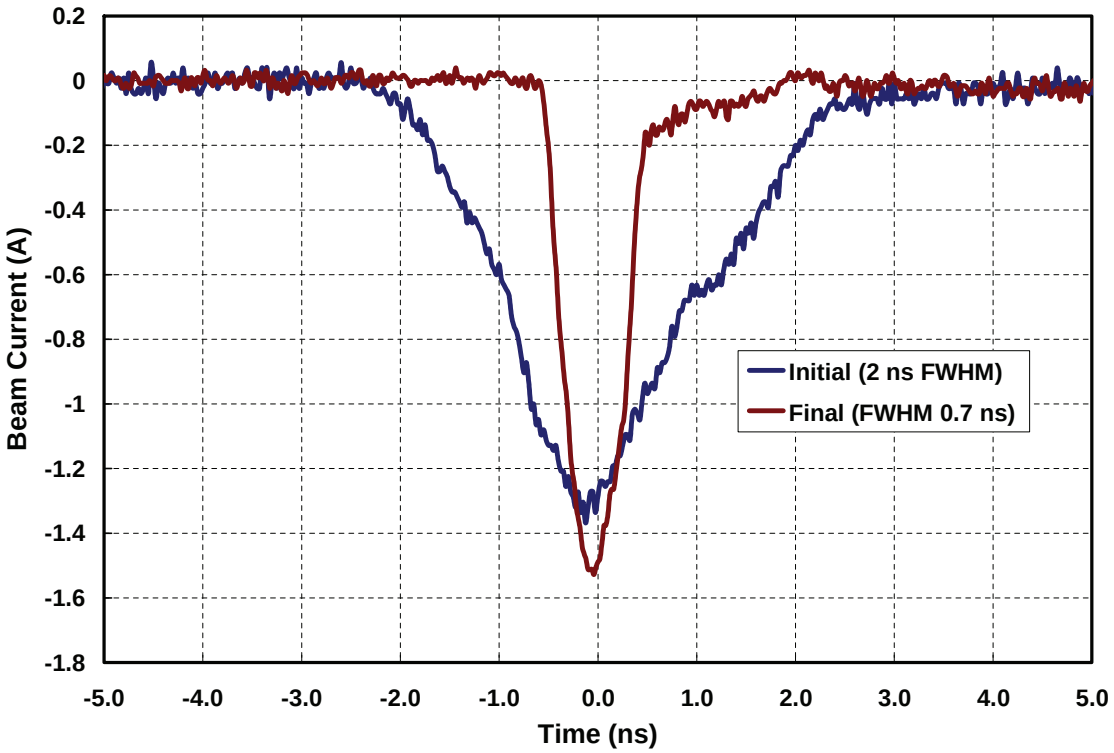

Figure 2. Oscilloscope traces of initial and final injected electron pulses

Bunched Pulse

Initial calculations indicated that by increasing its power the subharmonic buncher would achieve the 350-ps specification. However, since modifications made to the injected pulse produced better than expected results, the existing subharmonic bunching system needed only minimal modifications. The initial buncher was designed for 216 MHz, the 12th subharmonic of the L-band frequency. The new system required a subharmonic of the 2856 MHz S-band frequency. It was determined that the existing buncher and drive electronics could be retuned to be resonant at 219 MHz, the 13th subharmonic of the S-band frequency. With the improved injected pulse, the existing 10-kW

RF power was sufficient at 219 MHz to bunch the pulse to the required 350 ps. The results for a 100-keV injected pulse are summarized in Table 1. Figure 3 compares the bunched pulse for the L-band system and the upgraded bunched pulse to be used on the S-band accelerator. The final pulse has a FWHM of 250 ps, well below the S-band period. This will allow the acceleration of a single, well-defined electron pulse by the S-band accelerator.

Table 1. Measured pulse widths for original and new configurations

	Original Design: Pulse Width	New Design: Pulse Width
Injected Pulse	2 ns	0.7 ns
Bunched Pulse	530 ps	250 ps

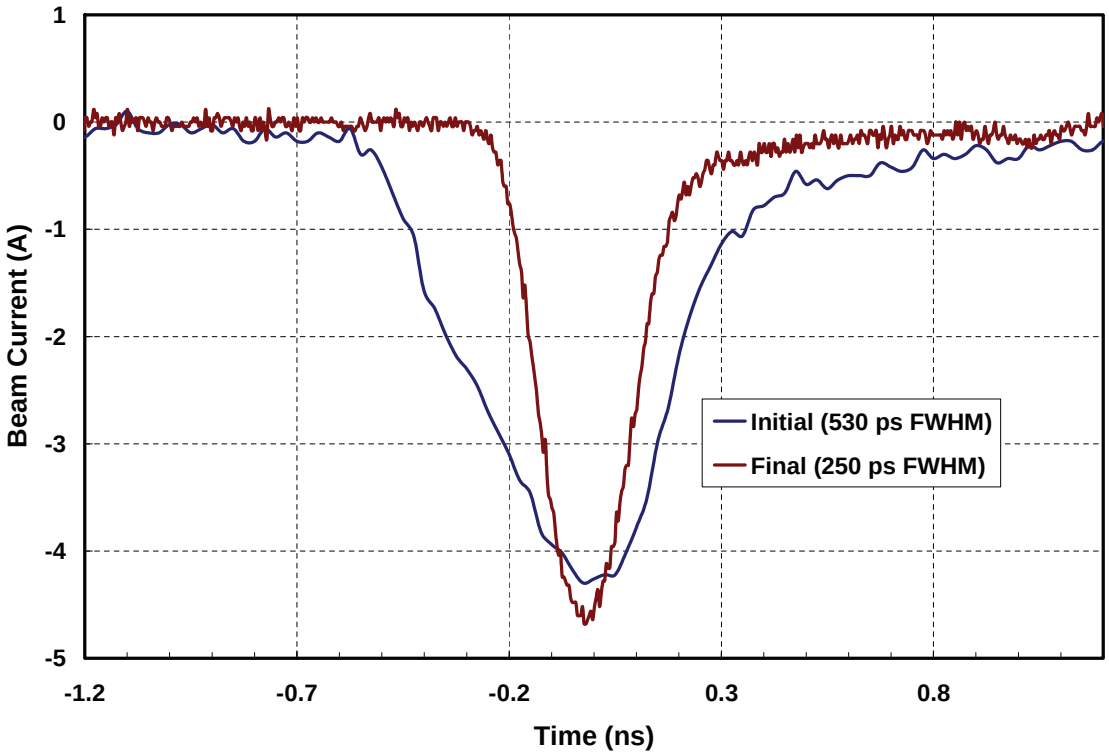

Figure 3. Oscilloscope traces of initial and final bunched electron pulses

Beam Transport

Throughout this project, beam transport calculations were performed and compared to measured results. Parmela, a particle tracking code developed by Los Alamos National Laboratory, was used for all beam transport studies, primarily because it was used to conduct the beam dynamics studies made during the accelerator design. Of primary interest for the reduced pulse width were space-charge effects as the pulse was transported to the RF accelerator. Parmela studies showed beam shape (spatial and temporal) at various points along the beam line. The beam line was modified to allow measurement of the beam's temporal characteristics at various points for comparison. The measured results were consistent with the calculations, indicating that the transport code as used was valid for future studies of this beam line. Representative Parmela results appear in Figure 4.

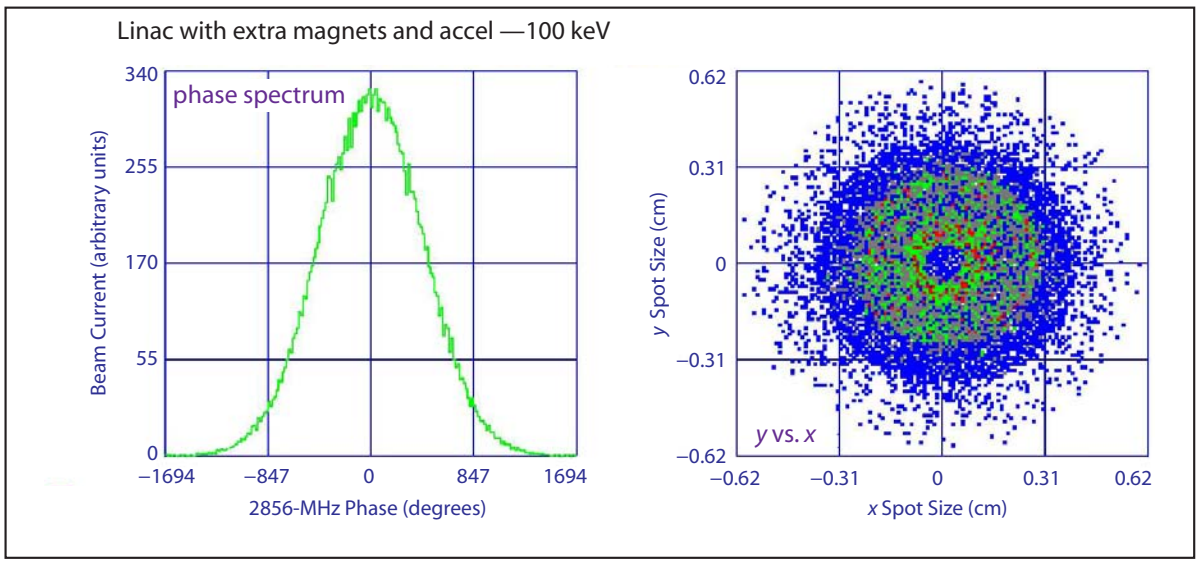

Figure 4. Representative Parmela outputs. The phase spectra show relative output as a function of RF phase in degrees. The range plotted (±1694) represents ±1.6 ns. The y vs. x plot gives beam size in cm.

Conclusion

Our team met this project's primary goal to design an injector capable of delivering a 100-keV electron pulse <350 ps wide at the input of the S-band accelerating section. The designed injector performed well enough to be integrated into the S-band accelerator at a later date. Since the bunched pulse is clearly less than one S-band period, the final accelerator should be able to convey a single pulse. A new, low-jitter pulser was identified and procured. The low-jitter pulser was bench-tested

and promises to give similar pulse width and peak current as the HYPS pulser, but with improved time jitter (<5 ps). This will yield a more stable, accelerated pulse, since the injected electron bunch will be better synchronized with the accelerating RF.

Sintered Optical Materials for Shock Physics Experiments

James R. Tinsley[1]
Special Technologies Laboratory

Currently available velocity interferometer systems for any reflector (VISAR) windows and "optical analyzers" do not adequately cover the range of mechanical impedance that is encountered by experimenters. The purpose of this project was to investigate the possibility of using sintering technology to produce suitable windows or analyzers in polycrystalline form with different impedances than are currently available with standard, single-crystal window materials.

Background

Matching the impedance of a VISAR window to that of the material being studied is very useful for simplifying the analysis of shock experiments. However, there are few materials in common use (e.g., LiF and Al_2O_3), leaving large gaps in impedance for which there are presently no suitable window materials. A similar situation exists for optical analyzers that are used to determine rarefaction wave velocities at very high pressures. These bear the additional requirement of exhibiting triboluminescence (that is, they produce light under pressure). There is especially a need for analyzers that have impedances similar to the actinides.

In FY 2005 and FY 2006, we began collaborating with Dr. Olivia Graeve at the University of Nevada, Reno (UNR) (Tinsley, 2006; 2007). Dr. Graeve has developed a process for sintering very fine ceramic powders into macroscopic pieces having very good optical qualities (i.e., good clarity and uniformity). We speculated that the same methods might permit the manufacture of new materials, or existing materials with modified properties, that would fill in the gaps noted above. For example, a crystal of LSO:Ce produces triboluminescence only when shocked above the elastic limit, but powdered LSO:Ce (randomly ordered crystals) does so at lower pressures. We determined it was a reasonable conjecture that LSO sintered from powder into a polycrystalline solid might also work for pressures below the elastic limit. Similar arguments would hold for YAG:Ce and YSO:Ce as well. Another advantage of a sintered piece would be that an optical analyzer could be made as a reciprocal part for a stepped sample that is used to measure acoustic velocity in some experiments. This would make it possible to eliminate Bromoform, a fairly toxic substance frequently used in such experiments.

[1] tinslejr@nv.doe.gov, 805-681-2282

Project

The primary goal of this project was to produce a sintered version of an existing VISAR window material, Al_2O_3, and test it at the Special Technologies Laboratory Boom Box to verify that its properties would not be degraded (i.e., would not darken under pressure and its impedance would not be adversely affected). Al_2O_3 was chosen as a test case because of its similarity to other high-temperature ceramics with which Dr. Graeve has some experience.

The Al_2O_3 powder was produced in a straightforward combustion synthesis:

$$Al\left(NO_3\right)_3 + a\left(H_2NNH\right)_2 \Rightarrow Al_2O_3 + yH_2O + zCO_2 \quad \textbf{(1)}$$

The x-ray diffraction spectrum of this powder showed that it was of excellent purity (Figure 1). However, a scanning electron microscope (SEM) image (Figure 2) shows that the individual particles were not as uniform in size as would be preferred; they also had irregular shapes and jagged edges.

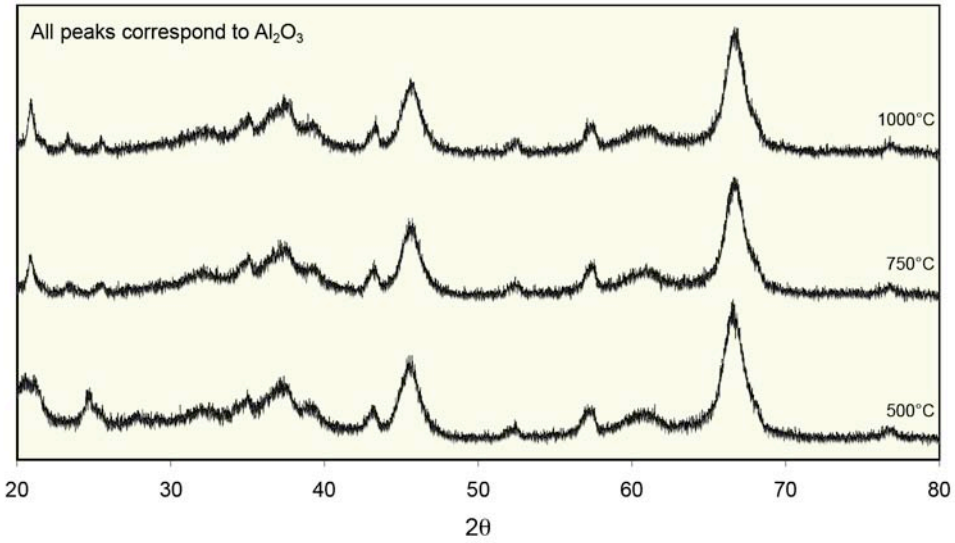

Figure 1. X-ray diffraction spectrum of synthesized Al_2O_3 powder, showing excellent purity

Once the starting powder has been synthesized, the final piece is made by pressing the powder into a tablet using a form of the desired size and shape; typical pressures are on the order of several tens of thousands of pounds per square inch. The tablet is then set in the furnace on a nonreactive material, such as iridium or some loose powder of the same material as that being sintered, to prevent

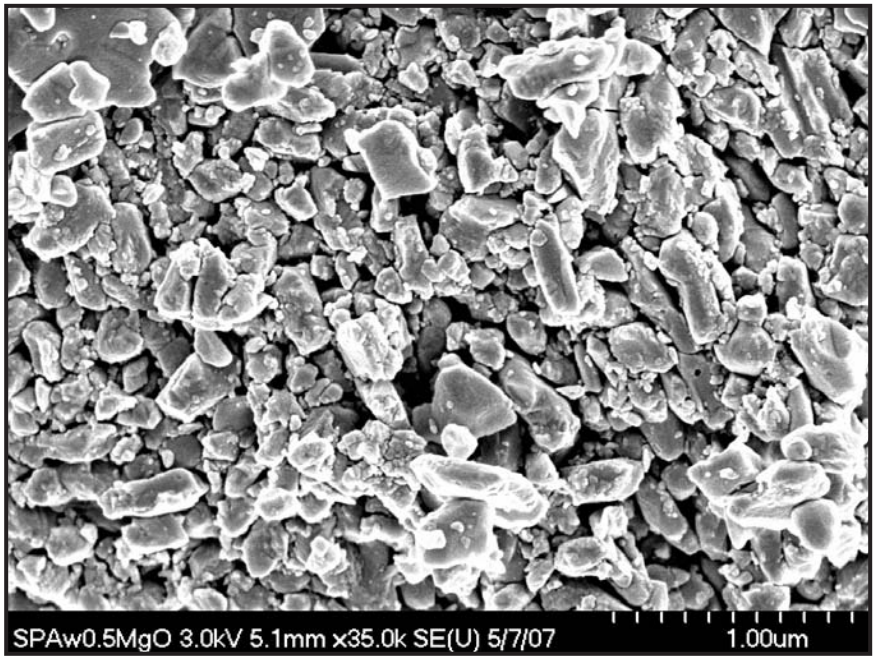

Figure 2. SEM image of synthesized Al_2O_3 powder, showing irregularity in shape and jagged edges

any contamination of the piece. The furnace is then ramped up to some final temperature at some prescribed rate, held at that temperature for a prescribed time, and then ramped down to room temperature at some other prescribed rate. The times and temperature are varied according to the melting point of the object material, as well as other considerations, to achieve the desired product. After sintering, the surface of the piece is invariably rough and must be polished for the true optical quality to be seen.

The characteristics of the Al_2O_3 powder made it difficult to press into tablets tightly enough to prevent voids in the sintered pieces. These voids scatter light, thus degrading the optical quality of the piece. We attempted to improve the particle packing. In some sinterings, MgO powder (a well-known sintering aid) was added to the Al_2O_3. In others, an organic binder, which acts as a lubricant, was also mixed with the powder in an attempt to improve the packing. (It should be noted that the organic binder is completely driven out of the samples during the sintering heat cycling.) In yet other tests, both of these methods were employed simultaneously. None of the tactics were completely successful alone or in combination. It was frequently the case that the final pieces had a density of 98–99% of single-crystal Al_2O_3. However, the voids that corresponded to this small amount of missing material were enough to make the sintered pieces merely translucent. A typical result is shown in Figure 3, in which visible light is transmitted through a 1951 U.S. Air Force resolution test pattern and then through a 1-mm-thick sintered piece. Only 0.4 line pairs per millimeter were resolved.

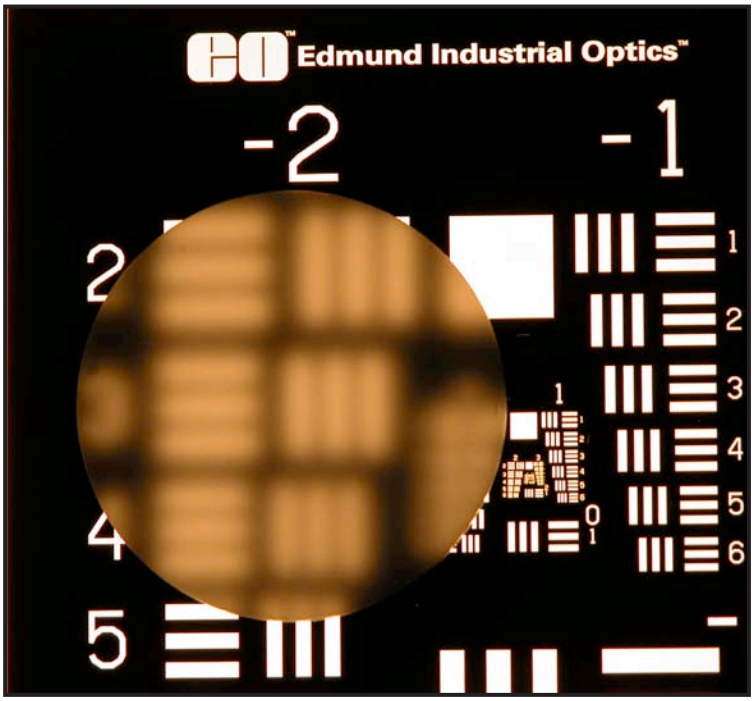

Figure 3. Typical example of a sintered single-crystal Al_2O_3, in which visible light is transmitted through a 1951 U.S. Air Force resolution test pattern and then through a 1-mm-thick sintered piece

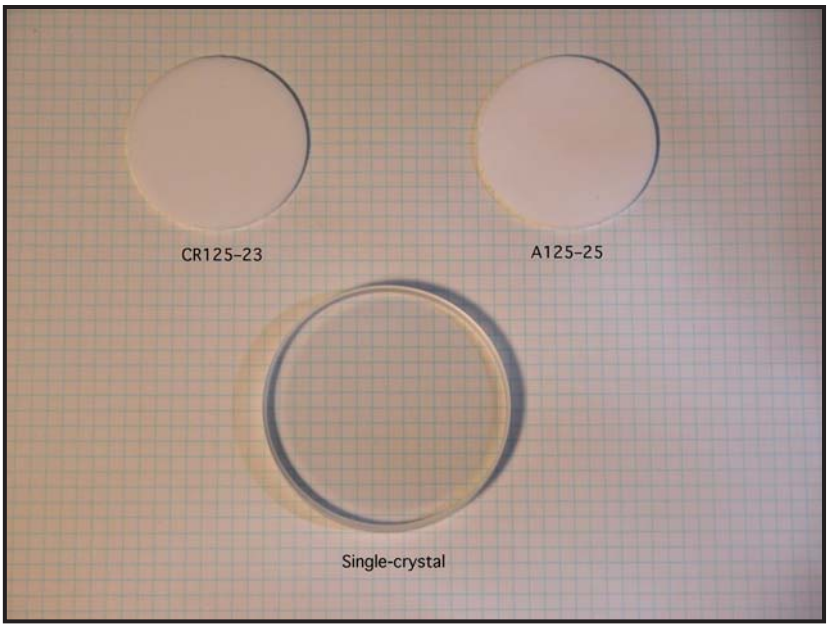

Figure 4. Samples run through various sintering parameters. The top left sample had MgO added and the top right did not.

Another method used to improve the characteristics of the starting powder was ball milling, a "brute force" method of mechanically polishing the particles to reduce their roughness. This gave somewhat better results, in terms of overall consistency in the finished pieces, but the problem of determining the sintering parameters that will lead to pieces with good transparency while remaining polycrystalline lingers.

Near the end of the project, an aggressive set of sintering parameters was used for a set of samples. This profile resulted in the powders melding into single crystals; Figure 4 shows one single-crystal example compared to two polycrystalline samples. Experiments with crossed polarizing filters showed that the crystal axes are oriented such that the extraordinary axis (c-axis) is perpendicular to the surface of the crystal. This is a valuable result: Al_2O_3 crystals with this orientation have especially high utility in shock physics experiments, and are costly to acquire. It is not yet known whether this favorable crystal orientation can consistently be produced by sintering, but if so, this may be a cost-effective method of producing them.

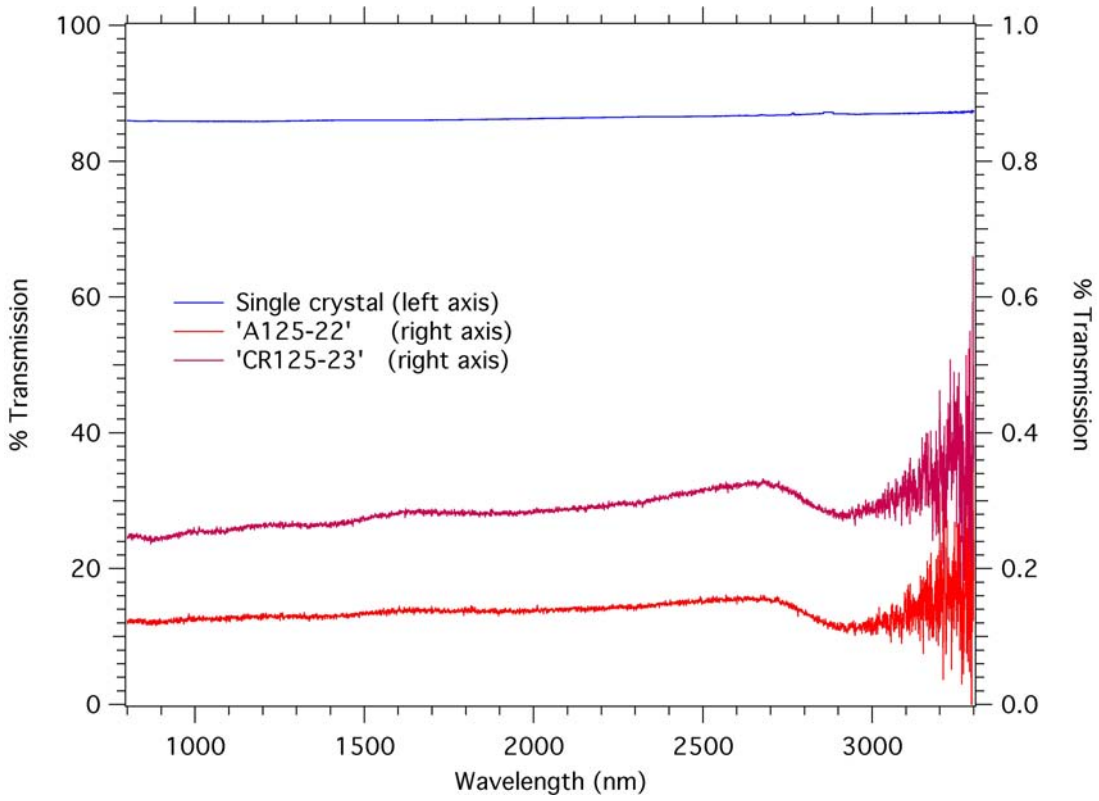

Figure 5. Results of measuring the samples' optical properties in the near infrared, showing strongly scattered light

To investigate the samples' optical properties in the near infrared, measurements of direct light transmission were made in the region between 700 and 3300 nm. The results showed that light at these wavelengths is very strongly scattered (Figure 5). While the direct transmission in the single-crystal sample is limited only by surface reflections (due to discontinuities in the index of refraction), those of the polycrystalline samples are down by more than two orders of magnitude.

Conclusion

In spite of the failure (so far) to attain good bulk transparency, the polycrystalline samples did uniformly exhibit the strength and hardness of single-crystal Al_2O_3. It was necessary to use diamond dust to polish the surfaces, and even early specimens that were severely cracked could not be broken without great effort.

It remains to be seen as to how well samples can be made with the necessary light transparency while remaining polycrystalline. Furthermore, sound velocity measurements must be made that will shed light on shock impedance differences between polycrystalline pieces and single-crystal Al_2O_3. Another future goal is to produce windows with impedances not presently available, using promising materials such as TiO_2.

The possibility of being able to produce single-crystal Al_2O_3 with the c-axis perpendicular to the crystal surface intentionally and consistently by sintering is exciting. If this ability is verified, it would be a significant advance in this field, and could lead to a paper and/or patent.

Acknowledgments

The author would like to acknowledge the contributions of Dr. Olivia Graeve, Brett Pearson, and other students in her lab at UNR.

References

Tinsley, J. R., "Large-Format Phosphor Imager," *Nevada Test Site–Directed Research, Development, and Demonstration*, FY 2005, Bechtel Nevada/National Security Technologies, LLC, Las Vegas, Nevada, 2006, 371–377.

Tinsley, J. R., "Large-format Phosphor Imager," *Nevada Test Site–Directed Research and Development*, FY 2006, National Security Technologies, LLC, Las Vegas, Nevada, 2007, 75–81.

Computer Sciences

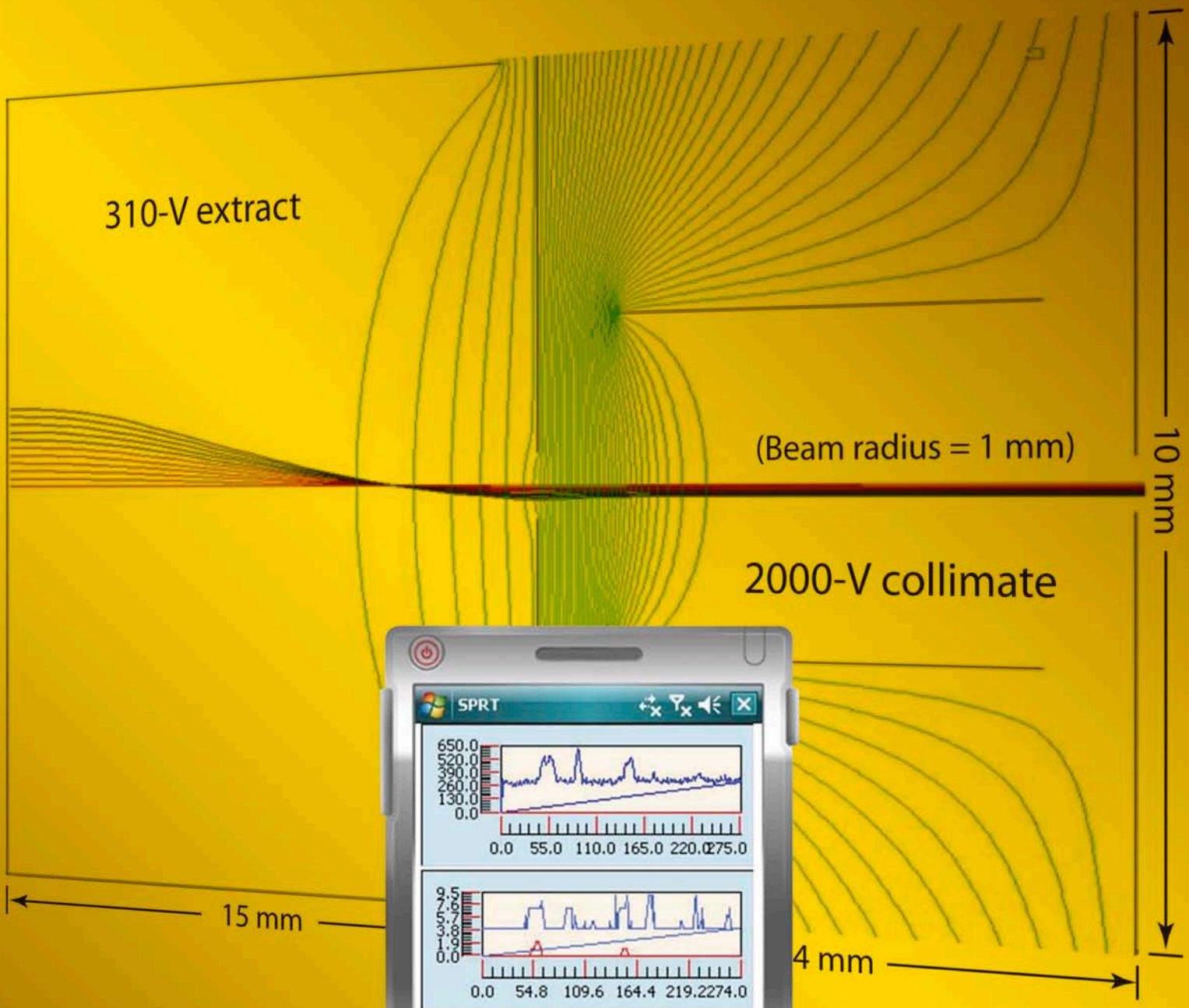

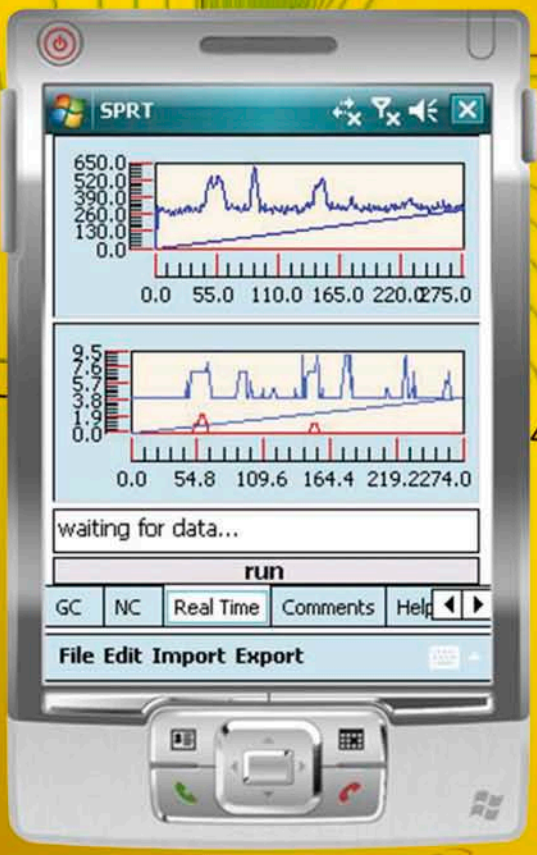

$$AL = Ceiling\left(Log_b\left(\frac{\mu_1 - \mu_0}{\rho\sigma_0}\right)\right)$$

High-speed Transient Waveform Recorder

Robert Buckles,[1] *Jerome M. Richter (former employee)*
Livermore Operations

This project investigated the feasibility of designing a viable replacement for high-speed transient recorders such as the Tektronix SCD5000 Transient Waveform Recorder, which is no longer in production. The SCD5000 is currently being used to record the photodiode output from the Dante diagnostic on the National Ignition Facility and is well-suited for other high-speed diagnostics in support of high-energy density physics and inertial-confinement fusion. The objective of this project was to design a replacement for the SCD5000 based on electron trajectory modeling. The Charged Particle Optics (CPO) two-dimensional (2-D) boundary element code (CPO, 2006) was used to conceptually model and design a complete tube, starting with the traveling-wave serpentine structure for the signal section and including the front-end beam extraction, collimation, and focus sections, plus the deflection plates for the sweep section.

Background

Oscilloscopes and waveform recorders use the input signal to deflect an electron beam vertically by an amount that is proportional to the signal amplitude. A second set of deflection plates sweeps the beam horizontally to generate the time axis. Recorders for high-frequency signals in the gigahertz range generally employ a traveling-wave signal section because the signal sampling interval must be shorter than the period of the sampled wave. For a 10-GHz signal with a 100-ps period, the sampling interval must typically be less than 40 ps to maintain adequate fidelity in the recorded signal. For a recorder operating with a 2-kV electron beam, the dwell time is 37.8 ps/mm, which implies that the signal sampling length must be on the order of 1 mm. Since a sampling interval of 1 mm will generally not provide adequate deflection of the electron beam, the signal is routed along a sinuous path such that it crosses the beam path repeatedly, thus increasing the beam deflection by imparting multiple impulses to the beam. To maintain the fidelity of the recorded signal, the signal transit time along one loop of the sinuous path must match the beam transit time from one loop crossing to the next. To maintain this phase-matching condition, dispersion of the input signal along the path must be kept to a minimum.

The SCD5000 provides a 512 × 1024 (amplitude vs. time) digital record with 11-bit amplitude resolution (centroided) for a 5- or 10-V input transient with up to 5 ps of temporal resolution. Temporal recording windows range from 5 ns to 100 μs. The 3-dB frequency response limit is 5 GHz. The tube

[1] bucklera@nv.doe.gov, 925-960-2520

uses an unbalanced helical signal section which suffers from "narrow-wide" distortion (Kocimski, 1991). It features a unique dual-gun structure with the source gun for the signal section at one end and a readout gun for the diode recorder at the opposite end.

Project

A block diagram of the proposed replacement tube is shown in Figure 1. The tube consists of an electron-beam source followed by beam extraction, collimation, and focus sections, a planar serpentine traveling-wave signal section, a sweep section for the time base, and a recording surface.

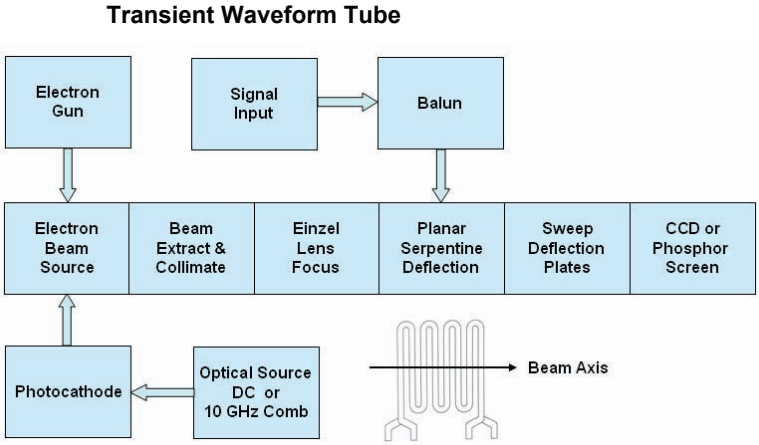

Figure 1. Transient waveform tube. Functional components of the transient waveform recorder. Either an electron gun or a photocathode could serve as the electron beam source. An external balun drives the dual push-pull serpentines. Either an internal CCD or a phosphor screen serves as the recording surface.

The 5-ns to 100-μs recording range of the SCD5000 implies a source intensity range of 20,000. This could easily be satisfied by an electron gun, but the design modeling was based on a photocathode pumped by an external optical source such as an LED or a 10-GHz comb. A comb generator would provide a self-calibrated temporal record with a fixed time increment between dots, but the comb rates and source intensity ranges needed to satisfy the targeted temporal range would require several different generators.

The beam source, extraction, collimation, and focus sections are cylindrically symmetric. The beam must be well collimated before reaching the Einzel lens, which focuses the beam to a spot on the screen. The dual serpentines and the sweep deflection plates are planar structures that deflect the beam in two orthogonal directions to yield a profile of signal amplitude versus time. A top view of a

balanced push-pull serpentine is shown in Figure 1, with separate input leads for the upper and lower serpentine planes. The electron beam travels between the two serpentine planes on the central axis of the windings as shown. An external balun converts the input signal to the required bipolar signal for the two serpentines.

An internal CCD recorder would provide high sensitivity to the swept electron beam, but a CCD in a sealed vacuum tube has never been attempted or demonstrated in the phototube facility at Livermore Operations (LO). A prototype tube would most likely be built with a phosphor screen. Digital recording of the phosphor image onto a CCD would be accomplished either via direct butt-coupling to the fiber-optic faceplate or via optical coupling.

To facilitate the operation of the proposed tube, an LED with output in the range of 500–550 nm would be used to match the peak response of the S-20 photocathode. The LED would be gated with a pulse width somewhat greater than the desired recording time window and with a pulse amplitude inversely proportional to the time width. The LED gate must be derived from a pre-event trigger to allow the LED to reach full output and to allow the resultant photoelectron beam to reach the sensing serpentine section before the transient signal to be recorded reaches the serpentine input.

The planar serpentines will be deposited on a pair of low-dispersion substrates to maintain signal fidelity. The backplane of each substrate will be at ground potential. Each serpentine loop will be isolated from its nearest neighbor by a guard electrode to minimize crosstalk. The serpentines must be designed such that the signal transit time along one loop exactly matches the electron transit time from loop to loop. Two parallel serpentines were studied via the CPO 2-D planar trajectory code, but a flared orientation would provide a higher deflection sensitivity at the cost of a more complicated serpentine design to maintain constant impedance. Transmission line designs (Shellman, 2006) will be used for both the serpentine and the sweep sections.

Initial modeling efforts addressed the balanced planar serpentine structure. Five CPO 2-D planar serpentine models with cell lengths of 2.5, 3, 3.5, and 5 mm, and deflection trace widths of 0.5, 0.7, and 1 mm were evaluated. The deflection impulse profiles, impulse FWHM, residual electric fields at cell boundaries, and deflection sensitivities from the five serpentine models were compared to select the optimum configuration for the final tube design. The configuration shown in Figures 2 and 3 consists of a balanced push-pull serpentine assembly with seven 3.5-mm cells composed of 0.5-mm trace widths with 1-mm deflection spacing. A 10-V deflection signal provides a 5-mm deflection for a 2-kV beam at 310 mm from the serpentine entrance.

As noted earlier, the effective sampling width of the serpentine traces needs to be on the order of 1 mm in order to faithfully impose a 10-GHz signal onto a 2-kV electron beam. Figure 4 shows the normalized electric field along the axis midway between the upper and lower serpentines for one of the 3.5-mm cells shown in Figure 2. The positions of the 0.5-mm signal trace and the two guard halves are shown. Note that the FWHM of the deflecting field is somewhat greater than twice the signal trace width. Also note that the field at the edge of the cell effectively vanishes.

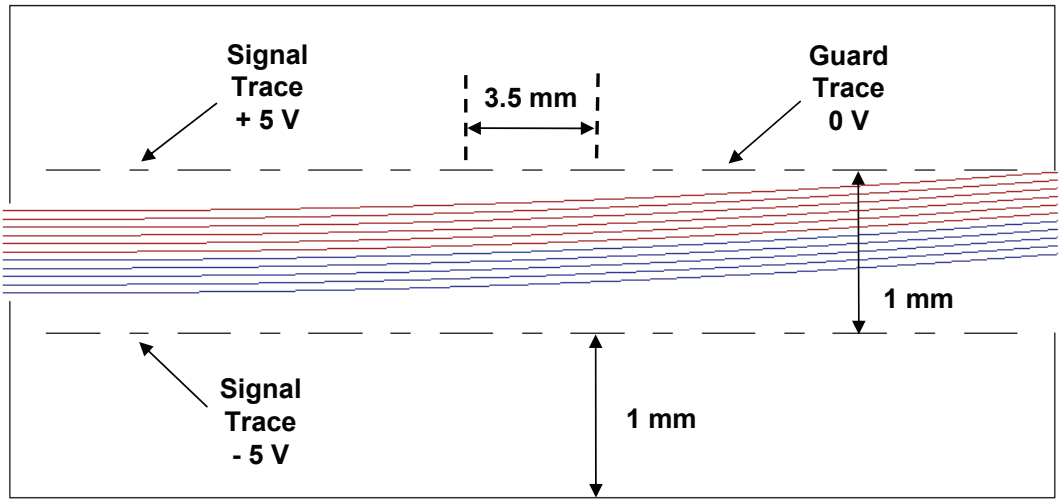

Figure 2. CPO 2-D planar model of a serpentine pair in profile (the serpentines wind in and out of the page on the signal traces; refer to Figure 3) separated by 1 mm with equal but opposite static potentials of 5 V on the upper and lower signal traces. Each of the seven 3.5-mm serpentine cells consists of a 0.5-mm signal trace separated from the 1.4-mm guard electrodes by 0.8-mm insulating gaps. The input and output apertures and the backplanes are at ground potential. The deflected trajectories for a 0.5-mm beam of 11 parallel 2-keV electrons entering from the left are shown. The total length for this serpentine structure is 28 mm.

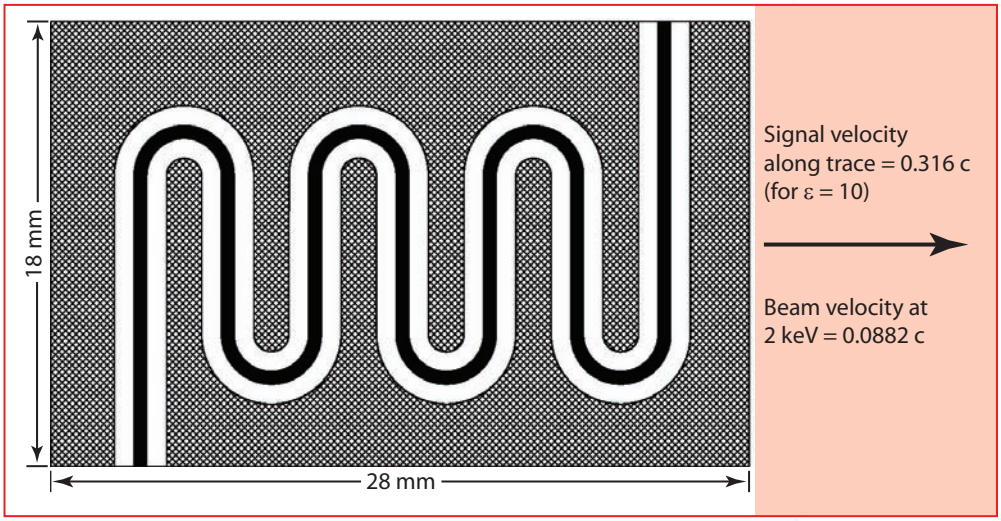

Figure 3. A drawing (top view) of the proposed serpentine with seven 0.5-mm-wide traces spaced at 3.5 mm along the horizontal beam path. The conductive serpentine (black) and guard (hatch) surfaces are deposited on a 1-mm thick alumina substrate which has a dielectric constant of 10. The 0.8-mm insulating gaps (white) are uncoated. The signal and beam velocities are given as a fraction of the speed of light. The substrate is 17.8 × 28 mm.

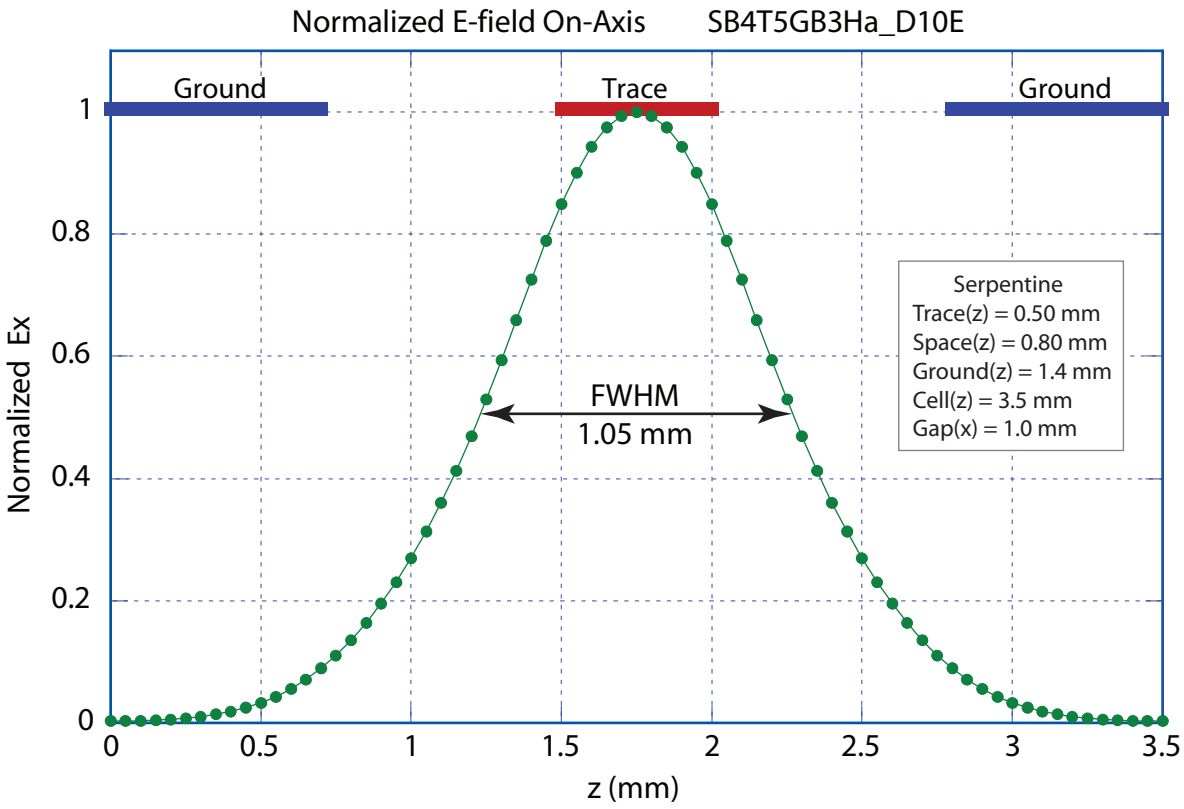

Figure 4. A plot of the normalized electric field along the axis of one 3.5-mm cell shown in Figure 2. Note that the field effectively vanishes at the edge of the cell.

The results from the five different serpentine deflection models are presented in Table 1. Note that the 2.5-mm cell yielded the narrowest field width (FWHM), but the highest residual field (percent of peak) at the cell boundary. The length of the serpentine section was determined by the requirement that the electron beam admitted through the 0.5-mm input aperture not impinge on the serpentine structure. The length of the drift region from the serpentine to the screen is determined by the transverse deflection velocity imparted by the serpentine, expressed in the table as deflection in μm per mm of axial drift. The total signal deflection length is the sum of the serpentine and drift lengths. Note that the deflection angle is very small, on the order of 1 degree.

A separate planar trajectory model showed that a pair of sweep plates 20-mm in length with 1.6-mm spacing and 5.5-V bias provided 5 mm of deflection at the screen for a 2-kV beam.

The cylindrical version of the CPO 2-D boundary element codes was used to design the front-end extraction and collimation section that provides a thin collimated electron beam along the tube axis.

To prevent damage to the photocathode from excessive photocurrent density, it is important to make the effective source area as large as possible while forming a well-collimated beam roughly 0.5 mm in diameter.

Table 1. Modeling results for five different serpentine geometries acting on a 2-keV electron beam with 10-V deflection across a 1-mm gap. The highlighted data corresponds to the serpentine model presented in Figures 2–4.

Serpentine Dimensions				Electric Field on Cell Axis		Serpentine Section			Drift Section	
Cell (mm)	Trace (mm)	Space (mm)	Ground (mm)	FWHM (mm)	E-min (% max)	No. of cells	Full Length (mm)	Total Deflect (μm)	Deflect Rate (μm/mm)	Drift Length (mm)
2.5	0.5	0.5	1.0	0.973	2.41	8	20	170.6	17.07	283
3.0	0.5	0.75	1.0	1.042	1.27	7	21	173.7	16.54	292
3.5	0.5	0.8	1.4	1.049	0.32	7	24.5	205.5	16.77	286
3.5	0.7	0.7	1.4	1.173	0.39	6	21	178.6	17.01	283
5.0	1.0	1.0	2.0	1.463	0.027	4	20	151.5	15.15	320

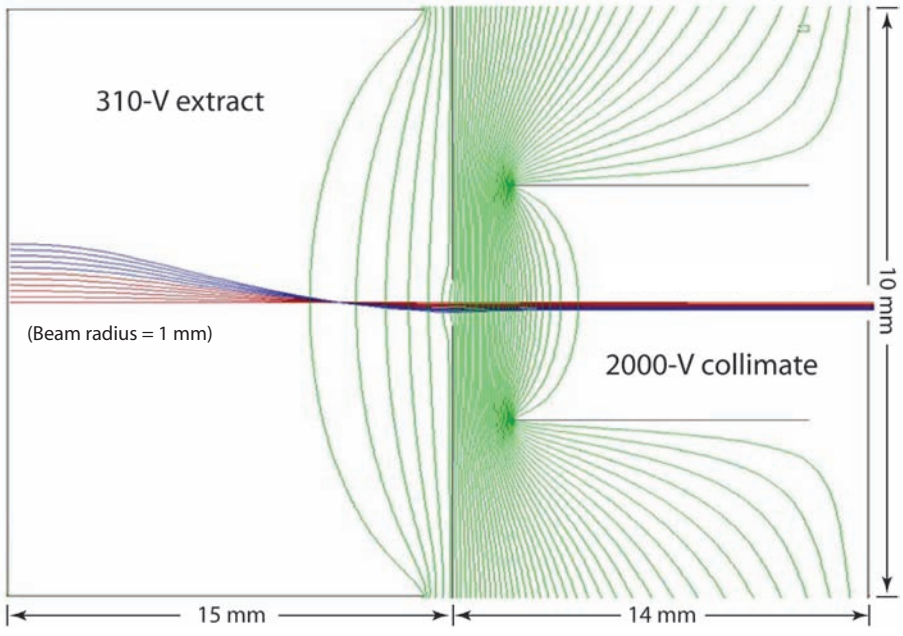

Figure 5. Beam extraction and collimation from a 1-mm radius on a flat cathode. The equipotential contour interval is 50 V.

Figure 5 shows a simple design consisting of a flat cathode inside a 10-mm-diameter cylinder at ground potential, a 0.8-mm aperture in a disk at 310 V, and a 4-mm-diameter cylinder at 2 kV. The parallel beam of 1-eV electrons emitted from a 1-mm radius at left is reduced to 0.24 mm at the 0.6-mm Einzel input aperture at right.

Figure 6 shows the trajectories in Figure 5 from the cathode to the sweep deflection plates. Note that the beam is slightly divergent, but this can be corrected by the triple-cylinder Einzel lens. The Einzel lens operates by adjusting the potential on the central cylinder while holding the input and output cylinders at a fixed potential. This allows the beam to be focused onto the output screen without affecting the beam velocity through the serpentine. The focusing half-angle for a collimated 0.5-mm beam traveling 310 mm from the serpentine entrance to the screen is 0.046 degree. This means that the beam entering the Einzel lens must have a divergence angle of <0.046 degree to achieve a sharp focus at the screen. The cylindrical model shown in Figure 6 also shows the relative length and spacing of the planar serpentine and sweep structures. In the actual tube one of these structures must be rotated by 90 degrees about the beam axis.

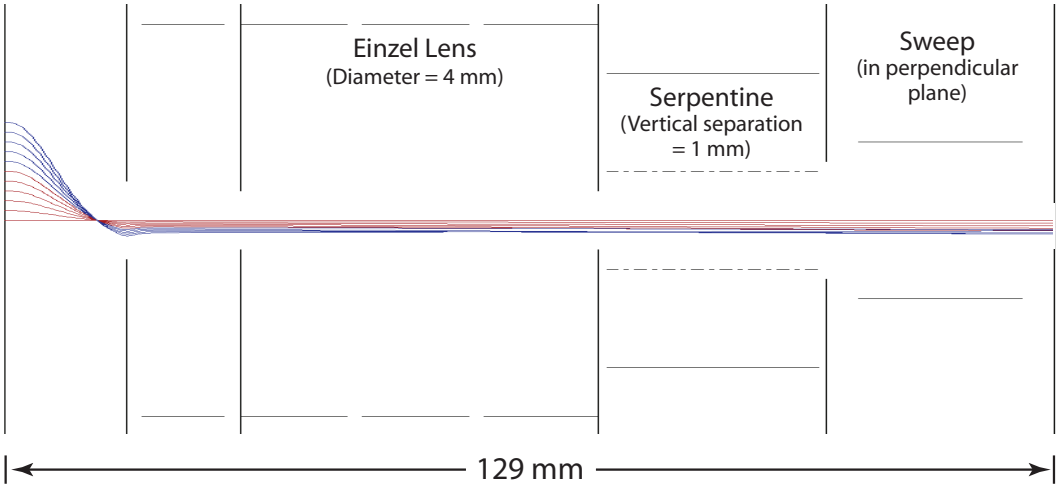

Figure 6. Extended view of the trajectories in Figure 5 with the 4-mm diameter collimation cylinder at left, followed by the triple-cylinder Einzel lens with 0.6-mm radius input and output apertures, the planar serpentine section with 1-mm deflection gap and backplanes at 1 mm, and the sweep deflection plates with a 1.6-mm gap. The total length of this section is 129 mm, which represents only one third of the entire tube since the drift region to the screen extends another 256 mm to the right.

As noted earlier, the electron beam entering the Einzel lens must be very well collimated. Since electron emission from a photocathode is characterized by a range of emission angles, a test run was made with six emission points ranging from 0 to 0.5 mm off-axis with emission angles of 0 ±1 degree from the cathode normal. The results are shown in Figure 7. Note that all the rays pass through the serpentine structure but those emitted at ±1 degree travel in separate groups roughly 0.18 degrees from the beam axis. Some of these rays would hit the deflection structures when deflected, but clearly most of the rays emitted in a cone with half-angle of 1 degree will reach the screen and form a 2-mm spot that will be swept across the 10-mm output screen.

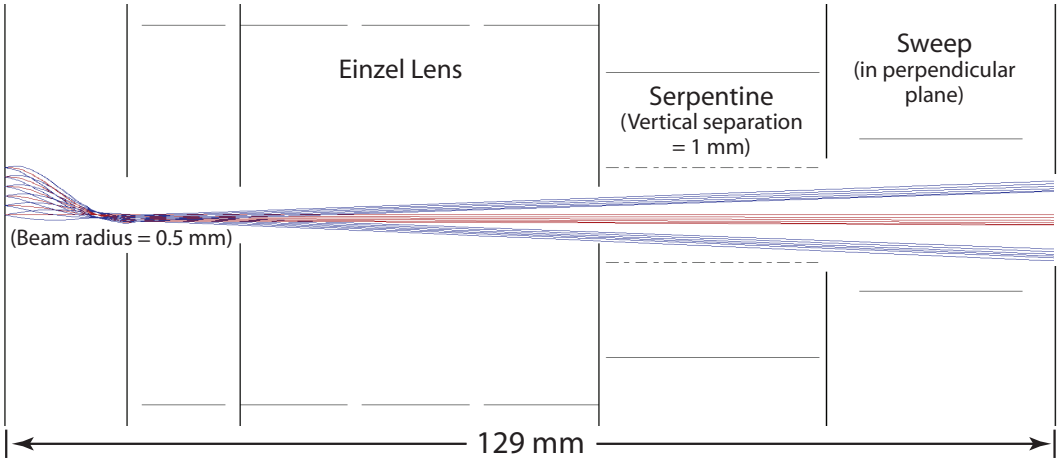

Figure 7. Electron trajectories for six emission points ranging from 0 to 0.5 mm off-axis with emission angles of 0 ±1 degrees from the cathode normal. The beam radius is 0.5 mm. The beam is not "collimated" through the deflection section, but spread out on various trajectories, nearly filling the aperture. The details of the lens design may impact the serpentine exit aperture. We envisioned having the plates angled apart to allow this spread.

The front-end models were run very late in the project, so this portion of the tube has not been optimized. It is possible that the extraction, collimation, and Einzel sections could all be shortened to allow for spatial filtering via a drift region with small input and output apertures preceding the Einzel focusing lens. This would serve to further collimate the beam by intercepting divergent rays. An extraction mesh or aperture near the photocathode plus a higher beam potential could also reduce the beam divergence. However, any increase in the beam potential would also require a longer serpentine section. Space-charge effects may need to be considered for the intense beam current required for high-speed sweeps. The overall tube length with input and output optics must be less than 440 mm in order to fit inside the photocathode process station.

Conclusion

This project used electron trajectory modeling to determine the tube geometry and operating conditions for a high-speed transient waveform recorder consisting of a photocathode pumped by an LED source; an extraction, collimation, and focus section; a traveling-wave signal section; a sweep section for the time base; and a phosphor screen/CCD combination for digital output. The front-end beam collimation needs to be improved via further modeling. Fabrication of a prototype tube will be pursued with programmatic funds.

Acknowledgments

Thanks are due to R. Buckles, LO, for consultation on serpentine, balun, and transmission-line theory and design; V. Tran, LO, for discussions and demonstrations of SCD5000 operation; and J. Blair, North Las Vegas, and K. Miller, Special Technologies Laboratory, for SCD5000 test reports and comparison tests with both analog and digital oscilloscopes.

References

CPO, Charged Particle Optics, boundary element code, CPO Ltd., http://www.electronoptics.com/, accessed September 28, 2006.

CPO, Charged Particle Optics, boundary element code, http://www.simion.com/cpo/, accessed September 28, 2006.

Kocimski, S. M., "Analysis and design of multi-gigahertz oscilloscope deflection structures," *IEEE Trans. Electron Devices* **38**, 6 (June 1991) 1524.

Shellman, R. A., "Optimization of Streak Tube Temporal Resolution," *Nevada Test Site–Directed Research, Development, and Demonstration*, FY 2005, Bechtel Nevada, Las Vegas, Nevada, 2006, 107–112.

this page intentionally left blank

Zero Wind Plume Model

Patrick Sawyer,[1] *Rick Venedam*
North Las Vegas

Atmospheric plume dispersion models are used for a variety of purposes including emergency planning and response to hazardous material releases, determining force protection actions in the event of an attack involving weapons of mass destruction, and for locating sources of pollution. Our project considered the principles used to derive air dispersion plume models and examined three specific models currently in use: Aerial Location of Hazardous Atmospheres (ALOHA), Emergency Prediction Information Code (EPIcode), and Second Order Closure Integrated Puff (SCIPUFF). Results from this study indicate over-prediction bias by the EPIcode and SCIPUFF models and under-prediction bias by the ALOHA model. The experiment parameters were for near field dispersion (less than 100 m) in low wind speed conditions (less than 2 m/sec).

Background

Gaussian plume dispersion models are widely used by emergency response personnel and environmental regulators. In wind speeds greater than 2 m/sec, advection dominates, and the plume forms a cone shape with the tip at the plume source. Within this cone, chemical species generally disperse in a Gaussian pattern, allowing for generally accurate prediction of downwind chemical plume concentrations by the plume models. In low wind conditions (0–2 m/sec), advection no longer dominates over diffusion, and the Gaussian distribution may no longer be valid. This may result in over-prediction of plume centerline concentrations under weak wind conditions.

Project

In this project, several plumes were produced in low wind conditions, and plume concentration data were collected to compare against three publicly available dispersion models. The models chosen for evaluation were ALOHA, EPIcode, and SCIPUFF. ALOHA and EPIcode are used by federal agencies for emergency planning and response operations, and SCIPUFF is the atmospheric dispersion model used by the U.S. Defense Department as part of their Hazard Prediction Assessment Capability (HPAC) program. The goal of this research was to determine the accuracy of these commercial models in predicting plume concentration in low wind conditions.

[1] sawyerps@nv.doe.gov, 702-295-4406

A total of 32 data sets were obtained from the release experiments. Two sets of data were not considered for further analysis due to zero readings from the photoionization detectors (PIDs). Factors such as a narrow plume width, meander, and loft can result in plumes missing detectors in the grid. To limit the lofting due to the high flow rates associated with the ethylene and propylene releases, a deflector plate was installed above the release tubes. This plate reduced the vertical velocity component at the release point, decreasing the chance that the plume would carry over the PID array.

Table 1A. Ammonia experiment (measured data)

Ammonia Experiment	Release									
	1	2	3	4	5	6	7	8	9	10
Mean Flow Rate (kg/hour)	0.73	0.49	1.10	1.54	2.04	0.68	2.02	1.65	1.03	0.76
Mean Temperature (°C)	1.26	1.44	2.05	2.27	2.33	3.38	5.33	7.00	8.29	9.10
Avg Wind Speed (m/sec)	1.46	1.21	0.88	1.20	0.80	0.75	0.74	1.59	2.16	2.60
Avg Wind Direction (°N)	40.76	97.98	80.10	63.68	67.85	186.33	198.86	162.53	208.03	236.34
Avg Wind Dir, Std Dev (σ_θ)	25.23	15.66	14.91	17.30	18.04	110.02	70.19	21.25	19.13	11.52
Stability Class	A	C	C	C	B	A	A	B	B	D
Run Time (min.)	0:07:06	0:05:00	0:05:04	0:04:56	0:04:58	0:20:00	0:20:02	0:20:00	0:20:02	0:20:02

Table 1B. Ammonia experiment (observed and predicted concentrations)

Release	1	2	3	4	5	6	7	8	9	10
PID Observations (highest 2-min. average on each ring)										
2-min. avg, 10 m C_o (ppm)	27.79	121.31	35.13	57.42	72.81	25.782	35.846	45.621	8.545	0.886
2-min. avg, 25 m C_o (ppm)	55.881	35.09	11.21	18.84	2.01	7.686	7.93	2.644	4.841	4.08
2-min. avg, 50 m C_o (ppm)	8.977	23.70	0.00	5.8	3.84	1.7	0.304	0.406	1.971	1.857
2-min. avg, 100 m C_o (ppm)	0.911	5.22	0.13	2.5	4.31	2.73	0.078	0.039	0.144	0.022
ALOHA Predictions										
Centerline, 10 m C_p (ppm)	7.83	2.28	6.89	7.24	33.2	11.8	35.3	15.6	7.21	0.251
Centerline, 25 m C_p (ppm)	1.91	5.06	15.3	16.1	17.1	2.87	8.6	8.03	3.71	4.54
Centerline, 50 m C_p (ppm)	0.507	1.85	5.6	5.88	5.04	0.764	2.29	2.37	1.1	2.29
Centerline, 100 m C_p (ppm)	0.129	0.512	1.55	1.63	1.32	0.194	0.581	0.62	0.286	0.708
EPIcode Predictions										
Centerline, 10 m C_p (ppm)	11.00	40.00	120.00	130.00	120.00	20.00	62.00	48.00	22.00	54.00
Centerline, 25 m C_p (ppm)	2.80	7.30	23.00	23.00	26.00	5.0	15	11	4.9	8.9
Centerline, 50 m C_p (ppm)	0.77	2.60	8.00	8.2	8.4	1.4	4.2	3.4	1.6	3.1
Centerline, 100 m C_p (ppm)	0.20	0.77	2.4	2.4	2.3	0.36	1.1	0.93	0.43	1.0
SCIPUFF Predictions										
Centerline, 10 m C_p (ppm)	20.94	18.36	41.39	49.52	93.01	22	62.87	53.94	29.58	14.43
Centerline, 25 m C_p (ppm)	7.67	6.01	13.46	17.76	26.58	7.41	21.07	20.95	10.87	8.1
Centerline, 50 m C_p (ppm)	4.18	3.02	5.75	8.7	7.47	3.7	10.96	9.01	5.37	3.88
Centerline, 100 m C_p (ppm)	1.99	1.39	1.23	2.61	1.27	1.48	4.14	5.27	2.97	2.11

Experimental Observations

Process data from the process control systems and weather data from the local weather stations for each of the chemical releases are shown in Tables 1A, 2A, and 3A for ammonia, ethylene, and propylene, respectively. The observed two-minute average PID and model-predicted centerline concentrations are shown in Tables 1B, 2B, and 3B.

Table 2A. Ethylene experiment (measured data)

Ethylene Experiment	Release								
	1	2	3	4	6	7	8	9	10
Mean Flow Rate (kg/hour)	1.00	2.00	4.83	10.42	1.01	2.00	5.07	10.27	19.74
Mean Temperature (°C)	3.12	3.59	3.77	3.77	3.76	3.76	3.77	3.77	3.77
Avg Wind Speed (m/sec)	1.54	1.53	1.86	2.22	1.13	1.17	1.14	1.50	1.12
Avg Wind Direction (°N)	199.16	158.98	96.73	92.68	142.50	96.31	242.91	217.60	150.65
Avg Wind Dir, Std Dev (σ_θ)	20.64	8.03	8.32	8.96	29.21	26.19	41.49	24.97	40.47
Stability Class	B	D	D	D	A	A	A	A	A
Avg Wind Pitch, Std Dev (σ_z)	5.04	5.31	6.46	6.53	8.68	10.49	16.01	12.66	17.82
Surface Roughness Length (z_o)	0.0003	0.0003	0.0003	0.0003	0.0003	0.0003	0.0003	0.0003	0.0003
Run Time (min.)	0:05:00	0:04:56	0:04:58	0:05:02	0:19:58	0:20:02	0:20:02	0:20:00	0:20:00

Table 2B. Ethylene experiment (observed and predicted concentrations)

Release	1	2	3	4	6	7	8	9	10
PID Observations (highest 2-min. average on each ring)									
2-min. avg, 10 m C_o (ppm)	9.083	13.55	101.85	234.871	20.502	18.414	57.77	167.782	118.977
2-min. avg, 25 m C_o (ppm)	1.917	0.13	29.67	101.85	6.23	4.898	13.373	54.545	70.354
2-min. avg, 50 m C_o (ppm)	0.987	0.90	12.28	28.91	0.58	1.687	4.564	5.08	23.028
2-min. avg, 100 m C_o (ppm)	0.197	0.70	2.44	11.108	0.488	0.16	0.499	1.785	2.438
ALOHA Predictions									
Centerline, 10 m C_p (ppm)	5.12	0.619	2.58	4.67	5.48	10.8	27.5	55.7	107
Centerline, 25 m C_p (ppm)	2.63	11.2	46.7	84.4	1.33	2.64	6.7	13.6	26.1
Centerline, 50 m C_p (ppm)	0.778	5.66	23.6	42.6	0.355	0.702	1.78	3.61	6.93
Centerline, 100 m C_p (ppm)	0.203	1.75	7.28	13.2	0.0902	0.179	0.453	0.917	1.76
EPIcode Predictions									
Centerline, 10 m C_p (ppm)	18	150	290	520	12	23	61	94	240
Centerline, 25 m C_p (ppm)	4.1	24	48	87	3	5.7	15	23	59
Centerline, 50 m C_p (ppm)	1.3	8.3	17	30	0.83	1.6	4.1	6.4	16
Centerline, 100 m C_p (ppm)	0.35	2.8	5.5	9.9	0.21	0.41	1.1	1.6	4.2
SCIPUFF Predictions									
Centerline, 10 m C_p (ppm)	19.78	30.7	54.83	114.48	20.09	39.73	71.05	118.65	249.8
Centerline, 25 m C_p (ppm)	7.57	15.18	26.47	49.88	7.11	14.03	31.06	61.63	103.37
Centerline, 50 m C_p (ppm)	3.74	7.5	14.93	28.85	3.48	6.88	16.98	30.15	59.12
Centerline, 100 m C_p (ppm)	1.83	3.67	8.39	16.24	1.98	3.81	9.05	17.47	29.1

Table 3A. Propylene experiment (measured data)

Propylene Experiment	Release										
	1	2	4	5	6	7	8	9	10	6B	Bonus
Mean Flow Rate (kg/hour)	1.00	2.00	9.80	19.39	1.03	2.04	5.18	10.16	19.76	1.28	1.04
Mean Temperature (°C)	14.00	13.92	3.77	3.77	5.00	2.68	3.77	16.12	14.81	0.73	6.20
Avg Wind Speed (m/sec)	1.42	1.79	1.35	1.48	1.62	1.64	1.84	1.63	1.27	1.98	1.38
Avg Wind Direction (°N)	240.72	269.60	173.49	147.49	98.21	64.53	163.20	193.27	207.51	104.44	139.29
Avg Wind Dir, Std Dev (σ_θ)	22.74	29.68	16.12	16.08	34.90	17.57	12.78	18.53	19.61	101.10	22.47
Stability Class	A	A	C	C	A	B	C	B	B	A	B
Run Time (min.)	0:05:00	0:04:58	0:04:58	0:04:54	0:20:56	0:20:58	0:20:00	0:19:56	0:19:56	0:20:14	0:30:04

Table 3B. Propylene experiment (observed and predicted concentrations)

Release	1	2	4	5	6	7	8	9	10	6B	Bonus
PID Observations (highest 2-min. average on each ring)											
2-min. avg, 10 m C_o (ppm)	3.324	0.16	69.681	30.17	11.161	28.127	52.91	107.911	5.886	66.904	10.639
2-min. avg, 25 m C_o (ppm)	4.934	2.66	20.34	28.44	4.391	4.445	22.724	43.11	37.701	12.397	6.22
2-min. avg, 50 m C_o (ppm)	3.85	0.76	2.97	8.012	0.355	1.114	6.113	11.735	15.871	4.82	0.196
2-min. avg, 100 m C_o (ppm)	1.759	0.19	0.271	5.283	2.134	5.033	3.526	20.851	29.054	2.408	1.992
ALOHA Predictions											
Centerline, 10 m C_p (ppm)	3.75	14.4	12.9	25.6	3.74	6.95	12.6	36.3	70.3	7.95	3.59
Centerline, 25 m C_p (ppm)	0.913	3.51	28.7	56.9	0.911	3.57	27.9	18.7	36.1	1.94	1.84
Centerline, 50 m C_p (ppm)	0.243	0.933	10.5	20.8	0.242	1.06	10.2	5.52	10.7	0.515	0.546
Centerline, 100 m C_p (ppm)	0.0618	0.237	2.91	5.75	0.0616	0.276	2.82	1.44	2.79	0.131	0.143
EPIcode Predictions											
Centerline, 10 m C_p (ppm)	6.4	10	290	530	5.8	23	110	120	290	5.9	14
Centerline, 25 m C_p (ppm)	1.6	2.5	53	96	1.4	5.2	21	26	65	1.4	3.1
Centerline, 50 m C_p (ppm)	0.44	0.69	19	34	0.39	1.7	7.3	8.3	21	0.4	1.0
Centerline, 100 m C_p (ppm)	0.11	1.8	5.6	10	0.1	0.45	2.2	2.2	5.6	0.01	0.27
SCIPUFF Predictions											
Centerline, 10 m C_p (ppm)	12.83	24.97	81.75	149.8	13.18	26.38	39.39	86.94	154.5	14.78	12.98
Centerline, 25 m C_p (ppm)	4.69	10.64	37.96	68.54	4.73	9.96	18.89	41.91	71.18	5.85	4.97
Centerline, 50 m C_p (ppm)	2.6	4.91	21.8	36.63	2.57	4.63	10.85	23.01	41.5	2.78	2.47
Centerline, 100 m C_p (ppm)	1.35	2.54	11.27	18.29	1.35	2.69	6.09	12.84	23.06	1.51	1.4

Statistical Analysis

Simple scatter plots of the predicted versus observed concentrations were used to compare the models' performance with the observed data.

The chart in Figure 1 includes trend lines to show the relative over-prediction of the EPIcode data and the relative under-prediction of the ALOHA data. The SCIPUFF trend line indicates relative over-prediction at lower concentrations and relative under-prediction at higher concentrations. The significant scatter in the EPIcode data is easily seen.

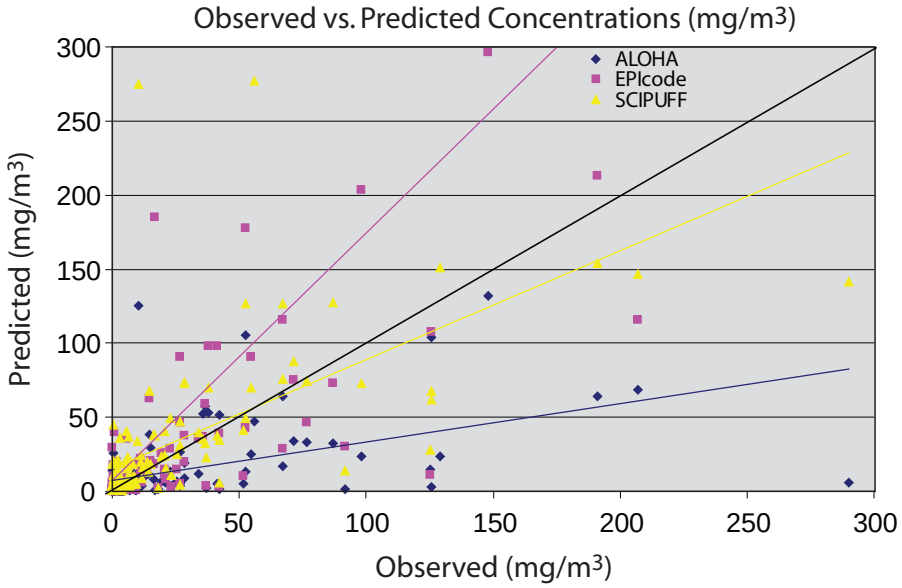

Figure 1. Observed vs. predicted concentrations

Figure 2 is a scatter plot of the data after it was normalized by dividing the observed and predicted concentrations by the flow rates for each experiment. The trend lines for all three models are below the 1-to-1 line, indicating general under-prediction, in the region above 0.04 s/m^3. Below that normalized value, the EPIcode and SCIPUFF trends are above the 1-to-1 line, indicating general over-prediction, while the ALOHA trend line only exceeds the 1-to-1 line in the region below 0.01 s/m^3.

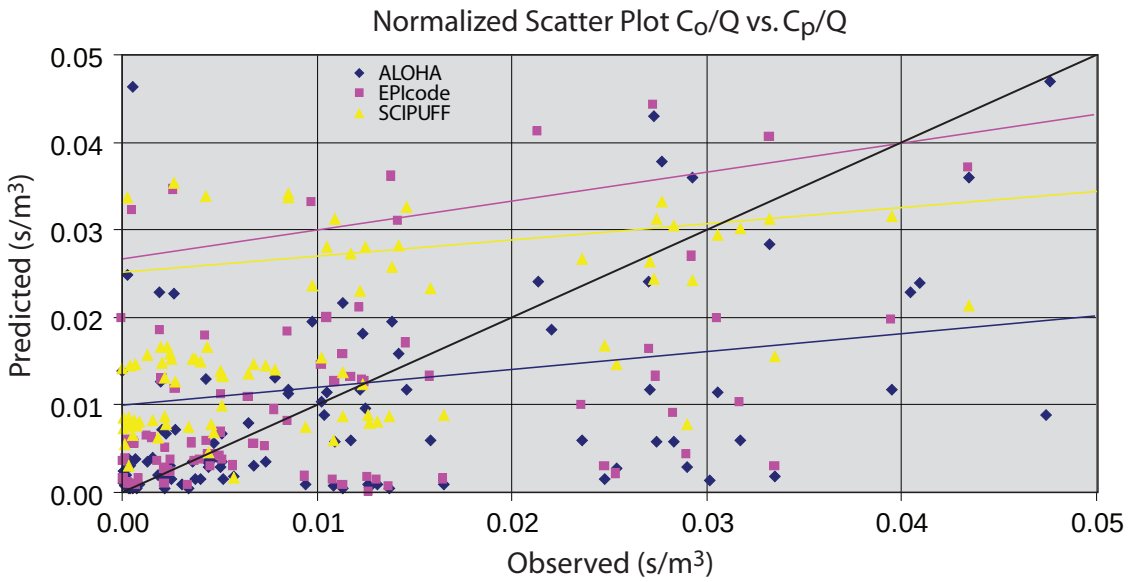

Figure 2. Observed vs. predicted concentrations (normalized)

Table 4 lists the data for the six statistical performance measurements considered for the thirty experiments analyzed. The FAC2 analysis shows the number of predictions within a factor of two of the observations. Chang and Hanna (2004) note that a FAC2 of greater that 0.5 is representative of a "good" model (for wind speeds over 2 m/sec).

Table 4. Overall model performance summary data

Factor	Summary		
	ALOHA	EPIcode	SCIPUFF
FAC2	0.4000	0.4583	0.4250
R	0.0343	0.0437	0.2099
NMSE	7.7366	4.0864	2.2912
FB	0.8863	0.1522	–0.0694
VG	25.5082	17.4223	51.5825
MG	1.6185	0.7093	0.4311

Legend: FAC2 = fraction of data within a factor of 2; R = correlation coefficient; NMSE = normalized mean square error; FB = fractional bias; VG = geometric variance; MG = geometric mean bias.

The FAC2 data (Figure 3) show all three models are below the 0.5; however, considering the fact that these data are all at low wind speeds in the near field region, the values of 0.40 to 0.45 should be considered reasonable.

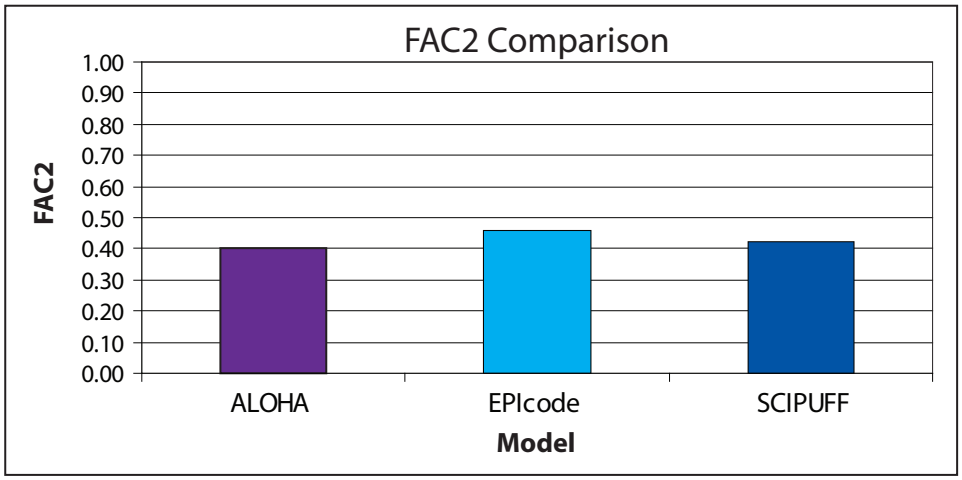

Figure 3. FAC2 data vs. model

The correlation coefficient (R) is a measure of how well the variables agree. A perfect correlation has a value of 1.0, while no correlation between the variables gives an R of 0. All three models have low correlation coefficients; the SCIPUFF predictions, R = 0.2099, shows the highest correlation to the observed data.

The normalized mean square error (NMSE) indicates the degree of deviation between predicted and observed data. A perfect model will have an NMSE of zero. If the mean value of the predicted data and the mean value of the observed data are the same, then the NMSE would equal 1.0. Using the NMSE performance measure, the SCIPUFF predictions show the closest agreement with the observations, followed by EPIcode and then ALOHA.

Fractional bias (FB) provides an indication of a model's tendency to over-predict or under-predict. Values for FB can range from –2 to 2 with 0 being ideal. ALOHA and EPIcode have positive FB values indicating a bias to under-predict plume concentrations. SCIPUFF, with an FB of –0.069, shows a slight bias towards over-prediction. It is worth noting that the FB calculation looks at the mean value of the observed and predicted data, which causes the FB data to favor the higher numbers. This is clearly demonstrated by looking at the EPIcode data. There are 120 pairs of observed-predicted data, and EPIcode over-predicted 72 of those data points and under-predicted 48. This would suggest an over-prediction bias. However, since most of the over-predictions are for low values, when the mean values are taken, the FB shows an under-prediction bias.

Geometric variance (VG) is a measurement of the mean relative scatter of the data points. SCIPUFF VG data indicate significant scatter among the predicted versus observed data points, while ALOHA shows moderate scatter, and EPIcode demonstrates the least amount of relative scatter.

Geometric mean bias (MG) measures the relative mean bias of the data; values below 1 indicate an over-prediction bias and values above 1 indicate an under-prediction bias. From the data in Table 4, ALOHA has an under-prediction bias, while EPIcode and SCIPUFF have an over-prediction bias. This is in line with the actual number of over-prediction versus under-prediction data points for the three models. ALOHA under-predicted 79 times and over-predicted 41 times, while SCIPUFF under-predicted 38 times and over-predicted 82 times.

Results

Figures 4 and 5 show the over-prediction versus under-prediction bias for the three models.

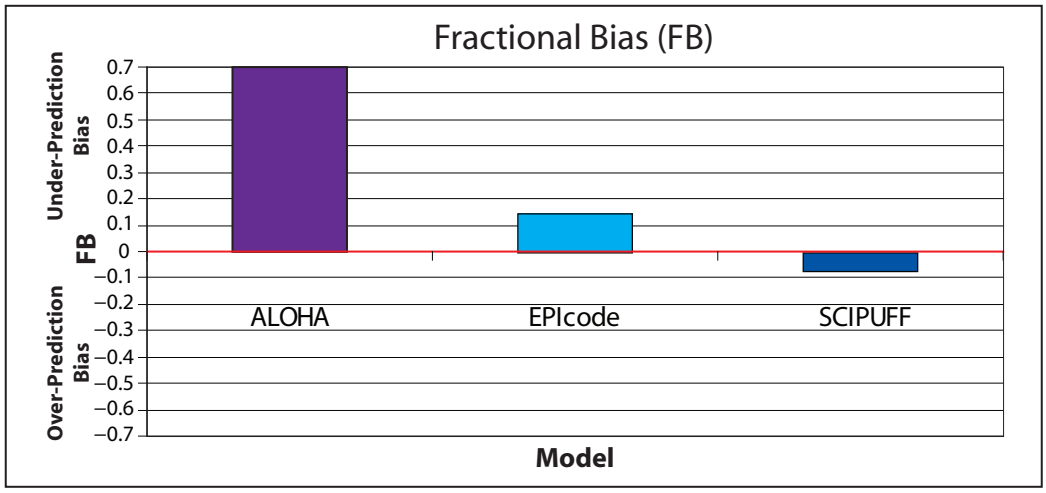

Figure 4. FB data vs. model

The results of these experiments demonstrate that the SCIPUFF model predictions agree with the hypotheses that Gaussian plume dispersion models tend to over-predict downwind plume concentrations in low wind conditions. The EPIcode analysis is not as clear. Although the FB data indicate a slight under-prediction bias, the MG data indicate a slight over-prediction bias. Just considering the number of under-predictions versus over-predictions of all the data sets, EPIcode over-predicted the concentrations nearly twice as often as it under-predicted. Since the FB data compare the mean observed and predicted values, the data are weighted for higher values; a few very large value under-predictions can outweigh many small value over-predictions. This suggests that EPIcode over-predicts at low values and under-predicts at high values.

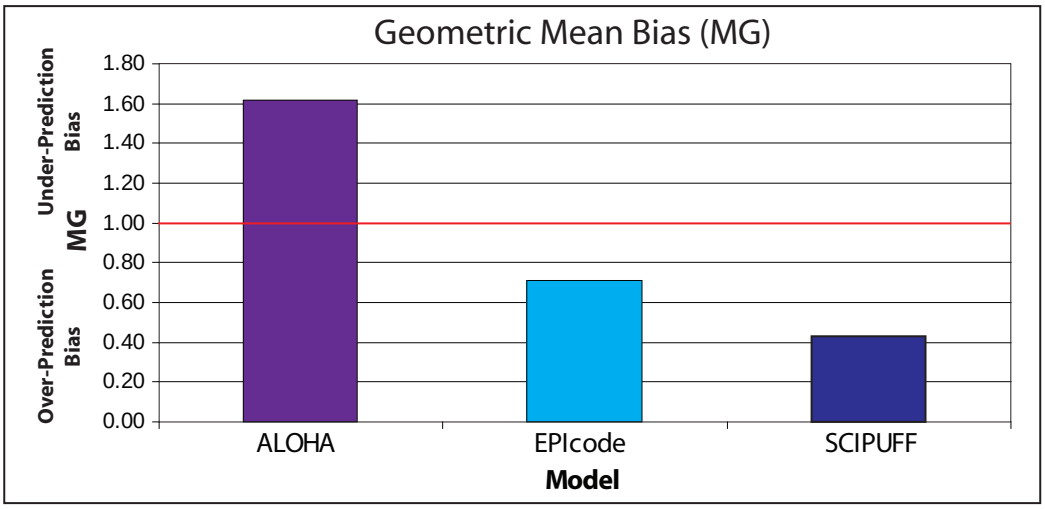

Figure 5. MG data vs. model

The ALOHA predictions agree with the null hypotheses that models under-predict downwind plume concentration in low wind conditions. The tendency of ALOHA to under-predict can be attributed to the model's tendency to force higher wind speeds than the input data based on internal model parameters that did not allow for the use of the actual observed meteorological data. ALOHA has minimum wind speeds for each stability class. In 19 out of 30 experiments, the observed wind speeds were below the minimum allowable wind speed input for the observed stability class. In each of the 19 cases, ALOHA forced a higher wind speed input, resulting in a lower predicted concentration.

The statistical analysis demonstrated that the EPIcode predictions were the most consistent with observations, with approximately 46% of model predictions within a factor of two of the observations. SCIPUFF was next with approximately 42% of predicted values within a factor of two of observations, and ALOHA produced nearly 40% of its predictions within a factor of two of the observed values. Considering the significant uncertainty associated with low wind speed plume dispersion, the FAC2 values seem very reasonable.

This experiment was set up to collect data relating to how models perform based on distance from the release point, mass flow rate, molecular weight, and duration of the release. The downwind distance comparison showed the highest correlation between model prediction and observation at the middle rings and significant deviation from observation at the innermost and outermost rings for ALOHA and EPIcode, while SCIPUFF predictions were closest to observation for distances of 10 and 25 m, followed by 100 m and, finally, 50 m. The mass flow rate comparison shows slightly more consistent results from high flow releases compared to low flow releases. However, this data may be somewhat

skewed in that the low flow data are predominantly ammonia, while the high flow data do not include any ammonia. Given that all the models poorly predict ammonia concentrations, the mass flow rate analysis should not be given too much weight in the overall analysis.

The use of ammonia, ethylene, and propylene was designed to detect any bias in how the models would predict based on molecular weight. ALOHA and EPIcode were most accurate in predicting ethylene concentrations. Ethylene, with a molecular weight nearly that of air, acts as a neutrally buoyant gas. The ammonia, which is lighter than air and acts as a buoyant gas, and the propylene, which is heavier than air and acts as a dense gas, both produced model predictions that were less consistent with observations than the ethylene predictions. In contrast, SCIPUFF was the most accurate with propylene, followed by ammonia, then ethylene. The release duration comparison was consistent with the hypothesis that the longer duration releases will result in less data scatter with less chance of extreme values in the prediction versus observation data sets.

In summary, all three models performed reasonably well considering the significant uncertainty associated with low wind speed releases. However, for the purposes of this analysis, EPIcode was the most accurate. EPIcode was also the easiest model to use. It comes with an extensive chemical database, and, since it generally over-predicted, it is considered a conservative model for downwind chemical concentration prediction. This experiment also demonstrated that caution should be exercised when using ALOHA to model low wind speed releases. The model is not designed for such conditions and the predictions tend to under-predict observed concentrations.

Conclusion

The goals of this study were to determine which model predictions most closely correlate with the observed data and to test the hypothesis that Gaussian dispersion models over-predict plume concentrations in low wind speed conditions. When comparing the performance of different models, the most important factor is how well the model predictions match actual data. The FAC2 data is the one statistical measure of how close the predictions come to matching the observations. Therefore, FAC2 is used to determine which model actually performs closest to reality. The FAC2 data, as shown in Figure 3, indicate that EPIcode agrees most closely with the observed data.

Reference

Chang, J., S. Hanna, "Air quality model performance evaluation," *Meteorology and Atmospheric Physics* **87**, 1–3 (2004) 167–196.

Prototyping Portable Detector with Multiple SPRT Options

Warnick Kernan, Ding Yuan[1]
Remote Sensing Laboratory – Nellis

A search software prototype for a Windows-driven mobile platform for an in-house portable detector has been developed. This prototype implemented the sequential probability ratio test (SPRT) algorithm, evaluated in FY 2006 and completed in FY 2007. This software offers multiple options on population distribution, confidence selection, stop handling, alarm calculation, and other execution controls. Initial evaluation suggests that this prototype offers three main advantages over the current algorithm for the in-house detector: adjustable mission-specific confidence levels, reduced false alarm rates, and reduced spatial uncertainties.

Background

The search algorithm investigated by this project was based on the SPRT method in its forward form proposed and studied by Wald (2004). In our FY 2006 project, we studied the SPRT algorithm in the forward form for radiation detection (Kernan and Yuan, 2007). The FY 2007 project developed a reversed SPRT scheme that better suited the field-continuous survey applications. The basic features of the SPRT method include dynamic sample size and two-way controllable confidence levels. The reversed SPRT scheme offers the additional capability of making decisions continuously, thus eliminating the waiting period needed for the forward SPRT scheme.

This year's work primarily focused on algorithm refinement, multiple options comparisons, and software prototype implementation. Although some algorithmic details about the SPRT method were reported in our FY 2006 report, for the purpose of continuity and thoroughness we will review the algorithm in order to better point out the differences between forward and reversed SPRT. We also describe improvements made to SPRT and the software implementation.

Project

Forward SPRT Method

The forward SPRT scheme shown in Figure 1 (left) is Wald's original form (Wald, 2004). Let us consider a one-second gamma gross counts (GC) sequence $x_1, x_2, \ldots x_k$, that can be either from a background, i.e., the null distribution $H_0 \sim f_0(x)$, or from a source (plus background), i.e., the alternative distribution $H_1 \sim f_1(x)$. The conventional search algorithm needs to make a decision by choosing

[1] yuand@nv.doe.gov, 702-295-8735

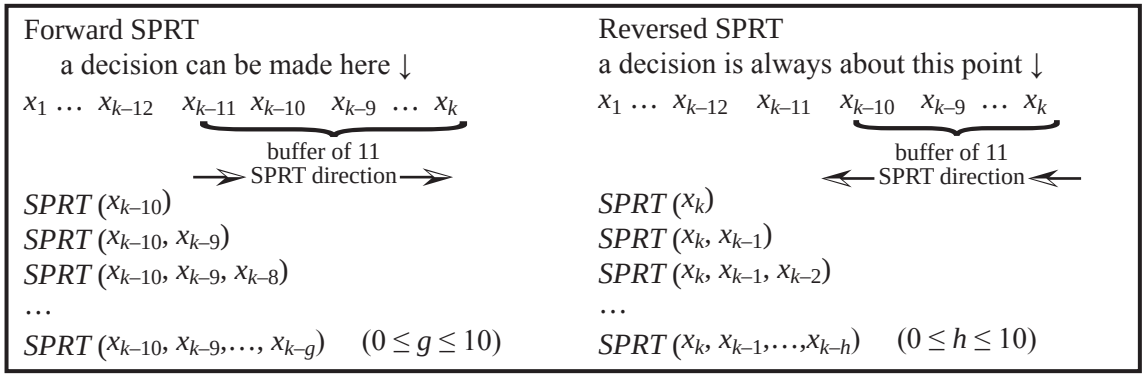

Figure 1. Schematic comparison of forward and reversed SPRT schemes

between the two hypotheses based on the current x_k and historical observations. The forward SPRT method offers a third decision option—no decision is made if prescribed confidence levels can not be reached. If this is the case, an additional sample is drawn or the algorithm waits for x_{k+1} to arrive. Essentially, the SPRT method computes the following log-likelihood probability ratio,

$$LLR_k = \log\left(\left(f_1(x_1)f_1(x_2)\ldots f_1(x_k)\right)/\left(f_0(x_1)f_0(x_2)\ldots f_0(x_k)\right)\right), \quad (1)$$

and makes decisions according to rules put forth by Wald:

If $LLR_k < A$, then accept H_0;

If $LLR_k > B$, then accept H_1;

If $A \le LLR_k \le B$, then take one additional sample and recompute LLR_k;

where $A = \log(\beta/(1-\alpha))$ and $B = \log((1-\beta)/\alpha)$ are decision thresholds; and $\alpha = \Pr ob(H_1 \mid H_0)$ and $\beta = \Pr ob(H_0 \mid H_1)$ are pre-specified, acceptable false positive and false negative rates.

The apparent advantage of the forward SPRT scheme is that it offers confidence control of decisions, as well as accepting potentially smaller sampling sizes. The drawback of the scheme is that it may not have a decision for every data point. This is not a desirable nature for field radiation technicians. In FY 2006, we attempted a backward-overlapping approach (originally called the FIFO or First-In First-Out scheme) that would force the program to make a decision at each data point. However, this backward-overlapping approach could potentially make a decision without even using the most recent data point. In other words, the decisions made by the backward-overlapping approach may contain spatial errors.

Reversed SPRT Method

In order to resolve the dilemma we faced in the forward SPRT approach, we devised a reversed SPRT scheme in FY 2007. In the reversed scheme, if x_k arrives, we compute the log-likelihood probability ratio in a reversed manner,

$$LLR_{k-i} = \log\left(\left(f_1(x_k)f_1(x_{k-1})\ldots f_1(x_{k-i})\right)/\left(f_0(x_k)f_0(x_{k-1})\ldots f_0(x_{k-i})\right)\right), \quad \textbf{(2)}$$

and make a decision according to the following rules:

If $LLR_{k-i} < A$, then accept H_0;

If $LLR_{k-i} > B$, then accept H_1;

If $A \le LLR_{k-i} \le B$, then take another data point from history and recompute LLR_{k-i-1}.

The difference between the forward and reversed SPRT schemes with a historical buffer of size 11 is shown schematically in Figure 1 (right). All notations follow early definitions. Assuming that the data history is sufficiently long, a decision would be made at some point (without need for waiting for x_{k+1} to arrive). The reversed SPRT scheme solved the dilemma inherent in the forward SPRT scheme.

The Software Prototype

A software prototype has been developed for a Windows mobile platform for an in-house radiation detector. This prototype offered both forward and reversed SPRT options. Selected screen captures of the prototype software are shown in Figure 2. The software prototype was demonstrated for Remote Sensing Laboratory (RSL) operation managers and field radiation technicians. The significant false alarm rate reduction in the prototype has attracted the attention of the observers.

Key Software Features

Hypothesis Options

Please note that neither forward nor reversed SPRT methods described earlier offered any specifics about the calculations of the background and distributions. Procedures were developed through this and previous SDRD projects (Yuan, 2007) for computing the distributions under various assumptions. The software prototype offers different hypotheses for background and sources. Generally, we recommend choosing normal for background and Poisson for source.

Figure 2. Selected screen captures of the software prototype for RSL in-house radiation detector; (left) hypothesis settings, (center) confidence settings, (right) execution window.

Confidence Settings

For generic emergency response missions, the recommended settings are: (1) generic applications (default) – α = 0.01 and β = 0.05, and (2) special nuclear materials detection – α = 0.05 and β = 0.01.

Forward/Reversed SPRT Selections

In the prototype, both forward and reversed SPRT algorithms were implemented. For operational adaptation, the forward version can be removed for improving the software efficiency.

Distribution Mean Estimations

For this prototype, two options were offered for estimating the Poisson population mean: the conventional arithmetic averaging method and the maximum likelihood estimator (MLE) derived by Mukhopadhyay (2004), where the MLE for the mean is:

$$\hat{\mu}_{MLE} = \sqrt{\frac{1}{n}\sum_{k=1}^{n} x_k^2 + \frac{1}{4}} - \frac{1}{2}. \quad \textbf{(3)}$$

Alarm Level Calculation

Once H_1 is accepted, the software uses the following scheme for computing the alarm level:

$$AL = Ceiling\left(Log_b\left(\frac{\mu_1 - \mu_0}{\rho\sigma_0} \right) \right), \quad \textbf{(4)}$$

where b is the base of the logarithm, μ_0 and μ_1 and are the sample background and source means, σ_0 is the sample standard deviation, and ρ ($0 < \rho$) is a scale factor. Both b and ρ are adjustable options, the software defaults are $b = e$ and $\rho = 1$.

Static/Dynamic Background

The software can be executed either in static or dynamic background mode. When the program is running in dynamic background mode, it will update the background μ_0 and σ_0 using the newest data point classified as background. Although the prototype has an internal control over the absolute ceilings for μ_0 and σ_0, caution is needed since dynamic background may lead to large background values and reduce the program sensitivity to the source.

Experiment Results

Field data (gamma gross counts) collected in FY 2006 at RSL in the area in front of the deployment building next to the truck scale were used for the evaluation of the software (Yuan, 2007). For comparison purposes, the data set was divided into five regions: (1) pre-source background, (2) pre-source up-transition, (3) source, (4) post-source down-transition, and (5) post-source background. Performances of the three algorithms (conventional, forward SPRT, and reversed SPRT) were compared using this data set region by region. The observed performance of the algorithms in the respective data regions are summarized in Figure 3. It was generally observed that all three algorithms behaved similarly in the source region. Both SPRT algorithms offered reductions in false alarm rates in the background region. Reversed SPRT did best in the transitional regions.

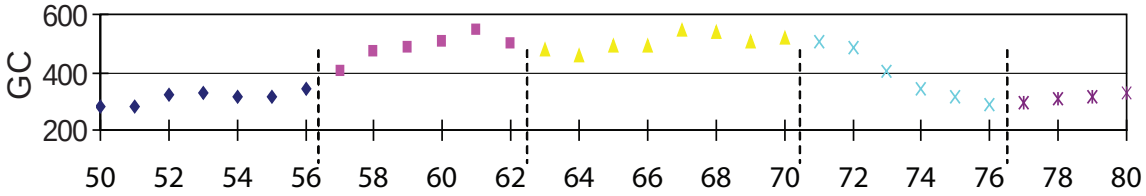

Alg.	Data Region				
	Background	Up-Transition	Source	Down-Transition	Background
CONV	False Alarm Rate High	Fixed Delayed Response High False Negative Rate	Without Confidence Similar Detection Results	Fixed Delayed Response High False Positive Rate	False Alarm Rate High
SPRTF	Reduced False Alarm Rate	Variable Delayed Response Medium False Negative Rate	With Confidence Similar Detection Results	Variable Delayed Response Medium False Positive Rate	Reduced False Alarm Rate
SPRTR	Similar to SPRTF	Immediate Response Low False Negative Rate	With Confidence Similar Detection Results	Immediate Response Low False Positive Rate	Similar to SPRTF

Figure 3. The observed performance of different alarm algorithms at different regions of the experimental data, where CONV = conventional algorithm, SPRTF = forward SPRT algorithm, and SPRTR = reversed SPRT algorithm.

Conclusion

A Windows mobile–based search software prototype with multiple SPRT algorithmic options has been developed and tested using field gamma data. The results suggest that the reversed SPRT scheme outperformed the conventional and the forward SPRT algorithms due to its ability to reduce false alarm rates, improve response speed, offer adjustable confidence levels, and minimize spatial uncertainties. We recommend that this prototype (with necessary modifications, such as removing the debugging portions) be adopted for emergency response missions.

Acknowledgments

A portion of the software engineering and evaluation work was performed by a team of graduate students supervised by Dr. Shahram Latifi at the University of Nevada, Las Vegas. The reversed SPRT was originally called a LIFELO (last in–first elected–last out) scheme in project correspondences; Dr. Paul Guss of RSL recommended changing the name to reversed SPRT.

References

Kernan, W., D. Yuan, "Prototyping Search Software with Multiple Algorithm Options," *Nevada Test Site–Directed Research, Development, and Demonstration*, FY 2006, National Security Technologies, LLC, Las Vegas, Nevada, 2007, 149–155.

Mukhopadhyay, N., G. Ciconetti, "Application of sequentially estimating the mean in a normal distribution having equal mean and variance," *Seq. Analysis*, **23**, 4 (2004), 625–665.

Wald, A., *Sequential Analysis*, 1947, reprinted by Dover Publications, Mineola, NY, 2004.

this page intentionally left blank

Detectors and Sensors

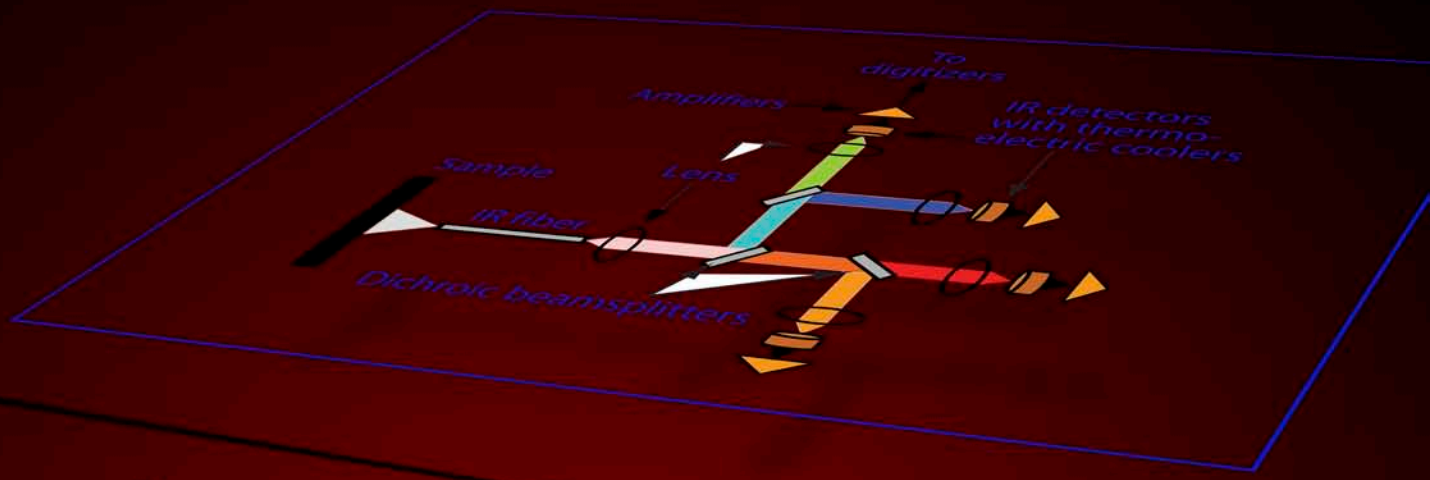

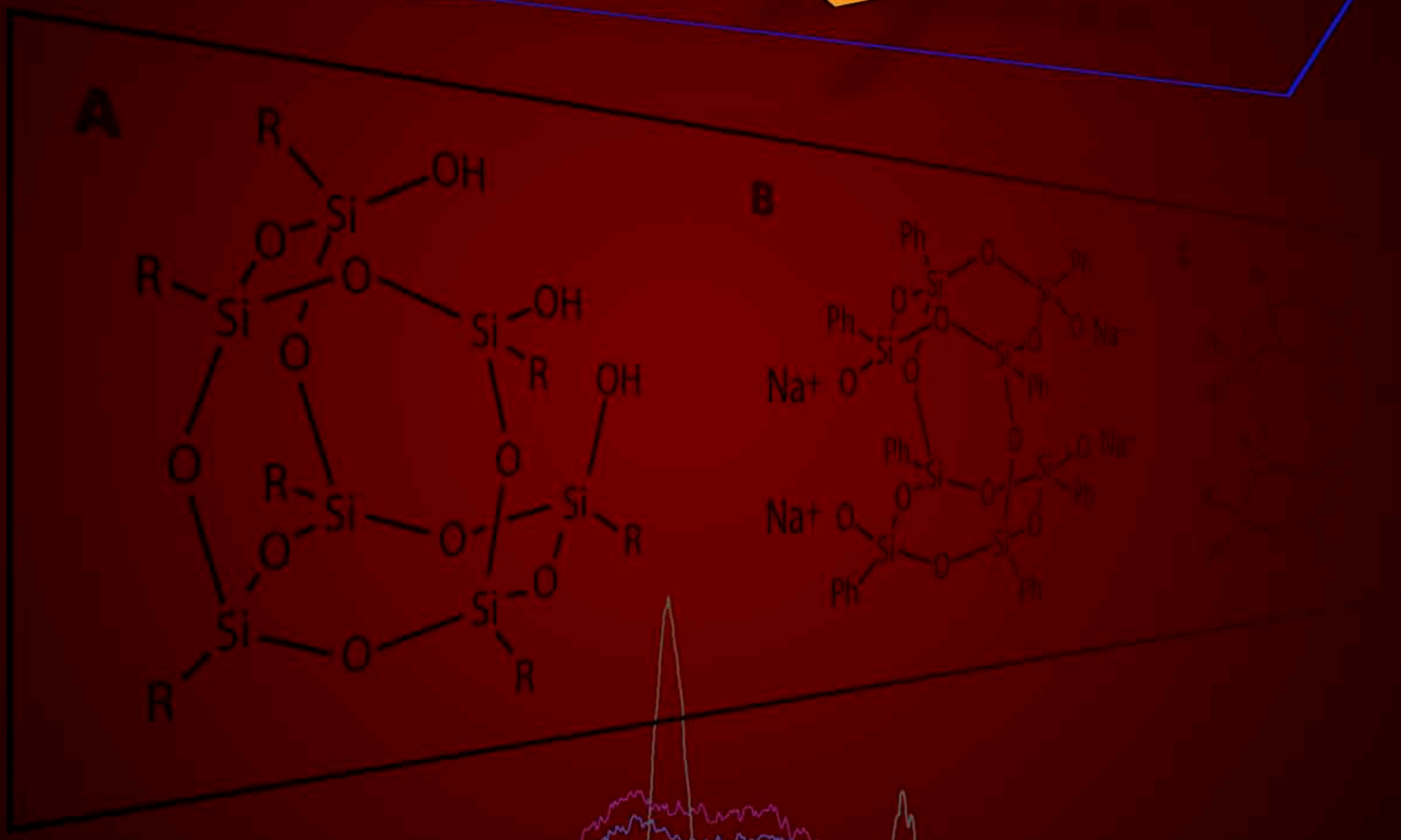

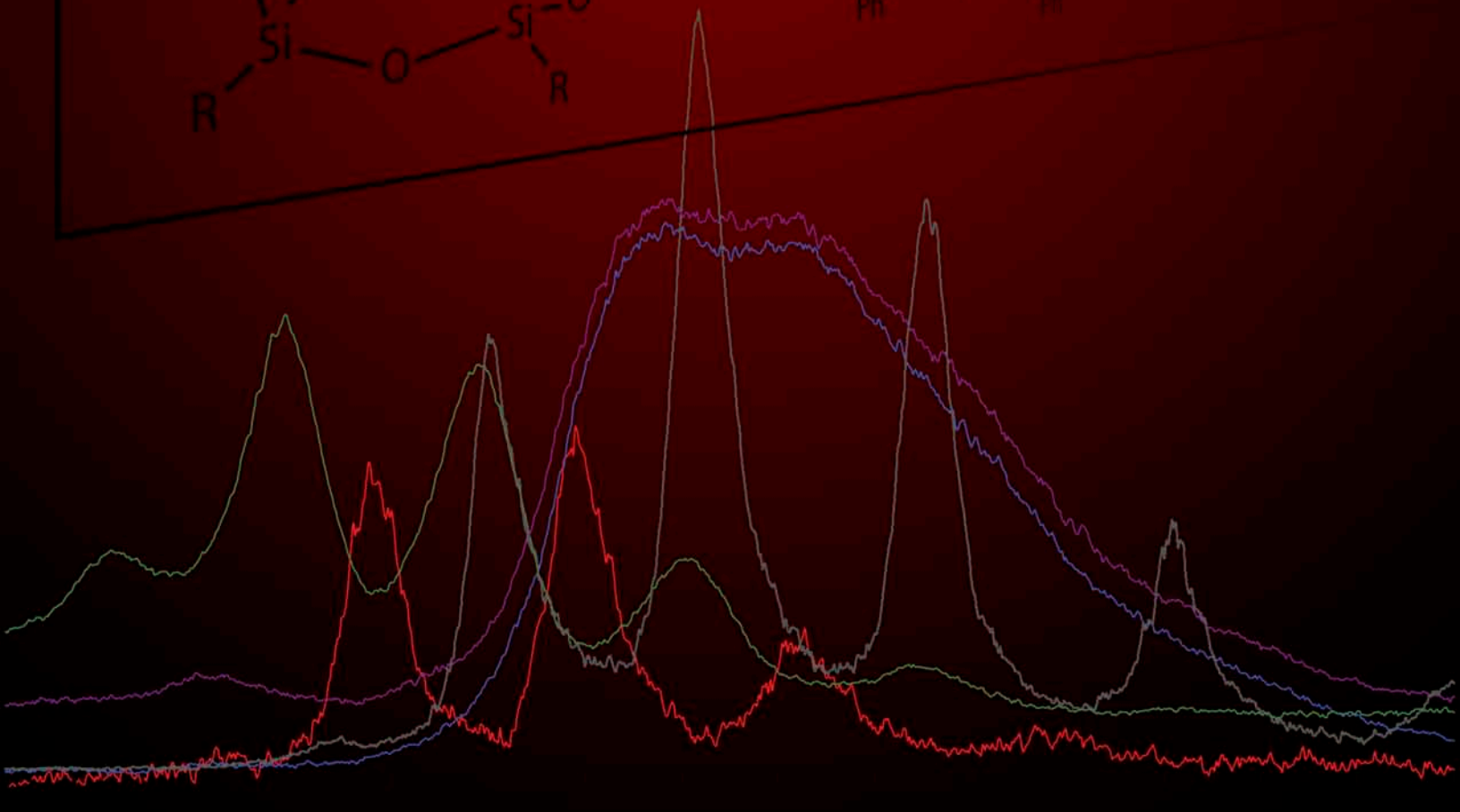

An Ultrasensitive Neutron Spectrometer

Timothy Ashenfelter,[1] *Julia You*
Remote Sensing Laboratory – Andrews

Robert Hayes
Remote Sensing Laboratory – Nellis

The concept to develop an ultrasensitive neutron spectrometer grew out of previous collaborations with the Environmental Measurement Laboratory (EML). The Remote Sensing Laboratory – Andrews (RSL–A) carried out measurements with the EML 14-element multisphere spectrometer during this collaboration (Heimberg, 2004). The function of both the EML and ultrasensitive neutron spectrometers is to measure neutron propagation in a macroscopic environment that is larger than a controlled laboratory. Although notable discoveries related to environmental neutrons were made using the EML spectrometer (Goldhagen, 2004; Gordon, 2004), its size requires several weeks of continuous measurements in order to obtain a spectrum. Because the EML multisphere spectrometer would require lengthy time integrations, this SDRD project conceived of a neutron spectrometer with a detector 100 times the sensitivity. This increase in detector size translates into a minimum integration time of one hour or less. The new detection system would specifically measure and quantify the macroscopic phenomena of neutron propagation in diverse environments with the targeted goal of discriminating between normal environmental elevations and fissile material. Because the detection of fissile material involves identifying subtle features in the background, it is imperative to either increase the signal or characterize the background more effectively. The ultrasensitive neutron spectrometer could be used to gain significant insight on both requirements. This project developed a theoretical and technical plan for a detector system capable of meeting these requirements, laying the foundation for future design work to include the supporting hardware.

Background

The primary impetus of the development of the ultrasensitive spectrometer was to quantify the phenomenon called the ship effect, in which the neutron background increases by up to an order of magnitude on large ships (Heimberg, 2004; Kernan, 2003). The ship effect is quite different from other sources of neutron background because the ship itself effectively becomes an indirect source that extends throughout the ship's proximity.

[1] ashenftp@nv.doe.gov, 301-817-3447

Ship effect is caused by the interaction of cosmic rays with the ship's metal. Cosmogenic neutrons, which are produced in cosmic ray showers, induce spallation reactions on atoms near the ground, assuming that their energy is sufficient. It just so happens that large atoms, such as those in steel, have more potential to fragment in these spallation reactions than do smaller atoms in soil, water, and wood. The net effect in a spallation reaction is a repartition of energy from the single-incident high-energy neutron toward multiple lower-energy neutrons. Through additional moderation, the spallated neutrons increase the flux of thermal neutrons aboard a large ship. The effective strength of that source scales with the mass of the metal material (high-Z) contained on the vessel.

Because the ship itself becomes the source for the ship effect, the measurements or simulations must also be macroscopic and scale to the size of the ship. While it would be far easier to simulate thousands of a ship's neutron spectral signature than to actually measure the neutron data, it would be difficult to ascertain the level of ship details needed in those simulations or the veracity of those simulations. To answer this question, one would also need empirical data for comparison. This would either require many exhaustive measurements by a single small spectrometer (to factor in this fine-structure and location variability) or several measurements from a single macroscopic detector. This issue is especially evinced when trying to quantify the propagation of a neutron flux on the ship from a point source. Because the smaller EML spectrometer takes weeks to measure a single spectrum, it would be impractical to use at different locations aboard a ship. Furthermore, the fine-structure detail of the ship would still need to be quantified. A detector with weeks of integration time would also be influenced by the effects of atmospheric depth, latitude, and solar activity (discussed below). The ultrasensitive neutron spectrometer design would integrate over enough of the fine detail to be of use in directly relating to macroscopic simulations, while also having a dramatically reduced integration time.

It should also be noted that the neutron background is affected by the same factors that affect cosmic ray propagation to the ground. Cosmic ray primaries are comprised of 90% protons. The neutrons measured on the ground result from secondary reactions of mostly the oxygen and nitrogen in the atmosphere with the cosmic ray primaries. The integrated mass of air above the source location (called atmospheric depth) affects the flux of secondary cosmogenic neutrons on the ground. At higher elevations, the flux is greater. For more extensive discussions of these phenomena, Gordon and his collaborators (2004) provide an excellent discussion. They determined that a change in the elevation to around 3500 meters from sea level increases the neutron flux by a factor of 15. This integrated mass of air is generally quantified by the air pressure, which is used for pressure corrections.

The cutoff energy or rigidity (measured in GeV) of cosmic ray primaries presents another influence on flux. The Earth's magnetic field bends the charged particles that induce cosmic showers. Closer to the equator, even greater amounts of energy are required for cosmic ray showers to reach sea level. This translates roughly into a factor of two variations in cosmic ray flux between the poles (maximum flux) and the equator (minimum flux).

Because the sun's magnetic field shields incident cosmic rays, the solar cycle also influences the background neutron flux. During the solar minimum in sunspot/solar flare activity, the cosmic ray flux is greater. When solar activity is at its height, the solar magnetic fields being pulled by the solar wind reduce the cosmic ray flux on earth. The variability of this effect on the neutron count rate is about 7% at the equator and 25% at the poles (Gordon, 2004). One confounding effect from solar activity is the potential for solar activity to emit neutrons directly. This may manifest as a temporarily elevated neutron flux on the ground. Because of their neutral charge, solar neutron primaries are unaffected by the magnetic field cutoff and can reach sea level despite being below the cutoff energy. An illustration of this enhancement from direct measurements will be elucidated below. An example of the phenomenon is given in Bieber (2005).

With an order of magnitude improvement in detection efficiency with the ultrasensitive neutron spectrometer, considerably more data analysis is available to quantify these macroscopic effects. In the same period of time as the EML spectrometer, hundreds of separate measurements would be possible, allowing for thorough examination of the temporal variability of the neutron spectrum as well as more statistically significant analyses. Also, during the course of a 14-day ship measurement, the background environmental factors such as pressure, rigidity, and solar variability will confound the analysis of a single long-dwell measurement. The variation in these environmental factors would not be a significant issue in a 1-hour measurement.

Project

Conceptual Design

The conceptual detector design leveraged extensively from legacy equipment; about a dozen detector pods that would have been excessed were claimed for use in the prototype detector. Each pod has eight (2" × 6') ^{3}He tubes, giving it a considerable increase in detection efficiency compared to the Bonner sphere EML design. Like the EML spectrometer, each pod would be outfitted with different shielding and moderators so that their energy response could measure the entire neutron energy range of interest. A bare detector would measure the thermal energy flux, while a pod surrounded by 2 in. of high-density polyethylene (HDPE) would span from the low MeV energy range to eV. On the far end, a pod containing several inches of steel or other high-Z material would mimic the ship effect and measure the hundreds of MeV energy range incident on the whole detector. An illustration of the detector arrangement in a shipping container is shown in Figure 1. It would be expected that simulations and pilot studies would be performed first to determine whether the separation distance between detectors is sufficient to minimize each detector's influence on its neighbors.

Each pod would be outfitted with several different layers of moderator and shielding so that an optimized configuration could be developed. Figure 2 provides a qualitative example of how the material changes the energy response function. For example, the addition of a thin layer of Gd foil provides an energy cutoff of around 0.1 eV for energy response.

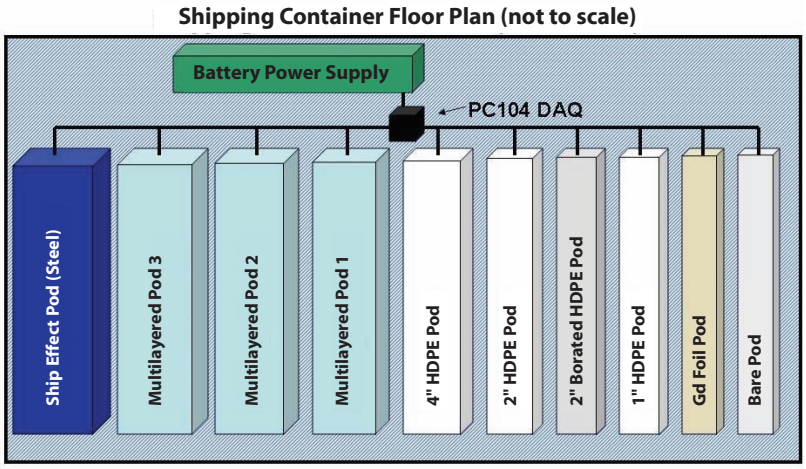

Figure 1. Conceptual design for the ultrasensitive neutron spectrometer. The large 10–12 pod system is intended to be installed inside a shipping container with its own self-contained power (battery) and data acquisition (DAQ) unit. Due to anticipated interactions between pods, the pods with the most significant layers would reside on the opposite end of the shipping container from the bare pod, which is most susceptible to effects from the other pods.

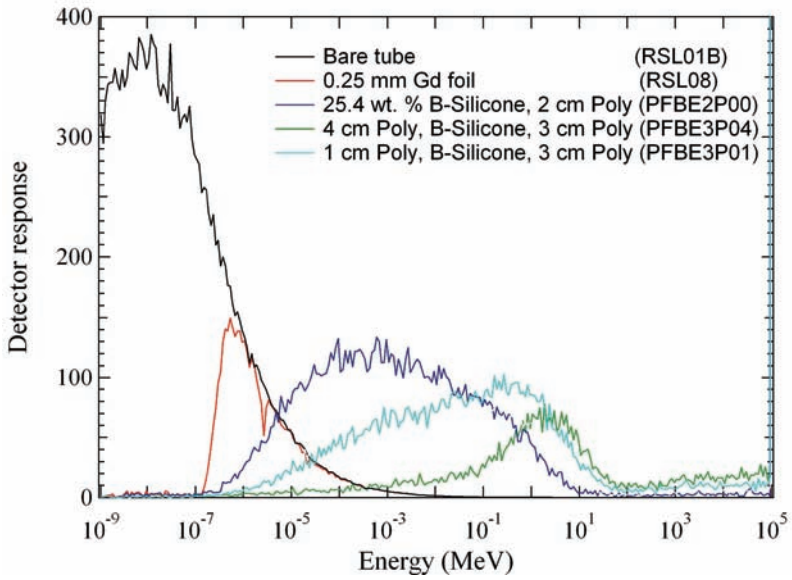

Figure 2. Monte Carlo N-Particle Extended (MCNPX) code simulations of a detector surrounded by various materials. The bare tube (black) responds to thermal neutrons, but can be confined to a tighter range with a thin layer of Gd foil (red). The difference between the bare tube and the Gd foil tube gives the neutron flux below the Gd threshold of 0.1 eV. These detector models were implemented in another smaller spectrometer design (Haard, 2005).

The choice for the material surrounding each pod would be determined from extensive MCNPX code simulations. In order to properly simulate the energy response, the high-energy neutron cross sections, cosmic ray propagation, and detector configuration should be modeled. The effectiveness of each configuration would be determined by the type of deconvolution algorithm used to translate the detector energy response functions into a neutron energy spectrum.

Components

The building blocks for the ultrasensitive neutron spectrometer are the legacy ^{3}He neutron pods. Each pod includes eight tubes (two four-tube layers) that are each 6 ft long and self-contained in a housing of thin HDPE. A preliminary characterization survey showed that of the fourteen available pods, eight operated qualitatively as expected (5–9 cps), three worked less optimally (2–4 cps), two were overworking (10+ cps), and one was inoperative. It is expected that a thorough cleaning and adjusting of the gain settings will resolve several of these issues, assuring twelve working detectors for a prototype neutron spectrometer.

Voltage to the detectors will be supplied by a power supply (Tri-M 60 Watt) on the PC104 DAQ unit. This power supply also operates the Parvus CPU (Elan 1421 133 MHz). The CPU runs a simple Linux operating system that receives the data from the detectors and sends data via Ethernet to an analysis computer. The detectors are connected to a 12-channel counter board designed at the Remote Sensing Laboratory – Nellis (RSL–N). A photo of the unit in operation is shown in Figure 3.

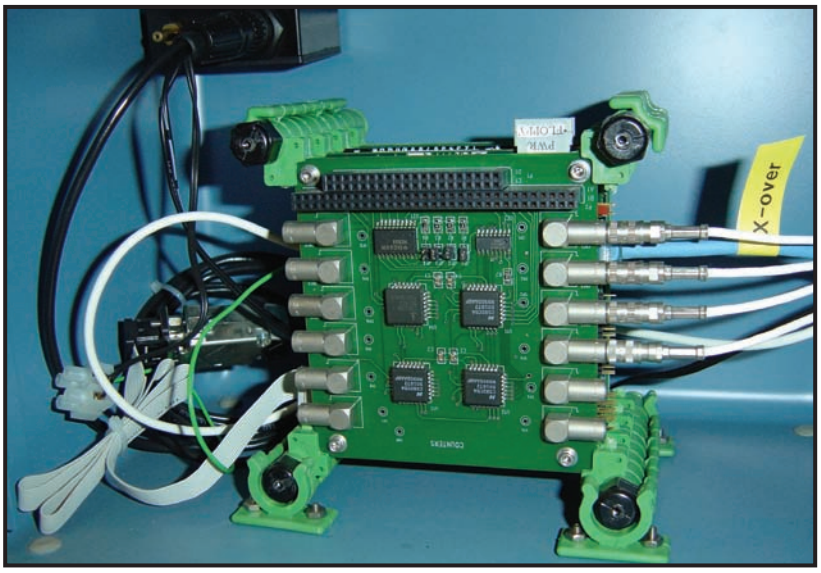

Figure 3. The PC104 DAQ unit for the ultrasensitive neutron spectrometer. The component stack includes a power supply (for the DAQ and detectors), CPU board, and a 12-channel counter board. The pressure and temperature gauge is shown in the upper left.

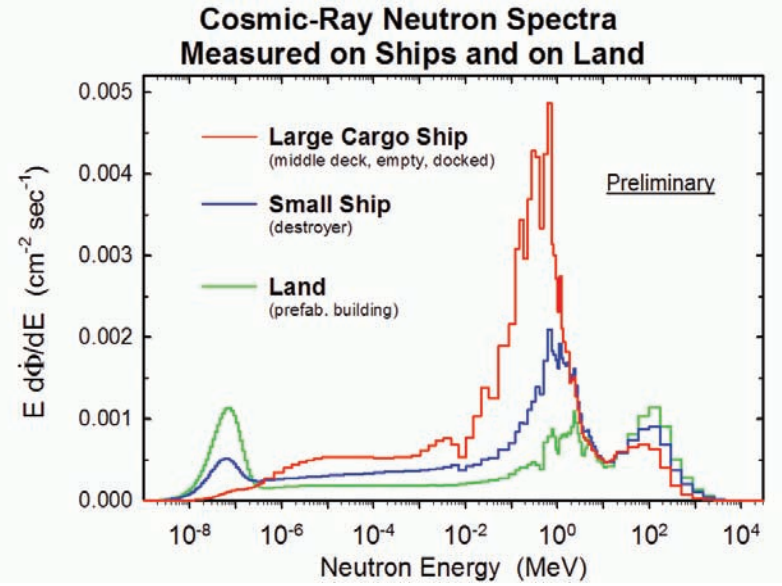

Figure 4. Preliminary energy spectrum from the EML spectrometer (RSL–A and EML collaboration) (EML, 2006). The important feature to note is that the ship effect increases the count rate near the 1-MeV range of fissile material.

Once the DAQ_CPU acquires 10 seconds of data from up to twelve pods, it bundles the data onto an output stream along with the temperature, pressure, and time data. This ASCI data stream is sent to the analysis computer, which runs a simple Java script to plot and combine that data onto a one-day ASCI file. Every 24 hours, at midnight, the data file is closed and a new file is opened with the date and timestamp used in the filename. As such, the automated system is capable of running uninterrupted for several weeks at a time.

The data would then have a deconvolution algorithm applied to transform the total corrected count data of each detector into a neutron spectrum. The EML spectrometer uses software called MAXED that makes an initial guess of the spectrum and uses a maximum entropy condition to best fit an energy spectrum. The fit is considered validated if the initial condition is varied and the same resulting spectra are repeated.

Results

The ultimate goal of the ultrasensitive neutron spectrometer would be to obtain spectra similar to those already obtained by the EML spectrometer as shown in Figure 4 using the MAXED software. This figure shows the energy × differential flux plotted versus the log(E); the distribution is flat with equal areas under the graph representing equal integral fluxes (Gordon, 2004). This plot provides

considerable insight into the nature of the ship effect. If we assume that the initial spectrum incident on the ship is represented by the land (green) spectrum, then the ship is effectively shielding the low-energy thermal neutrons. However, the 100-MeV neutrons are causing spallation reactions that dramatically amplify the flux of 1-MeV neutrons. The best way to look at this modified neutron source term is with respect to the partition of energy, where a single 100-MeV neutron can be repartitioned into a hundred 1-MeV neutrons. If one were to focus on the energy range of fissile material in this 1-MeV range alone, the ship effect could easily complicate any analysis or even induce false alarms.

The plot in Figure 4 illustrates this type of detector's potential to expand our knowledge about the ship effect. With a much larger detector, we could not only discriminate and quantify the ship effect, but also quantify the propagation of neutrons aboard a ship.

The ultrasensitive neutron spectrometer could also be used to examine temporal variability of the neutron flux. Using the neutron monitor (NEMO) and the DAQ system conceived for this project, evidence of an elevated neutron count rate was collected. The NEMO detector is a single detector composed of four pods encapsulated by 2 in. of HDPE. Figure 5 illustrates the detection of solar transients using a large-scale neutron detector. In order to accurately gauge the trend, the uncorrected (no pressure correction) data are shown. The overall subtle increase is due to the change in pressure

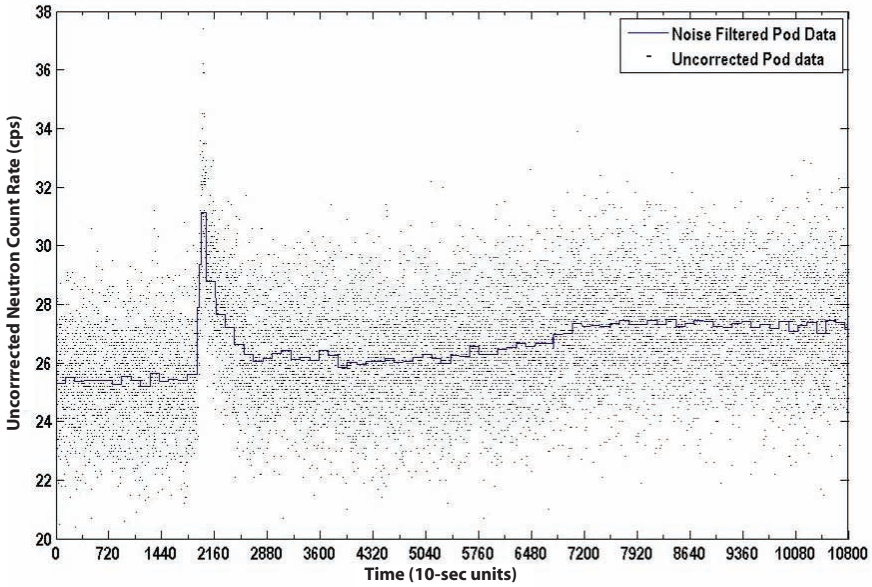

Figure 5. NEMO count rate during a large solar event on 12/14/2006. The 2-in. moderated neutron pods measured an elevation in neutron flux at sea level as a result of this solar storm. The count rate was measured every 10 seconds, so each tick on the time axis corresponds to 1 hour. The elevation in neutrons lasted ~2 hours.

over the course of the 30-hour span. The ~25% elevation in neutron count rate was due to this solar event. A denoising algorithm was applied to the raw data to better illustrate the trend. The data were filtered using the discrete Haar wavelet algorithm that applies a heuristic variant of Stein's unbiased risk signal threshold determination. The data were then rescaled once based on the level of measured noise. A more complete discussion of the denoising approach is found in the MATLAB wavelet toolbox documentation (Misiti, 2007).

Conclusion

The DAQ system and overall architectural design for the ultrasensitive neutron spectrometer has been affirmed beyond the proof-of-concept. In preparation for future work on neutron spectrometers, two spare PC104 DAQ systems were built at RSL–A. These systems have been shown to be economical and dependable, as is illustrated by the success of the NEMO pilot study. A thorough testing of the electronics is needed, as are improvements to the user interface, power supply, and the system's environmental ruggedness. These design improvements would likely need to be completed in the early stages of the production end of the neutron project.

In order to pursue this technology that benefits both science and homeland security, several additional steps should be completed. First, access to modelers of environmental neutrons for use in shielded configurations is needed. Second, adequate computer resources and manpower to execute the large array of simulations to support the optimization of the detector design are needed. The extensive modeling parameter space includes the type of shielding material, thickness, number of different layers, and depth order. These same computer resources should also examine the interaction effects between the detectors, with a goal of minimizing the detector's influence on itself. Third, unresolved questions regarding the validity of the deconvolution algorithm for this detector design remain and need to be addressed. Finally, the energy range distribution for neutrons is confounded by the fact that the energy range of interest spans over twelve orders of magnitude. To resolve this issue, the EML detector system implements the detection algorithm MAXED (Reginatto, 1998) on a 14-element detector to determine the neutron spectra as given in Figure 4. Because the number of energy bins (unknowns) is greater than the number of observations (detector counts), the results may be overly influenced by the initial guess in the deconvolution algorithm. This issue was tested by the algorithm creators by varying the initial guess to gauge if it influences the final result. If the result is stable, then it is considered reliable.

A more appropriate test would be to directly compare the results of this deconvolution with well-established and validated neutron spectrometers or well-established and calibrated neutron sources. The utility of the MAXED algorithm approach should be compared with other more established methods, which will lead to more unique solutions. One approach would be to establish a region of interest (ROI) for each detector, so that the system of equations could be solved uniquely. The divisions between these ROI could be adjusted to provide the most detail where the shape gradient

is the most significant. This technique is common in numerical modeling, where memory restrictions limit the grid density.

Another need is to develop thorough and self-consistent MCNPX input stacks. Current models used in spectrometer designs appear to combine the low-energy S-factor physics with high-energy tables. The integration of these two poles of the energy propagation scale would need to be verified empirically before a detector were manufactured.

By looking at only the energy range of fissile material, one is not able to deduce whether an elevated neutron count rate is caused by spontaneous fission, (α,n) reactions, or the environment. In order to detect threats using neutron spectral information, it is important to look at the 1-GeV end down to the thermal neutron range. Based on Figure 4, a viable design would look at the ratio of the three separate distribution peaks at the high-energy, low-MeV scale, and thermal scale. The ship effect could then be quantified by an increase in the MeV scale at the expense of both the thermal and high-energy end. Fissile material would likely be represented by an increase in the MeV component and thermal neutron range without any change in the high-energy component. A fourth component that can normalize the signal would provide the final key component for a complete detection system.

References

Bieber, J. W., J. Clem, P. Evenson, R. Pyle, "Relativistic solar neutron and protons on 28 October 2003," *Geophys. Res. Lett.* **32** (2005) L03S02.

EML, "Neutron 'Ship Effect', An Experimental Study" http://www.eml.st.dhs.gov/factsheets/ShipEffect.pdf, accessed 2006.

Goldhagen, P., J. M. Clem, J. W. Wilson, "The energy spectrum of cosmic-ray induced neutrons measured on an airplane over a wide range of altitude and latitude," *Radiat. Prot. Dosim.* **110** (2004) 387–392.

Gordon, M. S., P. Goldhagen, K. P. Rodbell, T. H. Zabel, H. H. K. Tank, J. M. Clem, P. Bailey, "Measurement of the flux and energy spectrum of cosmic-ray induced neutrons on the ground," *IEEE Trans. Nucl. Sci.* **51**, 6 (December 2004) 3427–3434.

Haard, T., P. Heimberg, "Optimized tool to search ships for fission sources," DOE TI Mid-year Review Report, 2005.

Heimberg, P. C., W. J. Kernan, R. Detwiler, T. M. Haard, C. Okada, "Experimental study of the neutron ship effect," DOE Report, 2004.

Kernan, W. J., R. S. Detwiler, T. M. Haard, C. Okada, "Vessel effect measurements aboard the USNS Regulus," DOE Report, 2003.

Misiti, M., Y. Misiti, G. Oppenheim, J-M. Poggi, "Wavelet Toolbox 4," *Wavelet Toolbox User's Guide*, MathWorks, Inc., Natick, Massachusetts, 2007.

Reginatto, M., P. Goldhagen, "MAXED, a computer code for the deconvolution of multisphere neutron spectrometer data using the maximum entropy method," USDOE Report EML-595, June, 1998.

Single-pulse Detection of Infrared Synchrotron Light

Steven Becker[1]
North Las Vegas

Richard Hacking, Robert Malone
Los Alamos Operations

Ken Moy, Gerald Stevens, Dale Turley
Special Technologies Laboratory

The goal of this project was to develop a high-bandwidth IR spectrometer capable of resolving individual synchrotron pulses such as those generated at the vacuum ultraviolet (VUV) line of the National Synchrotron Light Source (NSLS), <20 ns. The project leveraged FY 2006 detector development activities (Becker, 2007) to design and build a four-channel IR pyrometer using Si, photoelectromagnetic (PEM), and InGaAs detectors. This year's effort was to increase the collection efficiency of the spectrometer in order to improve the signal-to-noise ratio (SNR) and to study target reflectivity in order to better characterize the target temperatures. Project personnel designed, constructed, and fielded the optics and the IR spectrometer.

Background

Accurate hydrodynamic modeling codes require well-characterized thermodynamic equation of state (EOS) parameters, such as temperature. Two values, radiance and emissivity, must be measured or be assumed to determine the temperature of a dynamically compressed material. Radiance, emissivity, and temperature are related by Planck's law (DeWitt, 1988):

$$L = \varepsilon \frac{c_1}{\lambda^5 \left(e^{c_2/\lambda T} - 1 \right)}, \quad (1)$$

where L is the spectral radiance, ε is the object's emissivity, and T is its temperature.

Fiber-based optical pyrometers (Figure 1; Bergstresser, 2001) have been used to measure the radiance of accelerated materials, but reflectance (≈1 – emittance) measurements have not always been compatible with the experiment. Since emissivity can change during testing, the measured radiance from each detector was converted to temperature by bracketing the emissivity with the maximum emissivity of 1 and the static emissivity (Seifter, 2004) measured before the experiment (Bergstresser, 2004). An analysis can contain significant errors (Partouch-Sebban, 2003), especially at longer

[1] beckersa@nv.doe.gov, 702-295-0612

wavelengths. Previous reflectance measurements have been made employing flash lamps (Stevens, 2005) or lasers as the light source, but this was the first attempt to use the broadband-IR light generated at a synchrotron with an impact source.

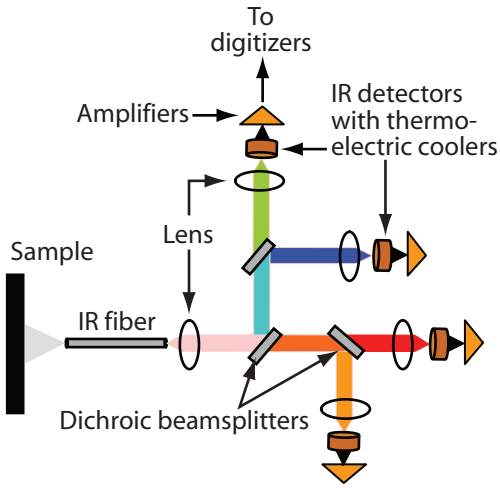

Figure 1. IR optical pyrometer layout

Dynamic temperature measurements can be technically challenging, as stray light (Poulsen, 2000) generated from lithium-fluoride (LiF) window edges, epoxy, air bubbles, and interference from other diagnostics can easily reduce accuracy. Extensive calibrations are also required before every test. A typical experiment generates stray light that can be much brighter than radiance emitted from a metal shocked at low pressures. Temperature discrepancies typically occur as a result of stray light contaminating the experiment. Large emissivity errors can be overcome if the measurements can be made at the shorter wavelengths; however, this area is susceptible to stray light, and the SNR is generally poor at low temperatures. Such measurements could be improved if a thin layer of high-emissivity material were applied to the target (Perez, 1992). This layer should have minimal effect on thermal diffusion while increasing apparent emissivity. Higher emissivity would yield an improved SNR and eliminate the need to characterize the surface of each target material. As part of this effort, several enhanced emissivity coatings were tested on compressed targets.

Project

This project was a follow-on to an FY 2006 SDRD project that focused on developing and testing high-bandwidth IR detectors (Becker, 2007). The only large-diameter, commercial detectors available, PEM detectors made by Vigo, were procured and tested. These 1-GHz-bandwidth instruments are designed for CO_2 laser-pulse detection but have low responsivity (40 mV/W). Unfortunately

the power supplies in these detectors were noisy, and Vigo redesigned their detector power supply in order to reduce detector noise. Recommendations made at the end of the FY 2006 work were completed in FY 2007, and this effort significantly improved data quality. All of the optics were anti-reflective coated. The team could not get the parabolic mirrors to recollimate the IR beam, so the parabolic mirrors were replaced with spherical mirrors. The beam is not conical, and the optical design was modified to compensate for the actual beam dimensions. Several iterations were made to optimize the optic design, which ultimately uses a prism mirror and spherical mirrors. The detector and preamplifiers were mounted in an electromagnetic interference/radio frequency interference (EMI/RFI)–shielded container. All of the AC-powered detectors and preamplifiers were converted to battery power so that electrical noise from the power grid could be eliminated.

Figure 2 shows the layout of the small impact source and the optic path. Figures 3 and 4 show the detector layout and a ray trace of the optic path, from the synchrotron, into the target chamber, reflected off the target, directed out of the target chamber, and separated into wavebands by dichroic beam splitters. Silicon (Si) photodiodes were used for visible light, indium gallium arsenide (InGaAs) photodiodes were used for near-IR light, and PEM photodiodes were used for the mid-IR properties.

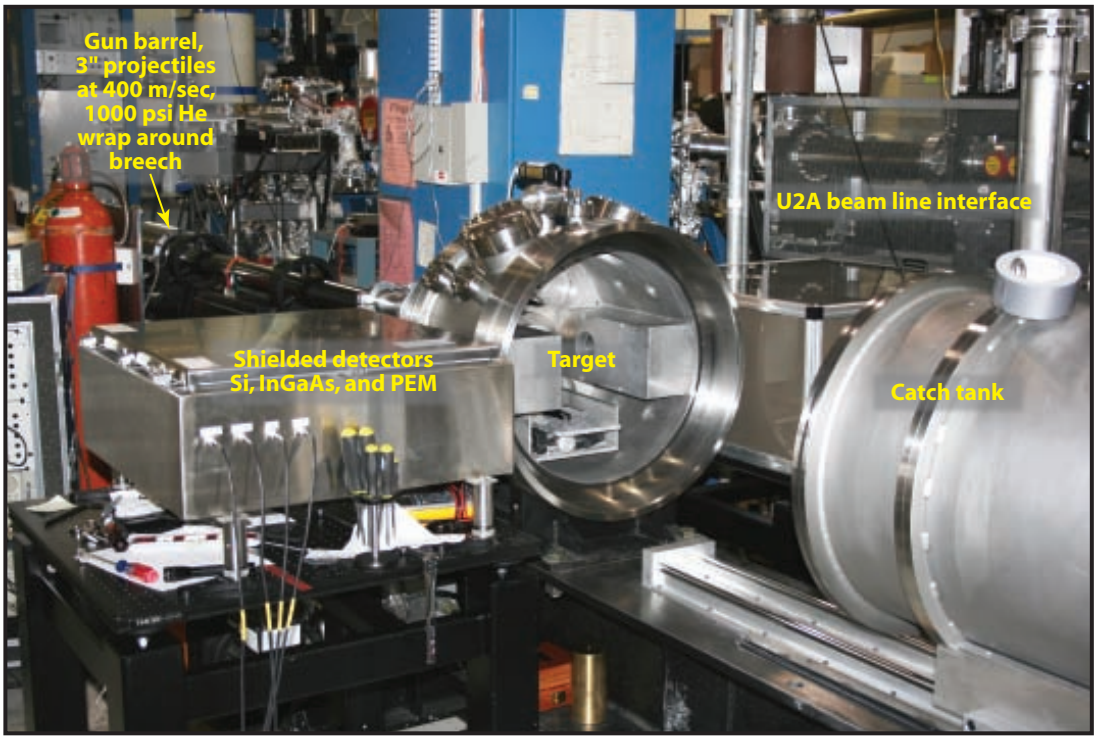

Figure 2. Detailed layout of small impact source and diagnostics at NSLS

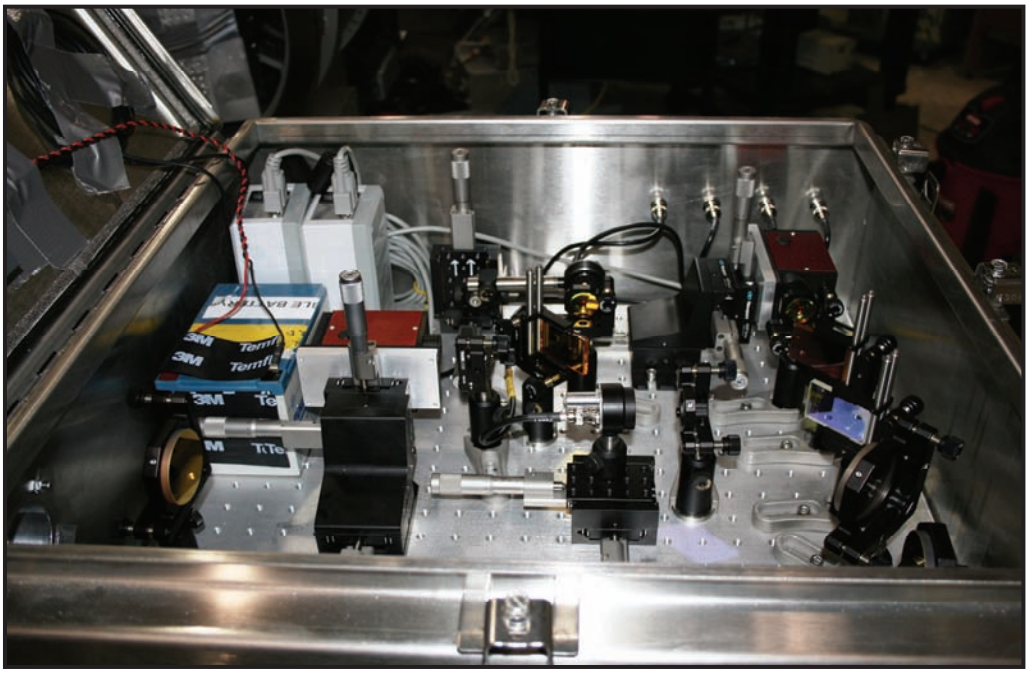

Figure 3. IR reflectance detectors

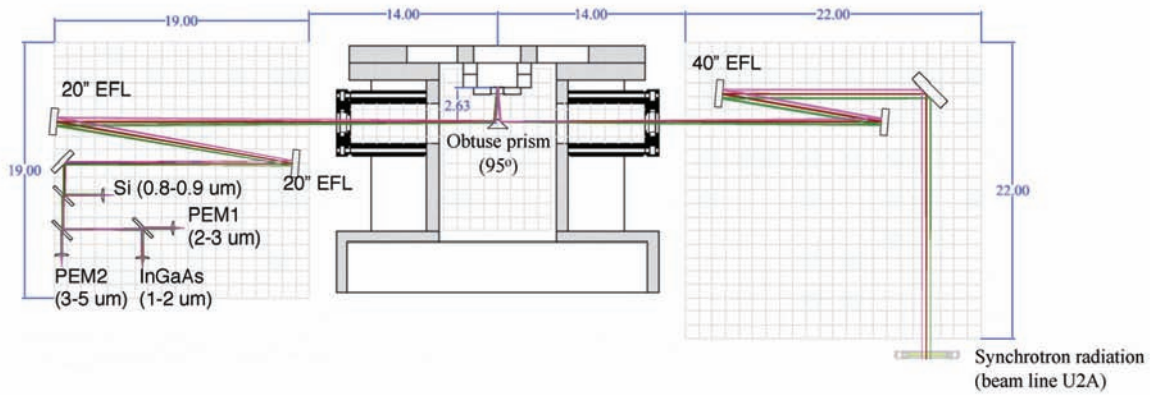

Figure 4. Ray trace of optic path

Figure 5 shows the three different target configurations used: standard, reverse, and separate. The standard configuration was used on most of our pyrometer experiments at other locations. The synchrotron light must pass through the epoxy layer twice in the standard configuration. The reverse configuration eliminated the epoxy layer from the beam path and the separate configuration allowed some separation between the target and the epoxy layer. The different target configurations were used to evaluate the light loss caused by the epoxy layer. Figure 6 (Dolan, 2007) shows sample data from a shot with the reverse configuration and Loctite 326 epoxy. Figure 7 (Dolan, 2007) shows two different experiments that used a chromium (Cr) target in the reverse configuration.

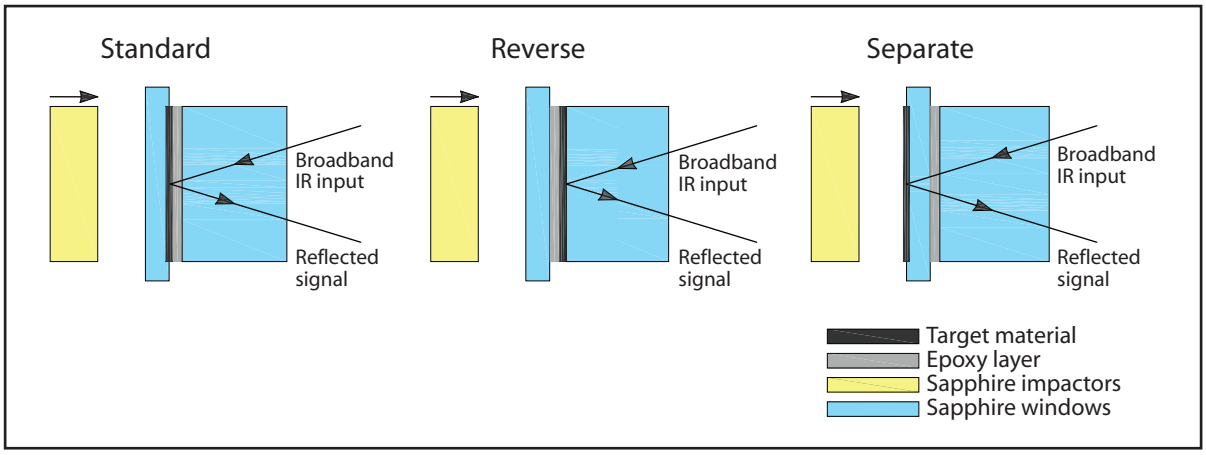

Figure 5. Target configurations for the IR reflectance experiments

Standard and reverse configuration experiments suggest that the bonding layer plays a role in the apparent reflectance of the compressed target. The signal drop in shot NSLS07-12 (standard), but little change in shots NSLS07-06 and NSLS07-19 (reverse), implies that epoxy absorption—not a change in emissivity—is creating a decrease in reflected light. Note that the synchrotron light in the reflectance measurement passes through the epoxy twice, while radiation emitted by the sample would only pass through the bond once. Bond thickness may also be a key parameter in assessing absorption strength, but precise measurements of the glue bond have not been completed. Currently the best epoxy thickness measurement obtained for this project is 0.002 mm. Some evidence indicates that the absorption of AngstromBond might be pressure-dependent, but without precise bond thickness comparisons it is impossible to quantify this effect.

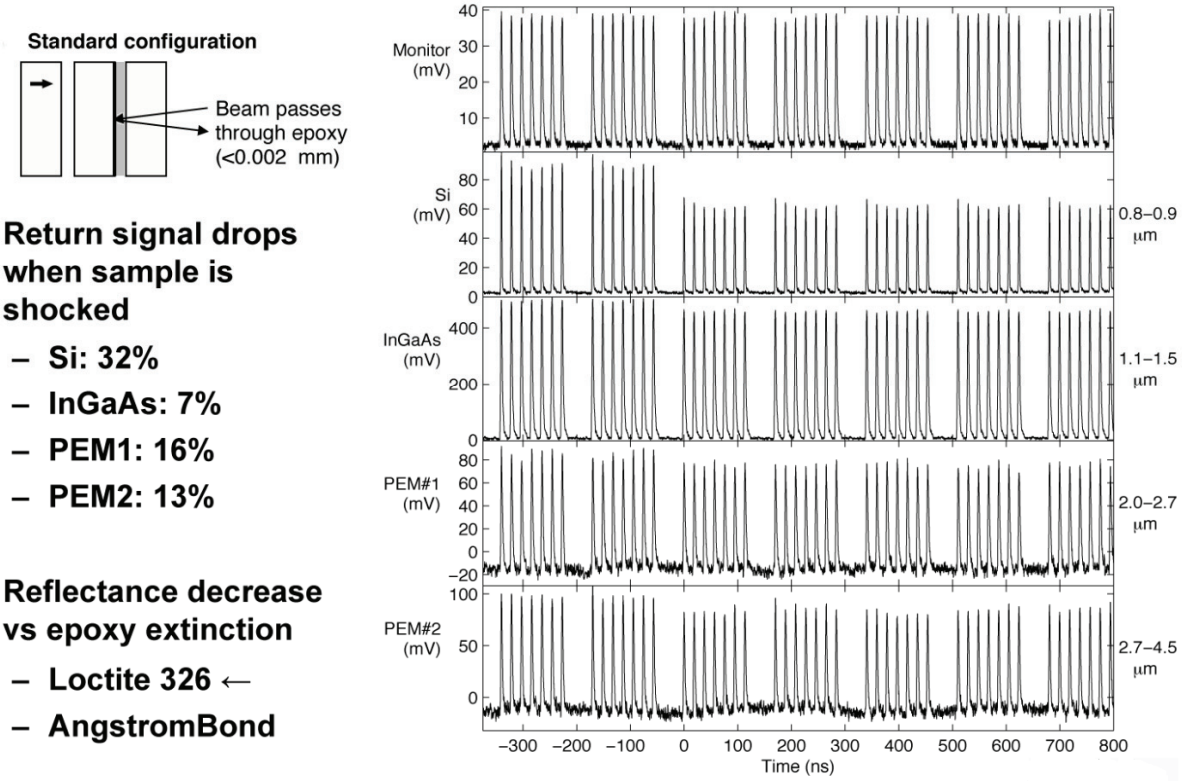

Figure 6. Bond layer absorption example (NSLS07-12, Loctite 326 epoxy)

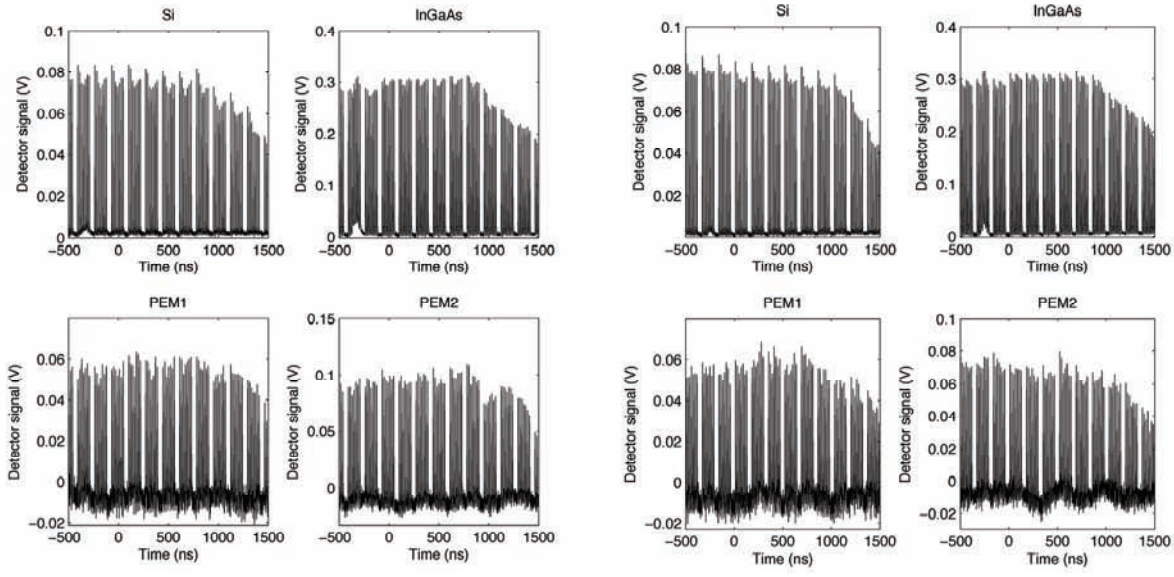

Figure 7. Raw data from NSLS07-06 (reverse Cr at 8 gigapascals [GPa]) and NSLS07-19 (reverse Cr at 8 GPa)

Conclusion

A high-bandwidth IR spectrometer was designed and fielded at the NSLS VUV beam line that employed Si, PEM, and InGaAs detectors developed on a prior year SDRD project. An optical relay was designed and constructed to couple synchrotron light into and out of the gas gun target chamber for specular reflectance measurements. Near- and mid-IR measurements were demonstrated with single-pulse resolution in support of a Sandia National Laboratories Laboratory Directed Research and Development project to develop a material phase diagnostic. Metal samples (Al, Cr, Cu, and Pt) maintained their ambient reflectance or became slightly less reflective during compression up to 9 GPa. The epoxy layer absorbed some of the synchrotron light on the experiments in the normal configuration. The enhanced emissivity coatings provided promising data and may still be developed as an emissivity standard. Projectile tilt, light flash from epoxy compression, epoxy thickness, and pin holes in some of the targets complicated the analysis. Quantitative data analysis is still under way at SNL, and a detailed description of the experiment can be found in Dolan (2007).

References

Becker, S., R. Hacking, R. Malone, K. Moy, G. Stevens, D. Turley, "Single-Pulse Detection of Infrared Synchrotron Light," *Nevada Test Site–Directed Research, Development, and Demonstration,* FY 2006, National Security Technologies, LLC, Las Vegas, Nevada, 2007, 157–164.

Bergstresser, T., S. Becker, "Temperature measurement of isentropically accelerated flyer plates," in *Shock Compression of Condensed Matter 2001: Proceedings of the Conference of the American Physical Society, Topical Group on Shock Compression of Condensed Matter*, June 24–29, 2001, M. D. Furnish, N. N. Thadhani, Y. Horie (eds.), American Institute of Physics, Melville, New York, 2001, 1169–1172.

Bergstresser, T., Sandia National Laboratories, lecture, "Pyrometry Experiments on Saturn," March 25, 2004.

DeWitt, D. P., G. D. Nutter (eds.), *Theory and Practice of Radiation Thermometry,* Wiley-Interscience, New York, 1988.

Dolan, D., "Characterizing the emissivity of materials under dynamic compression (final report for LDRD project 79877)," SAND2007-6376, Sandia National Laboratories, Albuquerque, New Mexico, October, 2007.

Partouch-Sebban, D., "High speed multi-wavelength pyrometry and emissivity measurement of shocked metals," in *Shock Compression of Condensed Matter 2003*, *Proceedings of the Conference of the American Physical Society, Topical Group on Shock Compression of Condensed Matter*, M. D. Furnish, Y. M. Gupta, J. W. Forbes (eds.), American Institute of Physics, Melville, New York, 2003, 1293–1298.

Perez, M., "Residual Temperature Measurements of Shocked Copper and Iron Plates by Infrared Pyrometry," in *Shock Compression of Condensed Matter 1991,* S. C. Schmidt, R. D. Dick, J. W. Forbes, D. G. Tasker (eds.), Elsevier, Amsterdam, Netherlands, 1992, 737–740.

Poulsen, P., D. Baum, P. Fiske, D. Holtkamp, "Temperature measurement on shocked surfaces," UCRL-JC-139909, Lawrence Livermore National Laboratory, Livermore, California, August, 2000.

Seifter, A., M. Grover, D. B. Holtkamp, J. R. Payton, P. Rodriquez, D. Turley, A. W. Obst, "Low-temperature measurements on shock loaded tin," DOE/NV/11718--996, Bechtel Nevada, Las Vegas, Nevada, September, 2004.

Stevens, G., D. Turley, L. Veeser, "Optical diagnostics for phase changes," *Nevada Test Site–Directed Research, Development, and Demonstration,* FY 2004, Bechtel Nevada, Las Vegas, Nevada, 2005, 281–286.

Frequency Modulated Detection of Phosphorescence on Surfaces

Gene Capelle, Linda Chandos, John Di Benedetto,[1] James Herning, Ian McKenna, Peter Ryan, R. Trainham
Special Technologies Laboratory

Phosphorescent samples of known lifetimes were examined using frequency domain detection schemes. The data were fit to a Laplace transform–based multiexponential lifetime model. The measured phase shifts and modulation amplitudes yielded lifetimes that were consistent with time-resolved measurements of the same samples. The technique was robust in the presence of fast fluorescence contamination, as well as with high levels of DC ambient light. Design parameters were established for a down-sized system that could make the hardware field-portable.

Background

Introduction

The recent advent of high-intensity blue and UV LED technology (specifically, GaN:In, gallium nitride doped with indium LEDs) permits a well-known laboratory technique of optical detection and identification to be adapted to portable field use. The work undertaken here used the new LEDs in a frequency domain spectroscopic technique to identify long-lifetime phosphorescent materials in the presence of substantial optical contamination. To our knowledge, this technique has never been taken out of the laboratory into field conditions where the experimental signals are subjected to high levels of ambient light and contamination from fast-decay fluorescence of common materials. The frequency domain technique is complementary to laser-induced fluorescence (LIF), and can actually surpass the performance of LIF in certain environmental conditions. Before describing the technique, let us define some terms.

Luminescence is the release of radiant energy from electronic transitions occurring within atoms and molecules. Photoluminescence is a type of luminescence induced by the absorption of photons. The photon absorption promotes electrons into excited states, which then decay to lower states emitting photons of lower energy. Fluorescence is photoluminescence from electron transitions that are called "electric dipole–allowed," and fluorescence occurs on a very short time scale, typically a few hundred nanoseconds. Phosphorescence is photoluminescence from "forbidden" or non-dipole-allowed transitions (usually resulting from a change of spin multiplicity). Phosphorescence happens on a much longer time scale, ranging from 100 microseconds to many seconds.

[1] dibeneja@nv.doe.gov, 805-681-2240

LIF is a luminescence technique using short-pulse, high-powered laser light. Fluorescence from laser-induced excitation is very characteristic of the particular atom or molecule involved, such that the wavelength and decay lifetime of a LIF process are often seen as fingerprints of the atom or molecule. The ability to identify chemicals by shining a laser onto them is obviously a very useful concept, and for a number of years the Special Technologies Laboratory (STL) has been using various LIF techniques in imaging applications called laser-induced fluorescence imaging (LIFI). The STL devices utilize wavelength filtering and time-resolved decay lifetimes for the study of both fluorescence and phosphorescence materials, and these systems have been very successful in forensics and environmental monitoring. In essence, LIFI takes the LIF concept into the photographic realm, enabling the identification and mapping of chemicals in the environment.

Being laser-based techniques, LIF and LIFI require expensive, bulky, and power-hungry lasers, which can be unsuited to certain field applications, where lightweight, compact, battery-powered devices are required. So, there is a clear need to adapt a luminescence technique for field use. Phosphorescence detection is an obvious first choice because the longer lifetimes involved do not demand the high bandwidth of a fluorescence technique. Additionally, a frequency domain technique is attractive since it constantly pumps the luminescence. Light levels remain constant and the detection does not have to dynamically scale over several orders of magnitude trying to follow luminescence decays. It must be stressed, however, that phosphorescence is often accompanied by fluorescence, so the phosphorescence technique must be robust in the presence of fluorescence. By the same token, the technique must have a certain immunity to ambient light. As an aside, we note that the driving light levels of the frequency domain technique can be substantially lower than light levels used in the time domain technique, so certain molecules that would be bleached or denatured by the intense light of the time domain technique can be successfully probed in the frequency domain.

In this undertaking, we showed that the frequency domain detection technique is valid for field use in the presence of high levels of optical contamination. Furthermore, the technique can be implemented using low peak-power UV LEDs and photodiode detectors of limited bandwidth. Using a benchtop setup consisting of commercially available instrumentation, we quantified a range of intensities of UV light required to excite a phosphorescent sample under conditions of varying levels of ambient light and large amounts of prompt fluorescence contaminants. From this brassboard assembly we can generate a set of specifications and identify components for the design of a low-power, portable phosphorescence measurement.

Technical Background

Time and frequency domain measurements of fluorescence lifetimes can be handled mathematically in a complementary and consistent fashion. The essence of the time domain technique is to rapidly transfer population into one or many excited states, and to then monitor the evolution of light emitted by the free decay of these states. The data from a time domain measurement show characteristic exponential decay. The frequency domain technique, on the other hand, consists of constantly driving

the exciting transition and monitoring the phase shift and demodulation of the fluorescence light relative to the driving light. This technique continuously replenishes the excited states, so the data are not as intuitive as that of the time domain method. The appearance of the plotted data depends very much on the waveform of the initial drive signal.

In the time domain, the rate equations governing the depopulation of the fluorescing excited states are homogeneous first-order differential equations. In the frequency domain they are non-homogeneous equations. For both, however, the equations can be written as follows:

$$\sum_i \frac{dN_i}{dt} - \Gamma_i N_i = g(t), \tag{1}$$

where the N_i are the excited state populations, the Γ_i are the decay rates, and *g(t)* is the driving function.

If *g(t)* is zero, or a delta function, then we have homogeneous equations of the time domain measurement. If *g(t)* is periodic, then we have non-homogeneous equations of the frequency domain. These are the same rate equations found in analog filter theory of electronics (Lacanette, 1991), where they represent simple first-order, low-pass filters. In electronics, the solution makes use of the Laplace transform and introduces the concept of the transfer function.

The transfer function for Equation 1 is:

$$F_i(s) = \frac{1}{(s + \Gamma_i)}, \tag{2}$$

where the variable *s* is the complex frequency variable of the Laplace transform. From this we can determine the phase shift and modulation amplitude of the filter response to a periodic driver function *g(t)*. This is accomplished by restricting *s* to the imaginary axis, and computing the mod of the transfer function for the modulation amplitude, and the ratio of the imaginary and real parts for the tangent of the phase shift. Further details of this technique can be found in an expanded version of this report (Trainham, in preparation). To analyze our data, we numerically computed these relations using complex arithmetic. Multiexponential decay was handled as a straightforward sum of the various single-state terms. Bandwidth limitations in the detection, which involve a convolution in the time domain, become a simple product of terms in the frequency domain.

The phase shift and modulation amplitude evolve on a frequency scale determined by the reciprocal lifetime. The range of frequencies is typically two orders of magnitude, and is centered at $2\pi\tau$ (i.e., the angular frequency of the reciprocal lifetime). Figure 1 shows the theoretical response assuming a single lifetime emission for various values of τ.

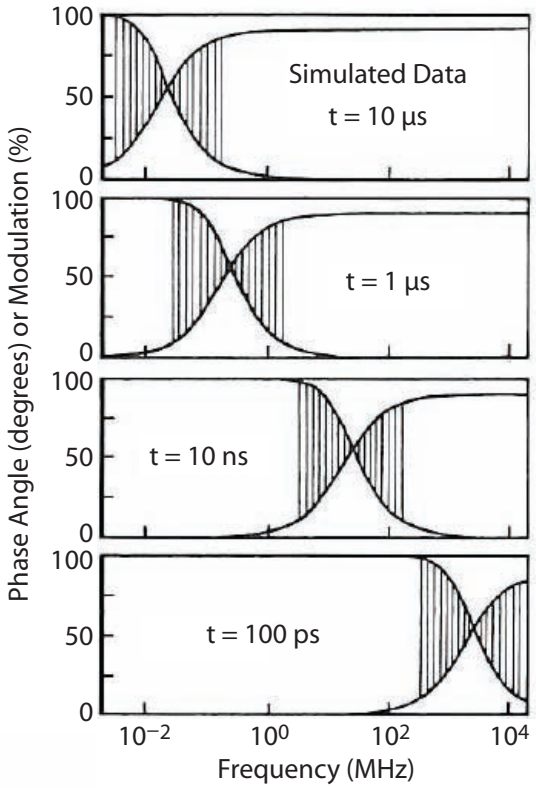

Figure 1. Relationship between the decay time and the useful range of light modulation frequencies (reprinted from [Lacowicz, 2006] sec. 5.1.A)

The frequency domain model used in our work differs slightly from that of prior published work (Lakowicz, 2006), in that previous models did not address bandwidth limitations of the detection system, nor did they consistently handle the addition of multiple lifetime components. Using the Laplace transform technique, these limitations and extensions are handled very elegantly.

Project

Experimental Setup

The basic experimental technique used in this work involved shaping the light emission from commercially available 365-nm UV-emitting LEDs into a sine or square wave, then ramping the frequency from tens of hertz into the hundreds of kilohertz range while directing the light onto a

phosphorescent sample. By measuring at each frequency the phase shift and modulation amplitude of the light emission from the sample, we were able to determine the component lifetimes. The data were analyzed by means of nonlinear least squares fits to the model functions.

Two experimental approaches were utilized in this project. The first was a commercially available device from TauTheta called a Multi Frequency Phase Fluorimeter (MFPF). The MFPF unit operated successfully, although the signal levels from the onboard LED were limited. We found that the MFPF could only measure single lifetimes over a limited range. This shortcoming was due to a combination of hardware limitations and inadequate software algorithms. Our second configuration was a tabletop assembly of discrete components. On the driver side, it consisted of a 365-nm LED array powered by a function generator coupled to a power amplifier, and focusing optics. On the receiver side, there was a PIN photodiode with a wavelength filter and a digital lock-in amplifier. All of the components, as well as the data acquisition, were under computer control. Figure 2 shows the arrangement of the tabletop brassboard assembly.

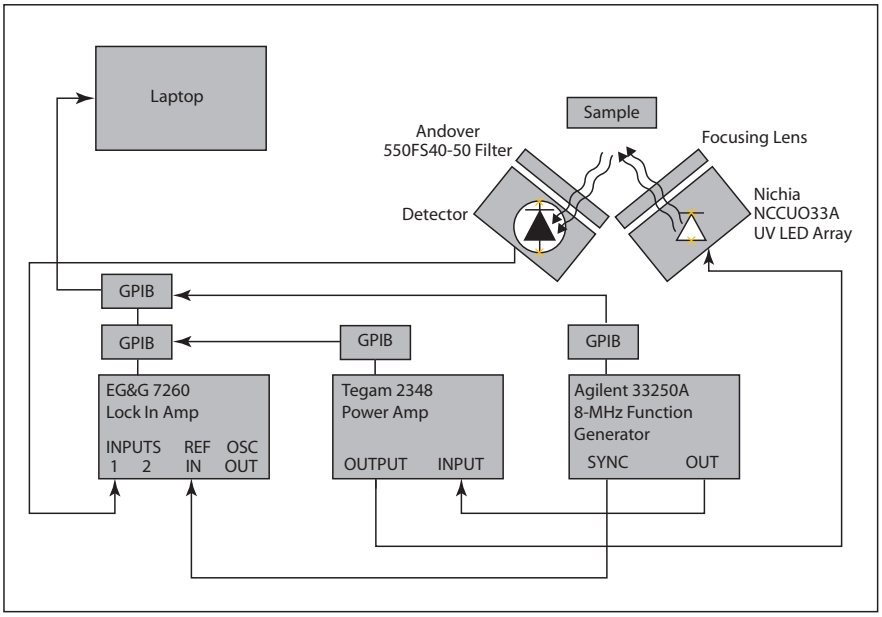

Figure 2. Block diagram showing the benchtop brassboard assembly

Data Collection and Analysis

Frequency domain data for phase and modulation amplitude are shown in Figure 3. The solid curves are least squares fits to models of one and two decay channels. The phase shift data clearly show indications of a two-component decay. The presence of a short lifetime component is the reason why the

curve peaks at <90 degrees, and then turns over. The fitted lifetimes are 910±13 μs and 0.245±0.006 μs. The amplitude data, however, do not clearly show sufficient structure to resolve a fast lifetime, so only a single lifetime model was used in the fit. The fitted lifetime is 900±4 μs. It is obvious from the forms of the curves that the amplitude fit is less sensitive to multi-lifetime structure, and that phase data is more sensitive to the fast decay component. The proper handling of fast decay components requires the detection system to have adequate bandwidth. If the bandwidth is limited, then the fitting model must explicitly account for that limitation. In the case of amplitude data, additional structure should not be assumed if there is no clear evidence of it.

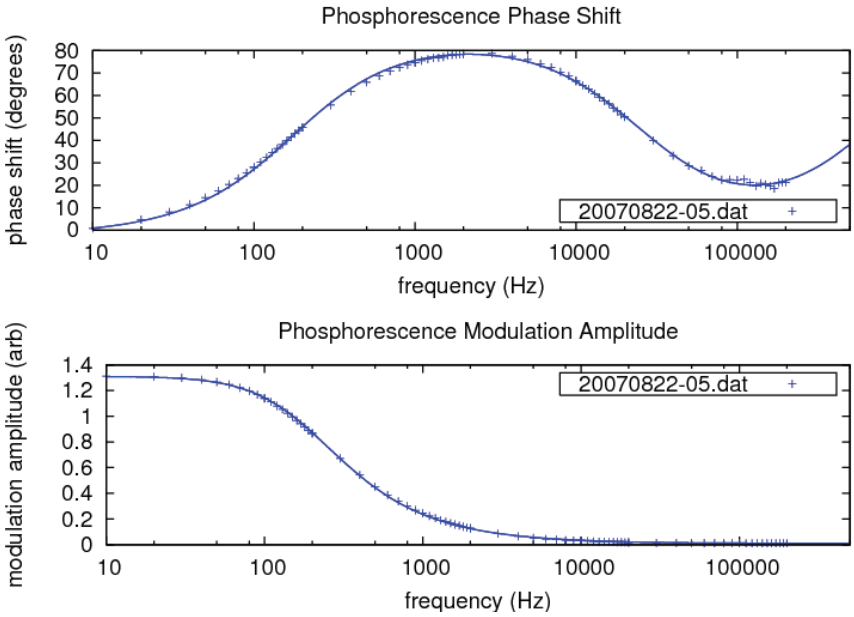

Figure 3. Phase and amplitude signals measured in the frequency domain. The solid curves are the result of fits to (top) two-component decay model for the phase data, and (bottom) single-component decay model for the amplitude data.

To gauge the effect of varying amounts of fast decay components in the fluorescence, we collected data from the same sample, but added fluorescence light of a short lifetime (τ ~2.5 ns) Coumarin 522B sample. We placed the sample next to the phosphorescent sample with both located in the field of view of the detector photodiode. By moving the Coumarin progressively into and out of the field of view, we were able to vary the amount of prompt fluorescence contamination. In this manner we were able to measure prompt contamination from 0% up to 100%. These data are shown in Figure 4 for the phase measurement, and in Figure 5 for the modulation amplitude. The solid lines through the data are results of least squares fits to the multicomponent decay model. We note that not only is the model qualitatively correct in form, but is also quantitatively correct for the levels of fast fluorescence contamination.

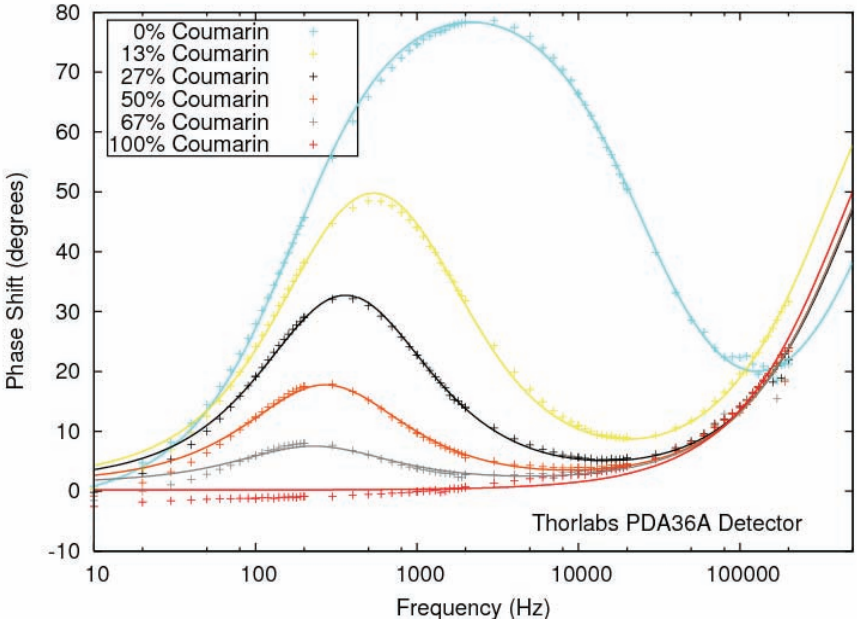

Figure 4. Phase data of phosphorescence in the presence of varying amounts of fast fluorescence contamination

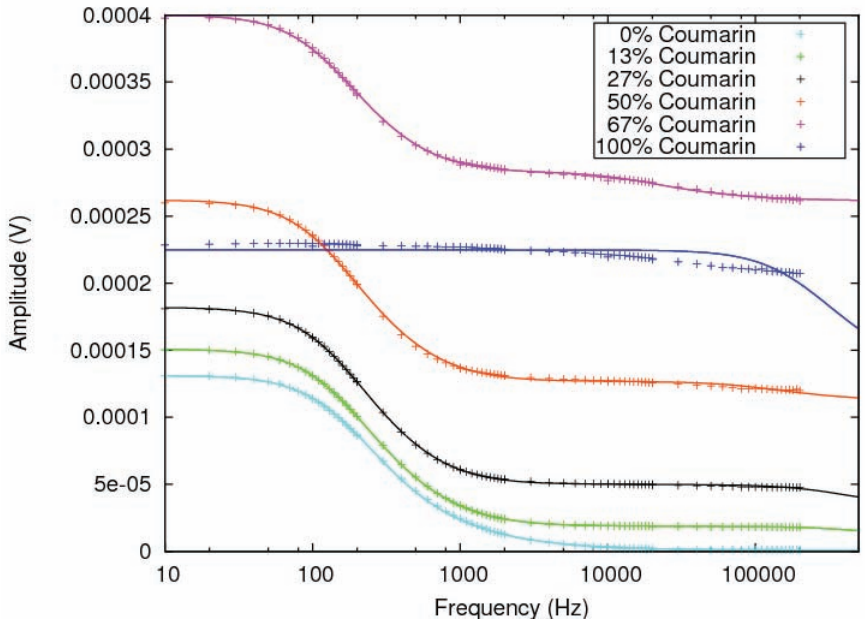

Figure 5. Modulation amplitude of phosphorescence in the presence of varying amounts of fast fluorescence contamination

Finally, we measured the immunity of the frequency domain technique for different levels of ambient light. Ambient daylight is constant (DC) light, and although the lock-in detection scheme rejects DC signals, the photodetector loses dynamic range when it is flooded with constant illumination. At some point the detection scheme must fail, but, a priori, it is unclear if the failure would be gradual or sudden. For a PIN photodiode detector the failure is sudden, showing a threshold beyond which the technique breaks down catastrophically (Figure 6). Beneath that threshold, however, the technique is robust and reliable. The ambient light level at failure is comparable to full daylight with the detector staring directly at the sun. Since it is unlikely that any use of the technique would involve aiming a detector directly at the sun, we conclude that the frequency domain measurement would be robust in full daylight. This is in contrast to pulsed time domain measurements, which cannot be operated in full daylight, because the long integration times needed to follow the decay tails of the luminescence would allow ambient light levels to destroy the intensified detectors. Quite simply, the time domain technique tries to follow a luminescence signal that dies away with time, whereas the frequency domain technique measures signals that remain strong because the pumping light constantly drives the luminescence.

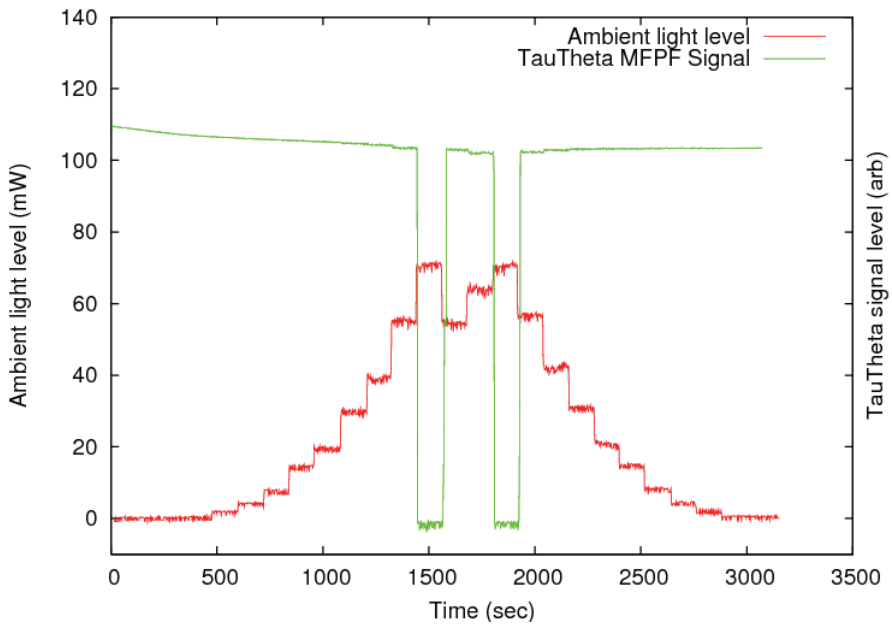

Figure 6. Solar immunity of frequency domain fluorescence detection. The green curve represents data of the modulation amplitude, and the red curve is the ambient DC light level. These data show that frequency domain detection is robust up to a failure threshold.

Conclusion

A benchtop test apparatus was assembled to demonstrate a frequency modulation measurement technique for phosphorescence lifetimes. The technique was robust in the presence of prompt fluorescence and with strong ambient DC background light. Our data was analyzed using a Laplace transform-based model to extract lifetimes, where this model was selected in part for its ability to effectively handle multiple exponential decay and detector bandwidth limitations. Our experimental results were in good agreement with data taken in a time domain measurement. Basic design parameters for a field system were established, enabling the future development of a prototype.

References

Lacanette, K., "A Basic Introduction to Filters—Active, Passive, and Switched-Capacitor," *National Semiconductor Application Note 779* (April 1991), http://www.national.com/an/AN/AN-779.pdf, accessed August, 2007.

Lakowicz, J. R., *Principles of Fluorescence Spectroscopy*, 3rd Edition, Springer Science+Business Media US, New York, New York, 2006.

Trainham, R., I. McKenna, J. Di Benedetto, "Frequency Domain Spectroscopy," Special Technologies Laboratory, Santa Barbara, California (in preparation).

this page intentionally left blank

Uranium Visualization Chemistry

John Di Benedetto,[1] *James Herning, Steve Jones, Clare Kimblin*
Special Technologies Laboratory

Marc Schrier
Calchemist, San Carlos, California

Craig Bias, Ken Czerwinski
University of Nevada, Las Vegas, Nevada

A new method for enhancing uranium phosphorescence was investigated. The strategy for developing the enhancing reagent was based on the photophysical properties of uranium(VI) [U(VI)] complexes. Variants of polyhedral oligomeric silsesquioxanes (POSS) ligand systems were investigated as tridentate structures for chelation of uranium. The efficiency of optical excitation/emission of the phosphorescence was used as the metric for success, as emission enhancement would be the final application. Spectra and time-resolved imagery data are presented in support of the primary conclusion that these compounds will enhance emission under the required environmental conditions expected in field use. Preliminary studies demonstrating the effect of iron, in the presence of ligands, on uranium phosphorescence are also described.

Background

Remote detection of uranium oxide phosphorescence has been useful for locating uranium at contaminated sites (Di Benedetto, 1999; 2007). Often the detection of the target emission is diminished by incomplete oxidation or matrix effects that either quench the emission or inhibit excitation of the material by the laser. The overall goal of this project was to develop a method, chemical formulation, and kit that could be used for remote delivery and detection of enhanced phosphorescence of uranium complexes on surfaces. The multi-component formulation would (1) mechanically or chemically extract the uranium complex to the surface of the material being probed for improved visualization, (2) oxidize reduced uranium to U(VI), and (3) chelate U(VI) with a ligand that enhances its phosphorescence by choosing a suitably absorbing chelating agent that separates it from iron.

The project team enlisted the help of the University of Nevada, Las Vegas (UNLV), to help understand the role of iron quenching as a competitive pathway for loss of emission intensity. After project initiation, it was determined that a great deal of effort would be required to perform reactions with

[1] dibeneja@nv.doe.gov, 805-681-2240

trace quantities of reagent-grade uranium acetate at National Security Technologies (NSTec). We chose instead to use an off-site contractor for test sample preparation. Dr. Marc Schrier, (Calchemist LLC) prepared sealed samples for optical analysis as part of this work.

Technical Motivation

Because the project goal was to enhance uranium phophorescence, the brightness of the emission was a primary metric for success. In pulsed time-resolved measurements, the U(VI) single-species lifetime typically displays a first-order decay that can be fit to a single exponential as in Equation 1, where k_1 is the observed rate constant. However, in most environmental conditions, mixtures of U(VI) oxide complexes are found and the emission lifetime is better determined by a series of exponentials (Equation 2), which are fitted with a nonlinear least-squares algorithm:

$$I(t) = I_o * \exp[k_1 * t] \quad \textbf{(1)}$$

$$I(t) = I_1 * \exp[k_1 * t] + I_2 * \exp[k_2 * t] + I_3 * \exp[k_3 * t] \quad \textbf{(2)}$$

Understanding the processes that enhance the phosphorescence is critical to system design. Fluorescence results from luminescence by a spin-allowed optical transition between singlet states. Spin-allowed radiative rates are high, on the order of 10^7 sec^{-1} or greater, and result in lifetimes on the order of nanoseconds, as observed with organic dyes. Phosphorescence is luminescence generated by a spin-forbidden transition between the lowest-energy triplet (T_1) and the electronic ground state, S_0 (Figure 1). Examples include triplet-to-singlet emissions from inorganic compounds such as transition-metal complexes, uranium oxides and fluorides, and dyes containing heavy atoms in solid matrices. The generalized observed phosphorescence lifetime (τ_{obs}) is the reciprocal of the sum of *all* rates (k) that depopulate the triplet excited state (Equation 3). The fraction of fluorophores that decay by emission is represented by the quantum yield (ϕ). The observed quantum yield is equal to the product of the observed lifetime and the radiative rate constant. If the radiationless decay rates are much smaller than the radiative decay rate, then quantum yield approaches unity, as

$$\tau_{obs} = 1/k_{obs} = \frac{1}{k_r + k_{nr} + k_q}, \quad \textbf{(3)}$$

$$\phi_{obs} = k_r * \tau_{obs} = \frac{k_r}{k_r + k_{nr} + k_q}, \quad \textbf{(4)}$$

where

ϕ_{obs} = observed yield,

k_r = radiative rate,

k_{nr} = non-radiative rate, and

k_q = quenching rate constant.

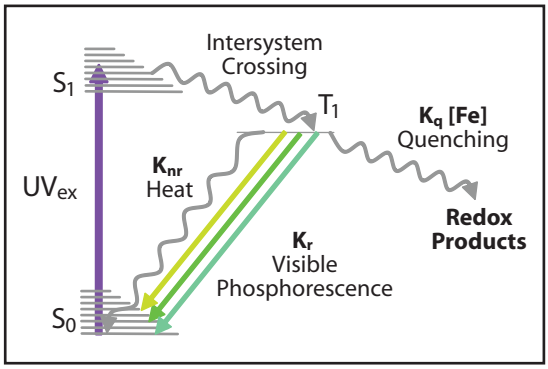

Figure 1. A Jablonski diagram of triplet emission

For U(VI), when the UO_2^{2+} ion is supported in a crystalline or polycrystalline lattice, non-radiative deactivation is blocked and k_r is on the order of 10^3 sec^{-1} (Brina, 1992). While some metal complexes have long lifetimes as solids and at low temperature, phosphorescence emission lifetimes can often be highly quenched by nonradiative (k_{nr}) and reactive (k_q) processes leading to lifetimes in the hundreds of nanoseconds (Yamamura, 1999). Coupling of the metal-centered excited state to the surrounding molecules through high-energy vibrational transitions is a particularly effective loss mechanism where the absorbed energy is lost as heat to the surrounding molecules. For lanthanides, actinides, and transition metals, water molecules in the first coordination sphere are particularly effective due to the strong O-H stretching frequencies in the infrared. The long-lived phosphorescence emissions of lanthanides display nearly linear loss of lifetime as the number of bonded water molecules increases (Beeby, 1999). In the case of uranium complexes, such thermal mechanisms are operating along with a second mechanism involving weakly bound solvents such as ethanol. Weakly bound ligands can cause quenching due to rapid bond breaking of the solvent in the first coordination sphere (Formosinho, 2003). The strong phosphorescence that can be observed for organophosphate uranium complexes may be due to strong ligand binding, which prevents water complexation. For this reason, we considered phosphorescence enhancement in which bonding to the metal ions involved non-labile

ligands with low numbers of protons. Bimolecular quenching can also be a major loss mechanism for phosphorescence, and in both diffusion-controlled and static mechanisms, iron can contribute significantly to loss of signal. Due to the ubiquitous nature of iron in the environment, part of this work focused on the effects of iron in solution and on dried samples.

Based on these considerations, we chose to investigate multidentate ligands based on silicon oxides. A literature search found research on silica gels (Sutton, 2003) and silico-chelates (Lorenz, 2000) demonstrating promising templates for long-lived emissions. In our approach, tridentate and tetradentate (with two bidentate coordination sites) functionalized silanols, or silanol salts, from Hybrid Plastics were used. Figures 2a and 2b show the ethyl-substituted trisilanol POSS (SO1444)[2] and the sodium salt of a phenyl-substituted tetrasilanol POSS (SO1460), respectively. The pendant group influences solubility. The ethyl substituent was chosen because ethanol is the target solvent for the final formulation. Figure 2c shows a proposed six-coordinate uranyl complex coordinated by SO1460.

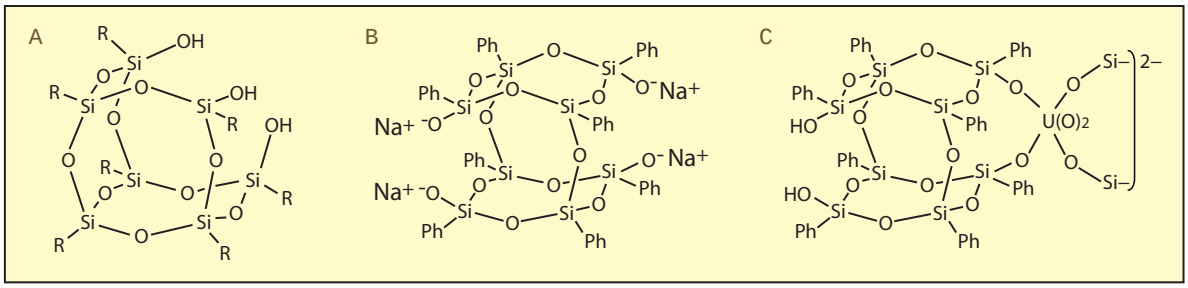

Figure 2. (a) TriSilanolEthyl-POSS® (SO1444); (b) Tetrasodium salt of TetraSilanolPhenyl-POSS® (SO1460Na); (c) proposed coordination of uranyl by SO1460Na

Project

Experiments in the Absence of Iron

Thirteen samples made by Calchemist are listed in Table 1. The first five samples were created to look at ligand fluorescence. For samples 8–13, dissolved uranium acetate was reacted with an excess of dissolved POSS ligand. Solvents were selected in which both starting materials were soluble. Two classes of end products were obtained: washed precipitate (the supernatant was not saved) or evaporated solution (when no precipitate was observed). Each resulting sample was deposited in a 1-in.-diameter Delrin sample holder and sent to the Special Technologies Laboratory (STL) for spectral/temporal analysis. The sample holders were fabricated at STL and fitted with a quartz window and expansion

[2] 1,3,5,7,9,11,14-Heptaethyltricyclo[7.3.3.1(5,110]heptasiloxane-endo-3,7,14-trisodiumsilanolate. Product Name: TriSilanolEthyl-POSS, Product Number: SO1444

plug (foam) to assure a good seal during shipping and handling. (The holders were drop-tested from 25 ft onto blacktop with no failures of the cell integrity.) Fluorescence spectra were collected using a F4500 Hitachi Spectrofluorimeter. Slit widths were constant for 5-nm resolution. The sample holders were oriented so that the excitation beam struck the samples at an angle of 30 degrees to normal, and the emission beam exited the samples at an angle of 60 degrees to normal relative to excitation and emission spectrometers. To further minimize first surface reflection of the incident excitation beam reaching the detector, the sample was angled in the third dimension with respect to the excitation/emission plane. Fluorescence spectra were collected from 380 to 700 nm at a 355-nm excitation wavelength. Spectrometer emission calibrations were performed prior to these measurements. Samples that exhibited emission were also evaluated using time-resolved laser-induced fluorescence imaging (LIFI).

Table 1. List of sealed samples delivered by Calchemist. Films were evaporated onto sample holders. Precipitates were placed in sample holders.
◊◊◊ indicates emission * indicates no emission**

POSS Standards (deposited without uranium)			
1	TrisilanolEthyl POSS (SO1444)		Film from POSS dissolved in MeOH
2	TrisilanolIsobutyl POSS, Li salt (SO1450Li)		Film from POSS dissolved in THF
3	TrisilanolPhenyl POSS (SO1458)		Film from POSS dissolved in MeOH
4	TrisilanolPhenyl POSS, Li salt (SO1458Li)		Film from POSS dissolved in MeOH
5	TetrasilanolPhenyl POSS, Na salt (SO1460Na)		Film from POSS dissolved in MeOH
U-Standards (deposited without added ligand)			
6	$UO_2(OAc)_2$ w/out added POSS	◊◊◊	Powder dispersed in $CHCl_3$ (not soluble)
7	$UO_2(OAc)_2$ w/out added POSS	◊◊◊	Film from sample dissolved in MeOH
U-POSS reactions to form complexes			
8	U-SO1444 from IPA	◊◊◊	No ppt formed, XS POSS in solution
9	U-SO1450Li from Acetone	***	Washed ppt, so U and free-POSS-free
10	U-SO1458 from MeOH	***	Washed ppt, so U and free-POSS-free
11	U-SO1458Li from IPA	***	No ppt formed, unknown stoichiometry
12	U-SO1460Na from H2O	***	Washed ppt, so U and free-POSS-free
13	U-SO1460Na from EtOH	◊◊◊	Washed ppt, so U and free-POSS-free

MeOH: Methanol
THF: Tetrahydrofuran
EtOH: Ethanol
IPA: Isopropanol (aka 2-propanol)
ppt: precipitate
XS: excess
$CHCl_3$: Trichloromethane

LIFI images were collected using a 355-nm pulsed Nd:YAG (7 ns) laser and an intensified camera (Di Benedetto, 2007). The camera lens had a 525 × 70 nm band-pass filter. The camera's electronic shutter is a microchannel plate, and the timing relative to the laser excitation is reported in terms of delay from excitation and gate width. Ten gate-and-delay values are used to capture the maximum emission during the phosphorescence decay (longer gate widths are used at longer delay times). Each sample in the image was treated as a separate region of interest (ROI), and the average pixel value at each ROI was used to evaluate the emission decay of each sample as a function of time. A nonlinear least-squares routine was used to fit the observed decay to three exponential terms (Equation 2).

UNLV Experiments on Iron Interference

To study the dependence of uranyl phosphorescence on relative concentrations of uranyl, iron, and ligand, a series of solutions were prepared at UNLV. Aqueous stock solutions of uranyl perchlorate, iron(III) perchlorate, citric acid, ascorbic acid, disodium hydrogen phosphate, and solutions of uranium and SO1444 in acetone were prepared.

In the following, [U], [Fe], and [L] refer to molar concentrations of uranium, iron, and ligand, respectively. To establish baseline uranyl phosphorescence in the solution matrix and at the parameters chosen for laser fluorescence spectroscopy measurement, solutions containing $0 < [U] < 5$ mM were prepared in water and in acetone. The quenching effects of iron were verified using solutions ranging from [Fe]:[U] = 2:1 up to [Fe]:[U] = 50:1 in water and in acetone. To study the phosphorescence enhancement effects of each ligand in the absence of iron, solutions ranging from [L]:[U] = 2:1 up to [L]:[U] = 50:1 were prepared in either water or acetone, as applicable. Finally, solutions containing [U] = 5 mM, [Fe] = 50 mM, and $0 < [L] < 50$ mM were prepared in either water or acetone, as applicable, to study the phosphorescence enhancement effects of each ligand in the presence of iron. All solutions prepared in water were hand-adjusted to pH = 2 (with the final diluent volume to minimize precipitation), centrifuged, and the supernatant decanted for analysis. The solution phases of each prepared solution were measured by UV-Vis spectrometry for absorbance, inductively coupled plasma atomic emission spectroscopy for concentration, and laser spectroscopy for phosphorescent intensity. Precipitates from the above series were dried pending further analysis. SO1460Na and SO1458 were not studied in this initial effort.

Results and Discussion

Experiments in the Absence of Iron

The diamonds and asterisks in Table 1 indicate whether or not emission was observed for samples 1–13, respectively. Given the aliphatic structure of the ligand, it was not surprising that little or no visible fluorescence was observed during optical analysis of ligand-only samples 1 through 5. Samples 6 and 7 contain emissive, dried uranium acetate without addition of POSS ligands.

The uranium acetate dissolved in methanol (MeOH), but remained a solid in trichloromethane ($CHCl_3$). We assume that the $CHCl_3$ solvent did not interact with the polycrystalline salt, and refer to it as the washed or powder sample. Samples 8 through 13 were collected after the uranium acetate was mixed with the POSS ligands and dried. Note that samples 9, 11, 12, and 13 are made with sodium or lithium salts of the POSS ligands. This is important, as the sodium and lithium POSS ligands will have very different complexation properties relative to the protonated neutral ligand. However, at this time we do not have pK_a measurements for the ligands, and it is not clear how quickly these salts will reprotonate in protic solvents, such as alcohols. Solution pH will likely change reactivity. Of the thirteen samples tested, only four showed significant uranium phosphorescence in the spectrometer and imaging measurements (6, 7, 8, and 13 [Table 1, red diamonds]). Samples 9, 10, 11, and 12 did not show uranium emission (Table 1, blue asterisks). These sample preparations will be repeated in experiments next year in a second run by Calchemist.

Figure 3 shows the emission spectra for the four emitting samples, a polycrystalline sample of UO_2F_2, and peak separations. The spectra for polycrystalline UO_2F_2 and the UO_2:SO1460 complex (for which we assume there is some U-POSS complexation) were plotted at ⅒ of recorded intensity. The $UO_2(OAc)_2$ in methanol and product of the reaction of $UO_2(OAc)_2$ and SO1444 in isopropanol were plotted at ½ intensity. Figure 3 shows that there are major spectral differences between samples that were dissolved, dispersed, and reacted with one of the POSS ligands. Both samples that dissolved in alcohols have a structureless emission centered at 525 nm. The uranium acetate, UO_2F_2, and UO_2:SO1460 samples exhibit structured emissions with significant shifts between the peaks of each compound. The POSS complex is shifted to higher energy relative to both uranium acetate and UO_2F_2. Although we cannot make peak assignments to the individual spectra, these data are consistent with strong bonding between the uranium and the tridentate POSS ligand. Minor differences in the peak separation (same spectra) indicate that the energy levels are not significantly altered between complexes.

Figure 4 shows a cropped photo of eight of the thirteen samples. Note the lack of uniformity in the sample deposition. This makes raw *intensity* comparisons between samples suspect, and this is an equally strong variable in field measurements. For now we can only tackle spectral difference with Figure 3, addressing true brightness later using time-resolved imagery with the lifetimes and rate equations for yield.

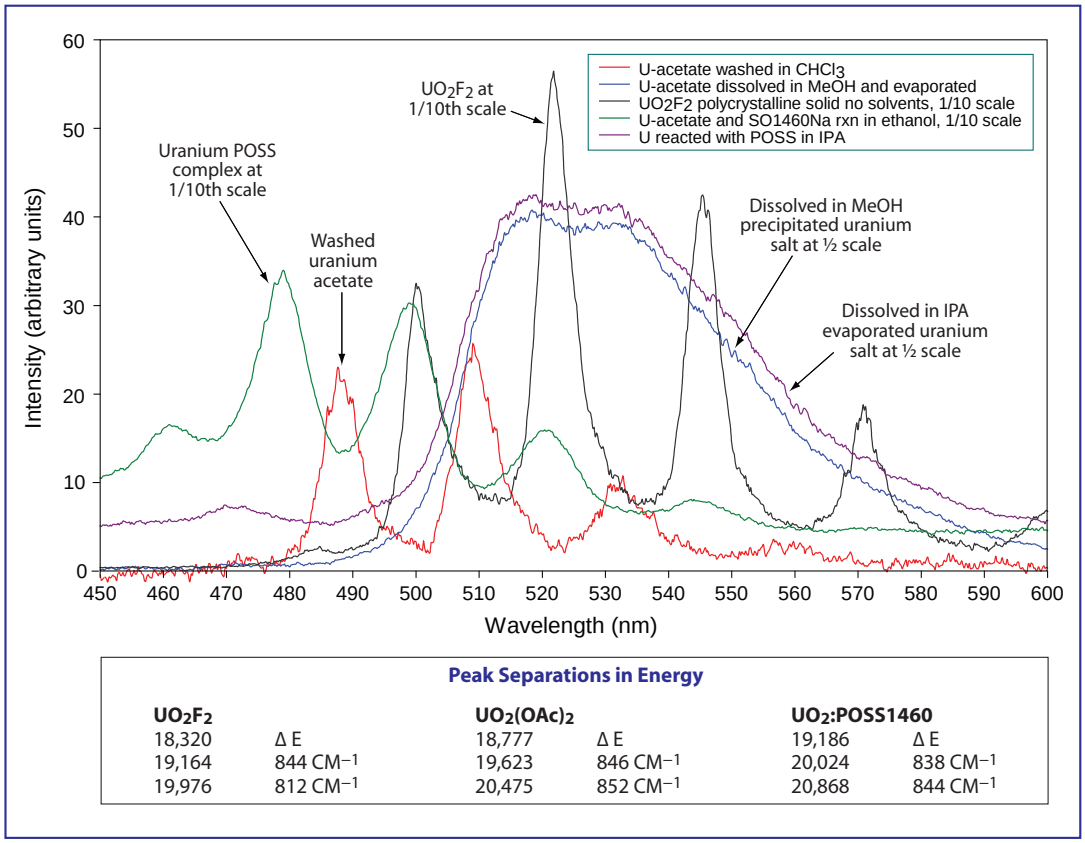

Peak Separations in Energy

UO_2F_2		$UO_2(OAc)_2$		UO_2:POSS1460	
18,320	Δ E	18,777	Δ E	19,186	Δ E
19,164	844 CM^{-1}	19,623	846 CM^{-1}	20,024	838 CM^{-1}
19,976	812 CM^{-1}	20,475	852 CM^{-1}	20,868	844 CM^{-1}

Figure 3. Fluorescence spectra of uranium samples and a table of peak separations in energy

Table 2. Lifetime fits for each sample

Sample	Lifetime Estimates	Yield Factors
$UO_2(OAc)_2$ from $CHCl_3$	200 ns	0.45
	2.23 µs	0.34
	44.84 µs	1.00
$UO_2(OAc)_2$ from methanol	**150 ns**	1.00
	1.27 µs	0.92
	3.49 µs	0.52
UO_2 SO1444 from IPA	**140 ns**	1.00
	1.23 µs	0.80
	3.80 µs	0.94
UO_2 SO1460 from ethanol	410 ns	0.06
	20.18 µs	0.45
	87.26 µs	1.00

Figure 4. (a) Photograph of test samples and (b) LIFI imagery. Panel is a false-color composite (RGB), with the red (R) given from the longest band (delay = 99.9 µs, width = 99.9 µs), green (G) at 5.94 µs and below, and blue (B) from the shortest/earliest band (d = 81 ns, w = 285 ns).

Figure 4 shows the LIFI imagery corresponding to the photograph. The RGB representation uses three of the ten bands collected (Band 1:Band 5:Band 10). By using a 2% linear stretch of each of the bands, blue intensity represents shorter lifetimes, while red indicates those pixels containing predominantly long-lived emission. Note that the solutions from methanol (MeOH) and isopropyl alcohol (IPA) exhibit bright blue emission with no indication of a long-lived component. While this visual is qualitatively useful, processing all ten bands in the nonlinear least-squares routine produces the three-component lifetime data in Table 2. The dominant lifetimes are shown in bold text. The UO_2:SO1460 reaction has produced a complex that is both structured and long-lived. This passes our design criteria for a material that is robust to oxidation, displays a long-lived emission, and is compatible with common solvents.

UNLV Experiments on Iron Interference

Phosphorescence in the Absence of Added Ligand

As expected, solution-phase sample measurements in both water and in acetone verified that in the absence of iron, phosphorescence increased linearly with increasing uranyl concentration. In the presence of iron, phosphorescence decreased linearly with increasing iron concentration. Phosphorescence was greater in acetone than in pH = 2 water for samples with equivalent uranyl concentrations.

Phosphorescence in the Presence of Added Ligand

Results are summarized in Table 3. In the absence of iron, uranyl phosphorescence was significantly increased when SO1444 was added to uranyl in acetone. The other ligands had limited or no effect on solution phosphorescence. For phosphates used in the presence of iron, iron continued to substantially quench uranyl phosphorescence in solution until [Fe] = [PO_4^{3-}], where the total precipitation of iron as strengite ($FePO_4$) results in the phosphorescent intensity of the residual, non-coprecipitated uranyl nearing that of solutions with equivalent uranyl concentrations without ligand or iron. In the presence of both citrate and ascorbate, iron substantially quenched uranyl phosphorescence in all measured samples. Iron substantially quenched uranyl phosphorescence in POSS SO1444 uranyl solutions except when [POSS] and [Fe] were significant relative to [U]. The sample containing [U] = 5 mM and [Fe] = [POSS] = 50 mM fluoresced.

Table 3. Summary of ligand effect on uranium phosphorescence in the presence and absence of iron

	Phosphate (aq.)	Citrate (aq.)	Ascorbate (aq.)	SO1444 (acetone)
No iron	Supernatant had only moderately enhanced phosphorescence	No enhancement	Inconclusive	Significantly higher phosphorescence than observed in solution samples containing only uranyl in acetone
With iron present	Fe quenched uranyl phosphorescence until [Fe] = [PO_4^{3-}], when iron precipitated out as strengite	Substantial quenching by iron in all measured samples	Substantial quenching by iron in all measured samples	Iron quenching observed, except with the sample containing [U] = 5 mM and [Fe] = [POSS] = 50 mM

Conclusion

When uranium acetate and SO1460 were dissolved in ethanol, a complex precipitated. The photophysical behavior is consistent with chelation by the phenyl-substituted POSS ligand. Bright phosphorescence was found, indicating this complex as a good candidate for further development.

However, given the simplistic chemical preparation of these complexes, and the limited number of test samples made, additional samples must be tested to optimize the formulation. This will likely involve a combinatorial study involving changes to ligand structure, solvent pH, etc. Also needed is a better understanding of variations in the chemistry that may occur on surfaces that are less benign than plastic and glass. Solution buffering should also be investigated.

Without question, iron quenching will become a more important element of this work as the formulation's oxidative properties are further investigated. Initial iron studies were performed with SO1444, phosphate, citrate, and ascorbate. Only the use of phosphate and SO1444 indicated enhanced uranium phosphorescence, both in the presence and absence of iron. The uranium phosphorescence observed with phosphate and high concentrations of iron, was a result of the precipitation of iron as strengite. It is not yet known if a similar coordination of iron by POSS occurs. Many questions remain. While these iron interference studies were performed only with SO1444, some of the behavior is expected to be generic for these ligands; the performance of additional POSS ligands needs to be investigated. The choice of solvent for the system also needs to be evaluated to facilitate uranium sequestration by optimizing uranium-ligand complexation in the presence of iron. Further efforts should focus on the precipitates formed from complexation or coprecipitation of the uranium, iron, and ligand. Future analysis of samples should also include fluorescence intensity and lifetime measurements. Furthermore, the [L]:[Fe] ratio should be much higher than unity in future systems, since that is nominally the threshold at which the effects of iron quenching begin to decrease.

Acknowledgments

We gratefully acknowledge the contributions of Glen Anthony and Tom Keenan to the design and execution of selected experiments during this project.

References

Beeby, A., I. M. Clarkson, R. S. Dickins, S. Faulkner, D. Parker, L. Royle, A. S. de Sousa, J. A. Gareth Williams, M. Woods, "Non-radiative deactivation of the excited states of europium, terbium and ytterbium complexes by proximate energy-matched OH, NH and CH oscillators: an improved luminescence method for establishing solution hydration states," *J. Chem. Soc., Perkin Trans. 2* (1999) 493–504.

Brina, R., A. G. Miller, "Direct detection of trace levels of uranium by laser-induced kinetic phosphorimetry," *Anal. Chem*. **64**, 13 (1992) 1413–1418.

Di Benedetto, J., "Laser-induced fluorescence imaging," *Arms Control and Nonproliferation Technologies: Partnering with Law Enforcement: Forensic R&D*, Department of Energy, DOE/NN/ACNT-SU99 (Summer 1999) 16, http://ftp.fas.org/sgp/othergov/doe/acnt/1999.pdf, accessed September 30, 2007.

Di Benedetto, J., K. Kyle, C. Morgan, "Portable uranium survey tool using laser-induced fluorescence imaging," Ames Lab: Characterization, Monitoring, & Sensor Technology Crosscutting Program, Ames, Iowa, 97–100, http://www.external.ameslab.gov/cmst/CMSTSite/Projects/TSB/D5_DiBenedetto.pdf, accessed September 30, 2007.

Formosinho, S. J., H. D. Burrows, M. da Graça Miguel, M. Emília, D. G. Azenha, I. M. Saraiva, A. Catarina, D. N. Ribeiro, I. V. Khudyakov, R. G. Gasanov, M. Bolte, M. Sarakha, "Deactivation processes of the lowest excited state of $[UO_2(H_2O)_5]^{2+}$ in aqueous solution," *Photochem. Photobiol. Sci*. **2** (2003) 569–575.

Lorenz, V., A. Fischer, S. Giessmann, J. W. Gilje, Y. Gun'ko, K. Jacob, F. T. Edelmann, "Disiloxanediolates and polyhedral metallasilsesquioxanes of the early transition metals and *f*-elements," *Coordination Chemistry Reviews* **206–207** (September 2000) 321–368.

Sutton, M., P. Warwick, A. Hall, "Uranium(VI) interactions with OPC/PFA grout," *J. Environ. Monit.* **5** (2003) 922–928.

Yamamura, T., Z. Fazekas, M. Harada, H. Tomiyasu, "New mechanism in deactivation of excited uranyl(VI) ion by lanthanide(III) ions," *Phys. Chem. Chem. Phys.* **1** (1999) 3491–3496.

Field Testing a Gamma-ray Telescope for Search and Consequence Management Missions

Carrie Fitzgerald,[1] *William Noonan (former employee), Jack Tueller*
Remote Sensing Laboratory – Andrews

The National Aeronautics and Space Administration (NASA) has designed, built, and put into orbit a wide field of view gamma-ray telescope to survey the sky for extragalactic gamma-ray bursts. This telescope, the Burst Alert Telescope (BAT), comprises a coded aperture and a focal-plane array of 32,768 CdZnTe (CZT) detectors. The NASA Goddard Space Flight Center (GSFC) maintains a smaller engineering model of this instrument on the ground. Collaboration between the Remote Sensing Laboratory – Andrews (RSL–A) and GSFC was initiated in order to test this 2048-element model for the detection and location of terrestrial radiation sources. For use in the field, the engineering model will require modifications to ruggedize the instrument against stresses commonly encountered during search and consequence management missions. Furthermore, the algorithms that reconstruct the images must be modified for earth-based (i.e., noninfinite) source distances.

Background

Gamma-ray imaging is useful in search missions, since it allows the searcher to survey a scene from a single vantage point and pinpoint any sources in a single measurement. NASA chose a coded-aperture approach for the BAT because of its superior sensitivity when imaging point sources. For this same reason, it is a good choice for search missions.

Other coded-aperture cameras developed for homeland security purposes generally suffer from low energy and spatial resolution. Further collaboration between RSL and GSFC will provide the opportunity to push the limits of coded-aperture technology.

Imaging with Coded Apertures

A coded aperture or coded mask is a pattern that creates a shadow on an image plane. For a point source, if the position of the image and mask are known, then the direction of origin of a source can be derived. This method can be applied even if multiple sources are present. The shadows may not be recognizable to the naked eye, but the positions of the sources can be deconvolved by computer reconstruction. While in principle any shape can be used for the mask, it can be shown that the most efficient mask pattern is one that is 50% open and 50% closed. A more closed pattern obstructs too much of the detectors, which leads to low efficiency; however, a more open pattern reduces the contrast (Phlips, 2006).

[1] fitzgecm@nv.doe.gov, 301-817-3361

The BAT Instrument and the Engineering Model

The orbiting BAT consists of 32,768 pieces of 4 × 4 × 2–mm CZT to form a 1.2 × 0.6–m sensitive area in the detector plane. Groups of 128 detector elements are assembled into 8 × 16 arrays and each array is connected to 128-channel readout application-specific integrated circuits. Detector modules contain two such arrays and are further grouped by eights into blocks. The engineering model to be tested consists of one of the 2,048 element blocks and will use electronics identical to those on the BAT. A single 8 × 16 array is shown in Figure 1.

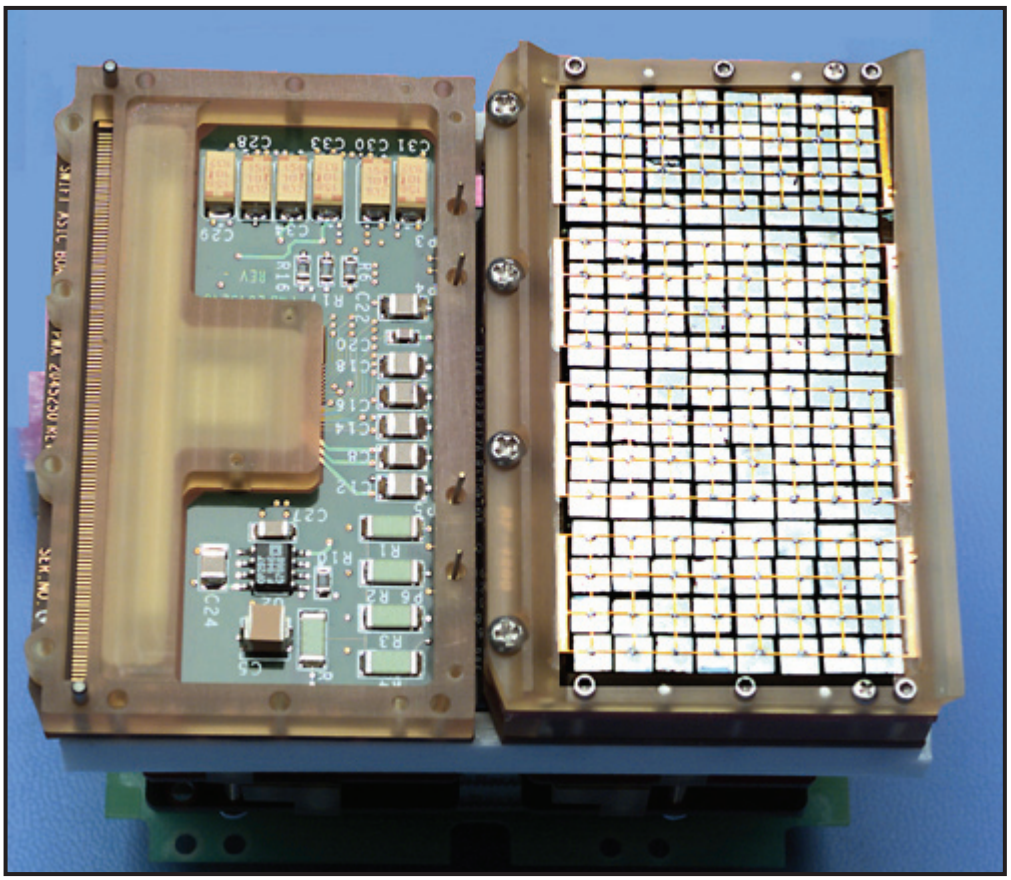

Figure 1. An 8 × 16 pixel array of the BAT (NASA, 2006). This is one of the 256 modules composing the BAT. It contains 128 separate CZT detectors with an aggregate sensitive area of 20 cm^2.

The BAT has a coded-aperture mask consisting of approximately 54,000 5 × 5 × 1–mm lead tiles mounted on a 5-cm-thick composite honeycomb panel. The panel is mounted 1 m about the detector plane. The BAT coded aperture uses a completely random, 50% open/50% closed pattern rather than the commonly used uniformly redundant array pattern. The engineering model to be tested employs a similar type of coded aperture, only it will be scaled to the smaller size of the detector. Unlike the BAT, however, the aperture-to-detector distance will be variable.

CZT as a Detector Material

CZT is the acronym for the ternary compound $Cd_{1-x}Zn_xTe$, where x is the blending fraction of ZnTe in CdTe. The range of x is generally between 0.04 and 0.2, corresponding to band gap energies of 1.53 eV and 1.64 eV (Knoll, 2000). CZT has many advantages when compared to other gamma-ray detecting materials; for example, the large band gap energy and the sufficiently low amount of energy needed to create an electron-hole pair. The wide band gap allows CZT detectors to be operated at room temperature, a desirable feature for field use. A result of the low energy for electron-hole pair creation is better resolution when compared to other room-temperature gamma-ray detectors (5%, or 3.3 keV at 60 keV). A spectrum of ^{241}Am taken with one of the BAT detector modules is shown in Figure 2 (NASA, 2006). Other advantages of CZT are its superior intrinsic photopeak efficiency and good photopeak-to-Compton ratio, both of which derive from CZT's high atomic number.

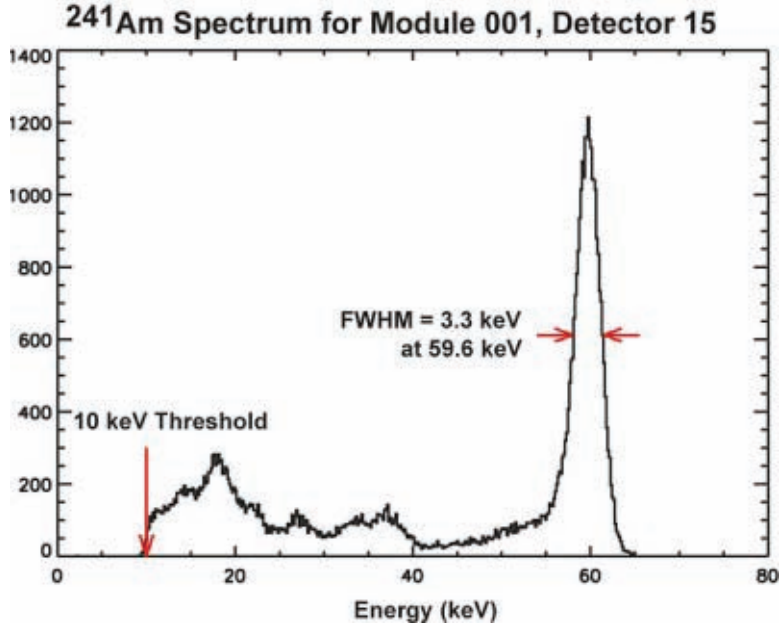

Figure 2. A spectrum of ^{241}Am taken with a BAT detector module (NASA, 2006)

CZT also has several disadvantages that should be noted. First, both the mobility and lifetime of the electrons are very different from that of the holes. The measured mobilities are 1,350 $cm^2/V \times s$ for electrons and 120 $cm^2/V \times s$ for holes (Knoll, 2000). The measured hole lifetime is between 100 ns and 3 μs for electrons, and from 50 to 300 ns for electron holes (Knoll, 2000). However, the low mobility and short lifetime of the holes result in their being trapped very quickly, and therefore they do not contribute to the formation of a full-energy signal. Consequently, the photopeak suffers from low-energy tailing. Another disadvantage of CZT is the difficulty in producing high-quality, large, homogeneous single crystals. CZT is currently in high demand and remains one of the more expensive detector materials. Nevertheless, it is expected that new manufacturing techniques will develop, allowing the production of thick CZT. Also, the price of CZT is expected to decrease over time.

Project

Originally the scope of work had five major steps:

1. Modification of the instrument for field use
2. Experiment planning
3. Bench testing at GSFC
4. Experiments at the Nevada Test Site
5. Experiments at the Federal Law Enforcement Training Center

Unfortunately the project suffered an eight-month delay due to funds not being transferred to GSFC. The result of this delay is that the group could not begin work on the instrument until late July 2007, two months before the end of FY 2007. The delay forced us to modify the scope of work, resulting in the following steps:

1. Modification of the instrument for field use
2. Experiment planning

GSFC is in the process of making the machine more rugged so that it meets requirements for field use. These modifications will allow the detector to operate in environments with changing temperature, humidity, and pressure. Requirements for shock, vibration, microphonics, and radio frequency interference will also be addressed. In addition to physical and environmental modifications, the instrument's image reconstruction algorithm will need to be changed to accommodate sources at noninfinite distances.

The experiment planning was completed at RSL–A. The test plan originally included detector characterization of properties such as efficiency, energy resolution, and spatial resolution. The plan specifies the sources to be used and source-detector geometries. These characterization measurements would be performed at GSFC during bench testing of the project. Once the detector is fully characterized,

it would be taken to RSL–A where a set of experiments designed to determine the effectiveness of the instrument in field-like, reproducible conditions using realistic sources and shielding would be performed.

Conclusion

This project did not meet the initially planned milestones. Nevertheless, progress has been made in modifying the detector block, and characterization measurements have begun. Evaluation of CZT as a field-usable detector material certainly has technical merit, and the exploration of coded-aperture detectors for detection and location of radiation sources is a promising area of research that should be pursued.

References

Knoll, G. F., *Radiation Detection and Measurement, 3rd ed.,* John Wiley & Sons, Inc., New York, New York, 2000, 486–488.

National Aeronautics and Space Administration, Goddard Space Flight Center, Swift's Burst Alert Telescope (BAT), 2006, http://swift.gsfc.nasa.gov/docs/swift/about_swift/bat_desc.html, accessed September 20, 2007.

Phlips, B., Naval Research Laboratory, private communication, 2006.

this page intentionally left blank

Fissile Material Detection Using Borated Paint

Raymond P. Keegan,[1] *Scott Wilde*
Remote Sensing Laboratory – Nellis

The technique explored in this project converted a gamma spectrometer into a dual gamma-neutron detection system while maintaining normal gamma spectrometer capability. This dual detection system exploits the neutron-gamma count rate buildup from a borated plane to enhance the neutron count rate. A 5% borated polyethylene panel with a neutron source on one side and a high-purity germanium spectrometer immediately opposite was used. The count rate buildup factor for the described setup was 4.4 ±0.3. We investigated the application of this technique to portal systems through both experiment and simulation, and the results were in reasonable agreement. We also quantified the efficiency of the technique when used in the manner described in this report.

Background

This work used borated polyethylene to convert a gamma spectrometer into a dual gamma-neutron detection system while maintaining normal spectrometer capability. Our investigation was similar to that described by Ghanbari (2001), where borated polyethylene caps were placed over a sodium iodide detector. In this project, a plane of borated polyethylene was placed in front of a high-purity germanium (HPGe) detector to exploit the expected neutron-gamma count rate buildup in the detector. Although we proposed to use borated paint, we ultimately used borated polyethylene due to its neutron thermalization properties, and because it presented fewer safety and health hazards. Neutron detector designs that use boron usually place borated material inside the detector or within close proximity, where the borated material dimensions tend to be roughly the same as the detector's active volume. Our work concentrated on portal system applications; however, the ideas could be applied to other types of gamma spectrometry instrumentation.

This paper focuses primarily on the application of the ^{10}B thermal neutron-induced fragmentation reaction:

$$^{10}B + {}^{1}n \rightarrow \begin{cases} {}^{7}Li + {}^{4}\alpha & (6\%) \\ {}^{7}Li^{*} + {}^{4}\alpha & (94\%) \end{cases}. \qquad \textbf{(1)}$$

[1] keeganrp@nv.doe.gov, 702-295-1005

The excited $^{7}Li^{*}$ nucleus has a half-life of about 10^{-13} sec, and loses energy through emission of a 478-keV photon while still recoiling, resulting in Doppler broadening of the gamma peak. The reaction has a cross section of 3840 barns, and the abundance of ^{10}B in natural boron is 19.8%.

This work supported two related missions, combating terrorism and supporting nonproliferation, thereby strengthening national security. Our goal was to enhance detection of hidden, shielded fissile material in shipping containers. Our dual detection system could provide spectral information that, when coupled with gamma peak analysis software, would likely reduce the number of false alarms observed with portal systems. Such systems usually employ a combination of gamma spectrometers and ^{3}He tubes to detect and identify radioisotopes. The technique we proposed eliminates the need for ^{3}He tubes, simplifies portal system engineering, and improves system reliability.

Project

We performed analytical mathematical work for a hypothetical setup comprised of a borated panel placed between a plane detector and a neutron source (Figure 1).

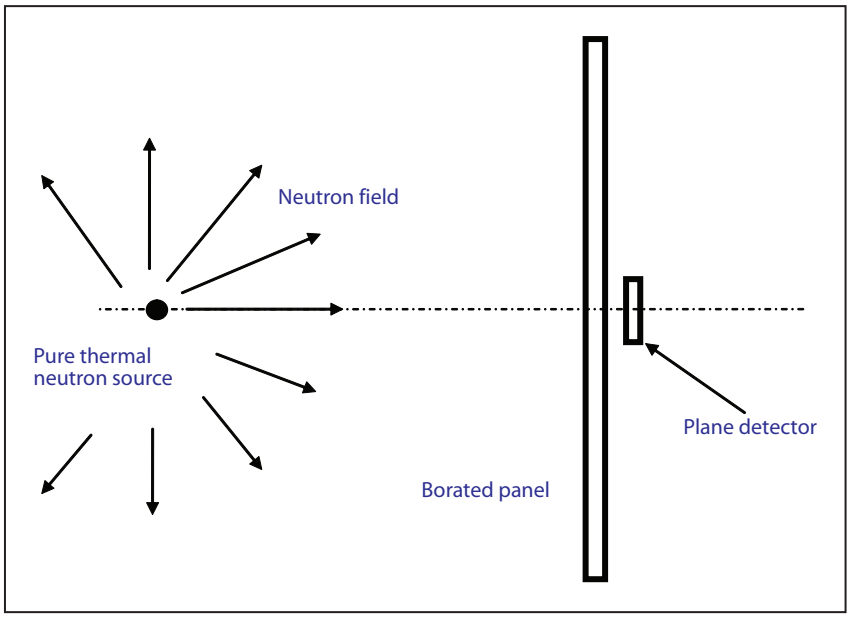

Figure 1. Hypothetical setup for converting a gamma spectrometer into a dual gamma-neutron detection system

In this setup, neutrons from the source radiate to the panel and are captured to produce a flux of 478-keV gamma rays, some of which are detected by the detector. The expression that gives the gamma ray flux distribution as a function of gamma ray angle of incidence at the detector face was calculated and found to be:

$$\frac{d^2F}{dA_w d\theta} \approx \pi C \sin 2\theta, \quad \textbf{(2)}$$

where C represents the strength of the radiation field and is a constant at the detector, A_w is the front surface area of the detector, and θ is the angle of incidence of the gamma ray on the front surface of the detector.

We found that an isotropic radiation field appears to a plane detector as an arrival angle distribution that peaks at 45 degrees. In other words, for an isotropic field, the most likely angle of arrival of a gamma ray on the front face of the detector is 45 degrees. We performed Monte Carlo N-Particle (MCNP) calculations in which a source was placed 50 cm in front of the panel, and the detector was placed 50 cm behind the panel. These calculations supported our analytical calculations, giving a peak at 43.6 degrees. The modeling results imply that gamma rays that do not arrive normal to the detector are expected to contribute significantly to the count rate. It is reasonable to expect that such an effect would also be observed when using a thick detector. (A thick detector could be considered to be a stack of plane detectors that form the thickness of the detector in the direction perpendicular to the panel.)

We measured the buildup factor using a borated polyethylene panel, a ^{252}Cf source, and an HPGe spectrometer. The borated polyethylene panel had a boron content of 5% and dimensions of 2.54 cm × 1.22 m × 1.22 m. Before taking measurements, we cut a small 10 cm × 10 cm piece from a corner of the panel. The ^{252}Cf source—Frontier Technology Corporation Model 10 series—had a neutron activity of 1.11 × 10^6 n/s on the assay date of March 16, 2001, according to the source certificate of neutron emission rate. We placed the source inside a cylinder of polyethylene to aid thermalization of 5.3 cm wall thickness for all of the measurements. The detector's relative efficiency was 103.2% at 1332 keV (^{60}Co), and the crystal dimensions were 77.7 mm in diameter and 102.1 mm in length. The detector crystal was located 5 mm back from the endcap. Spectral analysis was done using ORTEC MAESTRO version 6.01 software.

The apparatus was set up on February 5, 2007, as shown in Figure 2, with the source placed 1 m in front of the panel's center on the left-hand side; the detector end-cap was placed on the same axis as the source, 1.5 cm behind the panel. Data were collected for a live-time of 1800 sec. Both gross and net counts were computed for the same energy ranges across the 478-keV peak and are shown in the "First Run" column in Table 1. A disk of 96-mm-diameter (2.54-cm thick) that matched the diameter of the detector endcap was prepared from the corner previously removed from the panel.

The borated panel in the setup shown in Figure 2 was removed and replaced by the disk at the same distance from the panel, as shown in Figure 3. Once again, the live-time was 1800 sec. The neutron-gamma buildup factor was measured to be the ratio of the net counts for the panel to that of the disk, or 4.6 ±0.5.

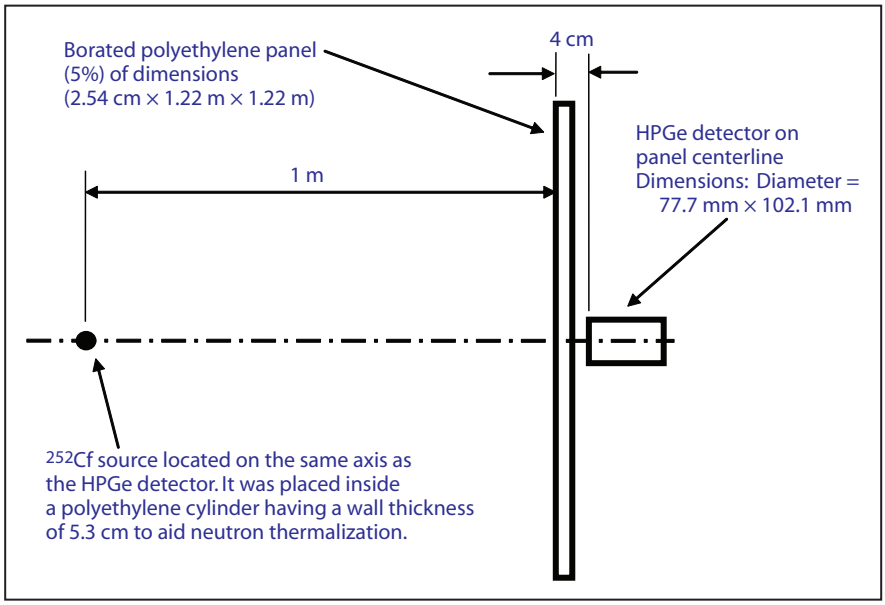

Figure 2. Experimental apparatus designed to measure net counts from a borated panel, using an HPGe system

Table 1: Buildup factor measurements

	First Run: February 5, 2007		Second Run: June 7, 2007	
Borated Polyethylene Geometry	96-mm-diameter x 2.54-cm disk	1.22-mm x 1.22-mm x 2.54-cm panel	96-mm-diameter x 2.54-cm disk	1.22-mm x 1.22-mm x 2.54-cm panel
Distance: Source to Panel	1 m	1 m	1 m	1 m
Live-time	1800 sec	1800 sec	7200 sec	7048 sec
Gross Counts	13,491	26,092	49,945	90,813
Net Counts	2462 ±268	11,286 ±324	6678 ±529	28,054 ±652
Buildup Factor	4.6 ±0.5		4.3 ±0.4	
Average	4.4 ±0.3			

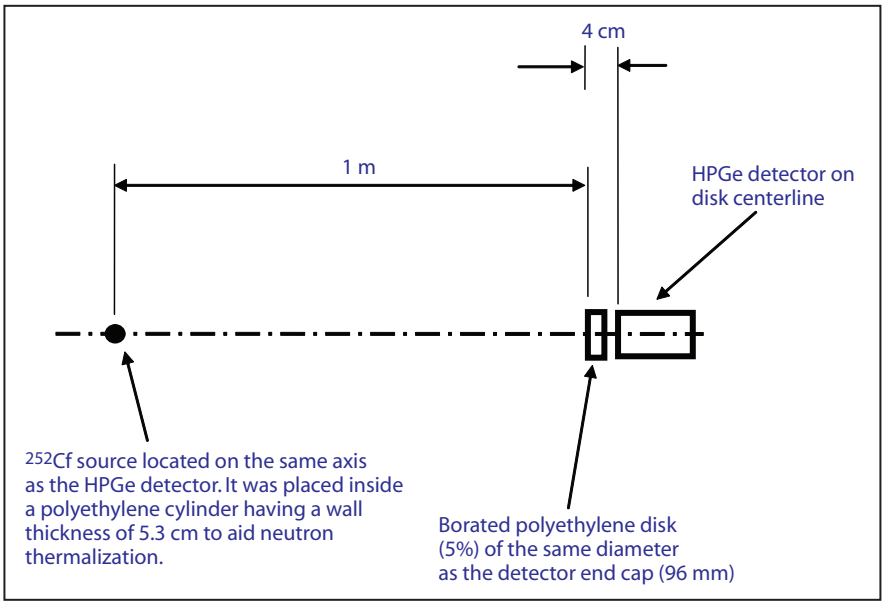

Figure 3. Experimental apparatus used for measuring net counts from a borated disk, using an HPGe system

These measurements were repeated for both the panel and disk arrangements on June 7, 2007, for both the panel and disk; the results are shown under the "Second Run" column in Table 1. The live-times were 7048 sec and 7200 sec, respectively. The buildup factor this time, after correcting for the difference in live-times, was calculated to be 4.3 ±0.4. The two results were averaged together to give a buildup factor of 4.4 ±0.3.

The efficiency of the borated panel system was calculated to be the ratio of the net counts per second in the 478-keV peak to the yield of the neutron source at the time of the study. The efficiency of the measurements taken with the panel in place was determined to be $(2.9 \pm 0.1) \times 10^{-5}$ counts per neutron for the February run, while it was found to be $(1.8 \pm 0.1) \times 10^{-5}$ counts per neutron for the June run. The difference in these numbers was due to slight differences in how the apparatus was set up, which impacted count rate more than buildup factor.

We evaluated the potential of this technique for use as a portal system through both experiment and MCNP simulation. In our work, one detector was placed behind the panel; however, a portal system would have an array of these detectors counting simultaneously. It is important to note that both the buildup factor and the efficiency results presented apply to every detector in the array. A 10^6 n/sec source placed at 1 m would measure on average 24 counts/sec; however, a portal system using 20 such detectors clustered close together would measure about 480 counts/sec. This means that a source placed in the portal system would measure ~2400 counts in only 5 sec. The apparatus

could be fine-tuned by forming a corridor using "walls" and a "ceiling" of borated polyethylene to significantly enhance the count rate. Boron could be placed in the road beneath the portal system, in the paint used to coat the system, or as a constituent in the alloy used to form the structure of the system.

We discovered that a neutron source behind the borated panel behaves as a "virtual gamma source" superimposed on top of the neutron source. Both MCNP calculations and experimental results are in reasonable agreement. The count rate due to this virtual source varies according to the inverse square law in which the distance is measured between the source and the detector face. In other words, the system behaves as though the borated panel is not present; this leads to a much simplified calculation. We calculated an efficiency curve for various locations of the source in the portal system. We also calculated count rate profiles for neutron sources having a range of yields moving through the system at various speeds. Based on these results, an efficiency table can be developed that provides integrated count information for sources moving through the system at speeds of 5, 10, 15, 20, 25, and 30 km/hour.

Conclusion

A borated panel placed in front of an HPGe detector effectively converted the detector into a dual neutron and gamma detector system with a neutron-gamma buildup factor of 4.4 ±0.3 over a disk of the same diameter as the detector endcap. A borated polyethylene panel is recommended, as it both thermalizes and captures neutrons even when nonthermalized neutron sources are present. However, any plane of borated material would produce similar enhancement, but with a different buildup factor. The work described here used a 2.54-cm thick, 5%-borated polyethylene panel, due to its availability at the time this work was performed, and a polyethylene cylinder to aid neutron thermalization. In practice, the borated panel should be prepared with enough thickness to thermalize and capture any incident neutron. The efficiency of the apparatus described herein was $(2.4 \pm 0.1) \times 10^{-5}$ counts per neutron emitted by the source.

The neutron-gamma buildup effect could be exploited (e.g., in portal monitors and mobile radiation measurement systems) by adding a borated plane of material to the environment of the detection system. The neutron source would behave as a virtual gamma source superimposed on the neutron source. Efficiency curves could then be generated for sources at various locations relative to the detector. This would lead to count rate profiles for neutron sources having a range of yields moving through the portal system at various speeds. The "sweet spot" of the arrangement is located with the detector in contact with the center of the plane at the point closest to the neutron source. It should be noted that the plane of borated material could be placed behind the detection system, instead of in front, to minimize any concerns about attenuation by the panel material. A poster paper on the buildup effect alone was presented at the Laboratory Directed Research and Development Symposium in Los Alamos on August 28. A full paper on this effect is being prepared for publication

in *Applied Radiation and Isotopes* by Elsevier in the near future. A further peer-reviewed paper on portal system application is being formulated at the time of writing. An invention disclosure was filed for the technique in December 2006.

Acknowledgments

MCNP support was provided through a subcontract with Battelle Energy Alliance that operates Idaho National Laboratory (Contact Name: Dr. Leo Van Ausdeln).

Reference

Ghanbari, F., A. H. Mohagheghi, "Use of gamma-ray spectroscopy for direct detection of thermal neutrons," *J. Radioanal. Nucl. Chem.* **248**, 2 (May 2001) 413–416.

this page intentionally left blank

Quantum Wire II

Paul Guss, Warnick Kernan[1]
Remote Sensing Laboratory – Nellis

Biswajit J. Das
University of Nevada, Las Vegas, Nevada

This project built on our FY 2006 study of solid-state materials with rich potential for alpha and neutron counting, in order to produce nanowire detectors sensitive to alphas and neutrons (Kernan, 2007). The ultimate goal of this year's work was to investigate the fabrication of detectors using wires having nanometer diameter and micrometer length with the objective of discovering whether the confinement of charge leads to unique properties such as improved charge collection, and/or reduced susceptibility to radiation damage. These structures inherently have high spatial resolution. As well, these structures have thicknesses comparable for ranges of alpha particles, and are suited for direct alpha detection and neutron detection via a converter layer. The mission of the experiment team was to build the foundation for effectively growing nanowire structures and to solve the problem of neutron detection using a solid-state approach. One of the goals of this task was to demonstrate the ability to grow nanowires that detect radioactive particles. We successfully prepared the microwire solid-state structure using silicon (Si), and developed the process for growing cadmium telluride (CdTe) nanowires, which we describe here.

Background

There is great interest in the technical and user communities for small, lightweight (flexible configuration) neutron sensors. There are quite a large number of solid-state neutron sensors to evaluate. One scheme employed by these sensors is to exploit the popular $^{10}B(n,\alpha)$ reaction for the conversion of slow neutrons into directly detectable particles (Knoll, 2000). The range of a 5-MeV α particle in aluminum is well in excess of 10 μm, as can be seen in Figure 1 (range of ^{3}H is shown in Figure 2). Energies of this magnitude are easily available from commercial α sources such as ^{241}Am. Assuming a conversion of deposited energy to the creation of electron-hole (e-h) pairs of 4.3 eV/e-h in the wire material, approximately ~1×10^6 e-h pairs are created for every α particle that completely deposits its energy. However, e-h pairs that are created in the dead portion (i.e., in the matrix material) are not collected and counted and thus do not contribute to the possible signal. If the results with the α

[1] warnick.kernan@pnl.gov, 509-376-1417

particles are encouraging, interest would turn to attempting to make position-sensitive, fast-response neutron detectors by adding a layer of boron or lithium on the surface, using the following reactions (Knoll, 2000):

$$^{10}B + n \rightarrow {}^{7}Li + \alpha, \text{ or} \quad (1)$$

$$^{6}Li + n \rightarrow {}^{3}H + \alpha. \quad (2)$$

While the second reaction has a higher Q value and α particle range, which may improve the energy deposition, the cross section is higher for the first reaction.

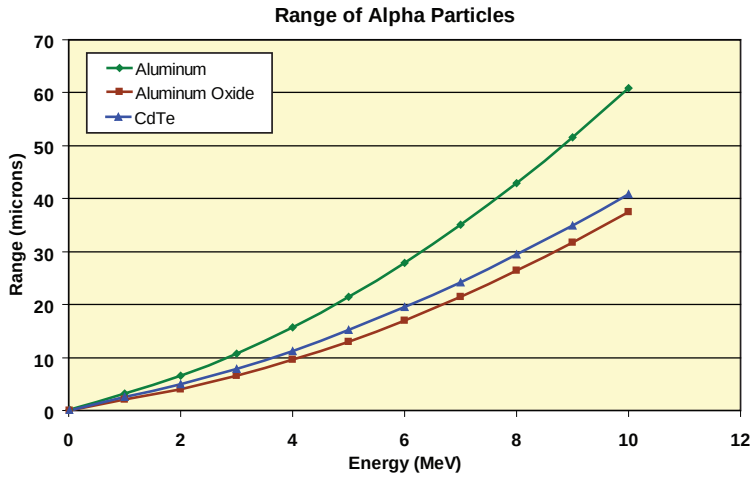

Figure 1. Range of α particles (^{4}He) (calculations made using the stopping and range of ions in matter [SRIM] code, written by Ziegler [2007])

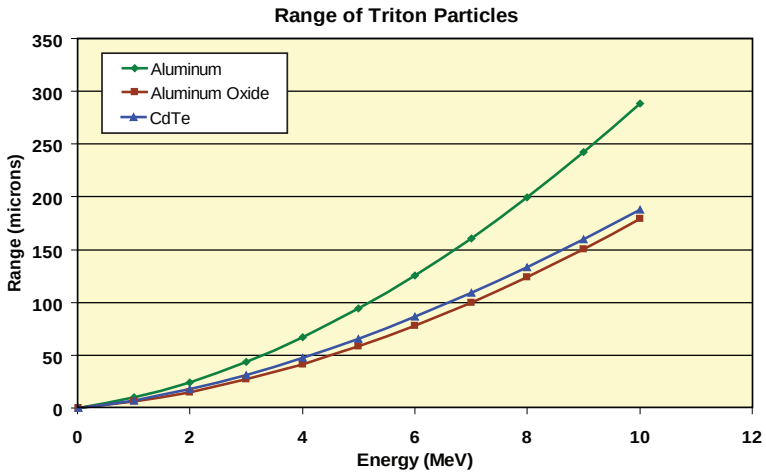

Figure 2. Range of tritons (^{3}H) (calculations made using SRIM [Ziegler, 2007])

Project

In this year's project we aimed to extend the preliminary, micron-scaled designs investigated in FY 2006 to detectors based on quantum wires, where the quantum mechanical confinement suggests an enhancement in the collection efficiency. We developed a generic laboratory setup to evaluate semiconductor neutron sensors. In this study, we report the fabrication of templates with cylindrical nanopores formed after anodization of aluminum thin films. We have succeeded in electrodepositing CdTe semiconductor thin films and nanowires into the nanoporous templates.

Prototype Microwire Radiation Detector

We completed the fabrication of the prototype microwire detector, begun in FY 2006. In this fabrication, photolithographic patterning of gold defines the bottom ohmic contacts; optical lithography of deposited Si defines the microwires; and deposition of the top electrode completes the device (Figure 3). When we tested the electrical contacts of our initial device, we found a short circuit between the top and the bottom electrodes. We observed that in some areas the top electrode penetrated through the inter-wire gap and connected to the bottom electrodes.

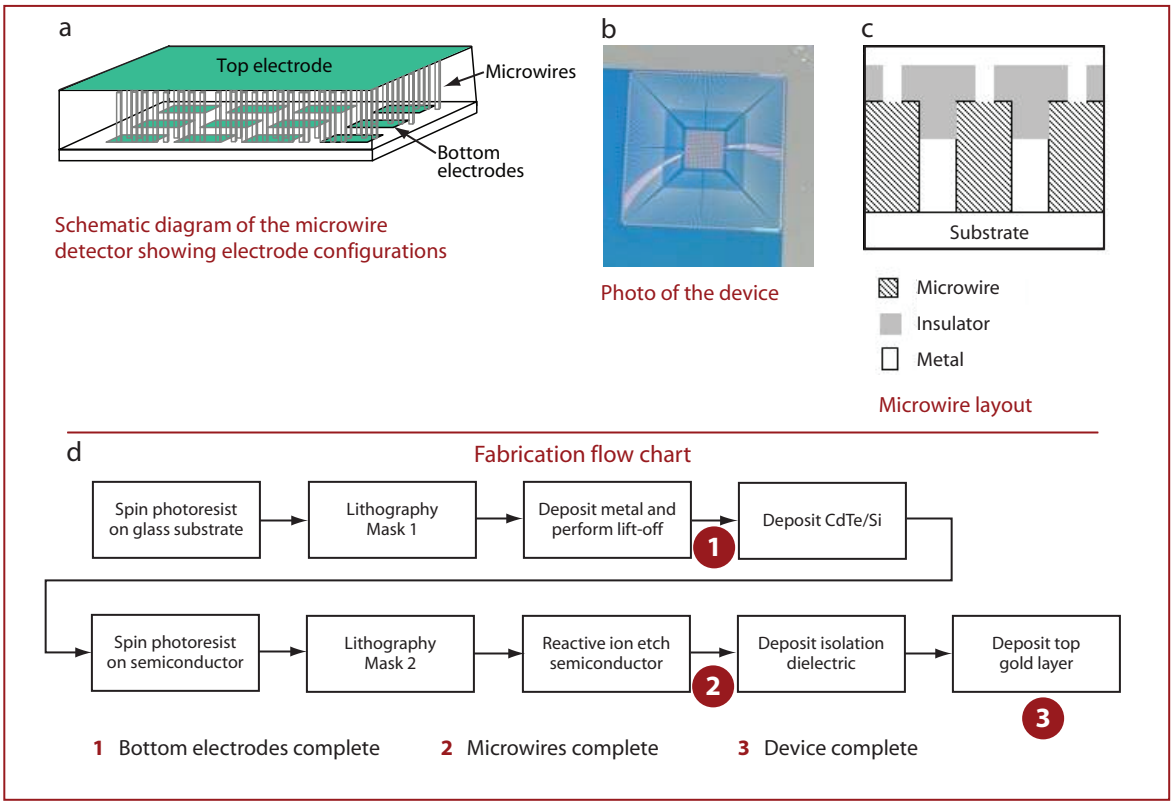

Figure 3. (a) schematic diagram of the microwire detector showing electrode configurations; (b) photo of device; (c) microwire layout; (d) fabrication flowchart

We also discovered that almost all the contact pads had some areas that electrically shorted. Our experience in depositing thin metal layers on nanowires did not show such problems. We attributed the short circuit in this case to the large gap between the microwires. To eliminate this problem, in the second pass of device fabrication we sputter-deposited a layer of insulator on the microwires; following this, we used optical lithography to open windows on top of each wire, and then finally we deposited the metal electrode (Figure 3c). This ensured that the top metal would not penetrate through the interwire gap and short the bottom electrodes. The deposition of the insulator layer and using photolithography to open the contact windows was successful.

Nanowire Radiation Detector

This project also implemented the use of quantum wires via a nonlithographic nanofabrication technique developed at the University of Nevada, Las Vegas (UNLV). In parallel to the microwire detector project, we have been developing the process technology to implement a nanowire radiation detector, which is the final objective of this project. We envisioned a nanowire radiation detector based on CdTe nanowires employed inside the pores of a nanoporous alumina layer using nonlithographic nanofabrication techniques. First, we fabricated nanoporous alumina layers. A thin layer of tantalum was deposited on the semiconductor surface followed by a layer of aluminum. Next, we anodized the aluminum film to form an alumina template using the substrate as the back contact. We used a two-step anodization process to improve pore uniformity and periodicity. In addition, we conducted an extensive literature search to identify the synthesis process for the deposition of the CdTe inside the nanoporous alumina layer. Due to the extremely small dimension of the nanopores, it is essential one uses an electrochemical synthesis technique for the deposition of the CdTe material. Another restriction is that one must carry out the synthesis of CdTe at room temperature in order to avoid damaging the nanoporous film. Based on the literature and the above criteria, we identified the following process recipe for the deposition of the CdTe nanowires. Using an electrochemical bath: $3CdSO_4 .8H_2O$ -- (25.6 g per liter) -- Cd^{2+} (0.1 mol per liter), TeO_2 -- (1.6 g per liter [0.01 mol per liter]), H_2SO_4 -- (98 g per liter [1.0 mol per liter]).

Using this process, we electrochemically deposited CdTe on a plain, aluminum-coated silicon substrate to confirm the process. Next, we performed an experimental study to determine the optimum process parameters for the deposition of CdTe inside the pores of a nanoporous alumina layer. In this process, we made use of the back contact of the alumina layer as one of the electrodes for electrodeposition. Preliminary results indicated successful initial deposition of the CdTe nanowires as shown in the scanning electron microscope (SEM) image in Figure 4. We continued to experiment to determine the optimum process parameters to deposit very long CdTe nanowires inside the nanoporous alumina layers required for the implementation of the detector. We then removed the porous alumina layer by etching in a phosphoric/chromic acid solution to form freestanding CdTe pillars. We employed reactive ion etching to transfer the pillar structures to the substrate material, thus forming the desired quantum wires.

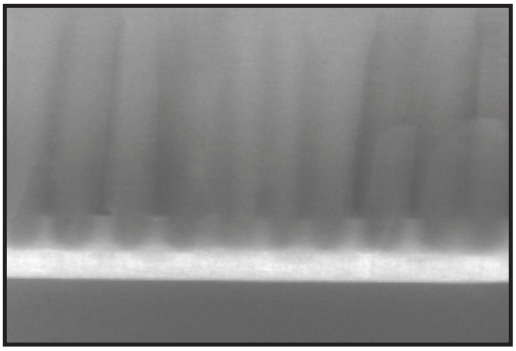

Figure 4. Cross-sectional field emission SEM image of the initial growth of CdTe nanowires inside the pores of nanoporous alumina. The nanowires are ~50 nm in diameter and 100 nm in length. A systematic study is currently in progress to optimize the process parameters to make the nanowires microns tall.

Process Optimization for the Deposition of CdTe

We employed cylindrical nanopores of an anodized aluminum oxide layer on the surface of bulk aluminum as templates for the electrochemical growth of CdTe. We have confirmed that we obtained the desired composition (50:50) of Cd and Te by controlling cathodic potentials during the growth process. The elemental composition of CdTe was verified using a field emission-scanning electron microscope (FE-SEM) (JEOL 6500, University of Minnesota) for analyzing the samples, along with electron dispersive x-ray analysis (EDS) (Oxford Instruments).

Template Synthesis

Figure 5 shows the composition of the multilayered wafers specially made for the preparation of the template. A typical wafer had a layer of tantalum of 200 nm thickness and of aluminum of 700 nm thickness. A layer of aluminum (500 nm) provided the back contact.

Anodization Process

First, the templates were electrochemically polished in a solution of ethanol and perchloric acid (75 vol % of ethanol, 25 vol % of perchloric acid) to achieve a mirror-like surface. Next, we anodized the polished aluminum sheets in an aqueous solution containing 0.3 M oxalic acid at 17°C to obtain a nanoporous aluminum oxide layer on the surface.

We used a constant current of 36.072 mA for the anodization process. The voltage varied with time. Figure 6 displays the voltage–time characteristic curve.

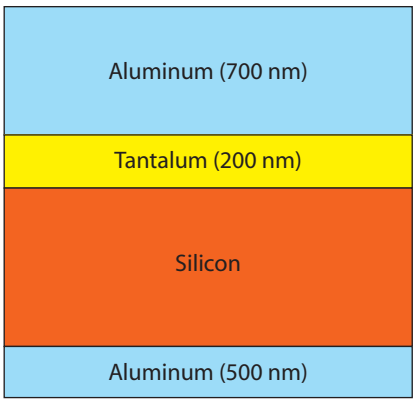

Figure 5. Composition of wafer used as template

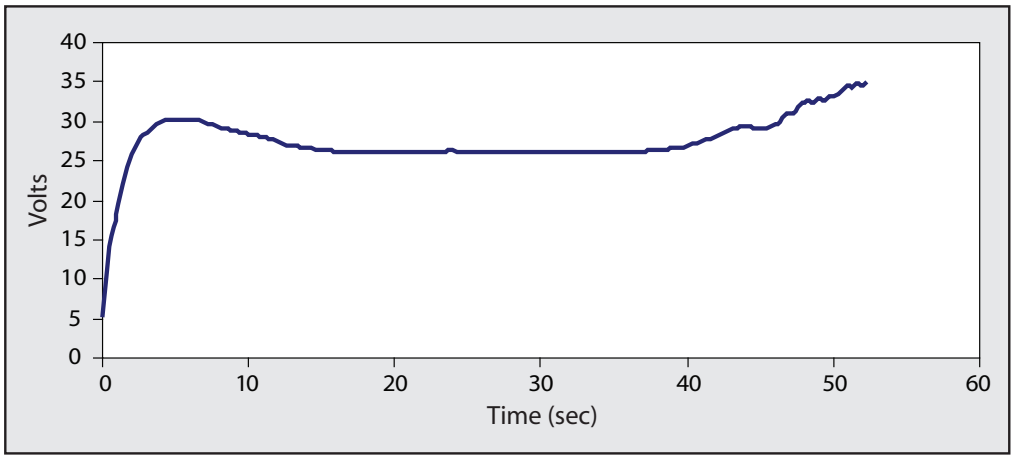

Figure 6. Time vs. voltage characteristic curve obtained during anodization process

Figure 7(a) shows the SEM image (top view) of the anodized alumina. Figure 7(b) shows the cross-sectional view of the anodized template. We used 3% phosphoric acid to etch the templates and then applied citric acid to widen the pores. We determined that the pores were ~50 nm in diameter and the pillars of alumina oxide were ~350 nm in height.

CdTe Growth

Solution Preparation

For the electrodeposition of CdTe into the anodized aluminum templates, we prepared electrolytic solutions using deionized water containing the following chemicals: $3CdSO_4.8H_2O$ (25.6 g L^{-1}), TeO_2 (1.6 g L^{-1}), and H_2SO_4 (98 g L^{-1}).

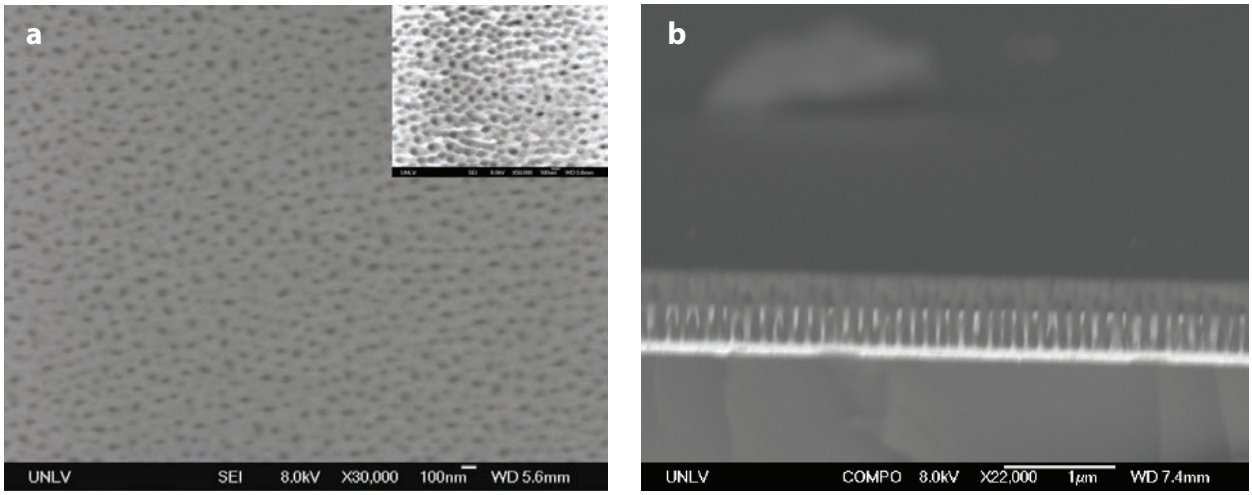

Figure 7. Anodized porous alumina (a) top view and (b) cross section

Electrochemical Reaction

With a 9-V cell as the power source, we configured the platinum mesh as the anode and the template as the cathode. The reaction follows the kinetics as below:

$$HTeO_2^+ + 3H^+ + 4e^- \rightarrow Te + 2H_2O, \quad \textbf{(3)}$$

$$Cd^{2+} + Te + 2e^- \rightarrow CdTe, \quad \textbf{(4)}$$

$$Cd^{2+} + 2e^- \rightarrow Cd. \quad \textbf{(5)}$$

We analyzed the CdTe–deposited alumina thin films using the SEM, Figure 8, along with EDS.

We also determined the composition of the CdTe films using EDS. The representative EDS spectrum is shown in Figure 9. From this spectrum, we find the ratio of Cd:Te to be 50:50—in good agreement with earlier reports. We investigated reproducibility of the data with additional samples. We continued the process development to increase the CdTe layer thickness. We carried out initial process development on a silicon substrate coated with Pt.

We conducted an extensive investigation to optimize the process, eventually obtaining CdTe layers that were >2.5 μm thick. This is a very positive achievement since thick layers of CdTe are necessary for the implementation of the radiation detector. Since these depositions were carried out at room temperature, the CdTe showed irregular polycrystalline nature (the CdTe can be made into single crystal material through an annealing step that is currently in progress). EDS measurements show that we deposited CdTe on the plain template and the composition of Cd and Te is as expected (nearly 50:50). Figure 10 shows an SEM image (cross section) of CdTe deposited on the plain template prior to annealing.

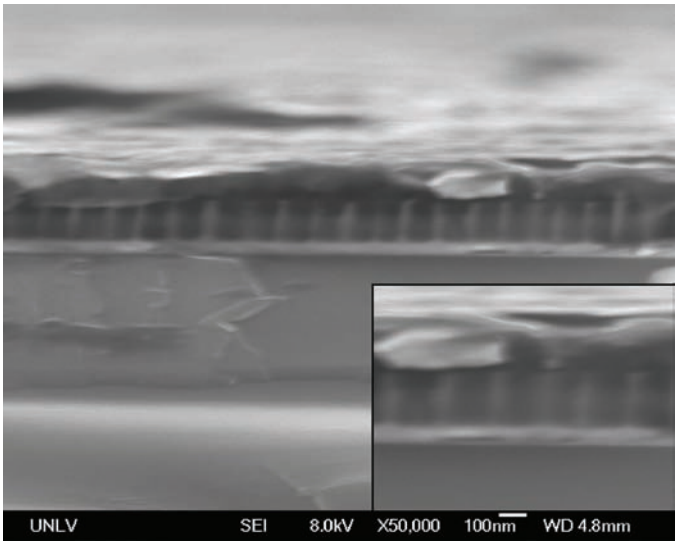

Figure 8. Representative SEM image (cross section) of the CdTe deposited anodized aluminum thin film. Inset shows magnified SEM image.

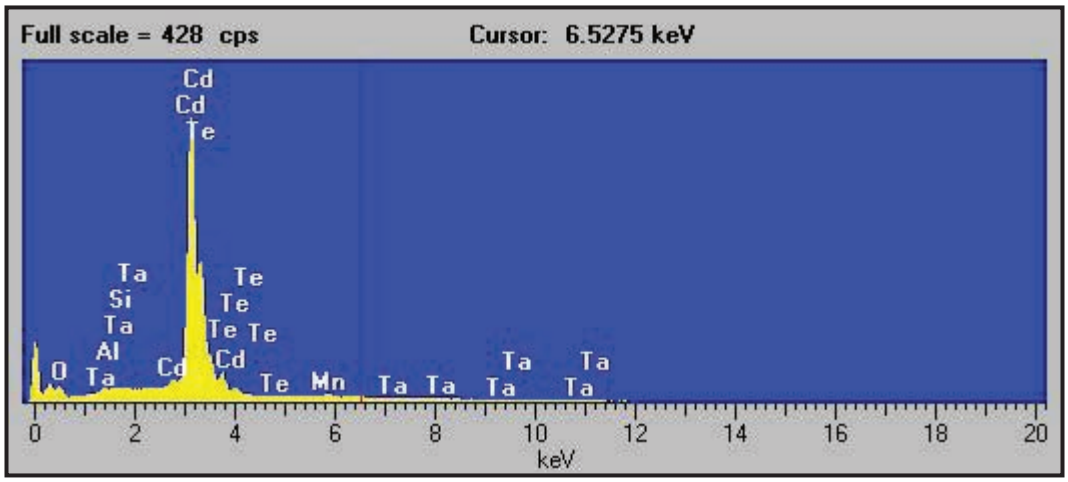

Figure 9. Representative EDS spectrum showing the elemental composition of electrochemically deposited CdTe in an anodized aluminum template

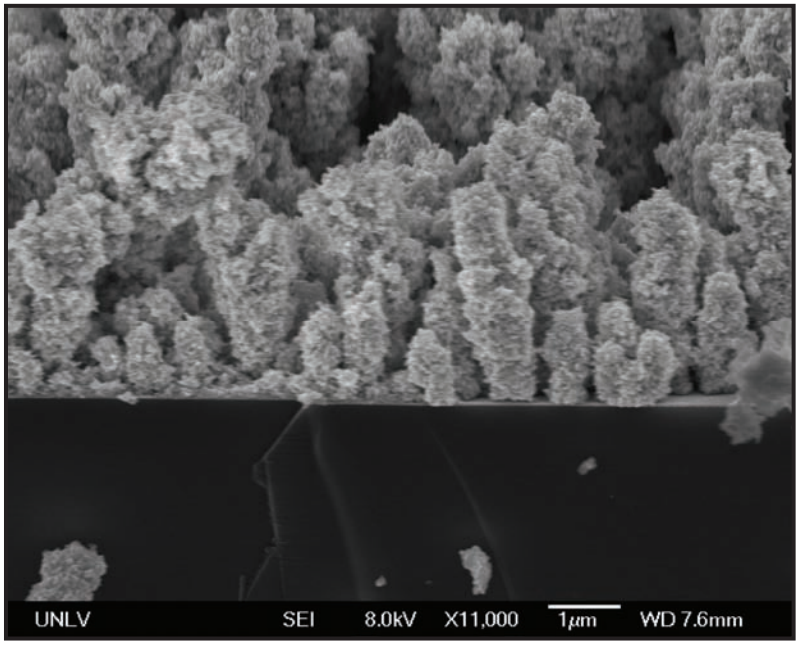

Figure 10. SEM image (cross section) obtained for CdTe deposited on Pt-coated silicon substrate showing thick layer of CdTe. The composition analyzed using EDS confirmed the Cd:Te ratio to be 1:1.

We conducted light testing on the samples to confirm the semiconducting nature of the nanowires, which is a prerequisite for the efficient detection of high-energy particles. For light testing, we formed a specialized contact layer on the nanowire layers as shown in Figure 11. We first deposited a thin layer of gold (4 nm) on the CdTe nanowires, which was semitransparent. Although such thin layers of gold provide electrical contact, they are mechanically fragile. To circumvent this problem, we covered a part of the device with a thicker layer of gold (10 nm) on top of the thin layer of gold. The thicker layer of gold is mechanically more stable; it is, however, opaque to light. We made external electrical contacts to the device by applying silver paint to the thick gold layer and the substrate. We measured the resistance between the two external contacts using a sensitive AC resistance bridge, while the device under the thin gold layer was excited with light of different wavelengths from an Argon ion laser. Figure 12 depicts the experimental setup.

Table 1 presents the light testing data. The dark resistance of the device was 1.05 kΩ, which is a reasonable value considering the length and the width of the nanowires. We recorded a 1% to 4% change in device resistance under different optical excitation wavelengths, depending upon the wavelength. The change in resistance conforms to the semiconducting nature of the CdTe nanowires, and the dependence of the resistance upon wavelength change confirms the quantum confinement

in the nanowires. The small change in the resistance occurs because light only excites a small area of the device and the semitransparent gold layer reflects most of the incident light. However, the fact that resistance depends on the optical excitation confirms that the devices are ready for radiation-detection testing. We have discussed the packaging requirements for such radiation testing; this testing should be carried out in the near future.

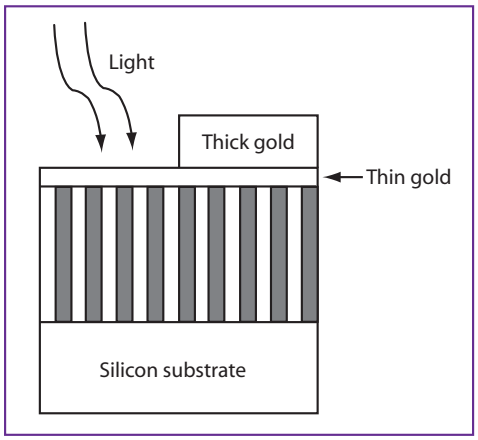

Figure 11. Schematic diagram showing the contact formation for light testing. The thin gold contact is semitransparent to light, while the thick gold layer provides mechanically reliable electrical contact for external connections.

Table 1. Percent change in resistance across the nanowire system as a function of the wavelength of the incident light. This dependence is consistent with the quantum confinement nature predicted for nanowires.

Optical wavelength (nm)	Change in resistance (%)
514	1
496	2
488	2
472	4
457	3

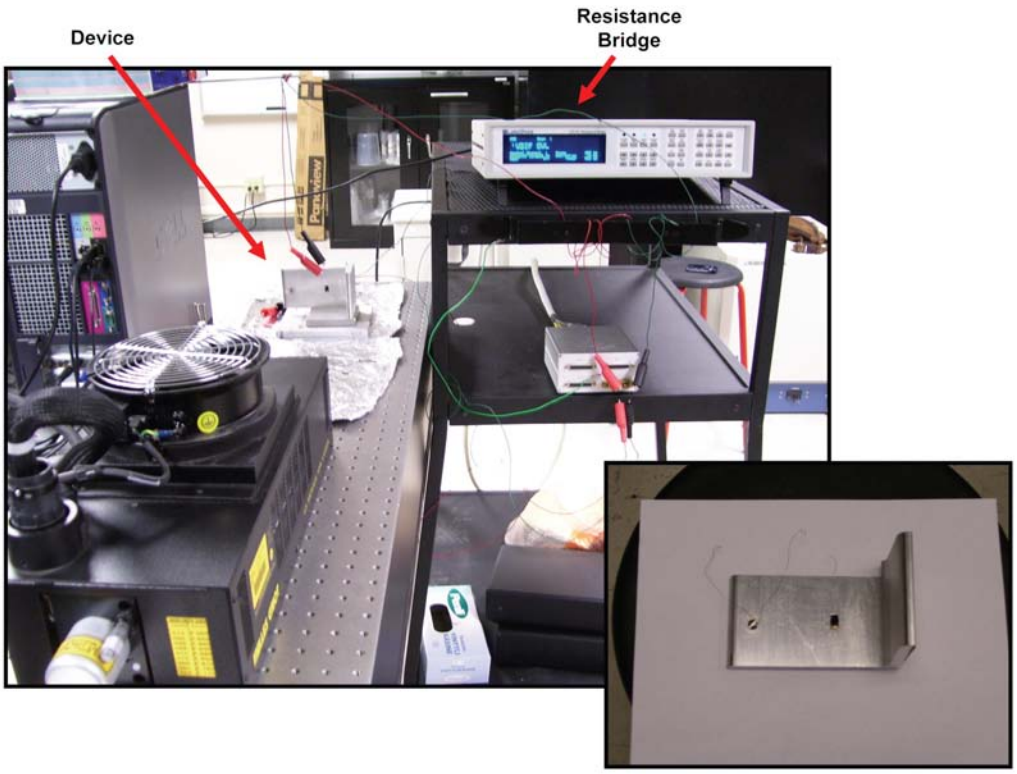

Figure 12. Experimental setup for light testing of the nanowire device. Inset shows a close-up view of the mounted device.

Conclusion

A first step towards creating a structure containing pillars having diameters on the order of nanometers was to build a device having micrometer-scale pillars. We used Si for such pillars due to the availability of tools to deposit Si at the University of California, Santa Barbara (UCSB). For the microwire system, having already manufactured the mask, we completed etching of microwires we patterned, and deposited an insulator layer to prevent the electrical shorting of the microwires. Lithography for microwire etching is also complete. In FY 2007, we extended the work from micrometer-scale wires to nanometer-scale wires to investigate detectors based on quantum wires, where we expected the quantum mechanical confinement to enhance the collection efficiency. We used a nonlithographic nanofabrication technique developed at UNLV to produce the quantum wires. For the nanowire system, we identified and developed a procedure for the synthesis of CdTe nanowires inside nanoporous alumina templates. We demonstrated the synthesis of seed layers of CdTe using this process. We have optimized, and continue to optimize, the process parameters for increasing the thickness of the CdTe layers. As well, we have completed the synthesis of 40-nm-diameter CdTe

nanowires with a minimum height of 1 μm, and have fabricated top contacts on the nanowires. For both the microwire and nanowire systems, complete testing of the devices against light, and then with radioactive particles, still needs to be performed. Characterizing the systems for α particles with the hope of laying the groundwork for building and testing a neutron detection device would be a logical next step. A publication detailing our progress and the results of these tests is forthcoming.

Acknowledgments

The authors wish to acknowledge UNLV and UCSB for making staff and facilities available for this work.

References

Kernan, W. J., "Quantum Wire Detector," *Nevada Test Site–Directed Research and Development*, FY 2006, National Security Technologies, LLC, Las Vegas, Nevada, 2007, 165–170.

Knoll, G. F., *Radiation Detection and Measurement*, 3rd ed., John Wiley & Sons, New York, 2000, Chapter 14.

Ziegler, J., "The Stopping and Range of Ions in Matter," Version SRIM-2006.02, http://www.srim.org/, accessed September 21, 2007.

Conducting Polymers for Neutron Detection

Glen Anthony, Mike Grover, Clare Kimblin,[1] Harry McHugh, Steve Jones, Kirk Miller, Bill Quam, Bob Vogel
Special Technologies Laboratory

Conjugated polymers have emerged as an attractive technology for large-area electronic applications. As organic semiconductors, they can be used to make large-area arrays of diodes or transistors using fabrication techniques developed for polymer coatings, such as spraying and screen printing. We have demonstrated both neutron and alpha detection using diodes made from conjugated polymers and have conducted the preliminary work to integrate a boron carbide layer into the conventional polymer device structure to capture thermal neutrons. The polymer devices appear to be insensitive to gamma rays, due to their small physical thickness and low atomic number.

Background

Solid-state neutron detectors would provide a compact, low-power replacement for the helium-3 (^{3}He) tubes typically used for neutron detection. While quite reliable and accurate, ^{3}He tubes are very expensive and relatively large. The cost of ^{3}He tubes (~$40/sq in.) is the principal reason they are not widely employed in portal detectors. Alternatively, conductive polymers can be applied to inexpensive substrates such as plastic or metal using simple techniques such as spin coating or spraying. Detectors fabricated from multilayer conductive polymers have the potential to be less expensive and more ve rsatile neutron detectors than ^{3}He tubes, with low gamma sensitivity.

Project

Energy Deposition and Electrical Charge Generation/Collection

To make the proposed solid-state detector, boron-10 (^{10}B) was used to capture thermal neutrons, resulting in emission of an alpha particle that can then generate electron-hole pairs, which are detectable by the polymer diode. Calculations show that a ^{10}B layer thickness of 1.5 μm presents an optimum thickness for neutron capture while ensuring a significant chance of an alpha escape with substantial energy intact. For a layer of this thickness, there is an ~3% probability of capturing a thermal neutron. Refer to Figure 1 for a theoretical plot of alpha energy vs. boron thickness.

[1] kimblicw@nv.doe.gov, 805-681-2257

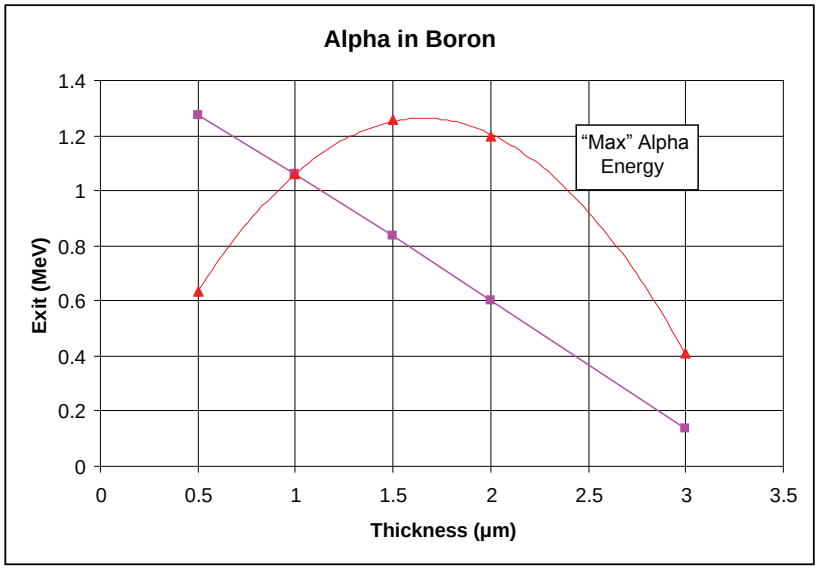

Figure 1. Alpha particle (1.47 MeV) exit energy (magenta trace) and relative average alpha energy yield on escape (orange trace) vs. thickness of ^{10}B

For this discussion, we shall analyze a 30-µm-thick polymer detector. At this thickness, almost all of the 1.5-MeV alpha energy will be trapped in the polymer. The ionization energy of this polymer is ~5 eV, leading to one electron-hole pair created for each ~15 eV deposited (Encyclopædia, 2007). In the case of a 1.5-MeV alpha, this equates to the creation of approximately 100,000 pairs carrying a charge of 1.6×10^{-14} coulombs. If all the electron-hole pairs generated by the alpha particles could be collected, the single-event pulses from the 30-µm polymer detector should be about 80 mV, well above the peak noise.

Figure 2 shows a display of the waveform obtained from a 5-MeV alpha capture in a 30-µm-thick polymer detector. The peak of the waveform is only about 15 mV (negative direction). The baseline noise peaks are <7 mV. The low value of the peak voltage implies that only about 20% of the charge generated from the alpha capture reaches the detector. The cause of the charge loss is not known at this time, but further optimization of the materials and device structure may lead to improvements.

Experiment and Data

Polymer Devices

The polymer devices used for this work were derived from the solar-cell designs being widely developed for power generation (Brabec, 2001). The solar cell design blends a conjugated polymer (poly-3-hexyl-thiophene [P3HT]), and a sensitizer ([6,6]-phenyl-C61 butyric acid methyl ester [PCBM])—a soluble derivative of buckminsterfullerene [C_{60}]). Upon photoexcitation of the P3HT, the electron

transfers to the PCBM, while the hole resides on the P3HT. The internal electric field (the sum of any externally applied bias and the mismatch of electrode work functions) then sweeps out the charges to their respective electrodes. The device architecture is typically a glass substrate coated with indium tin oxide (ITO, a transparent conductor), a thin layer of poly-ethylene-dioxy-thiophene, a spin-coated layer of the active material, then an aluminum electrode vacuum-evaporated on top.

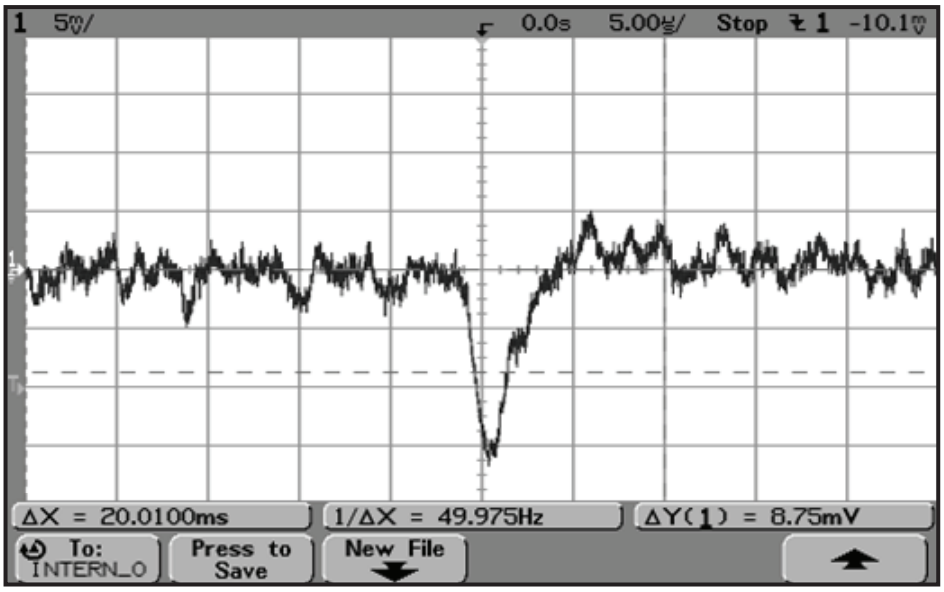

Figure 2. Waveform of alpha capture in a 30-µm detector

We determined that the active layer of conventional polymer solar cells, ~100-nm thick, would be too thin and the capacitance too high for radiation detection. Therefore, our first intensive alpha-irradiation testing was done with a series of devices from 1 to 30-µm thick, with small-area electrodes. With this first generation of devices, we discovered that static charge dissipation in the nitrogen glove box was crucial to having data that can be accurately interpreted.

We also learned that device fabrication techniques needed improvement for such thick films, so a second generation ("Gen-2") of devices was made using a "doctor blade" technique on glass/ITO substrates. With the Gen-2 devices, we sought to test various thicknesses, from 2.5 to 15 µm, and to control the experiment with devices of similar geometry. Instead of the P3HT/PCBM blend, poly-vinylcarbazole (PVK) was used in control devices. The P3HT/PCBM devices could be characterized by their light and dark currents; we found that the 10-µm device had the highest ratio of light-to-dark current. Data presented in Figure 4 are from that device, with its matching control (PVK) device.

Based on these observations, and to test the integration of the polymer devices with a boron-rich substrate, our colleagues at the University of California, Santa Barbara (UCSB), prepared a third generation of samples ("Gen-3"), with thicknesses of 10 and 25 μm plus 10-μm-thick PVK devices, on both glass/ITO and aluminum substrates coated with boron carbide.

Circuit Configuration

The polymer detector was connected to a 3-V reverse bias through a 100-MΩ resistor. The junction of these devices was connected to a high-impedance, low-noise charge preamplifier with a junction field-effect transistor (JFET) front end and a gain of 5×10^{12} V/coulomb for an input capacitance of ~4–10 pF (dominated by the capacitance of the polymer device). The detector contacts were connected to the amplifier via a commercial integrated circuit (IC) clip that squeezed the detector contacts against flat copper pins. The entire assembly was mounted inside a sealed Faraday enclosure designed to reduce pickup of external electromagnetic interference. Extensive filtering was used on all of the power inputs, and all leads were shortened to a minimum.

In a low-count-rate, low-signal-level situation such as this, one must be careful not to confuse spurious electrical pulses with actual signals. The alpha-induced ionization of air near the preamp generated signal pulses. Also, static electric discharges in the dry air created spurious signals that tended to dissipate with time. It is essential to be able to either eliminate these spurious signals or to distinguish between them and true signals. As one measure, we installed an ionizing air blower in the glove box to more quickly dissipate static.

Alpha Irradiation Measurements

Since detection of the neutrons hinges on detection of alpha particles, we initially tested polymer devices under alpha-irradiation from a 5-MeV ^{239}Pu alpha source. Counting was initially performed with a storage oscilloscope, but then a multichannel analyzer (MCA), the Health Physics Instruments "Rainbow," was implemented to better visualize the pulse heights being generated during data collection. The resolution of the Rainbow was ~0.25 mV/channel, with the low-level discriminator (LLD) set to approximately channel 35. Data were typically collected for 5 minutes for alpha-irradiation experiments, and 20 minutes for neutron-irradiation experiments.

The alpha source, which consisted of a thin foil of metal, was placed ~5 mm above the detector surface. An aperture with a 1-cm diameter was used to collimate the alpha particles and reduce the volume of ionized nitrogen. The electronic chassis box, polymer device, and alpha source are shown in Figure 3.

We used the 5-MeV alpha-emitting source to irradiate the Gen-2 and Gen-3 devices, and sheets of Mylar, 10-μm-thick, to slow the alpha particles and increase the energy deposited in the active layer. Using the National Institute of Standards and Technology's ASTAR database (NIST, 2007), we estimated the stopping distance for the 5-MeV alphas and 1.5-MeV alphas to be 40 μm and 8.5 μm,

respectively, in Mylar. Hence, we expect alphas generated by neutron capture in ^{10}B to be stopped by a single sheet of Mylar, while the more energetic alphas from the alpha source will be slowed, but not stopped, by one sheet.

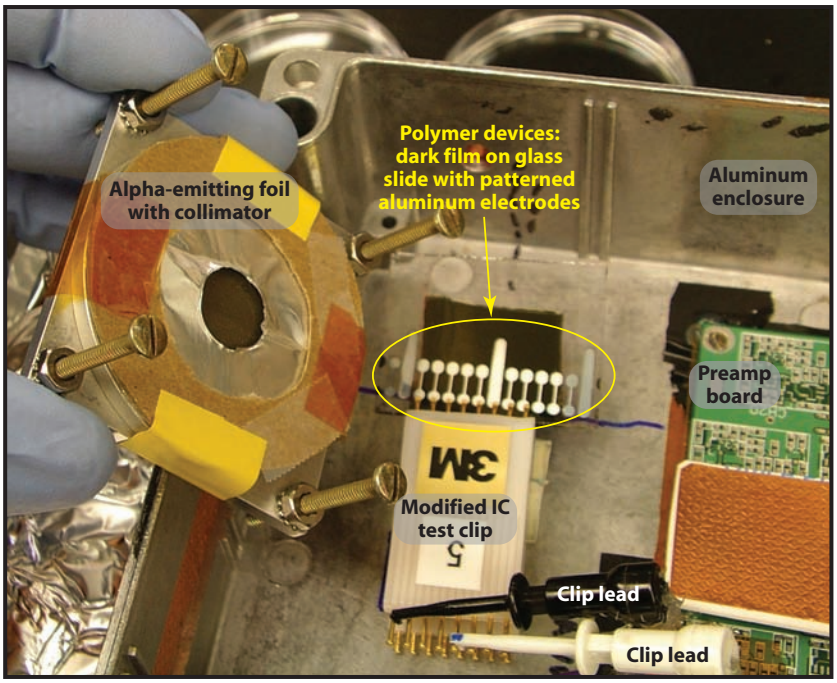

Figure 3. Electronic chassis box with polymer devices and alpha-emitting foil

Data in Figure 4 were taken with the Gen-2 10-μm device and the Gen-2 control device under alpha irradiation. The structure in channels 0–35 is entirely due to imperfections in the LLD circuitry in the Rainbow MCA. The sensitivity to alpha particles can be seen in channels 50–90, where the heavy black curve rises above the background when using the 10-μm Mylar film. While these data were encouraging, they raised some questions that we have not yet answered. What is the source of the large number of counts in both the active polymer and control devices when they are directly exposed to the alpha source? Why is the background count level so high, even with no source?

The aluminum substrate devices demonstrated a great reduction in background counts, with almost no counts in the channels above channel 45, when no radiation source was present. Data on the aluminum substrate devices, at 25-μm thicknesses, are shown in Figure 5. One important observation is

the shift of the signal peak away from the LLD (channel 35) out to channel 45 with the insertion of the 10-µm Mylar film. In addition, channels 50–80 showed higher counts when the Mylar film was added, in agreement with the data taken on the glass/ITO substrate devices.

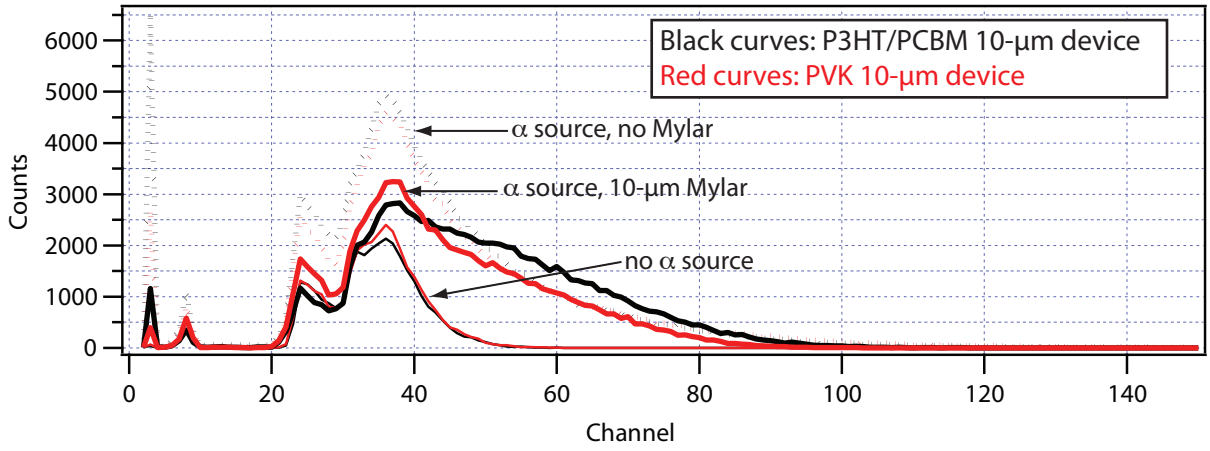

Figure 4. Five minute, alpha-irradiation spectra of 10-µm-thick conducting polymer and control devices on glass/ITO substrates. The bulge in the heavy black curve demonstrates the detection of alpha particles above the background.

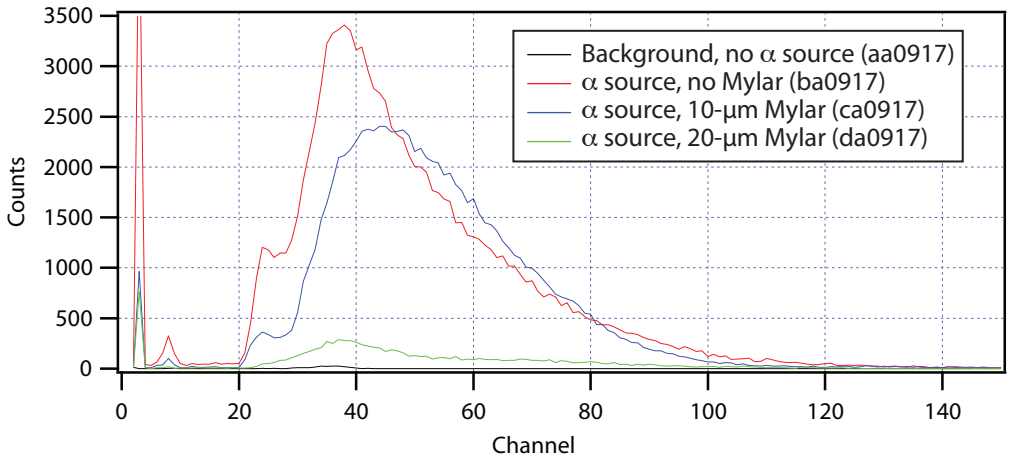

Figure 5. Alpha irradiation spectra using 25-µm-thick P3HT-PCBM aluminum-substrate device. Mylar was used to slow down alpha particles. Five-minute integration time.

Neutron Irradiation

To test the full sequence of neutron capture, alpha emission, and electronic detection, we used a neutron source moderated with polyethylene and a ^{10}B-carbide ($^{10}B_4C$) hemisphere placed close to the active polymer film. The distance from the ^{10}B-carbide to the active polymer layer was ~3 mm. Since the count rates were much lower than those for alpha irradiation, we chose to use the aluminum substrate devices, with their much lower noise floor. Data presented in Figure 6 are for the 25-µm-thick polymer device.

The data in Figure 6 show spectra taken with no neutron source present (background), with the neutron source present, and with the neutron source plus 10 µm of Mylar between the ^{10}B-carbide and the polymer film. The stopping distance for the 1.5-MeV alpha particles is ~8.5 µm in Mylar, so the addition of Mylar blocks all of the alpha radiation from reaching the polymer film. The high ratio of signal-to-background strongly suggests that alpha particles from the ^{10}B disintegration are being detected by the polymer detector.

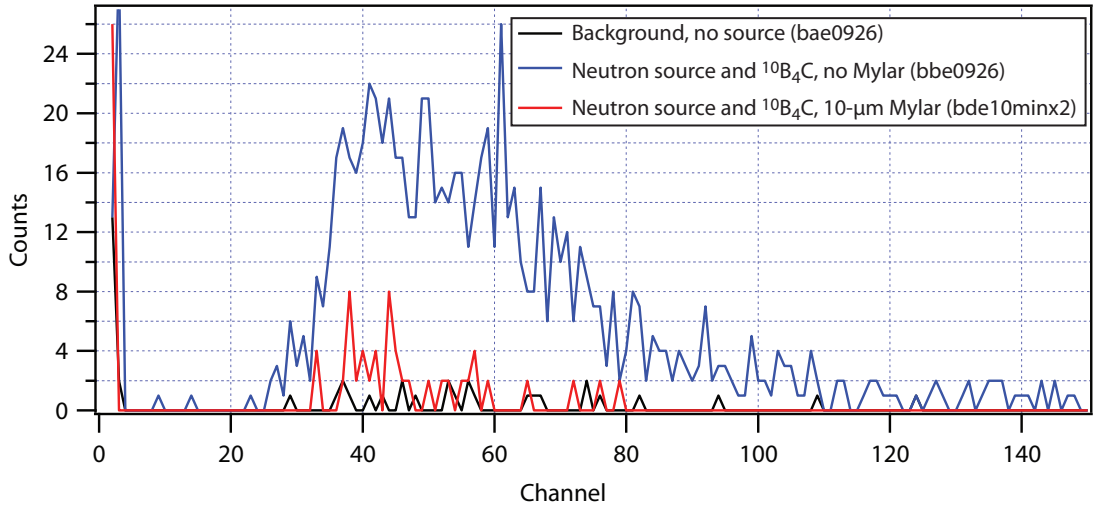

Figure 6. Neutron irradiation spectra using 25-µm-thick P3HT-PCBM aluminum-substrate device. The signal above the background demonstrates the detection of alpha particles emitted after neutron capture by ^{10}B. The Mylar sheet blocks the alpha particles. Integration time was 20 minutes.

Conclusion

The successful detection of neutrons in this prototype configuration suggests that integration of the ^{10}B-carbide layer into the device structure would yield an all-solid-state neutron detector made primarily from conjugated polymers. Device geometry and material optimization may lead to improved

charge collection. The origin of some spurious signals, such as the high background count rates for devices on glass/ITO substrates and the high count rates for control devices exposed to alpha irradiation, must be clarified, but may be due to RF pickup by the device, which could be shielded in a packaged detector.

Acknowledgments

Polymer devices for this work were prepared in the laboratory of Dr. Guillermo Bazan at UCSB by Corey Hoven, Dr. Je Jun, and Jeffrey Peet.

References

Brabec, C. J., N. S. Sariciftci, J. C. Hummelen, "Plastic Solar Cells," *Adv. Funct. Mater.* **11**, 1 (February 2001) 15–26.

Encyclopædia Brittanica Online, s.v. "Radiation measurement," www.britannica.com/eb/article-80706/radiation-measurement, accessed September 28, 2007.

National Institute of Standards and Technology, Gaithersburg, Maryland, ASTAR database, http://physics.nist.gov/PhysRefData/Star/Text/ASTAR.html, accessed February 1, 2007.

DNA Capture Material

Linda Chandos, Kevin R. Kyle,[1] Austin Moy, Kory Plakos
Special Technologies Laboratory

A means of capturing whole genomic deoxyribonucleic acid (DNA) from evidentiary samples was investigated. Human DNA from bodily fluid samples was utilized as the specific target of this investigation, with the end goal of collecting DNA suitable for subsequent short tandem repeat polymerase chain reaction (STR–PCR) analysis for individual identification. The efficacy and efficiency of various nucleotide sequences for capturing DNA was investigated using DNA primer probes. These probes were subsequently used as DNA capture probes covalently bound to polystyrene PCR tubes. Capture of whole genomic DNA was demonstrated. Protein nucleic acid (PNA) capture probes were designed as a means of binding DNA with greater affinity and specificity.

Background

A need exists for the collection of genetic materials (e.g., DNA) for the identification of biological targets of interest. This need spans a broad spectrum of customers, from forensics investigators to intelligence-collection personnel. For example, the forensics community desires extraction of DNA from chemically developed latent fingerprints in cases where the prints are not of good evidentiary quality when developed by standard means. DNA extraction would be required as a secondary means of suspect identification when primary identification fails. One requirement of the intelligence community is the collection of evidence of biological materials of interest from a number of matrices (surfaces, soils, fabrics, etc.). A capture matrix that binds and stabilizes DNA samples for potential long-term storage would satisfy this need. While the DNA from these examples represent highly disparate sources (human for the forensics community, microbial for the intelligence community), the chemistry involved in formulating a capture matrix for different species is similar, based on the pairing characteristics of the component nucleoside bases.

In the simplest form, a DNA probe anchored to a capture matrix could serve as the collection agent. However, DNA itself is unstable with respect to heat, pH, oxidation, and enzymatic degradation when not actively maintained by a biological system. A more robust candidate is a PNA probe. Whereas DNA is a natural product consisting of nucleotides on a deoxyribose-phosphate backbone, PNA is a synthetic molecule consisting of nucleosides on an amino acid polypeptide backbone (Nielsen, 1991). PNAs are resistant to environmental degradation over a wide range of conditions. In contrast to DNA, the 2-aminoethylglycine polypeptide backbone of PNA has no net electrical charge. There

[1] kylekr@nv.doe.gov, 805-681-2283

is therefore no electrostatic repulsion to overcome in the binding of DNA (net negative charge) to PNA, resulting in high binding affinity (Egholm, 1993) and a high sensitivity to nucleotide base pair (bp) mismatch (Orum, 1993). The environmental stability and strong binding of PNA strands to DNA strands makes them excellent candidates for sequestering and stabilizing specific strands of DNA.

Project

The goal of this project was the design and synthesis of PNA probes for the extraction and binding of DNA. The tasks leading to the realization of this goal were (1) selection of nucleotide capture-probe sequences for the target DNA, (2) screening of these probe sequences for their DNA capture efficiency by PCR, and (3) synthesis of PNA probes for DNA capture. A fourth task, PNA probe testing and material fabrication, was not achieved during this project.

The target analyte selected for this project was human DNA collected from saliva samples provided by investigators throughout the course of this project. The samples were utilized directly without purification as a mimic of real forensic samples. Human DNA was chosen due to its relevance to forensic identification. Commercially available forensic STR–PCR kits for the identification of chromosomal DNA sequences were used for the analysis of captured DNA. Specific chromosomes captured by the individual DNA probes could be identified using STR–PCR (Balogh, 2003), thereby allowing evaluation of the collection efficiency of each of the capture probes. The STR–PCR kit used throughout this investigation, the Promega PowerPlex 1.1, targeted STR loci on 12 of the 23 human chromosomes (Table 1). The kit protocol was modified to adapt it for PCR amplification on a Bio-Rad Tetrad 2 thermal cycle, with subsequent agarose gel electrophoretic analysis of the PCR amplicon products. A 4% gel was used to allow resolution of amplicons in the 100 to 300 bp size range. The presence of a target chromosome was indicated by a PCR amplicon of the correct bp length as measured relative to a DNA length standard coeluted on the agarose gel.

Probe Selection

Capture probes based on Alu contiguous genomic DNA regions were initially considered. These Alu regions, called Alu repeats, are comprised of noncoding DNA sequences about 300 bp long that are repeatedly interspersed throughout the genome of primates. The human genome is comprised of 10% Alu repeats by mass (Xing, 2004). The AluY subclass of Alu repeats is specific to the human genome (Batzer, 1996). Their specificity to and frequency throughout the human genome made them attractive candidates as capture probes for this project. A search of the National Center for Biotechnology Information GenBank database (NIH/NCBI, 2006) using the Entrez search engine yielded AluY repeat sequences suitable for DNA capture probes on eight of the twelve chromosomes represented in the PowerPlex STR–PCR kit. Probe sequences, 20 to 30 bp in length called oligonucleotides (oligos), were generated from the AluY sequences to serve as both DNA capture probes and PCR forward and reverse primers. However, during the search it was discovered that the primer pair sequences for the

Promega STR–PCR kit had been publicly disclosed (Masibay, 2000). Rather than test the efficacy of the AluY primers for their DNA binding ability, the Promega primers were chosen for use as DNA capture probes. The results of the AluY search and the Promega probe sequences are given in Table 1. Sequences are listed from the 5′ (phosphate) to 3′ (hydroxide) ends of the oligos.

Probe Development and Testing

The thirteen Promega primers listed in Table 1 were screened for the subset of the most efficient DNA binders as measured by the yield of PCR produced in the presence of a saliva DNA sample. Yield was measured as a function of the fluorescence intensity of ethydium bromide intercalated into the amplicon on an agarose gel. This process yielded five primers, CSF1PO, D7S820, D13S17, D16S539, and TPOX, on chromosomes 2, 5, 7, 13, and 16, respectively, which were utilized in the subsequent capture probe development.

The next phase of the project was to determine the functionality of the selected DNA primers as surface-bound DNA capture probes. The capture probes were chemically bound to a commercially available polystyrene PCR tube with pendant secondary amine groups grafted to the inner surface of the tube (NucleoLink tubes, Nalge Nunc International). DNA capture probes were designed based on the forward and reverse primers identified above, with a 9-mer thymine linkage group covalently bound to the 5′ end of the oligos and terminating in a 5′ phosphate group. The terminus of the thymine linkage was covalently bound to the NucleoLink tube pendant amine via a phosphoramidate bond via reaction with methylimidazole and carbodiimide. In this way, tubes were labeled with capture primers specific to a single chromosome.

The capture efficiency of the DNA probes was tested by first adding bovine serum albumin (1 mg/ml) to the capture tube to block nonspecific adhesion of the DNA and DNA polymerase enzyme to the tube wall. Next, template DNA (saliva) was added to the tubes in a 0.1-M sodium chloride solution, and hybridized for one hour at 37°C. It is during this step that binding of DNA to the capture probe takes place. The tubes were then washed with deionized water to remove unbound DNA. PCR primers and reaction master mix (PAQ 5000 DNA polymerase, $MgCl_2$, nucleotide bases, and buffer) were added to the tubes and PCR amplification reactions run. The expectation was that the bound primers would specifically capture their corresponding STR loci (e.g., CSF1PO would capture chromosome 2), but the results showed that one capture probe primer alone was sufficient to capture the chromosomal DNA in its entirety from a raw biological sample (in this case, saliva). Figure 1 shows the results of 4% agarose gel electrophoresis of DNA from saliva captured by DS13S317. The amplified PCR products from the DS13S317 capture probe exhibit the same band as the full genomic DNA positive controls. The most clearly visible bands are from chromosome 7 (D7S820), 2 (TPOX), 8 (LPL), and 13 (DS13S317). These data indicated that one single DNA capture probe for one STR locus was sufficient to capture a whole genomic DNA strand in its entirety, reducing the required probes to a single sequence.

Table 1. DNA and PNA primer probe sequences

STR Name	Chromosome	Primer Pair Sequence (Promega)[a,b]	STR size (bp)	Alu Element	Alu primer[a]	PNA Probe[a,c]
CSF1PO	5	AAC CTG AGT CTG CCA AGG ACT AGC TTC CAC ACA CCA CTG GCC ATC TTC	291-327	Yb9NBC6	GCA GAC CGT ATG TTC AAT AAA TGA C CCA CTT GGA AAA ACA CCC AAA	AGT CTG CCA AGG ACT
D5S818	5	GGT GAT TTT CCT CTT TGG TAT CC AGC CAC AGT TTA CAA CAT TTG TAT CT	135-167	Yb9NBC6	GCA GAC CGT ATG TTC AAT AAA TGA C CCA CTT GGA AAA ACA CCC AAA	ACA GAA GTC TGG GAT
D7S820	7	ATG TTG GTC AGG CTG ACT ATG GAT TCC ACA TTT ATC CTC ATT GAC	212-244	Yc1RG67	AAA CTA CCT TCC CCA GAC TCC CCC TAA GGA CTT TAT AAT GGG ACT	
D13S317	13	ACA GAA GTC TGG GAT GTG GA GCC CAA AAA GAC AGA CAG AA	165-197	---		
D16S539	16	GGG GGT CTA AGA GCT TGT AAA AAG GTT TGT GTG TGC ATC TGT AAG CAT	264-304	Yb9NBC18	CGT TTG AAA GCT ACG TTA CC TCC CAT GAG GTA GTG ATG AT	GGT CTA AGA GCT TGT
F13A01	6	GAG GTT GCA CTC CAG CCT TTG CAA TTC CTG AAT CAT CCC AGA GCC ACA	281-331	Yb9NBC21	TTC ATG TAG CCA AAA CTA CCT GTT C TTA ACA GCT TAC AGT TTG GCA GAG	
F13B	1	TGA GGT GGT GTA CTA CCA TA GAT CAT GCC ATT GCA CTC TA	169-193	Yb9NBC11	AAA GAC TTT TCA GGT TCT TGT AGC A ATG CAT GTC TAT GCA AAC TAT CAA A	
FESFPS	15	GCT GTT AAT TCA TGT AGG GAA GGC GTA GTC CCA GCT ACT TGG CTA CTC	222-250	---		
HPRTB	X		259-303	Yb9NBC54	TAG GAT GAG AAT GAA CTT TGA GAT G CCA TTT ATA ACC AAT GAC GAC AAA G	
LPL	8	CTG ACC AAG GAT AGT GGG ATA TAG GGT AAC TGA GCG AGA CTG TGT CT	105-133	---		
TH01	11	ATT CAA AGG GTA TCT GGG CTC TGG GTG GGC TGA AAA GCT CCC GAT TAT	179-203	---		
TPOX	2	ACT GGC ACA GAA CAG GCA CTT AGG GGA GGA ACT GGG AAC CAC ACA GGT TA	224-252	Yc1RG65	GCA GCC TGG ATA TCA ATT AAG G ATG GGT TAA AAC TCC TAG CAC TG	ACA GAA CAG GCA CTT
VWA	12	GCC CTA GTG GAT GAT AAG AAT AAT CAG TAT GTG GGA CAG ATG ATA AAT ACA TAG GAT GGA TGG	127-167	Yb9NBC1	AGT ATC TTT AGA TCC AGG GTG AAG C TTC CAG TGG TAA GTC TAT GGG AAT	

a) Sequences are listed from 5' to 3' end. For primer pairs, the first is the forward primer, the second the reverse primer.
b) For DNA capture probes, the sequences listed are preceded by TTT TTT TTT on the 5' end
c) For PNA capture probes, the sequences listed are preceeded by an unlabeled octamer of the amino acid lysine, KKK KKK K, on the 5' carboxyl end. The 3' amino end is capped by an acylated lysine, K-AC.
A = adenine, T = thymine, C = cystine, G = guanidine

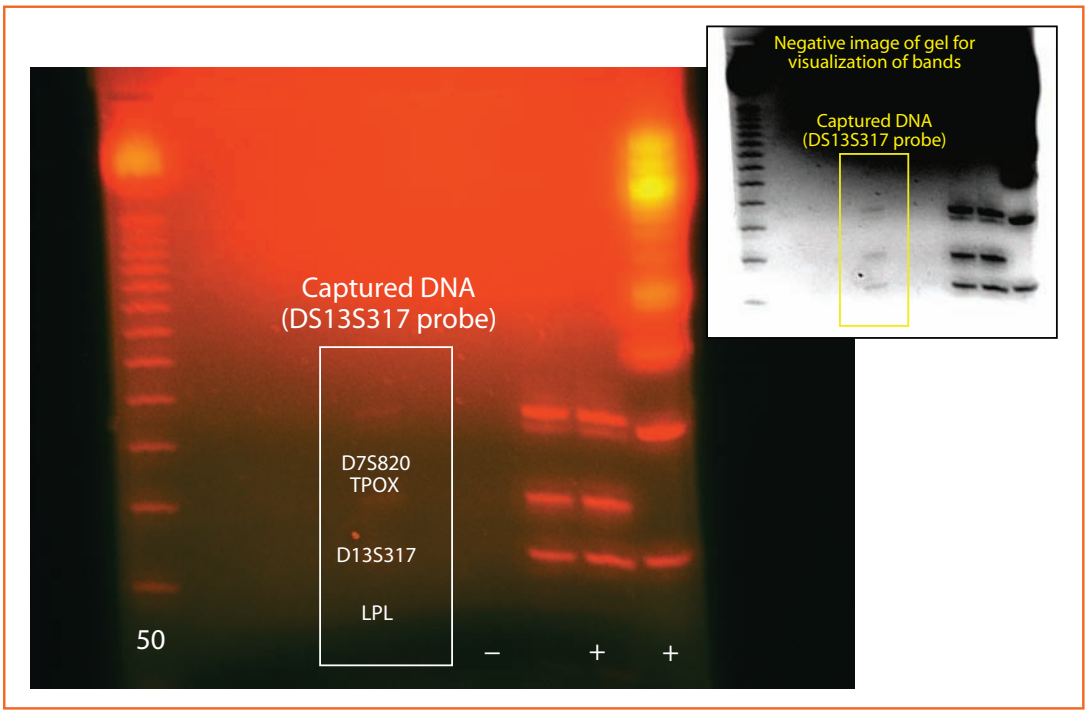

Figure 1. Gel electrophoresis of human DNA captured by D13S317 probe. Labeled bands correspond to DNA amplicons from various chromosomes.

PNA Probe Design

A set of four PNA primers was designed for use with the NucleoLink secondary-amine-labeled PCR tubes for evaluation as DNA capture probes (Table 1). With an amino acid polypeptide backbone, the terminal carboxyl group is the 5′ end, and the terminal amine is the 3′ end. While binding to the NucleoLink tube was desired through the 5′ terminus, the linkage chemistry (addition of carbodiimide to form acylurea, followed by sulfo-hydroxy succinimide to form a succinyl ester, which subsequently reacts with the pendant secondary amine forming a covalent amide bond) would also add through the 3′ terminus. Thus, the PNA probes were designed with either an acyl or fluorescein protecting group bound to the 3′ end. An 8-mer of the amino acid lysine was used as the linkage group on the 5′ end. The probes were procured from Panagene Incorporated in South Korea, the solely licensed worldwide producer of commercial PNA. Due to delays in international procurement and U.S. Customs entry into the United States, the PNA arrived at the end of the project cycle, and capture tests were not performed.

Conclusion

Proof of concept of the use of DNA probes for capture of whole genomic DNA was demonstrated. DNA from unprocessed biological samples was captured using a probe that hybridizes 20 to 30 bp out of the nearly 3×10^9 bp comprising the human genome. PNA probes for DNA capture were designed but not tested under this project. We anticipate that the strength and specificity of the PNA/DNA interaction will result in much greater capture efficiency, as well as providing a stabilizing environment for DNA samples. Additionally, the polypeptide backbone of the PNA probes is readily incorporated into polymers as block copolymers or organosilicate cross-linked matrices as part of a hydrogel (Schlaad, 2003). These matrices could provide a solid or gelatinous reagent for capturing DNA from surfaces and environmental samples, forming in effect a DNA-specific sponge. The applicability for DNA capture extends beyond human DNA into other species, including ribonucleic acid (RNA)–based genomes. The choice of organic component will dictate the form of the copolymer (e.g., polystyrene and poly-methylmethacrylate for films, polybutadiene or poly-t-butene for flexible rubbers, and nylon or rayon for fibers). Fibers could form the basis of woven collection materials.

References

Balogh, M. K., J. Burger, K. Bender, P. M. Schneider, K. W. Alt, "STR genotyping and mtDNA sequencing of latent fingerprint on paper," *Forensic Science International* **137**, 2–3 (November 2003) 188–195.

Batzer, M. A., P. L. Deininger, U. Hellman-Blumberg, J. Jurka, D. Labuda, C. M. Rubin, C. W. Schmid, E. Ziętkiewicz, E. Zuckerkandl, "Standardized nomenclature for Alu repeats," *Journal of Molecular Evolution* **42**, 1 (January 1996) 3–6.

Egholm, M., O. Buchardt, L. Christensen, C. Behrens, S. M. Freier, D. A. Driver, R. H. Berg, S. K. Kim, B. Norden, P. E. Nielsen, "PNA hybridizes to complementary oligonucleotides obeying the Watson-Crick hydrogen-bonding rules," *Nature* **365**, 6446 (October 1993) 566–568.

Masibay, A., T. J. Mozer, C. Sprecher, "Promega Corporation reveals primer sequences in its testing kits," *Journal of Forensic Science* **45**, 6 (November 2000) 1360–1362.

National Institutes of Health (NIH), National Center for Biotechnology Information (NCBI), GenBank, http://www.ncbi.nlm.nih.gov/Genbank, accessed November, 2006.

Nielsen, P. E., M. Egholm, R. H. Berg, O. Buchardt, "Sequence-selective recognition of DNA by strand displacement with a thymine-substituted polyamide," *Science* **254**, 5037 (December 1991) 1497–1500.

Orum, H., P. E. Nielsen, M. Egholm, R. H. Berg, O. Buchardt, C. Stanley, "Single base pair mutation analysis by PNA directed PCR clamping," *Nucleic Acids Research* **21**, 23 (November 1993) 5332–5336.

Schlaad, H., M. Antonietti, "Block copolymers with amino acid sequences: Molecular chimeras of polypeptides and synthetic polymers," *European Physical Journal E - Soft Matter* **10**, 1 (January 2003) 17–23.

Xing, J., D. J. Hedges, K. Han, H. Wang, R. Cordaux, M. A. Batzer, "Alu element mutation spectra: molecular clocks and the effect of DNA methylation," *J. Mol. Biol.* **344**, 3 (November 2004) 675–682.

this page intentionally left blank

Aerial Neutron Detection – Phase II

Manuel Avaro, Andre Butler, Lars Caspersen, Mansie Iyer, Carl Jackson, Steve Kegeler, Jeff LeDonne, Rick Maurer,[1] Tim Rourke, Greg Shore, Ethan Smith
Remote Sensing Laboratory – Andrews

Gary Hall, Tom McKissack, Tom Stampahar, Ed Zachman
Remote Sensing Laboratory – Nellis

This research, which continues a comprehensive study of aerial neutron detection begun in FY 2006, involved conducting aerial measurements with the Remote Sensing Laboratory (RSL) helicopter over a neutron point source, a nuclear power plant, spent fuel dry casks, depleted uranium hexafluoride cylinder yards, and depleted uranium crane counterweights. In addition, baseline measurements were obtained over land and water at altitudes from 200 to 5000 ft above ground level (AGL) in Maryland and Nevada. Finally, a baseline survey was conducted in Nevada over a large area free of radiation sources to determine if the effect of geologic features on neutron rates could be measured. The project includes data acquired from over thirty-four hours of helicopter flight time.

Background

Work performed in FY 2006 included making a series of static baseline measurements using a crane to elevate the neutron detectors over neutron sources in an open field (Maurer, 2007). Two neutron point sources were studied—Californium-252 (^{252}Cf) and Americium-Beryllium (^{241}Am-Be). The neutron energies from the ^{252}Cf and ^{241}Am-Be were 2–3 MeV and 4–5 MeV, respectively. The neutron detectors were elevated on a crane from 10 to 80 ft directly above the neutron sources. The count rates were measured as a function of distance to the source. The results indicated that the neutron detectors were readily sensitive to the neutron sources at the 80-ft distance, indicating that aerial measurements were feasible.

Project

Equipment

The aerial measurements were conducted using the RSL Bell 412 helicopters located at Andrews Air Force Base (AFB), Washington, D.C. and Nellis AFB, Las Vegas, Nevada. Each Bell 412 was outfitted with the Aerial Measuring System (AMS) shown in Figure 1.

[1] maurerrj@nv.doe.gov, 301-817-3367

Figure 1. Bell 412 helicopter with AMS external gamma detector pods (left) and the two neutron modules mounted on the helicopter's floor (right)

The AMS consists of two external pods each containing six 2" × 4" × 16" sodium iodide (NaI) detectors and an internal Realtime and Environmental Acquisition Recorder (REDAR), version 5. The REDAR records detector signals into four analog-to-digital converters (ADCs) along with the GPS position and radar altimeter. Two neutron modules were installed on a foam shock mount pad, lengthwise across the floor of the helicopter (Figure 1). Each module consisted of eight 6' long × 2" diameter tubes filled with 3 atm of ^{3}He. One module was moderated with ¼-in. polyethylene honeycomb matrix and one module was unmoderated (bare tubes). The neutron signals from the eight individual detectors were counted using the scaler inputs on the REDAR. All data were collected in 1-sec intervals. As such, simultaneous gamma and neutron data correlated with GPS coordinates and the radar altimeter were recorded for post-processing.

Aerial Measurement Flight Profiles

Two types of measurement flight profiles were conducted over the neutron sources, altitude and grid pattern profiles, as shown in Figure 2.

An altitude profile consisted of flying 1-min lines at a series of altitudes directly over the neutron source. This measurement was designed to determine the neutron count rate as a function of distance and determine the maximum detection range. Altitude profiles, from 100 to 3000 ft, were made at regularly spaced intervals. The count rate data were plotted as a function of altitude. The grid pattern profile consisted of flying in a series of parallel lines to form a box over the neutron source. This measurement was designed to show the spatial extent of the detection pattern for the neutron source. Typically, three grid pattern altitudes were selected for each neutron source—the lowest altitude possible, an intermediate altitude, and the highest altitude at which neutrons were still detectable. The line spacing for the grids ranged from 100 to 200 ft. The data from the grid profiles were contoured and overlaid on a high-resolution aerial photograph.

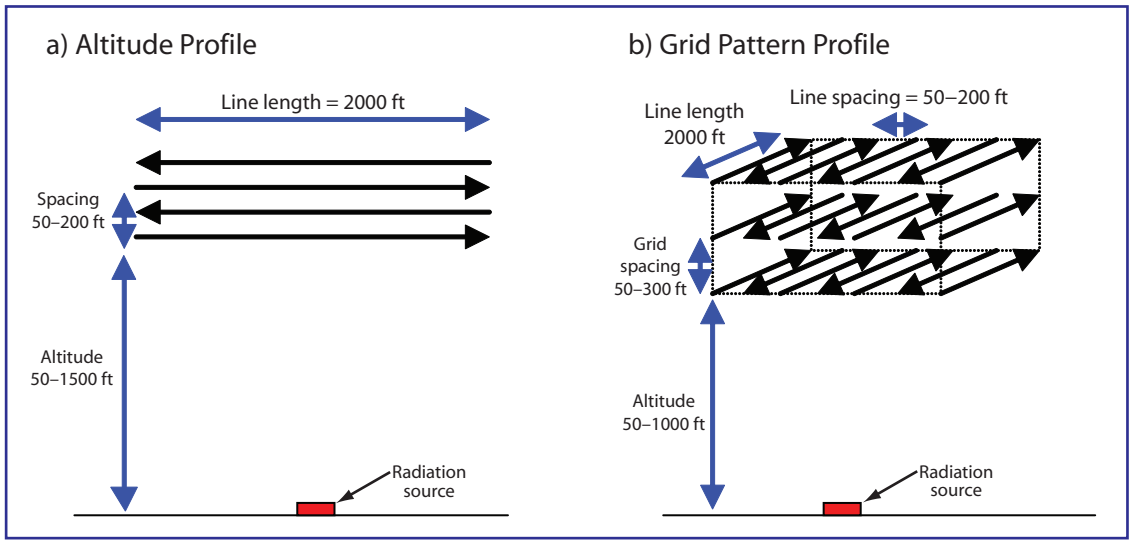

Figure 2. Aerial flying patterns for the (left) altitude profile and the (right) grid pattern profile

Baseline Background Measurements

Baseline neutron background count rate measurements were conducted over both water and land. The purpose of the measurements was to determine the background count rates as a function of altitude. The neutrons in the atmosphere originate from cosmic rays interacting with nitrogen in the upper atmosphere, which then produce a shower of neutrons toward the earth. As such, the source of the neutrons in aerial measurements was actually located above the aircraft and not terrestrially, as was the case with gamma arrays.

The background measurements over water and land were conducted in Maryland at the Chesapeake Bay and Calvert County Test Line, respectively. Similar measurements were also conducted in Nevada over Lake Mead and the Government Wash basin. Plotted in Figure 3 are the average neutron count rates for 1-min measurements as a function of altitude for the unmoderated and moderated neutron detectors as a function of altitude from 200 to 5000 ft for the Maryland data. It is evident from the graphs that the slopes of the count rates as a function of altitude are significantly different for the two detectors. This difference is a measure of the detection efficiency for thermal neutrons. Both detectors showed an increase in count rate as a function of altitude, with the slope for the moderated count rate increasing more rapidly. The moderated and unmoderated detectors exhibited a factor of three increase over the range of altitudes from 200 to 3000 ft.

It is also evident that the relative magnitudes of the minimum and maximum count rates from 200 to 3000 ft are also the same. Therefore, we deduced that the influence of the surface medium (air-ground interface) below the aerial neutron measurement contributed very little to the neutron count rates,

and that aerial neutron measurements above 200 ft were not influenced by the terrestrial environment. However, evidence from ground-level measurements (Dirk, 2003) and the previous SDRD work with crane measurements (Maurer, 2007) show that below 200 ft AGL, geological features may have an effect on measurable neutron rates.

Neutron Source Measurements

The following section presents representative samples of the contour data acquired over a point source, a nuclear power plant, and a spent fuel dry cask yard.

Point Source

Aerial measurements were conducted over a Californium-252 (^{252}Cf) source with a neutron flux of 10^7/sec. The ^{252}Cf source was placed on the ground at the south end of the runway in both shielded (2-in.-thick Delrin container) and unshielded (bare) configurations. This resulted in a series of four simultaneous measurements: (1) moderated detector/shielded source, (2) moderated detector/unshielded source, (3) unmoderated detector/shielded source; and 4) unmoderated detector/unshielded source.

First, an altitude profile was conducted over the source at distances ranging from 50 to 300 ft AGL at 50-ft intervals. Second, a series of grid patterns were flown at altitudes from 50, 100, and 150 ft with 100-ft grid line spacing. The flight lines were 2000 ft long. Thirteen lines were flown for each profile. These measurements required precision flying to maintain the altitude, line spacing, and aircraft speed. All measurements were conducted at 60–70 knots. Representative data for the 50-ft AGL grid pattern profile are shown in Figure 4.

It is evident from the graphs that the aerial neutron data provided a clear "bull's-eye" pattern on a relatively flat background, whereas the patterns produced by the gamma terrestrial background make it difficult to identify the location of the ^{252}Cf source.

Nuclear Power Plant

Aerial measurements were conducted over a nuclear power plant with an operating reactor. First, an altitude profile was conducted over the operating reactor at 300 to 1000 ft AGL at 100-ft intervals. Second, grid patterns were flown at altitudes of 300, 500, and 700 ft with 100-ft line spacing. The length of the flight lines was 2500 ft, and twenty-five lines were flown for each profile. Representative data for the 500-ft AGL grid pattern are shown in Figure 5.

It is interesting to note that there is no evidence of neutron emission from the nuclear reactor. On the other hand, the gamma data show a prominent bull's-eye centered on the reactor and an adjacent waste storage site directly below it. The gamma rays are primarily from cobalt-60 (^{60}Co), a by-product of neutron activation.

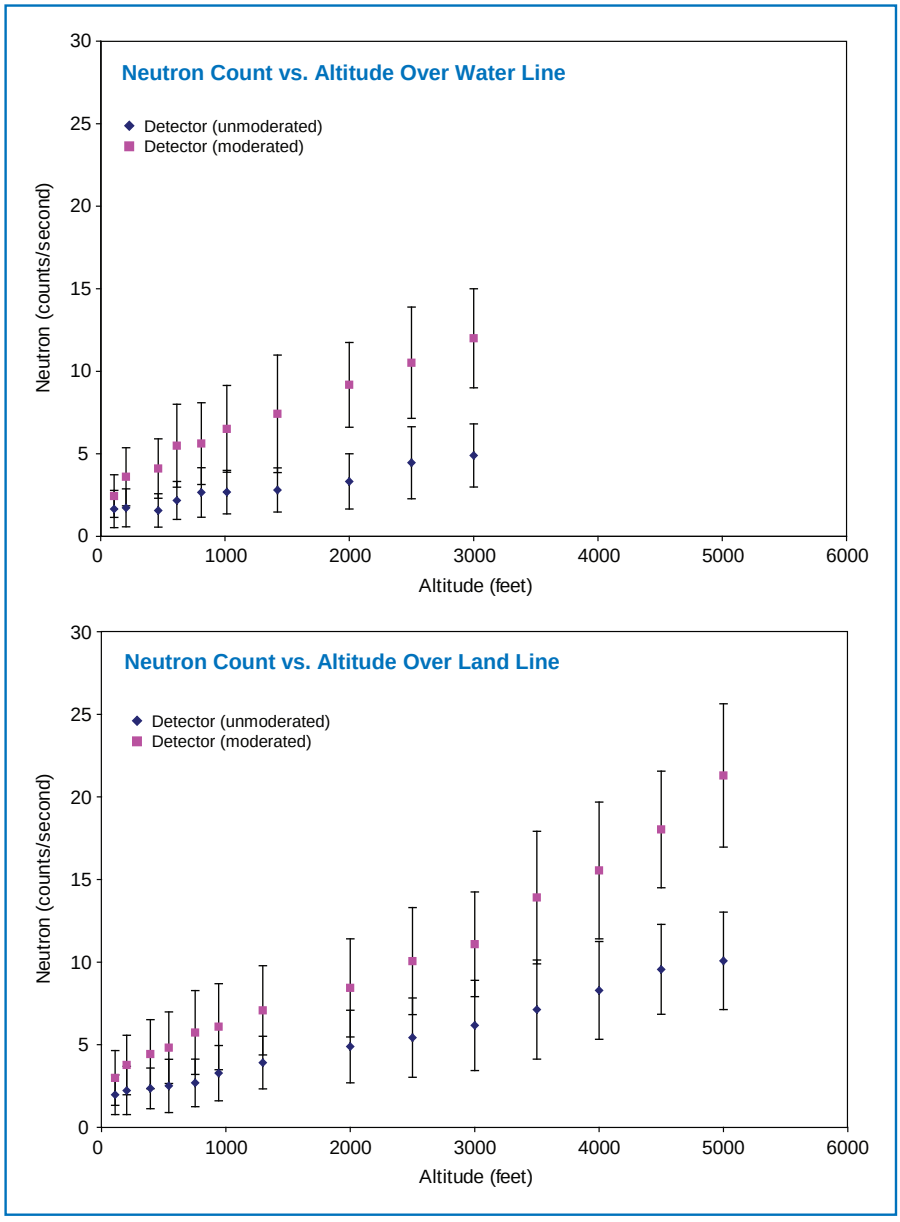

Figure 3. Neutron altitude profiles over (top) water and (bottom) land for both the moderated and unmoderated neutron modules

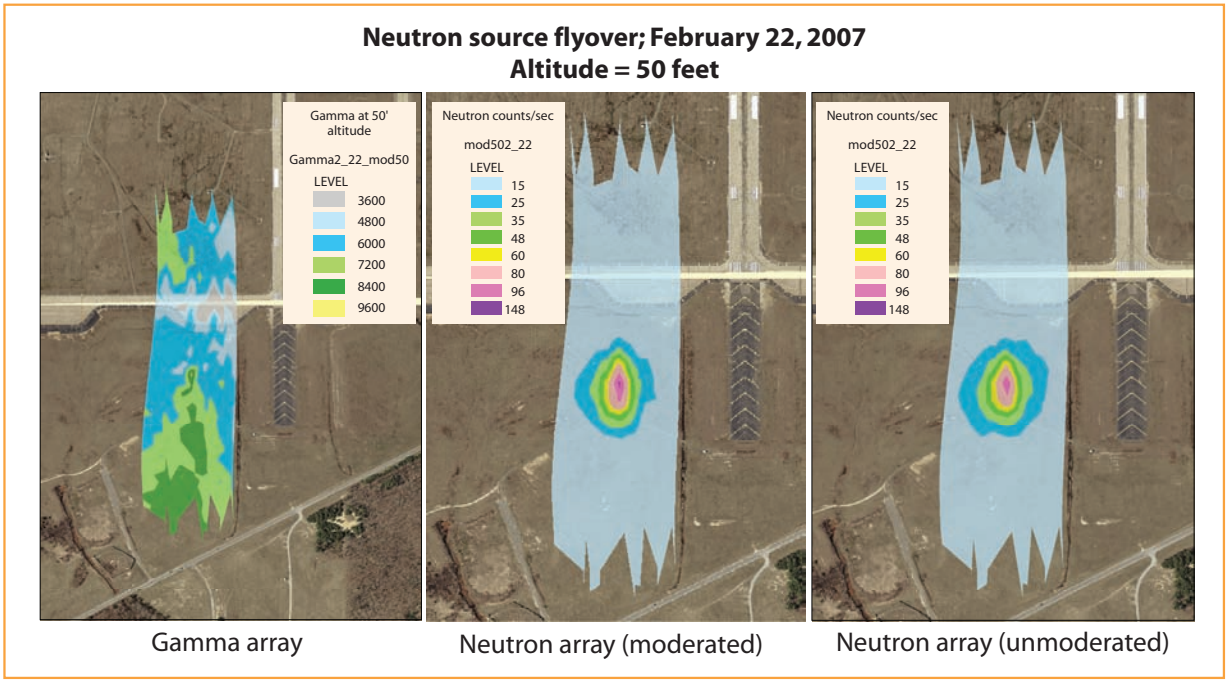

Figure 4. Aerial grid pattern data over the ^{252}Cf at 50 ft AGL and 100-ft line spacing for gamma gross count and moderated and unmoderated neutron arrays

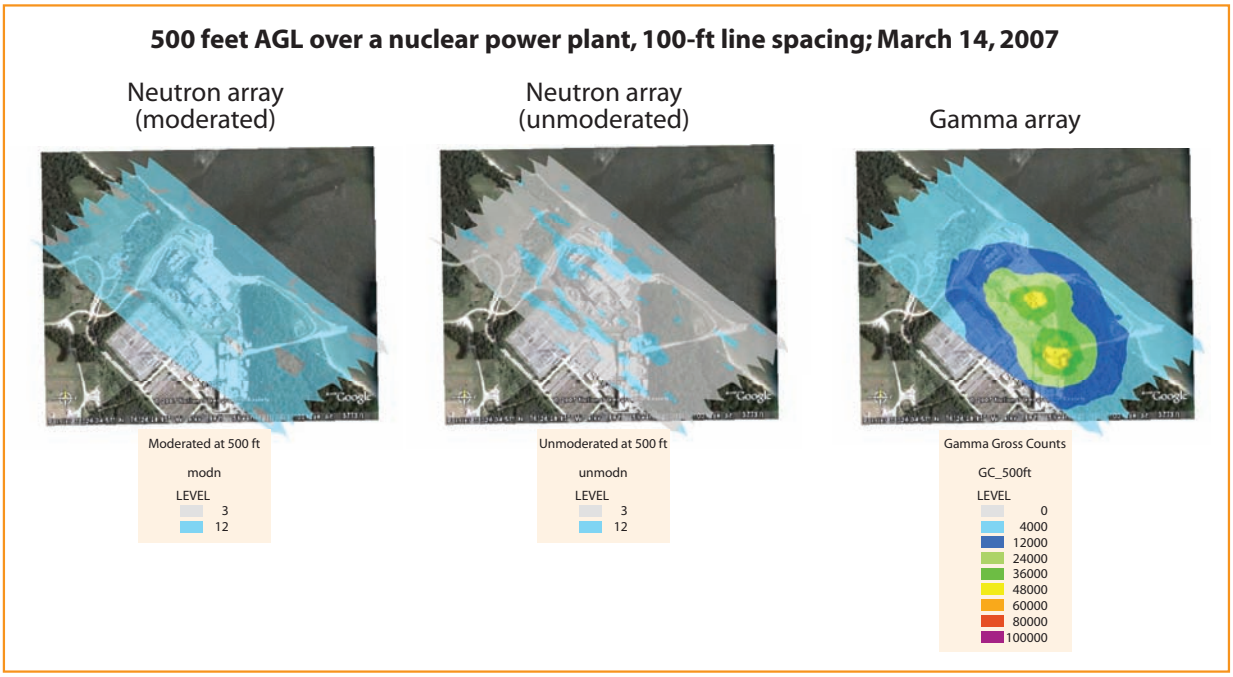

Figure 5. Aerial profile data for the 500-ft AGL grid pattern with 100-ft line spacing for moderated and unmoderated neutron arrays and gross count gamma array

Spent Fuel Dry Cask Yard

Aerial measurements were conducted over a spent fuel dry cask yard near a nuclear power plant. First, an altitude profile was conducted over the operating reactor at distances ranging from 300 to 1000 ft AGL at 100-ft intervals and then from 1000 to 3000 ft AGL at 500-ft intervals. Second, a series of grid patterns were flown at altitudes of 300, 600, and 1000 ft with 200-ft line spacing. The length of the flight lines was 2500 ft. Twenty lines were flown for each profile. Representative data for the 1000-ft AGL grid pattern are shown in Figure 6.

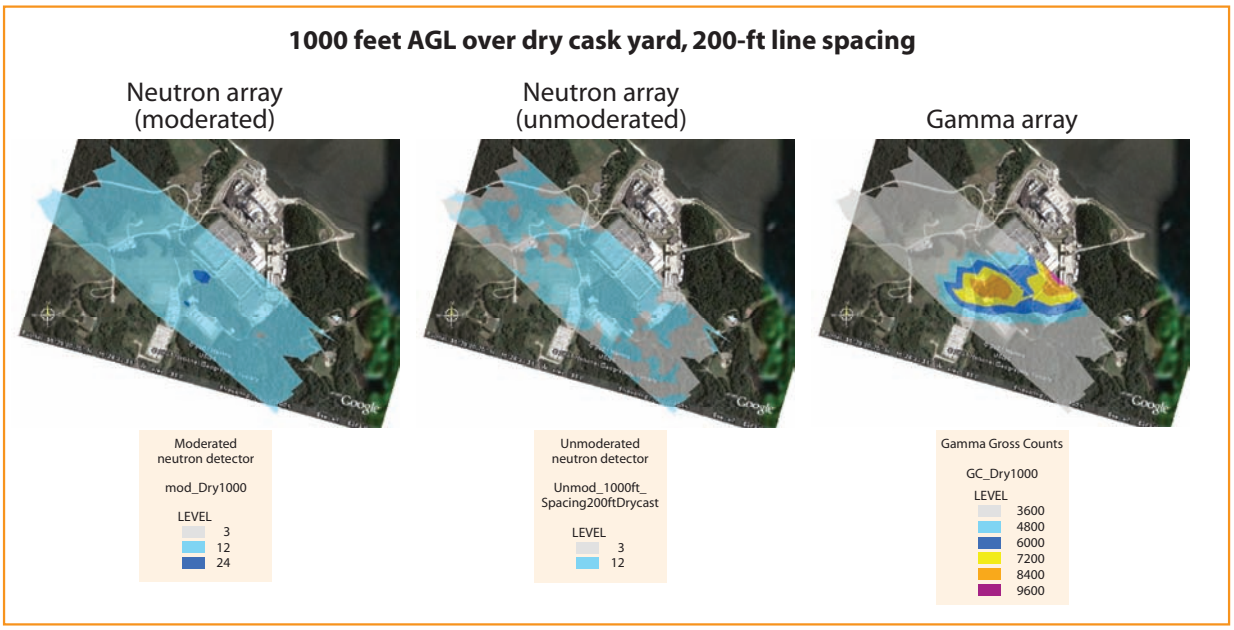

Figure 6. Aerial profile data for the 1000-ft AGL grid pattern with 200-ft line spacing for moderated and unmoderated neutron arrays and gross count gamma array

Evidence of neutrons from the dry cask yard are seen at an altitude of 1000 ft. Typically, fission neutrons have average energies of 1–2 MeV and a mean free path in air of ~600 ft. The neutrons detected at 1000 ft most likely originate from the alpha decay on low Z (such as oxygen) from the transuranics in the spent fuel. This reaction produces neutrons with energies from 4–5 MeV with a considerably longer mean free path in air.

Conclusion

Aerial measurements were conducted over a series of neutron sources to study the long-range detection of neutrons. The goal was to determine the detection distance and detection profile for a variety of neutron sources. Radiation measurements consisted of altitude profiles and survey grid profiles. Baseline background data were collected over land and water in both Maryland and Nevada with the same detectors for comparison. Data were collected over a neutron point source, a nuclear reactor, and a spent fuel dry cask storage site, and representative data were presented in this report. Also surveyed were a depleted uranium hexafluoride cylinder yard and depleted uranium metal from crane counterweights. These data will be included a future report.

References

Dirk, Lt. J. D., M. E. Nelson, J. F. Ziegler, A. Thompson, T. H. Zabel, "Terrestrial thermal neutrons," *IEEE Trans. Nucl. Sci.* **50,** 6 (December 2003), 2060–2064.

Maurer, R., T. Stampahar, E. Smith, "Aerial Neutron Detection," *Nevada Test Site–Directed Research and Development,* FY 2006, National Security Technologies, LLC, Las Vegas, Nevada, 2007, 199–204.

Concealed High-sensitivity Directional Detector

Jim Castelaz, Sarah Clemente, Rick Maurer,[1] Lance McLean, Lonnie Swindell, Ron Wolff
Remote Sensing Laboratory – Andrews

Currently available instrumentation to search for radioactive materials is housed in either a handheld meter or backpack form factor, neither of which is considered low profile. Typically containing a single detector element, the instruments are designed to detect the presence of a radiation source and notify the operator via an alarm level indicating the strength of the source. The operator then must locate the radiation source using a detector that has an isotropic response. It has been demonstrated that an instrument containing four detector elements can be employed to not only identify the presence of a radiation source but also determine its direction for tracking and localization. Although prototypes of directional detectors exist, they tend to be rather bulky and require the backpack format. The goal of this research effort was to develop a concealed directional detector system as a technology for the next generation search instrumentation. The prototype system is embedded in a belt to be worn by the operator. It consists of four equally spaced, high-sensitivity detectors with associated electronics, computer, and operator interface. The system provides radiation detection, direction, and tracking capability and is designed to be low profile, lightweight, and have hands-free operation.

Background

Over the years, searches for radiation sources have been conducted with a variety of instrumentation. In each case, however, the instrument was designed to advise the operator only that a radiation source was present nearby, with the assumption that the source remained in a fixed location, i.e., was stationary. The technique for locating the source required the operator to make several passes by it, eventually narrowing in on the site. This was a relatively inefficient, conspicuous, and time-consuming process. Search instrumentation has been developed in many form factors, from handheld meters to briefcase detectors to backpack systems, all which have their advantages and disadvantages. The most obvious disadvantage is the size and format of these systems: typically large, heavy, and most importantly, not considered low profile. In today's security environment, backpacks of any style draw attention and are typically not allowed into large-scale events for obvious reasons.

Therefore, a lower profile system that offers the sensitivity of the larger backpack systems and provides more advanced operator capabilities is desired. Determination of the source direction is especially

[1] maurerrj@nv.doe.gov, 301-817-3367

important when the radiation source is moving among a crowd. By incorporating multiple smaller detector elements within a single system, it has been demonstrated that radiation source direction and, thus, tracking and localization can be accomplished.

Project

The conceptual design of the concealed directional detector appears in Figure 1. The preferred format was a belt-type system with the detectors oriented at 45 degrees off-axis. Detector elements oriented at 45 degrees off-axis ensure that the operator's arms are not shielding the side detectors and provide a rear space for the supporting electronics. Each detector has an amplifier, multichannel analyzer (MCA), and power supply; data are recorded and monitored by a computer. When a source is detected above a preset background level, an algorithm calculates the source strength (i.e., alarm level) and the source direction based on the count rates in the four detectors. The computer then indicates source strength and direction to the operator through an interface.

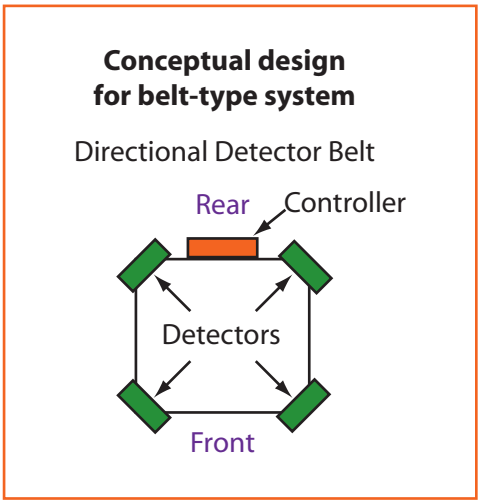

Figure 1. Conceptual design (top view) for the concealed directional detector in the format of a belt with four detectors positioned off-axis

In order to research this type of detection system, we prepared a list of desired functionalities and conducted a technology review, as outlined in Table 1.

After conducting the technology review, we prepared a design schematic (Figure 2) to begin system development.

Table 1. Desired functionality list and technology review for concealed directional detector

Desired Functionality	Technology Review
Directional detection	Detector materials
User in frame of reference	Compact computers
Sensitivity comparable to current systems	Audio interfaces
Wearable	Software requirements
Lightweight	Interface peripherals
Hands-free operation	Power supplies
Audio interface	Belt types
Low power, long life	
Upgradeable	

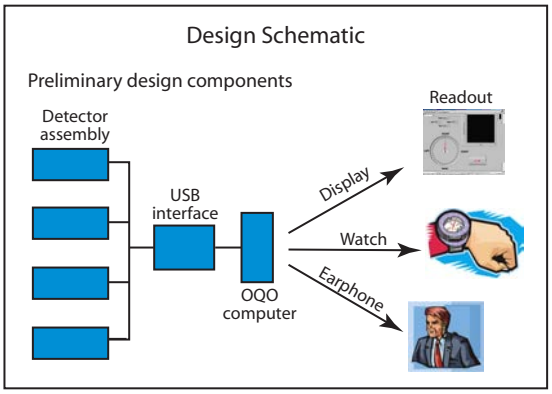

Figure 2. The concealed directional detector schematic

The system would consist of four gamma-ray detectors, an interface, a computer, and an operator display. The computer would record, store, and provide the directional algorithms. Several user interfaces were considered.

The algorithm for calculating the radiation source direction based on a four-detector system is:

$$X = GC1 - GC3$$

$$Y = GC4 - GC2$$

$$\theta = \text{Arctan}\,(Y/X),$$

where GC(i) is the gross count rate in detector i and θ is the angular direction of the radiation source.

Components

The detector selected for this system is custom-made by Scionix. It consists of a thallium-activated cesium iodide, CsI(Tl), with the dimensions 2.5" × 4" × 0.5", coupled to a photodiode and preamp, all sealed in an aluminum casing. Voltages of 6–12 V for preamplifier power and 35–70 V for the photodiode are required. The detectors were coupled to an eMorpho MCA, which has dimensions of 2" × 2" × 0.5" and contains a shaping amplifier, discriminator electronics, and a 12-bit waveform analog-to-digital converter (ADC). All signal processing, including peak detection, pulse discrimination, and pileup rejection, is performed on the digitized waveform. The use of this electronic package results in maximum detector throughput and optimal resolution. The MCA consumes only a few milliwatts of power that is supplied though the USB connection to the data acquisition computer. For the prototype, 9-V batteries were configured to provide both preamp power and bias voltage.

For the computer system, several concepts were evaluated. Initial plans included an OQO subcompact computer. The OQO computer is a 3.5" × 5" computer weighing 1 lb, which would add considerable weight and bulk to the system but was available for concept development from previous R&D projects. Further evaluation of compact computer technologies led to a Gumstix computer (1.25" × 3.75" × 0.25"; 1 oz). The Gumstix computer product line provides the ability to mix and match basic computer components, resulting in the construction of a custom-tailored, tightly packaged, powerful computer at a very low cost. The Gumstix configuration used for this project consisted of a CPU with a 600-MHz processor with 128 MB of RAM. The custom-configurable Gumstix Linux operating system, which is based on the 2.6 Linux kernel, resides on the internal 32-MB flash ROM. Also included in this configuration were two expansion cards: one housing three PS2 serial ports and a USB host port, and the other housing a compact flash adapter and an Ethernet port. The prototype system also combined an LCD/LED display with a six-button keypad. The Gumstix computer and LCD peripheral appear in Figure 4.

Results

The prototype system was assembled and preliminary tests conducted. The system was shown to monitor the background radiation, detect an increase in radiation level, and determine the radiation source direction. The computer was programmed to conduct an initial self-test, then automatically begin signal analysis for radiation source detection and direction.

The graphical representation in Figure 5 shows the two primary LCD screen messages. The first screen shows the count rates for the four detectors in counts/second. When the count rate exceeds a preset alarm level setting of 4 (indicating the magnitude of the count rate excess above background), the screen then displays the calculated direction of the radiation source in degrees in the reference frame of the operator and a directional arrow quantized in 45-degree increments.

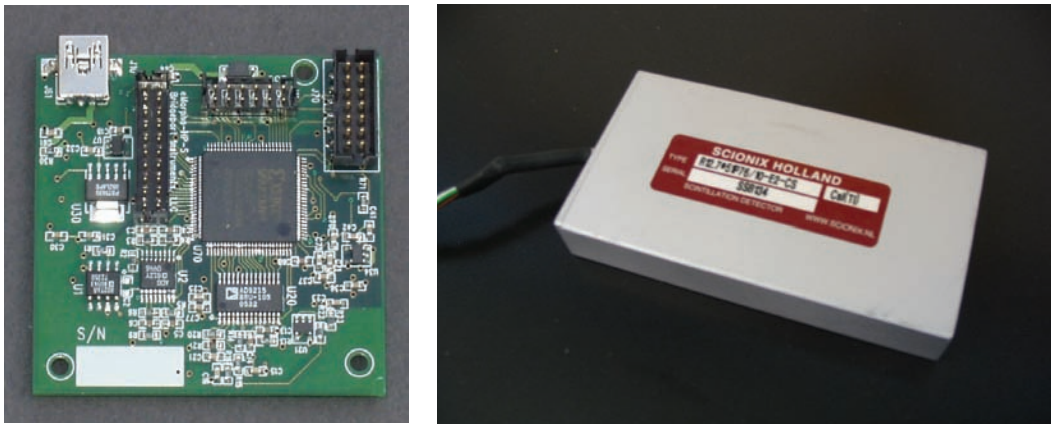

Figure 3. The eMorpho MCA (left) and Scionix CsI detector/photodiode (right)

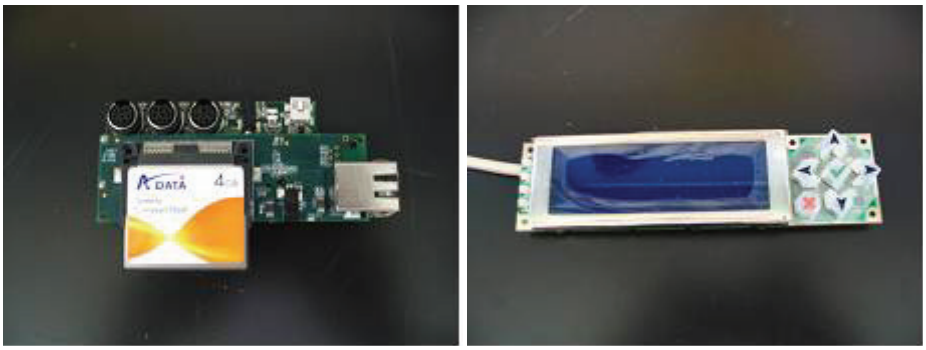

Figure 4. The (left) Gumstix computer and (right) LCD display peripheral

LCD Display 1. Startup screen

LCD Display 2. Alarm level and direction indicators

Figure 5. LCD Display 1, showing detector counts per second, and LCD Display 2, showing alarm level, direction angle, and direction indicator arrow

A front view of the prototype system appears on the display model in Figure 6. Four detectors are equally spaced around the body—two visible from the front and two from the rear. At the center rear of the operator is a 6" × 6" × 2" pouch, which contains the supporting electronics, computer, and power supply. As shown, the detectors are offset 45 degrees to the forward axis to eliminate shielding from the operator's arms and allow for a space behind the operator for the pouch.

Figure 6. Display model showing prototype concealed directional detector

Conclusion

A prototype concealed directional detector was developed and preliminary tests conducted. The tests indicated that the system can monitor the radiation background, determine when the trip level is exceeded, and calculate and display the direction of the radiation source. The system is both low profile and lightweight, and easily worn beneath a light jacket. It is designed to detect, determine direction of, and track a moving radiation source.

Nanosecond Single-photon Detection of Diffracted X-rays

Michael Madlener, Dane Morgan[1]
Los Alamos Operations

Mike Grover, Gerald Stevens, Dale Turley
Special Technologies Laboratory

The initial scope of work for this project was to develop a new, fast, single-photon microchannel plate (MCP) detector for use in conjunction with single-pulse x-ray diffraction (SPXRD). The project sought to address an ongoing need for a rigorous phase transition diagnostic for dynamic materials studies. Because x-ray diffraction (XRD) provides a direct correlation between the diffracted image and solid-state structure of the material under investigation, such a diagnostic would be extremely useful to the entire Stockpile Stewardship community. Previously, dynamic experiments have been limited to single-crystal experiments, in which the diffracted signal intensity is a factor of ~1000 greater than that reflected by common polycrystalline materials. Early in our investigation, we discovered that the combination of the Supersaver Marx bank, a newly designed x-ray diode, and a low-noise imaging detector could be used to observe x-ray diffraction images from virtually any polycrystalline material. Hence, with SDRD program approval, the work scope was expanded to include the first-ever dynamic polycrystalline materials experiments with SPXRD as the primary diagnostic. This report describes SPXRD diagnostic experiment test results. Although the MCP detector design was completed and parts were procured, the assembly and testing of the MCP detector in conjunction with the SPXRD diagnostic will be the focus of future work.

Background

The scientific concept for use of an MCP as an x-ray detector in the 17–22 keV energy range is based on new measurements by Greg Rochau (2006) and others at Brookhaven National Laboratory's National Synchrotron Light Source (NSLS) beam line X8A. For this experiment, MCP sensitivity was monitored as the beam line energy was increased through the lead and gold M_4-M_5 edges at energies of 2–3 keV. A significant increase in detector response was observed at the M_4-M_5 edges of lead; however, no measurable change in response occurred at the M_4-M_5 edges of gold. Conducted for x-ray energies ranging from 100 eV to 6 keV, NSLS experiment results were consistent with a leaded-glass photocathode and not a gold photocathode. This discovery opened the possibility of using 17–22 keV gated MCP detectors. Figure 1 suggests a mechanism for the high quantum efficiency possible for such detectors.

[1] morgandv@nv.doe.gov, 505-663-2047

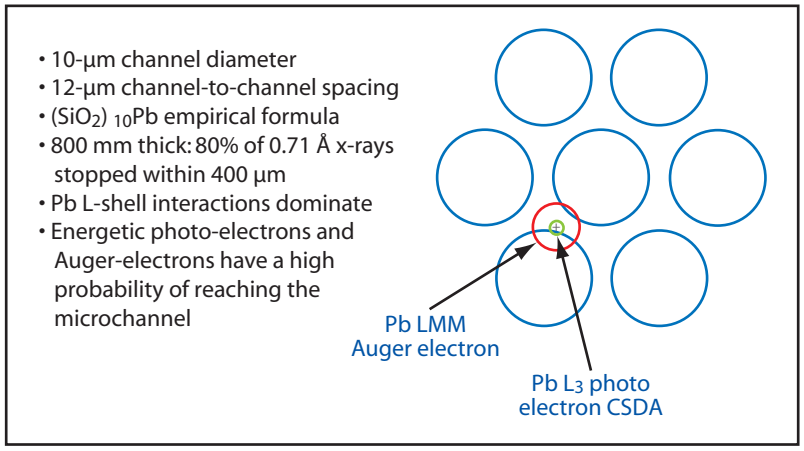

Figure 1. Continuous slowing down approximation (CSDA) electron range data from the National Institute of Standards and Technology shows a high probability that Pb Auger-electrons will reach a channel and start the electron cascade. The atomic data are available at http://physics.nist.gov.

Project

Design drawings were made for a prototype MCP detector, including windows, feedthroughs, and CCD camera couplings. MCPs were ordered from Burle Industries, and the fiber-optic faceplate phosphor, an item with a long lead time, was also ordered. We then turned our attention to developing the SPXRD diagnostic experiments.

To begin developing a viable SPXRD diagnostic, bench tests with a prototype SPXRD system were made. The high-voltage pulse used to generate the x-rays was provided by a Supersaver Marx bank (Figure 2). The Supersaver is a 37-stage Marx with 8.1 nF per stage, charged to –30 kV. The Marx develops a pulse >400 kV, which travels through a DS-2158 coaxial transmission line to a needle-and-washer x-ray diode that generates line and bremsstrahlung x-ray emissions in a 35-ns pulse.

The first prototype SPXRD system appears in Figure 3. A 1.5-mm-diameter tungsten pinhole collimator limits the spot size on the sample and the beam divergence to about 1 degree. The x-ray imaging detector is a P-43 phosphor that converts the x-rays into light. A coherent fiber-optic bundle couples the image generated at the phosphor to a CCD camera. For benchtop melt experiments using a hot plate, the system was rotated so the melting surface was parallel to the tabletop (Figure 4).

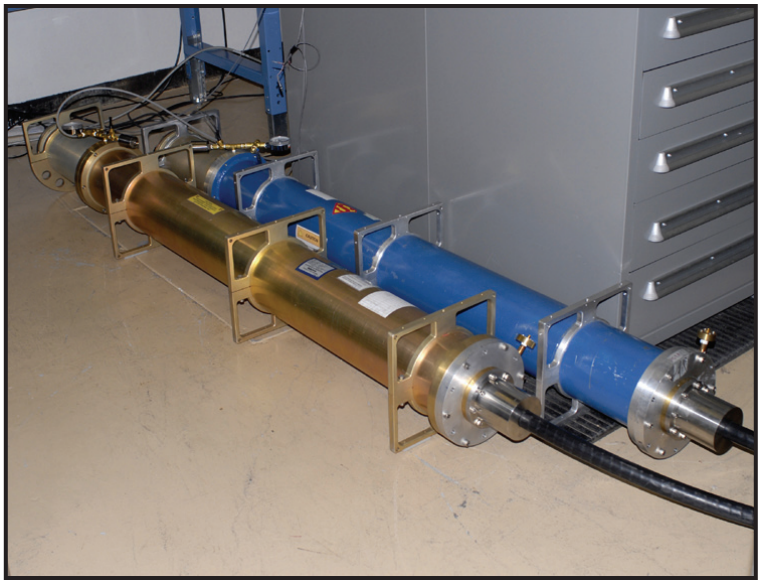

Figure 2. Supersaver Marx banks. The Supersaver is a 37-stage, 8.1-nF-per-stage, 150-joule Marx bank. It delivers a 400-kV, 35-ns pulse to the load.

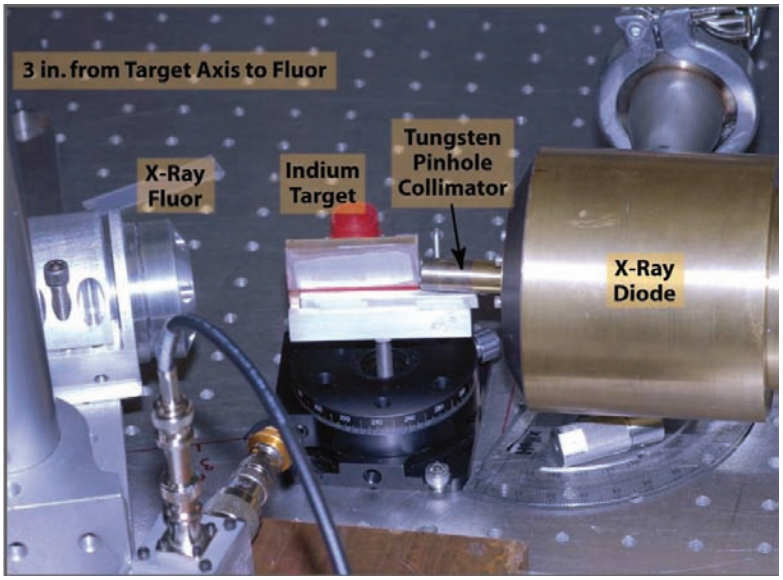

Figure 3. Single-pulse x-ray diffractometer. The x-ray diode on the right is shielded by brass and tungsten. The pinhole collimator is placed as close as possible to the sample. The distance from the target axis to the imaging phosphor (at left) is ~3 in.

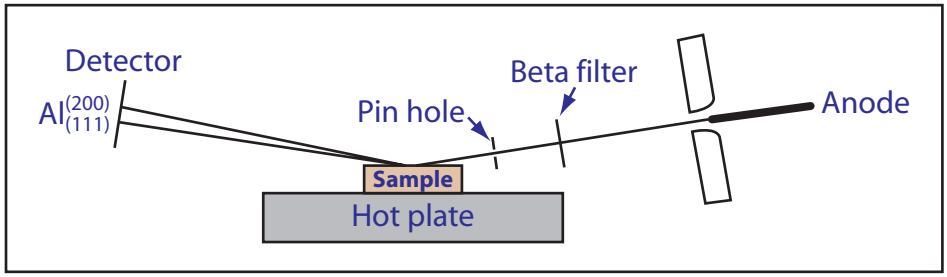

Figure 4. Configuration for benchtop high-temperature experiments

High-Temperature Benchtop SPXRD Experiments

Because of their low melting points, tin and indium were chosen as samples. At room temperature, tin is in the β phase. The structure of the tin β phase is face-centered tetragonal, with a second identical lattice offset from the original basis at coordinates (*a*,*a*,*c*)/4 (Ashcroft, 1976). The result is a diamond-like tetragonal structure with values for *c* and *a* of 3.17 Å and 5.82 Å, respectively. With this basis, x-ray reflections will occur for the same Miller indices as a cubic diamond. Indium has a body-centered tetragonal structure at room temperature, with c = 4.95 Å and a = 3.25 Å. For this study, part of the beam was incident on the sample, while part of the beam was incident on a stainless-steel sample holder. Results of the tin melt experiment appear in Figure 5.

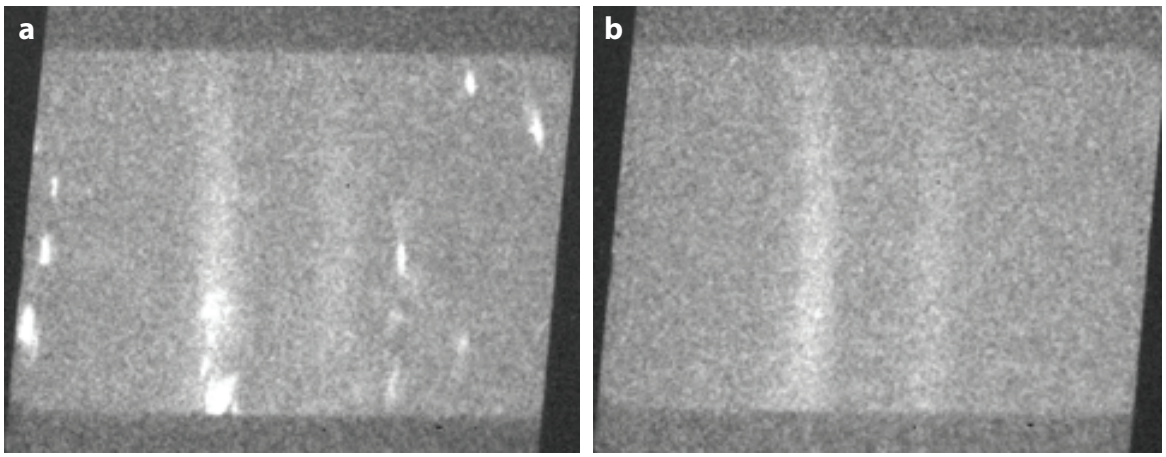

Figure 5. (a) Image obtained at room temperature using a 0.56-Å silver anode. Diffraction lines are apparent from both the tin and the stainless-steel holder; however, the tin has a much larger grain size. (b) Image obtained at 230°C, well above tin's melting point. The diffraction "spots" associated with the large-grain solid-state tin β phase have disappeared, indicating melt.

Coherent scattering from atomic centers in a solid-state lattice results in diffraction lines that are observed at angles for which the difference in path lengths is an integral number of wavelengths. As a solid's temperature rises, the atoms' average displacement from their equilibrium positions in the lattice increases. This causes a random phase shift in the scattered wave front from adjacent scattering atoms. Therefore, the intensity of the diffraction lines decreases as the temperature increases, as expressed by the Debye-Waller factor (Warren, 1990). For a solid lattice with a single type of atom, the reduction in the diffracted x-ray intensity is given as:

$$I/I_0 = \exp-\left\{16\pi^2 \langle u_s^2 \rangle \sin^2 \theta_B / \lambda^2\right\}, \quad \textbf{(1)}$$

where $\langle u_s^2 \rangle$ is the mean-square displacement of the atom's position from its equilibrium position perpendicular to the Bragg plane, θ_B is the Bragg angle, and λ is the x-ray wavelength. From Equation 1, we see that the reduction in intensity is greatest when the Bragg planes are closely spaced and the scattering angle is large. Using the harmonic approximation, the mean-square displacement of the atom from its equilibrium position is approximated as:

$$\langle u_S^2 \rangle = \frac{3\hbar^2}{4m_a k\Theta_D}\left(\frac{\phi(x)}{x} + \frac{1}{4}\right), \quad \textbf{(2)}$$

where $\hbar$ is Planck's constant, m_a is the mass of the atom, k is Boltzmann's constant, Θ_D is the Debye temperature, and $x=\Theta_D/T$, where T is the sample temperature. The term $\phi(x)$ (Warren, 1990) in Equation 2 is written as:

$$\phi(x) = \frac{1}{x}\int_0^x \frac{\xi\, d\xi}{\exp(\xi)-1}. \quad \textbf{(3)}$$

Although more recent theoretical calculations consider the anharmonicity of the atomic vibrations as well as thermal expansion (Nicklow, 1966), for the initial test of our single-pulse diffraction system as a temperature diagnostic, the harmonic approximation described above was adequate.

Because the diffraction line intensity depends on atomic mass, Debye temperature, and scattering angle, aluminum was chosen for the initial single-pulse diffraction tests. Aluminum has a comparatively low Debye temperature (395K) and low atomic weight (27 g/mole). Furthermore, at wavelengths ranging from 0.56 to 0.71 Å, aluminum's x-ray reflectivity is high. This allowed high sensitivity to high-order reflections with large scattering angles.

For our experiments, we used aluminum 6061-T6 0.25-in.-square bar stock. The sample temperature was measured using a thermistor calibrated to the melting points of indium and tin in the experiments described previously. Shot-to-shot variations of the x-ray source intensity were ~10%. The results of

three single-pulse (400) diffraction line observations are compared with the harmonic Debye-Waller model in Figure 6. The trend for reduced intensity with increasing temperature is apparent. The simple theoretical model shown in Figure 6 does not include anharmonic or thermal expansion effects.

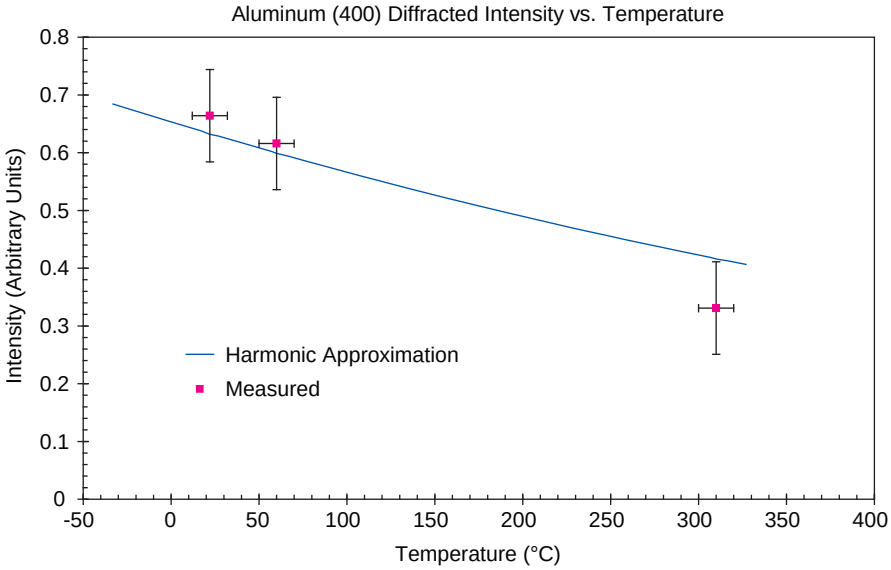

Figure 6. Measurement of the intensity variations with temperature of the aluminum (400) line compared with the harmonic model for 0.71-Å diffracted x-rays

Boom Box Experiments

We performed a set of SPXRD diagnostic experiments at the Special Technologies Laboratory (STL) Boom Box to observe phase transitions and temperature variations in real time during a high-explosives-driven shock experiment. We designed, built, and tested a containment system that allowed the source and detector to fit inside the Boom Box, close to the sample. The SPXRD diagnostic and its containment vessel are shown attached to and from inside the Boom Box in Figures 7 and 8.

Experiments were performed on shocked samples of tin and aluminum. Both free surfaces and shock-loaded samples were studied. Shock-loading was provided by 1-mm-thick sheets of vitreous carbon (VC), supplied by Alpha Aesar. This thickness of VC provided approximately 400 ns of shock loading, which was required because of the great timing uncertainty associated with the high-explosives' detonation. Unfortunately, this VC thickness causes difficulty with broadband coherent scatter and attenuation of the diffracted signal from the sample.

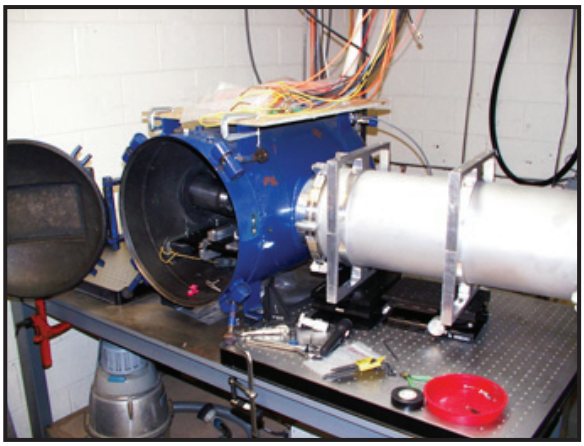

Figure 7. The Boom Box is the blue high-explosives chamber at left. The x-ray diode is contained inside the 10-in.-diameter tube at right.

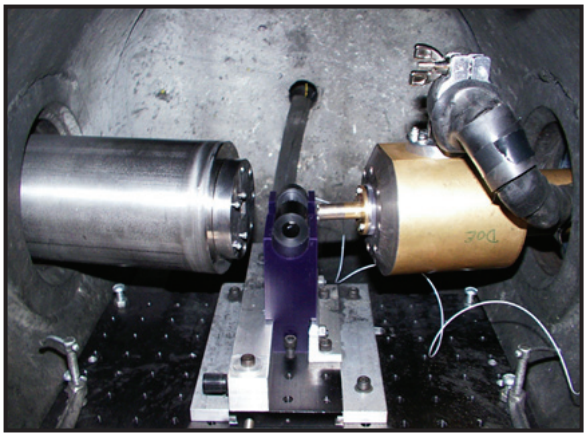

Figure 8. Inside the Boom Box are the x-ray diode and collimator (right), and the containment for the x-ray imaging system (left). The black high-explosives package is in the violet wax cradle on the near side. A photon Doppler velocimetry diagnostic is in a cradle on the far side.

We attempted to observe a solid-solid phase transition in tin. The tin beta-to-gamma phase transition occurs above 70 kbar, as predicted by a Wondy calculation. Experiment results show the tin shifting away from the beta phase as the grains are observed to disappear. However, it was impossible to infer a new solid-state phase from the dynamic data.

Better success was obtained with our shock-loaded aluminum experiments at 70 kbar. The shock reflection from the interface transversed a distance approximately three times greater than the penetration depth of the 0.56-Å x-rays into the aluminum, so the entire observed region was shock-loaded. The lines were observed to shift to larger scattering angles consistent with the aluminum shock compression (see results in Figure 9). The compression of both the (200) and (220) crystal orientations showed $\Delta d/d$ of ~1.8%.

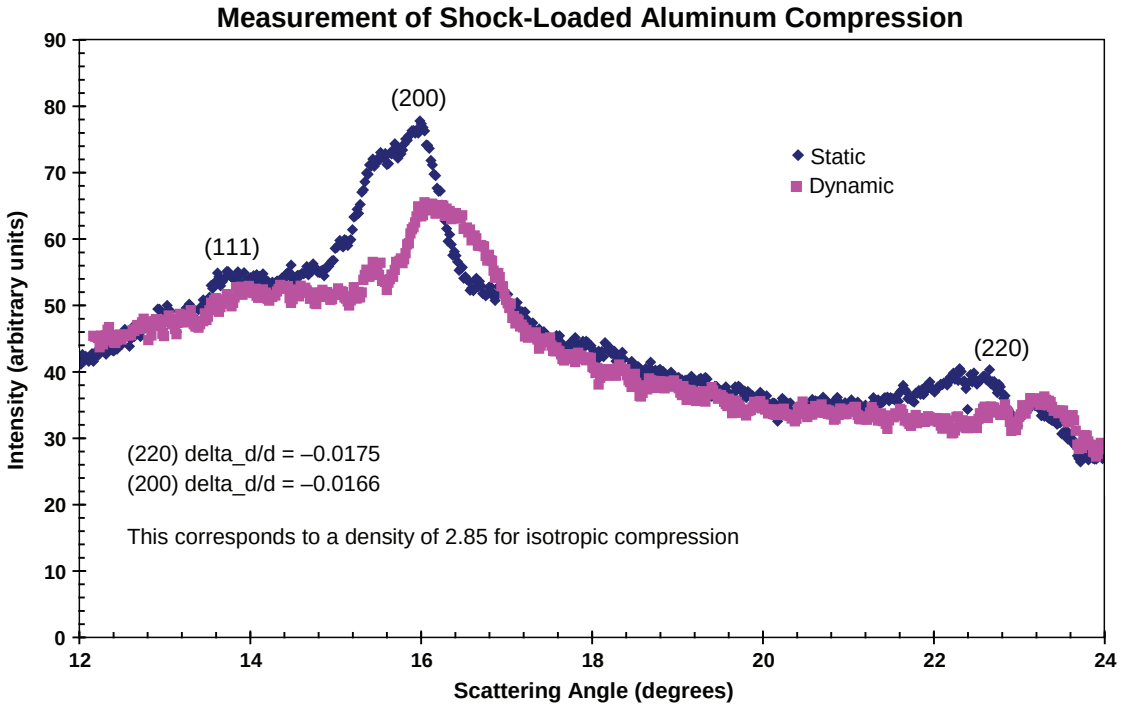

Figure 9. Aluminum line shift to higher scattering angles is consistent with shock-loaded compression

Large-format SPXRD Images and Analysis

To obtain a larger field-of-view and observe the entire diffraction pattern, we used large-format imaging plates. The image plates were bent to a 3-in.-radius cylinder about an axis defined by the intercept of the beam with the sample. This allowed simultaneous observation of the direct x-ray

beam and the entire diffraction pattern. Figure 10 illustrates a large-format image of a 0.71-Å diffraction pattern from aluminum. Analysis can show many of the material properties of the sample under study, including grain size distribution, preferred grain orientation (texture), and temperature.

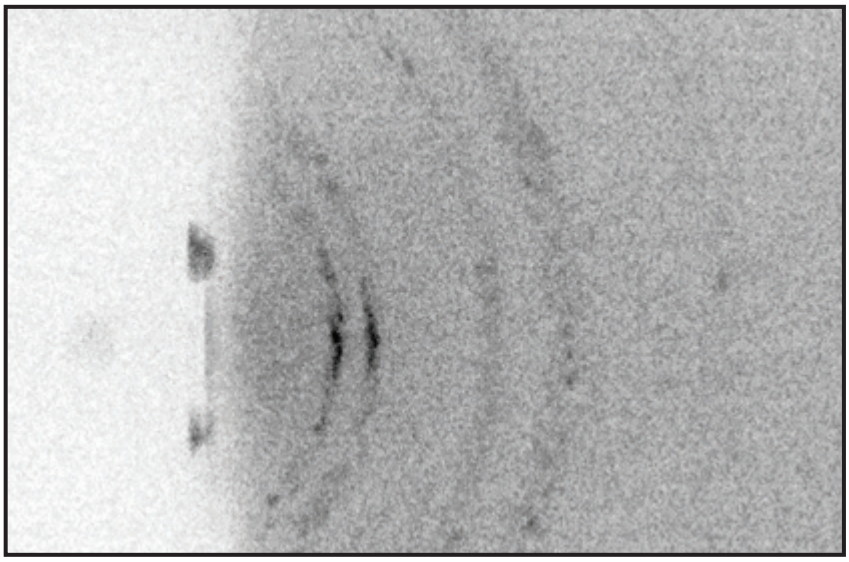

Figure 10. Large-format SPXRD image of an aluminum sample with 0.71-Å wavelength x-rays. The sample is 6061-T6 bar stock. The direct beam was blocked with ¼-in. tungsten; however, some hard x-rays, visible at left, still penetrated the beam block.

Conclusion

During this project, we completed the design and drawings of the prototype nanosecond single-photon detector. Delays were experienced in procuring the fiber-optic faceplate; however, with all the components for the nanosecond single-photon detector in hand, we are ready to assemble and test the unit.

Acknowledgments

We would like to thank Don Macy, Jiaming Morgan, and Lynn Veeser for their contributions to this work.

References

Ashcroft, N. W., N. D. Mermin, *Solid State Physics*, W. B. Saunders Company, Philadelphia, Pennsylvania, 1976.

Nicklow, R. M., R. A. Young, "Lattice vibrations in aluminum and the temperature dependence of x-ray Bragg intensities," *Phys. Rev.* **152** (1966) 591–596.

Rochau, G. A., J. E. Bailey, G. A. Chandler, T. J. Nash, D. S. Nielsen, G. S. Dunham, O. F. Garcia, N. R. Joseph, J. W. Keister, M. J. Madlener, D. V. Morgan, K. J. Moy, and M. Wu, "Energy dependent sensitivity of microchannel plate detectors," *Rev. Sci. Instru.* **77,** 10 (October 2006) 10E323-1-4.

Warren, B. E., *X-Ray Diffraction*, Dover Publications, New York, New York, 1990, 35–38.

Gel/Liquid Bubble Neutron Detector

Paul Hurley, Austin Moy, Ken Moy,[1] James R. Tinsley
Special Technologies Laboratory

Total fusion yield from inertial confinement fusion (ICF) experiments conducted at U.S. DOE national facilities can be measured using a time-integrated neutron detector. A robust and neutron-sensitive high-resolution imaging medium can extend this measurement and provide a picture of the spatial distribution of the reactions. Exploratory work conducted by R. K. Fisher of General Atomics and colleagues from Lawrence Livermore National Laboratory (LLNL) and the Laboratory for Laser Energetics (LLE) (Fisher, 2002) using a gel bubble detector from Bubble Technology Industries (BTI) coupled to a pin-hole collimator has yielded some robust diagnostic images of capsule burn. Recently, BTI and the U.S.–Canada PICASSO Dark Matter Search Group have teamed up to produce a more sensitive formulation. The goals of this project were to establish a collaborative effort with these researchers, procure and evaluate detectors to verify their original results, and develop the new and more sensitive formulation into a suitable format for neutron imaging diagnostics. However, these goals were only partly realized due to the heavy demand for BTI products that stalled their development for the new-formulation bubble detectors.

Background

Ignition and high-yield experiments planned for ICF facilities at the LLNL National Ignition Facility (NIF), LLE's Omega EP, and Sandia National Laboratories' (SNL's) ZR in service of the U.S. DOE High Energy Density Physics (HEDP) mission require robust diagnostics to detect neutron production. These experiments concentrate a high flux of photons or energetic x-rays to uniformly illuminate microspheres filled with deuterium-tritium (D-T) gas to initiate fusion burn. A time-integrated image of the neutron output provides a measure of burn efficiency and a picture of the spatial distribution of the fusion burn as a function of drive condition. High-resolution images can only be produced in a medium that coherently preserves the spatial signature. Past techniques have made use of a scintillating fiber array coupled to a readout camera. Circa year 2000, the gel-bubble medium commonly used in personal neutron dosimetry (Ing, 1997; 2001) (Figure 1), originally shaped as a pen-like cylinder, was reformatted into a disc for imaging (Fisher, 2002).

[1] moykj@nv.doe.gov, 805-681-2284

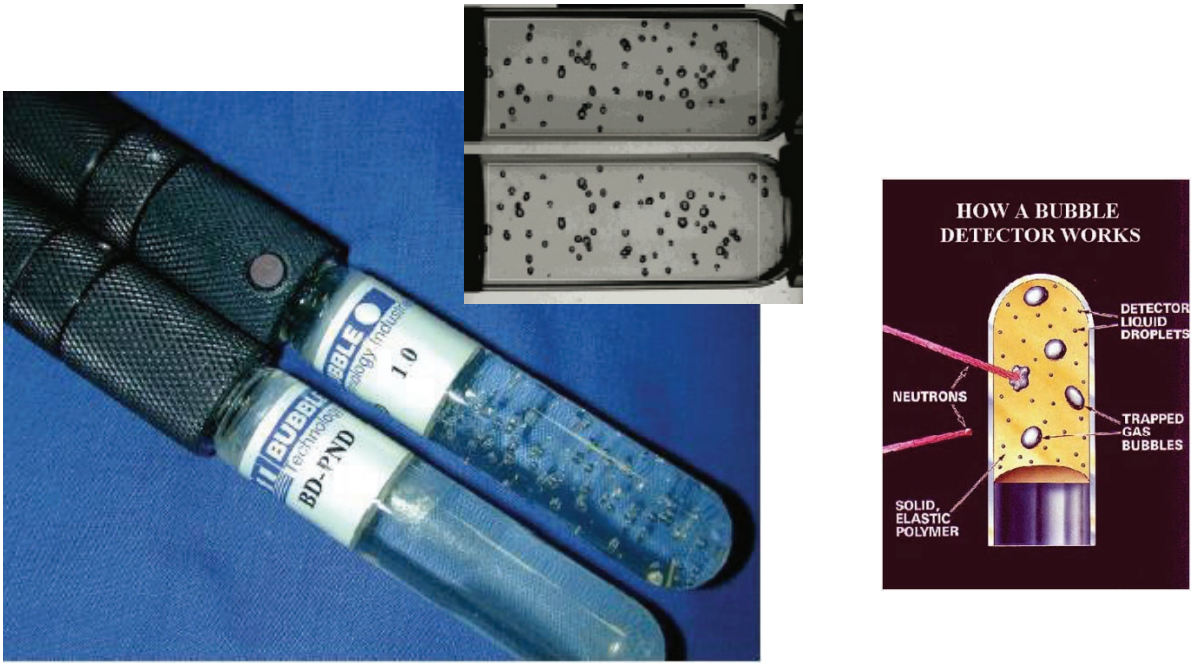

Figure 1. (left) BTI's Defender neutron detector; inset shows bubbles formed after neutron exposure; (right) Elastic scattering of incident neutron with fluorine atoms in a superheated liquid droplet vaporizes the droplet to form a gas bubble.

A gel bubble detector is a small-scale bubble chamber tailored for detecting neutrons. The detection medium is made with freonlike superheated liquid droplets dispersed in an elastic polymer. When neutrons interact with the droplets by elastic scattering with the fluorine atoms, the droplets vaporize to form gas bubbles that are trapped in the polymer. These bubbles can be counted to provide a direct measure of the neutron dose. Past formulations were quite inefficient, producing ~1 bubble per 10^5 incident neutrons per centimeter (n/cm). Exploratory tests (Fisher, 2002; Lerche, 2003) conducted at LLE using this formulation in a disk format (Figure 2) have shown some nice neutron pin-hole images at high (6×10^{13}) neutron yields. A very recent development (Fisher, 2006) employed in the detector shown in Figure 3 uses larger-diameter liquid drops, thicker samples, and more complex formulations to increase the sensitivity to ~0.1% (1 bubble per 10^3 n/cm), an improvement of ~100X. This significant advancement in sensitivity, and therefore signal-to-noise, has extended neutron pin-hole imaging to lower yield (~10^{12}) experiments and improvement in failure mode detection. In addition to being insensitive to x-rays (<10^{-14} bubble per ^{60}Co gamma), this passive medium does not require an electronic system for in-situ recording (such as a photomultiplier or CCD) that would be susceptible to electromagnetic pulses and x-rays.

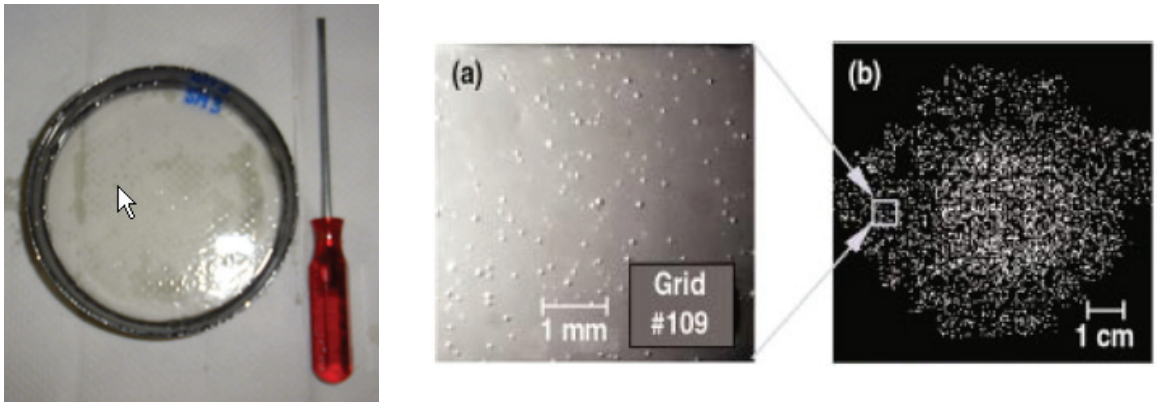

Figure 2. BTI bubble detector (left) in disc format, 8.5-cm diameter, 1-cm thick, fielded at LLE's Omega for neutron pin-hole images. Pin-hole image recorded after neutron exposure (middle). Unfolded image (right) yielded 25-μm spatial resolution at object plane.

Figure 3. BTI Defender: ultra-sensitive formulation in personal dosimeter format (~1000 counts/ mrem, 100 counts/μSv)

Project

Working with R. K. Fisher of General Atomics, we established the necessary contacts to investigate and procure the BTI gel bubble detectors for neutron imaging. But with BTI's commitment to delivering a large order of personal dosimeters for DHS, it was difficult to gain their attention for a small-scale, time-critical R&D effort that required nonproduction equipment. The gel-bubble medium formatted as a disc also needed a 200+ psi pressure vessel (Figure 4), obtainable only from a specialized fabricator, to maintain the medium in an unexposed state and to reset and deactivate for reuse after neutron exposure. The high-pressure requirement also posed procurement challenges and additional delays to the project.

Figure 4. Pope 200+ psi pressure vessel for BTI gel bubble detector storage and reset

In the meantime, we focused on adapting the FY 2006 SDRD-funded $LiTaO_3$ pyroelectric crystal–based neutron source (Figure 5) to meet our test requirements. Using deuterated (TiD_2) targets received in early FY 2007, and a sensitive BC400/photomultiplier tube–based neutron detector (National Security Technologies [NSTec] model NPM-2X-247-LV), we were unable to discern a measurable neutron signal.

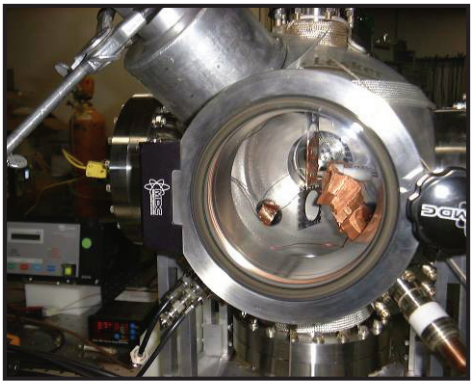

Figure 5. Pyroelectric crystal–based neutron source

With no discernable signal, we attempted to understand the neutron production and detection efficiency of our experimental system via Monte Carlo N-Particle (MCNP) modeling. Simulations showed that despite the large volume of BC400 (5-in. diameter by 3-in. thick) used in the detector, the signal could be improved by ~3–5X with additional surrounding BC400 to provide side- and back-scatter contributions, even for a normally incident line source of neutrons (Figure 6). Further study and discussions with Professor Yaron Danon of Rensselaer Polytechnic Institute led us to suspect that our TiD_2 targets may not have been infused properly with D_2. Unfortunately, Professor Danon did not have any spare deuterated polyethylene films nor the materials and resources to fabricate more targets for us to confirm or invalidate these suspicions.

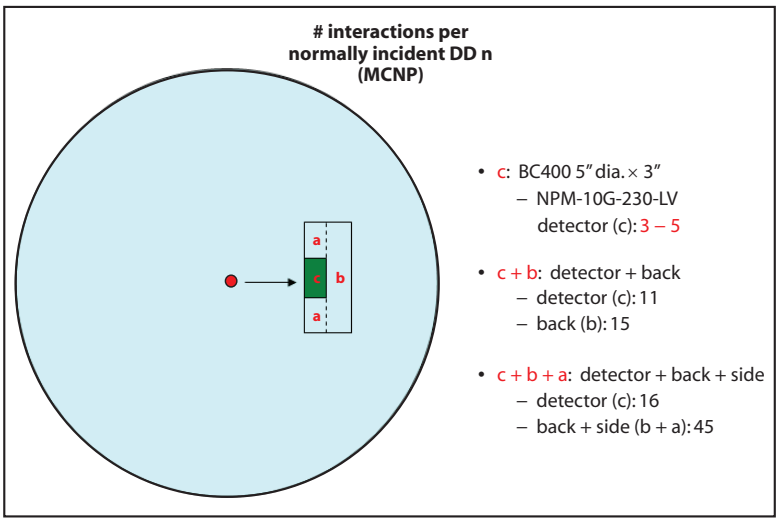

Figure 6. MCNP calculations showing detection efficiency enhanced by additional BC400

When the BTI gel bubble detectors were received, we set up the Special Technologies Laboratory sealed-tube neutron generator (STNG) source to characterize them using 14.1 MeV D-T neutrons. The results from this test are shown in Figure 7. A careful count of the bubbles formed showed ~400/cm^2 for SM1 (Figure 7, top) and ~200/cm^2 for #16 (Figure 7, bottom). Using a calibrated neutron survey meter (Far West Technology, REM 500) and assuming a point neutron source, the calculated neutron areal density incident at the respective BTI detectors correspond to 5.3×10^7 and 2.9×10^7 n/cm^2. These values yield sensitivities of ~0.75×10^{-5} and 0.7×10^{-5} bubble/neutron respectively, confirming the previously noted data taken at LLE.

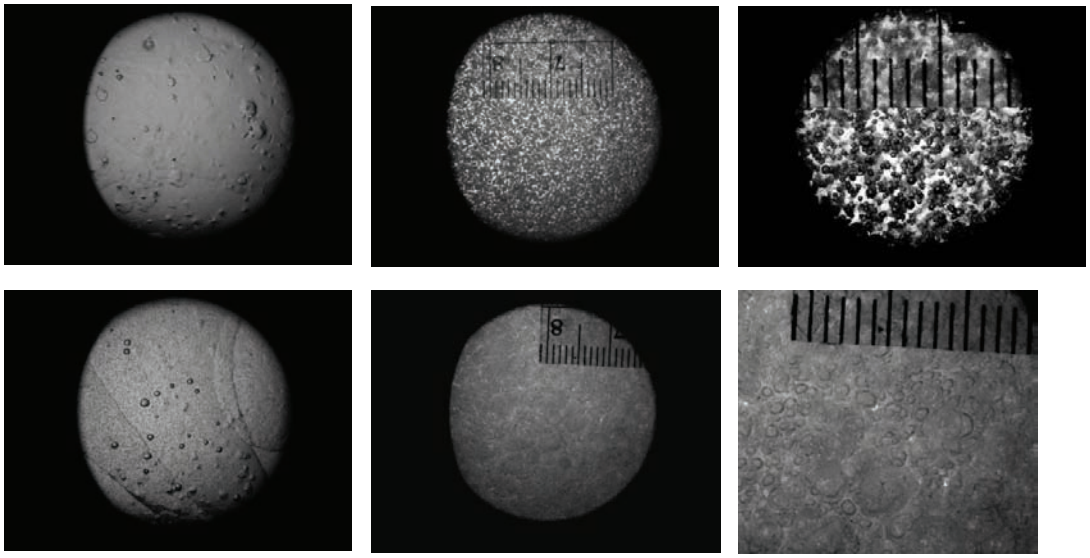

Figure 7. BTI gel bubble detectors irradiated with D-T neutrons: (top row) SM1: space medium type with 1-MeV neutron detection threshold; (bottom row) #16: 100–200 keV neutron detection threshold. In each row, the left is unirradiated, the center is post-irradiation, and the right is magnified post-irradiation. (Small tick marks on overlaid ruler correspond to millimeters.)

Conclusion

This project introduced us to contacts and forefront researchers investigating the use of gel bubble detectors for neutron imaging. We have procured samples in a disc format based on the standard gel bubble formulation and, using D-T neutrons, have corroborated their sensitivity with published results. We have gained sufficient experience and developed resources to field these detectors for HEDP programmatic applications and will explore opportunities to collaborate with national weapons

laboratory researchers for ride-along experiments at LLE's Omega, SNL's ZR, and NIF. Future efforts could be extended to neutron penumbral imaging and HEDP neutron pin-hole diagnostics using gel bubble detectors.

Since the existing formulation of gel bubble detectors is relatively insensitive, thereby limiting our measurement capability to high yield (10^{13} n/shot) experiments, a significant progression for this project would be to engage BTI to develop the high sensitivity (~0.1% [~100X increase]) imaging medium based on their Defender formulation.

Acknowledgments

The authors wish to thank Rob Noulty of BTI and Ray Fisher of General Atomics for their advice and general assistance with the development of these bubble detectors. We also thank Brent Davis, Ron Head, and Pat O'Gara from our Las Vegas facility for providing the photomultiplier-based neutron detectors. We are indebted to Kelley Rangel and especially Kelly McCarthy for their dedication with the difficult procurement process that required a foreign vendor and a pressurized vessel.

References

Fisher, R. K., R. B. Stephens, L. Disdier, J. L. Bourgade, A. Rouyer, P. A. Jaanimagi, T. C. Sangster, R. A. Lerche, N. Izumi, "High-resolution neutron imaging of laser fusion targets using bubble detectors," *Phys. Plasmas* **9,** 5 (May 2002) 2182–2185.

Fisher, R. K., "Neutron imaging of inertial confinement fusion target plasmas using high-resolution gel bubble detectors," *Rev. Sci. Instrum.* **77**, 10E714 (2006) 1–4.

Ing, H., R. A. Noulty, T. D. McLean, "Bubble detectors—a maturing technology," *Radiation Measurements* **27**, 1 (February 1997) 1–11.

Ing, H., "Neutron measurements using bubble detectors—terrestrial and space," *Radiation Measurements* **33**, 3 (June 2001) 275–286.

Lerche, R. A., N. Izumi, R. K. Fisher, L. Disdier, J.-L. Bourgade, A. Rouyer, P. A. Jaanimagi, T. C. Sangster, "Neutron images recorded with high-resolution bubble detectors," *Rev. Sci. Instrum.* **74,** 3 (March 2003) 1709–1712.

this page intentionally left blank

RadOptic Sensor Performance Enhancement and Product Development

Ke-Xun "Kevin" Sun[1]
Livermore Operations

RadOptic sensors are a new type of radiation detector utilizing radiation-induced refractive index change as the optical readout mechanism. We proposed to use gallium nitride (GaN) as a new sensing material, to investigate new pump-probe experimental configurations, and to design a prototype that could be deployed at the Nevada Test Site (NTS) and the National Ignition Facility (NIF). The goal of this research was to substantially improve RadOptic sensor performance in temporal response and sensitivity. In the first phase of this research, we designed the experiments and acquired key equipment, such as the ultrafast laser. We have established working collaborations with Lawrence Livermore National Laboratory (LLNL) and Lawrence Berkeley National Laboratory (LBNL). We have successfully secured the supply of GaN materials and have also acquired GaN thin films grown on sapphire substrates.

Background

RadOptic sensors are a new class of fast semiconductor detectors, relying on x-ray–induced refractive index change as the detection mechanism. When energetic ionizing radiation is absorbed by the semiconductor material, electron-hole (e-h) pair productions alter the spectral refractive index, which changes the phase of another optical probe beam. Laser interferometry is then used to read out the phase variation. The difficulties in detecting broadband x-rays thus become a problem of optical interferometric detection, which is frequently an easier task.

LLNL recently demonstrated a gallium arsenide (GaAs) material–based RadOptic sensor (Vernon, 2006; Lowry, 2005), using optical readout in the IR region. We saw an opportunity in LLNL's significant accomplishment to make many improvements in our project and utilized their experiment specifications as a stepping off place for our own work. First, we aimed to improve the temporal response of the RadOptic sensor, now limited to several hundred nanoseconds due to material relaxation time in GaAs. The LLNL work also used an oscilloscope as the recording device, which is potentially slower than the temporal response of the sensing materials. We proposed using GaN materials (Nakamura, 2000) as sensing materials and a streak camera as the readout. The RadOptic system with the GaN sensor head and the streak camera readout can achieve 5–6 orders of magnitude improvement in detector response time over GaAs–based sensors with an oscilloscope.

[1] sunke@nv.doe.gov, 925-960-2514

Ultrafast RadOptic sensors as high-bandwidth x-ray and particle detectors will have numerous applications at the NTS, the national laboratories, and NIF, which require ultrafast detectors for energy measurements.

Project

The main tasks for this year were to explore product concepts, design the experiment, establish collaborations, acquire GaN materials, and acquire equipment, especially lasers. These tasks represented a substantial amount of time and compose the bulk of this report.

Experimental Configuration

The basic configuration for the RadOptic sensor is a pump-probe setup, as shown in Figure 1. The pump beam is the x-ray or other short-wavelength radiation to be detected. The nonlinear optical interaction between the pump beam and the sensing material produces a transient distribution of e-h pairs that alter the semiconductor refractive index. A laser interferometer is used to detect the phase shift induced by the change of the refractive index and absorption. The interferometer output is recorded by an oscilloscope or streak camera.

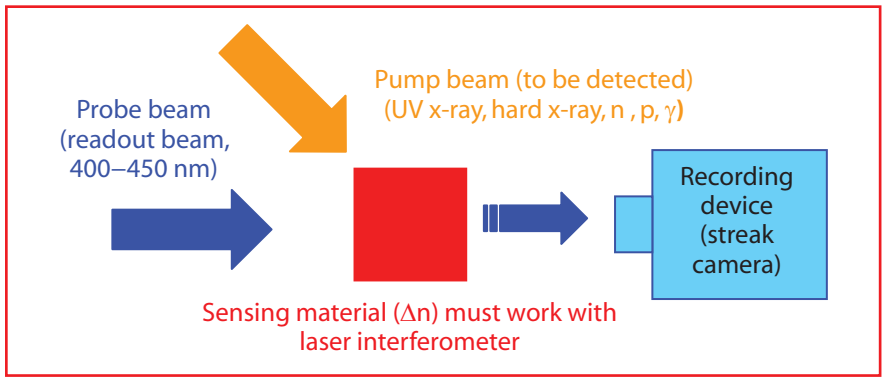

Figure 1. RadOptic sensor block diagram. The three essential functional blocks are the probe laser, the semiconductor material, and the recording device. The pump beam, the signal to be detected, can be ultraviolet, x-ray or particle radiation.

For the first proof-of-principle experiments, the x-ray pump source that generates e-h pairs was replaced with a short-wavelength laser whose photon energy was higher than the semiconductor band gap. The setup required two laser inputs to function as pumps and probes. For reasons detailed below, the first probe laser was operated at ~400 nm. The pump laser was operated at ≤350 nm.

The recording device in the LLNL experiments was an oscilloscope with a bandwidth of 6 GHz, implying a rise time of ~57 ps, which is quite fast. However, streak cameras have time resolution capability in the subpicosecond region. Moreover, a streak camera has higher dynamic range than an oscilloscope and real-time imaging capability. This directly matches a large-area RadOptic sensor in terms of high-speed imaging. Practically, streak cameras have been one of the core product lines at Livermore Operations (LO), so support was readily available. Therefore, using a streak camera as the recording device can further improve the RadOptic sensor.

Streak Camera Selection

Because IR light was used as the probe beam in the LLNL experiment, we initially tested a streak tube with an S-1 photocathode test-manufactured at LO. However, the S-1 photocathode deteriorated significantly over time, showing quantum efficiency of ~10^{-6}. On the other hand, the S-20 photocathode demonstrated much higher efficiency over a longer time period. Therefore, we selected the S-20 streak camera. The S-20 photocathode response to input light peaks at 400–450 nm.

Tunable Lasers

The experiment had wavelength requirements for both the pump and probe laser sources. The pump laser wavelength needed to be shorter than that of the corresponding band gap, so that the pump beam would create enough e-h pairs. The probe laser wavelength needed to be equal to or longer than that of the band gap wavelength, for effective nonlinear optical interaction. This was realized by using tunable lasers.

A more detailed, desirable experimental setup, where both the pump and the probe are tunable, is shown in Figure 2. The lasers can be very expensive. Our collaborators at LLNL loaned us the Tsunami laser, and National Security Technologies (NSTec) internal collaborators loaned us the Verdi pump laser. Nonlinear optical frequency conversion processes will be necessary to produce the required wavelength at 345~410 nm.

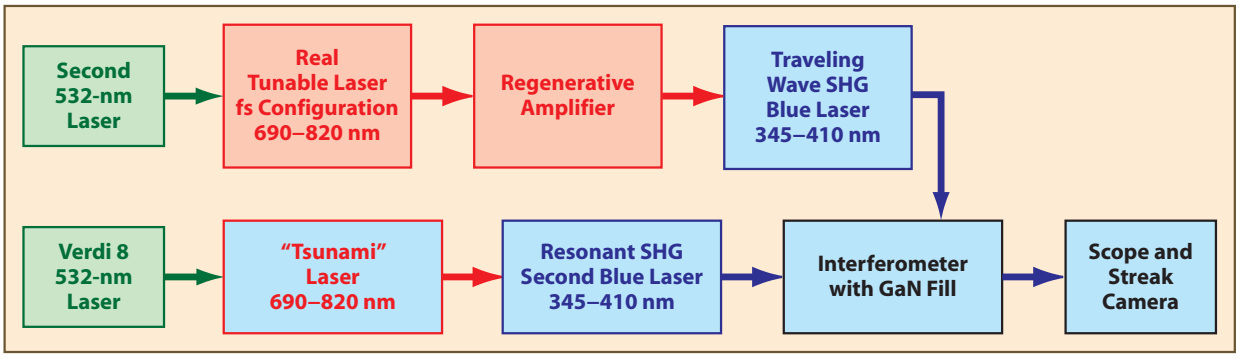

Figure 2. Detailed system diagram of the RadOptic sensor. Preferably, both the pump laser chain and probe laser would be tunable lasers.

GaN as the RadOptic Sensor Material

In the LLNL experiments, GaAs–based $In_{1-x}Ga_xAsP$ materials were used as the sensing material for the RadOptic sensor. Our choice to use GaN materials over GaAs materials was based on the following considerations:

- Similar to GaAs, GaN material is a direct transition material. However, GaN–based materials have much shorter relaxation times than GaAs. The energy relaxation time of GaN can be as short as 5–10 fsec (Stanton, 2001). The momentum relaxation time of hot electrons in GaN structures is ~0.4–1.4 ps (Matulionis, 2002).
- Based on this performance, the GaN–based RadOptic sensor should achieve temporal response several orders of magnitude better than previously demonstrated using GaAs material.
- GaN is transparent at blue wavelengths of 400–450 nm. This should enable the use of S-20 cathode streak cameras as recording devices.
- GaN materials can be doped with heavy elements that have higher absorption for x-ray and particle radiations. Particle detectors can be constructed using this property.

GaN Material Search and Measurement

We required band gap engineering to tune the resonant wavelength. Therefore, we initially contacted a university for collaborative research. Eventually, we found a small commercial vendor that grows GaN thin film on a sapphire substrate. LBNL and the University of California, Santa Barbara (UCSB), provided free GaN measurement services. LBNL measured the photoluminescence (PL) spectra, spectral transmission, and reflection. UCSB measured x-ray diffraction, which determined density of defects.

The characterization of GaN material is critical to the performance of the RadOptic sensor. First, the GaN transmission and absorption determine the wavelengths of the pump and probe lasers. Second, interferometric probing requires good optical quality to obtain reasonable fringe contrast, thus achieving a higher signal-to-noise ratio (SNR).

Figure 3a shows the measurement results for PL spectra. The samples were 5-µm- and 7-µm-thick GaN films grown on 1-mm-thick sapphire that was optically polished on both sides. The samples were round with 2-in. diameters. The measurements for each sample were made at three different locations (center and two edges) to determine the uniformity of the GaN material. At all locations, the PL spectrum consistently peaked at ~3.42 eV (~363 nm in wavelength), reflecting the GaN band gap.

Figure 3b shows the measurement of GaN transmission or absorption. The absorption edge was centered at ~3.43 eV (~362 nm in wavelength), consistent with the PL measurement. For wavelengths shorter than the absorption edge, GaN samples exhibited strong absorption. The wavelength of the pump beam should be within the strongly absorptive region. For wavelengths longer than the absorption edge (starting from 375 nm), the GaN material and the substrate exhibited ~85% transparency.

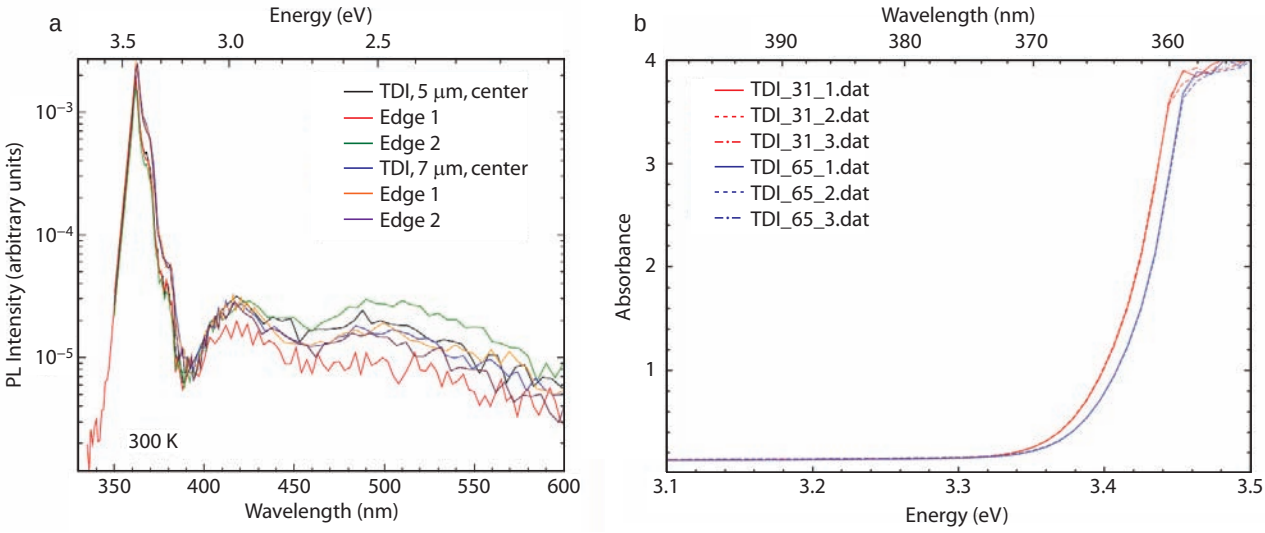

Figure 3. GaN material characterization, showing (a) the PL spectra and (b) GaN transmission or absorption

Figure 4 shows the GaN reflectance measurement. The measurements were extended to the longer wavelength region thanks to the instrumentation capability. The spacing and depth of the fringe are wavelength-dependent. From the fringe separation in wavelength, we determined that the observed interference fringes mostly originated from the GaN film, not the substrate. The interference fringes demonstrated good optical quality. Figures 4a–d show the measurement results at several locations of the GaN thin film sample. Again, good optical uniformity is demonstrated.

Further Work on GaN Materials

The current GaN material requires a pump wavelength shorter than 350–360 nm, and an optimal probe wavelength of ~370 nm. To achieve the desired wavelength of 400–450 nm for the S-20 photocathode, we have requested that the supplier investigate new alloy materials. Our plan was to create an InGaN and GaN alloy to narrow the band gap. The first cut sample showed PL wavelength peaking at 450 nm.

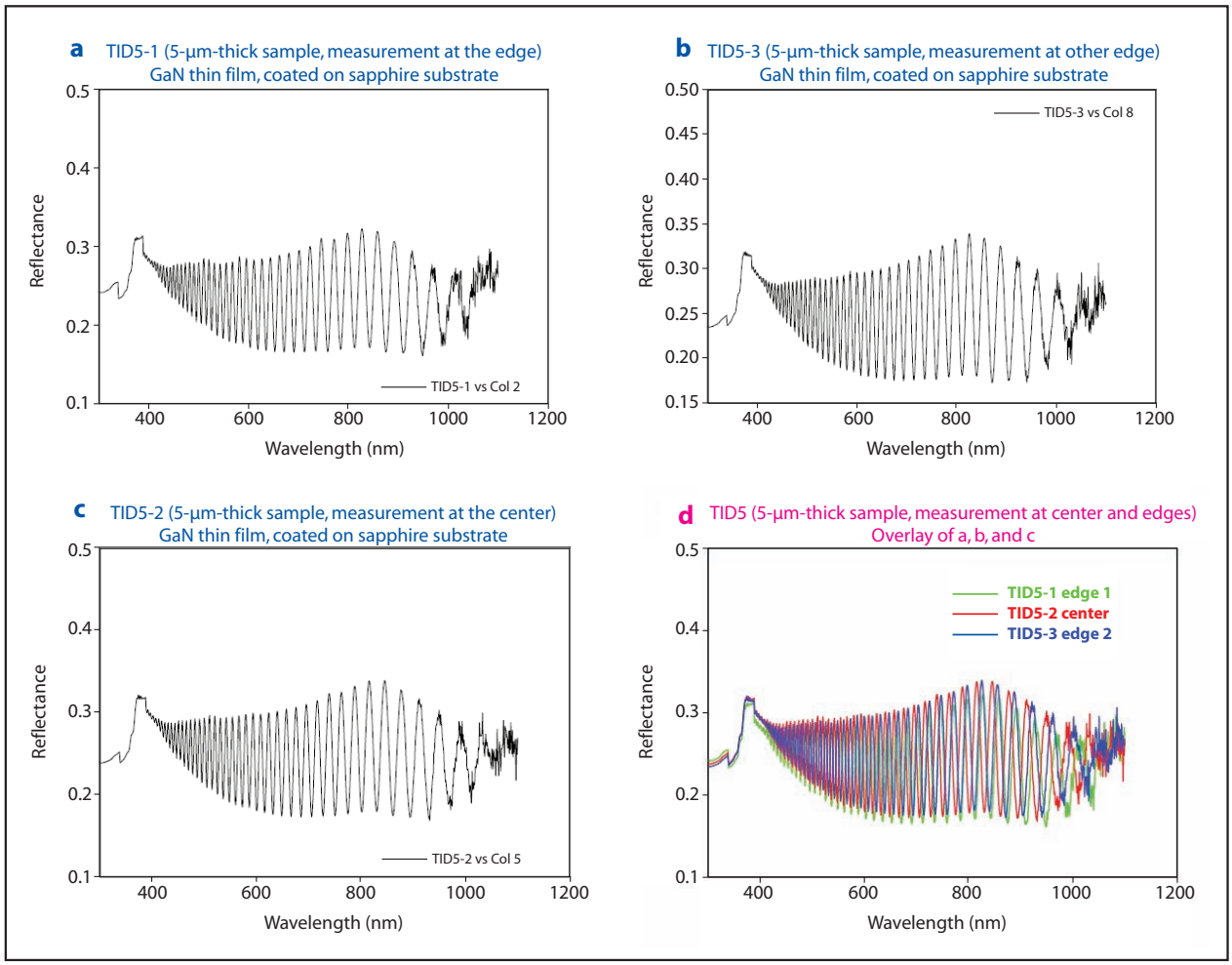

Figure 4. GaN thin film reflection measurements. The sample was a 5-mm-thick GaN thin film grown on a 1-mm-thick sapphire substrate. Measurements of the film are (a) left edge; (b) center; and (c) right edge; and (d) is an overlay of (a), (b), and (c) that shows GaN thin film uniformity. It was determined that the interference fringes originated in the GaN film, not the substrate.

For higher sensitivity at the x-ray region, high Z-element doping is needed. We have been in contact with LBNL for possible collaborative work in doping high Z elements into GaN thin film, and have discussed the possibility of using an ion implantation machine for this purpose.

Pump-probe Experiment Configurations

The first experimental goal was to demonstrate the RadOptic sensor in the probe wavelength region of 400~450 nm. Figure 5 shows several designs with different features and complexity levels. Figure 5a

shows an intensity-correlated experiment, in which there is no optical interference involved; therefore, the setup is simpler. GaN is placed in front of a detector. The signal detected will be the amplitude change due to pump beam irradiation. The intensity correlation will be used to reduce the probe noise. Similar arrangements can be used for the pump beam.

Figure 5b shows a Mach-Zehnder interferometer, having one arm filled with GaN material subject to pump irradiation. The pump-induced refractive index change, and thus the phase shift of the probe beam, will be interferometrically detected. This scheme has higher sensitivity, but will require active stabilization of the interferometer. Additional complexity of electronics and mechanics will arise.

Figure 5c shows a Fabry-Perot cavity filled with GaN material. The cavity is tuned to resonate with the probe beam, enhancing the interaction between the probe beam and the GaN. A free-space cavity can be constructed with traditional mounts and mirrors. Alternatively, the cavity can be formed by coating the GaN thin film with high reflectors at both sides. Either the cavity length or the probe laser wavelength should be tunable to search for the resonance. The cavity photon lifetime should be designed to be shorter than the required temporal response time.

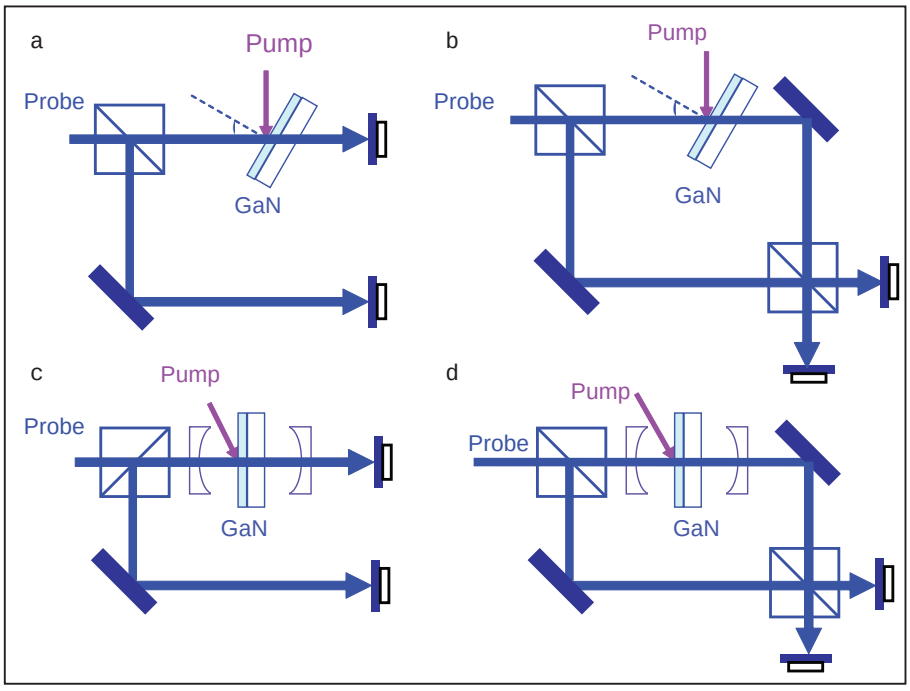

Figure 5. Interferometer configurations for the RadOptic sensor: (a) Intensity correlated measurement; (b) Mach-Zehnder interferometer; (c) Fabry-Perot cavity enhanced intensity correlator; (d) Fabry-Perot cavity enhanced Mach-Zehnder interferometer. Reflective versions of these configurations can be constructed by using the beam reflected off the GaN sample.

Figure 5d shows a combined version of Mach-Zehnder and Fabry-Perot interferometers. Both the phase and the amplitude of the probe beam exiting from the cavity will be detected. This is useful when the finesse of the Fabry-Perot cavity cannot be set too high. However, this method is complicated in terms of operation and device stabilization.

In all configurations the pump beams will be injected from a spatial angle and polarization different from the probe beam, so that the probe beam detectors will not be affected by direct pump illumination. In addition, optical color filters will be used to further attenuate the pump beam by only allowing the probe wavelength to pass through.

Sagnac Interferometer Pump–Probe Configuration

Using a single streak camera requires that the probe light presents only when the streak camera is taking the image. For a single-shot ungated streak camera, like the one typically used at LO, continuous illumination on the streak camera may saturate the CCD camera before the image is recorded, or at least lower the SNR. Therefore, the interferometer outputs should remain dark, unless the GaN sample is illuminated with a powerful signal pump pulse. For Mach-Zehnder interferometers, this requirement may incur more work, due to the active stabilization needed. More intrinsically, Mach-Zehnder interferometers maximize their signal at mid-fringe.

A Sagnac interferometer could provide a possible solution to this problem. The Sagnac interferometer is a common configuration for laser gyro applications, where its bright port is typically used for signal extraction. The less-used dark port, which remains dark for slow arm variations, will also have a response when a fast transient signal arrives. Figure 6 shows a Sagnac interferometer with a GaN–sensing material placed asymmetrically in the Sagnac loop. In the most simplified case, the electrical output pulse shape, $E_{out}(t)$, of the Sagnac interferometer is given by:

$$E_{out}(t) = r^2 E(t-\tau_1) - t^2 E(t-\tau_2), \quad \textbf{(1)}$$

where E is the probe field perturbation produced by the pump laser pulse; r and t are the amplitude reflection and transmission coefficients, respectively; and τ_1 and τ_2 are the time separations from the GaN location to the beam splitter. To simplify, we have omitted pulse-broadening effects and only considered the time delays, which are large when compared with pulse width.

Each pump pulse will produce two sequential pulses at the dark port. The dark port remains at low output, and is determined by the interferometer contrast ratio (Figure 6). The dual-pulse-out feature simultaneously allows determination of the pulse width using delay time, which is easily measurable. The Sagnac pump-probe experiment should be explored experimentally along with the Mach-Zehnder configurations.

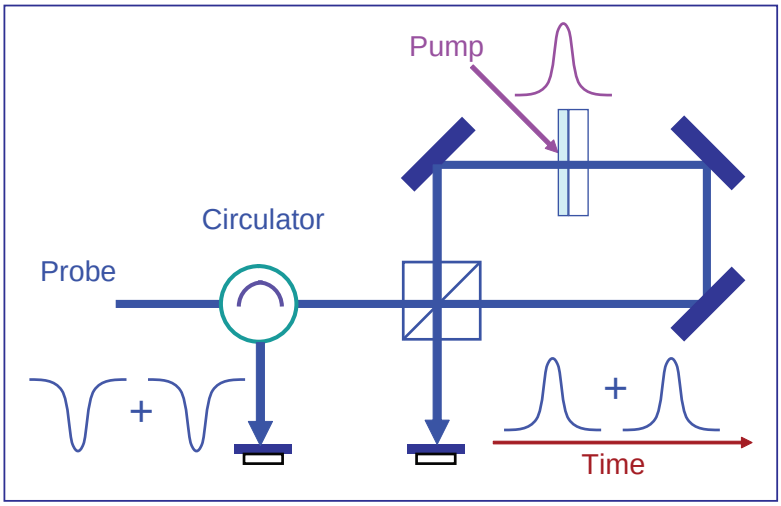

Figure 6. Sagnac interferometer for the RadOptic sensor. For an asymmetrically placed GaN converter, each pump pulse will produce two sequential pulses at the dark port. The dark port remains dark when there is no signal. The Sagnac interferometer is therefore suitable for streak camera recording.

Conclusion

In our RadOptic sensor research, we have made substantial progress in many areas. Using GaN–based material for the new generation of RadOptic sensors is recommended; it should improve the RadOptic sensor temporal response by several orders of magnitude. Furthermore, by using a streak camera as the recording device, this integrated RadOptic sensor system will further help to realize the potential of GaN sensing material. We have successfully secured the supply of GaN materials, and have also acquired GaN thin film grown on sapphire substrates.

We established collaborations with LLNL, LBNL, and UCSB, and our work greatly benefited from their contributions, including a loan of expensive equipment (LLNL) and the detailed characterization of the GaN material (LBNL and UCSB). We have made substantial progress in experimental design and associated hardware purchases.

Acknowledgments

Dr. Steve Vernon at LLNL provided stimulating discussions about the RadOptic sensor. He also provided the Tsunami laser. Prof. Nakamura, Prof. DenBarr, and graduate students at UCSB provided x-ray measurement for GaN samples. Prof. Eugene Haller, Dr. Joe Ager, and several graduate students at LBNL provided measurements on spectral transmission, reflection, and photoluminescence

of GaN. Roderick Tiangco at the Special Technologies Laboratory loaned us the Verdi laser. Rob Buckles (LO) and I shared the same laboratory and other equipment, and helped each other with laboratory setup.

References

Lowry, M. E., C. V. Bennett, S. P. Vernon, T. C. Bond, R. Welty, E. M. Behymer, H. E. Petersen, A. Krey, R. E. Stewart, N. P. Kobayashi, V. R. Sperry, P. L. Stephan, C. Reinhardt, S. Simpson, P. Stratton, R. M. Bionta, M. A. McKernan, E. Ables, L. L. Ott, S. W. Bond, J. Ayers, O. L. Landen, P. M. Bell, "RadSensor: x-ray detection by direct modulation of an optical probe beam," *Proc. SPIE* **5194** (2005) 193–204.

Matulionis, A., J. Liberis, L. Ardaravičius, M. Ramonas, I. Matulioniene, J. Smart, "Hot-electron energy relaxation time in AlGaN/GaN," *Semicond. Sci. Technol.* **17** (2002) L9–L14.

Nakamura, S., G. Fasol, S. J. Pearton, *The Blue Laser Diode: The Complete Story*, Springer-Verlag, Germany, 2000.

Stanton, N. M., A. J. Kent, A. V. Akimov, P. Hawker, T. S. Cheng, C. T. Foxon, "Energy relaxation by hot electrons in *n*-GaN epilayers," *J. Appl. Phys.* **89**, 2 (January 2001) 973–979.

Vernon, S. P., M. E. Lowry, "Ultrafast radiation detection by modulation of an optical probe beam", UCRL-TR-219486, Lawrence Livermore National Laboratory, Livermore, California, 2006 (https://e-reports-ext.llnl.gov/pdf/330937.pdf).

Active Infrared Sensor Investigation

Kevin Thomas,[1] *Mark Dayson*
Remote Sensing Laboratory – Nellis

This investigation focused on the characterization and evaluation of active infrared (AIR) sensors with an eye toward identifying vulnerabilities and potential performance improvements. Our work concentrated on assessing external, multibeam AIR sensors, commonly stacked to produce an IR beam "fence." Five commercial off-the-shelf (COTS), stacked-beam AIR sensors were assembled, tested, and evaluated. Based on the results, we identified modulation technique improvements that could be implemented in such sensors.

Background

Multibeamed AIR security sensors are increasingly being used to protect high-value facilities. Projecting up to four beams, these sensors are often stacked on top of each other to create a tightly spaced IR beam "fence." AIR sensors are popular in providing protection in multilayered security systems where increasing levels of security are desired in each successive zone. Such sensors are used at the Nevada Test Site (NTS) as well as at other DOE/NNSA facilities. Because adjacent AIR sensor beams are so tightly spaced, mutual interference has been recognized as a problem, and manufacturers have used modulation techniques to mitigate it. These techniques include dual-frequency modulation and digitally encoded pulse trains. This project sought to characterize and assess the existing modulation techniques and recommend methods for improving detection performance, interference rejection between adjacent beams, and tampering immunity.

Project

Measurement and analysis techniques developed for single beam AIR sensors that use analog modulation were applied to this project. The first step was to acquire COTS stacked-beam AIR sensors, particularly those employing digital modulation. These were the Optex MKIII, Optex RedNet, Takex PB-IN-50HF, Honeywell Perimbar Vindicator, and the Integrated Design Ltd. Rayonet (Figure 1). We then assembled a laboratory sensor system that could detect IR beams and digitize their modulation. This was accomplished by coupling an IR detector diode to a digital receiver (Figure 2). Based on the investigation results, methods for improving detection performance, interference rejection between adjacent beams, and tampering immunity were identified.

[1] thomask1@nv.doe.gov, 702-295-8799

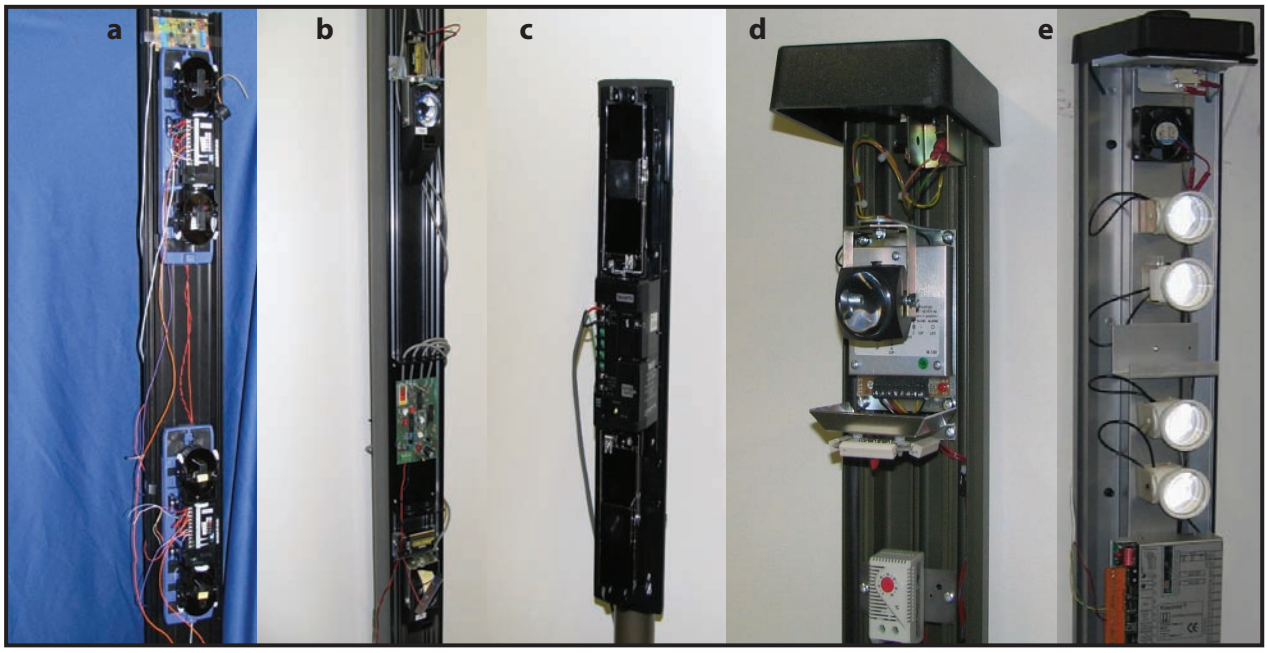

Figure 1. The five AIR systems that were characterized and studied: (a) Optex MKIII; (b) Optex Rednet RN4/10-25; (c) Takex PB-IN-50HF; (d) Honeywell Perimbar Vindicator; (e) Integrated Design Ltd. Rayonet

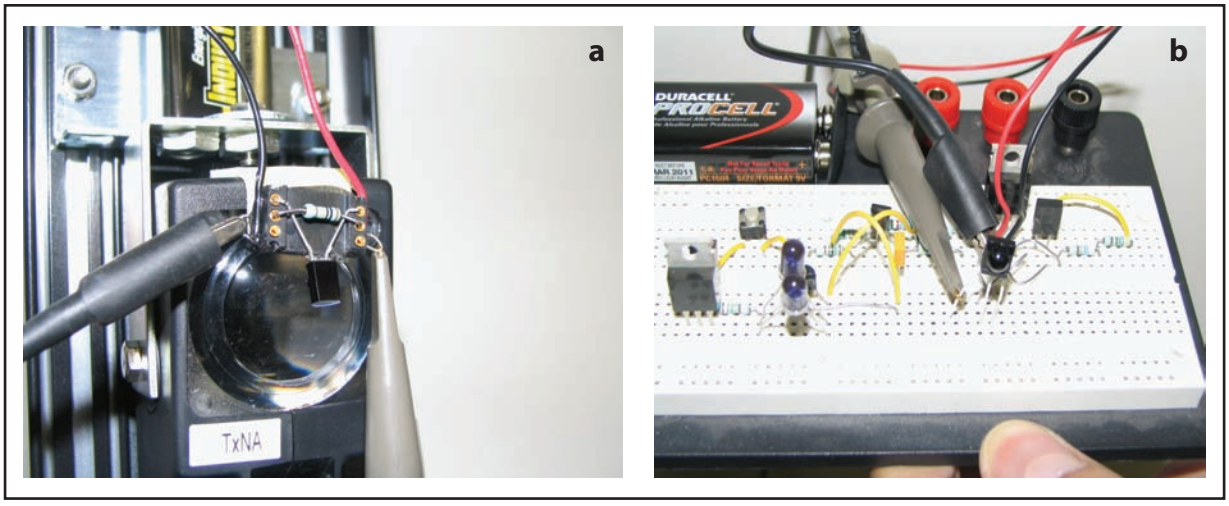

Figure 2. The (a) IR photodiode and (b) receiver diode module were used to help characterize the transmitted beams

The Optex MKIII AIR system (Figure 3) proved to be quite sophisticated. Interference rejection between adjacent beams was handled by different communication channels and varying protocols. The faux/unused lens and the capability of the towers to transmit and receive data between each other contributed to tampering immunity. Therefore, our suggestions for improving this Optex system were minimal.

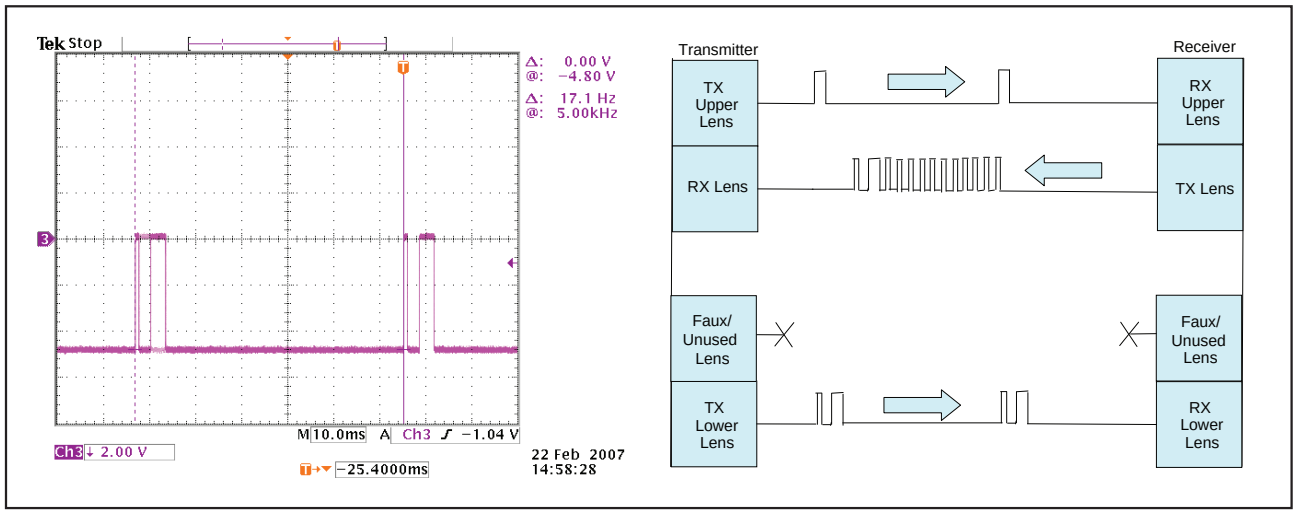

Figure 3. Optex MKIII AIR security system and virtual diagram

More potential improvements were identified in the Optex RedNet AIR system (Figure 4). These included providing different communication channels so that the system does not risk interfering with other, same-frequency systems, as well as communicating with a distinct protocol that modifies data transmission, instead of using the same protocol and frequency for each transmitter head.

For the Takex PB-IN-50HF AIR system (Figure 5), suggested improvements resembled those of the Optex RedNet, except that the Takex system incorporated multiple-frequency selections for its IR beams. It also included beam transmission-strength selection and programmed automatic gain control, both of which improved sensor detection performance.

After investigating the Perimbar Vindicator AIR system, we established that its data communications protocol needed enhancement because of the constant IR signal it transmitted. As evident in the virtual diagram (Figure 6), the four transmitter heads send out identical IR beam signatures (as did the Takex and Optex Rednet AIR systems).

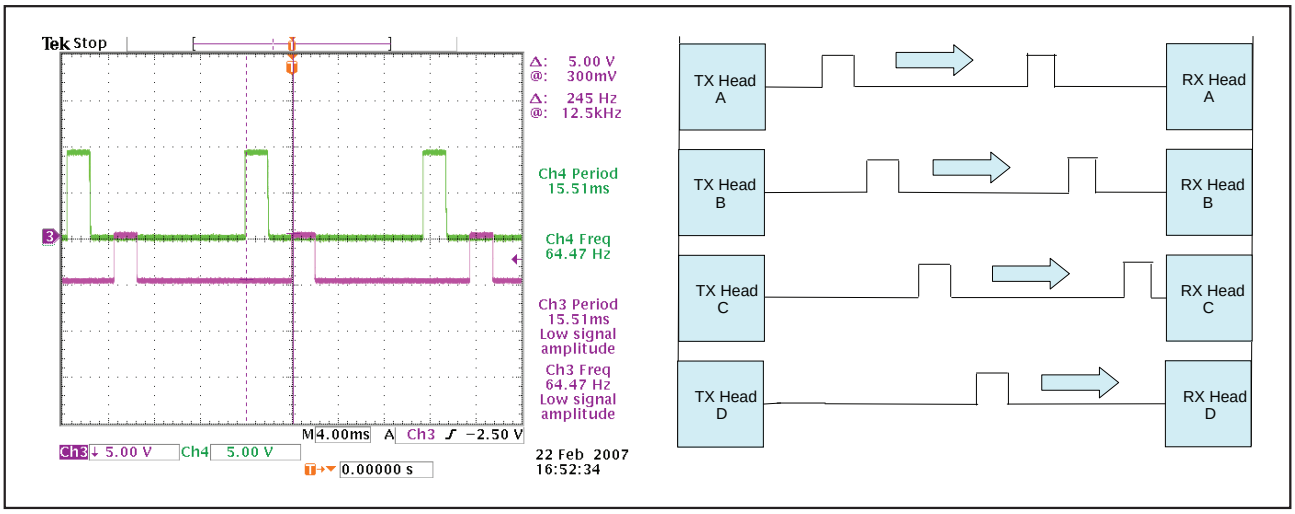

Figure 4. Optex Rednet AIR security system and virtual diagram

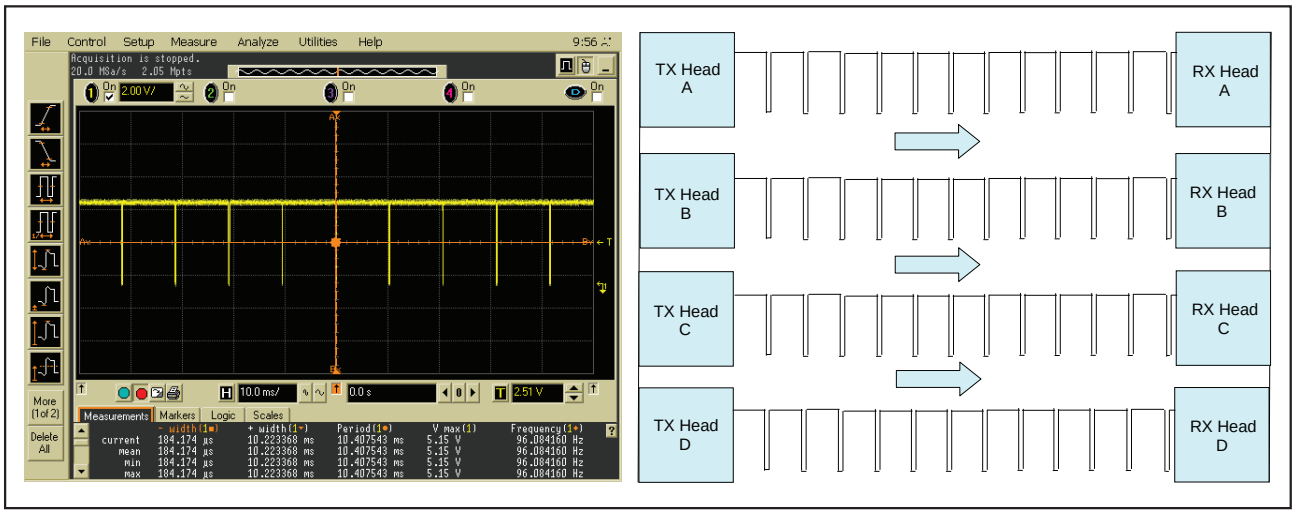

Figure 5. Takex PB-IN-50HF AIR security system and virtual diagram

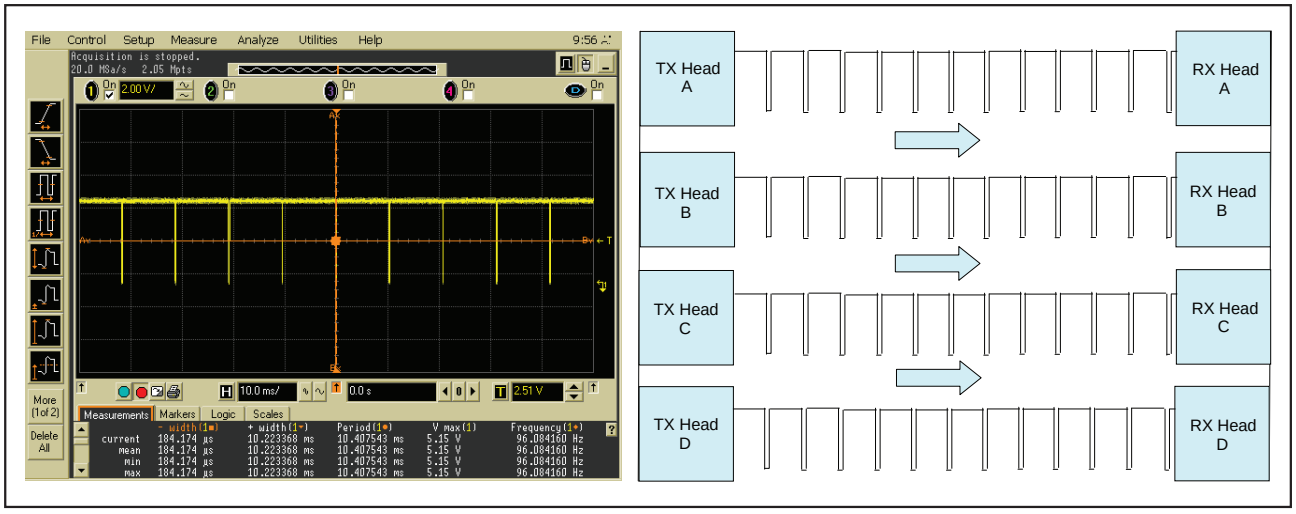

Figure 6. Honeywell Perimbar Vindicator AIR security system and virtual diagram

During testing, the Integrated Design Ltd. Rayonet AIR system exhibited an interesting beam signature (Figure 7) of a linear amplitude signal followed by a constant pulsed signal. In essence, the linear amplitude signal determined the transmitter's beam strength, thus providing system information and status. Again, with a fixed-frequency transmitted signal, detection performance, interference rejection, and tampering immunity are compromised.

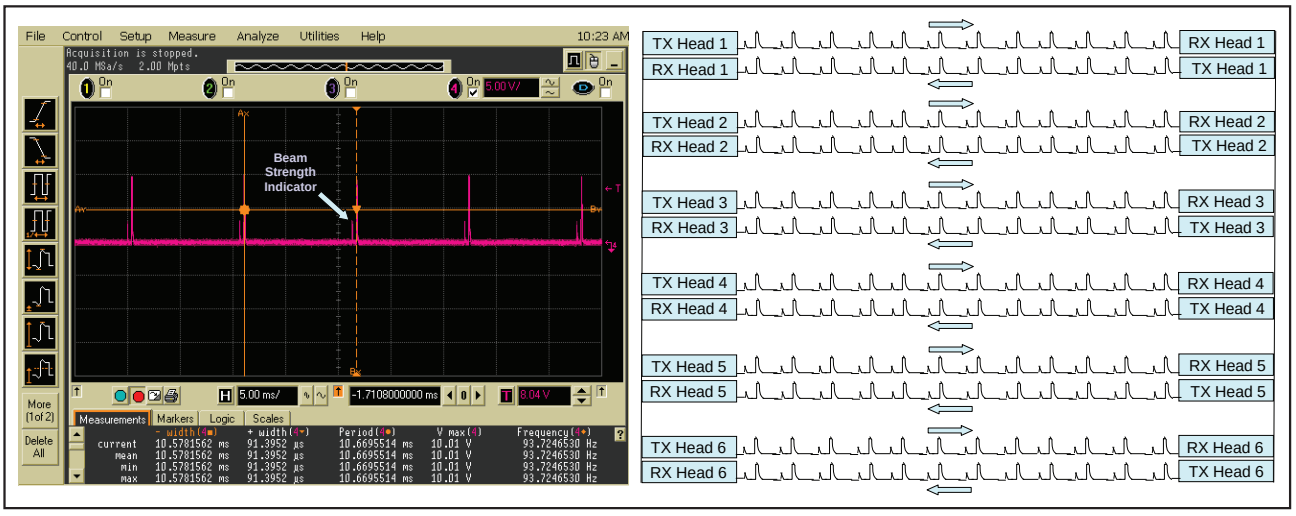

Figure 7. Integrated Design Ltd. Rayonet and virtual diagram

Microcontroller–based IR Transceiver Circuit Test

To fully test the AIR systems' modulation techniques, we added a test procedure, which employed a microcontroller-based IR transceiver circuit that duplicates the transmitter's beam signature (Figures 8 and 9).

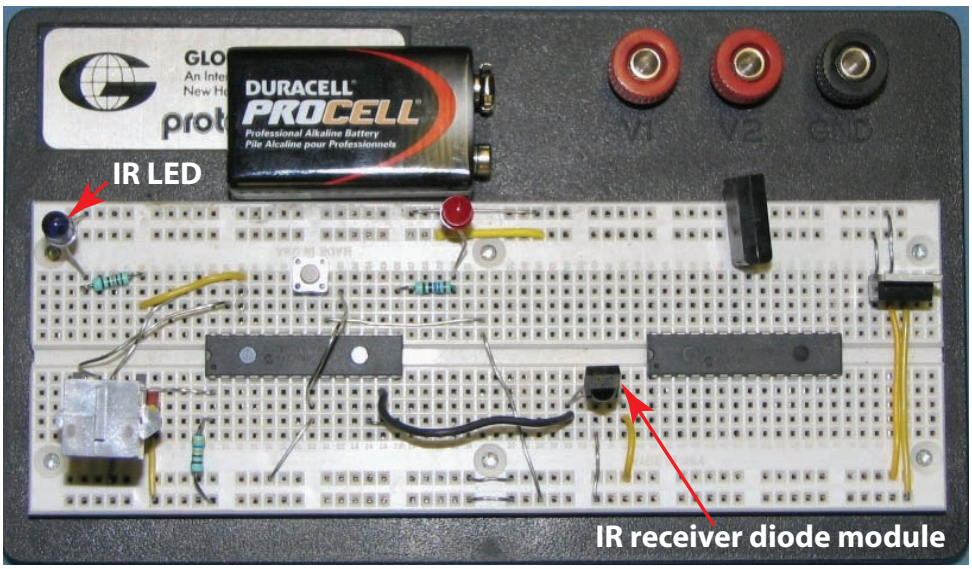

Figure 8. Microcontroller-based IR transceiver circuit prototype board

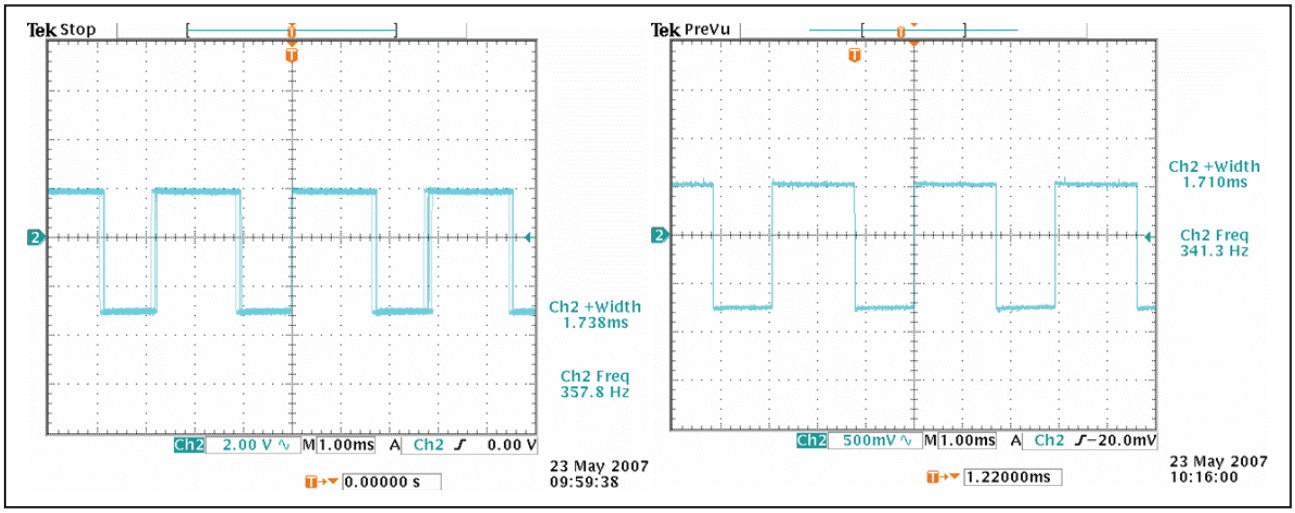

Figure 9. Left, beam signature of the Takex AIR system; right, successful duplication of the beam signature by the microcontroller test circuit

The microcontroller test circuit's primary objective was to "read" the transmitter's beam signature and automatically output the same beam characteristic to an IR LED on the board. It was only programmed to duplicate constant, fixed-frequency IR beam signatures, mainly, to prove the ease of replicating the IR beam signatures of the studied AIR systems that did not vary their beam characteristics.

Conclusion

The microcontroller-based transceiver circuit failed to successfully replicate the modulated "data communication" IR signals (particularly from the transmitter's bottom transmit lens) of the Optex MKIII AIR system, due to the unpredictable changes of its data communications. It is easier to record and store an IR signal that does not vary its signal characteristics (i.e., frequency, pulse width, etc.). In addition, AIR system vulnerability significantly decreases when the transmitter also supports the receiving of modulated IR signals from the receiver, which is not a typical technique with AIR systems. Finally, incorporating various channels of frequency to avoid adjacent beam interruption can greatly help prevent system vulnerability.

NOTE: Additional details are available from the authors in an Official Use Only report.

this page intentionally left blank

Embedded Piezoelectric Microcantilever Array

Rick Venedam[1]
North Las Vegas

Tim L. Porter
Northern Arizona University, Flagstaff, Arizona

Embedded Piezoresistive Microcantilever Array (EPMA) sensors were deployed in Las Vegas–area tortoise burrows, some known to be occupied by a tortoise and some known to be unoccupied or occupied by box turtles. When a tortoise was present, the sensor responded to its presence within a few seconds, at a distance of ~8–10 in., and reached equilibrium in ~5 seconds.

Background

The desert tortoise is an endangered species that lives in the Las Vegas area, among other places. While it is known to be present, an accurate count of tortoises in the area has been difficult to achieve. Use of the EPMA may allow a more complete census to be taken.

Project

Desert tortoises are known to use chin-gland-secretion olfactory cues in their social behavior, mating, and movements. Analysis of these secretions by Rose (1969) reveals the presence of caprylic, capric, lauric, myristic, palmitic, palmitoleic, stearic, oleic, and linoleic acids. These fatty acids have characteristic odors, and are complex molecules that interact with organic polymer-based sensing elements (Eastman, 1999). The EPMA is a small "array" of three to four (or more) individual sensing units, all queried by a single scanning multimeter, that detects the unique signature of the desert tortoise chemical excretions and does not respond to those of the box turtle. The EPMA was tested in Las Vegas–area tortoise burrows, some known to be occupied by a tortoise and some known to be unoccupied or occupied by box turtles. An infrared imaging camera with a focal length of 8–10 in. was used to verify the presence of a tortoise.

The initial data from the field trials are summarized in Figure 1, and Figure 2 captures us with a friendly tortoise.

[1] venedarj@nv.doe.gov, 702-295-5458

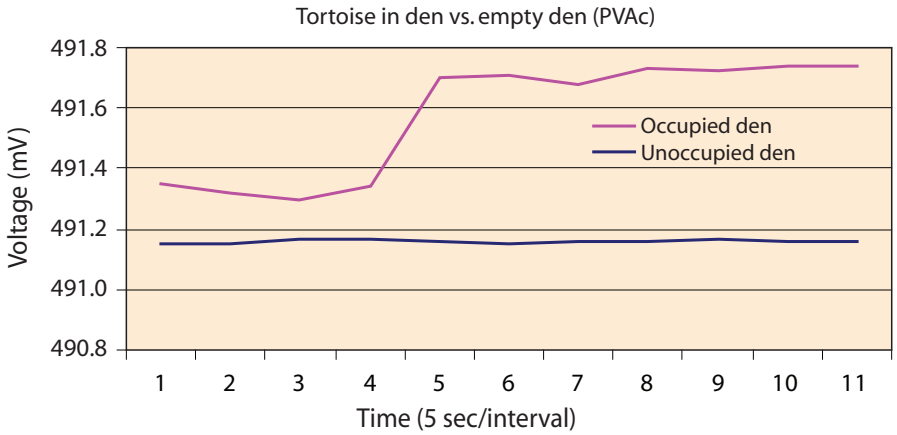

Figure 1. Tortoise den vs. empty den sensor test results

Figure 2. Project participants and tortoise

The blue data trace (lower at ~491.15 mV) is indicative of an unoccupied burrow. The magenta trace shows, during the insertion period of ~1–15 seconds, a flatness indicative of either a lack of occupation by a tortoise or simply excessive distance from the tortoise. At the inflection point, at ~20 seconds, the sensor was ~8–10 in. from the tortoise. Equilibrium was established in ~5 seconds.

Conclusion

The EPMA sensor was able to detect the presence of a desert tortoise at a distance of 8–10 in. The sensor was able to discriminate between a burrow occupied by a desert tortoise (positive inflection), and another burrow either occupied by a box turtle or unoccupied (flat response).

A full publication and a presentation at the American Chemical Society's national meeting in New Orleans in March 2008 are forthcoming.

Acknowledgments

Thanks to Tim L. Porter of Northern Arizona University, Dept. of Physics and Astronomy, Flagstaff, AZ, for participating in this research and co-authoring this paper.

Special thanks to Mr. Peter M. Munding, NNSA, Nevada Site Office.

References

Eastman, M. P., R. C. Hughes, G. Yelton, A. J. Ricco, S. V. Patel, M. W. Jenkins, "Application of the solubility parameter concept to the design of chemiresistor arrays," *J. Electrochem. Soc.* **146**, 10 (October 1999) 3907–3913.

Rose, F. L. "Tortoise chin gland fatty acid composition: behavioral significance," *Comp. Biochem. Physiol.* **32** (1969) 577–580.

this page intentionally left blank

Room-temperature, High-resolution Spectroscopy on Nanostructures

Stephan J. Weeks[1]
Special Technologies Laboratory

Colloidal suspensions of functionalized quantum dots (QDs) in polymer matrices were bound in densely packed ensembles to glass surfaces. These nanoscale QD-molecular complexes can selectively interact with target analytes as well as employ a fluorescent resonance energy transfer (FRET) mechanism to indicate target analyte attachment. The densely packed ensembles were fabricated and characterized for their physical properties. The formation of unique attachment sites and superlattice minibands was explored to investigate the conditions necessary for analytes to form well-defined quantum states that may yield the desired narrow-line luminescence spectra at room temperature. The target analyte selected was a surrogate of the explosive TNT.

Background

Many National Security Technologies (NSTec) customers and Nevada Test Site Test & Evaluation programs would greatly benefit from the development of highly selective and sensitive chemical, biological, and explosive (CBE) real-time field analytical capabilities. Such analyses would greatly reduce or eliminate false positive and negative signals, allowing critical decisions to be made with more confidence due to the improved measurement certainty in the supporting data. In this project, two principal barriers to making high-resolution fluorescence measurements in the field were addressed: (1) molecular spectra are broad, making qualitative and quantitative analytical measurements difficult, particularly in multicomponent real sample matrices where detectability, selectivity, and the absence of interferences are critical; and (2) high-resolution, laser-based spectroscopy techniques are performed at low temperatures (4–77K) and low pressures ($<10^{-4}$ Torr). If high-resolution luminescence techniques could be performed under ambient conditions in real time, this would enable CBE detection method development for many applications. The breakthrough technology would be the development of functionalized nanostructures, allowing high-selectivity, trace-level molecular analysis at room temperature in an open environment.

The scientific challenge is to limit spectral broadening effects at room temperature. Nanotechnology may hold the key to producing ordered, functionalized arrays that could restrict the available (electronic/vibrational/rotational/lattice) transitions to allow interrogation by wavelength-tunable laser excitation to result in high-resolution spectroscopy.

[1] weekssj@nv.doe.gov, 805-681-2262

From an analytical fluorescence measurement point of view, increased number density within specific energy level(s) results in higher absorption of photons (up to saturation) through monochromatic laser excitation of allowed transitions, thus providing higher populations in excited states, leading to greater photon emission and increased signal. Decreased line broadening results in narrower spectral absorption and emission bandwidths and provides enhanced selectivity and specificity, thereby reducing interferences in complex matrices. The analytical advantages that have made laser-based techniques powerful tools in low-temperature and solid-state luminescence spectroscopy include the capability of high intensity, monochromaticity, spatial and phase coherence, and the ability to discriminate the homogeneous lines from the inhomogeneous bands (Vo-Dinh, 1997). These techniques can be used to improve analytical figures of merit such as detection limit; precision; signal-to-noise ratio; accuracy; sensitivity; linear dynamic range; selectivity; and spatial, temporal, and spectral resolution. All are related to how well one can perform qualitative and quantitative analysis.

Optimal conditions for high-resolution molecular luminescence are currently obtained at cryogenic temperatures or in supersonic molecular beams. The natural linewidth of an isolated molecule is determined as temperatures approach 0K. Absorption and emission bands are the result of a broad distribution of homogeneous guest molecule lines in solid host matrices. The interaction of molecular energy states with the different individual molecular microenvironments results in inhomogeneously broadened spectra. Energy uncertainty related to molecular excited-state lifetimes and energy level population relaxation processes contribute to the homogeneously broadened linewidth; both are only weakly temperature dependent. However, phase relaxation processes, which contribute to the homogeneously broadened linewidth, are strongly temperature-dependent and reflect fluctuations of the optical transition frequency induced by host dynamics and guest-host coupling. The broad inhomogeneous linewidths are due to distribution of the population of guest molecular energy states with different individual molecular microenvironments. Quanta of lattice vibrational energy in the host matrix are referred to as phonons. A narrow zero-phonon line corresponds to a purely electronic transition of the analyte in which the vibrational state of the host lattice does not change. Electron-phonon coupling produces broad phonon wings corresponding to electronic transitions of the guest molecule coupled to changes in the vibrational state of the host lattice. High-resolution spectrochemical methods include low-temperature Shpol'skii, line narrowing, hole-burning, and matrix isolation spectroscopies, plus laser photolytic and supersonic jet spectroscopies. Examples of enhanced spectral resolution using Shpol'skii spectrometry are shown in Figure 1 (Vo-Dinh, 1997).

Advances in the fabrication of functionalized semiconducting, metallic, and insulating materials with nanoscale dimensions are opening up novel approaches to sensor development. High-resolution, room-temperature spectroscopy would require the production of functionalized, ordered nanostructure arrays that trap specific analytes uniquely on their surfaces for CBE-sensing applications. Self-assembly and molecular templates produce selective coatings or films on substrates. Nanostructured supports can be formed by ordered arrays of QDs, carbon nanotubes, nanowires, photonic crystals, nanoparticle arrays, or microporous substrates. Block copolymers have been integrated with silicon-based technologies to

produce nanoscale structures. These copolymers bring chemical selectivity, functionality, and organic synthetic methodologies to inorganic semiconductor surfaces (Chai, 2007). Chemical self-assembly of ordered networks of colloidal QDs has been demonstrated (Ramadurai, 2006).

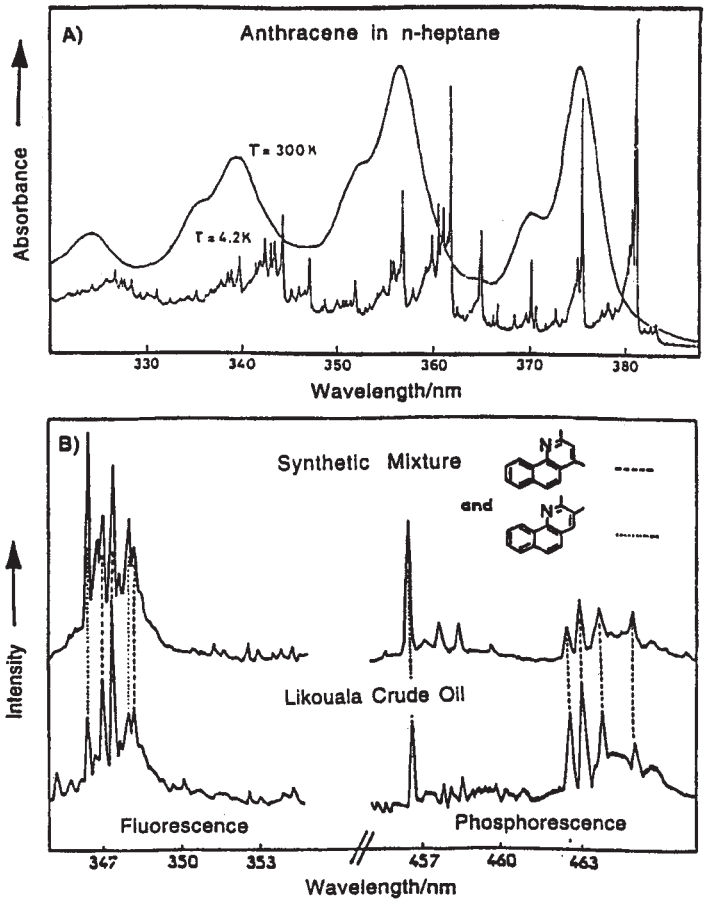

Figure 1. The Shpol'skii Effect reduces both the electron-phonon coupling and the inhomogeneous broadening in absorption and luminescence spectra. (a) Line narrowing of absorption spectrum occurring upon cooling an anthracene solution in n-heptane from room temperature to 4.2K. (b) Luminescence spectra of 2,3- and 2,4-dimethylbenzo[h]quinolines in a synthetic mixture and in a di- and triaromatic base concentrate from Likouala crude oil, frozen in n-hexane at 15K. Excitation was at 330 nm. Each isomer is identified by fluorescence and phosphorescence peaks (Vo-Dinh, 1997).

Project

An approach was developed where arrays of QDs may form a 3-dimensional superlattice by an alternating structure of colloidal QD complexes and matrix materials (such as polymers). Colloidal synthesis produces solution-based QDs, which are flexible in fabrication and convenient for molecular conjugation. These colloidal QD-based complexes can be functionalized for interaction with specific target analytes. Biomolecules (e.g., short-chain peptides) of various lengths can also be conjugated to QDs in order to form ordered networks with varying interdot spacings. Novel architectures with limited nanoenvironments for interacting analytes may be able to be fabricated that would provide narrow line excitation and emission. Additionally, superlattice minibands formed would lead to well-defined extended quantum states, and that may lead to modified (enhanced spectral resolution) optical linewidths at room temperature (Stroscio, 2007).

Our collaborators at the University of Illinois at Chicago (UIC) (Stroscio, 2007) prepared triplicate trinitrobenzenesulfonic (TNBS) samples and blanks in a CdS QD ensemble containing ~2×10^{14} QDs of ~3-nm radius each. The samples had 5.5×10^{-19} g of TNBS (2,4,6-trinitrobenzenesulfonic acid) deposited on the ensemble. Two sample/blank sets were prepared from a nearly monodisperse suspension. The QDs formed colloidal close-packed ensembles on the glass slide substrates. The third set was a previously prepared suspension that more readily formed colloidal ensembles due to van der Waals interactions. Another sample simply had 5.5×10^{-19} g of TNBS on a glass slide with coverslip. A sample with PbSe QDs embedded in Poly(2-methoxy-5(2-ethyl) hexoxy-phenylene-vinylene (MEH-PPV) conductive polymer was prepared by spin-casting on an indium-tin-oxide (ITO) substrate. Duplicate sample/blank pairs with 1.01 μl of 5×10^{-17} g/ml TNBS deposited on CdSe-ZnS QD ensembles were also prepared.

A stepwise approach was developed toward examining the use of FRET complexes of these colloidal QD suspensions that form densely packed ensembles on substrates and may form superlattice minibands. The initial experiments examined the energy levels in the QD-based ensembles, the energy levels in the analyte, and then the energy levels of the system with the analyte deposited on the surface of the QD-based ensemble. Unfortunately, the definitive experiments to examine colloidal suspensions of functionalized QDs bound in densely packed ensembles to glass surfaces or other substrates were not completed within the time frame of the project. These QD-based FRET-altering complexes (composed of QD, simulant molecule, and quencher) could be synthesized so that when an analyte molecule interacts with one molecular complex the quencher-labeled molecule will be replaced with the analyte; accordingly, the QD will be unquenched and will emit. These complexes and their use are illustrated in Figure 2. Samples examined thus far contain the QD-simulant (surrogate) complex, but not the quencher.

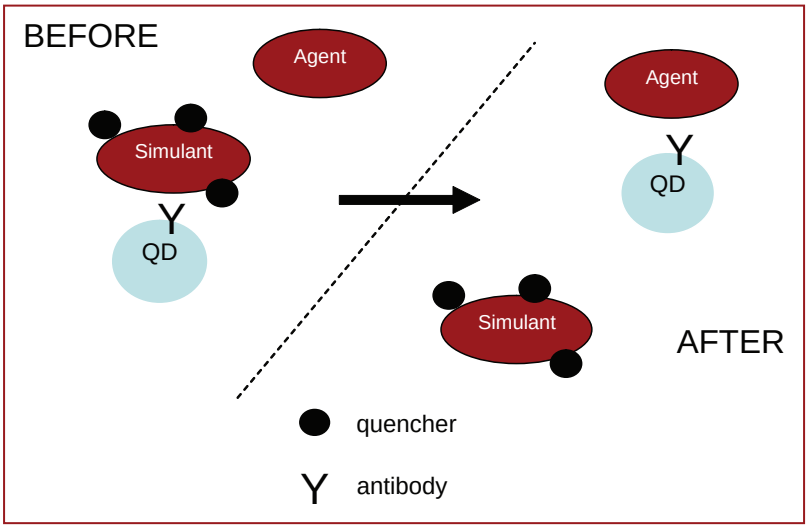

Figure 2. QD-based FRET-altering complexes

The target analytes chosen for study were explosives. Well-characterized and commercially available simulants for antigens, including those for hexahydro-1,3,5-trinitro-1,3,5-triazine (RDX) and TNT, are available. Since similar functionalized QD complexes have demonstrated selective molecular detection of ricin-A-chain, anthrax, and E. coli through FRET emission detection, using the commercially available antigen simulants was determined to be a conservative sensor development approach. Additionally, single-molecule detection has been demonstrated using a QD blinking mechanism as an indicator (Dutta, 2006). The QD-based complex for the detection of 2,4,6-trinitrobenzene (TNB) was chosen for study since it is a well-known TNT surrogate. QDs can be conjugated with either of two available anti-TNB-antibodies, 11B3 or A1.1.1 (from Strategic Biosolutions). Initially, CdS QD ensembles were investigated with 2,4,6-TNBS deposited on the ensemble. TNBS is a surrogate for TNB (Goldman, 2005). Clusters of QDs formed on the glass substrate due to van der Waals attraction. A transmission electron microscope (TEM) image of the ensemble of QDs fabricated by our collaborator at UIC is shown in Figure 3. Figure 4 shows a photoluminescence spectrum of the sample containing an MEH-PPV matrix with embedded PdSe QDs on an ITO substrate. MEH-PPV is a conductive polymer being studied for minibands formation in QD arrays under bias (Sun, 2007).

Critical to note for the formation of superlattice minibands is that densely packed ensembles of colloidal QDs differ from self-assembled QDs. Self-assembled QDs are grown on a substrate as a result of a lattice mismatch between the substrate and the QD material. As a result, the spacings between the QDs are not very uniform, and it is difficult to stack them in the third dimension. This makes it difficult to obtain high-quality minibands. The colloidal QDs (initially in a colloidal suspension) may be linked together using molecules as spacers, or by coating the QDs with thin surfactants that cause

the dots to bind in close proximity to each other, ideally in close-packed ensembles. If the dot-to-dot separation is small, common quantum states are formed and arrays with almost uniformly spaced (10–20% variation is tolerable) minibands are formed. However, in our project superlattice formation was not as important as it would be in carrier collection in QD-based photodetector applications. In our case, it would have been nice to have well-defined minibands so that states associated with the analyte could have been easily identified in the energy spectrum. If the minibands are not well formed, the energy states will be spread out and might mask the states we are trying to resolve.

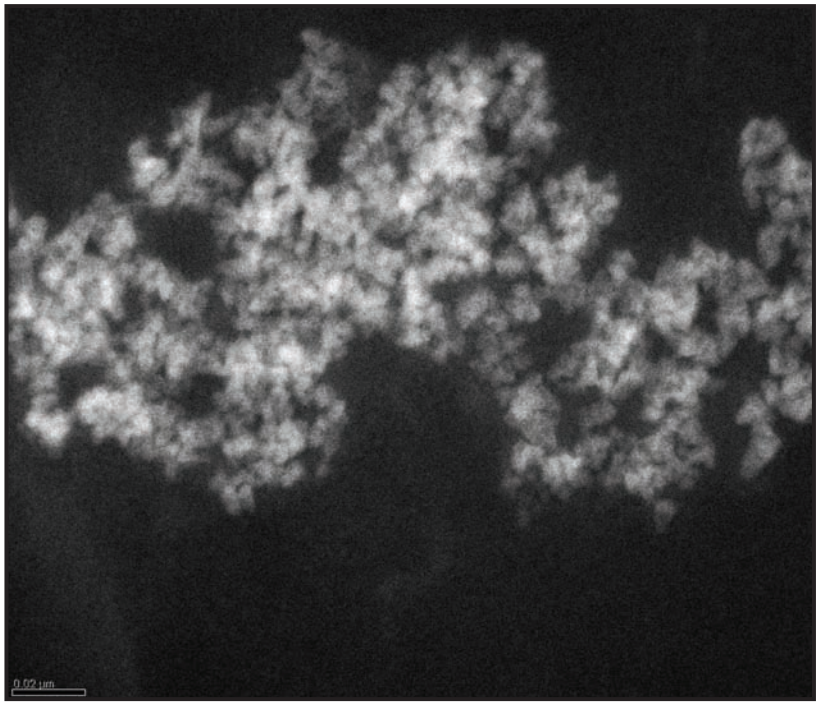

Figure 3. TEM image of ensemble of QD fabricated at UIC, in which clusters of QDs form on the substrate due to van der Waals attraction

Equipment assembled for the laser-based studies included an Nd:YAG Q-switched optical parametric oscillator (OPO) laser (Vibrant LD 355 II, OpoTek, Carlsbad, CA) with 1–25 mJ/pulse at 10 Hz, 5-ns pulse width, 410–2400-nm tuning range, and 4–7-cm^{-1} linewidth; a Stirling microcooler (FLIR Systems, Inc., Wilsonville, OR) capable of cooling samples to –150°C; and a fiber-optic spectrometer (Ocean Optics Inc., Dunedin, FL) with a wavelength range of 410–774 nm and a resolution of 0.78 nm FWHM. However, the collaboration formed late in FY 2007 and, therefore, the QD samples arrived too late to perform the required laser experiments.

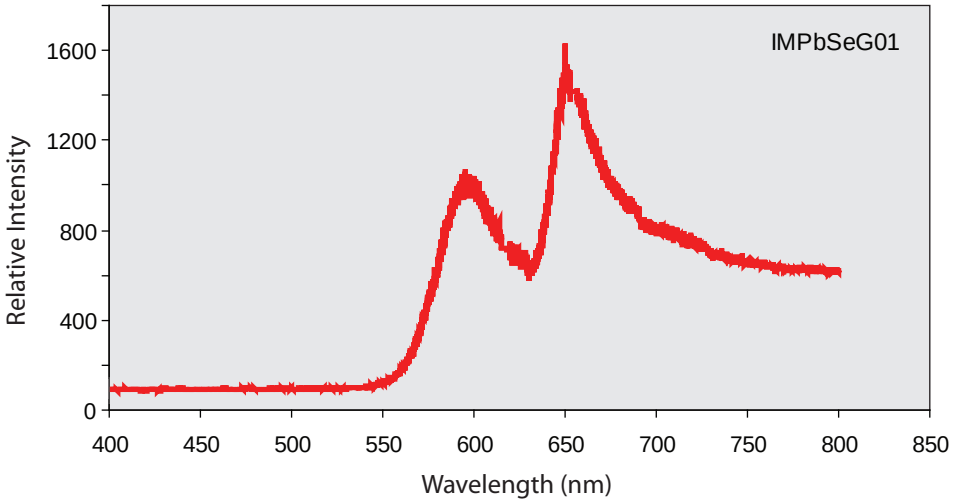

Figure 4. Photoluminescence spectrum of MEH-PPV matrix with embedded PdSe QDs on ITO substrate, fabricated at UIC

Conclusion

A novel approach was developed to investigate the possibility of obtaining high-resolution spectra from analyte molecules that interact with a functionalized, ordered nanostructure. Colloidal suspensions of QDs functionalized to detect a TNT surrogate were created based on a FRET scheme. A methodology was developed for the densely packed QD-based ensembles to be characterized by traditional photoluminescence and TEM techniques.

Further work needs to be performed to investigate the application of laser-based techniques to functionalized, ordered nanostructure arrays and to study the formation of superlattice minibands. FRET emission or QD blinking could be monitored in such a way that, when blinking is observed, a diode laser scan is initiated at the appropriate wavelength to identify the analyte. This project was an initial effort to explore the forefront topic of the formation of superlattice minibands in densely packed ensembles of QDs that may lead to well-defined extended quantum states, which, in turn, may lead to modified (enhanced spectral resolution) optical linewidths. Additional studies may provide a selective method of enhancing the detectability of target analytes trapped in ordered nanostructure arrays using ultraviolet-visible-infrared luminescence spectroscopy. QD complexes using conductive polymers may yield complementary detection techniques to luminescence spectrometry.

Future applications may include the development of motes using tunable diode lasers and analyte-selective functionalized nanostructures, as well as remote sensing using large arrays of functionalized nanostructured layers. It should be noted that <1 mJ of tuned laser diode excitation should yield near-saturation conditions for many analytes. Wavelength or time modulation can be used to enhance detection.

Acknowledgments

Dr. Michael A. Stroscio, Director, Center for Integrated Networks of Nanoscale Sensors for Biomedical Applications, University of Illinois at Chicago, provided technical collaboration and fabricated the QD ensemble used for the experiments. Dr. Gene Capelle (Special Technologies Laboratory) provided valuable laser and spectrometer resources and technical advice.

References

Chai, J., D. Wang, X. Fan, J. M. Buriak, "Assembly of aligned linear metallic patterns on silicon," *Nature Nanotechnology* **2**, 8 (August 2007) 500–506.

Dutta, M., M. A. Stroscio, B. J. West, "Mechanism for blinking of colloidal semiconductor quantum dots in electrolytic suspensions," *J. Nanoelectron. Optoelectron.* **1**, 1 (2006) 99–103.

Goldman, E. R., I. L. Medintz, J. L. Whitley, A. Hayhurst, A. R. Clapp, H. T. Uyeda, J. R. Deschamps, M. E. Lassman, H Mattoussi, "A hybrid quantum dot-antibody fragment fluorescence resonance energy transfer-based TNT sensor," *J. Am. Chem. Soc* **127**, 18 (April 2005) 6744–6751.

Ramadurai, D., Y. Li, T. Yamanaka, D. Geerpuram, V. Sankar, M. Vasudev, D. Alexson, P. Shi, M. Dutta, M. A. Stroscio, T. Rajh, Z. Saponjic, N. Kotov, Z. Tang, S. Xu, "Colloidal quantum dots as optoelectronic elements," *Proc. SPIE* **6127** (2006) 61270L-1–61270L-13.

Stroscio, M., M. Dutta, "Formation of minibands in close-packed ensembles of quantum dots," Private communication, September 2007.

Sun, K., M. Dutta, M. Stroscio, "Transmission coefficients for minibands formed in quantum dot arrays under bias," manuscript in preparation for *Proceedings of 12th International Workshop on Computational Electronics*, Amherst, Massachusetts, October 8–10, 2007.

Vo-Dinh, T., N. H. Velthorst, D. S. Moore, B. Schrader, "Laser-based Molecular Spectroscopy for Chemical Analysis—Luminescence," (IUPAC Recommendations 1997), *Pure & Appl. Chem.* **69**, 7 (1997) 1435–1449.

Electronics

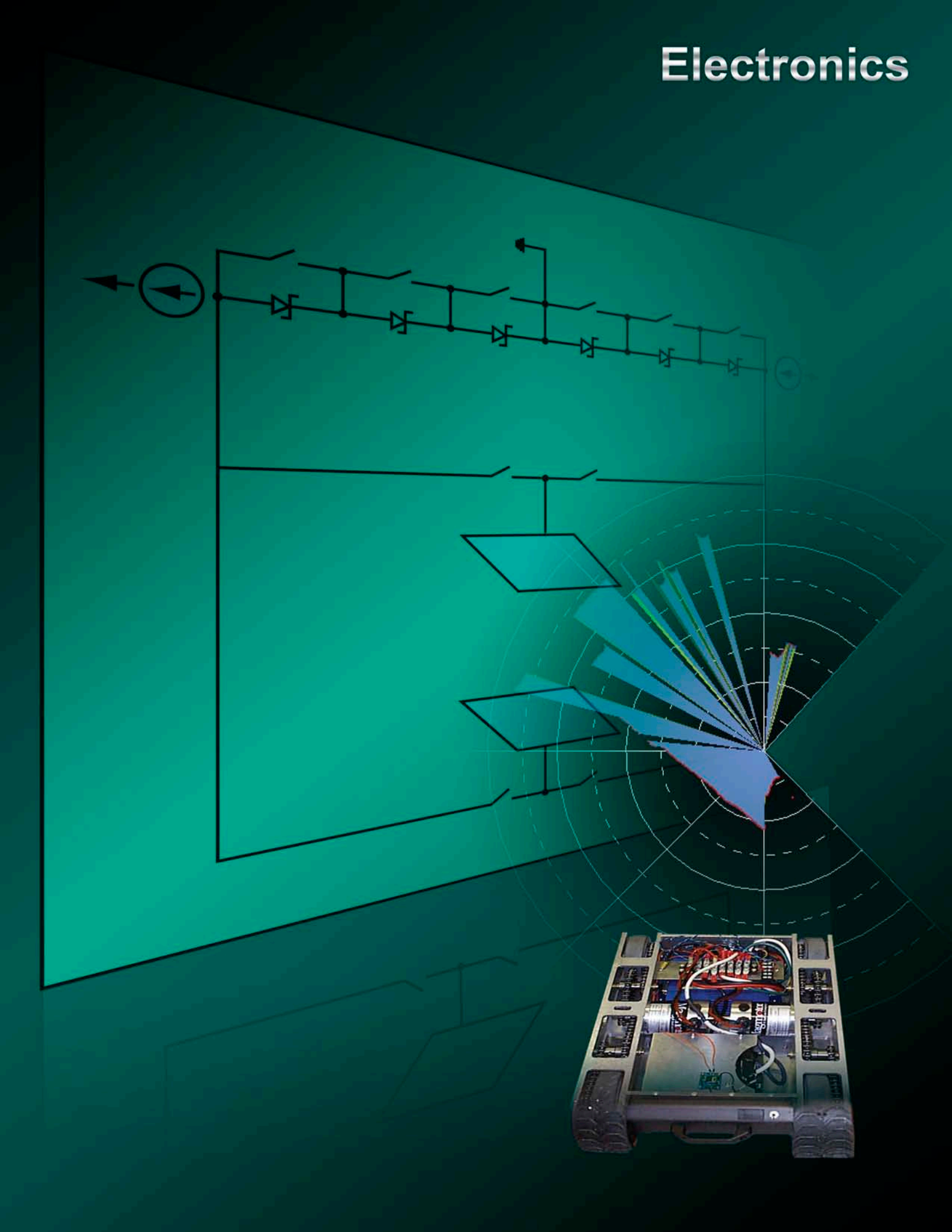

Pulse Discriminating Microchannel Plate Beacon/Receiver

Michael Buss,[1] *Duane Gardner, Eric Larson*
Special Technologies Laboratory

Our team investigated the effectiveness of detecting an optical beacon (pulse-modulated light) by monitoring the electrical bias parameters in a microchannel plate (MCP). Specific investigations were conducted to measure the effect modulated light has on the MCP strip current, in comparison to the optical response. By altering the effective bias impedance on the MCP, bias currents flow more readily at modulation frequencies where the MCP and bias circuitry are at resonance. This increase in current flow is used as an electrical presence detector for a specific pulse modulation frequency. Our experiments showed that the frequency selectivity function does occur, but that the optimal implementation of bias resonance circuitry could not be attained due to the unavailability of high Q components at the desired resonant frequencies. Alternate resonator topologies could enable the use of lower Q components, thus making this technique a viable beacon detection method.

Background

The NNSA, the U.S. DOE Safeguards and Security programs, and various non-DOE agencies have a continuing interest in technology enhancements for protective forces, as well as tagging, tracking, and locating (TTL) technologies for counterproliferation activities. Several different technologies are employed, and personnel carry and use an assortment of equipment for each operation. Modifying a piece of gear already being carried to function as a dual-use device would relieve the operator from having to bear excessive equipment. A standard set of night-vision goggles (NVGs) that have been modified for use as an optical beacon detector would be desirable for many special operations teams.

The MCP is the primary optical element used in night-vision goggles. MCP-based NVGs are of great interest to TTL programs due to their very high gain and sensitivity to light and, hence, their ability to operate over very long distances. The MCP-based imaging tube functions as a light-amplification imaging device. Incoming light is focused onto the photocathode, where it is directly converted to photoelectrons. These photoelectrons are accelerated toward the MCP structure by a –200-V bias voltage. The MCP is biased with a variable voltage (700–1000 V) that controls electron multiplication ratios and, hence, tube current. The maximum amplification of photoelectrons is a factor of about 10,000. Photoelectrons exiting the MCP are accelerated by a –6-kV bias voltage and strike the phosphor screen at high velocity; they are then converted back into photons visible to the eye.

[1] bussmn@nv.doe.gov, 805-681-2493

This image-amplification device has electrical characteristics that are defined by its physical configuration. The three main elements of the imaging tube are the photocathode-to-MCP gap, the MCP-in to MCP-out gain region, and the MCP-out to phosphor converter acceleration region. Current flow is generated between these regions due to the photo-induced current originating at the cathode.

Physically, these regions are large (18-mm diameter) flat plates separated by narrow gaps. The electrical contact to these plates is made through rings that encircle the plates. These contacts have very low inductance and resistance. A major characteristic of these regions is the capacitance formed by the proximity of the plates and the vacuum gap between them. Measurements of the tube used for this effort indicated a photocathode-to-MCP capacitance of 42.3 pF, and an MCP-in to MCP-out of 74 pF.

The goal of this research was to selectively tune an MCP optical element in an NVG, using an electrically tuned circuit, to receive a pulse-modulated optical signal. The MCP, altered to produce a greater gain to the selected/tuned pulse duration, would reject undesired pulses. The modulated optical signal would be produced by a field-deployed tag or beacon. The net result would be a bright spot in the NVG display at the location of the incident photons corresponding to the modulated optical signal.

A pulse-modulated optical signal would be very difficult to detect in the presence of background illumination without the properly tuned receiver, and would therefore have an inherently low probability of detection. As such, this technology would make an excellent tagging and tracking system. This technique would allow tracking of optical tags using NVGs.

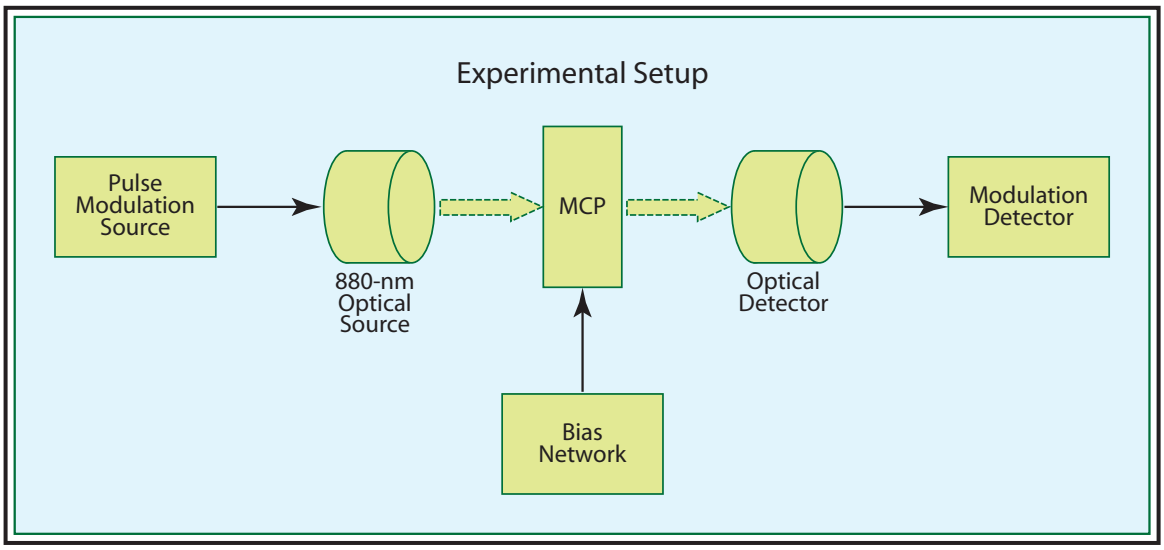

Figure 1. MCP experimental test setup

Project

The first phase of this investigation was to obtain a baseline characterization of a stock MCP. A Delft Electronic Products #2040 MCP was chosen. This MCP is designed to operate in the near-IR, 880-nm optical region. An appropriate LED was chosen as a simulated pulsed optical source, and optical detector circuitry was designed and built to measure the frequency response of the optical display. The experimental setup is depicted in Figure 1.

Extreme care was taken to isolate the incoming modulation signal from the modulation detector. As a result, a very accurate measure of the "dark current" could be obtained for the MCP baseline. Using the test fixture shown in Figure 2, a baseline was obtained for both the optical path frequency response (Figure 3) and the electrical path frequency response. The electrical frequency response was obtained by monitoring the high-voltage bias line with a spectrum analyzer. A high-voltage isolation buffer was used to protect the analyzer from the high voltage.

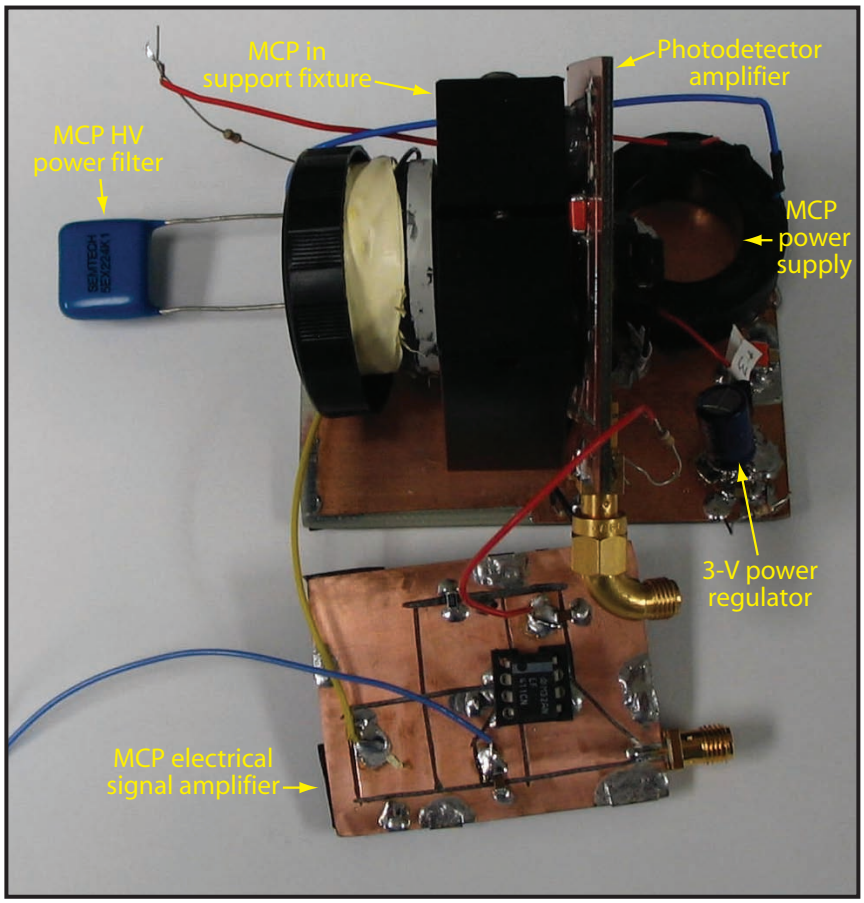

Figure 2. MCP test fixture

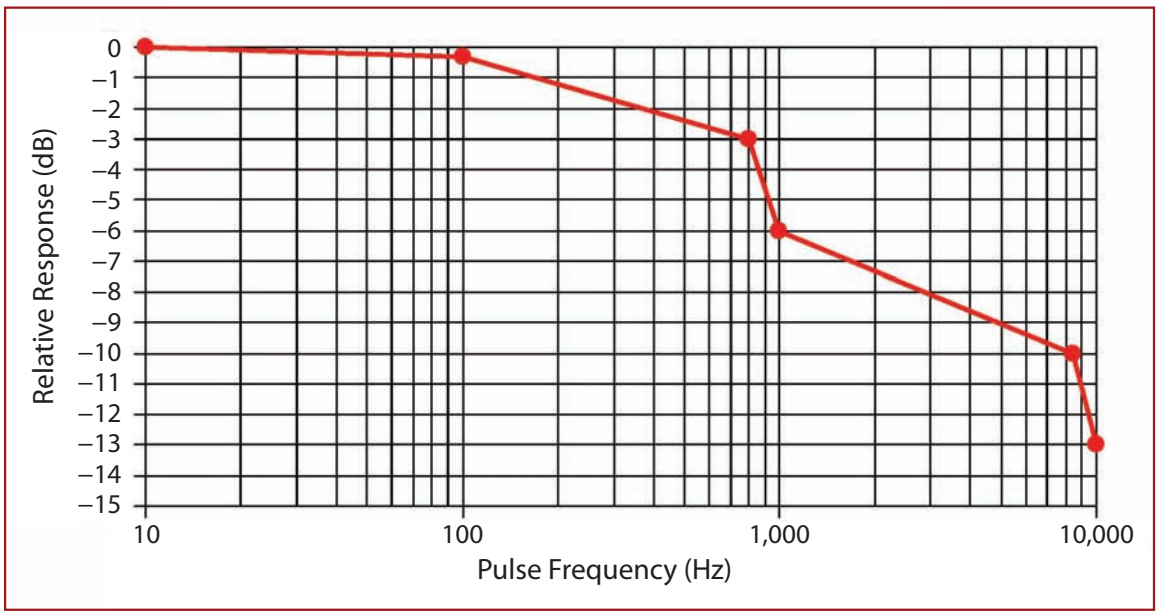

Figure 3. MCP incident optical modulation frequency response

After the baseline was obtained, an external resonator, in a shunt-to-ground configuration, was installed at the MCP high-voltage bias node. This resonator consisted of multiple resonator crystals in series, permitting their use at the high voltages of the MCP. The external resonator had the effect of adding a large AC load to the MCP. This effectively reduced the gain of the overall MCP amplifier. However, upon close examination a very small enhancement of the gain, relative to the reduced gain, could be detected. This gain enhancement was much less than a decibel, but it was detectable. Additional shunt-resonator circuits were built and tested, but because of the lack of very high Q components capable of working at high voltage, low Q components were substituted. This dampened the resonance features and further degraded the MCP gain. The availability of high Q components is not a supply issue, but rather of manufacturability and device physics limitations.

Conclusion

Our experiments have shown that the frequency selectivity function of an MCP does occur and can be manipulated by altering the external high-voltage bias structure to form a desired resonance. Optimal implementation of bias resonance circuitry could not be obtained during this investigation due to the unavailability of high Q components at the desired resonant frequencies. Alternate resonator topologies could enable the use of lower Q components, thus making this technique a viable beacon detection method.

Networked Unmanned Ground Vehicle-based Data Acquisition

Paul Ainsworth, Ben Davison, James Essex,[1] Bob Fisher, Ron Guise, Joe Hassen, Jon Mrugala, Key Senh, Terry Smith, Patrick Whitely
Remote Sensing Laboratory – Nellis

Robotic surrogates for hazardous human activities are rapidly evolving from unintelligent teleoperated platforms to intelligent, autonomous systems that adapt to unmodeled environments. This effort focused on the design and development of a low-cost, flexible unmanned ground vehicle (UGV) and the software/networking architecture to support acquisition and telemetry of radiation data. Accomplishing this goal required a plug-and-play approach to sensors, base platforms, radiation detection subsystems, and configuration-aware control software. In this report, we present our design goals, evaluate key aspects of this effort, and illustrate the feasibility of achieving these goals using a terrestrial test bed developed as part of this effort, the Networked Unmanned Ground Vehicle for Autonomous Radiation Detection Indoors/Outdoors (NUGVARDI/NUGVARDO), as a demonstration.

Background

Current emergency response field operations require the ability to rapidly collect radiological deposition data over large areas at high resolution, or to collect data on a suspect area or container without compromising the health and safety of field teams. Flexibility is the primary challenge to meeting the needs of this community. Commercially available systems address requirements from the perspective of a single class of environment, single mode of operation, and/or single mission. Solving the flexibility issue necessitates rethinking requirements such as clearance height, speed, payload, total weight, sensing capability, sensing resolution, and modes of operation.

Project

Overview of Design

Common scenarios during U.S. DOE emergency response missions were evaluated and used to prioritize operational goals for our system. A small selection of missions were identified as test cases and used to formulate prototype UGV design requirements to demonstrate modularity. Our operational goals included the ability to rapidly collect contamination data over large areas at high resolution, acquire radiation measurements on a suspect area or container, and perform repeatable measurement tasks both indoors and outdoors.

[1] essexjj@nv.doe.gov, 702-295-8714

The key design strategy the team adopted at the outset of this effort was a system of modular components. The NUGVARDI (Figure 1) needed to adapt to different terrain types and modes of operation, have plug-and-play sensor and detector packages, and algorithms that could be adjusted for environments and configurations. Software structures needed to support and coordinate elements of perception, localization, planning, and control, while reactively handling and mitigating internal and external uncertainty.

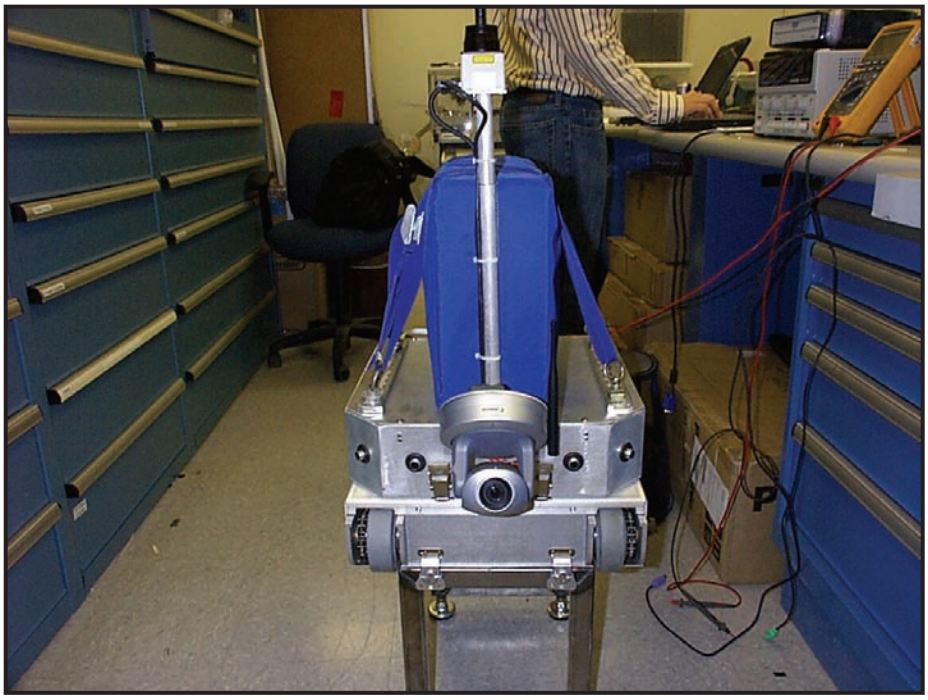

Figure 1. Final assembly of NUGVARDI on test stand

This effort required defining and bounding classes of terrain, modes of operation, networking options, and basic functional and physical characteristics. Our overall design goals included:

Basic Attributes

- The basic physical and functional attributes required that the system be man-portable, cost less than $10K and be primarily commercial off-the-shelf (COTS)–based
- The system also needed to include hardware, sensors, and software in support of basic functional attributes including configuration recognition, localization, obstacle avoidance, and radiation detection

- Specifications for the ground vehicle platform to include:
  - » Navigation of semi-rugged terrain (parking lots, fields, streets, etc.)
  - » Maximum speed of 15 mph
  - » Travel distance of 10 miles before refueling
  - » Low noise emission
  - » Cost of ground vehicle less than $1K

Modes of Operation

- Manual control via external handheld controller, and line of sight via laptop with optional connected controller or over commercial infrastructure accessed via a Web interface available both internally or externally over clientless virtual private network (VPN)
- Execution of GPS track or navigation to GPS coordinates while avoiding obstacles
- Autonomous mode for execution of search or survey based on predefined boundaries

Networking Options

- Networking capabilities to support different modes of operation, including Bluetooth (10 miles), 802.11 (100 miles), Internet protocol (IP) mesh networking (1–10 km), and the Global System for Mobile Communications (GSM) (no geographic boundaries–1000 km)

Engineering NUGVARDI

We approached the issue of modularity in its simplest form: indoor vs. outdoor. This in no way addresses the gamut of unique operational hazards that an implemented system may encounter, but it served as a starting point and demonstration. Alternative platforms that could be explored in the future include boats, crawlers, and terrestrial platforms of various sizes.

Two skid steering chassis were acquired from commercial vendors as platforms for our outdoor and indoor models (Figure 2). Each chassis was retrofitted with power subsystems, serial controllers, and plates for mounting the modular electronics package (Figure 3). These subsystems met all requirements for noise emission, cost, speed, travel distance, and navigational characteristics for the respective operational environments.

The electronics package (Figure 4) is a custom enclosure designed and fabricated in-house. The enclosure contains all power, data I/O, perception, communications, computation, and control components with the exclusion of the detector subsystem. The electronics package has aviation-grade rails for mounting a detector package weighing <50 lbs.

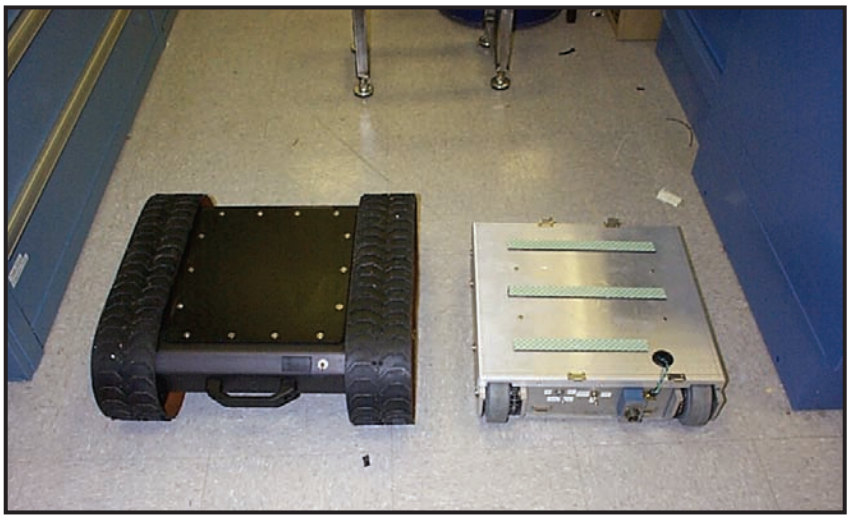

Figure 2. Chassis used to demonstrate modular design

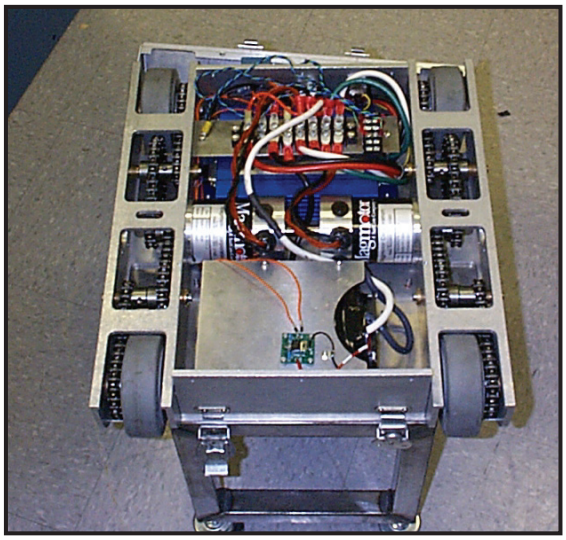

Figure 3. Open chassis displaying battery, motors, controllers, and drive train

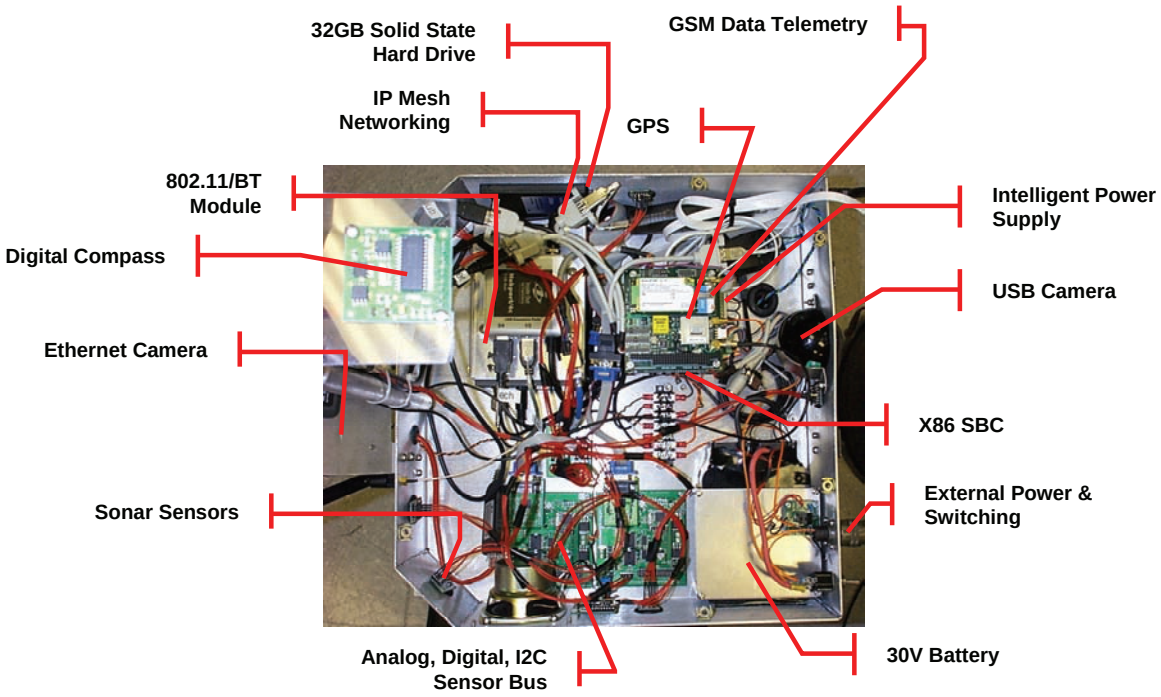

Figure 4. Open electronics package with key design elements labeled

Achieving the modular design required the chassis, electronics, and detector systems to have independent power sources. The electronics and chassis power comes from 30-V nickel-metal hydride batteries with a 12-ampere hour capacity. In the electronics package, the power is managed by a 100-W intelligent Tri-M power supply. Fully charged, this supply will run the electronics package in an active mode for nearly four hours.

The data I/O standards utilized in the electronics package included serial, USB, Ethernet, analog, I2C, and PC104 bus. A low-power, 800-MHz Geode processor with 1 GB of RAM from PC104 Modules is responsible for data handling from all component connections.

Software and Networking Infrastructure

The software effort included two key development strategies. The first strategy was modular software components that could be easily developed, modified, and tested. The second strategy was an all IP-based communications framework that would allow control and reporting functions to occur over either commercial or stand-alone communications infrastructures (Figure 5). These strategies resulted in a well-defined set of classes that supports all three software components including: (1) the onboard UGV application, (2) the Web services–based server communications layer, and (3) the operator interface.

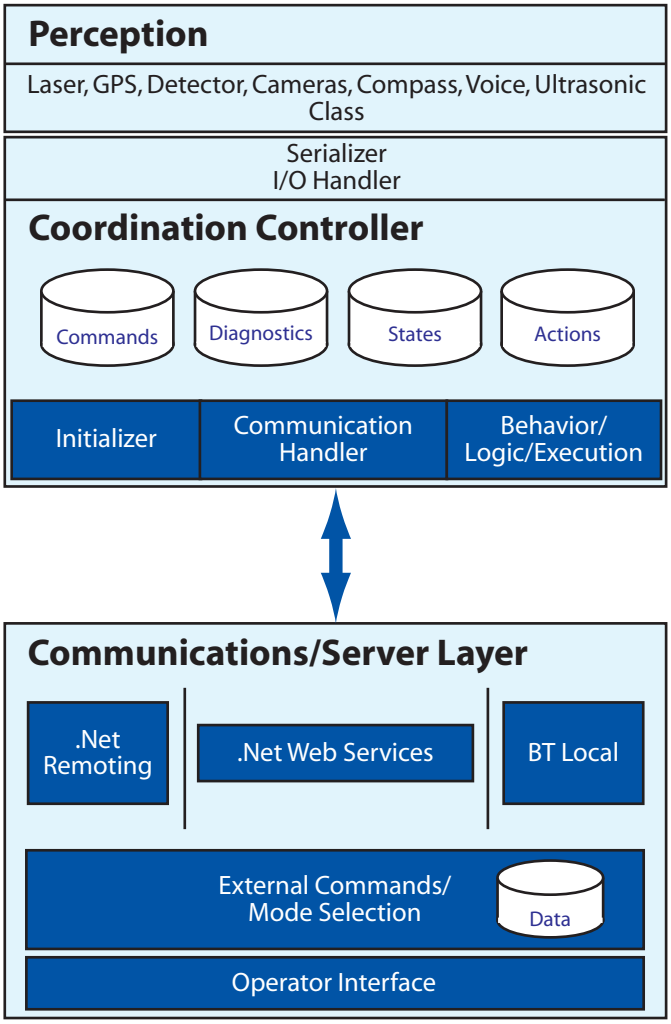

Figure 5. NUGVARDI software architecture

The onboard UGV application handles all aspects of data acquisition, buffering, and storage, and is responsible for system initialization, communications, and actuation of movement. Each function is handled in a separate thread that receives, processes, and stores data asynchronously.

The server communications layer is based on the Real-time Data Acquisition and Dissemination (RDAD) architecture developed under a previous SDRD project (Essex, 2006). This architecture provided the backbone for distributed, service-oriented, secure IP communications between operator and NUGVARDI. The server layer leverages several programming structures including .Net Remoting, .Net Web Services, and Bluetooth serial streams.

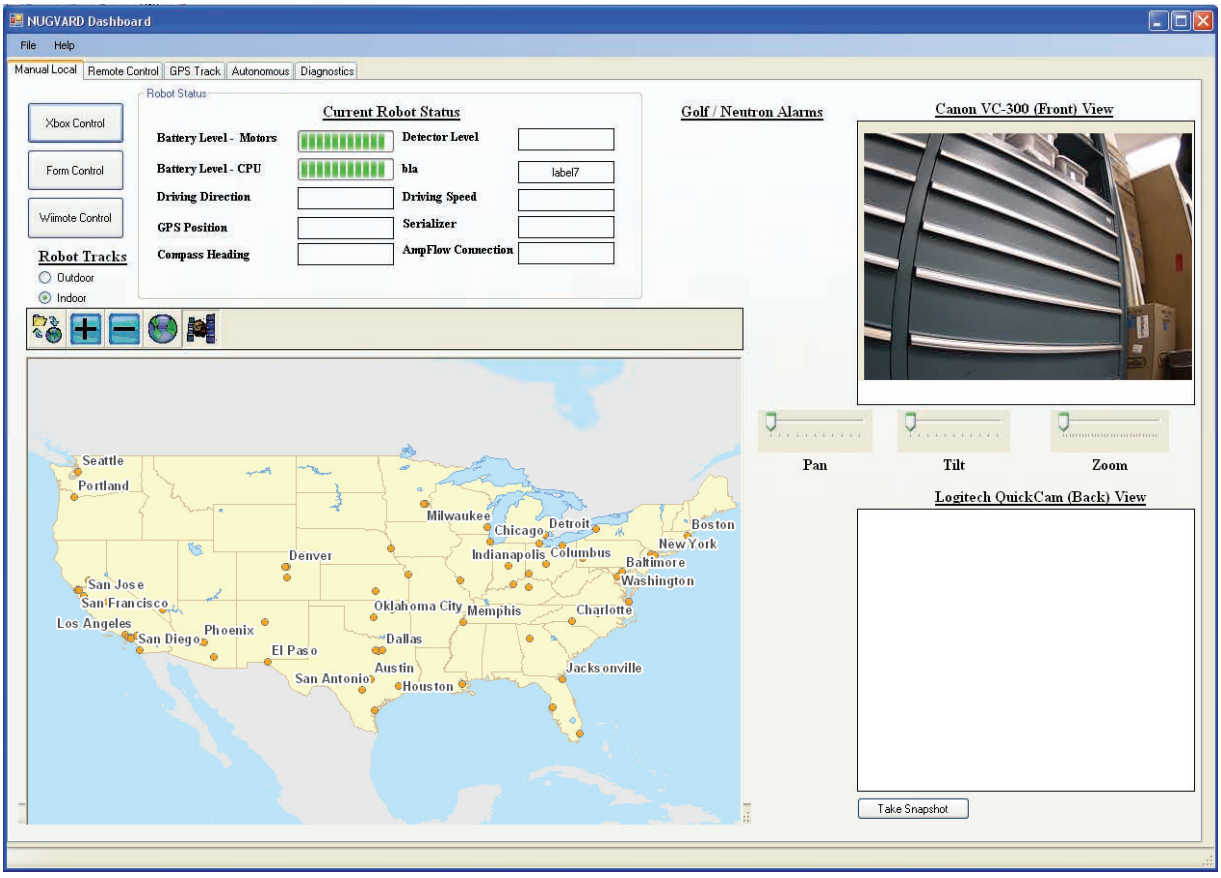

Figure 6. Prototype operator interface

The operator interface includes controls for selecting the mode of operation, and displaying diagnostics, radiation detector alarms, mapping, and camera images (Figure 6). The application intelligently switches between multiple data sources determined by initialization and the communication channel available.

All source code was written in the .Net framework 2.0 using the integrated development environment, Visual Studio 2005. This choice afforded the team access to multiple reusable application programming interfaces (APIs) and drivers made available by vendors for respective components.

Perception

Multiple components for perception and localization were included in the design. The requirements included: (1) short-range obstacle avoidance, (2) long-range motion planning, (3) global outdoor localization, and (4) indoor localization.

The short-range obstacle avoidance requirement is handled by seven srf235 sonar sensors. These are narrow beam sensors operating at 235 kHz over 15 degrees. The data is retrieved multiple times per second by the serializer I/O bus which is passed to a thread that analyzes immediate obstructions to motion. This capability is utilized during both indoor and outdoor operations.

The long-range motion planning requirement is handled by a Hokuyo URG-04LX laser range finder (Figure 7). Although relatively expensive, it is extremely successful at identifying both obstacles and potential travel paths out to nearly 4 m. The sensor resolution is 2 degrees with a 270-degree field of view. The data is captured via USB and handled by a coordination thread that analyzes these data both for potential obstacles and travel path estimation and planning.

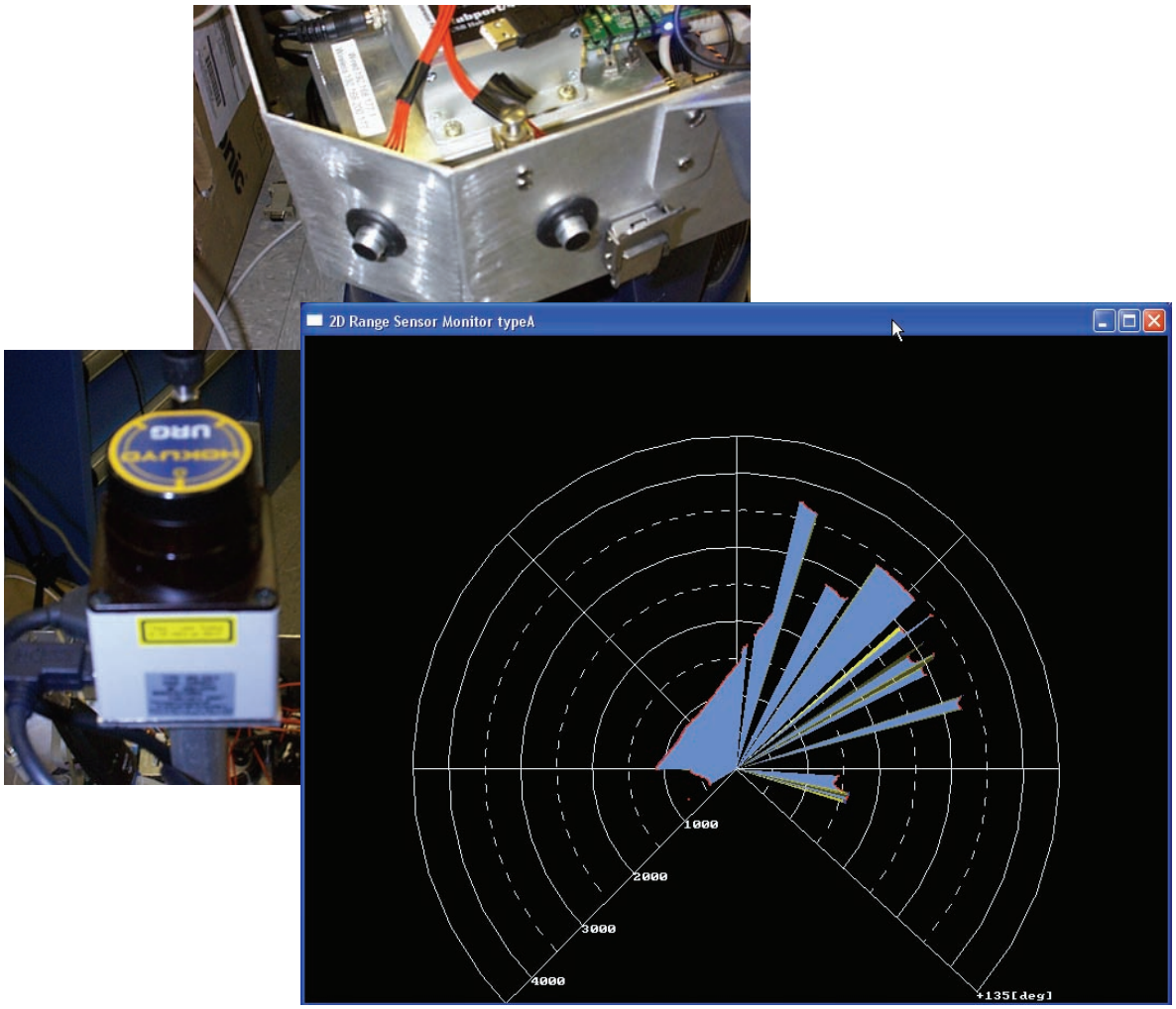

Figure 7. Ultrasonic and laser modules with display representing obstacles

Global outdoor localization is achieved using a Trimble GPS module on a WinSystems PCM-GPS carrier board. These data are captured in a serial stream via the PC104 stack, stored in the data source, and analyzed via the coordination thread when in outdoor mode.

Indoor localization is handled by a mapping capability developed using the ESRI ArcEngine software development kit. This software module determines travel path when the system is being used indoors in autonomous mode. An algorithm that utilizes odometry is coupled with the compass measurements and used to determine the vector of travel. A new vector is calculated each time the speed or direction changes by more than 5%. Vectors are stored in the local data source and transmitted to the operator interface by the communications handler.

Operational Modes

NUGVARDI is capable of several guidance modes, including (1) manual control via external controller, (2) GPS track while avoiding obstacles, or (3) autonomous mode.

We explored several options for manual control and chose two commercial game controllers based on several attributes including communications, ease of programming, and ease of operation (Figure 8). The Wii handheld controller has several advantages, including one-handed operation and an intuitive motion-based operation. The motion control is based on an ADXL 330 accelerometer that converts x-y-z controller motions and velocities to digital signals. An API was developed to translate signals into drive commands that were transmitted to and executed by NUGVARDI. The USB Xbox controller has a basic paddle and button design and is controlled via a similar API.

Figure 8. The Xbox and Wii external controllers

The "GPS track" and "GPS point" modes allow a user to draw a multisegment line or select a single point on a map in the operator interface. These data are transmitted to NUGVARDO and compared to the current location. The difference calculation, combined with basic obstacle avoidance, gives the system the ability to navigate based on GPS data.

Defining and bounding the requirements for autonomous mode was the most challenging component of this effort. The ease of testing was the determinate factor in focusing on the capability of NUGVARDI to search the hallways of a building (e.g., a hotel, office complex, or warehouse) while avoiding obstacles. The algorithm developed uses a combination of data from the laser rangefinder, ultrasonic sensors, radiation detection system, and indoor localization capability to map travel paths and radiation source locations.

Results and Performance

Extensive benchtop testing was conducted on all sensors, hardware components, and communication modules with positive results. Functional testing was also conducted in several modes of operation (Figure 9). The manual and autonomous mode results include expected behavior, power consumption, and communications. If this research is continued, we plan to execute a rigorous test plan to evaluate necessary enhancements to meet our design goals.

Figure 9. Operational testing

Conclusion

Creating a robotic system to replace a human searcher or field-team operator is an extremely difficult challenge. The difficulty arises from having to mimic with machinery the supreme perception and localization capabilities of human senses.

If this research is continued, we plan to execute extensive operational testing of all modes of operations and explore enhancements to the NUGVARDI test bed including:

- Indoor localization and mapping
- GPS with accelerometer
- Enhanced detector capabilities including directional detection
- Power modifications to increase travel distance
- Additional laser for stereo capability
- Voice recognition
- Antenna mast, external light
- Longer-range ultrasonic systems
- Terrain recognition with active laser grid
- Algorithm enhancement for autonomous decision-making
- Lightweight, mobile, all-weather packaging

Acknowledgments

This was a Remote Sensing Laboratory–wide collaboration with major contributions made by the nuclear instrumentation engineering group, fabrication, and the nuclear instrumentation software group. The team would not have met with success without the hard work and dedication of all involved.

Reference

Essex, J., P. Ainsworth, K. Chin, B. Davidson, M. Stacey, E. Wagner, "Multipath Communication Device," *Nevada Test Site–Directed Research, Development, and Demonstration,* FY 2005, Bechtel Nevada/National Security Technologies, LLC, 2006, 231–237.

this page intentionally left blank

Photonics

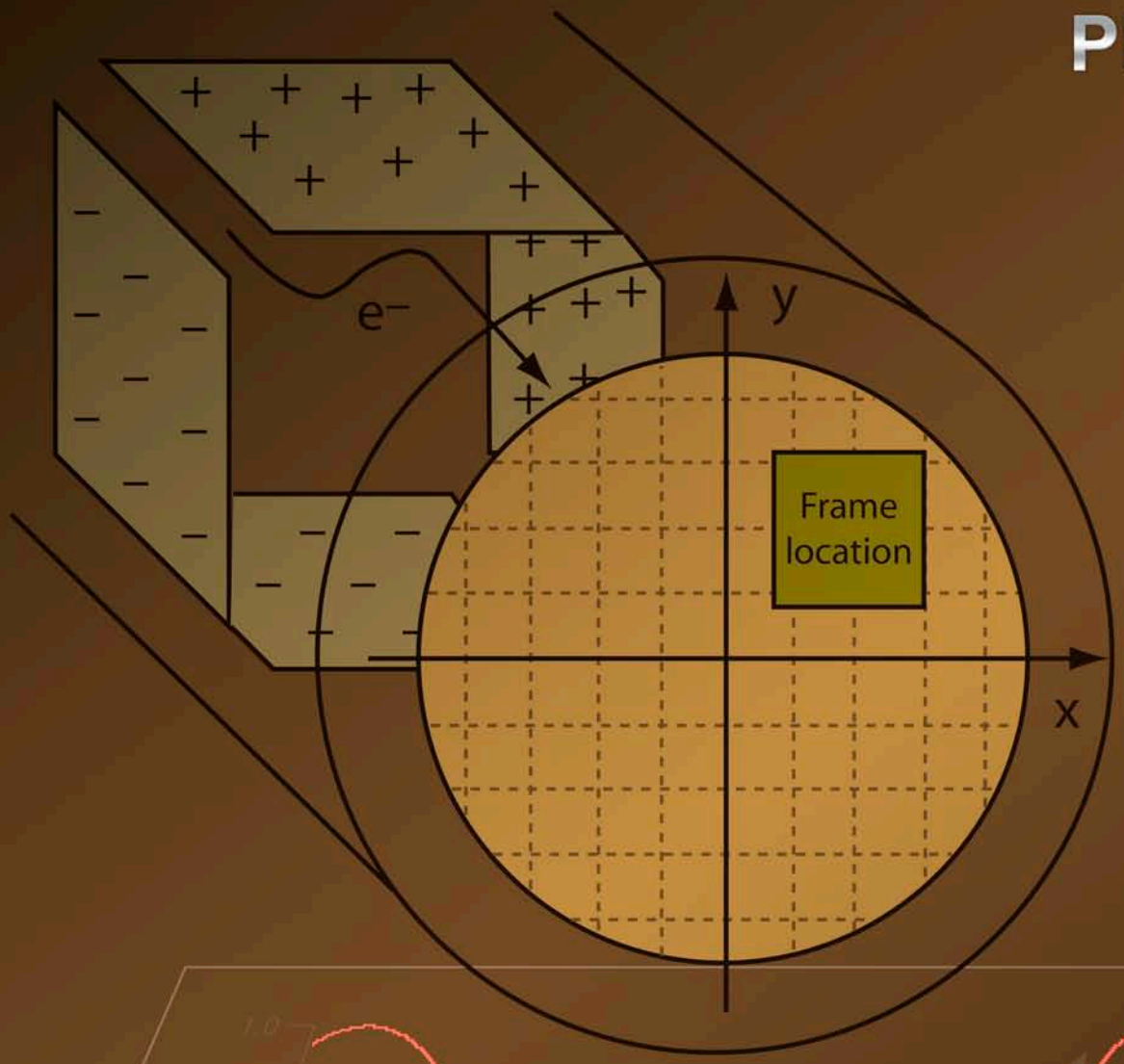
e–
y
Frame
location
x

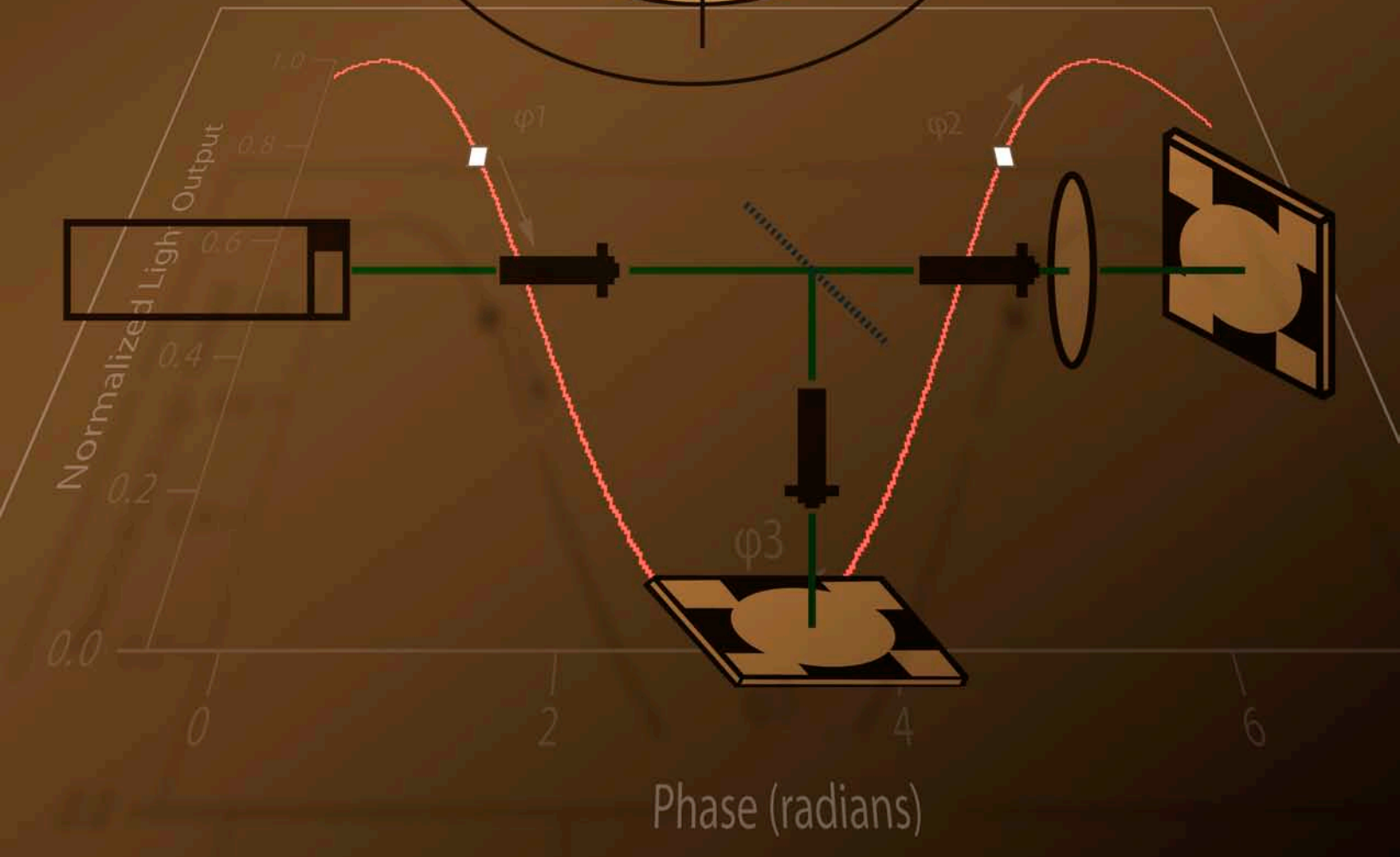
Normalized Light Output
1.0
0.8
0.6
0.4
0.2
0.0
φ1
φ2
φ3
0
2
4
6
Phase (radians)

Stereo Borescope

Stuart A. Baker[1]
Los Alamos Operations

The second year of this project intended to research and develop techniques in microvideo photogrammetry to view three-dimensional (3-D) explosive surfaces. Areas of investigation included small-format optics for visible stereo image data acquisition in the absence of direct lines of sight, and photogrammetry for image data processing to correlate stereo-view image data into a 3-D digital elevation model (DEM). A small-format lens was used to image objects through a flexible, coherent, fiber-optic stereo image bundle to a recording camera. The flexible image bundle was used as an optical relay capable of routing the optical path into areas difficult to reach with standard lens-viewing, such as surfaces of explosive experiments executed inside containment vessels. Static objects were recorded onto standard CCD cameras, and a series of dynamic explosive surface shots were recorded onto a framing camera. Software research was performed to adapt an internally developed program called One-Path Photogrammetry Program (OPPP). We also researched the use of 3DM Analyst, a commercial, short-range photogrammetry program from ADAM Technology (Australia). 3DM Analyst seems better suited to our short-range, close-proximity imaging application. Software reconstruction appears possible with manual interaction.

Background

Single line-of-sight borescope diagnostics, currently identified as surface-visible imaging (SVI), have been fielded on past subcritical activities with mixed results. The original borescopes suffered from very poor sensitivity and provided no depth-of-field details in image data. Single line of sight diagnostics have shown the transition of surface shock waves but with no depth perception, providing no quantitative measure of the amount of surface disturbance. In order to provide depth of field, a stereo view is necessary.

Stereo photogrammetry is not a new concept. The technique is used to correlate two separate views of a 3-D object into a 3-D DEM. The challenge is in applying the technique to short-range photogrammetry applications, and addressing borescope image quality restrictions.

The first borescopes we used for imaging diagnostics were made up of long, thin, tube-housing optics that allowed the probe to be inserted and positioned to view the surface of an experimental package assembly during explosive detonation. The optical relay contained inside the ~1-m-long tube utilized very-small-format lenses 3–5 mm in diameter. The optical relay borescope did allow installation into

[1] bakersa@nv.doe.gov, 505-663-2039

tight locations but resulted in poor optical efficiency and resolution. Experimental results exhibited weak signal-to-noise and no depth of field due to the single line of sight. On dynamic explosive experiments, the signal level can be increased with exposure time, but this increases motion blur. To minimize motion blur, fast exposure times (~100 ns) are desirable. Future surface imaging experiments can benefit from improved optical relays with the ability to record and process stereo image data, thus providing scaled depth-of-field information.

The first year's developments for this SDRD effort were described in the FY 2006 report "Stereoscopic Borescope" (Baker, 2007).

Project

The general schematic and system design concept of the stereoscopic borescope appear in Figure 1. The optical image system uses a flexible, coherent, quartz fiber-optic image bundle to relay the image of the shocked surface to the recording camera. The single image bundle relay reduces the number of coupling interfaces and eliminates the dependence on miniature optics, greatly improving system efficiency.

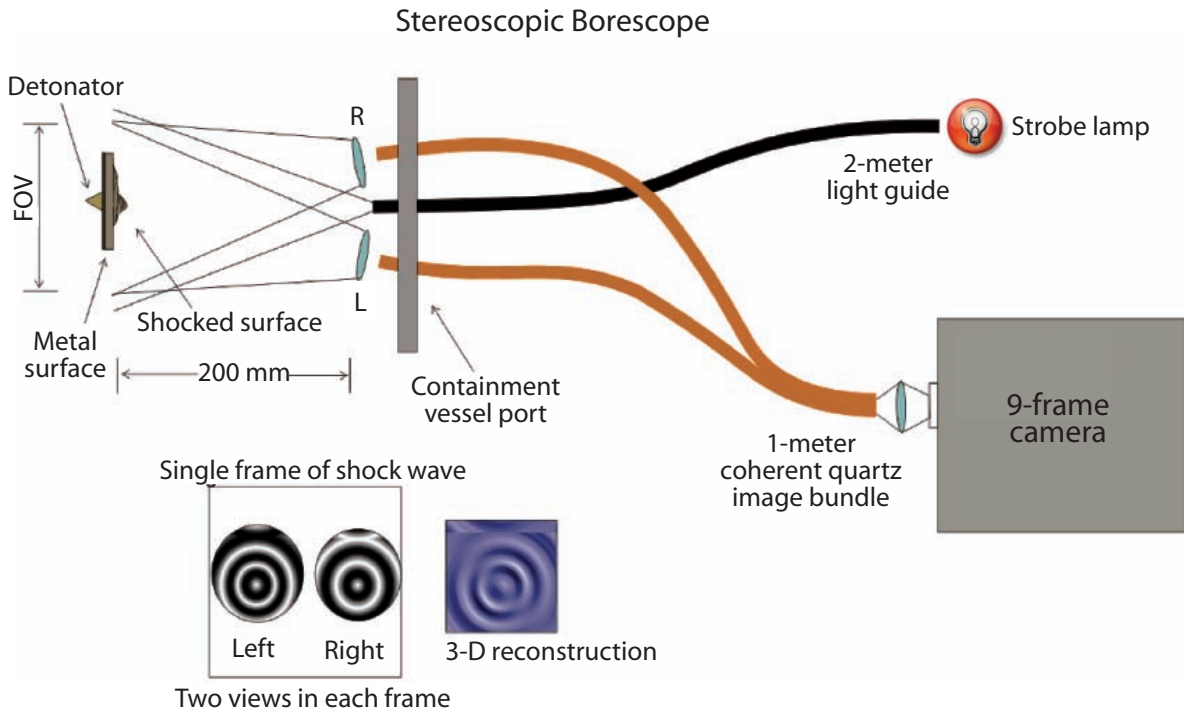

Figure 1. Stereo borescope system

Our stereo image system utilizes two separate coherent image bundles to view the shocked surface from two different perspectives. We use a toe-in angle of ±5 degrees for the left and right views. The two image bundles are combined at a framing camera to record both views in each camera frame. The image bundles are intended to be inserted through a gas pressure–blocked containment vessel port. In some configurations the object lens can be attached to the bundle end after the bundle is inserted through the gas block port. This allows for larger-diameter lenses with better collection efficiency for greatly increased signal levels.

The surface is illuminated by a strobe lamp external to the containment vessel. The strobe is coupled through the containment vessel port to illuminate the surface with the natural numerical aperture divergence of the light guide. For longer standoff distance, a lens can be used to focus the strobe light and control the area of illumination. The images at the bottom of Figure 1 illustrate the acquired stereo image and reconstructed 3-D DEM results.

Software

Software research originally aimed at adapting an existing automated photogrammetry program, OPPP, which had been developed for aerial photogrammetry (Wu, 2004). The basic photogrammetry processing functions for our configuration were tested using Boeing SoftPlotter software. Before adapting a customized version of OPPP, we used SoftPlotter for proof of principle for photogrammetry processing with our configuration. Despite its many capabilities and features, SoftPlotter required considerable manual interaction to correlate the stereo images. Early image-processing tests were conducted on static 3-D objects. With extensive manual interaction, the stereo images were correlated to produce 3-D orthophotos. Figure 2 shows the stereo view of static objects and the rectified orthophoto. The orthophoto's evident distortion can be attributed to the repetitive patterns evident on the objects used. The automated orthophoto rectification process attempts to identify unique pixel regions to correlate the stereo images. The repetitive pattern in these images results in many similar pixel regions, causing difficulty in correlation. This problem was expected to be less of an issue with dynamic images of shocked surfaces due to a less-ordered surface pattern.

Sample images were sent to Mira Solutions, the software company that wrote the OPPP program. Although the OPPP is an automated routine requiring minimal interaction, our system configuration is very specific and these specifications would need to be input to the software. Our intent was to produce an OPPP version customized for our system. Mira Solutions concluded that our configuration was incompatible with the automated processing of OPPP.

We began discussions with ITT, the developer of Interactive Data Language (IDL) image analysis software. ITT's ENVI program has a canned DEM module, which we thought might suit our needs. However, this DEM, which is designed for satellite imaging of the earth and uses a global

coordinate system, would require extensive customization to adapt to our configuration. To better fit our requirements, ITT suggested searching for a program specifically designed for short-range photogrammetry.

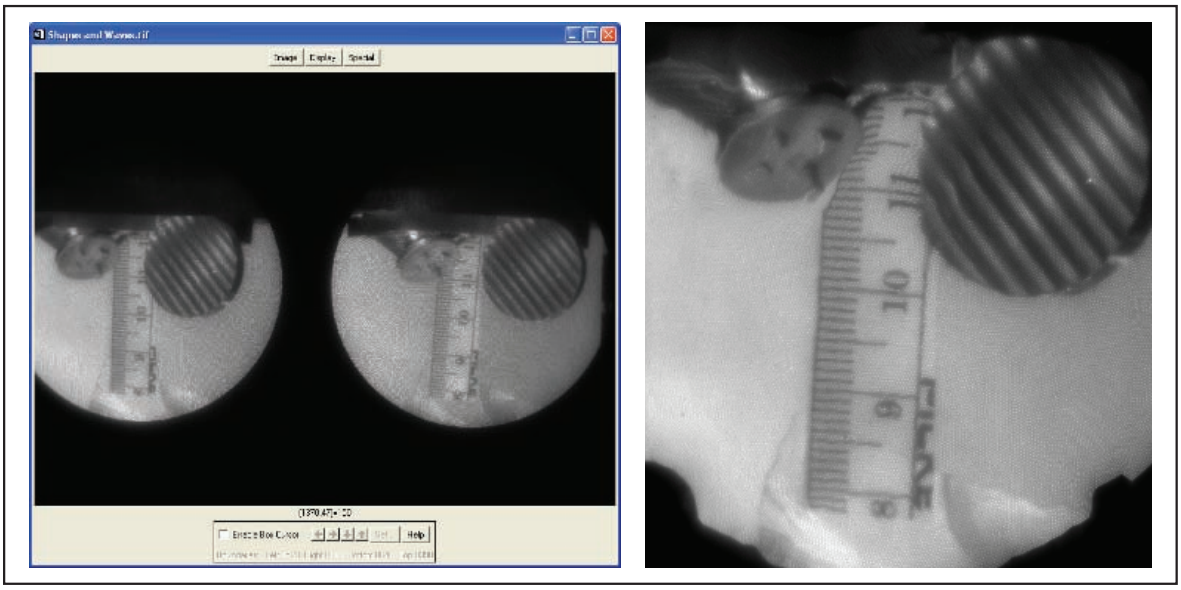

Figure 2. (Left) stereo view of static objects; (right) rectified orthophoto from SoftPlotter DEM

An Internet search for short-range photogrammetry programs revealed a number of possibilities. The most promising option was 3DM Analyst (ADAM, 2007) from Australian vendor ADAM Technology (http://adamtech.com.au/). Mining companies have extensively used 3DM Analyst to examine results of surface excavations as well as other photogrammetry applications with an imaging distance of a few feet. Several examples appear on the company's Web site. We sent the simulated images shown in Figure 3 to ADAM Technology so they could evaluate the results of their process on one of our data sets. The top left and right views in Figure 3 show the points the program assigned to correlate the stereo images and generate the DEM. The scaled DEM illustration can be rotated and zoomed, and can indicate the camera lens' proximity to the object. These results appeared ideal, and we purchased the program for further evaluation of test data. The program handles high-quality images extremely well but requires assistance in identifying correlation points in real images with signal noise and distortion. The simulated images have nearly ideal features, making correlation straightforward. Actual camera data have such features as limited signal-to-noise, resolution blur, and optical distortion. Some image conditioning or preprocessing may be needed to achieve good stereo image correlation in real data.

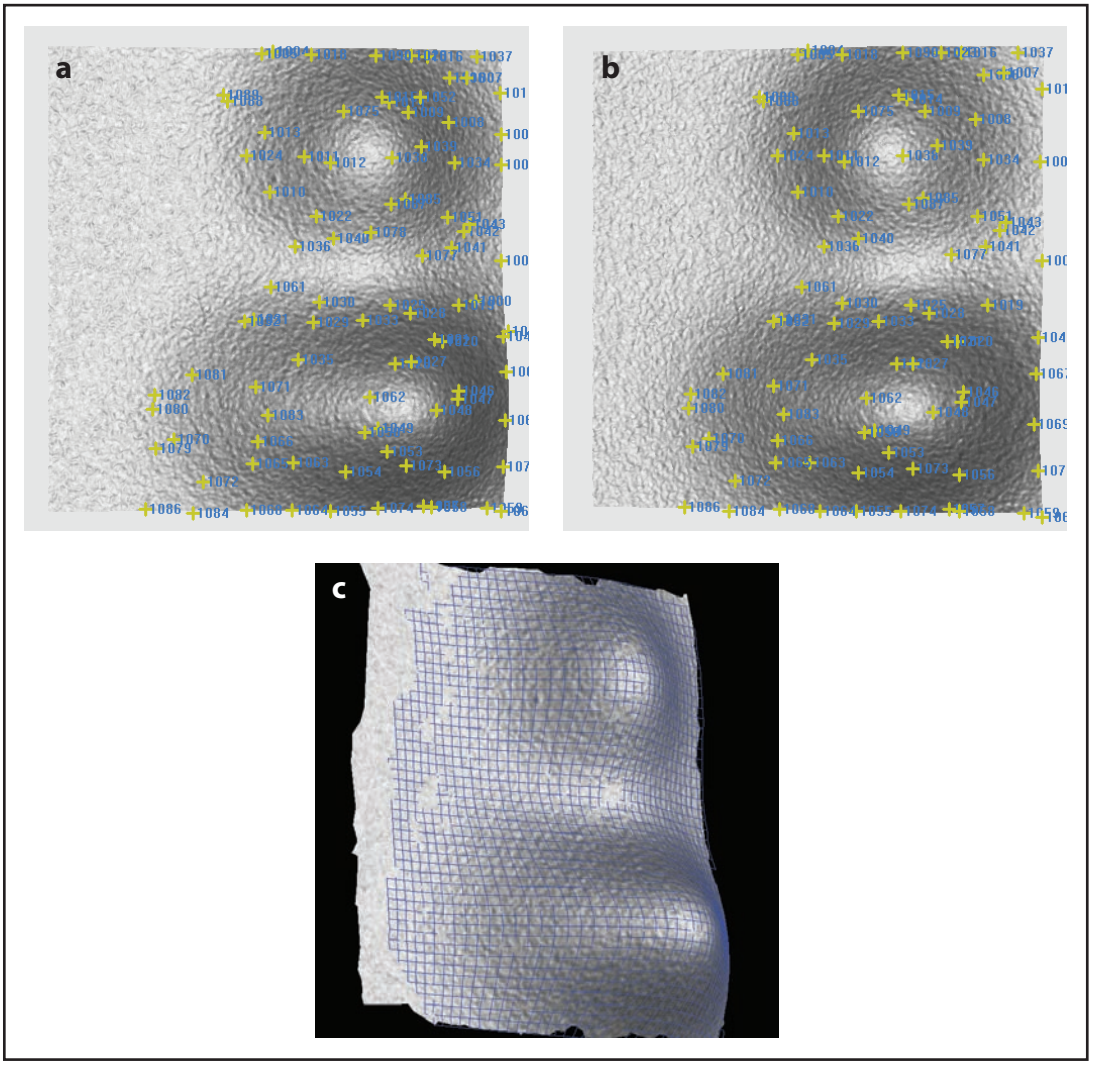

Figure 3. Simulated (a) left and (b) right views of 3D objects; (c) ADAM Tech 3DM Analyst software 3D reconstruction with scaled elevation

Dynamic Experiment

We planned to use an upgraded optical system to record a new dynamic experiment at the Special Technologies Laboratory (STL) Boom Box. The setup appears in Figure 4. The object lens is attached outside the Boom Box on a flange to allow viewing of a copper coupon through a protective blast window. We were able to upgrade our distal object lens from a tiny microprobe-type lens to a larger commercial microvideo lens. The original microprobe lens was set up for a larger 50-mm field of

view. The new microvideo lens was set up for a zoomed-in view of the 20-mm target copper coupon and resolved 1-mm lines with high contrast, allowing focusing to be accomplished with a target of 0.5-mm line spacing.

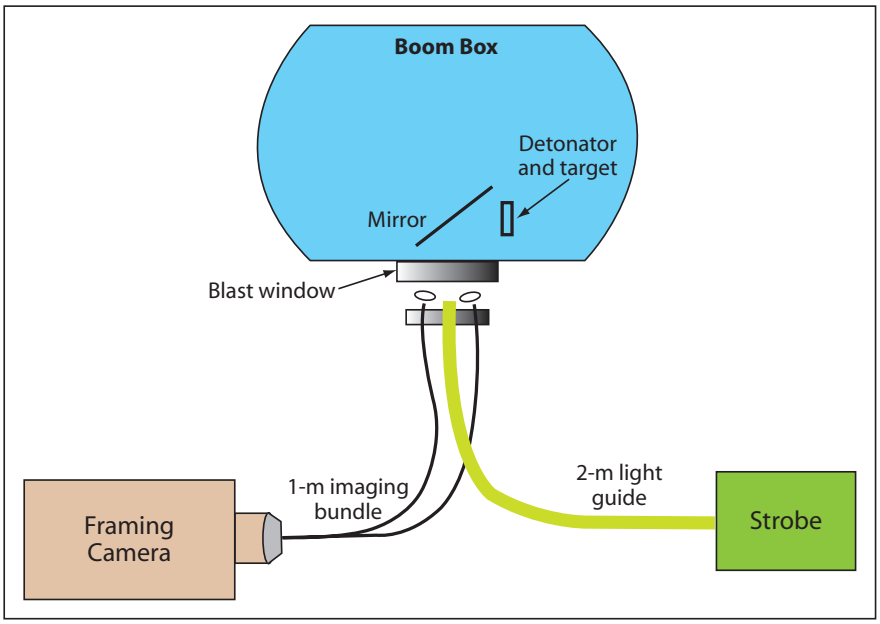

Figure 4. Boom Box setup

The larger-diameter object lens increases light collection by a factor of approximately five and improves limiting resolution approximately six times. Limiting resolution is the maximum viewable resolution in line pairs per millimeter (lp/mm). Table 1 shows the increase in shot data average signal and in system resolution.

Table 1. Object lens improvement

	Object Lens	Exposure Time (ns)	Signal	System Resolution Limit (lp/mm)
Jul-06	microprobe	500	330	1.8
Aug-07	17.5-mm microvideo	400	1240	11

Table 2 describes our shot series. We recorded a series of five shots on 2-mm-thick copper coupons 20 mm in diameter, with either slots or v-grooves machined into the front surface of the coupon. The machined slot was designed to create a strong jet of material emerging from the shocked surface, to have a nice 3-D surface to view. We started the series with longer exposure times to look for good signal levels, at the expense of seeing motion blur on longer exposures. Two shots were taken in air, and three had the coupon target chamber purged with helium. Air resistance in the target chamber caused the jet to mushroom out as it left the surface. The helium environment had less air resistance, resulting in a pencil jet leaving the surface. Shot 2 had a weak helium purge, and the image appears as an air shot. Shot 3 is shown in Figure 5. With the aid of a stereo viewer, these frames are easily fused visually by the eye, indicating that we have recorded good 3-D content. Shot 3 has dramatic 3-D effects and appears to be a good test case for photogrammetry correlation with 3DM Analyst. The software was able to automatically correlate simulated stereo data but not actual shot data. The program includes functionality that allows a user to identify correlation points, but we were unable to verify that with our data this fiscal year.

Table 2. Shot series with copper coupons

	Pattern	Slot Depth and Width (μm)	Gate Exposures (ns)	Environment
Shot 1	cross slot	500 × 150	820	air
Shot 2	cross slot	500 × 150	820	helium/air
Shot 3	cross slot	500 × 150	400	air
Shot 4	cross slot	500 × 150	400	helium
Shot 5	cross groove	60 × 240	300	helium

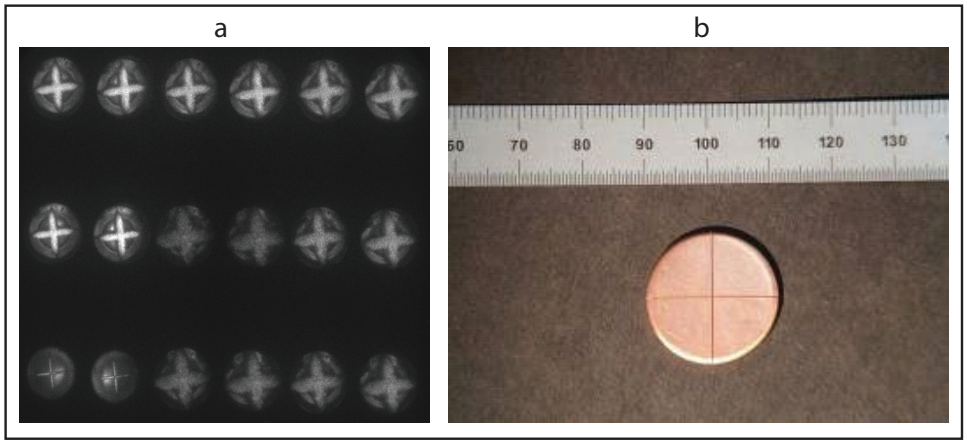

Figure 5. (a) Dynamic nine-frame image, Shot 3; (b) copper coupon with machined slot

Conclusion

Much effort was spent pursuing the OPPP solution. This approach showed promise when used with an in-house-developed code but required a great deal of manual interaction. Desired results of an automated stereo image correlation program were not achieved, and OPPP had to be abandoned. The selection of a short-range photogrammetry program appears to be the correct solution, but further work with stereo image correlation of test cases is needed to provide a firm conclusion. Although the 3DM Analyst program has worked well in correlating simulated images in an automated fashion, it struggles with actual data. Additional research is needed to develop correlation techniques for actual non-ideal image data. Manually identifying a 2-D or 3-D grid of correlation points may allow the program to automate processing. Image preprocessing, such as data smoothing to improve signal-to-noise ratio and/or edge sharpening to reduce resolution blur, may also help.

The image bundle used combines two views into one camera. This combining creates a resolution element limit, due to the number of available pixels. Recording each view on individual cameras would improve system resolution but would double the number of cameras needed. Better resolution would upgrade image correlation factors. The larger commercial object lenses were a big step in enhancing system performance. Future improvements may include removing the lens at the camera end on a larger area image bundle, coupling the bundle directly to the camera, which would greatly improve optical efficiency and resolution.

Single line-of-sight SVI is currently in use regardless of its depth perception limitation. The stereo Boom Box shots show dramatic 3-D effects, which have sparked interest in the diagnostic community. Successful data processing would present a strong case for fielding stereo SVI on a future dynamic explosive experiment.

Acknowledgments

We would like to acknowledge the following individuals: Doug Devore, Paul Flores, Brent Frogget, Daniel Marks, Joshua Tybo (Los Alamos Operations); Heather Gledhill, Sherman Wu (Remote Sensing Laboratory); Mike Grover, Gerald Stevens, Dale Turley (STL); and Dan Sorenson and Mark Wilke (Los Alamos National Laboratory).

References

ADAM Technology home page and reference information, http://adamtech.com.au/, accessed March 10, 2007.

Baker, S. A., "Stereoscopic Borescope," *Nevada Test Site–Directed Research and Development,* FY 2006, National Security Technologies, LLC, Las Vegas, Nevada, 2007, 287–294.

Wu, S. S. C., "Real-time Photogrammetric Mapping System," *Nevada Test Site–Directed Research, Development, and Demonstration,* FY 2003, Bechtel Nevada, Las Vegas, Nevada, 2004, 149–154.

Wide-range Streak Camera

D. Taner Bilir[1]
Livermore Operations

This research continued FY 2006 work in which a wide-range (800 ps–300 μs) ramp generator was designed (Bilir, 2007). In FY 2007, we constructed, tested, and revised the wide-range ramp generator, demonstrating ±1200-V ramps from 2 ns to 3 μs. We designed and constructed a power distribution circuit for ±3000-V deflection supplies, a –500-V common-mode bias supply, and also a variable, wide-range gating circuit that demonstrated –1000-V square-width pulses from 100 ns to 100 μs. These components make up the greater part of a new set of streak camera electronics that will provide flexibility and cross-platform compatibility for streak cameras designed by National Security Technologies (NSTec).

Background

Streak cameras are primary diagnostic tools in many large-scale U.S. DOE experiments. As such, the quantity and quality of data collected is of the utmost importance. In recent years, there has been a trend toward using inferior streak camera systems due to ease of use, flexibility, and cost considerations. NSTec produces some of the highest quality streak camera systems available today, but due to high cost and lack of flexibility, scientists have been choosing cameras produced by commercial manufacturers, which can have less than 5% of the data record (Bilir, 2007), and lower quality data in terms of both spatial and temporal resolution.

NSTec streak cameras are more expensive and offer less fielding options than commercial cameras in part because they currently require a different set of electronics for several sweep ranges. Maintaining several versions of electronics is difficult from a documentation perspective, and the labor to install and configure the unique sets of electronics is considerable. A wide-range NSTec streak camera could obviate the need for several sweep range designs, while adding the desirable flexibility. Additionally, if the electronics were compatible with many types of streak tubes, cross-platform savings could be achieved.

This project strove to produce a set of streak camera electronics that could be used in either the Los Alamos Operations (LAO) Gen V or the Livermore Operations (LO) LOE07 streak cameras. Amy Lewis of LAO had previously demonstrated ±1200-V ramps, which achieved 300 μs (Bilir, 2007). We planned for sweep operation from 2 ns to 500 μs with enough linear ramp voltage, specifically a linear ramp of 1200 V into a deflection plate capacitance of 15 pF (Bilir, 2007), to drive the deflection electrodes of the commercial Photek and Photonis tubes, as well as the LO BN50 streak tubes.

[1] bilirdt@nv.doe.gov, 925-960-2626

Project

This project continued FY 2006 SDRD work (Bilir, 2007), which was the design of a fast- to medium-range negative-going sweep board that covered continuous 800 ps–1 μs ramps. We had not yet fabricated the PCBs or completed testing. We developed the following project task priorities:

- Ramp circuit development and testing
  - » Fabricate negative fast/medium ramp board (NFMRB)
  - » Construct NFMRB and test performance
  - » Revise design based on tests
  - » Design and fabricate positive fast/medium ramp PCB when NFMRB is complete
- Gate circuit development and testing
  - » Determine devices and core circuitry
  - » Design wide-range gating circuit
  - » Layout design on PCB
  - » Fabricate and test
  - » Revise design based on tests
- Power circuit development
  - » Determine power supplies
  - » Design power circuit
  - » Layout design on PCB
  - » Fabricate and test

Since these were separate efforts, we approached the processes in parallel. This allowed us to design one circuit while another was being laid out, and a third was being fabricated. This methodology worked fairly well for the duration of the project.

Ramp Circuit Development

For the ramp development, we determined that the 3000-V ramps were higher than needed, so we reduced the supply voltage to 2500 V. This allowed us to remove some stages from our avalanche diode and metal-oxide semiconductor field-effect transistors (MOSFET) stacks, decreasing the size of our circuit. This also had the effect of slowing down the avalanche stack ramps from 800 ps to 2 ns, which was our design goal. Should ramps faster than 2 ns be desired, only a simple design

modification would be required to achieve 800 ps again. The avalanche section of the board uses simple filter circuits to attenuate the slope of the ramps. The three fastest sweeps from the negative ramp board are shown in Figure 1.

For the medium speed section of this board, MOSFETs switch the voltage, and high-frequency capacitors connected between the MOSFET gates set the slope. Lewis' design for extended slow range ramps modifies these gate capacitors by switching in additional capacitances with high-voltage relays in order to change the ramp range. Some medium-speed section data without the Lewis modification are shown in Figure 2. This figure demonstrates a range of 80 ns to 1.5 μs, though a range of 30 ns to 3 μs was achieved in our work.

If the Lewis modification were added, this range could extend to several hundred microseconds (Bilir, 2007), thus achieving the desired range goal.

Gate Circuit Development

Developing the wide gate circuit was of major importance in our research. The gate circuit provides a pulse on a streak tube photocathode that biases the extraction field such that electrons travel toward the accelerator electrode. For the Advanced Sensor Development Group streak tube at LO, the required voltage is 1000 V. In order for this pulse to remain on for the longest sweep duration, it would need a maximum pulse width on the order of 1 ms. Previous SDRD research (Diamond, 2005; Bilir, 2006) suggested that IXYS Corporation's DEI275X2-102N06A power MOSFETs would have the requisite voltage and current capabilities desired for the gating circuit. Figure 3 shows the performance of the gating circuit as a function of pulse width between 100 ns and 160 μs. On the wider pulses, some drooping in the return amplitude can be observed. We believe this is due to the wide pulse on the trigger section of this circuit, but more testing must be done to confirm our assumption.

Power Circuit Development

Meanwhile, positive and negative 3000-V power supplies were researched for use with these new ramp circuits. Due to the sensitivity of electron optics, the ramps needed to be extremely stable; thus, linear supplies were chosen over switching supplies. The EMCO H30N and H30P supplies had sufficient power to deliver the full 3000 V into the deflection plate capacitance for the slowest sweeps, and had no noticeable ripple or drift when measured with a 1-GΩ probe. Additionally, a common-mode supply, the EMCO CA05N, was chosen to provide the common-mode bias on the deflection plates. This supply was chosen because it too was linear and highly stable, but did not need the same power delivery as the deflection supplies.

Conclusion

We constructed, tested, and revised the wide-range ramp generator, demonstrating ±1200-V ramps from 2 ns to 3 μs. Lewis had previously demonstrated ±1200-V ramps in FY 2006 (Bilir, 2007),

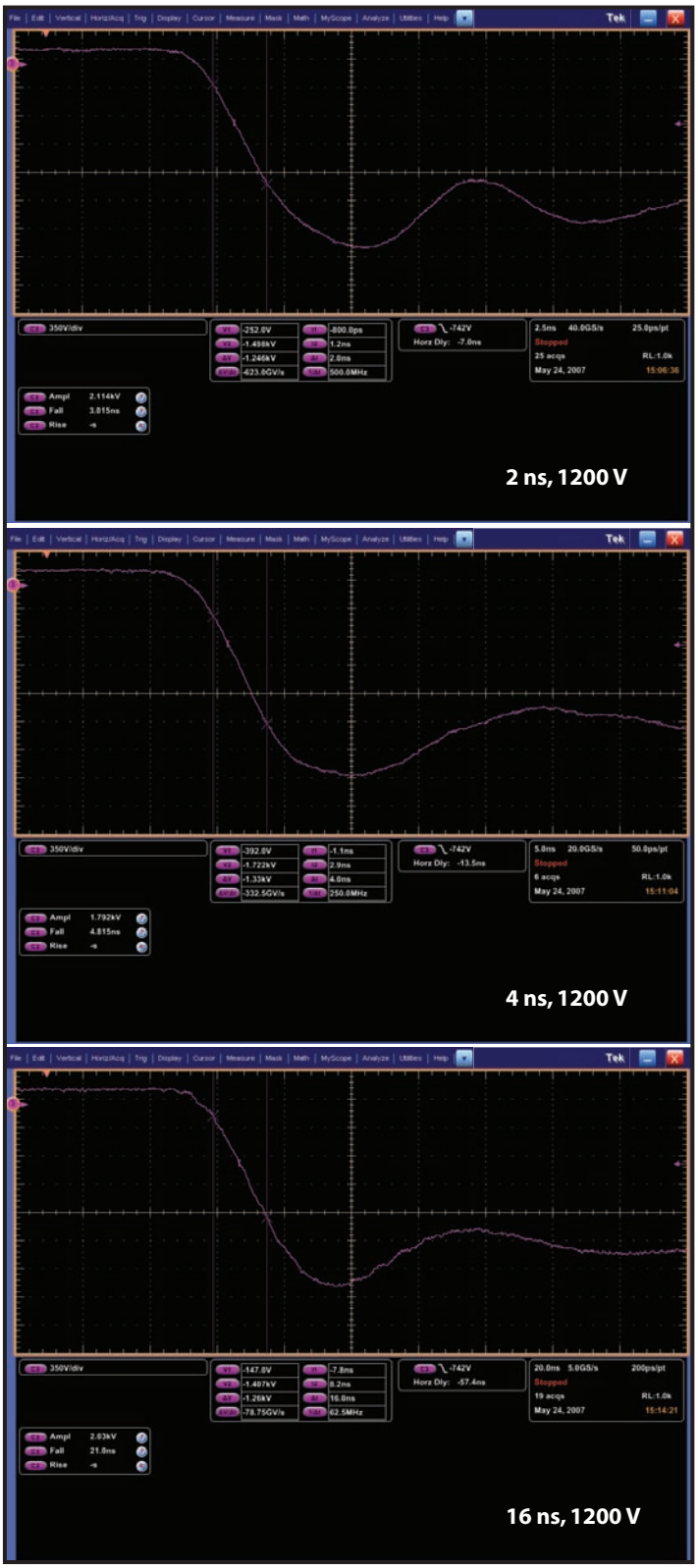

Figure 1. Three fastest sweeps (2 ns, 4 ns, and 16 ns) from negative ramp board, switching 1200 V. Filters can be designed to run longer than 40 ns.

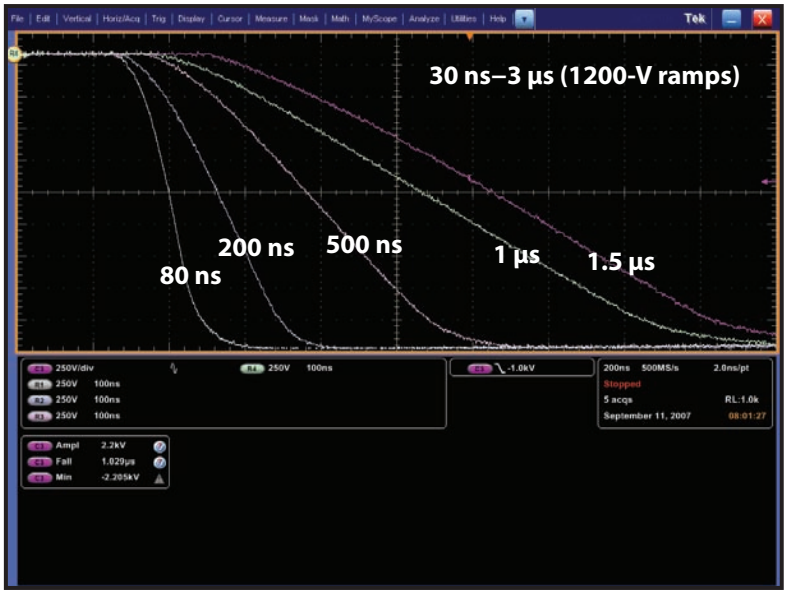

Figure 2. A range of ramps in the MOSFET stack section

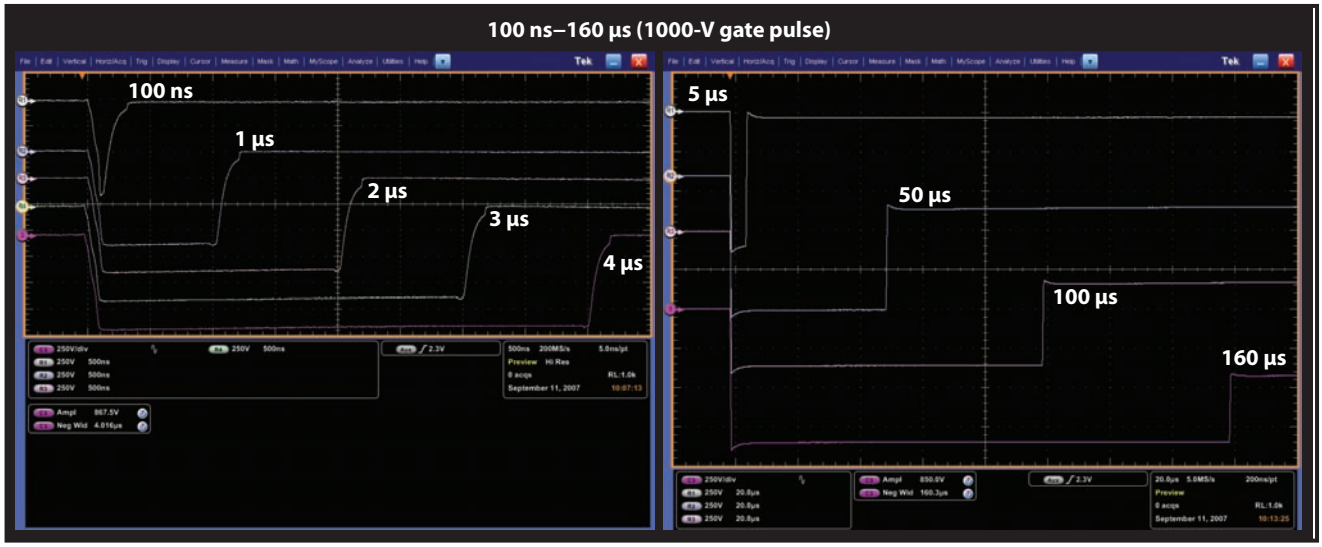

Figure 3. Wide-range gate performance

which achieved 300 μs. A power distribution circuit for ±3000-V deflection supplies and a –500-V common-mode bias supply were designed and constructed, as was a variable, wide-range gating circuit that demonstrated –1000-V square pulses from 100 ns–100 μs in pulse width. These circuits comprise most of the new set of streak camera electronics that will provide flexibility and cross-platform compatibility NSTec streak cameras. We believe this research is ready for programmatic application under stockpile stewardship activities.

Acknowledgments

The following team members were essential in the success of this research project: J. O'Connor, for his circuit design expertise; J. Cradick and W. Warthan, for all their efforts in fabrication and testing; and J. Mirador, for his circuit board design and prototype fabrication efforts.

References

Bilir, D. T., "High-Power Pulser," *Nevada Test Site–Directed Research, Development, and Demonstration,* FY 2005, Bechtel Nevada/National Security Technologies, LLC, Las Vegas, Nevada, 2006, 223–229.

Bilir, D. T., A. Lewis, "Wide Range Streak Sweep Circuits," *Nevada Test Site–Directed Research and Development,* FY 2006, National Security Technologies, LLC, Las Vegas, Nevada, 2007, 249–255.

Diamond, C. E., "High-Power Pulser," *Nevada Test Site–Directed Research, Development, and Demonstration,* FY 2004, Bechtel Nevada, Las Vegas, Nevada, 2005, 191–196.

Terahertz Time-domain Spectroscopy and Imaging

Robert Buckles[1]
Livermore Operations

The technical goal of this project was to assemble and demonstrate a terahertz time-domain spectroscopy (THz-TDS) system. The original scope included using an existing THz-TDS system, developed over the past six years in collaboration with Lawrence Livermore National Laboratory (LLNL) and the University of California, Davis (UCD), and modifying it for hydrodynamic THz imaging. However, UCD made a successful case to NNSA to grant the equipment to them. In lieu of that hardware, we had to reduce the scope to simply building up a new THz-TDS system. By borrowing the requisite lasers (8-W 532-nm diode-pumped solid-state [DPSS] continuous wave pump laser from the National Security Technologies [NSTec] Special Technologies Laboratory [STL], and 1-W 80-MHz titanium-sapphire oscillator from LLNL) and making a modest purchase of optics, we managed to achieve our new goal in just one year. The technical challenges faced and solutions achieved are presented here, many of which are similar to those found in the vast body of published literature on THz technology. Further experimentation using the system will be the focus of future work.

Background

The formation of high-Z beam target plasma in advanced radiography machines (the dual-axis radiographic hydrodynamic test [DARHT] facility, Experimental Test Accelerator [ETA], Z machine, the radiographic integrated test stand [RITS], etc.) is detrimental to dose and resolution (Ekdahl, 1975; Caporaso, 2007). High-voltage breakdown and plasma formation dynamics are widely present in such pulsed-power machines, and this remains a general field of study (Sampayan, 2001; Kolner, 2005). Researchers have sought means to investigate the plasma phenomenon, to better understand and perhaps mitigate its effects (Capelle, 2007; Jamison, 2003). It remains a tough problem, as most diagnostics indirectly probe the plasma, with charge collection or electromagnetic emission diagnostics. A direct diagnostic is one that invariably measures the instantaneous electron density and collision rate of the plasma. Microwave and millimeter-wave beams, far-infrared lasers, and optical lasers have been routinely employed in this regard for some decades, but are usually fixed in frequency, resulting in limited dynamic range. The plasma density range encountered in our experiments varies dramatically over a short microsecond time scale (10^{12}/cc to 10^{16}/cc) and can only be directly probed at the limits of this range with the wavelengths historically available to us (Heald, 1965). A single broad-band THz pulse has sufficient bandwidth to instantaneously probe this whole plasma range. THz technology has evolved quickly over the last decade, with components and

[1] bucklera@nv.doe.gov, 925-960-2520

systems becoming commercially available. High-powered, single-pulse THz imaging systems have recently been demonstrated in the laboratory (Shan, 2000). We aim to be the first researchers to apply the technology to probe a hydrodynamic sample and yield temporally and spatially resolved direct measurement. Other widespread interest includes reflectometry of shocked metallic surfaces to detect solid phase changes, and probing ultrafast electron beams (Kruschwitz, 2008).

This technology can also be used for inspection and security applications. With some limitations, THz waves can penetrate optically opaque materials and have sufficient spatial resolution to image objects. THz screeners are very similar to x-ray screeners, except they are nonionizing, and hence are being applied toward screening people at security checkpoints. Privacy issues stand in the way of widespread use, as clothing is quite transparent (NAP, 2007). The spectroscopic capability of THz technology is also well suited for security applications, as it provides molecular specificity. With probing capability, it is conceivably sufficient to detect sealed explosive material. We plan to direct the successes of this SDRD project at improvised explosive devices (IEDs) and homemade explosives detection, in addition to Stockpile Stewardship.

Project

The minimum project requirements included an ~100 fsec class-4 laser and a place to operate it. We installed a 4' × 8' optical table, built an equipment rack over it to house the needed hardware, installed laser interlock and access controls, prepared a laser safe operating procedure (LSOP), and turned the room into an authorized laser lab. Earthquake restraints for the table, load calculations, the LSOP, and mechanical and laser safety authorization took more than six months to complete once items were specified, leaving about one month for testing. We were loaned a Coherent 8-W DPSS Verdi laser for the pump source and a Spectra Physics Tsunami titanium sapphire (Ti:S) laser oscillator.

At mid-year all the pieces of the project coalesced sufficiently to drive a THz-TDS system. To make up for lost time, we started shopping for an inexpensive terahertz "kit," a fully specified collection of opto-mechanical hardware and optics, ready to be assembled. Such components can now be bought as commercial off-the-shelf equipment, from companies like Newport and Advanced Photonics, Inc. (Picometrix). We chose an intermediate solution, from Ekspla, mostly due to low cost and a short timeframe, but also due to our recent experience with the excellent quality of their picosecond Nd:YAG laser. The THz-TDS system was not a complete turnkey solution such as Picometrix offers, nor individual components such as Newport offers. However, it does come fully assembled on a breadboard, with various options, such as a nitrogen purge box, sample stage, dual-phase digital signal processing lock-in amplifier from Stanford Research Systems, and LabVIEW source code, all tested before shipment. Figures 1 through 4 show the assembled laser laboratory and equipment.

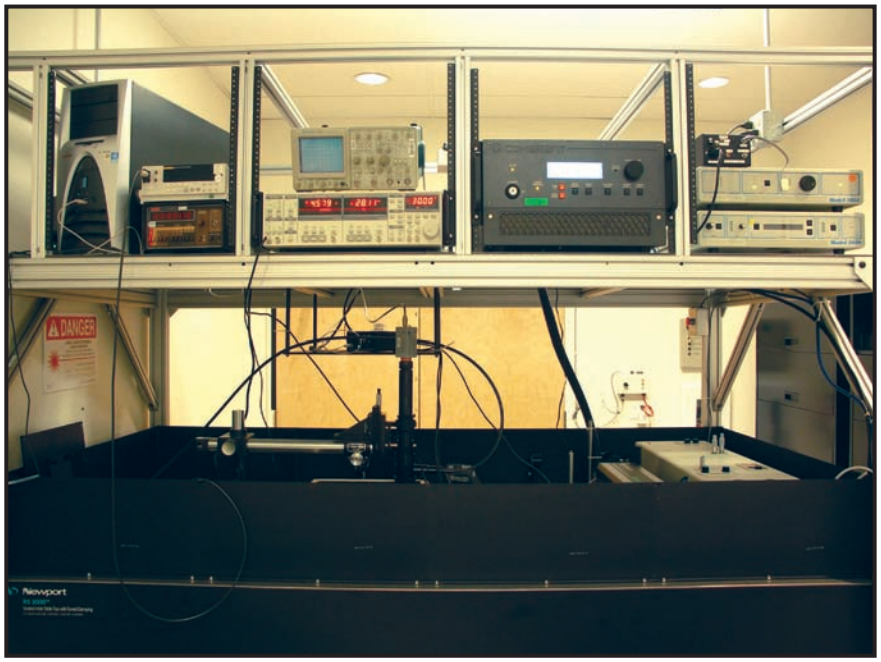

Figure 1. Laser laboratory and equipment. On the right are the Ti:S laser systems; on the left are the lock-in amplifier, scope, signal sources, and computer control and acquisition.

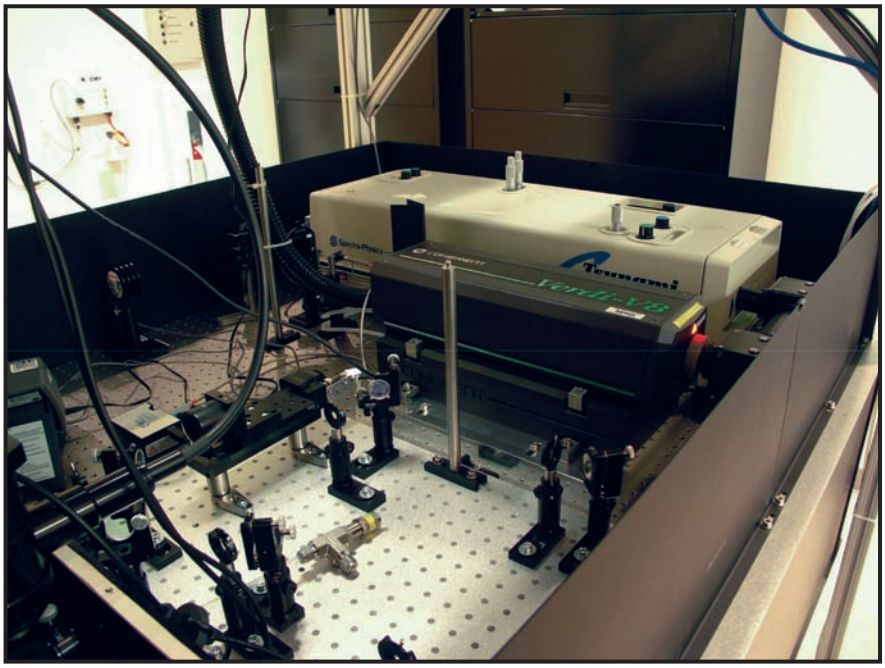

Figure 2. Verdi and Tsunami lasers. Interlock systems and storage in background, Ekspla THz-TDS in foreground.

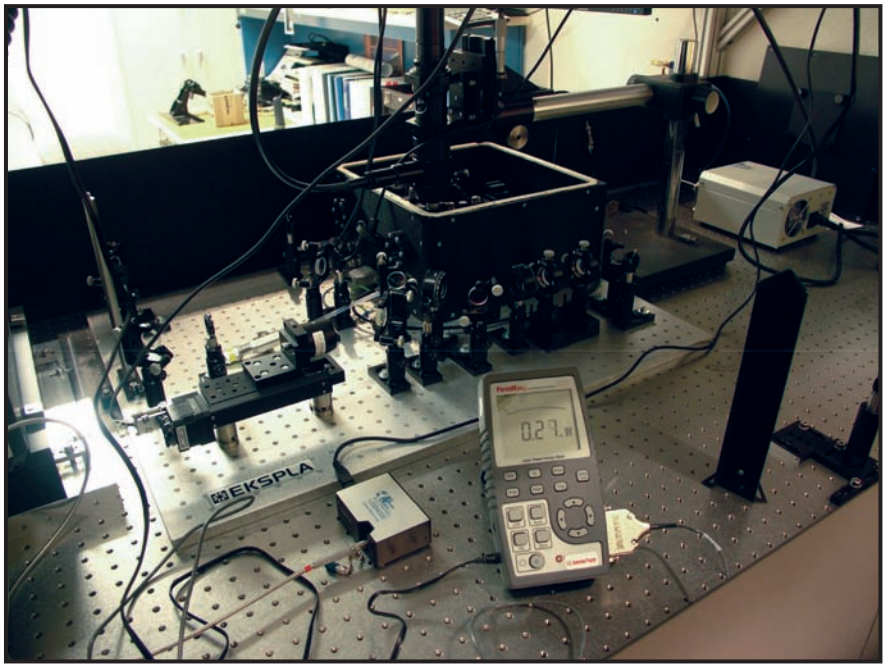

Figure 3. Ekspla THz-TDS system. Ocean Optics spectrometer, Coherent laser power meter in foreground. Time delay stage, beam relay optics, and purge box in background. Microscope placed above THz components is for inspection purposes.

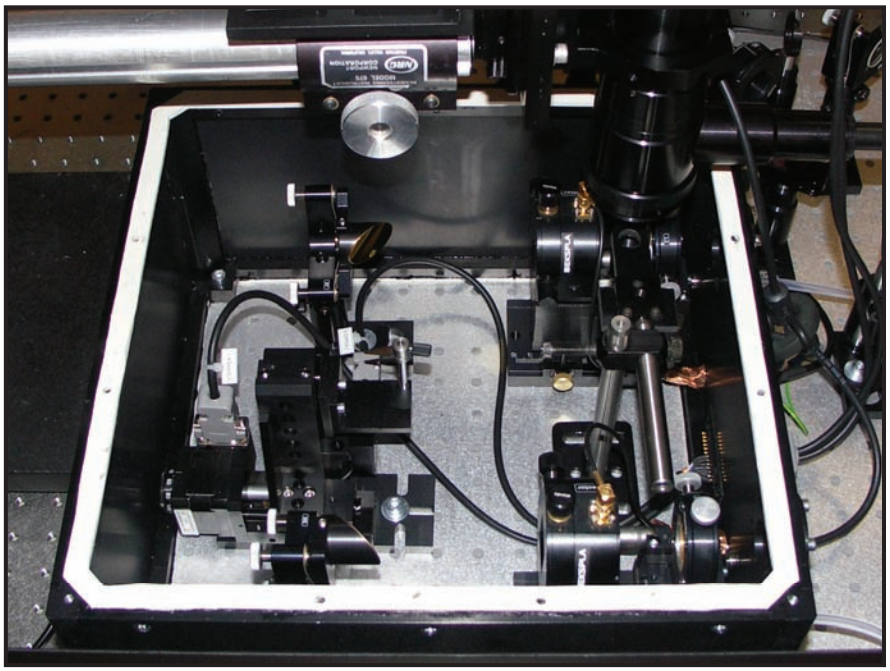

Figure 4. THz components inside purge box. Emitter and detector on right with laser windows and focusing optics. Off-axis parabolic mirrors and sample stage on left. Inspection microscope above.

The key components of any THz system are THz generation and detection. Two methods of each are generally used in a TDS system. Optical rectification and electro-optical detection are necessary for a veritable imaging system. The explanation of such details lies beyond the scope of this report, and is available elsewhere in published works (Auston, 1985; Zhang, 1990; Winnewiser, 1997). Such techniques will be used in the intended hydrodynamic THz imaging system. Photoconductivity is the preferred method for generation and detection of THz, and is widely used, especially in commercial systems. Much research and engineering has been devoted to the development of these devices over the past few years, so we offer only this abbreviated explanation.

A coplanar transmission line is lithographically deposited on the surface of a high-resistivity semiconductor substrate with the right band gap, absorption, and ultrafast recombination properties for sub-picosecond laser pulses (gallium arsenide [GaAs] in this case). Generally, the spacing of the lines scales with the available pulse energy. Fifty-μm spacing is adequate for nanojoule pulses. The biased electrodes will conduct photo-generated carriers when its substrate is exposed to light (above band gap). The dynamics can be quite prompt for a high-mobility material. A molecular beam epitaxy process is an excellent means of tailoring material properties. By adding excess arsenic and then annealing at a relatively low temperature (~300°C as opposed to ~900°C for standard GaAs), the excess arsenic will form finely dispersed metallic precipitates, providing recombination sites for electron hole carriers. This is referred to as "low-temperature"–grown gallium arsenide (LT-GaAs), and provides substantially faster recombination than standard GaAs, resulting in higher bandwidths.

Maxwell's equation for Ampere's Law summarizes the radiation effect, where E and B are electric and magnetic field respectively, and J is photo-induced current density:

$$\vec{\nabla}\times\vec{\nabla}\times\vec{E} = -\frac{\partial\vec{\nabla}\times\vec{B}}{\partial t} = -\mu_o\frac{\partial\vec{J}}{\partial t}. \quad \textbf{(1)}$$

Essentially, this is a wave equation, but more apropos for the radiated THz field magnitude:

$$E(t) \propto \frac{\partial J}{\partial t}. \quad \textbf{(2)}$$

The current density is unipolar, and nominally follows the envelope of the optical pulse. It increases on the rising edge and decreases on the trailing edge (for sufficiently fast recombination time); hence, the radiated THz electric field is a single monocycle, approximately the width of the optically stimulated current pulse. The radiation pattern is that of a dipole point source; however, it is constrained by the substrate. The high dielectric constant of the material allows total internal reflection except in a narrow cone near normal incidence. To circumvent this, a high-resistivity silicon hyper-hemisphere is placed against the back of the substrate. Not only does this increase coupling (all air interfaces are near-normal) but it provides some collimation of the output radiation.

It is not clear whether this photoconductive switch technology is "owned" by any one entity. It appears to be in the public domain, being based on the work of hundreds of investigators. Nevertheless, Ekspla has engineered a very compact package with all the right controls for a developmental system. The LT-GaAs chip is mounted and wire-bonded to a circuit package with an SMA connector, and the mount also retains the silicon ball lens pressed to the back of the chip. The ball lens can be translated in the plane with an X-Y adjustment. Likewise, the laser input lens has an X-Y adjustable mount, and both mounts are held on a carrier with either or both translatable in Z individually or as a unit. This is the best possible optomechanical configuration. Picometrix offers a more compact sealed unit with fiber coupling, which is great for a turnkey solution. However, fiber coupling has certain limitations as well, which do not suit our needs for an imaging system.

The detector is fashioned in the same manner, except the optimal laser focal spot is close to the positive electrode (due to thermally generated space-charge) and spacing is smaller than in the emitter. Rather than applying a DC bias to the electrodes, the optically gated photo-carriers are integrated over time. The average current amounts to a few hundred picoamperes for this system. The signal-to-noise ratio (SNR) is improved dramatically by lock-in detection. The emitter bias is modulated at a few tens of kilohertz, enough to get clear of the 1/f noise of the laser, and the THz beam carries this same amplitude modulation. The detected photocurrent is imposed by the THz beam electric field on the detector and carries that same modulation. The lock-in amplifier is a tuned narrow-band receiver and filters out as much as 80–100 dB of the overall noise, enabling detection of very weak signals. It provides the same modulation frequency to the emitter bias circuit.

The time-domain aspect of this system is extremely significant. Since the receiving signal is stimulated by the temporal gating effect of the "probe" laser beam, it is a coherent system. The average photocurrent is representative of the THz electric field at the precise moment the optical probe arrives at the detector and stimulates carriers. By delaying the optical probe with respect to the THz "pump" beam, the THz electric field can be mapped. (This is quite similar to a sampling scope.) The advantage of this setup is that electric field is measured as opposed to intensity or power, such as is done with golay cells or bolometers. Bolometers are good for absolute power calibrations, or looking at nebulae, but they are far too slow for rapid, high-SNR measurements. And since electric field is measured, the THz-TDS system can measure the complex dielectric properties of materials (both absorption and phase shift simultaneously) without resorting to Kramers-Kronig relations, which would require more precise measurement of lineshape, and greater bandwidth. This is analogous to using a vector network analyzer as opposed to a spectrum (scalar) analyzer.

Figure 5 shows a simplified schematic of the system. Figure 6 shows a representative scan (no sample) with water vapor purged from the system, and its Fourier transform amplitude spectrum.

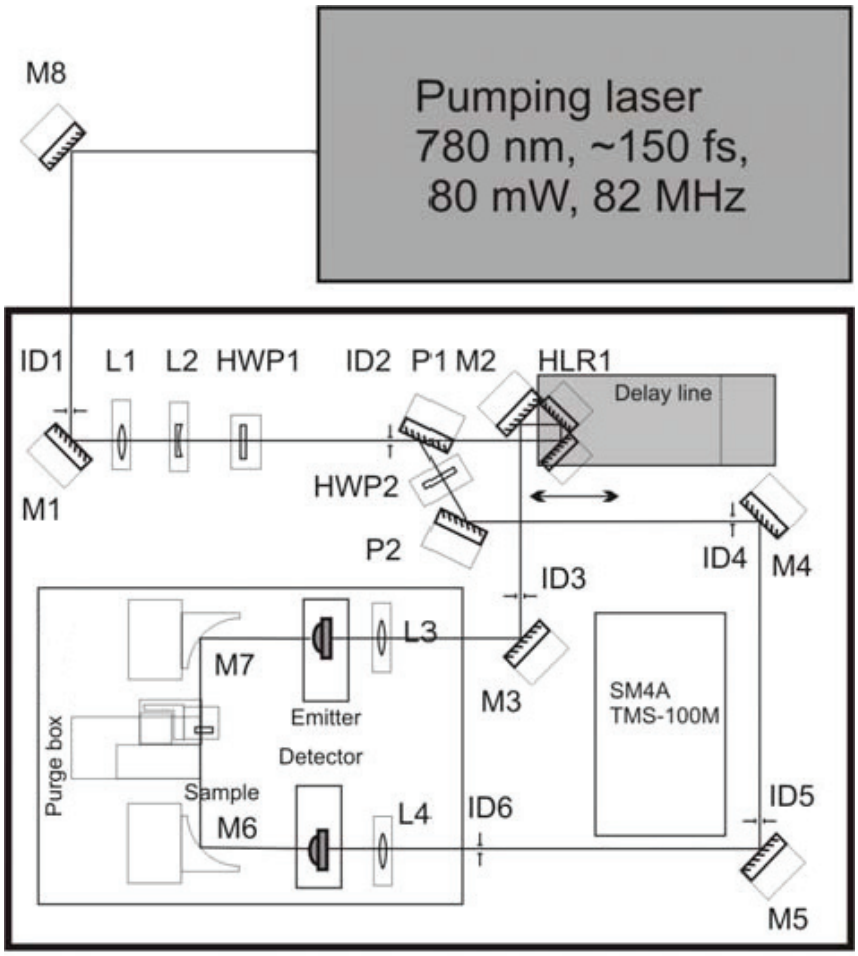

Figure 5. Schematic of THz-TDS system. Half-waveplates and polarizers split the beam into pump and probe arms, and set the input power level. SM4A stepper controller operates the delay line. The TMS-100M provides emitter bias modulation.

Spectroscopy is performed by simply acquiring a reference scan as in Figure 6, repeating with a sample in the THz path, and taking the ratio of the Fourier transforms (which are complex, having amplitude and phase), resulting in the absorption and phase shift through the sample. Knowing the length of the sample will yield attenuation and propagation coefficients as a function of frequency. However, a thin sample will produce triple and quintuple transit-time echoes for a long enough scan. Accounting for these in the analysis will yield material thickness, without knowing it a priori. Non-uniform distribution of material can be measured as well, such as a plasma. One must only make a best-fit model to the observed phase shift and attenuation data.

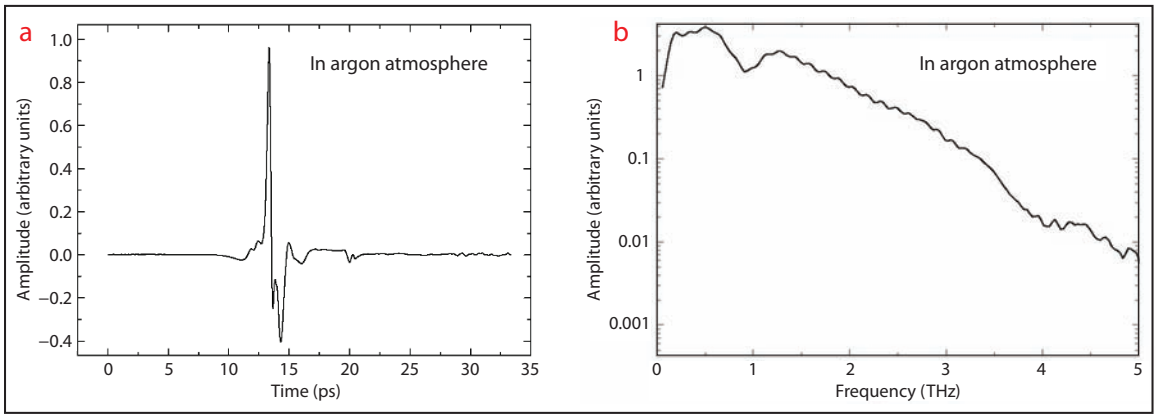

Figure 6. (a) Representative time-domain waveform - no sample. (b) Fourier transform of waveform. Courtesy of Ekspla.

Conclusion

We assembled and tested the THz-TDS system. Optimization to our laser beam propagation characteristics was under way at the time of this publication, as well as cable shielding improvements to reduce interfering feedthrough signals from the modulation source to the lock-in amplifier. In early FY 2008 we will begin measuring samples of interest to security screening and IED detection. We will also begin augmenting the system for electro-optical detection and optical rectification using ZnTe crystals instead of the LT-GaAs chips. It is an evolutionary process, as some signal indication is required before detecting the THz beam. We intend to use a focal-plane balanced photodiode array as the receiver, and construct a THz line-imaging system, with temporal delay, or spectra created by a geometrical delay rather than time-delay scan. This will evolve into a single-shot THz imaging system. An existing Quanta-Ray YAG laser and target chamber will be prepared for production of laser plasmas. Once ready, we will use an amplified Ti:S laser to generate high-powered THz pulses through electro-optic rectification. The laser plasma is a surrogate sample for more complex pulsed-power devices. We will explore the dynamics of laser plasma plume generation.

Acknowledgments

We are indebted to Roderick Tiangco at the Special Technologies Laboratory and Steve Vernon at LLNL for the generous use of their lasers. Kevin Sun was instrumental in brokering the loan. Many thanks go to the technical staff for obtaining equipment and establishing the laboratory: Albert Traille, William (Billy) Warthan, and Jerald Cradick.

References

Auston, D. H., K. P. Cheung, "Coherent time-domain far-infrared spectroscopy," *J. Opt. Soc. Am. B: Optical Physics* **2**, 4 (April 1985) 606.

Capelle, G., R. Tiangco, "Resonance Shadowgraphy," *Nevada Test Site-Directed Research and Development*, FY 2006, National Security Technologies, LLC, Las Vegas, Nevada, 2007, 1–6.

Caporaso, G. J., S. Sampayan, Y.-J. Chen, D. Blackfield, J. Harris, S. Hawkins, C. Holmes, M. Krogh, S. Nelson, W. Nunnally, A. Paul, B. Poole, M. Rhodes, D. Sanders, K. Selenes, J. Sullivan, L. Wang, J. Watson, "High Gradient Induction Accelerator," *Proceedings of the Particle Accelerator Conference*, Albuquerque, New Mexico (2007).

Ekdahl, C., M. Greenspan, J. Sethian, C. B. Wharton, "Beam energy transfer and propagation in a fully ionized magnetized plasma," *J. Vac. Sci. Technol.* **12**, 6 (November 1975) 1203.

Heald, M. A., C. B. Wharton, *Plasma Diagnostics with Microwaves*, John Wiley & Sons, New York, 1965.

Jamison, S. P., S. Jingling, D. R. Jones, R. C. Issac, B. Ersfeld, D. Clark, D. A. Jaroszynski, "Plasma characterization with terahertz time-domain measurements," *J. Appl. Phys.* **93**, 7 (April 2003) 4334–4336.

Kolner, B. H., P. M. Conklin, R. A. Buckles, N. K. Fontaine, R. P. Scott, "Time-resolved pulsed-plasma characterization using broadband terahertz pulses correlated with fluorescence imaging," *Appl. Phys. Lett.* **87**, 15 (October 10, 2005).

Kruschwitz, C., M. Wu, "Exploring Phase Transition/Shock Dynamics with THz Spectroscopy," *Nevada Test Site–Directed Research and Development*, FY 2007, National Security Technologies, LLC, Las Vegas, Nevada, 2008, 17–24.

National Research Council of the National Academies, Committee on Assessment of Security Technologies for Transportation, *Assessment of Millimeter-Wave and Terahertz Technology for Detection and Identification of Concealed Explosives and Weapons*, National Academies Press, Washinton, D.C., 2007.

Sampayan, S., R. Buckles, G. Caporaso, F. C. Chambers, Y.-J. Chen, S. Falabella, F. Goldin, G. Guethlein, D. Ho, M. Heino, T. Houck, E. Lauer, J. McCarrick, R. Neurath, P. Pincosy, R. Richardson, D. Sanders, J. Weir, "Beam-target interaction experiments for multipulse bremsstrahlung converters applications," *Proceedings of the 2001 Particle Accelerator Conference*, Chicago, Illinois (June 2001) 330–332.

Shan, J., A. S. Weling, E. Knoesel, L. Bartels, M. Bonn, A. Nahata, G. A. Reider, T. F. Heinz, "Single-shot measurement of terahertz electromagnetic pulses by use of electro-optic sampling," *Opt. Lett.* **25**, 6 (March 15, 2000) 426–428.

Winnewisser, C., P. U. Jepsen, M. Schall, V. Schyja, H. Helm, "Electro-optic detection of THz radiation in $LiTaO_3$, $LiNbO_3$, and ZnTe," *Appl. Phys. Lett.* **70**, 23 (June 9, 1997) 3069–3071.

Zhang, X.-C., B. B. Hu, J. T. Darrow, D. H. Auston, "Generation of femtosecond electromagnetic pulses from semiconductor surfaces," *Appl. Phys. Lett.* **56**, 11 (March 12, 1990) 1011–1013.

Resonance Shadowgraphy

Gene Capelle,[1] *Roderick Tiangco*
Special Technologies Laboratory

In FY 2006, an experimental setup consisting of a plume generator, a tunable laser illumination system, and a CCD–based detection system was constructed, and a resonance shadowgraph image of the plume was demonstrated in our laboratory (Capelle, 2007). In FY 2007, the quality of the resonance shadowgraph image was improved to the point of being a very useful diagnostic. Further, this image quality was demonstrated at a large-standoff (equipment-to-target distance), as would be encountered at radiographic accelerators or other such facilities where this technique might be used.

Background

At accelerator-based radiography facilities, an e-beam is directed onto high-Z targets to produce x-rays for radiographic imaging. During this process, plasmas are formed on both the anode and cathode of the accelerator diode. Since these plasmas affect the produced x-ray dose and its effective source size, it is desirable to understand the plasma formation and time evolution and behavior, in order to mitigate their effects. Conventional plasma imaging diagnostics are generally limited to densities greater than $10^{16}/cm^3$. Densities earlier in the pulse, when the plasma has already begun to interact with the e-beam, are lower ($\leq 10^{15}/cm^3$) and, hence, a challenge to measure directly. In FY 2006, we created a shadowgraph image of a plasma cloud using a pulsed, excimer laser–pumped, tunable dye laser with the wavelength tuned to an atomic resonance absorption line of one of the species in a surrogate plasma cloud that we created. Normal shadowgraphy depends primarily on scattering light out of the laser beam to produce a shadow image. However, when the illumination laser is of narrow linewidth and tuned to resonance, there is a resonant absorption effect that causes the plasma "plume" to remove additional light from the beam, thus increasing the effective opacity of the plume and allowing "thinner" (lower concentration) areas of the plume to be visualized (i.e., sensitivity increases and therefore makes it possible to track the time-space evolution of the plasma from earlier times during the course of its evolution). The resonant shadowgraphy images collected at the end of last fiscal year showed plume shapes, where none could be seen with off-resonance images (i.e., "normal" shadowgraphy), but the images were of relatively poor quality and only somewhat useful in visualizing the plasma. Our goal this year was to make significant improvements in the image quality and demonstrate data collection in an experimental configuration (i.e., with a large

[1] capellga@nv.doe.gov, 805-681-2252

standoff distance [≥25 ft] between the target and the measurement equipment, such as would be encountered during actual measurements where the equipment must be placed behind the radiation barrier, a significant distance away from the target chamber).

Project

For this project, we aimed to improve the laser beam quality and the optics of our shadowgraphy system so that it would produce much higher quality images (i.e., suitable for diagnostic use) while at greater standoff distances from the target. The FY 2006 laboratory experimental setup consisted of the plume to be studied, the probe laser, and the detector. The plume system consisted of a vacuum chamber with multiple quartz windows, typically operated at a pressure of 10^{-4} torr or less, and containing a flat aluminum target. When pulsed, a small, Nd:YAG laser, focused through the top chamber window onto the aluminum target, produced a plasma above the target. Two "goalposts," one in front of the plume and one behind it, served as alignment aids (Figure 1). The shadowgraphy illumination laser was an excimer laser–pumped tunable dye laser tuned to the aluminum resonance at 394.4 nm; output was sufficiently short (24 ns) to freeze the rapidly moving plume in time. Laser illumination occured <1 μsec after the Nd:YAG laser pulse. The illumination laser was located several feet away from the plasma chamber. After exiting the plume chamber, the laser beam was optically folded by two mirrors, to allow the detector to be placed at a standoff of ~25 ft or more from the

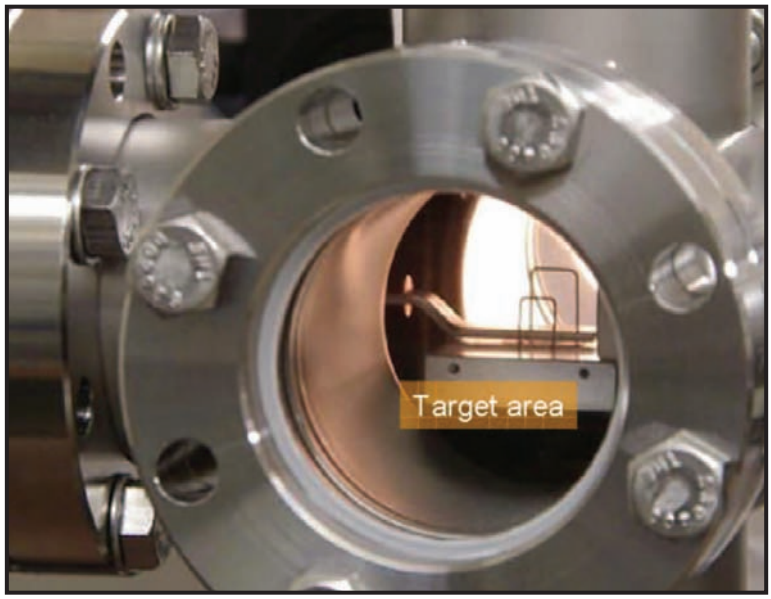

Figure 1. Plume generation area with alignment loops and movable aluminum target at base of the loops. The plasma generation laser enters through the top arm of the vacuum chamber.

target. The detector was an 8-in. diameter, 2000-mm focal length Cassegrain telescope with its input aperture masked to a 2" × 2" opening to collect light only from the area in which the dye laser beam entered the telescope; a narrow-band optical filter, plus neutral density filters, were placed in this input opening to reduce background light. A digital single-lens reflex camera (Nikon D50), mounted to the back of the telescope, recorded data. To increase sensitivity below 400 nm, the camera was modified by removing the UV/IR filter normally mounted in front of its 6-megapixel CCD chip. (This also tends to give some of the images a reddish tint.) With this configuration, the best images we could obtain last year are shown in Figure 2, and these images were taken with the laser very close to the target area.

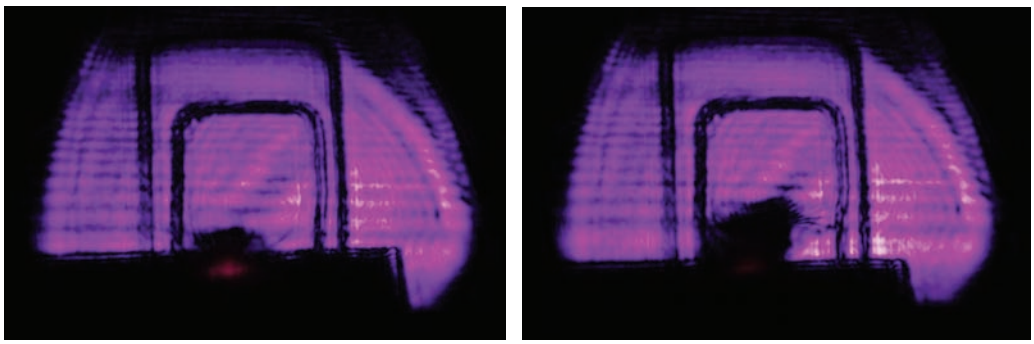

Figure 2. The two best resonance shadowgraph images from FY 2006 of the plume created by the Nd:YAG laser focused on an aluminum target were plagued by severe horizontal and diagonal fringes in illumination light. The aluminum target position was moved between shots.

Much of the beginning of this year's project was spent getting the excimer laser–pumped dye laser system back up and operating properly, after we received parts from Germany. Subsequently, we focused on improving shadowgraph image quality while at the same time moving the laser at least 25 ft away from the target area to more truly mimic actual experiment conditions. Improving image quality was synonymous with improving laser beam quality, since the dye laser output is of very poor quality, and roughly triangular in shape, with many permanent fringes.

Several ideas for improving laser beam quality were breadboarded, but most of them gave disappointing results. First, we tried spatial filtering. A conjugate pair of lenses (two plano-convex, 150-mm focal length lenses) were spaced such that the exit beam was collimated like the input; a small aperture was placed at the focus between the lenses to achieve filtering. Laser power was not high enough to cause sparking of the air with these focal lengths, so a vacuum tube was unnecessary. We started with a 500-μm-diameter aperture. This produced little change in the final beam appearance, although it was possible to transmit most of the dye laser power through the aperture. Next, we reduced the aperture to 200 μm; this attenuated the beam slightly, but the camera image recorded through the

telescope was not much improved. Finally, the aperture was set to 100 μm; hot spots around the edges of the aperture suggested that we could not go much smaller in aperture size, lest we risk ablating the aperture edges. Since the 100-μm aperture provided only a slight improvement in image quality, this technique was not deemed useful. The unfiltered dye laser beam is a triangular shape formed from successive bands, with the brightest, widest band at the base of the triangle and successively narrower (length and width) bands occurring toward the apex where intensity is minimal. The 100-μm aperture selected for the first (brightest) band; this is probably because the weaker bands are due to higher order modes that are, to some extent, removed by the spatial filter.

Next, we tried beam homogenization through a fiber. The idea was to inject the laser beam into a length of fiber, homogenizing the laser output; then the end of the fiber could be imaged onto the target area or the telescope (at 25 ft or more) with a lens having a focal length of 100–200 mm. The target plume would be located less than 12-in. in front of the fiber-lens combination. This was first breadboarded using white light and a 600-μm core, N.A. = 0.15 (for less divergence than standard N.A. = 0.22 fiber), and a 20-ft coil of fiber; the resultant performance looked good. Then, we used the dye laser. A lens having a 1-in. focal length was used to inject the laser beam into the fiber. With

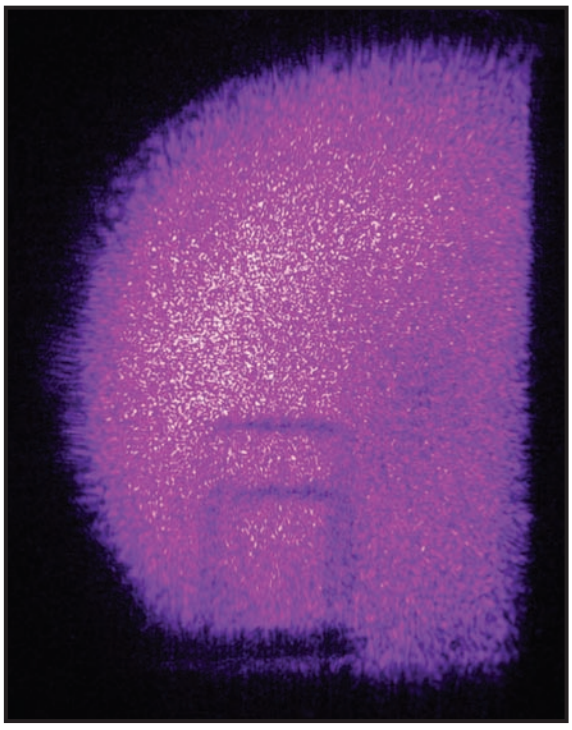

Figure 3. This image of the target through the telescope, illuminated with laser light passed through mixing fiber, shows severe speckle

the fiber placed just beyond the focus, so as not to damage the fiber end, about 50% of the laser energy was injected into the fiber, and the output end of the fiber was imaged as before to a point near the receiver telescope's input (to keep the telescope entrance aperture masked small). Results, unfortunately, were entirely unsatisfactory due to severe speckle problems (Figure 3). Because of the shortness of the pulse (24 ns), techniques such as vibrating the end of the fiber or putting a rotating transmissive plate in front of the fiber to smooth out speckle were not feasible, so this method was also discarded.

The earlier observation that the spatial filtering had selected for the brightest band in the laser output beam suggested that this same effect might be more easily achieved simply by expanding the dye laser beam with a Galilean telescope, using only the brightest band of the laser output for plume illumination and masking out the other parts. In all the experiments described herein, we initially expanded (using a Galilean telescope) the roughly triangular dye laser output to be about 15 × 15 mm. Following this, we used a –25 mm followed by a +150 mm focal length lens, with the lenses separated by about 125 mm. This increased beam size by 6X, which was enough expansion for the first (brightest) laser band to cover the plume region of interest. The beam-expanding telescope was fine-focused to greatly collimate the beam and thus maintain a relatively small-sized beam at the telescope input aperture. This method was successful: it resulted in much improved shadow images (Figure 4).

The plume shape changed depending on the shape and condition of the point on the aluminum surface that the Nd:YAG ablation laser struck. Uniformity of the laser illumination beam improved when the laser standoff distance was increased to 33 ft (Figures 4b, 4c, and 4d vs. 4a), presumably because some of the higher order laser modes do not propagate as well over the large distance. Due to the nature of the light source, there is some diffraction around all sharp edges (e.g., goalposts and base plate); we cannot improve upon this. Because the bright laser band used was much longer than it was wide, it seemed that a one-dimensional beam expander based on cylindrical lenses would result in less waste of laser power. (When the spherical Galilean scope expanded the height of the band by 6 to achieve minimum proper coverage of the plume, the length, which was already correct, was also expanded 6 times; hence ⅚ of the beam was wasted.) We then set up a cylindrical lens–based telescope, with –12.5-mm and 100-mm focal lengths, resulting in 8X expansion in the narrow dimension only. This also yielded good shadowgraph images, but setup and alignment were more difficult because of two added degrees of freedom: rotation of each lens.

Fine-tuning the lens spacing of both the spherical and cylindrical beam expanders gave us good control over beam collimation. Both beam expanders were placed fairly close in front of the plume area. During the above-described measurements, effective laser standoff was increased to 33 ft by adding three folding mirrors between the laser and the final beam expander, such that the laser beam had to travel 33 ft before reaching the target chamber (the plume). The expander was fine-tuned to keep the spot within a 2-in. area at the telescope input aperture, which was located more than 25 ft from the plume (Figure 5). We were able to obtain shadowgraph images of good quality with this setup, thus establishing that quality images can in fact be collected at a standoff of greater than 25 ft.

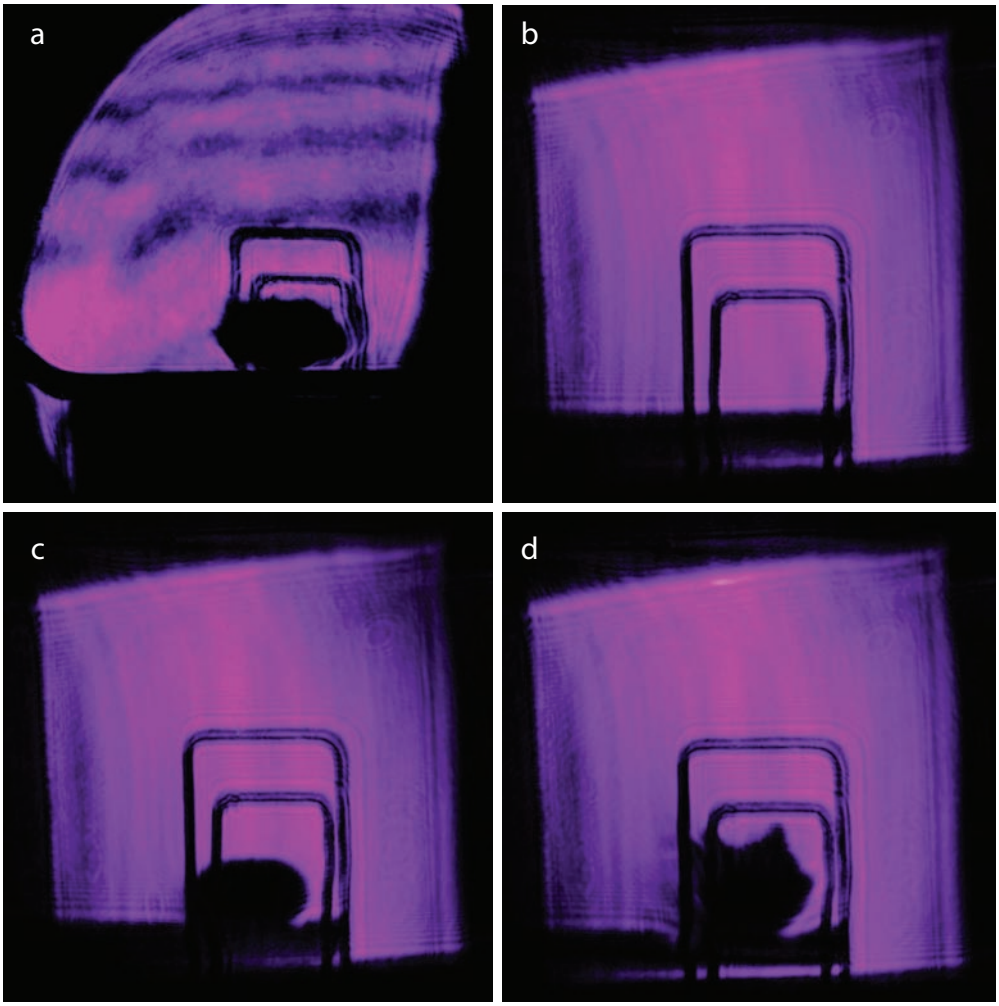

Figure 4. Photos through the telescope at 26 ft using the spherical beam expander/masking technique: (a) our first try with the laser close to target (note the detail visible in plume); (b) laser at a standoff distance of 33 ft; no ablation laser, hence no plume; shows improved uniformity of illumination; (c) and (d) with the ablation laser; total height of tallest goalpost is 10 mm, so the plume in 4d is about 5 mm high.

All resonance shadowgraph images were obtained using a 394-nm, 10-nm-wide band-pass filter at the telescope input aperture. To avoid overexposure, the dye laser output energy was reduced to 100 μJ or less per pulse; additionally, a Wratten neutral density filter as dense as OD2 (attenuation = 100X) was added in front of the band-pass filter. With the laser at full power (>1 mJ/pulse) and using the

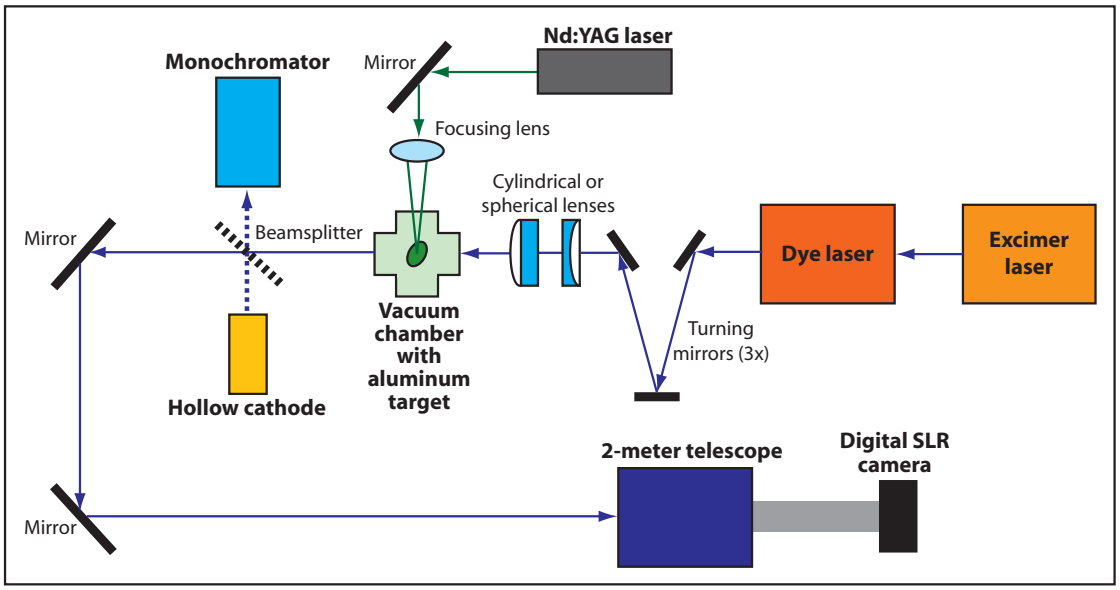

Figure 5. Experimental setup

cylindrical expander, an OD3 had to be used (attenuation = 1000X); this resulted in the ability to record the shadowgraphy images with the room lights on. Under these conditions, the bright plasma light flash generated by the Nd:YAG–aluminum target interaction was not visible at all. This bodes well for use of such a diagnostic at facilities such as the Z machine, where the plasma light is bright.

Conclusion

We developed a method of reliably producing good quality resonance shadowgraph images of an aluminum cloud that we generated in a vacuum system, and at a standoff distance of 25 ft or more, such as would be necessary in many experiment scenarios.

The only drawback we anticipate is the size of the illumination laser required for this system, which makes it difficult (but certainly not impossible) to move. A brief search turned up no real alternatives to the dye laser, since the laser source must be tunable (UV to visible, depending on the resonance), pulsed with short pulse length (tens of nanoseconds or less), of reasonable output power (at least 1 mJ/pulse), and fairly narrow linewidth (<0.1 nm, probably close to 0.01 nm).[2] The cylindrical

[2] With the advent of rugged, relatively small and compact, high-energy (>200 mJ at 355 nm) Nd:YAG lasers, one possibility would be to replace the excimer pump with one of these, and the pump laser head could probably be mounted right in the existing dye laser box. Also, while optical parametric oscillators (OPOs) are currently not field-rugged and are too broad in linewidth by at least a factor of 20 (4–7 cm^{-1} vs. the required 0.2–0.4 cm^{-1} [and preferably even less]), a compact, doubled OPO may be capable of doing the job within a few years.

beam expander is better for conserving energy but is more difficult to align because of the two extra degrees of freedom (rotation of each lens), so it is justifiable only if laser power is low or plasma light is particularly bright. If resonance lines further into the UV were to be used, a quartz or all-reflective telescope system should be considered.

Our results show that this resonance shadowgraphy technique would be very helpful at places like the Z machine and RITS (radiographic integrated test stand), since it would expand their plasma diagnostic capabilities to considerably lower concentrations and earlier times in the life of the plasma.

Reference

Capelle, G., R. Tiangco, "Resonance Shadowgraphy," *Nevada Test Site–Directed Research and Development,* FY 2006, National Security Technologies, LLC, Las Vegas, Nevada, 2007, 1–6.

Repetitive Motion Imaging

John Di Benedetto,[1] *Steve Lutz, Steve Jones, Seth Petersen*
Special Technologies Laboratory

Kenneth McGwire
Desert Research Institute, University of Nevada, Reno, Nevada

Motion sensing of plumes was investigated using frequency-domain image processing techniques. Two types of thermal imagery were analyzed: high-speed and video-rate. To better evaluate the use of high-speed thermal cameras, a re-registration algorithm was pursued in collaboration with Ken McGwire of the Desert Research Institute (DRI), and the method was developed into a software tool. Better than 0.1 pixel registration was achieved (for a full treatment of the software development involved in this project, please refer to McGwire [2008] published on p267 in this report). Processing with the software tool has led to the conclusion that frequency-domain processing is valid and should be pursued further using three-dimensional (3-D) wavelet techniques.

Background

Two important targets related to persistent site monitoring are gaseous effluents, thermal plumes, and objects in periodic motion (vibrating or rotating). Detection and characterization by the method studied here could help identify effluents at concentrations lower than those possible using conventional algorithms (e.g., the use of matched filters requires some estimate of spectral content and signal strength in the spectral response of the detector, and scene motion from passing plumes can be simply refractive index variation), and also could facilitate the detection of subtle repetitive motion. In remote sensing applications, static thermal images are usually acquired, and change detection involves revisiting a location to record small changes in temperature. Motion detection at video rates (for example, a helicopter-mounted video camera) is typically used in situations where moving objects, such as vehicles and people, are tracked. The purpose of our work was to determine how high-rate, multiframe imagery could be processed using frequency-domain techniques to enhance detection and characterization of concealed activities.

While frequency-domain techniques could be applied spectrally from the near-UV to the long-wave infrared (LWIR), we chose to focus on thermal imagery in the LWIR, which allowed day/night surveillance capability without scene illumination. This work sought to detect and characterize motion in the frequency domain, using many sequential frames to enhance the small changes in digital intensity at levels not possible with time-domain techniques. This report discusses the project concept,

[1] dibeneja@nv.doe.gov, 805-681-2240

a simple model for motion in turbulent air, and some experimental results using one-dimensional (1-D) fast Fourier transform (FFT) analysis. An Interactive Data Language (IDL) program written by Dr. Ken McGwire, DRI, is addressed briefly (for a complete treatment, see McGwire [2008]). Finally, some suggested paths forward are presented.

Project

Concept

National Security Technologies (NSTec) scientists have been pursuing applications of interferometer-based spectrometers for quantifying effluent concentrations. In both imaging and non-imaging instruments, moving-mirror Michelson interferometers are used to collect spectra of gases, which are then processed using the well-known FFT analysis. Michelson-based field instruments can be very susceptible to vibrations, as unwanted periodic modulation or vibration of the moving mirror can cause intensity modulations that appear as peaks in the transformed frequency spectra. NSTec researchers realized that motion in the *scene* of an imaging system would cause similar intensity fluctuations that would create features in the transformed image, so efforts were made to capture images at high frame rates. After the image cubes are processed using a 1-D FFT analysis, the new image cube is in units of frequency. With a known frame rate and pixel size, the frequencies can be related to velocity (Gonzalez, 2008) of motion. For clarity, raw data collected from both cameras (high-speed and video-rate) are referred to as frames. The FFT data, displayed as images, are referred to as motion "bands," analogous to spectral bands since both spectral and motion data are frequency-based, while the camera frames are time-based.

Figure 1 is a simplified model of processes that influence image stability. The intensity fluctuations at any pixel are considered here to be composed of three classes: camera motion, atmospheric scintillation, and variations related to the object and background. Camera motion causes a global image translation with equivalent pixel displacements in x and y coordinates. For this work, of the six degrees of camera motion, only pitch (ϕ) and yaw (θ) were considered to cause appreciable scene motion. Roll (ρ) influence was assumed to be minimal due to each camera's mounting configuration.

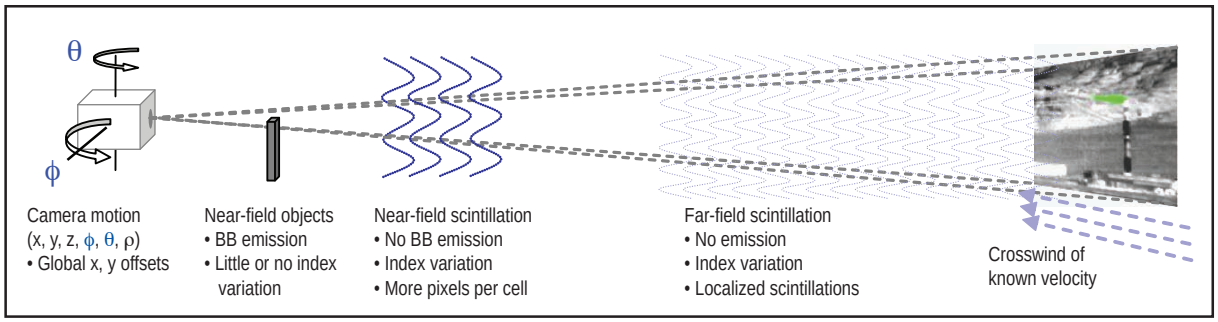

Figure 1. Some influences on image stability and degradation

Index of refraction changes in the path were considered the dominant optical effect of turbulence-induced scintillation, where intensity is transferred between pixels by the changes in index due to local heating, density changes, and the presence of gases and liquids. In the near field, the fluctuations were assumed to cause nearly global changes in image position as the volume of air traversed is on the order of the lens diameter. In the far field, heat rising from objects, gas plumes, dust swirls, and other local density fluctuations subtend a small number of localized pixels, and appear as objects themselves. Finally, motion and light fluctuations can occur from influences at the object. Examples include fan blades, motors, and thermal emission from gases and liquids.

While we had been studying the phenomenon for approximately 18 months, only toward the end of this time did we discover a large body of work known as spatio-temporal analysis (Price, 2007) that uses similar mathematical treatments of motion in the frequency domain. Early work describes the tracking of objects such as smoke (Privalov, 2007; Töreyin, 2005), athletes in training (Neumann, 2002), and cloud imagery (Milanfar, 1996) using FFTs, while more recent efforts use wavelets. In nearly all cases, the parameters most desired are the object velocity and direction (Milanfar, 1996), rather than a method to optimize plume visualization. FFT and wavelet analysis as three-dimensional (3-D) and projected two-dimensional (2-D) techniques were beyond the current scope of this work.

Experimental Setup

Two types of thermal imagery were analyzed. While both collected imagery in the LWIR (8–11.5 μm), the camera technologies have different noise and sensitivity characteristics.

High-speed Imager

The high-speed thermal imager is a shot-noise-limited Silicon Arsenide Blocked Impurity Band (BIB) sensor, cooled to liquid helium temperatures. The 128 × 128 pixel imager collects frames at 2 kHz. The 16-bit binary image files consist of 4096 (or 8192) frames for a total acquisition time of 2.048 (or 4.096) seconds. The imager frame acquisition was limited by overall system memory; 2^n images were used throughout this work. Acquisitions were made during field collections at the FY 2006 Tarantula test campaign at the Nonproliferation Test and Evaluation Complex (NPTEC), and these data were analyzed during this SDRD project.

Video-rate Imager

The video-rate imager was an uncooled microbolometer device collecting 320 × 240 pixel images at 30 Hz. The 16-bit TIFF files consisted of 512 frames, for a total acquisition time of 17.067 seconds (although 512 frames [2^9] were collected, the length of the frame acquisition was limited by available operating software). An internal blackbody provided flat-field calibration. Digital video was collected as part of the FY 2007 Black Widow test campaigns and made available for this SDRD project.

All data were processed using two graphical user interface (GUI)–based programs in the IDL environment. The DRI program, called MA_TOOL.pro, was used to re-register and evaluate images. The standard Environment for Visualization (ENVI) GUI, available from ITT Research Systems of Boulder, Colorado, was used for further analysis and visualization.

Results and Discussion

A motion data-capture and analysis example using the high-speed imager is shown in Figure 2. A filter wheel was spun at approximately 400 Hz. Figure 2b shows the intensity at one pixel location on the blades in each of the 4096 images. When 4096 frames were transformed using a standard FFT (4096 temporal points per each spatial pixel), the transformed bands corresponded to the modulation frequencies. Figure 2c shows a Z-slice through the first 500 bands of the transformed imagery at a pixel (red dot) that corresponds to the chopper blade aperture.

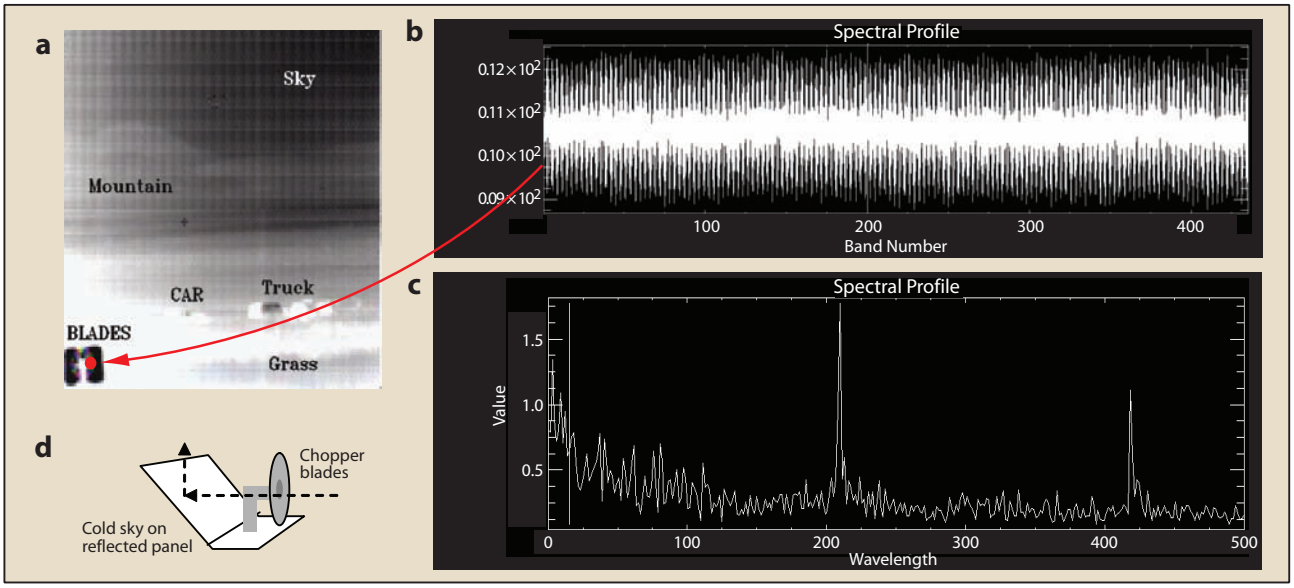

Figure 2. (a) Image captured by high-frame-rate camera; (b) intensity values at 1 pixel for each of 4096 images; (c) transformed pixel values in frequency domain; (d) cartoon of chopper wheel used in initial tests

Figure 3a is a thermal image obtained from the same high-rate camera, and Figure 3b shows a false color representation of select motion bands from this image. Red indicates low frequencies, and green and blue indicate higher frequencies. The small plume above the tall stack on the right is dwarfed by the largest feature in the image, a plume generated by the exhaust of a jet start cart. The purely

hyperspectral analysis of similar images did not identify this as a plume. The fact that such plumes containing insignificant amounts of effluent were detectable led us to consider this frequency-domain analysis technique for transient plumes.

In Figure 3b the bright blue line represents a known camera readout artifact associated with one of the camera's four digitizers. Since the noise is synchronous with the frame rate, the noise is amplified. The bright red vertical and horizontal features observed in the low-lying buildings were attributed to a mixture of camera motion (rocking the scene at lower frequency) and local heating of the structures. The scene motion due to camera motion was initially estimated to be <0.1 pixels. If the images were to be analyzed with greater fidelity, the camera motion would need to be diminished. The subpixel re-registration problem was given to Dr. Ken McGwire at DRI; McGwire developed an IDL tool for image registration as described in a companion report to this project (McGwire, 2008). This stand-alone IDL code (MA_tool.pro) was used to process examples of motion data collected with both the high-speed and the video-rate microbolometer cameras. When the image in Figure 3a was processed through the DRI re-registration tool, approximately 50% of the motion-induced intensity in Figure 3b was removed.

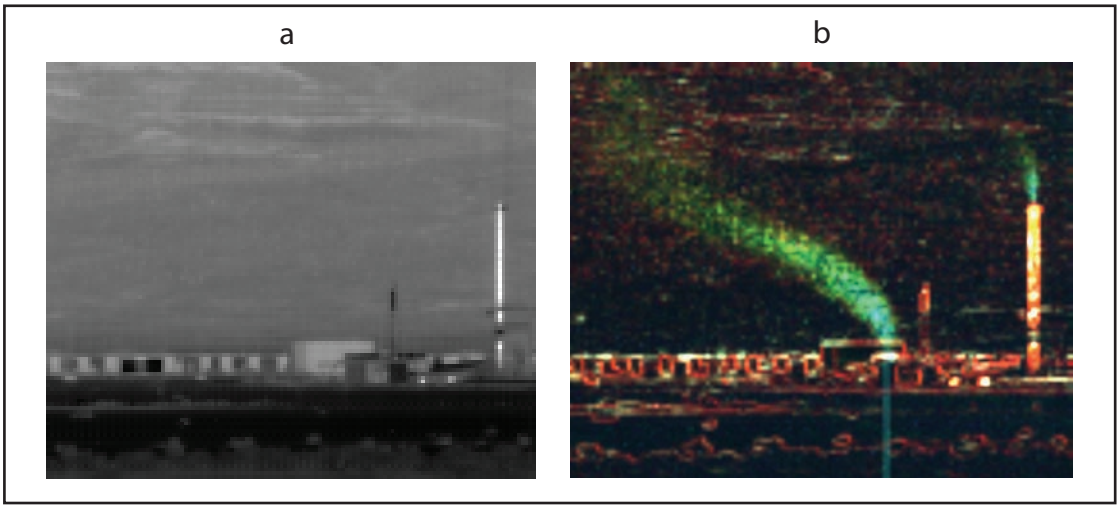

Figure 3. (a) Thermal image captured with camera; (b) false color composite of three frequency ranges

Figure 4 shows a mosaic of single images collected from four acquisitions (four release rates) using the video-rate imager during collections from an unheated source. Each individual image was intensity stretched to maximize the possibility of detecting plume before the mosaic was created. On this particular day, clear desert skies created a high thermal contrast of the ambient plume against the cold background sky. Due to this high temperature difference (ΔT), a plume is readily visible at

19 kg/hour, and visually detectable at 2.5 kg/hour. Note how the thermal blooming from the desert floor limits in-scene contrast stretching to improve visualization. Figure 5 shows the side-by-side comparison of the original thermal image and the FFT of the image for the 19 kg/hour release. Note how well the FFT suppresses the ground-level thermal bloom. The righthand image in Figure 5 is an RGB composite using the second (red), third (green) and eighth (blue) FFT bands from the 512 frames. The transform image represents 17 seconds of image information, causing the representation of any frequency band to be the average of the plume location over that time period. On this day, wind velocity created a left-to-right scene velocity of approximately 1 pixel per frame.

Figure 4: Mosaic of four images collected at four release rates

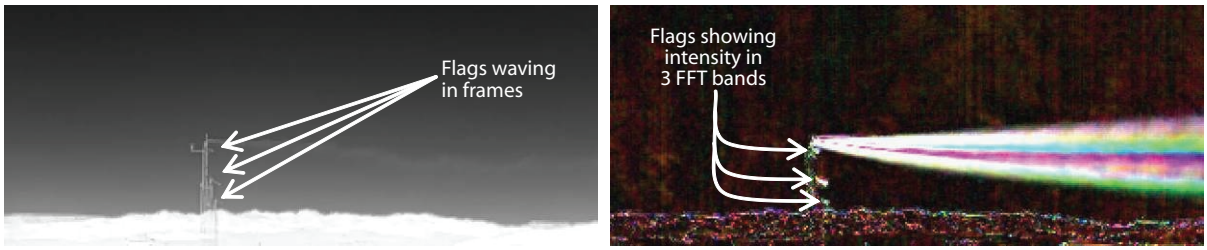

Figure 5. (left) 8-bit stretched thermal image; (right) 512-frame FFT image (red = band 2 at 0.0586 sec^{-1}, green = band 3 at 0.1172 sec^{-1}, and blue = band 8 at 0.410 sec^{-1})

Figure 6 shows two FFT analyses *using only the first 8 frames of the 512 frames recorded.* The left image shows an RGB representation of three FFT bands (#2, #3, and #4). Shorter time intervals lessen averaging of the plume location but increase scene noise. The right-hand image in Figure 6 shows that by summing FFT frames one can improve the visualization. Note the decreased smearing using only eight frames (8/30 second duration) as compared to the 17-second duration with 512 frames. However, using 8 frames instead of 512 trades away temporal resolution (frame separation is 0.0586 Hz at 512 frames vs. 3.75 sec at 8 frames). As the number of frames decreases at a constant frame separation, higher-frequency information is lost, and this lack of detail impacts the detection of rapidly moving objects. Also note the small white spots that are seen on the towers. These are three flags, each on top of the individual towers, blowing in the prevailing wind. The high contrast against the cold sky creates a strong return in the frequency domain.

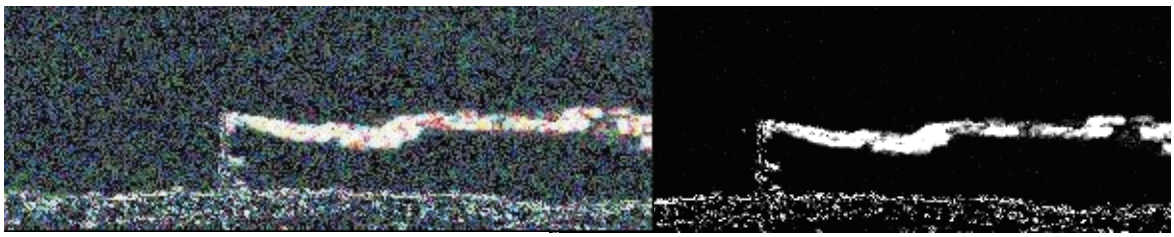

Figure 6. (left) 8-frame FFT image (red = band 2 at 3.75 sec^{-1}, green = band 3 at 7.75 sec^{-1}, and blue = band 4 at 11.25 sec^{-1}); (right) the sum of the three bands

Figure 7 shows FFT images acquired at four release rates. Each RGB false-color representation uses the same bands (#2, #3, and #8), and each image has been scaled independently. While the atmospheric noise appears to be increasing as the release rate decreases, this is a function of the processing of the 16-bit integers to 8-bit screen images using a 2% histogram stretch. If the image with the lowest concentration (1 kg/hour) were plotted at the same intensity as the highest concentration (19 kg/hour), the left-most image would be black except for the flag intensities, which are constant. An additional processing step using a principal component analysis (PCA) was investigated to increase the effectiveness of the 1-D FFT technique. Figure 8 shows the first or second principal component (PC) band for the four image data cubes. Increased contrast is consistent with the idea that summing bands of sufficient energy would increase detection. However, many more data cubes need to be processed before this can be validated.

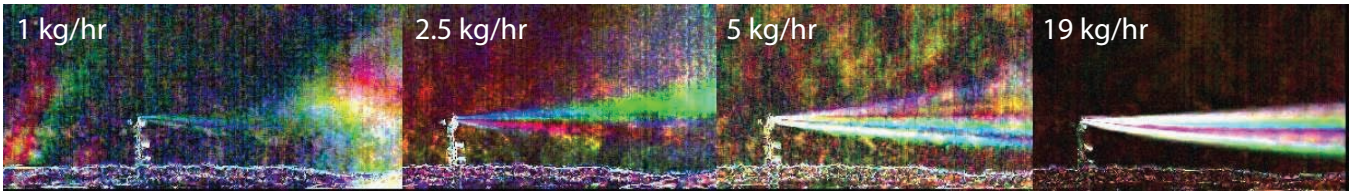

Figure 7. Mosaic of four FFT images collected at four release rates

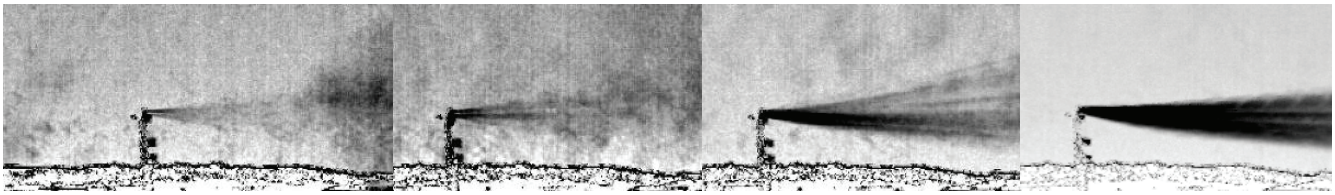

Figure 8. Principal component analysis: first rotation of FFT data

Conclusion

Using motion-detection algorithms, gaseous effluents and thermal plumes were detected using frequency-domain analysis. An image registration software tool was developed that allows subpixel re-registration of large numbers of images. The tool allowed for processing using spatio-temporal and principal component analysis. Image stabilization of <0.1 pixels was achieved in the limited data set investigated. Better stabilization will likely result when pixels of known stationary objects are isolated and used in the 2-D Fast Hartley Transform as opposed to a purely global 2-D spatial transform. Zero padding the isolated object pixels to a $2^n \times 2^n$ image may improve the accuracy of the resulting (x, y) offsets. The analysis of the limited number of video-rate images undertaken during this project indicates that visualizing release concentrations of <1 kg/hour should be feasible as an effluent diagnostic at NPTEC. Processing different numbers of sequential frames into frequency-domain bands showed that filtering for specific bands improved visualization. High-pass filtering using an inverse FFT (IFFT) will likely create an effective visualization tool. However, collecting FFTs over a number of time durations is equivalent to scaling in a wavelet analysis. The comparison of 512-frame to 8-frame durations supports the idea that a discrete wavelet transformation (DWT), followed by filtering and an inverse DWT (IDWT) would improve the visualization of weak plumes over those from a single FFT transform. Although computationally intensive, 3-D FFT techniques using matched-filter detection have been used successfully in the past as velocity measurement tools (Porat, 1990). Combined with a 3-D IFFT, this technique should work well. However, given the availability of faster 3-D DWT/IDWT techniques, plume detection by wavelets is likely a better path forward.

Acknowledgments

The authors would like to acknowledge the contributions of Kevin Kyle and Ian McKenna of NSTec. This work was also enhanced by the IDL tool developed by Dr. Ken McGwire of the Division of Earth and Ecosystem Sciences at DRI at the University of Nevada, Reno.

References

Gonzales, R. C., R. E. Woods, *Digital Image Processing,* Pearson Prentice Hall, New Jersey, 2008, 782–785.

McGwire, K., "Development of a tool for motion analysis and subpixel registration of high-speed image time-series," *Nevada Test Site–Directed Research and Development*, FY 2007, National Security Technologies, LLC, Las Vegas, Nevada, 2008, 267–275.

Milanfar, P., "Projection-based, frequency-domain estimation of superimposed translational motions," *J. Opt. Soc. Am. A* **13**, 11 (November 1996) 2151–2162.

Neumann, J., Y. Aloimonos, "Spatio-temporal stereo using multi-resolution subdivision surfaces," *Int. J. Comput. Vision* **47**, 1–3 (April 2002) 181–193.

Porat, B., B. Friedlander, "A frequency domain algorithm for multiframe detection and estimation of dim targets," *IEEE Trans. Pattern Anal. Mach. Intell.* **12**, 4 (April 1990) 398–401.

Price, K., "Annotated Computer Vision Bibliography: 18.7.3. Spatio-Temporal Filtering," University of Southern California, http://www.visionbib.com/bibliography/motion-i787.html#Spatio-Temporal%20Filtering, accessed August 1, 2007.

Privalov, G., J. A. Lynch, "Video Image Detection Systems for Fire and Smoke," axonX, LLC, Sparks, Maryland, http://www.axonx.com/White%20Papers-Reports/Testing%20Video%20Image%20Detection%20Systems%20for%20Fire%20and%20Smoke.pdf, accessed August 1, 2007.

Töreyin, B. U., Y. Dedeoğlu, A. E. Çetin, "Wavelet based real-time smoke detection in video," *Proceedings of the 13th European Signal Processing Conference (EUSIPCO)*, held September 4–8, 2005, Antalya, Turkey.

this page intentionally left blank

Development of a Tool for Motion Analysis and Subpixel Registration of High-speed Image Time-series

John Di Benedetto[1]
Special Technologies Laboratory

Kenneth McGwire
Desert Research Institute, University of Nevada, Reno, Nevada

This report describes work that was performed for the Special Technologies Laboratory (STL) by Dr. McGwire of the Desert Research Institute, under a subcontract through the University of Nevada, Reno. The goal of this effort was to develop methods for subpixel image registration on the order of 0.1 pixels or less in order to reduce the effects of camera vibration on high-speed image time-series. Reduction of artifacts from camera motion should aid investigations of atmospheric plumes and possibly allow novel explorations of atmospheric turbulence. This report provides detail on the software developed to accomplish the related FY 2007 SDRD project "Repetitive Motion Imaging" (Di Benedetto, 2008).

Background

(Please refer to "Repetitive Motion Imaging" by John Di Benedetto, 2008, published on p257 in this report.)

Project

Two image time-series from a high-speed thermal imaging system were provided by National Security Technologies (STL) for use in this work. Both images were identical views across a landscape collected at two different time periods. Each time-series consisted of more than 4000 frames. The first image, here named Shot-29, was acquired during a period of low atmospheric turbulence at the time of thermal crossover. The second, named Shot-22, was acquired during daytime conditions with noticeable atmospheric scintillation. The images contained a number of fixed structures and mountains, as well as objects and atmosphere that were in motion during the time-series. Subpixel camera motion was detectable at the edges of fixed objects in both image series, and a method was required for measuring this global shift in image position and resampling to reduce the effect.

Tools developed by Dr. McGwire in the analysis of the Shot-22 and Shot-29 images were packaged into a graphical user interface (GUI) for future use and development (Figure 1). The MA_Tool software program, which combines capabilities from the IDL computing environment and a Java-based image processing package called ImageJ (Rasband, 1997), was used to develop the GUI. MA_Tool

[1] dibeneja@nv.doe.gov, 805-681-2240

can ingest a monochrome image time-series in TIFF or Environment for Visualization (ENVI) image formats, and the user may choose to work with a range of image frames from the time series. The MA_Tool functions are organized under a number of tabs, which are described below.

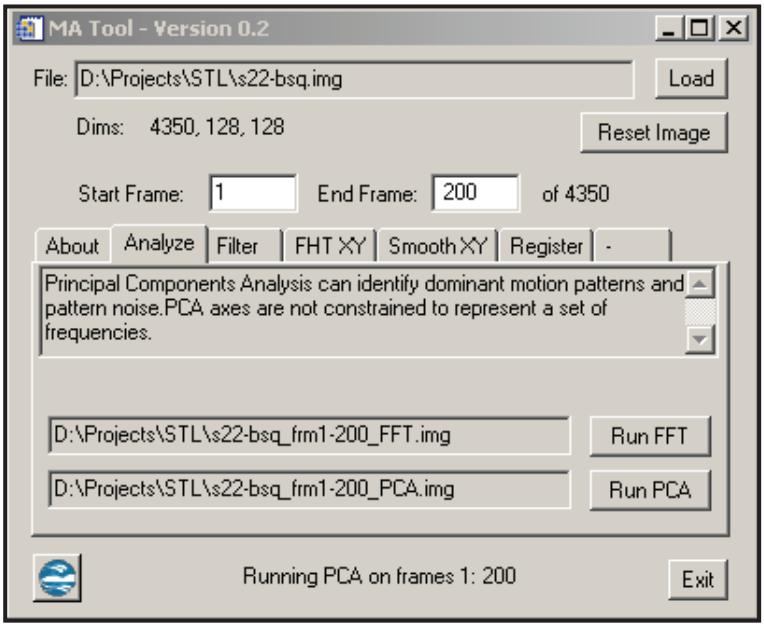

Figure 1. MA_Tool GUI

Analysis

Two methods for analyzing temporal variability in the image time-series were used in this analysis, a per-pixel fast Fourier transform (FFT) and whole-scene principal components analysis (PCA). MA_Tool calculates the FFT of the image time-series on a per-pixel basis, decomposing each location in the image into its spectrum in the frequency domain. After calculation, the user may click on a pixel in the image, and the power spectrum for temporal variation in that pixel is presented in a plot. The user may also animate a separate image representing the frequency components of the scene in order to visually identify the range of frequencies under which a phenomenon operates.

PCA provides a linear transformation of the image time-series that decomposes variance into a sequence of orthogonal synthetic axes. MA_Tool performs this analysis on a whole-scene basis, instead of a per-pixel one. The advantage of the PCA is that it is capable of reducing complex spatial/temporal patterns occurring at multiple frequencies down to a small number of dimensions

for visualization. The eigenvalue associated with a given principal components axis also provides a measure of the magnitude of the phenomena observed in that axis. Figure 2 shows selected PCA results for the Shot-29 scene.

The first PCA axis in Figure 2 captures the pattern of mean image brightness. PCA axis 2 is dominated by the shift in image position across the selected range of frames, showing that the effect of camera vibration dominates the residual variance in the data set. The images in Figure 2 show that pattern noise dominates other early PCA axes. Note that at high camera speeds, the presence of this noise in early PCA axes may have less to do with high signal-to-noise than with high frame rates, resulting in an enormous amount of cross-correlation.

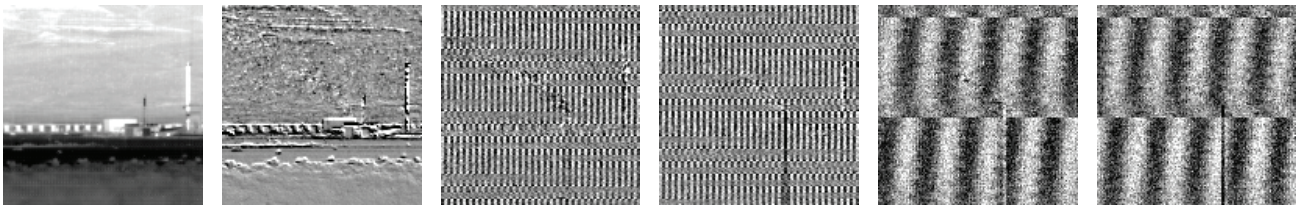

Figure 2. Motion and pattern noise in higher principal components axes of Shot-29

MA_Tool provides a plot of the PCA eigenvalues and allows the user to move through each PCA axis and examine a plot of the corresponding eigenvector and eigenimage. This allows simultaneous understanding of spatial and temporal variability in the image time-series. The eigenvector weighting in Figure 3 (blue line) shows how the roll pattern of PCA 12 in Figure 2 arises from variation at a number of frequencies.

Temporal Smoothing

Figures 2 and 3 demonstrate how high-frequency pattern noise may introduce spatially dependent shifts in image brightness that when superimposed on a scene will lead to apparent positional shifts of edges in the scene. Given the high-frequency nature of this noise in the provided data set, a low-pass digital filter was implemented that could reduce this artifact. The low-pass filter implements the digital sinc filter in IDL on a per-pixel basis in the time dimension with a user-specified full-width, half-maximum dimension in number of image frames. The kernel of the sinc function is extended to four lobes on either side of the peak.

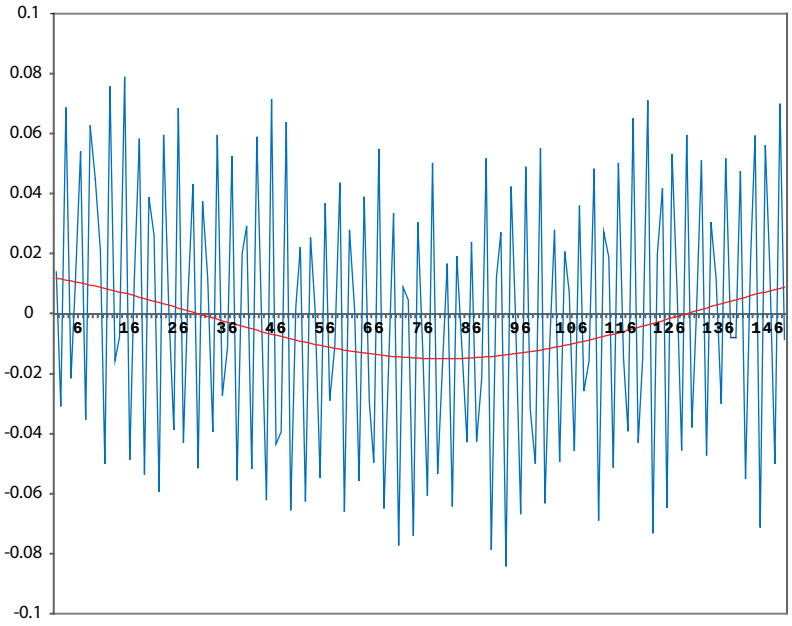

Figure 3. Eigenvector weights for PCA 12 (blue)

Calculating Subpixel Offsets

In order to reduce the effects of camera motion on the image time-series, a method was needed that could estimate global shifts in image position at a subpixel resolution. A deconvolution of FFT images is often used to estimate this offset as a phase shift in the frequency domain. While subpixel information content does exist in the frequency domain, practically all image processing software packages implement their Fourier transform using the FFT, which integerizes the transformation from the frequency domain back to the spatial domain. While this greatly accelerates computation, this discretization eliminates information at the subpixel level. In order to deal with this, an image processing package called ImageJ was joined to MA_Tool. ImageJ was written in Java for the National Institutes of Health, and unlike almost all other image-processing software, it implements its Fourier analysis using the fast Hartley transform (FHT). The foundation for the ImageJ implementation of the FHT is described in Reaves (1990). Like the FFT, the FHT accelerates conversion between the time and frequency domains, but the FHT performs these operations with real values. As a result, subpixel information content on the phase shift between images is maintained.

Figure 4 shows a single frame from the test data set and a copy that was shifted by 0.3 pixels in the x and y dimensions using a cubic convolution resampling. The images were converted to the frequency domain with the FHT, deconvolved, and transformed back to the spatial domain. The shift of the

resulting impulse function away from the center pixel indicates the degree of offset. A range of known subpixel image offsets were generated in *x* and *y* using cubic convolution resampling, and a second order polynomial was fitted to estimate shifts from the FHT results.

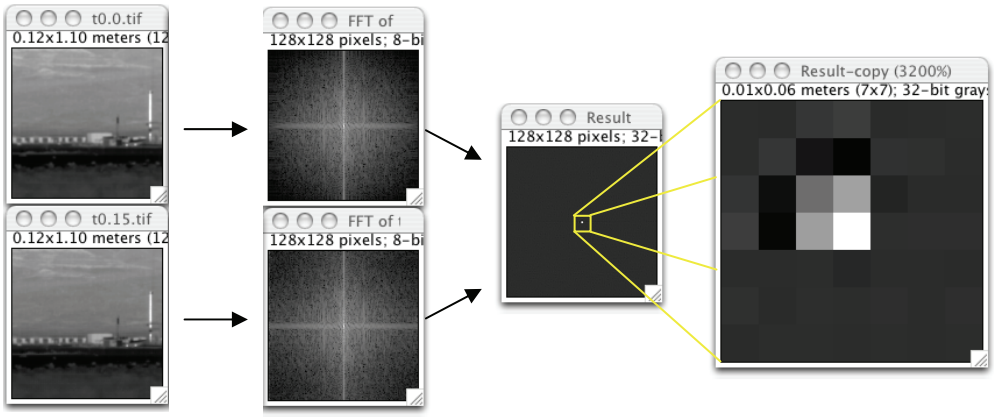

Figure 4. Using the FHT to calculate sub-pixel offsets

To calculate *x* and *y* offsets for each frame, MA_Tool outputs the image time-series from IDL and spawns ImageJ in batch mode. An ImageJ plugin written by Dr. McGwire iterates through each frame and uses the FHT phase shift to estimate camera motion relative to an image representing the average brightness of the entire time-series. The current implementation of this method assumes that all scene elements are static, which is limiting. However, future development efforts may provide methods of masking regions with high local variability. After the ImageJ batch job finishes, results are returned to MA_Tool; the user is then presented plots of *x* and *y* offsets and values for the RMS and maximum excursions in *x* and *y*. Figure 5a shows the FHT calculated offsets for the Shot-29 image time-series.

Smoothing X/Y

Estimates of image shifts derived from the FHT phase shift will contain errors due to image noise, influences of within-scene motion, and loss of precision. Also, as offsets approach 0.5 pixels, some of the phase shift may also be expressed at a distance from the impulse response, as shown in Figure 4. To ameliorate this, the user may smooth the estimates of *x* and *y* offsets using a combination of median and averaging filters of a user-specified width. After filtering, the user is presented with a plot of the filtered offsets and a new calculation of RMS and maximum excursions in *x* and *y*. Figure 5b shows the result of applying a 5-frame median filter to Figure 5a.

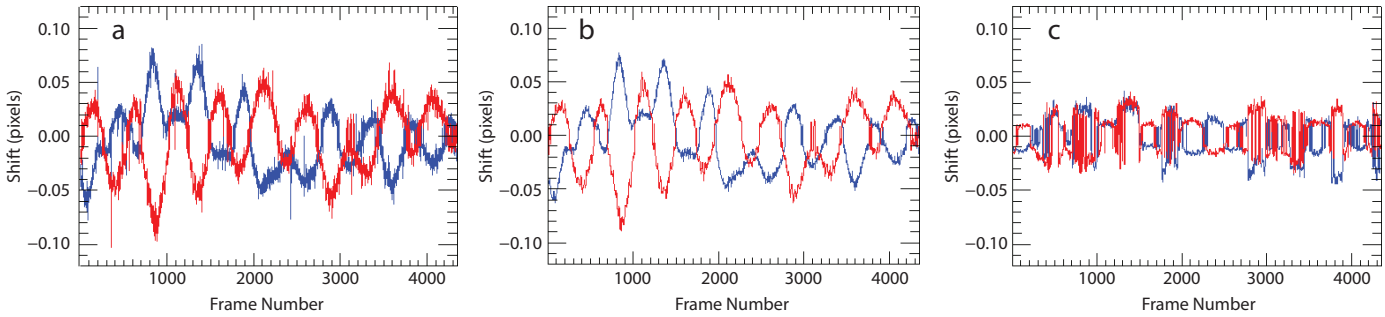

Figure 5. Estimated offsets for Shot-29, showing *x* axis in blue, *y* axis in red; (a) original; (b) 5-frame median filter; (c) after resampling

Resampling the Image Time-series

Finally, the user can resample the entire time-series to compensate for the global camera motion estimated by FHT phase shifts by using a cubic convolution resampling routine. The user may select either the initial FHT phase shift estimates or the filtered offsets. Cubic convolution approximates the optimal sinc function interpolation with cubic polynomials.

Results

Median-filtered estimates of global image motion for the Shot-29 image series taken at thermal crossover with a calm atmosphere are shown in Figure 5b. The fairly regular periodic pattern that is apparent is likely due to camera vibration. The RMS of this subpixel oscillation was 0.04 pixels, with a maximum excursion of 0.09 pixels. The image series was resampled by cubic convolution to remove the median-filtered offsets. The "corrected" image series was then run through the FHT offset calculation and a 5-frame median filter was again applied to the estimated residual offsets. Figure 5c shows that the correction did reduce the estimated image motion, but did not eliminate it. RMS for the corrected image series lowered to 0.03 pixels, with a maximum excursion of 0.05 pixels.

The reduction in temporal variation attributed to subpixel camera motion for Shot-29 is demonstrated in Figure 6 using PCA of the image time series before and after resampling. PCA axis 2 for the initial data set was completely dominated by global scene motion, as evinced by directional enhancement of edges along buildings and landscape features. In the resampled data set, the second PCA axis is dominated, instead, by local variation. Some global scene motion is apparent in PCA axis 3 both before and after resampling, though it is less pronounced in the resampled series.

Figure 7 provides estimated image offsets for the Shot-22 image, after applying a 5-frame median filter. Shot-22 was collected during daytime conditions with a more turbulent atmosphere. RMS for the original series was 0.05 pixels with a maximum excursion of 0.13 pixels (Figure 7a). Unlike the Shot-29 image, the pattern of variation for this series is much more erratic and it is difficult to

discern a similar periodicity. After correcting estimated image offsets for the image series with cubic convolution, there was little, if any, improvement (Figure 7b). RMS of the resampled series was the same, and though the maximum excursion was reduced to 0.11 pixels, residual variability in much of the time series seemed to increase.

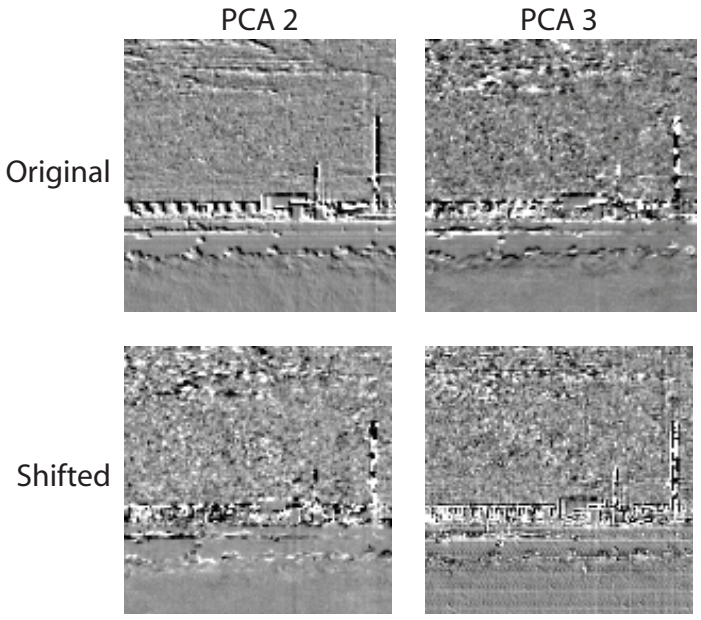

Figure 6. Reduction of variance attributed to motion in PCA of Shot-29

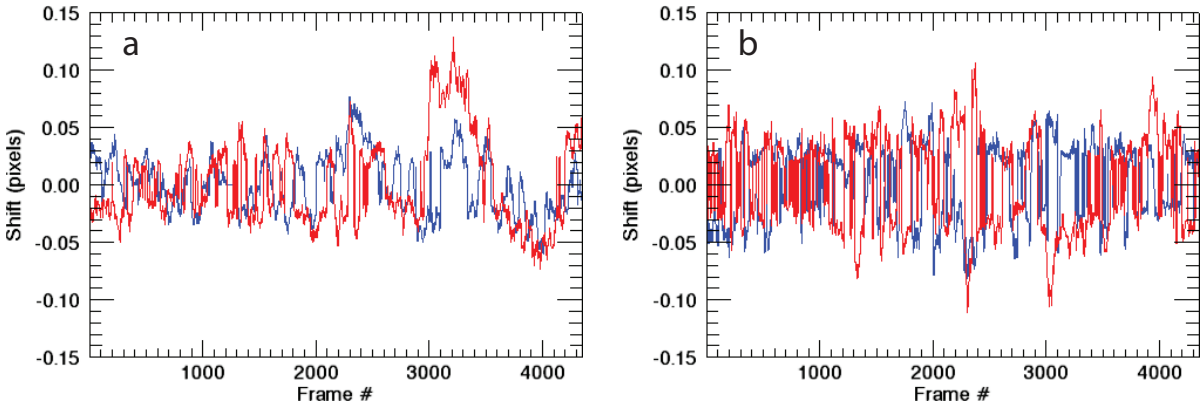

Figure 7. Median-filtered image offsets for Shot-22: (a) original; (b) after resampling

The poor result with Shot-22 is almost certainly due to the FHT method being overwhelmed by localized patterns of atmospheric scintillation. Though there may be underlying image information on global phase shifts, the FHT method was probably locking onto transient local shifts along edges in the image that had high contrast. This problem is illustrated in Figure 8, where transects of image brightness are shown for two small buildings on the left side of the image. The red and blue lines in Figure 8 indicate a horizontal brightness profile across these buildings at the times of greatest estimated displacement. Horizontal displacements in Shot-29 (Figures 8a and b) are seen to be consistent in magnitude and direction, while displacements in Shot-22 vary between buildings (Figures 8c and d), and even within the space of a single building (Figure 8d).

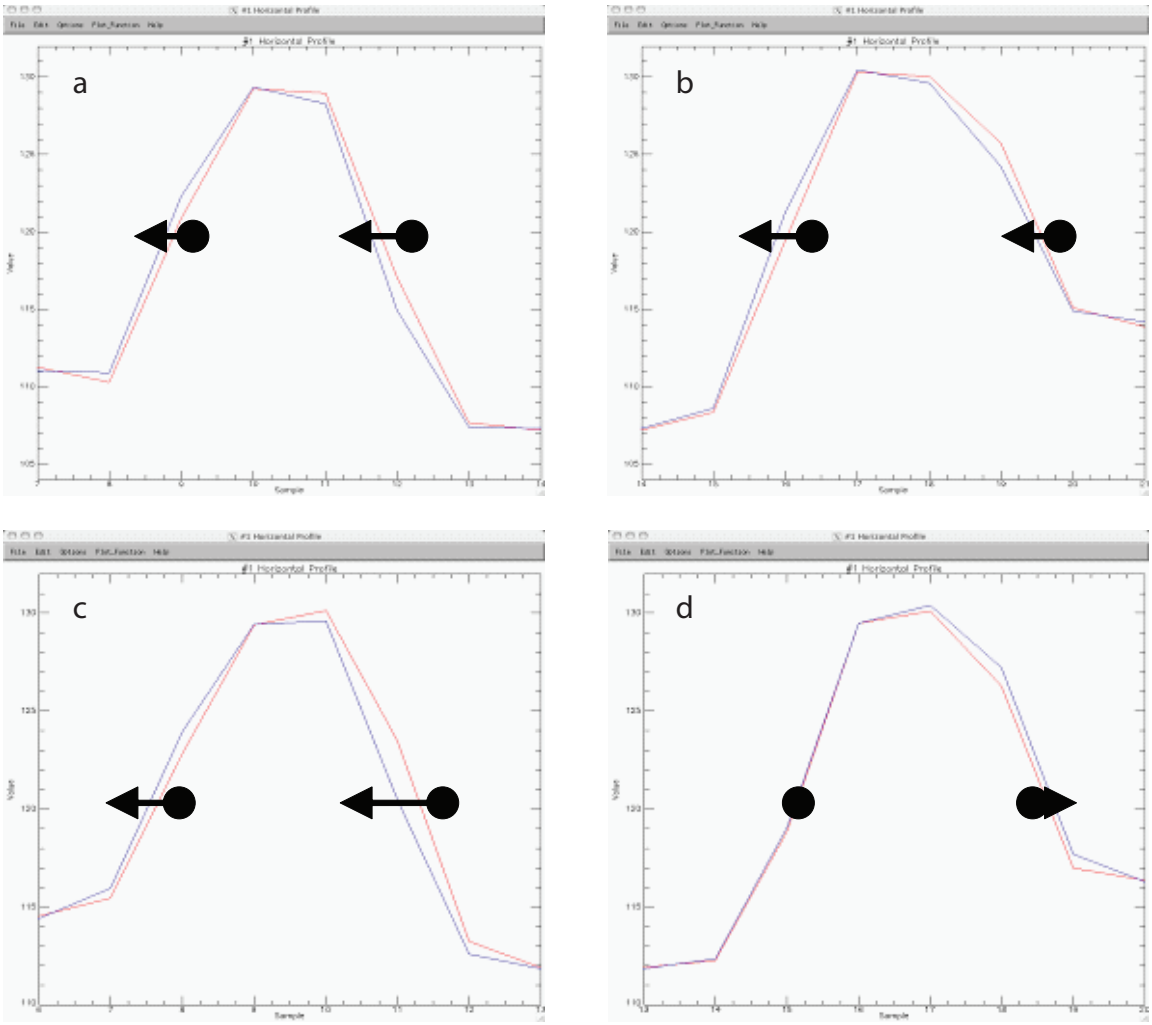

Figure 8. Horizontal transects: (a) Shot-29, building 1; (b) Shot-29, building 2; (c) Shot-22, building 1; (d) Shot-22, building 2

Conclusion

Based on the data sets used in this study, estimation of global image offsets and correction by resampling appears to be limited to cases where localized displacements due to atmospheric turbulence are relatively low. The sensitivity to turbulence is likely to be magnified by distance from target, so proximity to target would be expected to improve results during difficult conditions. Alternatively, it may be possible to confidently identify and reduce camera motion from the entire scene if a target is placed in the near-field and the FHT phase-shift analysis is performed on an image subset just around that target.

Original discussions with NSTec identified a target accuracy for image registration of less than 0.1 pixels. Based on the phase-shift calculations performed here, the test images that were provided for use in this study were already approximately at this level of precision, so it is yet to be verified that the tools developed in MA_Tool could move image data subject to greater camera vibration to the target registration accuracy. It is quite possible that MA_Tool might lock onto a pattern of global image motion even in a somewhat turbulent atmosphere, if the effect of camera motion was large relative to the scintillation. However, if this were the case, then more sophisticated methods for smoothing the resulting estimates of image displacements would be required in order to deal with scintillation dominating the periods of crossover between extremes in camera motion.

References

Di Benedetto, J., S. Lutz, S. Jones, S. Petersen, K, McGwire, "Repetitive Motion Imaging," *Nevada Test Site–Directed Research and Development*, FY 2007, National Security Technologies, LLC, Las Vegas, Nevada, 2008, 257–265.

Rasband, W. S., "ImageJ," U.S. National Institutes of Health, Bethesda, Maryland, 1997, http://rsb.info.nih.gov/ij/, accessed September 30, 2007.

Reaves, A. "Optimized fast Hartley transform for the mc68000 with applications in image processing," Master's thesis, Dartmouth College, March, 1990, http://rsb.info.nih.gov/ij/docs/ImageFFT/docs/thesis.pdf, accessed September 30, 2007.

NOTE: Final report for subcontract UNR 07-43 with the University of Nevada, Reno

Work performed by:
Kenneth McGwire
Desert Research Institute
Division of Earth and Ecosystem Sciences
2215 Raggio Parkway, Reno, NV 89512 (Ken.McGwire@dri.edu)

this page intentionally left blank

Optical Pin Measuring Machine

Brian Cox, Daniel Frayer, Amy E. Lewis[1]
Los Alamos Operations

As photon Doppler velocimetry (PDV) diagnostics advance and hydrodynamic experiments become more prominent, the need to produce high-quality optical pins and domes increases. But even though the design and fabrication techniques for optical and hybrid domes move forward, pin metrology methods lag behind. This project developed and tested metrology hardware and a technique to qualify an optical pin to <10 μm from its nominal location. Because new optical pin technology must correlate decades of archived electrical dome data, we chose a design strategy that fixed an existing optical detector into the pin-measuring hardware at Los Alamos National Laboratory's (LANL's) pin assembly laboratory. This report summarizes the design and testing of the pin measuring machine and metrology method on a sample dome; the data analysis is also presented.

Background

Spherical electrical and optical pin arrays allow diagnoses of explosively driven implosions. Electronic pin domes measure the implosion of explosive devices by recording the time when the individual pins are shorted by the shock front. For successful data collection, the electrical pin tips must be located and measured precisely in radius and angle. A dome, whether it is hemispherical or almost fully spherical, is made of an electrically insulated material, such as plastic or phenolic, that holds a large number of wires (pins) radiating from its center. The wires, usually spring steel, are inserted into individual holes in the dome and exit through the dome base. Before use, they are cut to specified lengths, likely several discrete radii. The number of pins in the dome can vary; older technologies may contain about 50 pins, while modern domes may have up to 600 pins. Pin domes are mounted on hardware designed to fit into a mock-up of a nuclear explosive device.

Because they transmit light from the imploding device until the implosion impacts the dome surface, optical pins, made of optical fibers, need not extend beyond the dome's surface. Because they continuously record data, such pins yield 2000 to 10,000 times more data points than electrical pins covering the same surface area. The angle and position of each fiber's tiny viewing area must be carefully measured to document the vector of the laser light emanating from the fiber probe. In this aspect, optical pin metrology varies considerably from that of an electrical pin, since the vector, rather than a single point in space, must be characterized. Figure 1 shows optical and hybrid (electrical and optical pins)

[1] lewisae@nv.doe.gov, 505-663-2053

domes. The optical dome in the figure was designed during an FY 2005 SDRD project (Romero, 2006), and a partially populated dome of this type was used to develop the alignment techniques in this year's project.

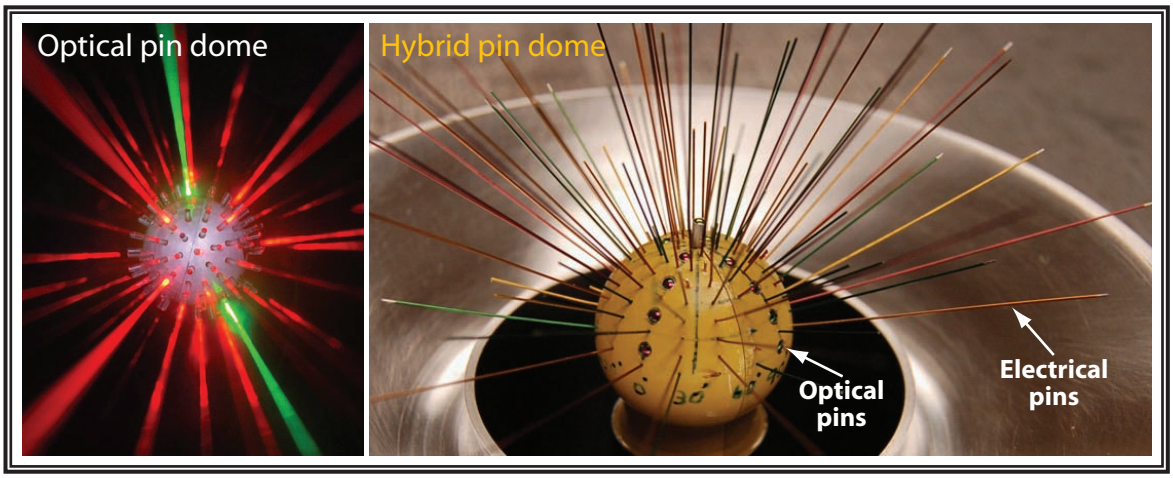

Figure 1. Sample optical and hybrid pin domes

An optical detector is used to precisely align and characterize the fiber probes in an optical dome. The detector assembly in our pin measuring machine was composed of commercial and custom-built components, including a commercial alignment head (the AlignMeter from Melles Griot) containing two quadrant detectors, as well as the custom hardware used to mount it into the existing translating arm. Figure 2 illustrates the component detail for the AlignMeter head. Combining two quadrant detectors allows detection and recording of the position and the angular deviations of an incident light beam. Measurements are computed by a special software package, enabling simultaneous calculation and display of beam characteristics.

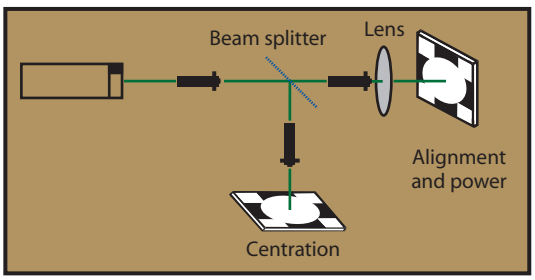

Figure 2. Melles Griot's AlignMeter quadrant detector configuration

Project

Mechanical Design

The core of the optical pin measuring machine was a commercial alignment system, the AlignMeter. To minimize potential damage, the mechanical design required that the AlignMeter mount fit the existing semikinematic mounting system and weigh no more than 300 g. Because future data sets measured using the AlignMeter must correlate with all previous data sets, the AlignMeter mount and other new probes must perform as well as or better than the existing probes in both self-weight sag and mounting repeatability. Finally, a simultaneous mastering scheme for the AlignMeter and pin measuring machine had to be defined.

The mounting apparatus on the LANL pin dome characterization machine utilizes a system of grooves and balls to exactly constrain the probe arm. Six point contacts on six flat surfaces ensure that the arm can repeatedly mount and dismount. An eccentric ball and pair of ball-tip setscrews provide three adjustable degrees of freedom that allow the user to precisely position the probe tip. Because the existing pin lab system is very old and undocumented, the mount has been reverse-engineered for fabrication and testing (Figure 3).

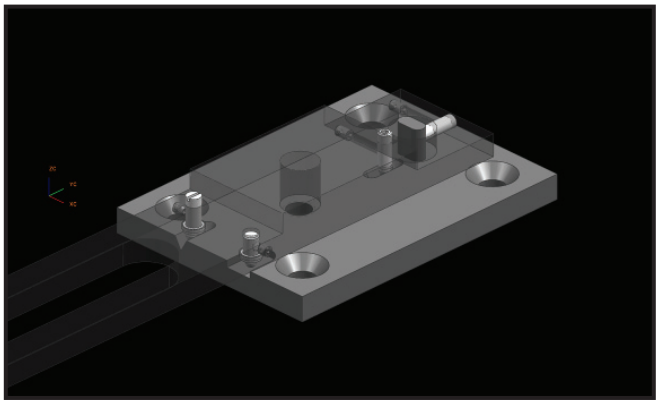

Figure 3. Ball-groove mounting system

As an experimental method of correlating wire data to optical data, a hybrid fiber (HF) probe was designed and fabricated. Using the same basic form factor as the wire pin dome probe, an optical fiber was installed into the probe tip to detect a collimated light source. Because of the fiber's small diameter, the probe could still characterize wire pins but could now also characterize a laser light source. Minor changes were made to help stiffen the probe arm and enable insertion of the fiber into the probe tip. The hybrid arm (Figure 4) retains all necessary degrees of freedom required to adjust probe tip location.

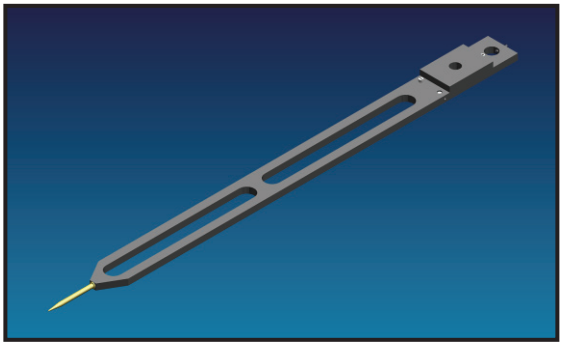

Figure 4. Hybrid fiber probe

The team produced a weight-optimized truss structure and I-beam design for mounting the AlignMeter onto the semikinematic mount. The parts were fabricated from 6061-T6 aluminum due to its excellent stiffness-to-weight ratio. The design's weight-saving features reduced the final weight of the AlignMeter head and mount to 270 g. Because the AlignMeter's aperture is much larger than the lasers being measured, it was not necessary to include three adjustable degrees of freedom, as needed for the hybrid probe. Instead, three fixed spherical points locate the AlignMeter's aperture with standard machine tolerances. A three-dimensional view of the AlignMeter mount appears in Figure 5.

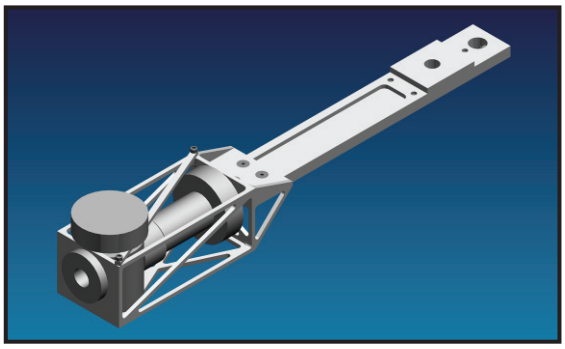

Figure 5. AlignMeter mount design

Finite element analysis studies using ANSYS were performed on both the wire pin dome probe and AlignMeter mount to evaluate the design's performance characteristics (Figure 6). The results show that the overall gravitational sag of the AlignMeter's mount was <50% that of the existing pin measuring probe, while weighing 50% more. Not only did this modeling help verify the performance of the original probe when subjected to self-weight, but it also confirmed that the AlignMeter's mount could very effectively constrain gravitational motion. The resulting maximum deflections for the pin probe and the AlignMeter mount are 30.4 μm and 15.1 μm, respectively.

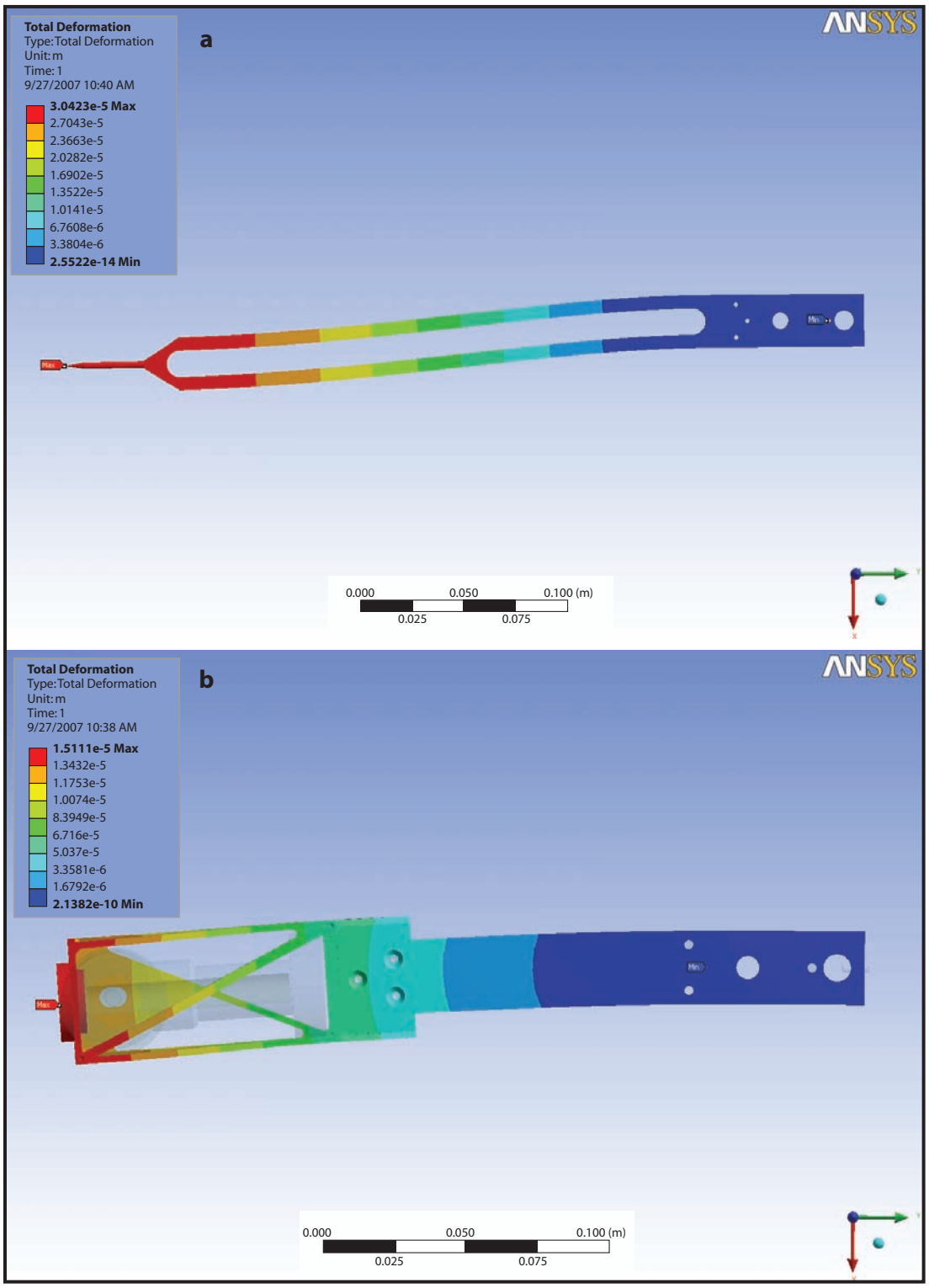

Figure 6. Finite element analysis of (a) pin probe and (b) AlignMeter mount

The test bed used to evaluate the experimental pin measuring technique had not been accurately mastered for production measurement. Therefore, a mastering scheme was defined to ensure that measurements taken with the AlignMeter were as accurate as possible. To do this, the team fabricated several parts modeled after those used in mastering techniques used in the production pin dome lab.

A mounted calibration sphere allowed us to find the system's center and align the perpendicular centers of rotation in the system. The sphere was a truncated and threaded ball with an overall diameter of 1 ±0.0001 in. and a measured sphericity of ≤10 micro-inches. To ease optical pin dome centering, the height and outer diameter of the calibration ball was the same as the mounted optical pin dome. A conical calibration point having a sharp tip was also available for gross mastering of the hybrid probe's tip. The height of the calibration point tip was the same as the center of the calibration sphere when mounted. Both calibration devices are pictured in Figure 7.

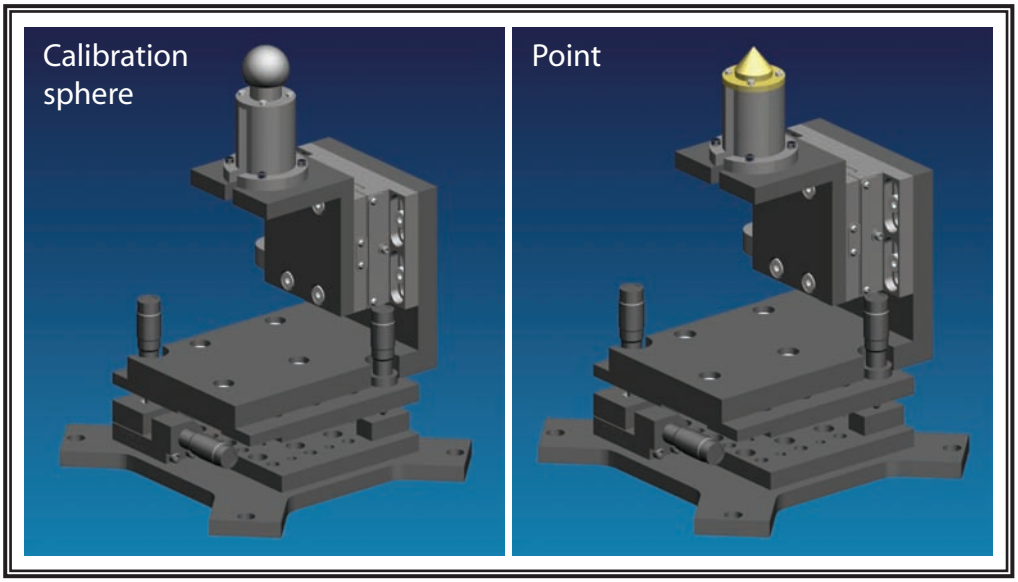

Figure 7. Calibration sphere and point

A highly effective piece of hardware, the Laser Calibration Assembly (LCA), was designed to master the system in conjunction with the AlignMeter and a laser source. The LCA employed a precision beam splitter to divide a collimated laser into two perpendicular beams. The LCA (Figure 8) was designed to master the location of machine components, confirm alignment of the system's two rotation stages, and provide a perfectly vertical zero reference for AlignMeter calibration.

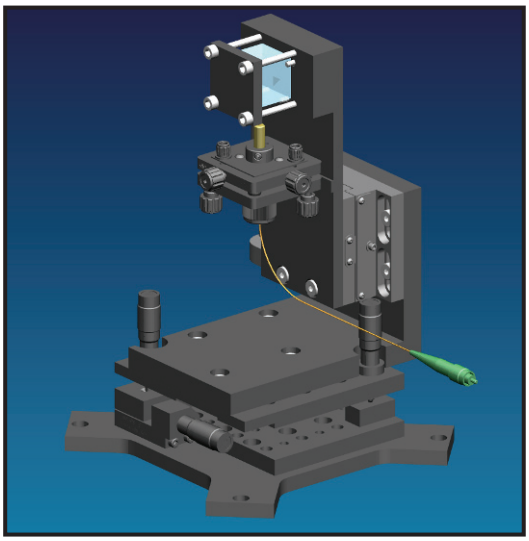

Figure 8. Laser calibration assembly

Data Collection

Prior to data collection, the existing test bed measurement machine was mastered according to this scheme:

1. The LCA was aligned such that its two emergent laser beams were both perpendicular to each other and aligned with the directions defined by the LCA's mounting scheme. The alignment required a standard optical table, sliding apertures mounted on long translation rails, and the AlignMeter.
2. The LCA was placed on the lower rotation stage so its vertical beam was colinear with the stage's axis of rotation by attaching the AlignMeter assembly to the machine and turning the rotation stage. First, the LCA system angles were adjusted to bring the beam and the axis into parallel, and then the position was adjusted in x and y to bring them into colinearity.
3. The radial translation stage on the machine was translated to determine parallelism in two directions. Any nonparallelism was considered in the data analysis calculations.
4. The lower rotation stage's position was adjusted so that its axis of rotation intersected the upper arm's axis of rotation by swinging the arm and lower rotation stage to ±90 degrees and observing, then bringing to zero the difference in the AlignMeter's measurement in the direction of the arm's swing.
5. The test pin dome was centered about the lower rotation stage's axis of rotation by replacing the AlignMeter assembly with the HF probe assembly and gently adjusting the dome position until the HF assembly contacted it at the ±90 degrees positions.

This process was implemented because of its utility for all-optical domes. For the measurement of hybrid domes, an alternate process that relied more on the HF assembly was envisioned. Prior to executing the mastering steps, the accuracy and repeatability of the AlignMeter itself were tested. The effective distance from the front face to the internal position measuring plane of the AlignMeter (r_{AM}) was also measured.

Multiple data sets were taken as follows: two supersets were taken at two different radii. Within each of these, one set was taken by zeroing the angle read by the AlignMeter and another by zeroing the position. This scheme was developed to allow a best fit on the data, as several constant offsets were not precisely defined, including the relationship between the radial measurement given by the machine and the actual center of the coordinate system, the translation angles of the radial stage (as mentioned in step #3), and the mounting angles of the AlignMeter assembly. The data collection arrangement appears in Figure 9.

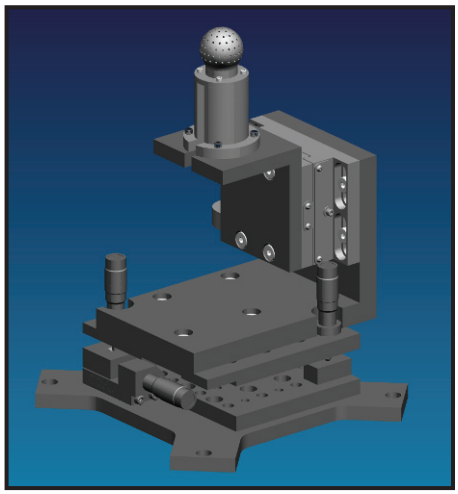

Figure 9. Test arrangement

Data Analysis

The reporting scheme for our resultant data consisted of (ϕ_T, θ_T, Δx, Δy): the two system angles (ϕ_T, θ_T) that describe the beam angle emitted from a given point, and the Cartesian offsets (Δx, Δy) that describe the distance from the real beam to an ideal beam emitted at (ϕ_T, θ_T) from the center of the coordinate system (and, consequently, the pin dome), where Δx is parallel to a sweep in Φ, and Δy is orthogonal to both x and the ideal beam. Measured data consisted of (Φ, Θ, ρ), the polar and azimuthal angles and radius reported by the measurement machine, and (x_0, y_0, ϕ_0, θ_0), the angles and positions reported by the AlignMeter software. The two schemes are related as follows:

$$\varphi_T = \Phi + \varphi_0, \tag{1}$$

$$\theta_T = \theta \left| 2 \cdot \tan^{-1} \left[\frac{\tan\left(\frac{\theta_0}{z}\right)}{\sin\left(\varphi_T\right)} \right], \right. \tag{2}$$

$$\Delta x = -R \cdot \tan(\varphi_0) + x_0, \tag{3}$$

$$\Delta y = -(R + \Delta r) \cdot \tan\left[2 \cdot \tan^{-1} \left[\frac{\tan\left(\frac{\theta_0}{z}\right)}{\sin(\varphi_T)} \right] \right] \cdot \sin(\varphi_T) + x_0. \tag{4}$$

The real radius R was found by summing the measured ρ and (1) the offset between the tip of the HF probe and the center of the system; (2) the difference in length between the HF and AlignMeter probes; and (3) r_{AM} such that

$$R = \rho - r_{HF-CMM} + r_{HF-AM} + r_{AM}. \tag{5}$$

Note that these equations take into account the sign conventions reported by the machine and the AlignMeter.

The formatted data were then compared to a set of numbers corresponding to the nominal vectors. Several least-squares-fit (LSF) routines were performed, to best align (1) the data from each of the two subsets, with a change in radius from that given by the machine as the variable; (2) the data from the two supersets, with translational angles as the variable; and (3) the average data from all four sets to the nominal vectors, with an angle about the axis of rotation of the lower rotation stage as a variable.

The LSFs showed that (1) the measured R was incorrect by a small amount; (2) the solved-for translational angles were very close to those independently calculated via step #3 in the mastering process; (3) once the correct R was used and the translational angles accounted for, the four-set scheme resulted in very precise data; and (4) once the rotational variable was accounted for, the data were very close to the nominal, with deviations within manufacturing tolerances. Table 1 shows the angular and positional deviations of the average from the nominal vectors, as well as the standard deviations (AlignMeter manual, 2005). It should be noted that fiber #7's position at the pole introduces large errors and rotational ambiguity, making it more difficult to measure and analyze.

Table 1. Angular and positional deviations from nominal

fiber	polar deviation (degrees)	stdev (degrees)	azimuthal deviation (degrees)	stdev (degrees)	x-offset (mm)	stdev (mm)	y-offest (mm)	stdev (mm)
1	1.42	0.01	1.37	0.08	−0.19	0.04	0.18	0.11
2	−0.78	0.01	0.23	0.04	0.29	0.01	0.05	0.10
3	1.43	0.01	−0.13	0.05	−0.17	0.02	0.09	0.09
4	−0.97	0.01	0.56	0.06	0.25	0.01	0.12	0.08
5	0.91	0.01	−1.07	0.22	0.06	0.02	−0.22	0.07
6	−0.20	0.00	−2.37	0.15	0.31	0.01	−0.06	0.09
7	0.00	0.30	−65.31	66.25	0.30	0.11	0.13	1.75
8	−0.28	0.01	0.59	0.20	0.01	0.01	0.18	0.04
9	−0.60	0.11	−2.17	0.26	0.11	0.08	−0.28	0.03
10	0.48	0.01	−0.31	0.10	−0.15	0.01	−0.13	0.06
11	0.38	0.01	−1.42	0.07	0.05	0.02	−0.04	0.09
12	−0.18	0.01	−0.39	0.05	0.15	0.01	0.14	0.10
13	1.57	0.00	0.13	0.07	−0.10	0.01	0.17	0.11
14	0.58	0.01	0.27	0.06	0.02	0.01	0.16	0.10
15	−0.38	0.01	−0.64	0.05	0.12	0.03	0.08	0.12
16	1.16	0.00	−0.66	0.14	−0.20	0.02	−0.04	0.10
17	−0.68	0.00	1.19	0.14	0.35	0.01	0.32	0.08
18	−0.72	0.25	0.88	0.07	0.39	0.02	0.18	0.11
19	−0.11	0.00	−1.04	0.07	0.33	0.01	0.00	0.09

The graphical representation of the tabular data is shown in Figure 10. Each vector, representing a PDV detector, emanates from the relevant dome hole. Once certain variables are known for a given system, it is conceivable that one or two data sets would suffice. Certainty in *R* would obviate the usefulness of zeroing both angle and position. More accurate mounting of the radial stage and/or knowledge of its errors would similarly preclude the need to collect data at different radii. Production optical pin domes will need a clocking feature either on the dome or the blast hardware to facilitate an accurate clocking measurement.

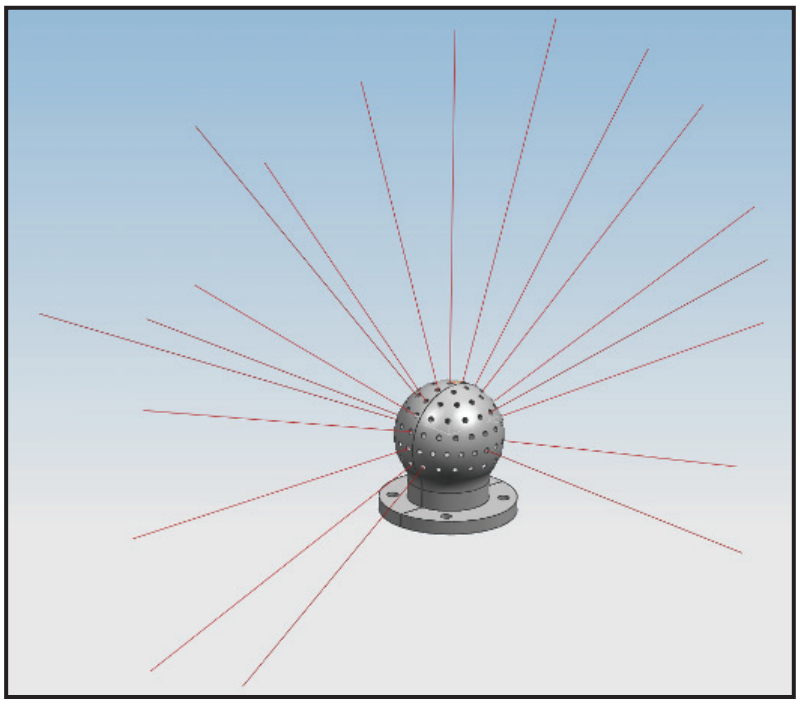

Figure 10. Final data

Conclusion

Advancements in optical pin metrology must continue to correlate data taken with electrical domes over the past 40 years, as we apply this immense database of knowledge to more advanced experiments. Hence, the equipment and techniques developed during this project will offer immediate advantages when used in the pin assembly laboratory alongside older techniques. Data from the test bed indicate that this technique is safe for arm manipulation and valid for dome characterization. The project team developed prototype metrology hardware, demonstrated its effectiveness, and documented a feasible test procedure.

Acknowledgments

We want to thank Matt Briggs, Lori Primas, and Wayne Scoggins (LANL) for providing access to their test bed and for sharing their PDV data.

References

AlignMeter Simultaneous Measurements of Position and Angular Displacements: User Manual, Version 5.1, April 2005, http://mellesgriot.com, accessed November 14, 2006.

Romero, V. T., "Development of a Multichannel Velocity Interferometer Optical Probe," *Nevada Test Site–Directed Research, Development, and Demonstration,* FY 2005, Bechtel Nevada/National Security Technologies, LLC, 2006, 343–348.

Zero Delay Velocimeter

Bruce Marshall[1]
Special Technologies Laboratory

Velocity interferometry system for any reflector (VISAR) diagnostics are widely used in the weapons test community for measurement of shock velocity. The delay time of a VISAR interferometer limits the time response of the measurement. This project was an attempt to produce an instrument similar to a VISAR, but with improved time response, using dispersion instead of delay to generate the transfer function. Unfortunately, it appears that this is a self-contradictory goal and is inherently impossible to achieve.

Background

A VISAR system uses a wide-field, delayed Michelson interferometer to measure the Doppler shift of laser light reflected from a moving target. In the VISAR cavity, the wavefront interferes with a delayed wavefront to generate fringes whose phase is determined by the delay time divided by the period of the optical wave. During a measurement, a change in target velocity can be determined simply and with high accuracy from the change in phase of the interferometer, as long as the velocity is stable on a time scale comparable to the delay. Any abrupt change in velocity or spatial coherence must propagate through the interferometer for the simple VISAR analysis to be applicable. If the velocity changes on a time scale that is shorter than that of the delay, a more complex analysis is needed and some assumptions about the shape of the acceleration may be necessary (Hemsing, 1991; Dolan, 2006).

Since the velocity per fringe (VPF) constant is inversely proportional to the VISAR delay, a VISAR optimized for low velocities has correspondingly poor time response. A 1000-meter/second/fringe VISAR requires a 0.266-ns delay, while a 100 m/s/f VISAR has a 2.66-ns delay. Applications with low velocities but rapid accelerations would benefit from an improvement in the tradeoff between velocity resolution and time response.

Project

A VISAR can be considered as an optical filter with a sinusoidal transfer function obtained via phase delay with negligible dispersion. It seemed reasonable to consider optimizing the time-bandwidth product of this filter primarily by using dispersion. For example, one could imagine an interferometer with highly dispersive zero delay at the unshifted laser wavelength whose phase would change with wavelength because the delay would be wavelength-dependent.

[1] marshabr@nv.doe.gov, 805-681-2266

Unfortunately, I made an error in the preliminary model and came to the conclusion that the idea was feasible. In fact, an interferometer with linear phase vs. frequency dependence and zero delay has zero phase sensitivity regardless of the dispersion in the optical media. Furthermore, an interferometer with nonlinear phase vs. frequency dependence would develop a finite delay as the wavelength shifted away from the zero-delay wavelength. A finite VPF implies a non-zero delay. In the course of the project, I demonstrated this fact theoretically in two different ways, and also built a dispersive interferometer that very clearly confirmed the fact.

Taylor Expansion

The response of a dispersive interferometer can be demonstrated fairly simply by approximating the phase using a Taylor expansion and then differentiating it to obtain the sensitivity to wavelength.

$$\Phi(\lambda) \cong \Phi(\lambda_0) + (\lambda - \lambda_0)\left.\frac{d\Phi}{d\lambda}\right|_{\lambda_0} + \frac{(\lambda - \lambda_0)^2}{2}\left.\frac{d^2\Phi}{d\lambda^2}\right|_{\lambda_0}$$
$$\frac{d\Phi}{d\lambda} \cong \left.\frac{d\Phi}{d\lambda}\right|_{\lambda_0} + (\lambda - \lambda_0)\left.\frac{d^2\Phi}{d\lambda^2}\right|_{\lambda_0} \quad (1)$$

The group delay τ_g is:

$$\tau_g(\lambda) = \frac{d\Phi}{d\omega} = \frac{d\Phi}{d\lambda}\frac{d\lambda}{d\omega} = \frac{-\lambda^2}{2\pi c}\frac{d\Phi}{d\lambda}, \quad (2)$$

$$\tau_g(\lambda_0) = \frac{-\lambda_0^2}{2\pi c}\left.\frac{d\Phi}{d\lambda}\right|_{\lambda_0}, \quad (3)$$

$$\frac{d\Phi}{d\lambda} \cong -\tau_g(\lambda_0)\frac{2\pi c}{\lambda_0^2} + (\lambda - \lambda_0)\left.\frac{d^2\Phi}{d\lambda^2}\right|_{\lambda_0}. \quad (4)$$

Therefore, if the group delay at λ_0 is zero ($\tau_g(\lambda_0) = 0$), then it follows that $\left.\frac{d\Phi}{d\lambda}\right|_{\lambda_0} = 0$, and $\frac{d\Phi}{d\lambda}$ is proportional to λ_0;

$$\frac{d\Phi}{d\lambda} \cong (\lambda - \lambda_0)\left.\frac{d^2\Phi}{d\lambda^2}\right|_{\lambda_0} \quad (5)$$

and $\Delta\Phi$ depends quadratically on λ, not linearly, as one would wish for a VISAR.

$$\Delta\Phi(\lambda,\lambda_0) \cong \frac{(\lambda-\lambda_0)^2}{2}\left.\frac{d^2\Phi}{d\lambda^2}\right|_{\lambda_0} \tag{6}$$

For a conventional VISAR with path lengths l_1 and l_2 of refractive indices n_1 and n_2, the phase is:

$$\Phi(\lambda) = \frac{2\pi}{\lambda}\left(l_1 n_1(\lambda) - l_2 n_2(\lambda)\right), \tag{7}$$

and the derivative of the phase with respect to wavelength is:

$$\begin{aligned}
\frac{d\Phi}{d\lambda} &= \frac{2\pi}{\lambda}\left(l_1\frac{dn_1}{d\lambda} - l_2\frac{dn_2}{d\lambda}\right) - \frac{2\pi}{\lambda^2}\left(l_1 n_1(\lambda) - l_2 n_2(\lambda)\right) \\
&= -\frac{2\pi}{\lambda^2}\left(l_1\left(n_1(\lambda) - \lambda\frac{dn_1}{d\lambda}\right) - l_2\left(n_2(\lambda) - \lambda\frac{dn_2}{d\lambda}\right)\right) \\
&= -\frac{2\pi c}{\lambda^2}\left(\frac{l_1 n_{1g}(\lambda)}{c} - \frac{l_2 n_{2g}(\lambda)}{c}\right) \\
&= -\frac{2\pi c}{\lambda^2}\left(\tau_{1g}(\lambda) - \tau_{2g}(\lambda)\right).
\end{aligned} \tag{8}$$

The inverse of the VPF can then be shown to depend linearly on the group delays at a given wavelength.

$$\lambda = \frac{\lambda_0}{1+\frac{2V}{c}}, \tag{9}$$

$$\frac{d\lambda}{dV} = -\frac{\lambda_0}{\left(1+\frac{2V}{c}\right)^2}\frac{2}{c} \cong -\frac{2\lambda_0}{c} \text{ for } V << c, \tag{10}$$

$$
\begin{aligned}
\frac{1}{VPF} &= \frac{d\Phi}{dV} = \frac{d\Phi}{d\lambda}\frac{d\lambda}{dV} = -\frac{2\lambda_0}{c}\frac{d\Phi}{d\lambda} \\
&= \left(-\frac{2\lambda_0}{c}\right)\left(-\frac{2\pi c}{\lambda^2}\left(\tau_{1g}(\lambda)-\tau_{2g}(\lambda)\right)\right) \\
&= \frac{4\pi\lambda_0}{\lambda}\left(\tau_{1g}(\lambda)-\tau_{2g}(\lambda)\right) \\
&\cong \frac{4\pi}{\lambda}\left(\left(\tau_{1g}(\lambda_0)+(\lambda-\lambda_0)\frac{d\tau_{1g}}{d\lambda}\right)-\left(\tau_{2g}(\lambda_0)+(\lambda-\lambda_0)\frac{d\tau_{2g}}{d\lambda}\right)\right) \\
&\cong \frac{4\pi}{\lambda}\left(\left(\tau_{1g}(\lambda_0)-\tau_{2g}(\lambda_0)\right)+(\lambda-\lambda_0)\left(\frac{d\tau_{1g}}{d\lambda}-\frac{d\tau_{2g}}{d\lambda}\right)\right),
\end{aligned}
\tag{11}
$$

where V represents the velocity of the target and c is the speed of light.

If the group delays of the two paths are equal at λ_0, then $\frac{1}{VPF}$ and $\frac{d\Phi}{dV}$

will be zero at λ_0 and will have linear dependence on $\Delta\lambda$.

If the wavelength changes sufficiently to give a finite value to $\frac{1}{VPF}$ and $\frac{d\Phi}{dV}$,

then the group delay at that wavelength will no longer be zero and the time domain response over a small range of wavelengths will be approximately that of a conventional VISAR. Also, the VPF will no longer be a constant, but will vary with velocity.

Fourier Transform

The zero-delay velocimeter model can also be addressed by means of the Fourier transform. We can consider the zero-delay velocimeter as an optical filter that has sinusoidal amplitude dependence in the frequency domain. Our goal is to minimize the width of the impulse response in the time domain. We can express the frequency domain response of the filter as

$$G(\omega) = \left|G(\omega)\right| e^{ih(\omega)}$$

where the phase component $h(\omega)$ is real. Since we want to maintain the sinusoidal amplitude dependence, the only degree of freedom lies in $h(\omega)$. By the convolution theorem, the Fourier transform of $G(\omega)$ is equal to the time domain convolution of the transforms of $\left|G(\omega)\right|$ and $e^{ih(\omega)}$.

$$
\begin{aligned}
f(t) &= \frac{1}{\sqrt{2\pi}} \int_{-\infty}^{\infty} F(\omega) e^{i\omega t} d\omega \\
&= \frac{1}{\sqrt{2\pi}} \int_{-\infty}^{\infty} \left|F(\omega)\right| e^{i\varphi(\omega)} e^{i\omega t} d\omega \text{ where } \varphi(\omega) \text{ is real} \\
&= \frac{1}{\sqrt{2\pi}} \int_{-\infty}^{\infty} G(\omega) H(\omega) e^{i\omega t} d\omega \\
&= g(t) \otimes h(t) \\
\text{where } G(\omega) &= \left|F(\omega)\right| \quad \text{and} \quad H(\omega) = e^{i\varphi(\omega)}.
\end{aligned}
\tag{12}
$$

$$
\begin{aligned}
\text{If } G(\omega) &= \cos(a\omega), \quad g(t) = \frac{\sqrt{2\pi}}{2}\left(\delta(t-a) + \delta(t+a)\right) \\
f(t) &= g(t) \otimes h(t) = h(t-a) + h(t+a).
\end{aligned}
\tag{13}
$$

Thus, the transform of the VISAR transfer function $\left|G(\omega)\right| = \cos(a\omega)$ is a pair of delta functions separated by 2*a* in the time domain. The corresponding filter time response will therefore consist of a pair of pulses separated by 2*a*. If the VISAR delay, and therefore the pulse separation, are set to zero, the transfer function *G(ω)* will be a constant and the VPF will be infinite. The effect of the $e^{ih(\omega)}$ component is only to shift the pulse pair in time or possibly to broaden the impulses. It cannot be used to eliminate one of the pulses or change their separation. Also, if the pulse separation is frequency-dependent due to dispersion, then the VPF will also be frequency-dependent, since it depends on *a*.

Experiment

I set up a dispersive interferometer using single-mode fiber components at 1550 nm. One leg of the interferometer used Corning SMF28, which has chromatic dispersion of ~+18 ps/(nm·km). The other leg consisted of 100 m of OFS Fitel single-mode fiber with –250 ps/(nm·km) dispersion. The length of SMF28 was adjusted to give zero delay, and a variable air delay was added for fine-tuning. The interferometer delay was measured using a short optical pulse and a fast receiver and oscilloscope. The tunable laser frequency was modulated sinusoidally, and amplitude modulation from the interferometer was observed on the oscilloscope.

With zero delay, no modulation occurred. If the delay was made non-zero either by changing the center wavelength of the laser or by changing the variable delay setting, modulation was observed as expected for an interferometer with that delay.

Conclusion

I have shown that an interferometer with linear phase vs. frequency dependence and zero delay has zero phase sensitivity, regardless of the dispersion in the optical media. Further, an interferometer with nonlinear phase vs. frequency dependence and zero delay at a particular wavelength will have non-zero delay at other wavelengths and will have a non-constant VPF. Therefore, this work concluded that it is not possible to improve the time response of a VISAR interferometer.

References

Dolan, D. H., "Foundations of VISAR analysis," SAND2006-1950, Sandia National Laboratories, Albuquerque, New Mexico, April 2006.

Hemsing, W. F., "VISAR: displacement-mode data reduction," in *SPIE Conference Proceedings: Ultrahigh- and High-Speed Photography, Videography, Photonics, and Velocimetry*, San Diego, California, July 10–13, 1990, P. A. Jaanimagi, B. T. Neyer, L. L. Shaw (eds.) **1346** (January 1991) 141.

Variable Framing Camera

Amy Lewis, Matthew Martin[1]
Los Alamos Operations

National Security Technologies (NSTec) fabricates framing cameras in four- and nine-frame configurations, often substituting a camera in an experimental setup as requirements dictate. This project targeted the development of a flexible circuit-and-control system to produce the deflection voltages during the interframe time. A user-selectable, 1- to 25-frame camera can result, a concept the authors call a VarFrame camera. This report presents the final prototype circuit and performance characteristics.

Background

A framing camera is a data acquisition instrument designed to capture information about a dynamic system by taking multiple images in a limited timeframe. Framing cameras are used in such areas as velocimetry, radiography, and shadowgraphy experiments. Los Alamos Operations has historically made one type of framing camera, which offers the capability to record either four or nine frames. Designed around an electrostatic image tube, this camera images the light present during each frame (at the photocathode) onto the tube's phosphor. Phosphor persistence allows the camera to display multiple frames on the phosphor at one time. During this persistence, a CCD camera is triggered and the analog image collected digitally. The tube functions by converting photons to electrons at the negatively charged photocathode. The electrons move quickly toward the more positive charge of the phosphor (typically, ground potential relative to the photocathode). To prevent phosphor exposure between frames, the image tube is shuttered between exposures. To do this, the gate grid, a ring located behind the photocathode, is held at a more negative charge than the photocathode. Thus, electrons are diverted from the phosphor, and a high-speed gate is realized.

Two sets of deflection plates (Figure 1) skew the electron's position in horizontal (x axis) and vertical (y axis) directions. Hence, each frame's electrons bombard the phosphor surface at a controlled location defined by the deflection-plate voltages. For the deflection to work correctly, each plate in an axis pair must be held at a voltage equivalent in magnitude but opposite in polarity to the other plate in the pair. In this way, each plate on the axis either pushes or pulls on the electrons with an equivalent electromotive force. For example, a frame can be positioned in the upper right corner of the phosphor by applying $+y$ V to the top deflection plate, $-y$ V to the bottom deflection plate, $+x$ V to the right side plate, and $-x$ V to the left side plate. A frame can also be positioned in the center by grounding all of the plates.

[1] martinma@nv.doe.gov, 505-663-2033

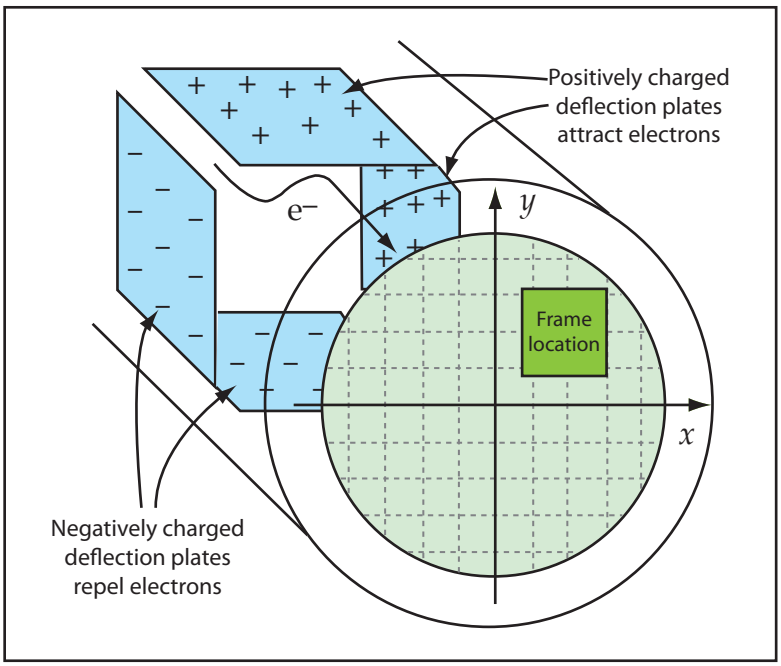

Figure 1. Framing tube deflection plates

The interframe time and number of frames are specified by the user but are limited by the camera electronics. The variable-frame circuit shifts the plate voltages of the first frame to those of the second frame during the user-specified interframe time.

Project

Commercial off-the-shelf (COTS) power supplies and amplifiers were evaluated as possible switching devices to allow voltage adjustment and stabilization during the interframe time. Most high-voltage (HV) power supplies are electronically adjustable. However, settling times, measured in milliseconds, make them unsuitable for driving the plates fast enough. COTS HV amplifiers are produced for the voltages required. The PA98A operational amplifier made by Apex Precision Power could not settle within the time specification of 100 ns. The actual device showed a slew rate of 1000 V/μs, meaning it could shift the plate voltages from rail to rail in 450 ns. Even then, these amplifiers (as others) take more time to settle on an intermediate voltage. With a simple resistive divider feedback circuit, the device took several microseconds to settle.

These devices had other disadvantages as well. Each drew as much as 25 mA of quiescent current. As such, they produced a significant amount of heat and required a significant power supply, even without a load. The circuit to drive a framing tube would conceivably demand at least four of these devices (two per axis). A power supply capable of producing such voltage and current would be hazardous to manipulate. Both the power supply and required heat sinks would require considerable space.

After the possibilities of designing the circuit around a COTS amplifier or power supply were eliminated, we opted to design a custom circuit. The first such circuit attempted control of a plate voltage with a chain of resistors or zener diodes. The voltage would be controlled by selectively shorting parts of the chain. The resistive or zener diode string method works by defining a constant current and varying resistance to produce the desired voltage. Each element of the string would be selectively shorted by a transistor switch controlling the cumulative resistance or reverse breakdown voltage with resistors or zener diodes, respectively. The number of elements would dictate the voltage steps achievable. A capacitive chain would operate differently—more as a traditional voltage divider circuit fed by a voltage source. Regardless of the components, two chains would control each axis. One would generate the variable positive voltage; the other would produce the mirrored negative voltage required by the other plate in the pair. Another set of switches would connect each of the plates to the correct polarity. The effect of capacitance must be minimized to switch from one plate voltage to the next quickly. Hence, the actual capacitance in key areas of the circuit must be minimized, and the current available to charge the capacitance when shifting voltages must be maximized. The output capacitance of the transistors in all the switches became the greatest challenge. The sample zener diode chain in Figure 2 allows for more current flow than the resistive chain. However, this technique's limited resolution and prohibitively high circuit count led us to consider a custom amplifier.

We designed a two-stage push-pull amplifier to amplify a 5-V analog signal (produced from a digital-to-analog converter) to the ±400-V plate voltage. Transistors for this design must tolerate (HV) at a very low conducting current. Most HV transistors target power applications. That is, these transistors have wide channel widths to handle higher conducting currents, which, consequently, increases their capacitance. When used in high-current applications, the capacitance has less impact. Avoiding a high-current, the HV circuit limits the system's safety hazards and bulkiness. Also, the deflection plates are very near an ideal load (high-resistance, near-zero capacitance), and submilliamps of current are necessary to drive them. Thus, we selected the Supertex VN0545 and VP0545, which are N- and P-channel-matched metal-oxide semiconductor field-effect transistors (MOSFETs). Very low capacitance values that would allow high speed with little quiescent current dictated our choice. The disadvantage is that these transistors hold off 450 V, short of the 800 V necessary for each axis. Several transistors can be used to divide the voltage across multiple transistors.

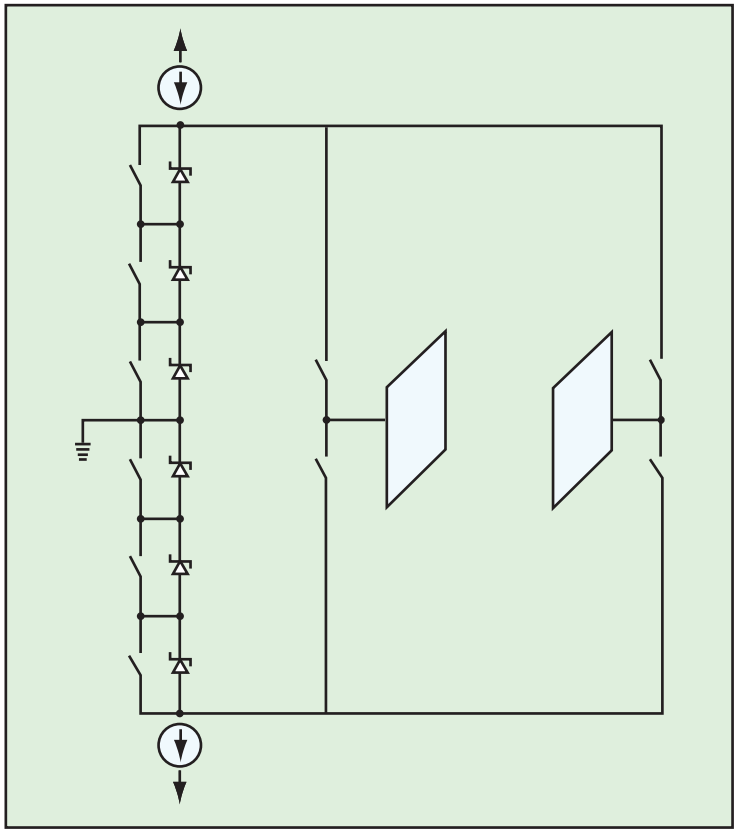

Figure 2. Zener diode chain and deflection plates

In simulation, the amplifier achieved an unacceptable, 14-μs settling time (Figure 3). Also, the simulation optimized the circuit for speed without regard for other considerations. For example, the circuit had poor linearity which would affect resolution and stability for certain input values. Even for a perfect amplifier, the circuit would be vulnerable to noise from the bandwidth and amplification required.

An HV switch design could fulfill the timing requirements but promised the least flexibility in frame positions. To increase voltage resolution, additional switch circuits, along with circuits to preset the voltages, would be necessary. Flexibility costs expensive PCB real estate to realize, but the speed would be achievable with transistors. Switching is simply what transistors do best. The circuitry eliminates any speed considerations in establishing voltage levels, allowing robust voltage preset circuits. The strategy virtually eliminates noise and stability issues.

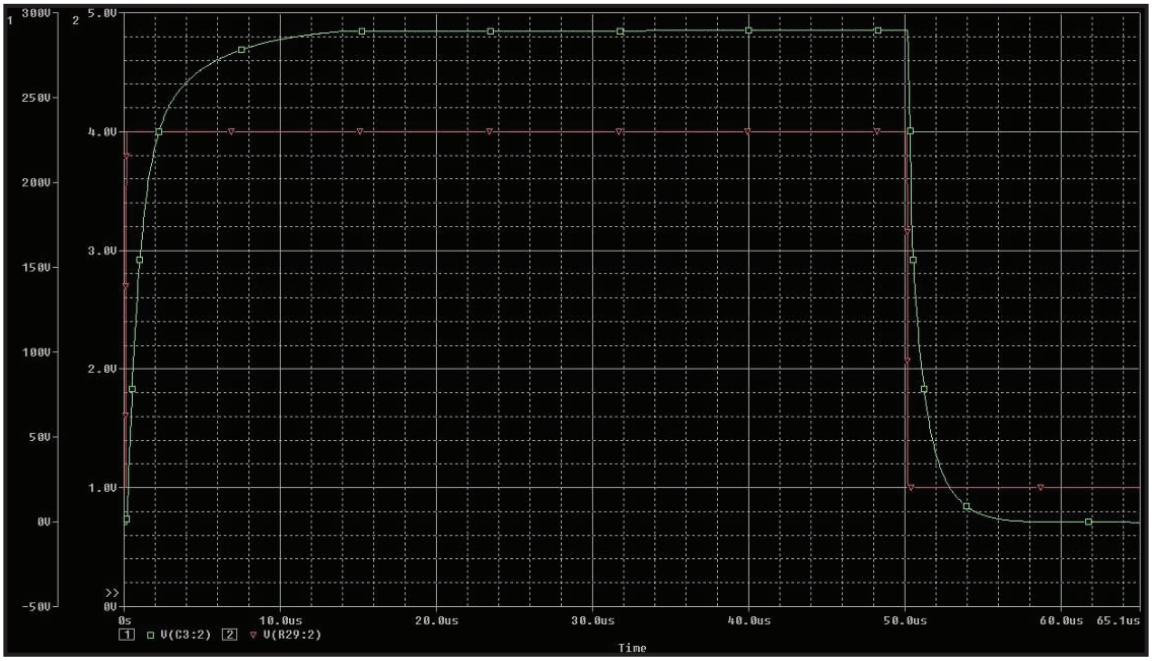

Figure 3. Amplifier circuit simulation

Similar to the amplifier, the switched circuit (Figure 4) rails the voltage to a preset potential. The switch does not experience the exponential speed decay that occurs when an amplifier approaches its settling voltage, making the switch very fast. The transistors are pushed well into their saturation region with a gate-source voltage only limited by what would damage the transistor. In simulation, a circuit consisting of one switch could change the output voltage in <200 ns. The real circuit's actual performance (with five switches capable of driving the output to five different voltage states) achieved a speed of <100 ns.

Results

We ultimately fabricated the HV switch. The final deflection circuit deflects to five different frame positions per axis (totaling 25 frames) including center position. To create the preset voltages, we selected electronically adjustable ±500-V power supplies from Emco (CA05P and CA05N). To control output voltage, they require a 0–5 V input. For simplicity, a potentiometer is used to set the power supplies. Future designs could employ digital-to-analog converters to provide digital control. The power supplies were clamped to ±400 V, so as not to exceed the transistors' voltage ratings. The switch timing (Figure 5) is <100 ns. A separate control board receives the trigger signal and

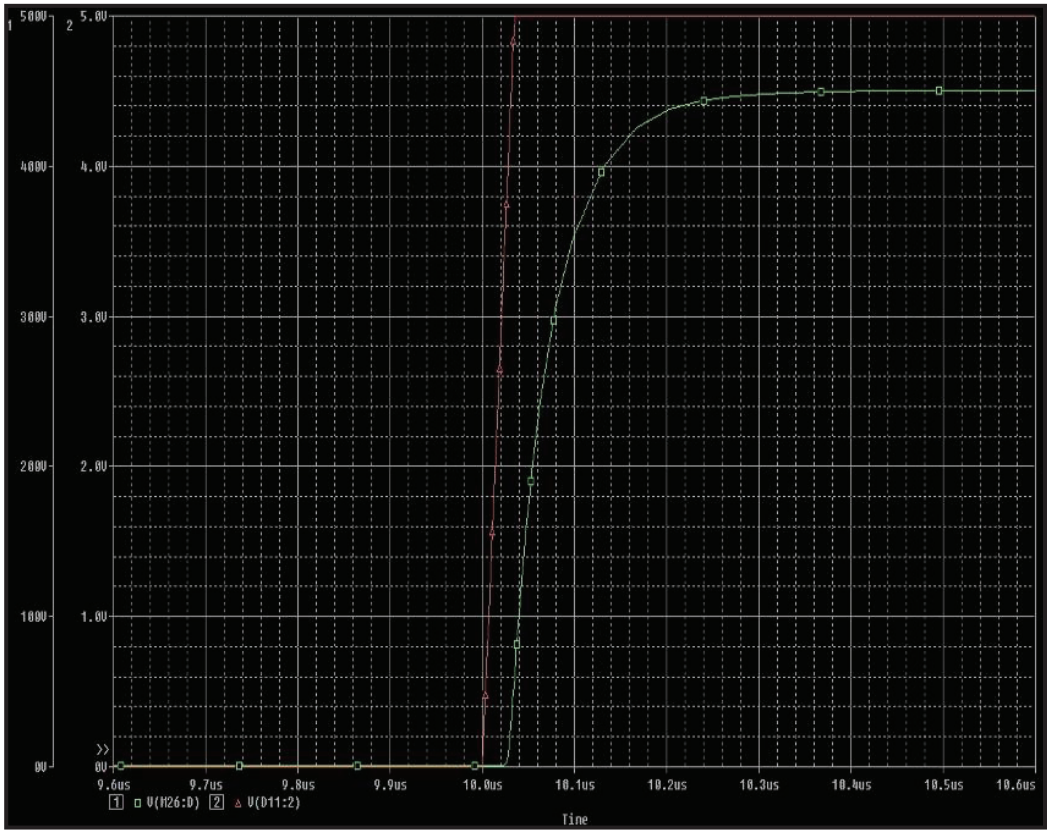

Figure 4. Switched circuit simulation

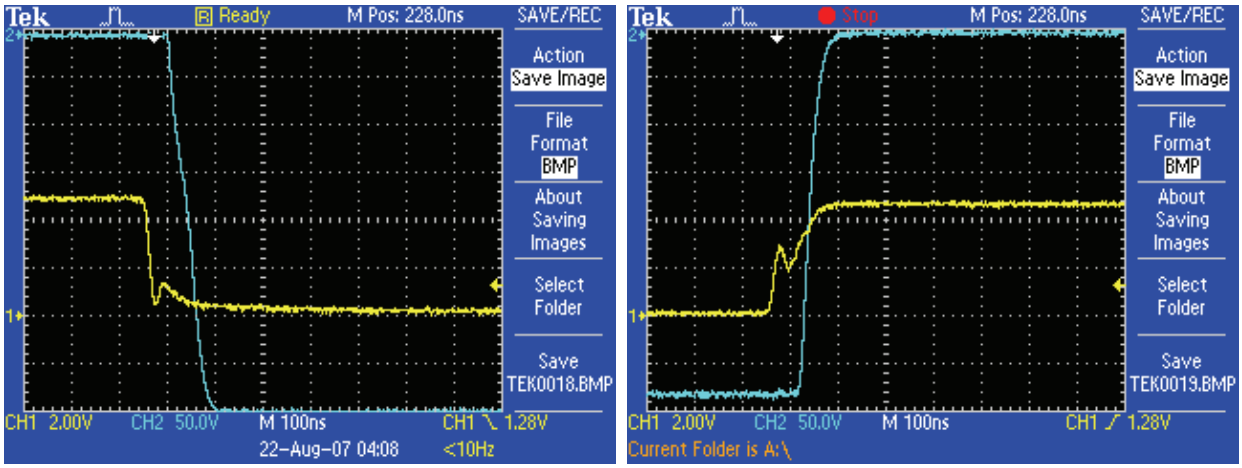

Figure 5. Scope trace from final switching circuit

calculates the combination of plate voltages for each frame. The control board also has provisions to attach a single-board computer for more complex control. The control circuit itself would be more easily integrated into the same PCB as the deflection circuit. Separating the analog portion from the control circuit allowed for two-stage design. The final PCBs appear in Figure 6.

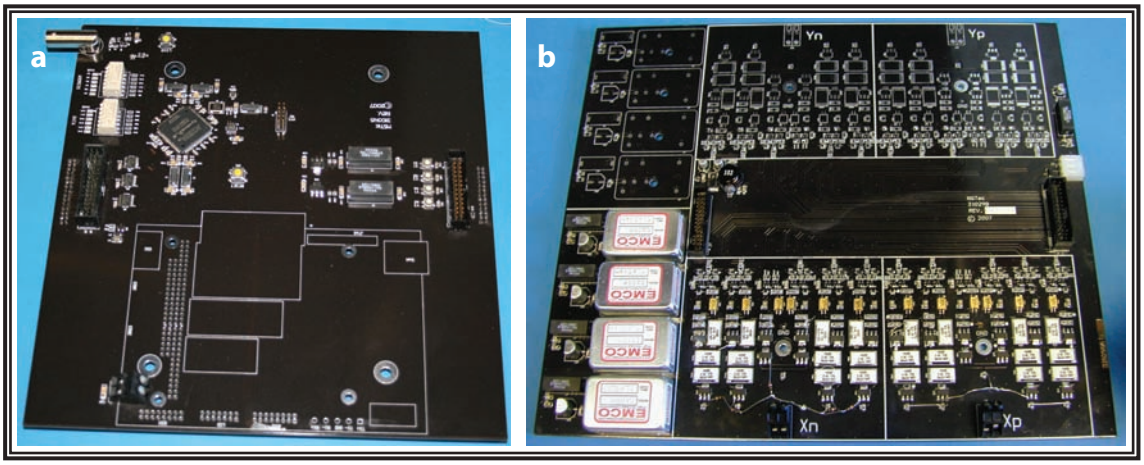

Figure 6. PCBs: (a) fabricated control and (b) HV switching

Conclusion

A control system allowing a user to program the number and location of frames in real time was realized. The tested prototype circuit design can switch to any position in the camera range in less than 100 ns. The current design still restricts the experimenter to a fixed number of frames, although that number is rather large. Design of a VarFrame camera can now begin providing users the tool to field diverse experiments.

References

Baker, R. J., B. P. Johnson, "Stacking power MOSFETs for use in high speed instrumentation," *Rev. Sci. Instrum.* **63,** 12 (1992) 5799–5801.

Dugad, S. R., S. S. Upadhya, M. S. Pose, K. S. Gothe, B. S. Acharya, "Optically isolated high-voltage digital-to-analog converter," *Nucl. Instrum. Methods Phys. A* **548** (2005) 590–596.

this page intentionally left blank

Hybrid Electro-optic Links

E. Kirk Miller[1]
Special Technologies Laboratory

This project created a fieldable fiber-optic data link based on phase-modulation for instrumentation of inertial-confinement fusion (ICF) experiments. In addition, the effects of intense, pulsed radiation on the transmission fibers were investigated, with new short-time and high-dose regimes explored for the first time.

Background

The use of electro-optic (EO) links (e.g., Mach-Zehnders) is gaining traction in ICF experiments, such as laser-driven experiments at OMEGA and the National Ignition Facility, and pulsed-power-driven experiments at Sandia's Z-machine and National Security Technologies' (NSTec's) Dense Plasma Focus (DPF). Compared with conventional Mach-Zehnders, the sophisticated data transmission and acquisition afforded by phase-modulated EO links will readily yield extended bandwidth and dynamic range while simplifying the link and isolating the experiment electrically from the recording system. Because they require high bandwidths and are conducted in an electrically noisy environment, ICF reaction history measurements are well suited to using EO links.

Project

This project was separated into two phases: the development of a prototype demodulation interferometer that would be suitable for high-bandwidth recording of phase-modulated signals, and radiation studies on transmission fibers to examine phase and attenuation effects during radiation pulses. All work was done at a wavelength of 1550 nm, with recorded optical power of ~1 mW, suitable for detection using commercially available 12-GHz photoreceivers.

For the demodulation interferometer, several configurations were investigated, with the initial goal of delivering well-defined, amplitude-encoded outputs 90 degrees out of phase (in quadrature). The decision was made to design the demodulation interferometer completely in-fiber. Due to delay times (and corresponding useful record lengths) greater than a few nanoseconds, a high-phase-stability fiber laser, the NP Photonics Scorpion, was used.

[1] millerek@nv.doe.gov, 805-681-2237

The first prototype used two interferometers, each consisting of a 2×2 coupler and a delay leg with a fiber stretcher controlled by a bias-control circuit. With two independently controlled interferometers, we could set one to its quadrature point (50% transmission) and one to its minimum transmission. We quickly found, though, that locking the bias of the interferometer at quadrature was too difficult due to the rate of bias drift (~0.2 rad/sec). This is because bias lock at quadrature is achieved by dithering the input to the stretcher and adjusting the DC bias to null out the second harmonic, which is a very small signal relative to the fundamental of the dither tone. Locking was feasible at minimum or maximum transmission, where the fundamental of the dither tone is nulled out by the bias controller.

Next, we considered using a 4×4 fused coupler, but upon evaluating several units from a trusted vendor, we discovered that the relative phases of the outputs were not consistent, nor were they anywhere close to 90 degrees out of phase.

This led us to using a 3×3 coupler, which, if well-balanced for power, will have very nearly 120-degree phase difference at the outputs (Choma, 2003). The interferometer is shown in Figure 1. One output can be locked at minimum transmission, and the other two can be set to ±120 degrees, as shown in Figure 2. The interferometer was enclosed in a foam-insulated compartment inside the chassis, but drift of the interferometer phase limited the time window for bias locking to ~1 min before the controller automatically reset. For a large experiment, this window would need to be extended to ~1 hour, either by increasing the output voltage from the bias controller (current limit is ±15 V), or by improved insulation of the interferometer to prevent differential expansion of the fibers in the two legs.

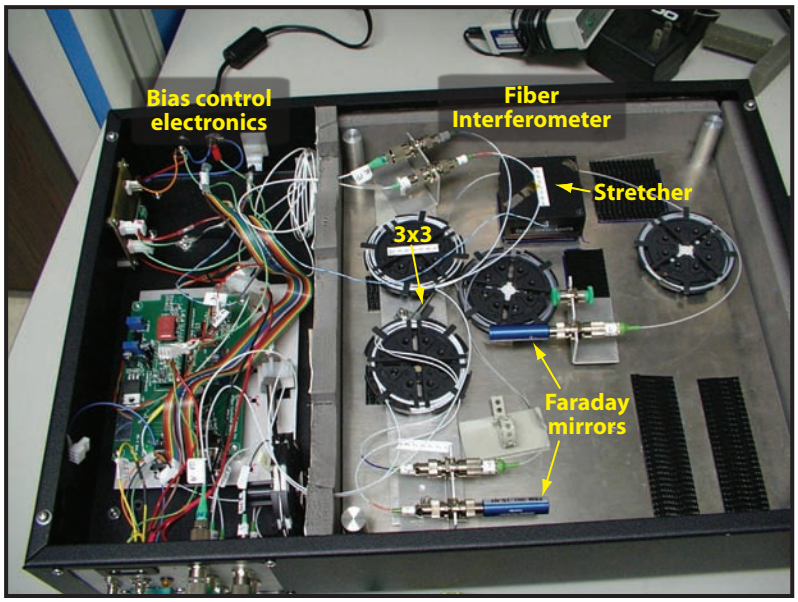

Figure 1. Interferometer based on 3×3 coupler

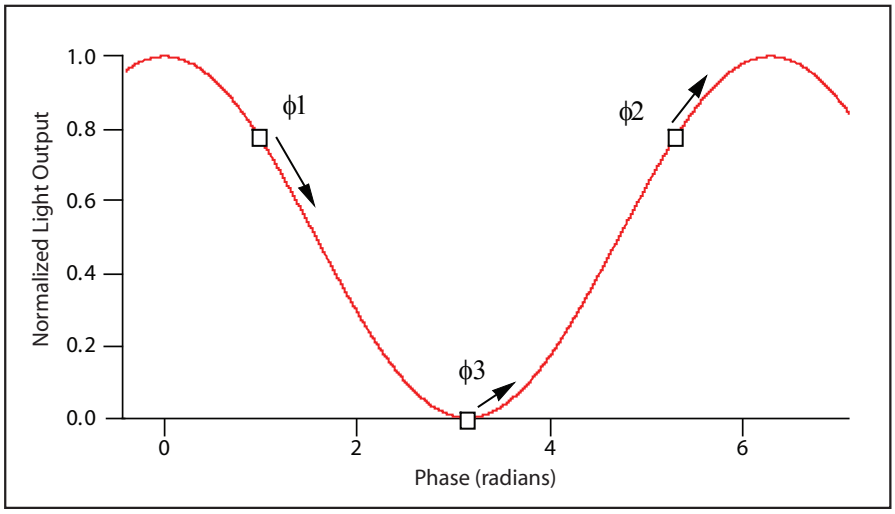

Figure 2. Transfer curve for interferometer based on ideal 3×3 coupler, showing one point locked at minimum transmission

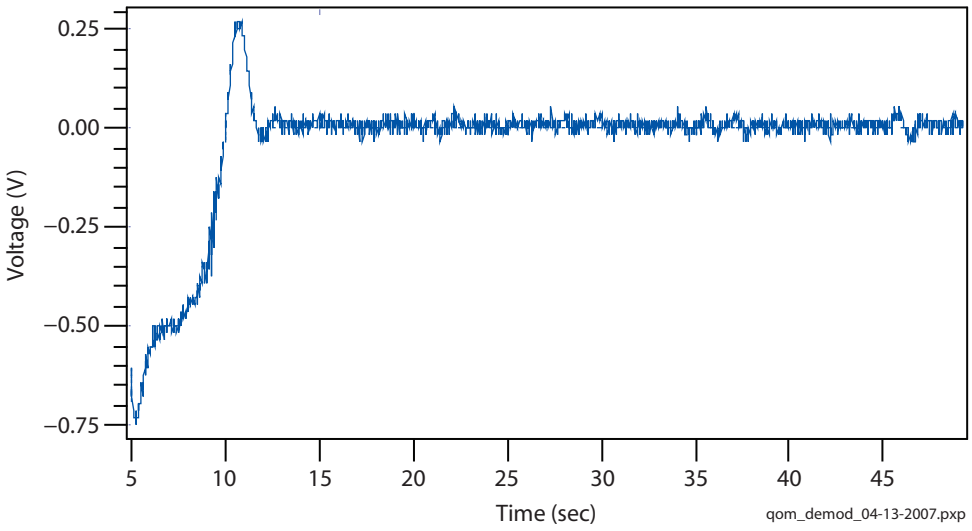

Figure 3. Bias stability of 3×3 interferometer, showing <5% short-term drift. The record starts with a reset of the bias controller, with locking achieved at t = 12 sec.

The second phase of this work examined how radiation affects fibers during an intense radiation pulse (Miller, 2007). Much work has been done on long-term exposure of fibers to radiation, and to recovery in the microseconds-to-seconds timeframe after a pulse (Friebele, 1990), but accurate transmission and recording of high-bandwidth data requires understanding of the effects during the pulse. To study this, we compared three fibers under high-dose electron beam irradiation at the Special Technologies Laboratory (STL) Febetron flash x-ray facility, and under 50-ps irradiation at the linear accelerator (LINAC) at the Idaho Accelerator Center at Idaho State University. The three fibers studied included a Corning SMF-28e (the telecommunications workhorse fiber), a radiation-hardened single-mode fiber ("rad-hard" SMF) manufactured by j-fiber, and a Crystal Fibre solid-core photonic crystal fiber (PCF). (For the radiation effects experiments, the light source was again the 1550-nm fiber laser, with ~10 mW coupled into the test fiber.)

The conclusions that we draw from the data discussed below are:

- All three fibers generally integrate the dose during exposure, with both amplitude and phase showing a sub-50-ps step-like response with long decays.
- The amplitude and phase responses are generally linear over the range of doses studied in this work (10 kRad to 300 kRad).
- The PCF showed somewhat lower phase sensitivity, but the amplitude sensitivity (though inconsistent) was comparable to that of the solid fibers. (A new generation of hollow-core PCF is now available and should be evaluated [Girard, 2005; Henschel, 2005].)

For the Febetron work, a 1-in. segment of fiber was exposed to the 30-ns-wide pulse of electrons, attenuated with various thicknesses of aluminum foil, and signal attenuation and phase shift were recorded simultaneously on a 10-GS/s oscilloscope. Dosimetry on each shot was done using radio-chromic film, which is sensitive down to ~10 kRad. Typical high-dose response curves are shown in Figure 4. The left plot shows phase shifts in the three fibers, overlaid with the time-integrated

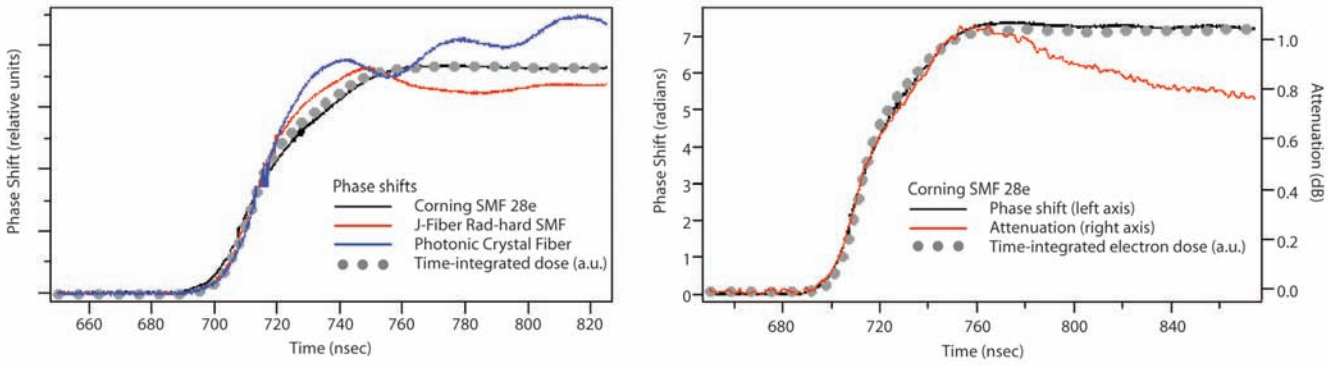

Figure 4. Time-domain data from Febetron experiments

electron current measured with a fast Faraday cup. The right plot shows both phase and amplitude response for the SMF-28e fiber, overlaid with the time-integrated current for comparison. The structure on the phase responses of the PCF and the rad-hard SMF are likely due to mechanical ringing after the energy deposition, though no extensive effort was made to study this effect.

The peak attenuation and phase shift vs. dose are plotted in Figure 5, with the sensitivity tabulated in Table 1. The scatter on the plot of attenuation vs. dose for the PCF may be due to inhomogeneity in the fiber, but the phase shift, measured simultaneously on the same shots, shows scatter comparable to all the other measurements, strongly suggesting that different physical mechanisms are responsible for the two effects.

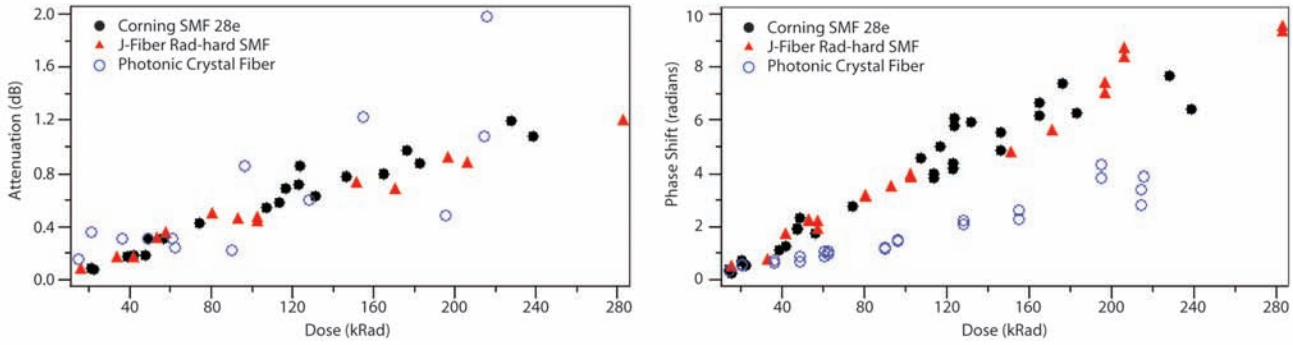

Figure 5. Response of attenuation (left plot) and phase shift (right plot) to radiation dose at the Febetron

Table 1. Sensitivities of three commercial fibers to pulsed radiation

Fiber	Phase (Radians/kRad/m)	Attenuation (dB/kRad/m)
Corning SMF-28e	1.54	0.21
j-fiber Rad-hard SMF	1.45	0.18
Photonic Crystal Fiber	0.67	0.23

For the LINAC work, a 1-cm length of fiber was exposed at the output of the accelerator, and pulses were 50-ps-long at 12-MeV electron energy. The amplitude and phase of the transmitted light were recorded by averaging many pulses with New Focus 1544-B photoreceivers and a Tektronix TDS6124C 12-GHz oscilloscope. The results are shown in Figure 6, with attenuation on the left and phase on the right. Both plots show essentially instantaneous response to the electron pulse with a long decay time. The PCF shows a more pronounced prompt recovery component in its attenuation, compared to the SMF-28e and rad-hard SMF.

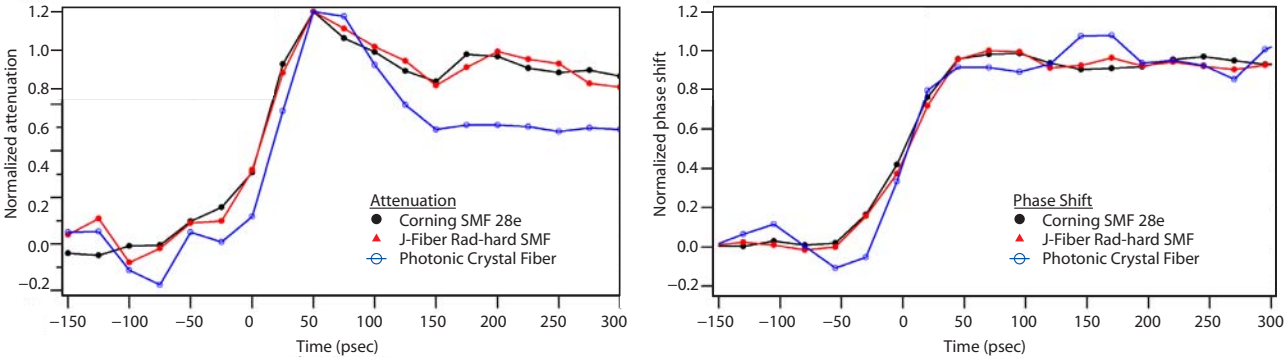

Figure 6. Time response of commercial fibers to 50-ps pulses, from data collected at the Idaho State LINAC

The interpretation of phase-sensitivity is crucial to effective implementation of phase-modulated links, since accrual of phase on the transmission fiber cannot be distinguished from the signal of interest: phase encoded by the phase modulator. The same can be true of amplitude changes (darkening) on an amplitude-modulated (e.g., Mach-Zehnder) link, especially for so-called partial-fringe or single-fringe operation. However, Mach-Zehnders can also be operated in a multi-fringe mode, which gives the data analyst a maximum and minimum transmission value for each half-cycle of the transfer function.

A few mitigation strategies are suggested for phase-modulated links:

- Monitor the amplitude of light in the fiber (e.g. using the spare output) and use the darkening to estimate the radiation-induced phase shift as a function of time.
- Heavily shield the transmission fibers for phase-modulated links.
- Deploy phase-modulated links only in areas where low radiation levels are expected (e.g., optical isolation of digitizers from coaxial cables).
- Demodulate the phase signal to one or more amplitude-modulated fibers before long transmission runs (though this introduces tens of nanoseconds of delay, which may only compound the problem).

Conclusion

We have built and characterized a bias-controlled demodulation interferometer for phase-encoded analog data. The outputs are 120 degrees apart in phase, giving good coverage over a wide range of electrical input levels applied to a high-bandwidth phase modulator. We fielded this interferometer at the STL Febetron and at the Idaho State LINAC to measure amplitude and phase response of three commercially available transmission fibers under intense, pulsed-electron radiation. The fiber

response integrates the radiation dose instantaneously, with a long decay time, though recovery dynamics are different for phase and amplitude, implying different physical phenomena underlying those effects. Phase shifts due to radiation will add to (and be indistinguishable from) the analog data encoded by the phase modulator, so care must be taken in designing phase-modulated links for high-radiation environments.

References

Choma, M. A., C. Yang, J. A. Izatt, "Instantaneous quadrature low-coherence interferometry with 3×3 fiber-optic couplers," *Opt. Lett.* **28**, 22 (2003) 2162–2164.

Friebele, E. J., P. B. Lyons, J. Blackburn, H. Henschel, A. Johan, J. A. Krinsky, A. Robinson, W. Scheneider, D. Smith, E. W. Taylor, G. Y. Turquet de Beauregard, R. H. West, P. Zagarino, "Interlaboratory comparison of radiation-induced attenuation in optical fibers. Part III: transient exposures," *J. Lightwave Technol.* **8**, 6 (June 1990) 977–989.

Girard, S., J. Baggio, J.-L. Leray, "Radiation-induced effects in a new class of optical waveguides: the air-guiding photonic crystal fibers," *IEEE Trans. Nucl. Sci.* **52**, 6, Part 1 (December 2005) 2683–2688.

Henschel, H., J. Kuhnhenn, U. Weinand, "High radiation hardness of a hollow core photonic bandgap fiber," *8th European Conference on Radiation and its Effects on Components and Systems (RADECS)*, Cap d'Agde, France, September 19–23, 2005.

Miller, E. K., G. S. Macrum, I. J. McKenna, H. W. Herrmann, J. M. Mack, C. S. Young, T. J. Sedillo, S. C. Evans, C. J. Horsfield, "Accuracy of analog fiber-optic links for inertial confinement fusion diagnostics," *IEEE Trans. Nucl. Sci.* **54**, 6 (December 2007) 2457–2462.

this page intentionally left blank

Applications of Semiconducting Nanowire to Phototubes

Donald Ng[1] (former employee)
Livermore Operations

The goal of this project was to fabricate semiconducting nanowires for use as a photocathode by field-emitting light-injected electrons in the nanowires. Two approaches were studied: nickel oxide (NiO) nanowires were grown with a bottom-up method, and Si pillars 0.1 μm across were etched into a silicon thin film using methods similar to those used in semiconductor device fabrication. The processes for growing NiO wires and for electron beam lithography patterning of a Si thin film were developed. A third approach, the growth of nanometer-scale porous tungsten oxide (WO_3), was also considered.

Background

Multialkali photocathodes of phototubes in image intensifiers and streak cameras are susceptible to degraded performance if exposed to contaminants or air. Replacing these alkali-based photocathodes with those not susceptible to reaction with air could improve phototube reliability and stability. Previous work at Livermore Operations (LO) involving the fabrication of silicon field emitter arrays (FEAs) using processes developed at the University of California, Davis (UCD), and Lawrence Livermore National Laboratory (LLNL) were successful, but problems with shorting and tip erosion were discovered (Lui, 2003). The UCD process experienced nonuniform lithography and broken wafers arising from the silicon-on-sapphire substrates used. The work with the LLNL process revealed a potential problem with shorting the metal gate to the substrate. Although the principle of optical injection of carriers in FEAs is sound and has been demonstrated (Figure 1), the fabrication techniques involved in earlier work often had low yield due to electrical shorting or current leakage between the gate and the substrate. Another factor affecting the use of the FEAs is the cone shape of the etched emission elements; although they have a sharp tip after fabrication, the tip can become blunt from localized heating and high-current densities, and the bluntness reduces field-emission efficiency.

To avoid the fabrication difficulties associated with the previous work and emitter tip erosion, it was proposed that semiconducting nanowires be used as field-emission elements. An array of semiconductor field-emission elements can function as a photocathode through optical injection of carriers into the conduction band for field emission at the tip of the nanowires. Fabrication can be done by using either a bottom-up method, growing the nanowires on a substrate with a seed layer, or a top-down method, using fabrication methods similar to those used in the semiconductor device industry.

[1] For more information, contact Robert Buckles at bucklera@nv.doe.gov, 925-960-2520

We selected these approaches to avoid some of the problems encountered in the processes tried at UCD and LLNL. Another advantage of using nanowires is that tip erosion would only shorten the length of the wire, but the wire would retain its sharp tip; having a sharp tip would eliminate field emission degradation that comes from tip blunting.

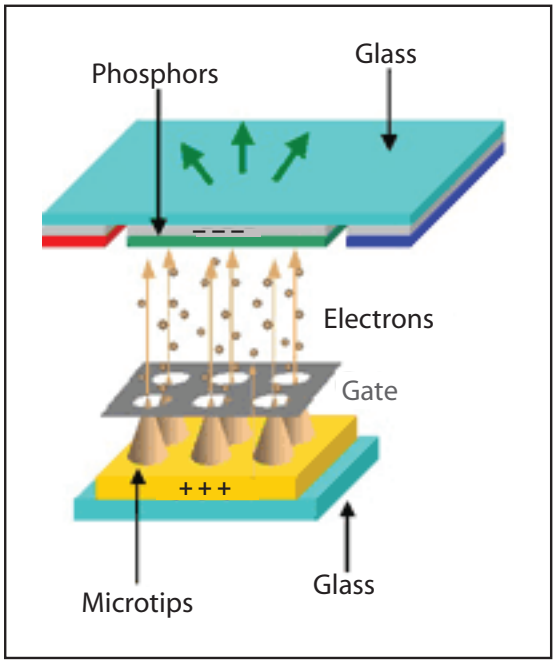

Figure 1. Schematic of silicon–based FEAs

Project

In FY 2007 we applied new materials and methods to work performed in FY 2006. The FY 2006 work utilized ZnO nanowires with a 3.4-eV band gap, wide enough to put the absorption edge in the near ultraviolet region (Ng, 2007). This year we chose to work with NiO nanowires having a band gap of 2.65 eV and an absorption in the visible blue region, and p-type silicon with a 1.1-eV band gap. The work was performed as two efforts, one at University of California, Berkeley (UCB), and the other at Lawrence Berkeley National Laboratory (LBNL) under the sponsorship of the Molecular Foundry.

Thomas Devine of UCB had built an autoclave large enough to accommodate a 40-mm image intensifier face plate. By controlling the temperature, solution chemistry, electrochemical potential, and metal thin film composition, NiO nanowires can be grown. The process begins with the deposition

of nichrome thin film onto a sapphire substrate. The coated substrate is placed in an aqueous solution containing 2 ppm Li^{+} and 1200 ppm B^{+3}, added as LiOH and $B(OH)_3$. The temperature is increased to ~285°C, and the electrochemical potential of the metal thin film is controlled by a potentiostat with a reference electrode and electrical contact to the metal thin film.

While the new autoclave was being developed, its heaters kept burning out. This problem was the result of the larger autoclave's higher thermal mass and the high solution flow rate. Another problem that surfaced was controlling and maintaining uniform electrochemical potential across the entire surface of the relatively large 40-mm substrate. A potential, stepped in time from –1600 mV to –850 mV to –25 mV, is applied to the thin nichrome film to induce and control NiO nanowire growth in three phases: nucleation, densification and vertical growth. Because of the large ohmic drop across the 40-mm surface from the electrical contact at the edge of the face plate and the increased resistivity from converting nichrome to NiO, controlling the electrochemical potential became a problem. Also, we had to reduce the growing time in order to produce short (~0.1 μm) nanowires, but reducing the growing time also reduced the density of nanowires nucleated on the nichrome surface; this created the possibility that the wires might bend or fall over from their own weight.

As a secondary effort, we explored the growth of nanometer-scale porous WO_3. Processing of WO_3 occurs at room temperature and atmospheric pressures, and does not require an autoclave. The anodic reaction of tungsten thin film in a sodium fluorine solution has been reported to produce semiconducting porous films with a band gap of 2.75 eV and increased photocurrent in electrochemical reactions. Unexpectedly, the WO_3 thin film we grew displayed two distinct morphologies: a nanometer-scale porous ("honeycomb") film and a nanometer-scale "prickly" film (Figure 2). The honeycomb surface was produced from a 1500-Å thin film of evaporated tungsten. The causes for the honeycomb and prickly growth remain unexplained, as attempts at reproducibility were beyond the scope of this work. However, the prickly morphology holds promising results for field emission, and should be further explored.

The heating elements of the autoclave were repaired and the thermal problems were solved, so we refocused our efforts on growing and characterizing NiO nanowires. To address the electrochemical potential problem, we decided to attempt to control the dissolved oxygen content of the aqueous solution to manage the electrochemical potential on the surface of the coated 40-mm optic (Figure 3). Several successful runs were made using this method, which also addressed the issue of wire density versus wire length. The revised process used custom formulated gas mixtures with controlled oxygen concentration to adjust and maintain a uniform electrochemical potential across the 40-mm surface, with no electrical contact at the substrate edges, and grew short NiO nanowires with reasonable areal density (Figures 4, 5, and 6).

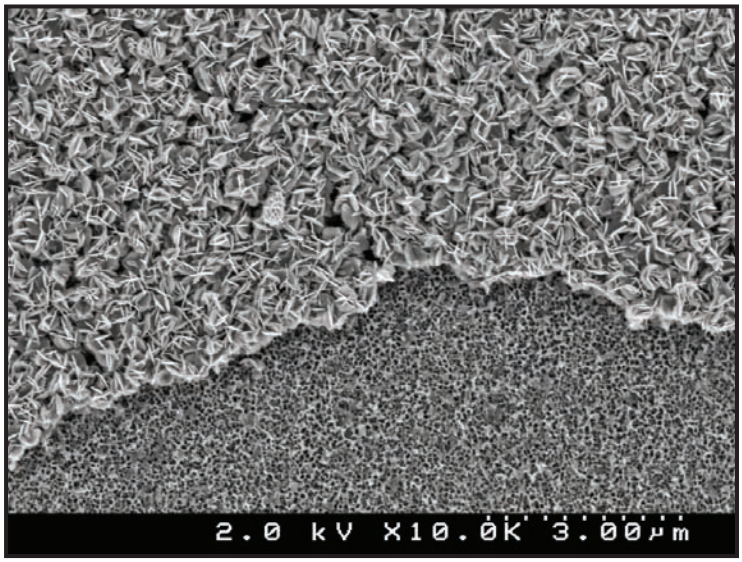

Figure 2. WO_3 nanometer-scale thin film growth, showing prickly (top portion) and honeycomb (bottom portion) morphologies

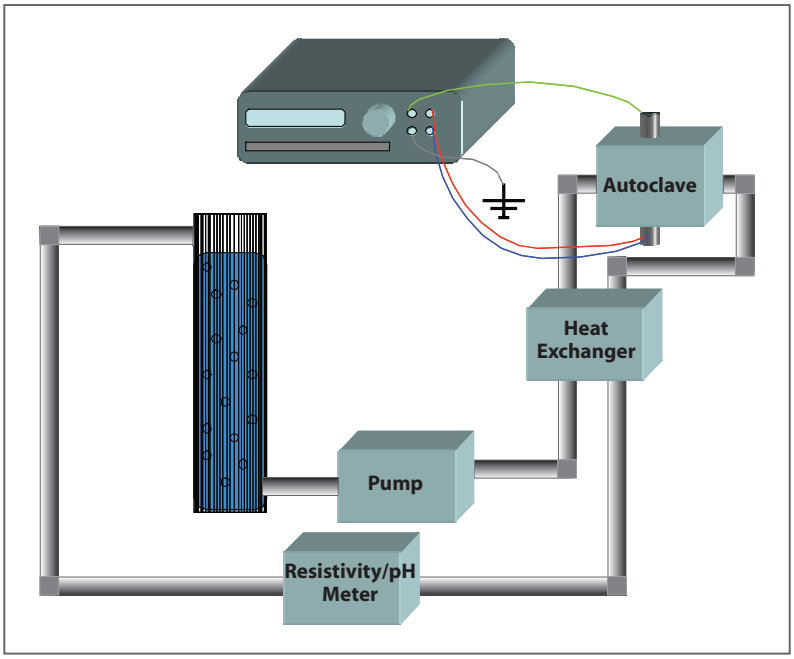

Figure 3. Water loop for the autoclave system

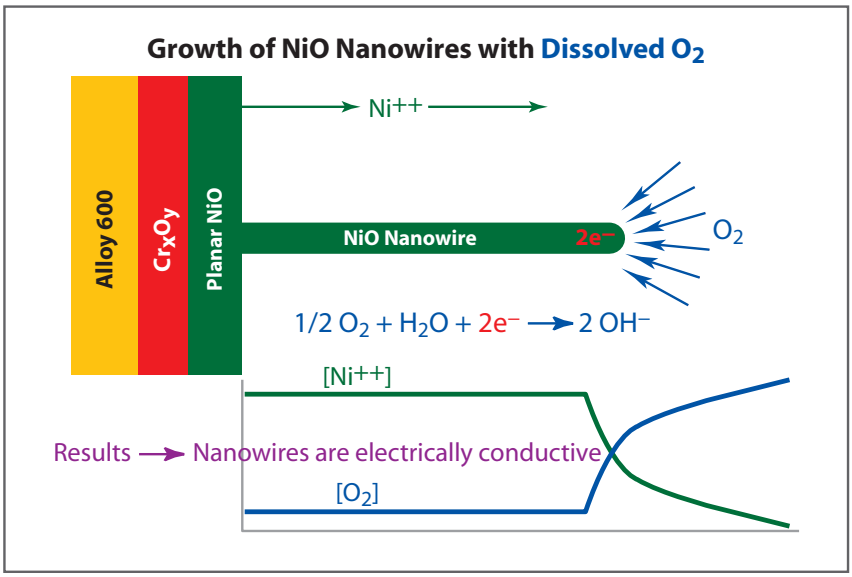

Figure 4. Growth mechanism of NiO nanowire on alloy 600, a Ni alloy used for early process development

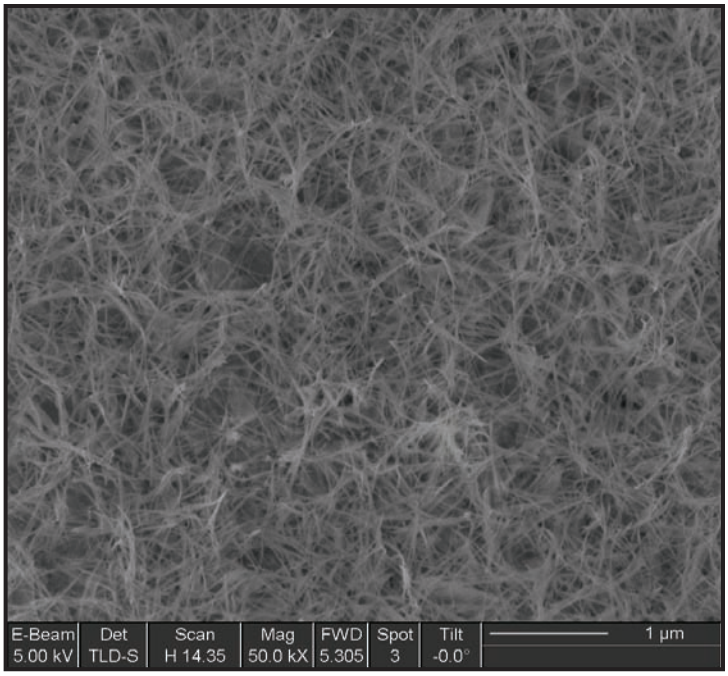

Figure 5. NiO nanowires grown at 288°C for two days, 209 ppb O_2, 2 ppm Li, 1200 ppm B, pH ~6.75

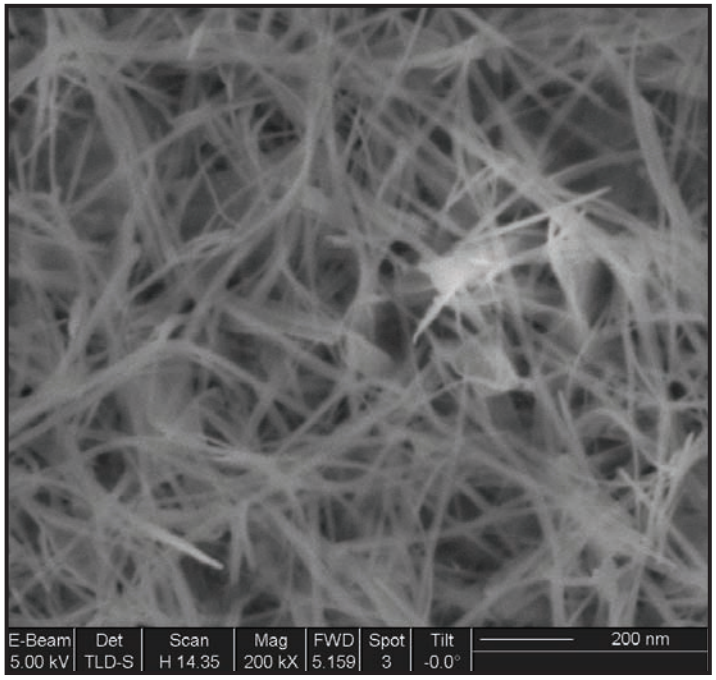

Figure 6. NiO nanowires

In our work with Deirdre Olynick at the Molecular Foundry at LBNL, we used a quartz 40-mm image intensifier face plate and a quartz wafer coated with p-type Si. Because the Foundry is a new facility and is still acquiring equipment and instruments, the Si sputtering deposition was done with the assistance of another department within LBNL. After Si deposition, nanowires 0.1-μm across were patterned with an electron beam lithography instrument. The samples were prepared for etching by a deep reactive ion etch (DRIE) process developed at LBNL, called the gas chop process, that is capable of etching high aspect ratio trenches without undercutting the mask. However, the etcher that was to be used for fabricating the nanowires is owned by another department at LBNL and availability was limited. Complicating the issue of machine availability was unanticipated equipment breakdown on the etcher. Etching the Si nanowires would have begun with process tuning and adjustments using the coated quartz wafer. Then the process would be tried using the 40-mm image intensifier face plate, which has a raised central active area of interest. Because the 40-mm face plate is not flat, as are the substrates used to develop the DRIE process, it was feared that the shape of the face plate could cause gas flow to differ from that experienced with a flat substrate and the etch process would not be what we expected.

The NiO nanowire growth process using the larger autoclave and controlled gas composition of the solution at UCB has been demonstrated, and the UCB group is ready to grow NiO nanowire on

40-mm image intensifier sapphire substrates. The work at the Molecular Foundry later rectified the equipment issues with their etcher, but actual etching was not performed on the patterned substrates.

Conclusion

In cooperation with UCB, this project has developed a method to grow NiO nanowires that can be used in the fabrication of a semiconducting field-emitter capable of detecting visible light in the blue region of the spectrum. It has also made progress in fabricating Si nanowire field emitters, which would allow detection of the entire visible light spectrum. Both of these efforts showed progress during the duration of this SDRD project and have advanced to the stage of preparing an initial test of a nanowire field-emitter photocathode. This concept could be demonstrated on a working 40-mm photodiode. The team also explored nanometer-scale growth with WO_3, which resulted in unexpected honeycomb and prickly surface growth. Reproducibility of these results should be attempted and further studied.

Acknowledgments

I would like to acknowledge the following collaborators for their respective contributions to this project: Professor Thomas Devine, Materials Science and Engineering, UCB; and Dr. Deirdre Olynick, Staff Scientist, Molecular Foundry, LBNL. Work at the Molecular Foundry was supported by the Director, Office of Science, Office of Basic Energy Sciences, Division of Materials Sciences and Engineering, of the U.S. Department of Energy under Contract No. DE-AC02-05CH11231.

References

Liu, K. X., "Broad spectral response photocathode using gated silicon field emitter array," *Nevada Test Site–Directed Research, Development, and Demonstration,* FY 2002, Bechtel Nevada, Las Vegas, Nevada, 2003, 129–131.

Ng, D. "Applications of Si nanowires and carbon nanotubes to phototubes," *Nevada Test Site–Directed Research and Development,* FY 2006, National Security Technologies, LLC, Las Vegas, Nevada, 2007, 377–383.

this page intentionally left blank

Commercial Sensor–based Digital Framing Camera

Larry Pirkl,[1] *Fred Sanders*
Los Alamos Operations

Framing cameras for radiographic imaging require a well-designed and -constructed, robust package to offer reliable imaging and data transmission in high-electromagnetic-interference environments. Our team designed new camera control circuits and software for a Teledyne solid-state sensor that will provide the basis for a highly integrated, state-of-the-art camera design. Because of time constraints, we purchased a camera head Dewar assembly from the Teledyne's supplier; the physical characteristics of the Dewar determined the prototype control logic form factor we chose. We succeeded in providing working control logic, computer interface, and control software that provides all the functionality of the existing design and the capability of providing an integrated, fiber-optic-based control/data interface and industry-standard software interface.

Background

Dynamic radiographic experiments at U.S. DOE laboratories utilize high-speed framing cameras to resolve ultrafast phenomena. A three-frame, solid-state imager recently developed by Los Alamos National Laboratory (LANL) and Rockwell Scientific (acquired by Teledyne in September 2006 and now known as Teledyne Scientific & Imaging, LLC) allows exposure times as short as 50 ns, with as little as 300 ns between frames. LANL owns the design for these imagers and presently purchases the imager and camera hardware from Teledyne for use on proton radiography experiments. The existing camera hardware is more a collection of parts than the integrated package that one would expect in a commercial scientific imaging system. An inadequate cooling system in the Teledyne camera limited the imager temperature to 0°C when operating in elevated ambient temperatures; therefore, because the sensor was not adequately cooled, we saw significant noise in the experimental data. Exposed interconnect cables have presented issues with reliability and intermittent operation and loss of event data. Because Teledyne subcontracts this camera's hardware design and construction, addressing design deficiencies and system upgrades is challenging.

The availability of a reliable, compact digital framing camera system would greatly enhance data acquisition opportunities in real-estate-limited radiography experiments. Having the hardware and control software designers accessible to the experimenters would allow greater flexibility in the design of imaging layouts for experiments and would provide additional experimental data by reducing downtime.

[1] pirklla@nv.doe.gov, 505-663-2019

Project

This project focused solely on the control and interface electronics and software for the camera system, reserving detailed thermal and mechanical design for future projects. A key to successfully completing the project was implementing a nondisclosure agreement (NDA) with Teledyne to obtain detailed, proprietary information about the imager interface requirements, operating parameters, and sequences, as well as obtaining an operating imager integrated circuit. Because of a prior SDRD project collaboration with Rockwell Scientific, an acceptable NDA was in place and design information was available very early. The other key requirement was satisfied when LANL made a fully functional sample imager available early in the project.

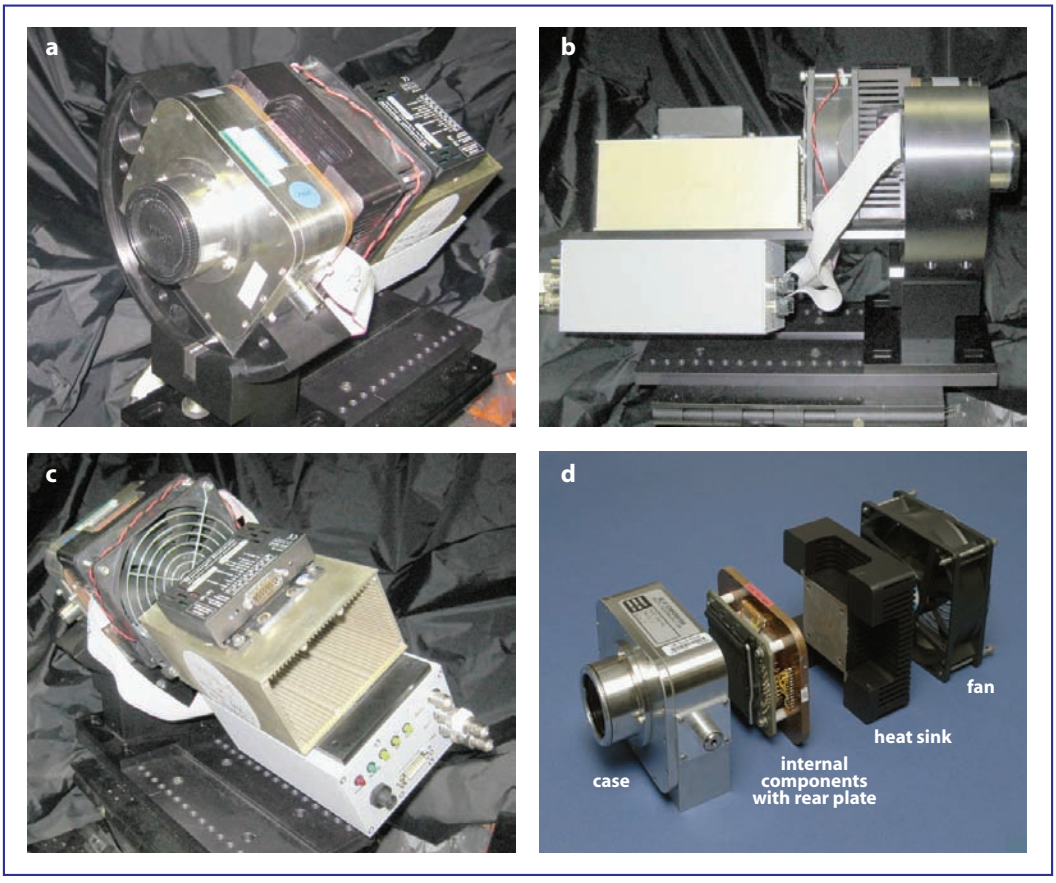

Figure 1. Existing camera hardware: (a, b, c) hardware installed in a LANL-designed camera mounting frame for proton radiography experiments (not shown are an external power supply, fiber-optic interface, and interconnecting cables); (d) the disassembled camera head (Dewar)

While we were looking at the design for the interface to the imager integrated circuit and providing an interim mechanical housing, we found that we could purchase a complete Dewar housing from the supplier (SE-IR) for the existing system (Figure 1). The cost of the Dewar, while significant, was less than the estimated design and fabrication cost of an in-house design.

The Teledyne imager is a hybrid chip with a 720 × 720 array of 26-µm photodiodes bonded to a complementary metal oxide semiconductor (CMOS) readout integrated circuit (ROIC). This provides a quantum efficiency of >90%, making short exposure times without intensifiers possible. The ROIC amplifies the signals from the photodiode array and successively stores the charge in sampling capacitors for each of the three image snapshots. After three images have been acquired, the ROIC enters a readout mode, multiplexing the data from the storage array to an on-chip analog-to-digital converter (ADC) and transferring the digital data to off-chip data-processing logic. All of the ROIC configuration data (operating modes, amplifier bias adjustments, ADC gain and offset, etc.) are entered in the ROIC configuration and control registers through a three-wire serial interface. No readout of these registers is available. The only other signals used to control the image acquisition are system clock and arm and trigger signals. The arm signal enables the image acquisition process, and three successive triggers control the timing and duration of image acquisition. A block diagram of the imager is shown in Figure 2.

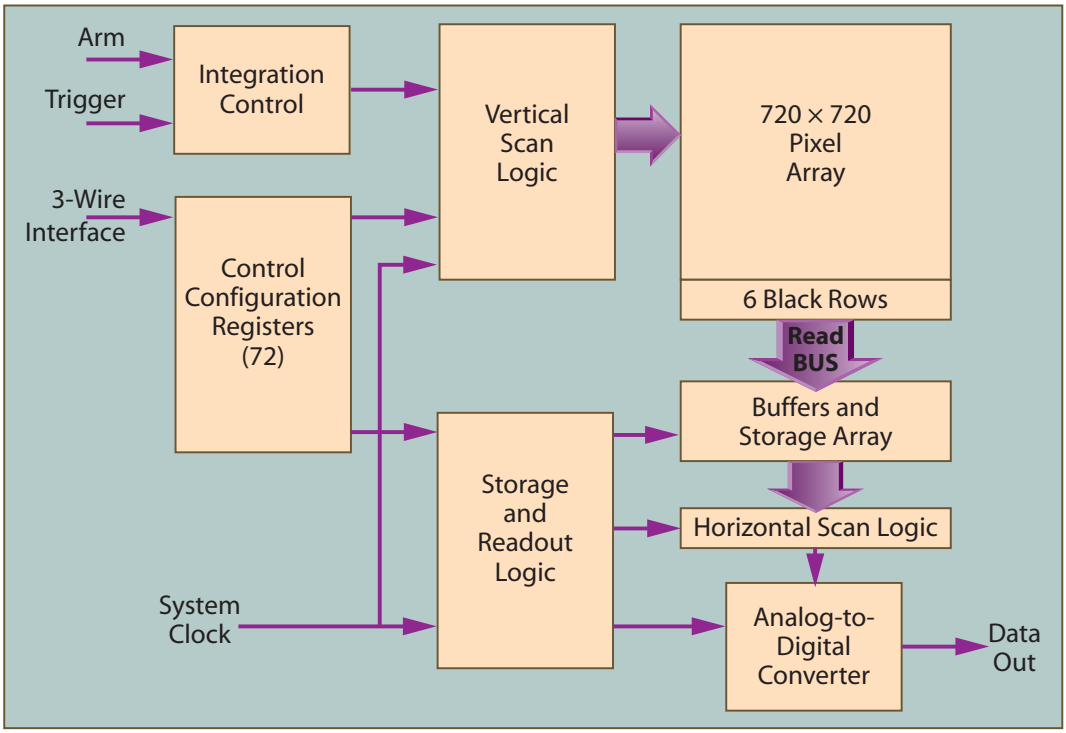

Figure 2. Imager block diagram

The existing camera control electronics (Figure 3) use a field-programmable gate array (FPGA) to implement a Camera Link interface to the host computer, convert Camera Link serial port type control and configuration data to the three-wire interface format for transmission to the imager, buffer and gate external arm and trigger signals to the imager, and transfer imager data to the host Matrox frame-grabber card. The Camera Link interface only reaches 10 m. For proton radiography experiments, a third-party, fiber-optic Camera Link extender is used (adding another box to the system) between the camera in the experiment area and the host PC. At the host PC, the user interface to the camera (via the Matrox frame grabber) is via a custom Interactive Data Language (IDL)-generated graphical user interface.

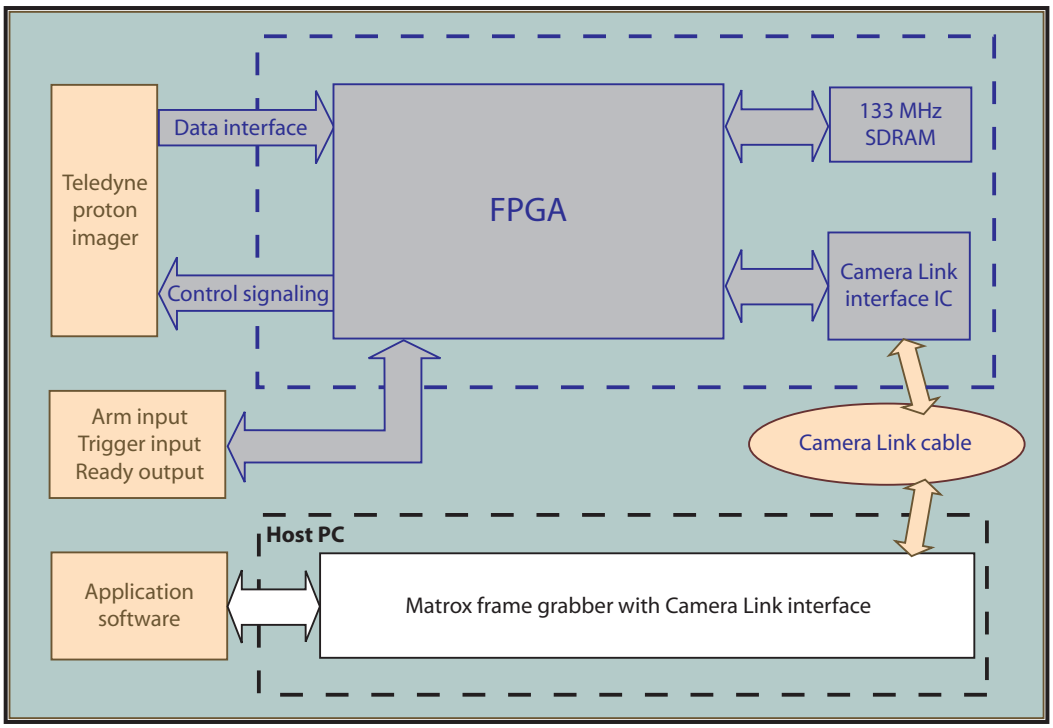

Figure 3. Existing camera control electronics

For our design, we decided to transition to the latest industry standard camera interface, Gigabit Ethernet Vision (GigE Vision). With this interface, camera-to-PC distance with wire is up to 100 m, and with fiber-optic up to 5 or more kilometers. At the PC side, the interface can share the built-in gigabit network connection or use a dedicated, low-cost ($100) Intel Pro gigabit Ethernet card. We also use an FPGA to execute the equivalent functions as in the existing design with a credit-card-sized PCB produced by Pleora (Figure 4) providing the gigabit Ethernet link functionality. This PCB is available with either an electrical or fiber-optic Ethernet connection.

Figure 4. Pleora hardware, boxed and unboxed

We attempted to develop the hardware (Figure 5) and software in parallel, using the boxed version of the Pleora hardware as a Camera Link to the GigE Vision interface. Pleora included Matrox Imaging Library (MIL)-equivalent drivers as part of the software development kit. We planned to plug the equivalent drivers in the existing IDL software and interface a Teledyne camera to the PC with this GigE Vision hardware. After we struggled with the supplied MIL drivers and were only able to send commands to the camera, Pleora support informed us that the MIL package had been deprecated when their focus shifted to supporting industry-standard, generic camera packages. At the same time, we lost use of the Teledyne camera, which was deployed to an experiment.

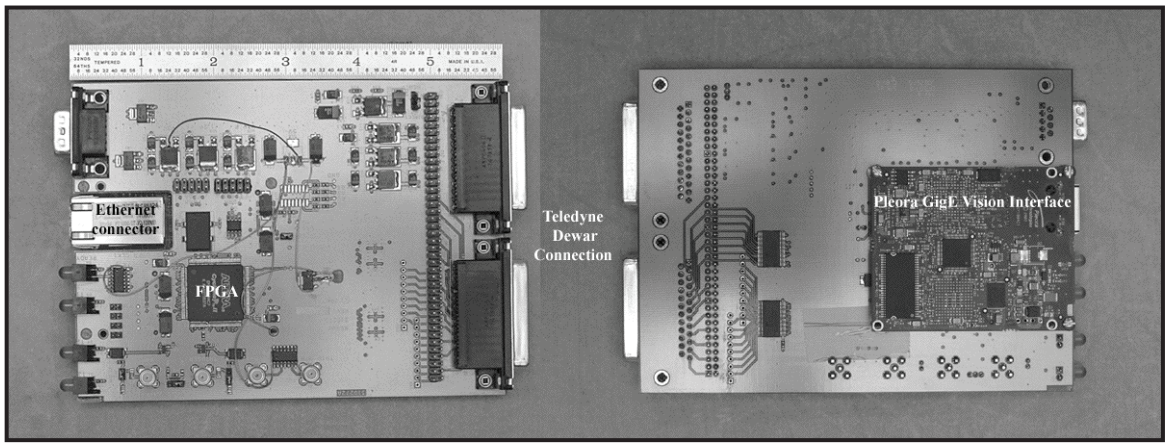

Figure 5. Prototype control hardware, top and bottom view

When our prototype hardware became available, we were able to gradually progress from sending commands to the camera to implementing the camera test mode (duplicating a function in the existing cameras). This mode exercises the camera arm and trigger requirements for shot mode and

substitutes image data with three test patterns generated in the FPGA. We used this sequence to implement the PC software data transfer and storage portion. Since we were no longer supporting the MIL drivers, the existing IDL software was discarded. However, for operator familiarity, we implemented the same look and feel (except for having to quit the program for error condition recovery). A sample of the developed software interface is shown in Figure 6.

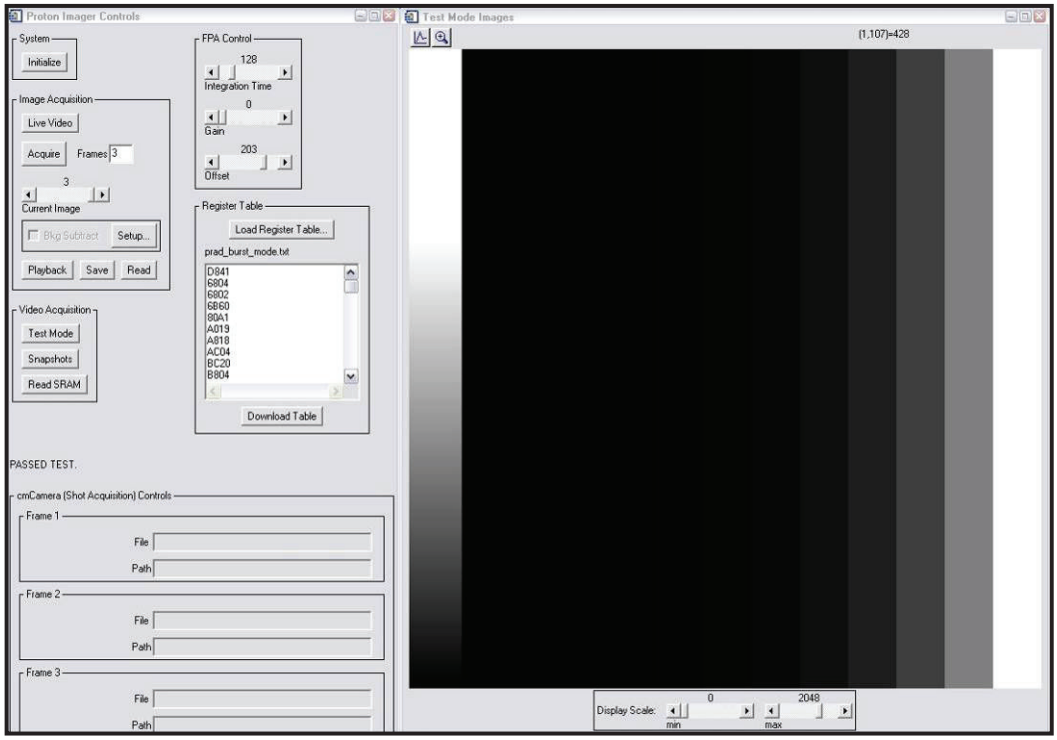

Figure 6. IDL interface with test image displayed

We then implemented the actual imager data transfer hardware in the FPGA and connected our hardware to the Teledyne imager installed in the purchased Dewar assembly. We succeeded in transferring image data without loss or distortion for all operating modes but only at low light levels (Figure 7). At normal to high light levels, the on-chip ADC misbehaved, acting as if certain data bits were "stuck." We connected this imager and Dewar assembly to Teledyne control electronics using our cables and found the imager to be behaving properly.

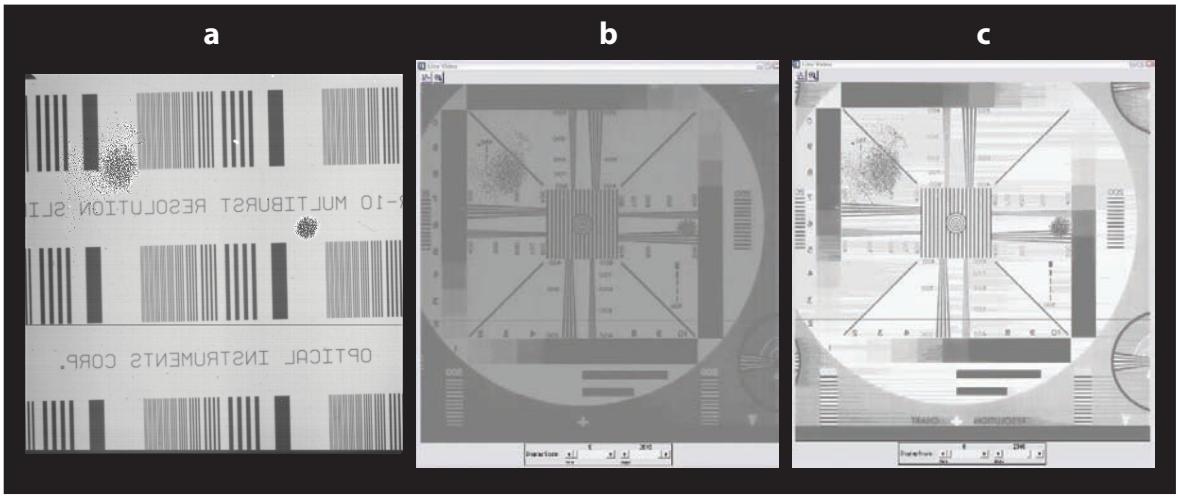

Figure 7. Imager with (a) Teledyne hardware, (b) NSTec hardware at low light level, and (c) NSTec hardware at normal light levels

Conclusion

Our team has successfully designed a new camera interface for this commercial digital framing camera imager. This interface can be used in developing a robust digital framing camera system with an integrated, fiber-optically coupled, gigabit Ethernet interface. The resultant experience and technology could easily be applied to our other camera systems, and we could develop a generic user interface with a common look and feel, thus reducing fielding difficulties and training requirements.

this page intentionally left blank

NNSA/NA-116

Lucille Gentry	(1)	Jamileh Soudah	(1)

NNSA Service Center

Russel Edge	(1)	Julianne Levings	(1)

NNSA/NSO

Carol Shelton	(2)	Laura Tomlinson	(1)

NSTec

Dennis Barker	(1)	Howard Bender	(2)	Rob Buckles	(2)
John Ciucci	(1)	Ken Cooke	(1)	Darryl Droemer	(1)
Jim Gatling	(1)	Paul Guss	(2)	Chris Hagen	(2)
John Hollabaugh	(1)	A. C. Hollins	(1)	Jim Holt	(1)
Steve Iversen	(2)	Bill Kost	(1)	Ping Lee	(1)
Wil Lewis	(1)	Dana Lindsay	(1)	Michael Martinez	(1)
Dave Nichols	(1)	Masafusa Nishimura	(1)	Brent Park	(1)
PIs	(1 ea)	Dave Post	(1)	Carson Riland	(1)
Bob Summers	(1)	Oliver Sweningsen	(1)	Tom Waltman	(1)
Steve Younger	(1)				

LANL

Drew Martinson	(1)
LDRD Office	(1)
(ATTN: William Priedhorsky)	

LLNL

Larry Wiley	(1)
LDRD Office	(1)
(ATTN: William [Bill] Craig)	

SNL

Raymond Leeper	(1)
John Porter	(1)
LDRD Office	(1)
(ATTN: Hank Westrich)	

OSTI

Electronic copy	(1)

Resource Centers

RSL-Nellis	(1)	Technical Library	(1)

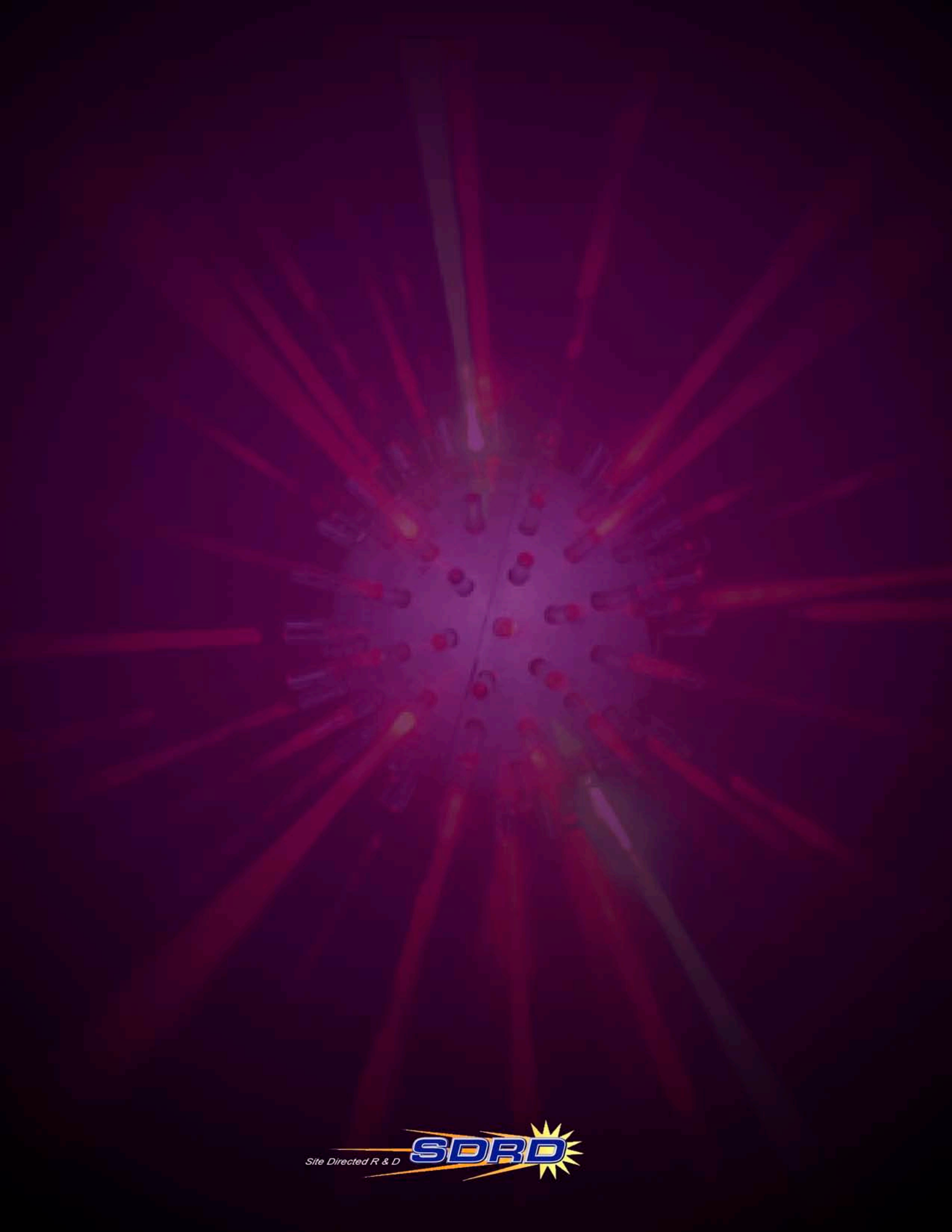
Site Directed R & D
SDRD